

JPL PUBLICATION 82-7

(NASA-CR-168848) PROCEEDINGS OF THE SECOND  
INTERNATIONAL COLLOQUIUM ON DROPS AND  
BUBBLES (Jet Propulsion Lab.) 400 P  
HC A17/HF A01 CSCL 20D

N82-23418  
THRU  
N82-23409  
Unclass  
09008

63/34

# Proceedings of the Second International Colloquium on Drops and Bubbles

Monterey, California

November 19-21, 1981

Dennis H. Le Croisette  
Editor



March 1, 1982

**NASA**

National Aeronautics and  
Space Administration

Jet Propulsion Laboratory  
California Institute of Technology  
Pasadena, California

JPL PUBLICATION 82-7

**Proceedings of the Second  
International Colloquium on  
Drops and Bubbles  
Monterey, California  
November 19–21, 1981**

**Dennis H. Le Croisette**  
Editor

March 1, 1982

**NASA**

National Aeronautics and  
Space Administration

**Jet Propulsion Laboratory**  
California Institute of Technology  
Pasadena, California

This publication was prepared by the Jet Propulsion Laboratory, California Institute of Technology, under contract with the National Aeronautics and Space Administration.

## INTRODUCTION

This is the *Proceedings* of the second international colloquium devoted to the science of drops and bubbles. It covers a wide variety of fields ranging from fundamental fluid dynamics to astrophysics and from theoretical considerations to material processing in space.

The first colloquium in this intermittent series was held at the California Institute of Technology in 1974. Both colloquia have provided an opportunity for scientists from a number of disciplines to discuss their common problems and learn from each other. In the intervening seven years between the first and second colloquia there have been substantial advances in most of the fields represented. In particular, the science of material processing in space has matured to the point where experiments are now being constructed. In a few years scientific investigations will be conducted in the substantially zero-g environment of space on board the NASA Space Shuttle. These experiments will uncover new information which will lead to a deeper understanding of the fundamental physics of this branch of science.

The colloquium included seven sessions where scientific papers were presented and one poster session. There were a total of ten invited papers at the colloquium and twenty scientific displays in the poster session. The invited papers and the papers representing the poster displays have been placed in the most appropriate scientific session in the *Proceedings*.

This colloquium, like its predecessor, was notable for the cross-disciplinary interactions among the participants. There were many scientific discussions carried out after the sessions were over and throughout the evenings. The benefit derived from these contacts made among the participants - often from different fields - is an intangible but valuable contribution that a specialized colloquium can make to a scientific field.

The colloquium organizers wish to recognize the support afforded to this colloquium by the Physics and Chemistry in Space and the Material Processing in Space programs of the National Aeronautics and Space Administration.

It is hoped that the *Proceedings* will become a valued reference source and will contribute to the literature in the science of drops and bubbles in the years to come.

Dennis H. Le Croisette  
Jet Propulsion Laboratory  
California Institute of Technology

## CONFERENCE CHAIRMAN

**C. P. R. Saunders**  
University of Manchester,  
United Kingdom

## STEERING COMMITTEE

**R. Brown**  
MIT

**N. Lebovitz**  
University of Chicago

**J. R. Carruthers**  
Hewlett-Packard

**M. Saffren**  
Jet Propulsion Lab

**P. Concus**  
Lawrence Berkeley Lab

**L. E. Scriven**  
University of Minnesota

**D. D. Elleman**  
Jet Propulsion Lab

**W. J. Swiatecki**  
Lawrence Berkeley Lab

**J. Hart**  
University of Colorado

**T. Wang**  
Jet Propulsion Lab

**C. D. Hendricks**  
Lawrence Livermore Lab

**F. Williams**  
Princeton University

**M. Ingram**  
University of Miami

## CONFERENCE ORGANIZATION

**D. H. Le Croisette**  
Jet Propulsion Lab

**G. McKay**  
Jet Propulsion Lab

**J. H. Van Dyck**  
Jet Propulsion Lab

## PROCEEDINGS EDITOR

**D. H. Le Croisette**  
Jet Propulsion Lab

## SESSIONS AND SESSION CHAIRMEN

1. **Material Science and Space Experiments** ..... 1 - 38  
T. Wang, Jet Propulsion Laboratory
2. **Combustion, Jet Stability and Inertial Fusion** ..... 39 - 128  
L. E. Scriven, University of Minnesota
3. **Bubbles** ..... 129 - 213  
R. Brown, Massachusetts Institute of Technology
4. **Astrophysics** ..... 214 - 226  
N. Lebovitz, University of Chicago
5. **Meteorology** ..... 227 - 259  
C. P. R. Saunders, University of Manchester
6. **Nuclear Science** ..... 260 - 279  
W. Swiatecki, Lawrence Berkeley Laboratory
7. **Poster Session**  
D. D. Elleman, Jet Propulsion Laboratory  
(Poster session papers have been included in the  
most appropriate technical session)
8. **Theory and Computation** ..... 280 - 383  
P. Concus, Lawrence Berkeley Laboratory

## ABSTRACT

This is the *Proceedings* of the Second International Colloquium on Drops and Bubbles, held at Monterey, California, on November 19-21, 1981. The 52 scientific papers reported here deal with the subjects of Material Science and Space Experiments, Combustion, Jet Stability and Inertial Fusion, Bubbles, Astrophysics, Meteorology, Nuclear Science, and Theory and Computation.

## CONTENTS

<b>Drops and bubbles in materials science</b> Robert H. Doremus . . . . .	1
<b>Normal modes of a compound drop</b> M. Saffren, D. D. Elleman, and W. K. Rhim . . . . .	7
<b>Interaction effects in thermocapillary bubble migration</b> M. Meyyappan, William R. Wilcox, and R. Shankar Subramanian . . . . .	15
<b>Dielectrophoretic levitation of droplets and bubbles</b> T. B. Jones . . . . .	17
<b>The motion of bubbles inside drops in containerless processing</b> N. Shankar, P. Annamalai, Robert Cole, and R. Shankar Subramanian . . . . .	26
<b>Acoustically induced oscillation and rotation of a large drop in space</b> Nathan Jacobi, Arvid P. Croonquist, Daniel D. Elleman, and Taylor G. Wang . . . . .	31
<b>Mechanisms of droplet combustion</b> C. K. Law . . . . .	39
<b>A numerical study of drop-on-demand ink jets</b> J. Fromm . . . . .	54
<b>Electrohydrodynamic (EHD) stimulation of jet breakup</b> Joseph M. Crowley . . . . .	63
<b>The stress system generated by an electromagnetic field in a suspension of drops</b> M. Emin Frdođan . . . . .	71
<b>Hydrodynamic performance of an annular liquid jet: production of spherical shells</b> James M. Kendall . . . . .	79
<b>Inertial confinement fusion targets</b> Charles D. Hendricks . . . . .	88
<b>Colliding droplets: a short film presentation</b> C. D. Hendricks . . . . .	94
<b>Behavior of liquid hydrogen inside an ICF target</b> K. Kim, I. Mok, and T. Bernat . . . . .	96
<b>Generation of a strong core-centering force in a submillimeter compound droplet system</b> Mark C. Lee, I-an Feng, Daniel D. Elleman, Taylor G. Wang, and Ainslie T. Young . . . . .	107
<b>Holographic studies of the vapor explosion of vaporizing water-in-fuel emulsion droplets</b> Stephen A. Sheffield, C. F. Hess, and J. D. Trolinger . . . . .	112
<b>Droplets generated from a new 'ogee' shaped, liquid, air-shear, electrostatic nozzle</b> I. I. Inculet, T. E. Base, and G. S. P. Castle . . . . .	120
<b>Liquid drop technique for generation of organic glass and metal shells</b> C. D. Hendricks . . . . .	124
<b>Surface tension and contact angles: molecular origins and associated microstructure</b> H. T. Davis . . . . .	129

## CONTENTS (Continued)

<b>Large amplitude drop shape oscillations</b> E. H. Trinh and T. G. Wang	143
<b>Bubble shapes in steady axisymmetric flows at intermediate Reynolds number</b> G. Ryskin and L. G. Leal	151
<b>The production of drops by the bursting of a bubble at an air liquid interface</b> J. S. Darrozes and P. Ligneul	157
<b>Resonances, radiation pressure, and optical scattering phenomena of drops and bubbles</b> P. L. Marston, S. G. Goosby, D. S. Langley, and S. E. LoPorto-Arione	166
<b>A numerical method for the dynamics of non-spherical cavitation bubbles</b> L. Guerri, G. Lucca, and A. Prosperetti	175
<b>Size distribution of oceanic air bubbles entrained in sea-water by wave-breaking</b> François Resch and François Avellan	182
<b>Collapse of large vapor bubbles</b> James Tegart and Sam Dominick	187
<b>A new droplet generator</b> W. E. Slack	195
<b>Non-axisymmetric shapes of a rotating drop in an immiscible system</b> T. G. Wang, R. Tagg, L. Cammack, and A. Croonquist	203
<b>Fragmentation of interstellar clouds and star formation</b> Joseph Silk	214
<b>Solidification of carbon-oxygen white dwarfs</b> E. Schatzman	222
<b>Drop processes in natural clouds</b> J. Latham	227
<b>A wind tunnel investigation of the shape of uncharged raindrops in the presence of an external, vertical electric field</b> H. R. Pruppacher, R. Rasmussen, C. Walcek, and P. K. Wang	239
<b>Raindrop oscillations</b> K. V. Beard	244
<b>Drop rebound in clouds and precipitation</b> Harry T. Ochs, III, and K. V. Beard	247
<b>The geophysical importance of bubbles in the sea</b> Ramon J. Cipriano	255
<b>Fluid dynamical description of relativistic nuclear collisions</b> J. R. Nix and D. Strottman	260
<b>Studies of the nuclear equation of state using numerical calculations of nuclear drop collisions</b> C. T. Alonso, J. M. LeBlanc, and J. R. Wilson	268

## CONTENTS (Continued)

<b>The size and shape of equilibrium capillary surfaces</b> Robert Finn .....	280
<b>The stability of the axially symmetric pendent drop</b> Henry C. Wente .....	286
<b>Capillary surface discontinuities above re-entrant corners</b> N. J. Korevaar .....	295
<b>Fluid mod. and simulations of biological cell phenomena</b> H. P. Greenspan .....	303
<b>Capillary forces exerted by liquid drops caught between crossed cylinders: a 3-D meniscus problem with free contact line</b> T. W. Patzek and L. E. Scriven .....	308
<b>The motion of a drop on a rigid surface</b> L. M. Hocking .....	315
<b>Profiles of electrified drops and bubbles</b> O. A. Basaran and L. E. Scriven .....	322
<b>A numerical method for integrating the kinetic equations of droplet spectra evolution by condensation/evaporation and by coalescence/breakup processes</b> Isaac M. Erukashvily .....	330
<b>Bubble in a corner flow</b> Jean-Marc Vanden-Broeck .....	336
<b>Asymptotic expansions and estimates for the capillary problem</b> Frédéric Paul Brulois .....	344
<b>The numerical analysis of the rotational theory for the formation of lunar globules</b> James Ross, John Bastin, and Kris Stewart .....	350
<b>Numerical methods and calculations for droplet flow, heating and ignition</b> H. A. Dwyer, B. R. Sanders, and D. Dandy .....	358
<b>Effects of rotation and magnetic field on the onset of convective instability in a liquid layer due to buoyancy and surface tension</b> Gabbita Sundara Rama Sarma .....	366
<b>A variational approach to the study of capillarity phenomena</b> Michele Emmer, Eduardo Gonzales, and Italo Tamanini .....	374
<b>Mechanics of couple-stress fluid coatings</b> Allen M. Waxman .....	380
<b>Colloquium Participants</b> .....	385
<b>Alphabetical Index of Authors</b> .....	391

## Drops and Bubbles in Materials Science

Robert H. Doremus

Materials Engineering Department, Rensselaer Polytechnic Institute  
Materials Research Center, Troy, New York 12181Abstract

The following applications of drops and bubbles in materials science are reviewed: Formation of extended p-n junctions in semi-conductors by drop migration; mechanisms and morphologies of migrating drops and bubbles in solids; nucleation and corrections to the Volmer-Weber equations; bubble shrinkage in the processing of glass; the formation of glass microshells as laser-fusion targets; and radiation-induced voids in nuclear reactors. These examples show that knowledge of the behavior of drops and bubbles is important in diverse areas of materials processing and properties, and deserves further fundamental study.

Introduction

Semiconducting junctions can be made in complicated shapes by migration of liquid bubbles in a solid semiconductor. Nucleation of solid phases must be controlled in processing solids and regulating their properties; the theory of nucleation was first derived for the formation of droplets in a vapor. Melting of clear and strong glass requires that bubbles be removed from viscous molten glass, and tiny microshells of glass as laser fusion targets are formed by blowing a bubble inside a drop of molten glass. These examples show the importance of drops and bubbles in processing solid materials. Radiation can form bubbles in reactor materials, weakening them. In each of these areas there have been recent advances or controversies, which will be described in this paper. These examples are not intended to provide a comprehensive review of drops and bubbles in Materials Science, but merely a sample of applications and opportunities.

Semiconductor processing and migration of drops

Commercial processes for making p-n junctions in semiconductors by migration of liquid drops, wires, or sheets have been developed by T. R. Anthony and H. E. Cline of General Electric.<sup>1-4</sup> Molten metallic drops or wires move through a solid semiconductor under a thermal or electrical gradient, leaving resolidified doped material in their wake. Drops of a low-melting metal that is a suitable dopant, such as aluminum, are deposited on the surface of the semiconductor, which is then heated and subjected to a temperature gradient or electrical field. In practice there are a number of problems in controlling the shape of the liquid region and its path that require careful control of the temperature and the gradients. Thus knowledge of the morphology and kinetics of the liquid drops and wires is important for successful production of a satisfactory device. Thermal gradients proved to be difficult to control, so electromigration was developed as an alternative.<sup>3</sup>

A lattice of columnar p-n junctions through a semiconductor wafer can be made by thermal migration of aluminum drops through silicon.<sup>5</sup> This "deep-diode array" can be used as an imaging target for x-rays and infrared radiation.

A liquid drop in a gradient of driving force in a solid moves by dissolution and reprecipitation of solid in the liquid. Driving gradients can be in temperature, mechanical force (accelerational field) or electrical potential. Anthony and Cline found that high force gradients were required to migrate brine drops in solid KCl,<sup>5</sup> suggesting that an impractically high sedimentation field would be required to move liquid drops in semiconductors.

The rate of droplet motion can be controlled either by the rate of diffusion of solute in the liquid or by the rate of dissolution of solid (interface control). This dissolution rate is usually proportional to the solubility of the solid in the liquid drop, and can be different for different crystallographic planes in the solid. At high temperatures convective flow in the drop can lead to rates higher than expected from the static diffusion coefficient of solute in the liquid.<sup>7</sup> For large drops diffusion in the liquid is more likely to control the rate of droplet migration, whereas for small drops interface rates become important. A similar influence of crystal size is found for the rate of crystallization from solution. For large crystals diffusion in the liquid controls the rate of growth, whereas for small crystals interface control is usual.<sup>8</sup>

At equilibrium the shape of a liquid drop in a solid is controlled by the interfacial energies of different crystallographic planes of the solid in contact with the liquid. The shape that minimizes the total surface free energy is the equilibrium one. In principle

this shape can be calculated from knowledge of the surface energy as a function of crystallographic orientation of a surface facet by the "Wulff" construction; in practice this function is hardly ever known in much detail, and the relative values of interfacial energies are often deduced from equilibrium shapes of crystals. One would expect that low index and closely-packed crystallographic planes should have the lowest energies, so that these planes should, and usually do, predominate in equilibrium shapes of crystals.

Brine droplets in  $KCl$  had mainly (100) planes as faces after seven years at room temperature, with edge roundings and some contribution from (110) faces.<sup>9</sup> Silicon exposes mainly (111) planes in contact with liquid, with some contribution from (100) planes.<sup>10</sup> When a droplet migrates in a force field, its shape can be distorted by nonuniformities in the field and in the rates of interfacial dissolution.<sup>10</sup>

The rate of migration of gas-filled bubbles in  $KCl$  in a temperature gradient was determined by the rate of evaporation of solid and by diffusion of  $KCl$  molecules in the bubble, in much the way as the liquid drops.<sup>11</sup> The bubbles were bounded by (100) planes, but stretched out in the direction of migration instead of remaining cubic.<sup>12</sup> The shape was determined by the interfacial rates of evaporation and deposition rather than by the equilibrium condition from surface energies. A trail of fine bubbles followed in the wake of the migrating bubble.

### Nucleation

The transformation of one phase into another almost always requires formation of a molecular cluster of the new phase in the old, after which the new phase grows at the expense of the old. This nucleation and growth mechanism is valid for pure materials and usually for mixtures; in some mixtures a uniform transformation called spinodal decomposition is possible, but it will not be considered here. When a cluster or nucleus forms the resultant surface energy can exceed the volume free energy difference driving transformation, so that a nucleation barrier exists even when a large sample of the new phase is stable with respect to the old. This situation is illustrated in Figure 1, where the chemical

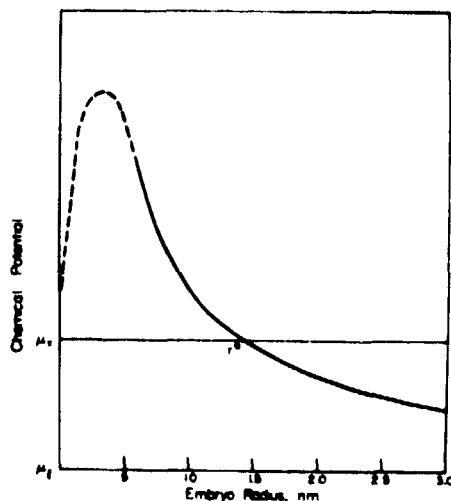


Figure 1. The chemical potential of ethanol drop at  $-9^{\circ}C$ , as a function of drop radius.

potential  $\mu_r$  in J/molecules of a drop of ethanol is compared to the chemical potential of supersaturated ethanol vapor  $\mu_v$  and the chemical potential of liquid ethanol  $\mu_l$ , all at  $-9^{\circ}C$ . When the chemical potential of a drop equals that of the surrounding vapor it is said to be of critical size (radius  $r^*$ ). Smaller drops are unstable and decompose; larger drops grow.

Volmer and Weber derived the number of critical nuclei as a function of supersaturation and temperature from the fluctuation theory of Einstein<sup>14</sup> and the calculation of Gibbs<sup>15</sup> of the reversible work to form a sphere of the critical size. The result is

$$N^* = N \exp(-W/kt)$$

(1)

where  $N^*$  is the number of critical nuclei per unit volume,  $N$  is the number of vapor molecules per unit volume,  $W$  is the reversible work to form the critical nucleus,  $k$  is Boltzmann's constant and  $T$  the temperature. Then the rate of nucleation  $I$  is the product of the number of collisions of vapor molecules with the surface of a critical nucleus with  $N^*$ :

$$I = Z A^* N^* \quad (2)$$

where  $Z$  is the collision frequency of molecules with a surface and  $A^*$  is the surface area of a critical nucleus. For a spherical nucleus:

$$W = 16\pi\gamma^3/3(\Delta P)^2 \quad (3)$$

where  $\gamma$  is the surface energy of the liquid and  $\Delta P$  is the difference in pressure between the inside and outside of the critical nucleus.

The equations of Volmer and Weber agreed well with experimental data in rain formation of various liquids in a cloud chamber<sup>16</sup> and with more recent results in the diffusion cloud chamber, especially in the calculated and measured values of the surface energies. Nevertheless a number of authors have suggested that the equations of Volmer and Weber need to be modified by correction factors that vary from a factor of  $10^{17}$  in the nucleation rate to a negligible correction.<sup>17-20</sup> These treatments involve questionable assumptions of equilibrium in chemical deposition reactions to form the critical nucleus or between embryos not of the critical size and the surrounding vapor. The equations of Volmer and Weber agree well with experiment, and there appears to be no need to correct them.

In a recent paper Carlon has found that even undersaturated water vapor and moist air contain multimolecular clusters of water.<sup>21</sup> Thus the initial condition of a vapor in a nucleation experiment may not be just individual molecules, but could contain an unknown distribution of clusters. Such a distribution would further complicate nucleation theories based on a series of condensation reactions, but should not influence the equilibrium fluctuation method of Volmer and Weber. Carlon also found that these clusters of water molecules lead to infrared absorption at wave lengths different from those for molecular water.

#### Bubbles in the processing of glass

Fining, or the removal of bubbles from a glass melt, is one of the major technological problems in glass melting. It is usually solved by holding the glass for some time at a temperature somewhat below the highest melting temperature, and by adding certain minor constituents to the original glass batch. The mechanisms by which these additions aid bubble removal are still somewhat uncertain, although much progress in understanding has been made in recent years.

Bubbles can be removed from a melt by either of two ways. They can rise to the surface or the gas in them can dissolve in the glass. The rate of rise is given by the following equation:

$$\frac{dh}{dt} = \frac{2\sigma g R^2}{9\eta} \quad (4)$$

where  $\sigma$  is the density of the glass,  $g$  is the gravitational constant,  $R$  is the bubble radius, and  $\eta$  is the viscosity of the glass. For a viscosity of 100 P, typical for melting temperatures, the rate of rise of bubbles 0.1 mm in diameter is about 10 cm/day, which is too small to eliminate them from a normal glass furnace. Thus small bubbles can be removed from glass melts only by dissolution of their gas into the glass melt, although larger bubbles can rise to the surface.

Arsenic oxide is a common fining agent added to glass to help remove bubbles. For many years it was thought that the arsenic released oxygen at glass melting temperatures, which "swept out" the bubbles in the glass. However, the calculation above shows that such a mechanism would not eliminate small bubbles, and the elegant experiments of Greene and co-workers showed that arsenic enhances dissolution of oxygen bubbles in glass.<sup>22-24</sup> Thus the importance of arsenic and antimony oxide additions to the glass is to aid in removal of fine bubbles, rather than to generate more gas.

Studies of bubble shrinkage in glass can help in understanding the kinetics of fining, the rates of diffusion of gases in molten glass, and the theoretical treatment of bubble dissolution. Greene and his co-workers observed the shrinkage of oxygen and sulfur dioxide bubbles in a number of silicate glasses between 1000°C and 1300°C.<sup>22-23</sup> They sealed a small amount of gas into a hole between two glass discs, which were then heated in a rotating silica cell. During the first few minutes of heating the temperature of the bubble changed,

so that reliable measurements were not possible. This technique also often introduced a small amount of foreign gas into the bubble. To avoid these difficulties Greene and Davis developed a technique in which the bubble was observed just after it was blown into the molten glass, and studied oxygen, nitrogen, and water bubbles in molten boric oxide.<sup>24</sup> Brown and Doremus<sup>25</sup> also used this technique to study the shrinkage of air oxygen, and nitrogen bubbles in molten boric oxide; an example of their work is shown in Figure 2.

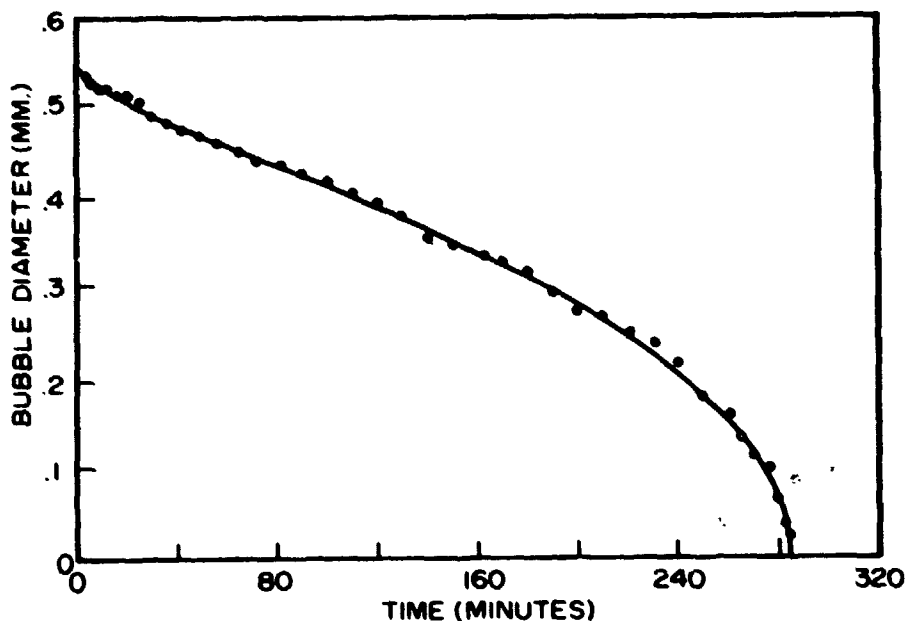


Figure 2. Diameter of an air bubble in molten  $B_2O_3$  at  $550^\circ C$  as a function of time. Circles data; line from eq. 5 with  $D = 2.3(10)^{-7}$   $cm^2/sec$  and  $B = 0.058$ .

The mathematical treatment of the growth or shrinkage of a bubble requires solution of a non-linear partial differential equation, and a general analytical solution has not been found. However, several limiting cases can be solved satisfactorily. If the gas dissolving in the glass has a low concentration (dilute solution in the glass), a relatively simple relation for the radius of the bubble  $R$  as a function of time  $t$  is found:<sup>25,26</sup>

$$R_0^2 - R^2 = 2DBt \left( 1 + \frac{2R_0}{r} \frac{dR}{dt} \right) \quad (5)$$

where  $R_0$  is the initial bubble radius,  $D$  is the diffusion coefficient of the dissolving gas in the glass, and  $B$  is a concentration factor  $B = (c_i - c_\infty)/c_s$ , where the subscripts denote concentrations of gas:  $s$  in the bubble,  $i$  dissolved in the glass at the bubble-glass interface, and  $\infty$  dissolved in the glass far from the bubble. Eq. 5 fits data for the dissolution of air in molten boric oxide as shown in Figure 2.

If the amount of gas dissolved in the glass is not small, ( $B \nless 1$ ), the solution becomes more complicated, because the flow of molten glass as the bubble shrinks leads to a "convection" term in the differential equation.<sup>27</sup> True convection in the glass melt is not significant because of the high viscosity of the glass. A perturbation solution of this expanded differential equation for bubble growth or shrinkage has been given by Duda and Vrentas;<sup>28</sup> the first term in their solution is eq. 5.

Further complications arise if more than one kind of gas is dissolving in the glass,<sup>26,29,30</sup> if the glass sample is not large compared to the bubble,<sup>26</sup> and if there is a surface chemical reaction of the gas dissolving in the glass.<sup>31</sup>

Hollow glass shells filled with deuterium and tritium can serve as laser-fusion targets. These shells are typically about 100  $\mu m$  in diameter with a wall thickness of a few microns, and can be made by dropping powder of a metal-organic gel through a furnace tower at temperatures of from  $1200^\circ C$  to  $1500^\circ C$ .<sup>32</sup> The organic material and residual water serve to blow out the glass into a spherical shell. The size and quality of the shells are dependent on the glass composition, the organic content of the gels, and the furnace conditions.

## Swelling of materials in fast reactors

The swelling of radiation-induced voids in metals and alloys in nuclear reactors can lead to serious degradation of these materials, and may become a problem in fast breeder reactors. The rate of swelling is strongly dependent upon the composition of the irradiated alloy; minor additions ("swelling inhibitors") can reduce the amount of swelling by up to two orders of magnitude.<sup>33</sup> Nucleation of the voids may be a critical step in their formation.<sup>34</sup> Bubbles of gas in irradiated metals can grow by migration and coalescence. The rate of migration of small bubbles is controlled by surface diffusion, and in larger bubbles by ledge nucleation, in niobium alloys and zirconium.<sup>35</sup>

### Acknowledgements

This work was supported by a grant from the National Aeronautical and Space Administration.

### References

1. Anthony, T. R. and Cline, H. E., "Random Walk of Liquid Droplets Migrating in Silicon", J. Appl. Phys., Vol. 47, pp. 2316-2324, 1976.
2. Cline, H. E. and Anthony, T. R., "High-Speed Droplet Migration in Silicon", *ibid*, pp. 2325-2331; "Thermomigration of Aluminum-rich Liquid Wires Through Silicon", *ibid*, pp. 2332-2336.
3. Anthony, T. R., "The Electromigration of Liquid Metal Inclusions in Si", J. Appl. Phys., Vol. 51, pp. 6356-6365, 1980.
4. Cline, H. E. and Anthony, T. R., "Migration of Fine Molten Wires in Thin Silicon Wafers", J. Appl. Phys., Vol. 49, pp. 2412-2419, 1978.
5. Anthony, T. R. and Cline, H. E., "Deep-Diode Arrays", J. Appl. Phys., Vol. 47, pp. 2550-2557, 1976.
6. Anthony, T. R. and Cline, H. E., "The Kinetics of Droplet Migration in Solids in an Acceleration Field", Phil. Mag., Vol. 22, pp. 893-901, 1970.
7. Cline, H. E. and Anthony, T. R., "High-Speed Droplet Migration in Silicon", J. Appl. Phys., Vol. 47, pp. 2325-2331, 1976.
8. Doremus, R. H., "Precipitation Kinetics of Ionic Salts from Solution", J. Phys. Chem., Vol. 62, pp. 1068-1075, 1958.
9. Cline, H. E. and Anthony, T. R., "Nonequilibrium Morphology of Liquid Inclusions Migrating in Solids", J. Appl. Phys., Vol. 48, pp. 5096-5104, 1977.
10. Cline, H. E. and Anthony, T. R., "On the Thermomigration of Liquid Wires", J. Appl. Phys., Vol. 49, pp. 2777-2786, 1978.
11. Carter, R. E., Rosolowski, J. H. and Nadeau, J. S., "Temperature Gradient Induced Migration of Gas-Filled Bubbles in KCl", J. Appl. Phys., Vol. 42, pp. 2186-2193, 1971.
12. Nadeau, J. S., Carter, R. E., Rosolowski, J. H., "Morphology of Migrating Bubbles in KCl Crystals", *ibid*, pp. 2194-2202.
13. Volmer, M. and Weber, A., "Keimbildung in übersättigten Gebilden" (Nucleation in Supersaturated Media), Z. Phys. Chem., Vol. 119, pp. 277-289, 1926.
14. Einstein, A., "Theorie der Opaleszenz von Homogenen Flüssigkeiten und Flüssigkeitsgemischen in der Nahe des Kritischen Zustandes", Annalen der Physik, Vol. 23, pp. 1275-1298, 1910.
15. Gibbs, J. W., The Scientific Papers, Vol. 1, Thermodynamics, Dover, New York, 1961, p. 254.
16. Volmer, M. and Flood, H., "Tropfenbildung in Dämpfen", Z. Phys. Chem., Vol. 170A, pp. 273-285, 1934.
17. Becker, R. and Döring, W., "Kinetische Behandlung der Keimbildung in übersättigten Dämpfen" (Kinetic Treatment of Nucleation in Supersaturated Vapors), Annalen der Physik, Series 5, Vol. 24, pp. 719-752, 1935.
18. Frenkel, J., Kinetic Theory of Liquids, Dover, New York, 1946, p. 366ff.
19. Lothe, J. and Pound, G. M., "Reconsiderations of Nucleation Theory", J. Chem. Phys., Vol. 36, pp. 2080-2085, 1962.
20. Reiss, H., "The Replacement Free Energy in Nucleation Theory", Adv. Coll. and Int. Sci., Vol. 7, pp. 1-66, 1977, and many other references in this article.
21. Carlon, H. R., "Infrared Adsorption by Molecular Clusters in Water Vapor", J. Appl. Phys., Vol. 52, pp. 3111-3115, 1981.
22. Greene, C. H. and Gaffney, R. F., "Apparatus for Measuring the Rate of Absorption of a Bubble in Glass", J. Am. Ceramic Soc., Vol. 42, pp. 271-275, 1959.
23. Greene, C. H. and Platts, D. R., "Behavior of Bubbles of Oxygen and Sulfur Dioxide in Soda-Lime Glass", *ibid*, Vol. 52, pp. 106-109, (1969).
24. Greers, C. H. and Davis, D. H., "The Behavior of Bubbles in Boric Oxide Glass", Proceedings of the Tenth International Congress of Glass, Kyoto, Japan, Vol. 3, pp. 59-62, 1974.
25. Brown, R. B. and Doremus, R. H., "Growth and Dissolution of Gas Bubbles in Molten Boric Oxide", J. Am. Ceramic Soc., Vol. 59, pp. 510-514, 1976.

26. Doremus, R. H., "Diffusion of Oxygen from Contracting Bubbles in Molten Glass", ibid, Vol. 43, pp. 655-661, 1960.
27. Ready, D. W. and Cooper, A. R., "Molecular Diffusion with a Moving Boundary and Spherical Symmetry", Chem. Eng. Sci., Vol. 21, pp. 917-922, 1966.
28. Duda, J. L. and Vrentas, J. S., "Mathematical Analysis of Bubble Dissolution", A. J. Ch. E. J., Vol. 15, pp. 351-356, 1969.
29. Weinburq, M. C., Onorato, P. J. K. and Uhlmann, D. R., "Behavior of Bubbles in Glassmelts II", J. Am. Ceramic Soc., Vol. 63, pp. 435-438, 1980.
30. Weinburq, M. C. and Subramanian, R. S., ibid, pp. 527-531.
31. Subramanian, R. S. and Chi, B., "Bubble Dissolution with Chemical Reaction", Chem. Eng. Sci., Vol. 35, pp. 2185-2199, 1980.
32. Nolen, R. L. and Downs, R. L. and Ebner, M. A., "Glass Shells from Metal-Organic Gels", Abstract, Am. Ceramic Soc. Bulletin, Vol. 60, p. 363, 1981.
33. Johnston, W. G., Rosolowski, J. H., Turkalo, A. M. and Lauritzen, T., "The Effect of Metallurgical Variables on Void Swelling", J. Metals, Vol. 28, pp. 19-24, 1976.
34. Hayns, M. R. and Wood, M. H., "Nucleation of Gas Bubbles in Steel", Proc. Roy. Soc., Vol. 368A, pp. 331-343, 1979.
35. Goodhew, P. J. and Tyler, S. K., "Helium Bubble Behavior in BCC Metals Below 0.65  $T_m$ ", Proc. Roy. Soc., Vol. 377A, pp. 151-184, 1981.

22

Normal Modes of a Compound Drop

M. Saffren, D. D. Elleman and W. K. Rhim

Jet Propulsion Laboratory  
California Institute of Technology  
4800 Oak Grove Drive  
Pasadena, CA 91109

Abstract

In this paper we discuss a theory of normal modes of oscillation of compound liquid drops and the experiments performed to determine its validity. The modes are characterized by their frequency, the attendant displacement of fluid boundaries, and the flow pressure fields within the fluids. The drops consist of three fluids; a core fluid, a fluid shell surrounding the core, and a host fluid surrounding the shell. These fluids are assumed to be inviscid and incompressible, and the core and the shell to be concentric. The theory is obtained by linearization of the equations of fluid motion to the lowest order of nonlinearity that yields the normal modes. Numerical values of mode frequencies and the associated relative displacements of the fluid boundaries are presented for several specific systems, and the results compared with our observations. The core-centering phenomenon whereby the oscillations of the system tend to drive the shell and the core to be concentric was observed in the experiments and will be fully analyzed in a sequel.

Introduction

This is the first in a series of reports on the study of compound liquid drop systems. The systems consist of three fluids: a host fluid infinite in extent, that surrounds a second fluid in the form of a shell, which in turn surrounds a third fluid that forms the core. In particular we will investigate the several normal modes of compound drops on the assumptions: (i) the density of the fluids and the interfacial tensions are arbitrary, (ii) the fluids are incompressible, (iii) they are inviscid, (iv) the equations of fluid motion are linearized to the lowest order of nonlinearity that yields the class of normal modes being studied, and (v) the two fluid interfaces are nearly spherical and concentric. In ensuing reports we relax conditions (iii) through (v).

The primary aim of the entire study is to gain sufficient understanding of the behavior of compound drops to plan and interpret experiments in the laboratories, in the weightless environment provided by flight on the KC-135 aircraft and the Space Shuttle.

Aside from its interest as a fundamental study of compound drops, the work can be applied to the fabrication of fusion target pellets, development of containerless materials processing techniques both terrestrial and extra-terrestrial, and development of techniques for liquid drop control that can be used for fundamental studies in other scientific disciplines such as superfluid drop dynamics.

Equations of motion

We consider a system of several inviscid, incompressible fluids that are in contact with one another at the fluid boundaries each of which is characterized by an interfacial tension. The equations of motion for the system are well known and in spherical coordinates are given as:

$\nabla^2 \psi = 0$  (1)

$\frac{\partial R}{\partial t} = \left( \hat{r} - \frac{\bar{v}_s R}{R} \right) \cdot \nabla \psi$  (2)

$\sigma \bar{v}_s \cdot \hat{n} = - \Delta \left[ \rho \frac{\partial \psi}{\partial t} + P - \sigma (\bar{v}_\psi)^2 \right]$  (3)

The first equation for the velocity potential in each fluid follows from the assumption of incompressibility. The second equation is also kinematic and states that the fluid boundary moves with the fluids; the equation of a boundary being given as  $r = R(\theta, \phi, t)$ . In eq. (2),  $\hat{r}$  denotes the unit vector along  $r$ , the vector from the origin to  $R(\theta, \phi)$ , and  $\bar{v}_s$  denotes the surface gradient operator given by

ORIGINAL FACE IS  
OF POOR QUALITY

$$\bar{\nabla}_s = \hat{\theta} \frac{\partial}{\partial \theta} + \frac{\hat{\phi}}{\sin \theta} \frac{\partial}{\partial \phi} \quad (4)$$

Equation (3) is a dynamical equation indicating that the stress across an interface depends solely on its interfacial tension,  $\sigma$ . The left side of eq. (3) is the stress at a point on the boundary.  $\hat{n}$  is the surface normal at the point, and  $\bar{\nabla}_s$  denotes the surface divergence operator. The right side of this equation is simply the pressure difference supported by the boundary stress, and  $P$  denotes the pressure in the resting fluid.

These nonlinear equations are rendered linear by assuming that the motion of the system produces small deviations of a boundary from the shape it had when the system was at rest. For a compound drop the boundaries are spherical, and the pressure difference across a boundary of radius  $\bar{R}$  and interfacial tension,  $\sigma$ , is

$$\Delta P = - \frac{2\sigma}{\bar{R}}. \quad (5)$$

For this system, retaining only first order terms, eq. (2) can be written as

$$\frac{\partial R}{\partial t} - \frac{\partial \psi}{\partial r} = 0, \quad (2A)$$

and eq. (3) after substituting eq. (5), becomes

$$\Delta \left( \rho \frac{\partial \psi}{\partial t} \right) = \frac{\sigma}{\bar{R}^2} (2 - L^2) \Delta R, \quad (3A)$$

where  $\Delta R = R - \bar{R}$ , and  $L^2$  is the surface Laplacian which results from the linearization of the curvature.

Normal modes of a concentric three fluid systems

We consider a concentric three fluid system as shown in Figure 1, and calculate normal modes using eqs. (1), (2A), and (3A). The solution of the equations involves finding flow potential,  $\psi$ , in the three fluids. Since  $\psi$  is nonsecular solution of Laplace equation, it can be expressed in the following forms in each region of the system:

$$\psi(\underline{r}, t) = \sum_{\ell, m} [A(\ell, m; t)r^\ell + B(\ell, m; t)r^{-(\ell+1)}] Y_{\ell m}(\theta, \phi) \quad (\text{shell}) \quad (6)$$

$$\psi_i(r, t) = \sum_{\ell, m} A_i(\ell, m; t)r^\ell Y_{\ell m}(\theta, \phi), \quad (7) \quad (\text{core})$$

$$\psi_o(\underline{r}, t) = \sum_{\ell, m} B_o(\ell, m; t)r^{-(\ell+1)} Y_{\ell m}(\theta, \phi). \quad (8) \quad (\text{host})$$

If the condition that the normal component of velocity across each boundary is continuous is imposed, we obtain.

$$A_i = A - \frac{\ell + 1}{\ell} B R_i^{-(2\ell+1)} \quad (9)$$

$$B_o = B - \frac{\ell}{\ell + 1} \bar{R}_o^{(2\ell+1)} \quad (10)$$

Therefore, only the flow potential in the shell remains to be determined.

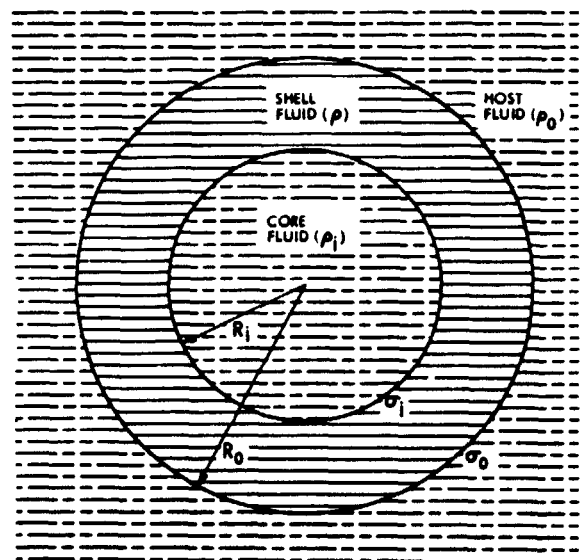


Figure 1. A concentric three fluid system used in the theory.

We now express the boundary functions in the following way:

$$R_{\begin{pmatrix} i \\ o \end{pmatrix}}(\theta, \phi; t) = \bar{R}_{\begin{pmatrix} i \\ o \end{pmatrix}} + \Delta R_{\begin{pmatrix} i \\ o \end{pmatrix}}(\theta, \phi; t) = \bar{R}_{\begin{pmatrix} i \\ o \end{pmatrix}} + \sum_{\ell, m} \delta R_{\begin{pmatrix} i \\ o \end{pmatrix}}(\ell, m; t) Y_{\ell m}(\theta, \phi). \quad (11)$$

If we substitute these expressions into eqs. (2A) and (3A), we show that the equations can be reduced to an eigenvalue equation which is essentially same as a coupled harmonic oscillator:

$$\begin{bmatrix} \frac{\sigma m_i}{\tau^3} & 1 \\ 1 & \frac{m_o \tau^3}{\sigma} \end{bmatrix} \begin{bmatrix} \Delta_o \\ \Delta_i \end{bmatrix} = -\frac{J}{W} \begin{bmatrix} \ddot{\Delta}_o \\ \ddot{\Delta}_i \end{bmatrix} \quad (12)$$

where

$$\sigma = \sqrt{\sigma_o/\sigma_i}, \quad \Delta_o \equiv \sqrt{\sigma} \delta R_o, \quad \Delta_i \equiv \delta R_i/\sqrt{\sigma}, \quad (13)$$

$$m_{\begin{pmatrix} o \\ i \end{pmatrix}} = (1 + \tilde{\Delta}_\rho \begin{pmatrix} o \\ i \end{pmatrix}) \tau^{(2\ell+1)} - \tilde{\Delta}_\rho \begin{pmatrix} o \\ i \end{pmatrix} \tau^{-(2\ell+1)}, \quad (14)$$

$$\tilde{\Delta}_\rho \begin{pmatrix} i \\ o \end{pmatrix} = \frac{(\ell+1)(\rho_i - \rho)}{(2\ell+1)\rho}, \quad \tilde{\Delta}_\rho \begin{pmatrix} o \\ o \end{pmatrix} = \frac{\ell(\rho_o - \rho)}{(2\ell+1)\rho} \quad (15)$$

$$J = (1 + \tilde{\Delta}_\rho \begin{pmatrix} o \\ o \end{pmatrix})(1 + \tilde{\Delta}_\rho \begin{pmatrix} i \\ i \end{pmatrix}) \tau^{(2\ell+1)} - \tilde{\Delta}_\rho \begin{pmatrix} i \\ i \end{pmatrix} \tilde{\Delta}_\rho \begin{pmatrix} o \\ o \end{pmatrix} \tau^{-(2\ell+1)}, \quad (16)$$

$$W = \left( \frac{\sigma_o \sigma_i}{[R_o R_i]^3} \right)^{1/2} \frac{(\ell-1)\ell(\ell+1)(\ell+2)}{(2\ell+1)\rho} \quad (17)$$

where  $\tau = \sqrt{R_o/R_i}$ . Note that the only dimensional quantity is  $W$  which has the dimension of frequency squared.

From eq. (12), the eigenvalues are given by

$$K = \frac{1}{2} \left( \frac{\sigma m_i}{\tau^3} + \frac{m_o \tau^3}{\sigma} \right) \pm \sqrt{\frac{1}{4} \left( \frac{\sigma m_i}{\tau^3} - \frac{m_o \tau^3}{\sigma} \right)^2 + 1}, \quad (18)$$

so that the normal mode frequencies  $\omega_{\pm}^2$ , are given by

$$\omega_{\pm}^2 = \frac{K}{J} W \quad (19)$$

From (11) and (17), we obtain the corresponding eigenvectors as

$$\frac{1}{\sigma} \begin{pmatrix} \delta R_o \\ \delta R_i \end{pmatrix}_{\pm} = \begin{pmatrix} \Delta_o \\ \Delta_i \end{pmatrix}_{\pm} = \frac{1}{d \pm \sqrt{d^2 + 1}} \quad (20)$$

where

$$d = \frac{1}{2} \left( \frac{m_o \tau^3}{\sigma} - \frac{\sigma m_i}{\tau^3} \right). \quad (21)$$

It follows from the orthogonality of eigenvectors that

$$\delta \left( \frac{\delta R_o}{\delta R_i} \right) = -\frac{1}{\sigma} \left( \frac{\delta R_o}{\delta R_i} \right)^{-1} \quad (22)$$

It is important to note that the positive square root in (20) corresponds to the positive square root in (18). Consequently for the normal mode with the higher frequency, the boundary oscillations are in-phase. We call this high frequency, "+", mode the "bubble" mode and the lower frequency, "-", mode the "sloshing" mode. From relation (22), the relative boundary displacement of the sloshing mode is out of phase. The relative boundary displacement of these two modes as they were observed in the neutral buoyancy tank is shown in Figure 2. The top figure shows "bubble" mode in which the two boundaries oscillate in-phase, and the bottom figure shows "sloshing" mode in which the two boundaries move out of phase. In this compound drop the core and the host were silicon oil, and the shell was water.

#### Velocity potential

We now obtain expressions of velocity potentials  $\psi_i$ ,  $\psi_s$  and  $\psi_o$  for the flow fields in the core, shell and the host respectively in terms of the interfacial displacements. From eqs. (6) through (11), the expressions for  $\psi_i$  and  $\psi_o$  are obtained as

$$\begin{aligned} (\psi_i)_{\ell m} &= \frac{s}{\tau} \tau^{\ell-1} \left( \frac{r}{s} \right)^{\ell} Y_{\ell m} \delta \dot{R}_i \\ (\psi_o)_{\ell m} &= -\frac{s}{\tau+1} \tau^{\ell+2} \left( \frac{s}{r} \right)^{\ell+1} Y_{\ell m} \delta \dot{R}_o \end{aligned} \quad (23)$$

where

$$s = \sqrt{\bar{R}_o \bar{R}_i} \quad \text{and} \quad \tau = \sqrt{\bar{R}_o / \bar{R}_i} \quad (24)$$

The result for  $\psi_s$ , interesting enough, can be expressed as

$$(\psi_s)_{\ell m} = (\psi_s^C)_{\ell m} + (\psi_s^H)_{\ell m} \quad (25)$$

where  $\psi_s^C$  is the shell velocity potential when the core is rigid and  $\psi_s^H$  is for the case when the host is rigid. When explicitly expressed, they are

$$(\psi_s^C)_{\ell m} = \frac{s_1^2}{(\ell+1)D} \left\{ (\ell+1) \tau^{\ell} \left( \frac{r}{s} \right)^{\ell} + \tau^{-(\ell+1)} \left( \frac{s}{r} \right)^{\ell+1} \right\} Y_{\ell m} \delta \dot{R}_o \quad (26)$$

$$(\psi_s^H)_{\ell m} = -\frac{s_1^{-2}}{\ell(\ell+1)D} \left\{ (\ell+1) \tau^{-\ell} \left( \frac{r}{s} \right) + \tau^{\ell+1} \left( \frac{s}{r} \right)^{\ell+1} \right\} Y_{\ell m} \delta \dot{R}_i \quad (27)$$

where  $D = \tau^{2\ell+1} - \tau^{-(2\ell+1)}$ . Of course, conditions

$$\left( \frac{\delta \psi_s^C}{\delta \dot{R}_o} \right)_{r=R_i} = 0 \quad \text{and} \quad \left( \frac{\delta \psi_s^H}{\delta \dot{R}_i} \right)_{r=R_o} = 0 \quad \text{were imposed to obtain (26) and (27).}$$

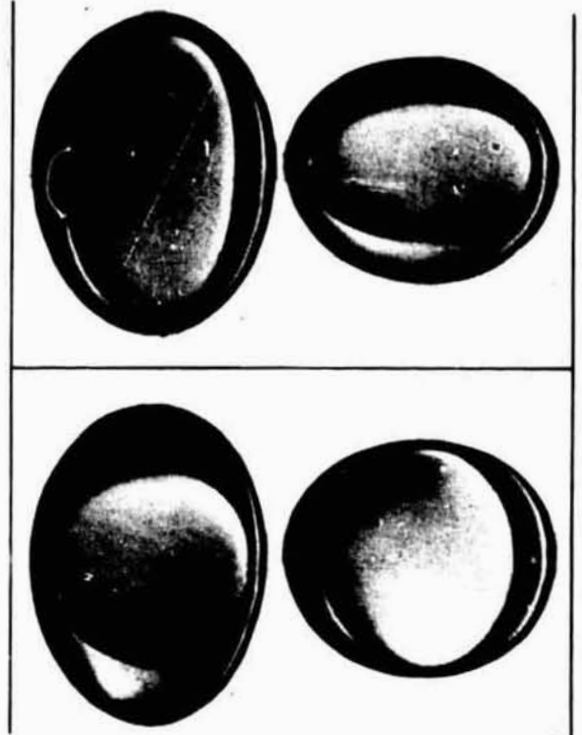


Figure 2. "Bubble" mode (top) and "sloshing" mode (bottom) oscillations of an oil-water compound drop.

Illustrative examples

Using eqs. (13) to (19), numerical values of the eigenfrequencies for various physical parameters can be readily obtained. Furthermore, simple expressions of several limiting cases as shown below can be deduced in a straightforward way.

(i) Simple Drop: We tested the present theory by deriving the well-known simple drop case. With  $R_1=0$  and following the procedure derived in the previous section, we get

$$\omega_L^2 = \frac{\epsilon(\epsilon+1)(\epsilon-1)(\epsilon+2)}{R^3 [\epsilon\rho_0 + (\epsilon+1)\rho]} \quad (28)$$

which is identical to Lamb's result.<sup>2</sup> Figure 3 shows various modes of a simple drop corresponding to the different values of  $\epsilon$ . A water drop immersed in a neutrally buoyant oil bath was axisymmetrically excited by a plunger which was in turn connected to a sinusoidally excited loud speaker. With 1.5cc of drop volume, the interfacial tension, 11.2 dynes/cm, was obtained using eq. (28) for  $\epsilon = 2$ . The higher mode frequencies obtained using eq. (28) is shown in Figure 4 (solid line) and it was compared with the actual measurements (circles). The agreement is excellent.

(ii) Rigid Host: When the compound drop was formed in the rigid host (i.e.,  $\rho_0 = \infty$ ), then  $\omega_- = 0$  and

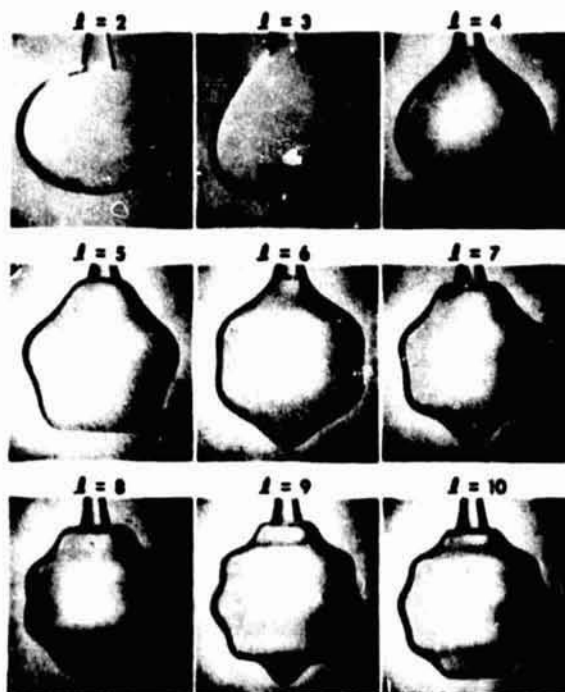


Figure 3. Various modes of a water drop oscillations in the silicon oil bath. The drop was mechanically excited.

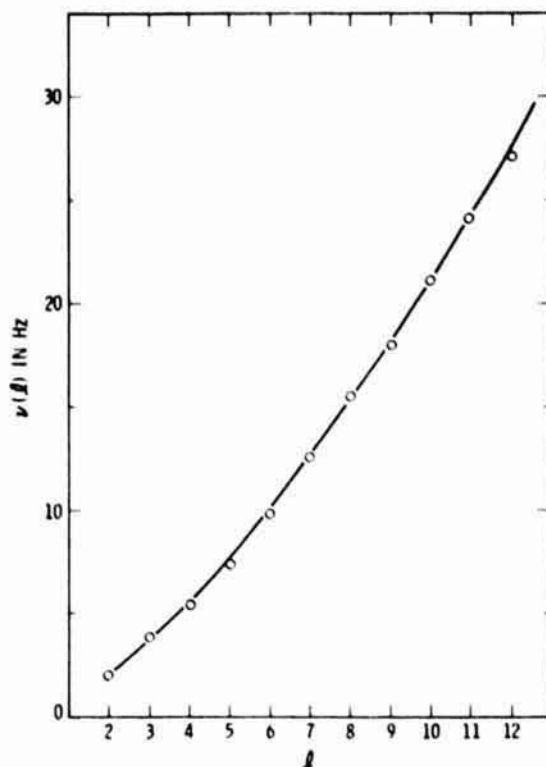


Figure 4. Frequency vs  $\epsilon$  of a water drop in silicon oil. Drop volume was 1.5cc, and  $\sigma = 11.2$  dynes/cm as measured for  $\epsilon = 2$  case. Under these conditions, the solid line was obtained using eq. (28), and the circles were as measured by the mechanically excited oscillations.

$$\omega_{\pm}^2 = \frac{\rho_1(\epsilon-1)\epsilon(\epsilon+1)(\epsilon+2)[\epsilon^{2\epsilon+1} - \epsilon^{-(2\epsilon+1)}]}{R_1^3 \{ [\epsilon\rho_0 + (\epsilon+1)\rho_1] \epsilon^{2\epsilon+1} + (\epsilon+1)(\rho - \rho_1) \epsilon^{-(2\epsilon+1)} \}} \quad (29)$$

If we normalize this with respect to  $\omega_L$  of a simple drop which is made out of shell fluid immersed in the core fluid, then  $N_0 = \omega_{\pm} / \omega_L$  for  $\epsilon=2$  and  $\rho_1 = \rho$  is as shown in Figure 5. Here  $V_T$  is the total volume (i.e.,  $V_T = V_{\text{shell}} + V_{\text{core}}$ ).  $N_0$  rises from zero at  $V_T/V_c = 1$ , then it approaches to infinity as the core shrinks. As the core shrinks with respect to  $V_T$ , the core motion becomes essentially decoupled from the host and approaches to the simple drop frequency. This can be readily observed from eq. (29) as

$$N_0 = \sqrt{\epsilon / R_1} \rightarrow \infty$$

(iii) Rigid Core: If the compound drop has rigid core (i.e.,  $\rho_1 = \infty$ ), then  $\omega_- \rightarrow 0$ , and

$$\omega_+^2 = \frac{\rho_0(\epsilon-1)\epsilon(\epsilon+1)(\epsilon+2)[\epsilon^{2\epsilon+1} - \epsilon^{-(2\epsilon+1)}]}{R_0^3 \{ [\epsilon\rho_0 + (\epsilon+1)\rho_1] \epsilon^{2\epsilon+1} + \epsilon(\rho - \rho_0) \epsilon^{-(2\epsilon+1)} \}} \quad (30)$$

Of course, when  $R_1 \rightarrow 0$ , this reduces to eq. (28) for the simple drop. If we let  $\omega_L$  be this simple drop frequency, then the normalized frequency,  $N_c = \omega / \omega_L$ , for  $l=2$  and  $\rho_0 = \rho$ , is as shown in Figure 6. Starting from a very thin shell (i.e.,  $V_T/V_C = 1$ ),  $N_c$  rises sharply to its maximum, then gradually approaches the single drop frequency as  $V_T/V_C$  increases. The agreement with the experimental points is fairly good.

(iv) Thin Shell: When the shell is very thin (i.e.,  $\tau = 1$ ), then  $\omega_- = 0$ , and

$$\omega_+^2 = \frac{(\sigma_0 + \sigma_1)(l-1)l(l+1)(l+2)}{R^3 [l\rho_0 + (l+1)\rho_1]} \quad (31)$$

Note that this is the same expression as that of a simple drop if its interfacial surface tension is replaced by  $\sigma_0 + \sigma_1$ . This particular result was also confirmed experimentally in the neutral buoyancy tank

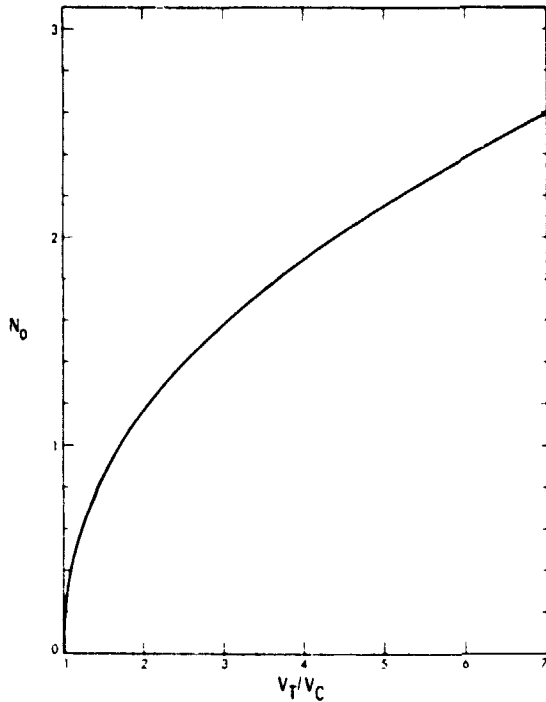


Figure 5. Normalized Frequency,  $N_0$  vs  $V_T/V_C$  when the hose is rigid.

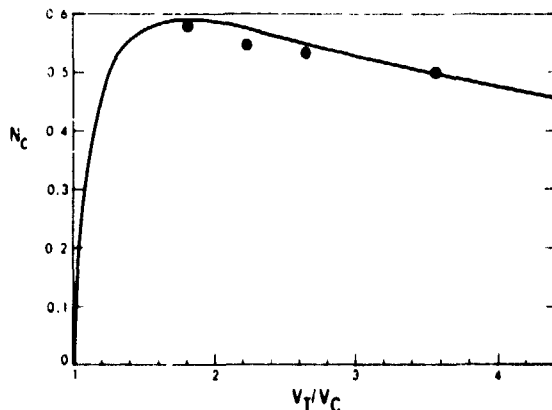


Figure 6. Normalized frequency,  $N_c$ , vs  $V_T/V_C$  when the core is rigid.

(v) Thick Shell: When the shell is very thick (i.e.,  $\tau \rightarrow \infty$ ), then we get

$$\omega_+^2 \rightarrow \frac{4\pi\sigma_1(l-1)l(l+1)(l+2)}{3V_C [l\rho + (l+1)\rho_1]} \quad (32)$$

and

$$\omega_-^2 \rightarrow \frac{4\pi\sigma_0(l-1)l(l+1)(l+2)}{3V_S [l\rho_0 + (l+1)\rho]} \quad (33)$$

where  $V_C$  and  $V_S$  are the core and the shell volumes respectively. These expressions tell us that in this limit the "bubble" and "sloshing" modes are no longer coupled since each mode represents simple drop oscillation.

(vi) For  $\rho_1 = \rho_0$  and  $\sigma_1 = \sigma_0$ : When the core and the host fluids are the same and the two interfacial tensions are the same the expressions for  $\omega_{\pm}^2$  cannot be made much simpler than eq. (19). However, the numerical results of these frequencies are shown in Figure 7, where  $V_T = V_C + V_S$ , and  $N_s = \omega_{\pm} / \omega_L$  where  $\omega_L$  is the frequency of a simple drop which is made out of the same compound drop when the core was reduced to zero. In this figure the upper five curves represent "bubble" modes for the specified values of  $\rho_1/\rho$  when  $\rho_1 = \rho_0$ , and the lower three curves represent corresponding "sloshing" modes. Experimental points taken in a neutral buoyancy tank ( $\rho_1/\rho = \rho_0/\rho = 1$ ) show good agreement with the theoretical curves. The results for the relative boundary displacements are shown in Figure 8 for an air-water-air type and an oil-water-oil type of compound drop systems. We see that our preliminary experimental results obtained in a neutral buoyancy tank also agree well with the theory.

#### Remarks on core centering

An interesting core centering phenomenon was observed in our neutral buoyancy experiments. Initially, a static compound drop was prepared so that the inner and the outer boundary surfaces were nonconcentric due to the slight density mismatch. However, as the drop began to oscillate in one of its normal mode frequencies (for  $l=2$ ), the two boundaries became concentric within the accuracy of our observation. Though this

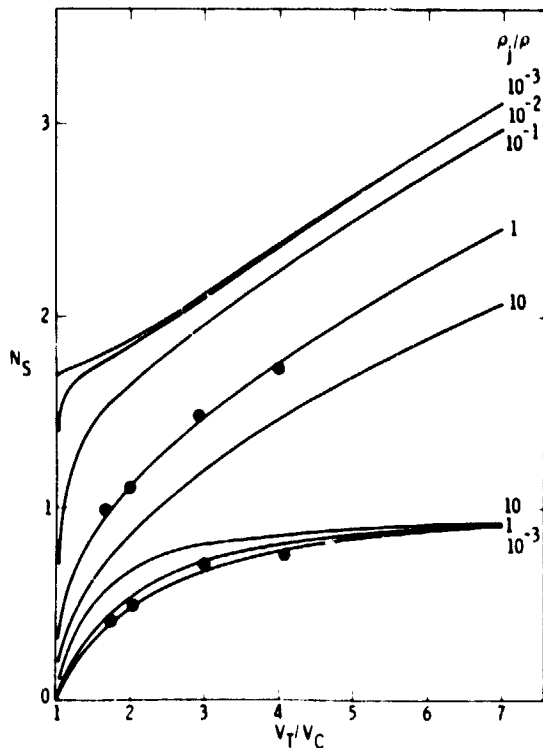


Figure 7. Normalized frequency,  $N_s$ , vs  $V_T/V_C$  when  $\sigma_1 = \sigma_0$  and  $\sigma_1 = \sigma_0$ . The upper five curves are for the "bubble" modes and the lower three curves are for the "Sloshing" modes.

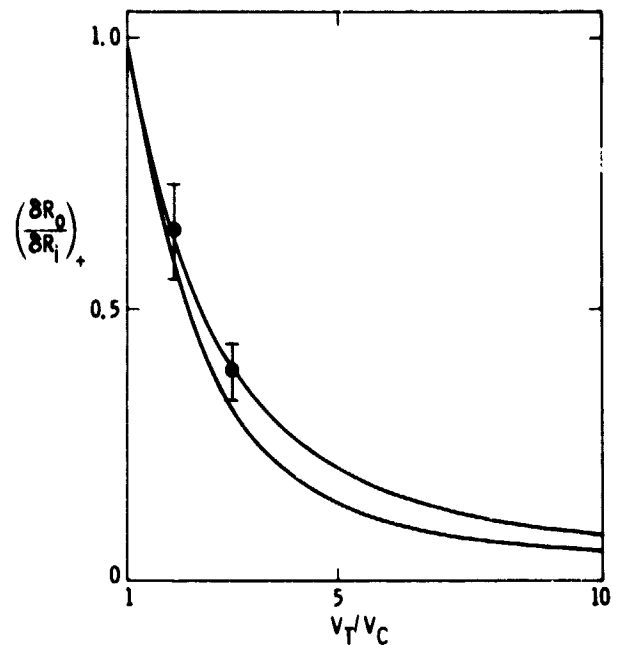


Figure 8. Relative boundary displacement of "bubble" modes. The upper curve is for an oil-water-oil type of compound drop and the lower curve is for an air-water-air type of compound drop. The experimental points are from the neutral buoyancy experiment.

centering phenomenon takes place within a few cycles of oscillation, the centering force seems to depend, among others, on the oscillation amplitude and the shell thickness. Within the approximations used in this paper, the positions of the core anywhere within the drop is neutrally stable. It is necessary to consider the next order of approximation to find the restoring forces responsible for the centering of the core and the shell. Work on the centering phenomenon and its more detailed description will be published elsewhere.

#### Experimental apparatus and procedure

(A) Neutral Buoyancy Tank: The heart of the experimental apparatus is a neutral buoyancy tank which is a lucite box filled with silicon oil (Dow Corning 200, lcs). Taking advantage of the fact that the density of silicon oil was less than water, we created a vertical density gradient by adding a small amount of freon to the silicon oil until the water droplet floated in the middle of the tank. Also imbedded within this box were several electrodes for the purpose of excitation and detection of the drop systems.

(B) Excitation and Detection Procedure: We adopted basically two different detection procedures: 1) frequency sweep, and 2) the pulsed transient technique. In the continuously driving method, the frequency of an oscillating electric field was swept through resonances while monitoring the oscillation amplitude using an optical recording and video systems (such as fast movie camera or TV video system). This method has the advantage of quick identification of the characteristic oscillations and provides detailed information about boundary motion. However, it was found that unless the driving field was kept at a low level, the resonance frequency measured in this method was erroneous. This is due to the fact that the large oscillating electric field changes the surface tension dynamically. The detection method which was used extensively in this experiment was the capacitance bridge method. The block diagram of this apparatus is shown in Figure 9. This method is similar in principle to more well-known transient techniques in nuclear magnetic resonance or optical spectroscopy. The basic idea of this technique is to record capacitance variation as the drop evolves freely toward equilibrium state from an initial nonequilibrium state. Application of an intense short electric pulse excites the droplet over a wide range of frequency simultaneously. Therefore, the Fourier transformation of this transient signal reveals characteristic frequencies simultaneously.

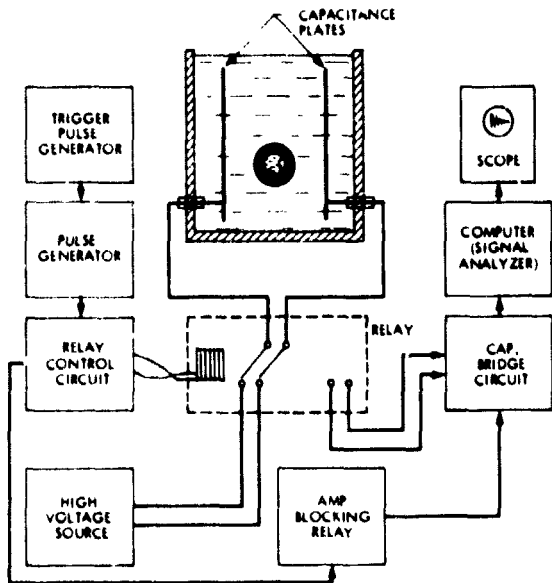


Figure 9. A block diagram of our apparatus which excites the drop electro-statically and detects the ensuing capacitance signal caused by the drop deformation.

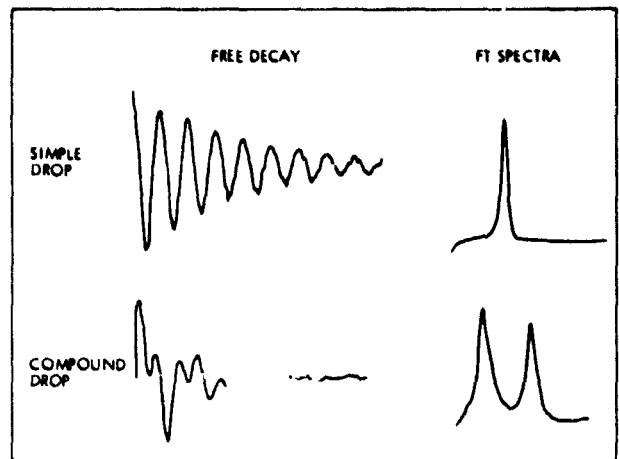


Figure 10. Signals obtained by the capacitance bridge and their Fourier transformed spectra.

This capacitance bridge system was constructed around a General Radio Capacitance Bridge Unit, a home-built relay system, an A/D converter, and a data processing minicomputer. Once the capacitance bridge was balanced with the relay connected to the bridge, an electric pulse could be fired by simply controlling the relay switch for the preset time duration. Upon the termination of the pulse, the electrodes were switched back to the bridge and the ensuing signal was detected and processed. In order to protect the amplifier during the pulse and to shorten the recovery time following the pulse, an amplifier blocking relay switch was inserted at the input of the amplifier.

Figure 10 shows a set of typical data obtained in this method. For the simple drop case, the signal is a damped monotonic oscillation which corresponds to a single peak in the frequency domain. Of course, the spectral line width is inversely proportional to the damping time constant of the time domain signal. The signal from a compound drop looks more complicated. However, Fourier transformation shows two well-resolved peaks each of which corresponds to the bubble mode and the slushing mode respectively. Though the capacitance bridge method provides a full spectrum without scanning through resonance frequencies, it does not provide information about boundary motion. For this reason it is more convenient to adopt both continuous and transient methods which will compliment each other.

#### Acknowledgement

The authors express their deep and warm appreciation to Dr. John Carruthers without whose interest, encouragement, and support this work would not have been possible. The authors also would like to extend their appreciation to J. Shanks and A. Croonquist for their assistance.

#### References

1. Landaw, L. D., and Lifshitz, E. M., Fluid Mechanics, (Pergamon Press, London), pp. 239.
2. Lamb, H., Hydrodynamics, Sixth Edition, Cambridge University Press, Reprinted by Dover, New York, 1945, pp. 475.

Interaction effects in thermocapillary bubble migration

M. Meyyappan, William R. Wilcox, and R. Shankar Subramanian

Department of Chemical Engineering, Clarkson College of Technology  
Potsdam, New York 13676

Abstract

The interaction effects between two bubbles migrating along their line of centers under the influence of an imposed thermal gradient are considered in the quasi-static limit. Results are reported for representative values of the governing parameters.

A gas bubble, when placed in a liquid with a non-uniform temperature field, will move in the direction of the temperature gradient. Such motion is a consequence of the dependence of surface tension on temperature. The temperature gradient at the bubble surface gives rise to a surface tension gradient. The resulting tangential stress at the interface will cause motion of the neighboring liquid in the direction of increasing surface tension, or toward the colder pole of the bubble. By reaction, the bubble will propel itself toward the warmer regions of the liquid. The thermocapillary motion of isolated bubbles has been the subject of much study. Both theoretical descriptions<sup>1-4</sup>, and experimental observations in general agreement with theory<sup>1,3,5,6</sup> have been reported.

Under conditions of creeping motion, the buoyant rise velocity of a gas bubble is proportional to the square of its diameter whereas its thermocapillary velocity (for negligible convective energy transport) is proportional to the diameter. Thus, it may be expected that on earth, very small bubbles will be influenced significantly by temperature gradients. In contrast, in reduced gravity processing, capillarity induced motion of bubbles and droplets will be important over a wide range of bubble sizes. Thus, there is renewed interest in this subject. At Clarkson, for instance, theoretical models of thermocapillary motion are being developed<sup>7-10</sup> and a reduced gravity experiment has been flown in collaboration with Westinghouse Research and Development Center on a NASA rocket in their SPAR (Space Processing Applications Rocket) program<sup>11</sup>. More rocket experiments as well as Space Shuttle experiments are being planned<sup>12,13</sup>.

The problem of the isolated bubble moving in a thermal gradient has received considerable attention as mentioned earlier. However, in many practical applications, interactions with neighboring bubbles and boundaries will be important. We have begun addressing such problems theoretically in the quasi-static limit. Work on bubble migration normal to a plane fluid or solid surface is reported in (8). Elsewhere in this Proceedings<sup>14</sup>, a brief discussion of the problem of thermocapillary motion of bubbles inside drops is presented in the context of applications to the containerless processing of glasses and other materials in free fall. The axially symmetric interaction problems for two unequal bubbles has been solved using bispherical coordinates, and a complete treatment is being reported elsewhere<sup>15</sup>. Details will be given in (16). Here, only a brief summary of the results will be presented.

When two bubbles, possibly of unequal diameters, are placed in a liquid possessing a linear temperature field such that the line of centers of the bubbles is parallel to the temperature gradient, the resulting problem is axially symmetric. Both bubbles will move in the direction of the temperature gradient. The problem, in general, is unsteady. However, when the Reynolds and Marangoni numbers are very small, the quasi-static assumption<sup>17</sup> may be made in order to obtain first order results. This involves ignoring the unsteady accumulation terms as well as the convective transport terms in the equations of conservation of momentum and energy. In physical terms, in part, it is assumed that the vorticity and temperature distributions for a given spacing of the bubbles relax quickly to their steady representations for that configuration compared to the time scale for the bubbles to move an appreciable distance and change the configuration. Further, the convective transport terms are ignored compared to molecular transport. For the small bubbles in glass melts used in our rocket experiments, the quasi-static assumption is a good one.

General solutions of the quasi-static equations in bispherical coordinates are available<sup>18,19</sup>. They are specialized for the boundary conditions of the present problem, a straightforward, but tedious process<sup>15</sup>. The quasi-static thermocapillary velocities of the two bubbles then are calculated by setting the net hydrodynamic force on the bubbles to zero.

It is convenient to discuss the results in the context of an interaction parameter  $\Omega$

which represents the ratio of the velocity of a given bubble in the presence of the second bubble to its velocity when isolated.  $\Omega$  will depend on the ratio of bubble radii,  $\lambda$

( $\lambda = \frac{R_{II}}{R_I}$ ) and the scaled separation distance between the bubbles,  $D$ . ( $D = \frac{d}{R_I}$ ). Here "d" is the actual separation distance,  $R_I$ , the radius of bubble I, and  $R_{II}$ , the radius of bubble II. Due to the neglect of convective transport effects, the order of two bubbles in the temperature gradient has no influence on the results. A representative set of values of  $\Omega_I$  and  $\Omega_{II}$  for the two bubbles as a function of scaled separation distance  $D$  is reported in Table I for a typical value of  $\lambda$ .  $\lambda = 1.5$  represents the case of bubble II being larger than bubble I.

TABLE I

Interaction Parameters  $\Omega_I$  and  $\Omega_{II}$  as a Function of  $D$  for  $\lambda = 1.5$

D	$\Omega_I$	$\Omega_{II}$
2.6	1.1432	0.9662
3.0	1.0728	0.9832
8.0	1.0033	0.9993

From the results in Table I, it may be seen that the larger of the two bubbles (II) moves slightly slower than it would if isolated. In contrast, the smaller bubble (I) moves more rapidly than it would, when isolated. Also, as the bubbles are separated further, the interaction becomes less important, and  $\Omega$  approaches unity. We might also observe that in view of the above behavior in the case of unequal bubbles, it is not surprising that when they are of equal size, both bubbles move at the same velocity that they would possess, if isolated.

#### Acknowledgments

This work was supported in part by the Materials Processing in Space Program Office of NASA, Marshall Space Flight Center, through a subcontract from Westinghouse Research and Development Center to Clarkson College of Technology. Computer time for some of the calculations reported here was donated by Clarkson College of Technology.

#### References

1. Young, N. O., Goldstein, J. S., and Block, M. J., J. Fluid Mech. 6, 350 (1959).
2. Bratukhin, Y. K., Thermocapillary Drift of a Viscous Fluid Droplet, NASA Report No. TT F-17093, June 1976.
3. Thompson, R. L., Dewitt, K. J., and Labus, T. L., Chem. Eng. Commun. 5, 299 (1980).
4. Subramanian, R. S., A.I.Ch.E.J. 27, 646 (1981).
5. McGrew, J. L., Rehm, T. L., and Griskey, R. G., App. Sci. Res. 29, 195 (1974).
6. Hardy, S. C., J. Colloid Interface Sci. 69, 157 (1979).
7. Shankar, N., Cole, R., and Subramanian, R. S., Int. J. of Multiphase Flow 7, 581 (1981).
8. Meyyappan, M., Wilcox, W. R., and Subramanian, R. S., J. Colloid Interface Sci. 83, 199 (1981).
9. Jayaraj, K., Cole, R., and Subramanian, R.S., J. Colloid Interface Sci. In Press, 1981.
10. Shankar, N., and Subramanian, R. S., J. Fluid Mech., Submitted.
11. Wilcox, W. R., Subramanian, R. S., Meyyappan, M., Smith, H. D., Mattox, D. M., and Partlow, D. P., Final Report to NASA Contract No. NAS8-33017.
12. Subramanian, R. S., and Cole, R., "Experiment Requirements and Implementation Plan (ERIP) for Physical Phenomena in Containerless Glass Processing." NASA Marshall Space Flight Center, Document 77FR010, August, 1979.
13. Annamalai, P., Shankar, N., Cole, R., and Subramanian, R. S., Appl. Sci. Res., In Press.
14. Shankar, N., Annamalai, P., Cole, R., and Subramanian, R. S., This Proceedings.
15. Meyyappan, M., Wilcox, W. R., and Subramanian, R. S., "The Slow Axisymmetric Motion of Two Bubbles in a Thermal Gradient" to be submitted for publication.
16. Meyyappan, M., Ph.D. thesis in Chemical Engineering, in progress, Clarkson College of Technology.
17. Happel, J., and Brenner, H., "Low Reynolds Number Hydrodynamics." Prentice-Hall, Englewood Cliffs, N.J., 1965.
18. Jeffery, G. B., Proc. R. Soc. A87, 115 (1912).
19. Stimson, M., and Jeffery, G. B., Proc. R. Soc. A111, 110 (1926).

## Dielectrophoretic levitation of droplets and bubbles\*

T. B. Jones\*\*

Department of Electrical Engineering, Colorado State University  
Fort Collins, CO 80523Abstract

Uncharged droplets and bubbles can be levitated dielectrophoretically in liquids using strong, nonuniform electric fields. The general equations of motion for a droplet or bubble in an axisymmetric, divergence-free electrostatic field allow determination of the conditions necessary and sufficient for stable levitation. Two cases of a bubble or droplet with dielectric constant ( $\kappa_2$ ) less than or greater than the liquid medium dielectric constant ( $\kappa_1$ ) emerge. For  $\kappa_2 < \kappa_1$ , passive levitation is possible, while for  $\kappa_2 > \kappa_1$ , active feedback-controlled levitation is required. The design of dielectrophoretic (DEP) levitation electrode structures is simplified by a Taylor-series expansion of cusped axisymmetric electrostatic fields. Extensive experimental measurements on bubbles in insulating liquids verify the simple dielectrophoretic model. Others have extended dielectrophoretic levitation to very small particles (<100  $\mu\text{m}$ ) in aqueous media. Zero-gravity DEP levitation remains to be demonstrated. This paper concludes with a discussion of applications of DEP levitation to the study of gas bubbles, liquid droplets, and solid particles. Some of these applications are of special interest in the reduced gravitational field of a spacecraft.

Introduction

Strong nonuniform electric fields exert effective forces on uncharged particles, liquid droplets, and gas bubbles. Pohl named this effect *dielectrophoresis* in 1951.<sup>1</sup> The dielectrophoretic phenomenon is most pronounced for small particles (<1000  $\mu\text{m}$ ). A cusped electrostatic field can stably levitate bubbles, droplets, and small particles suspended in dielectric liquids. Further demonstrations of the manipulation and control of droplets, bubbles, and solid particles exist that are relevant to the reduced gravitational environment of space. Zero-gravity dielectrophoresis offers some interesting prospects in a number of materials processing applications that are considered in this paper.

H. A. Pohl exploited dielectrophoresis in the separation of solid dielectric particles from a liquid insulant. One proposed application has been in the separation of living from dead blood cells.<sup>2</sup> Lin and Benguigui have used granular solid dielectric media stressed with strong electric fields to achieve high gradient DEP separations.<sup>3</sup> Veas and Schaeffer used a cusped electrostatic field to levitate small droplets of one dielectric liquid suspended in another.<sup>4</sup> Jones and Bliss studied the dielectrophoresis of small gas bubbles in insulating liquids and levitated these bubbles using an improved electrode geometry.<sup>5</sup> Kallio and Jones proposed the use of DEP levitation for the measurement of solid particle and liquid dielectric constants.<sup>6</sup>

In this paper, I discuss theoretical and experimental dielectrophoresis. Potential applications of DEP in a number of diverse fields (including zero-gravity experimentation) are reviewed in light of this recent work.

Theory

The theory relevant to dielectrophoresis is conveniently divided into sections dealing with the basic force calculation, properties of divergence-free electrostatic fields, frequency dispersion effects (charge relaxation), and the equations of motion.

Dielectrophoretic Force

The DEP force is nonzero if either the magnitude or direction of the Lorentz force ( $q\vec{E}$ ) exerted on the positive and negative ends of a dipole differ. The general expression is

$$\vec{F}^e = (\vec{p}_{\text{eff}} \cdot \nabla)\vec{E}, \quad (1)$$

\* To be presented at the Second Convention of the International Colloquium on Drops and Bubbles, Monterey, CA, November 1981.

\*\* Present address: Xerox Corporation, Webster, N.Y. 14580.

where  $\bar{E}$  is the imposed electric field and  $\bar{p}_{\text{eff}}$  is the effective dipole moment of the particle. If the particle is an insulating sphere of radius  $R$ , dielectric constant  $\kappa_2$ , and mass density  $\rho_2$ , in a dielectric insulator of dielectric constant  $\kappa_1$  and mass density  $\rho_1$ , and if the particle is sufficiently small, then

$$\bar{p}_{\text{eff}} = 4\pi R^3 \epsilon_0 \kappa_1 \left( \frac{\kappa_2 - \kappa_1}{\kappa_2 + 2\kappa_1} \right) \bar{E}. \quad (2)$$

Combining Eqs (1) and (2), the familiar result is

$$\bar{F}^c = 2\pi R^3 \epsilon_0 \kappa_1 \left( \frac{\kappa_2 - \kappa_1}{\kappa_2 + 2\kappa_1} \right) \nabla E^2, \quad (3)$$

which successfully predicts the observed behavior. Particles with  $\kappa_2 > \kappa_1$  are attracted to relative electric field intensity maxima, while for  $\kappa_2 < \kappa_1$ , the particles are attracted to minima.

Garton and Krasucki observed that liquid droplets and bubbles deform into prolate spheroids in the direction of the applied electric field.<sup>7</sup> For prolate spheroids, the DEP force becomes

$$\bar{F}^e = \frac{2\pi a b^2 \epsilon_0 (\kappa_2 - \kappa_1)}{3[1 + (\kappa_2 - \kappa_1)L_z/\kappa_1]} \nabla E^2, \quad (4)$$

where  $a$  and  $b$  are the semi-major and semi-minor axes of the particle, and  $L_z$  is the depolarization factor:

$$L_z = [1 + \frac{3}{5}(1 - \gamma^{-2}) + \frac{3}{7}(1 - \gamma^{-2})^2 + \dots]/3\gamma^2, \text{ and } \gamma = a/b. \quad (5)$$

The ratio  $\gamma$  is uniquely related to  $E$ . For small deformations, i.e.,  $\gamma < 1.1$ , an approximation may be used:<sup>8</sup>

$$\gamma \approx 1 + \frac{\sqrt{3} \epsilon_0 \kappa_1 r_0}{16\delta} \left( \frac{\kappa_1}{\kappa_1 - \kappa_2} - \frac{1}{3} \right)^{-2} (\cos \theta_0)^{-1} E^2, \quad (6)$$

where

$$\theta_0 = \cosh^{-1}(3\sqrt{3}Pr_0/4\delta)/3 \text{ and } r_0 = (R^3P/2\delta + R^2)^{1/2}. \quad (7)$$

$P$  is the absolute ambient pressure and  $\delta$  is the interfacial tension.

#### Properties of Electrostatic Fields

Theorems concerning electric field intensity maxima and minima are very important in DEP levitation. Consider a static, divergence-free electric field  $\bar{E}$  such that

$$\nabla \cdot \bar{E} = 0, \text{ and } \nabla \times \bar{E} = 0. \quad (8)$$

It is easily shown<sup>9</sup> that

$$\nabla^2 E^2 \geq 0. \quad (9)$$

This inequality specifically excludes the possibility of isolated three-dimensional electric field intensity maxima. The existence of isolated intensity minima (including zeroes) is demonstrated by reference to examples such as the quadrupole. Because of the above properties of electrostatic fields, stable, static levitation of particles is possible only for  $\kappa_2 < \kappa_1$ . This restriction places a serious limitation on the application of DEP levitation.

Certain properties of cusped axisymmetric electrostatic fields, useful in DEP levitation cells, may be examined using a Taylor-series expansion due to Holmes.<sup>9</sup> This field expansion, correct to second order in excursions  $(\rho, z')$  about some equilibrium point  $(0, z)$ , is:<sup>10</sup>

$$E_z = V \left[ \alpha_0 + \alpha_1 z' + \alpha_2 \left( z'^2 - \frac{\rho^2}{2} \right) \right], \quad (10)$$

$$E_\rho = V \left[ -\frac{\alpha_1}{2} \rho - \alpha_2 \rho z' \right], \quad (11)$$

where

$$a_n(z) = \frac{1}{Vn!} \left. \frac{\partial^n E_z}{\partial z^n} \right|_{\rho=0, z} \quad (12)$$

and V is the applied voltage. The stability of levitation for  $\kappa_2 < \kappa_1$  is determined by the dual conditions

$$\left. \frac{\partial^2 E^2}{\partial z^2} \right|_{0, z} > 0 \text{ and } \left. \frac{\partial^2 E^2}{\partial \rho^2} \right|_{0, z} > 0, \quad (13)$$

where  $E^2 = E_z^2 + E_\rho^2$ . Using Eqs (10) and (11), Eq. (13) can be reduced to conditions on the coefficients  $a_0, a_1, a_2$ .

### Frequency Dispersion

If the bubble, droplet, or particle and/or the fluid medium are slightly conductive, charge relaxation makes the effective dipole  $\rho_{eff}$  time dependent and dispersive. Benguigui and Lin arrive at a concise result for the time-average DEP force due to an ac dielectric field on a spherical particle with conductivity  $\sigma_2$  in a fluid of conductivity  $\sigma_1$ <sup>11</sup>

$$\bar{F}^e = 2\pi R^3 \epsilon_0 \kappa_1 \left[ \frac{\kappa_2 - \kappa_1}{\kappa_2 + 2\kappa_1} + \frac{3\epsilon_0 (\kappa_1 \sigma_2 - \kappa_2 \sigma_1)}{\tau (\sigma_2 + 2\sigma_1)^2 (1 + \omega^2 \tau^2)} \right] \nabla E_{rms}^2 \quad (14)$$

where  $\omega$  is the radian frequency,  $E_{rms}$  is the rms electric field magnitude, and

$$\tau = \epsilon_0 (\kappa_2 + 2\kappa_1) / (\sigma_2 + 2\sigma_1) \quad (15)$$

is a fundamental charge relaxation time. Equation (14) predicts that the DEP force is frequency-dependent, and a map of the stable regimes of levitation has been provided by Jones and Kallio.<sup>12</sup> (See Table 1.)

Table 1. AC Levitation Conditions

	$\kappa_2 < \kappa_1$	$\kappa_2 \sim \kappa_1$
$\sigma_2 \sim \sigma_1$	Stable levitation for $f > f_c$ only	No stable levitation at any frequency ( $f_c$ is not defined).
$\sigma_2 < \sigma_1$	Stable levitation for all frequencies ( $f_c$ is not defined).	Stable levitation for $f < f_c$ only

$$f_c = \sqrt{(\sigma_1 - \sigma_2) / \epsilon_0 (\kappa_2 - \kappa_1) \tau} / 2\pi$$

For a suddenly applied dc electric field, the DEP force is

$$\bar{F}^e(t) = 2\pi R^3 \epsilon_0 \kappa_1 \left( \frac{\sigma_2 - \sigma_1}{\sigma_2 + 2\sigma_1} \right) (1 - \exp(-t/\tau)) \nabla E^2 + 2\pi R^3 \epsilon_0 \kappa_1 \left( \frac{\kappa_2 - \kappa_1}{\kappa_2 + 2\kappa_1} \right) \exp(-t/\tau) \nabla E^2 \quad (16)$$

Charge relaxation, which governs the build-up and/or decay of free charge at the particle interface, causes these time- and frequency-dependent effects.

### Equations of Motion

The translational equation of motion for a bubble, droplet, or particle in a nonuniform electric field has a fairly general form:

$$m_{eff} \frac{d\bar{v}}{dt} = m_g \bar{g} - b\bar{v} + \bar{F}^e \quad (17)$$

where:<sup>13</sup>

$$m_{eff} = \frac{4\pi}{3} (\rho_2 + \frac{1}{2} \rho_1) R^3, \quad m_g = \frac{4\pi}{3} (\rho_2 - \rho_1) R^3 \quad (18)$$

$\rho_1$  and  $\rho_2$  are mass densities,  $\bar{g}$  is the gravitational acceleration vector,  $\bar{v}$  is the velocity, and  $b$  is a damping coefficient. In viscous fluids, the Stokes drag model for viscous drag can be used:

$$b = \begin{cases} 4\pi\mu_1 R & \text{for spherical bubbles,} \\ 6\pi\mu_1 R & \text{for solid spheres,} \end{cases} \quad (19)$$

where  $\mu_1$  is the dynamic viscosity of the fluid. For a fluid droplet of dynamic viscosity  $\mu_2$ :

$$b = 2\pi\mu_1 R (2\mu_1 + 3\mu_2) / (\mu_1 + \mu_2). \quad (20)$$

Equation (17) may be reduced to a set of linear dynamic equations if the Taylor-series expansion for axisymmetric electrostatic fields is used. Consider the geometry shown in Figure 1. Gravitational acceleration is directed in the  $-z$  direction, so Eq. (17) becomes:

$$m_{\text{eff}} \ddot{z} = -m_g g - b \dot{z} + K \frac{\partial E^2}{\partial z}, \quad (21)$$

$$m_{\text{eff}} \ddot{\rho} = -b \dot{\rho} + K \frac{\partial E^2}{\partial \rho} \quad (22)$$

where:

$$K = 2\pi R^3 \epsilon_0 \kappa_1 (\kappa_2 - \kappa_1) / (\kappa_2 + 2\kappa_1). \quad (23)$$

To linearize Eqs (22) and (23), let:

$$z(t) = z_0 + z'(t), \quad (24)$$

$$\rho(t) = \rho'(t), \text{ and} \quad (25)$$

$$V(t) = V_0 + v'(t) \quad (26)$$

where  $z'$ ,  $\rho'$ , and  $v'$  are all small time-dependent variables. Then, using Eqs (10) and (11),

$$\frac{\partial E^2}{\partial z} = [2\alpha_0 \alpha_1 + 2(\alpha_1^2 + 2\alpha_0 \alpha_2)z'] V_0^2 + 4\alpha_0 \alpha_1 V_0 v', \quad (27)$$

$$\frac{\partial E^2}{\partial \rho} = [2(\frac{\alpha_1^2}{4} - \alpha_0 \alpha_2)\rho'] V_0^2. \quad (28)$$

The equation of equilibrium

$$0 = -m_g g + 2\alpha_0 \alpha_1 K V_0^2 \quad (29)$$

determines the location  $z_0$  of the particle, bubble, or droplet. The perturbation equations are

$$\ddot{z}' + \frac{b}{m_{\text{eff}}} \dot{z}' - \frac{2KV_0^2}{m_{\text{eff}}} (\alpha_1^2 + 2\alpha_0 \alpha_2) z' - \frac{4KV_0}{m_{\text{eff}}} (\alpha_0 \alpha_1) v' = 0 \quad (30)$$

$$\ddot{\rho}' + \frac{b}{m_{\text{eff}}} \dot{\rho}' - \frac{KV_0^2}{m_{\text{eff}}} (\frac{\alpha_1^2}{2} - 2\alpha_0 \alpha_2) \rho' = 0. \quad (31)$$

For passive levitation  $v' = 0$ , and so Eqs (30) and (31) must have stable solutions for equilibrium to be stable. For  $K < 0$  ( $\kappa_2 < \kappa_1$ ), the prescribed conditions on  $\alpha_0$ ,  $\alpha_1$ ,  $\alpha_2$  can be met, but for  $K > 0$  ( $\kappa_2 > \kappa_1$ ), radial and axial stability cannot be achieved simultaneously. Thus, active means must be used to levitate particles or droplets when  $\kappa_2 > \kappa_1$ .

Consider the axisymmetric electrode geometry of Figure 2, which differs from the cusped configuration of Figure 1 in that the maximum electric field intensity is found along the center line. This configuration guarantees radial stability if

$$\alpha_1^2 < 4\alpha_0 \alpha_2. \quad (32)$$

To provide axial stabilization, an error signal proportional to  $z'$  must be generated. Assume that

$$v'/V_0 = -Gz'/L \quad (33)$$

where  $G$  is a dimensionless gain factor and  $L$  is a characteristic cell length. Then:

$$\ddot{z}' + \frac{b}{m_{\text{eff}}} \dot{z}' + \frac{2KV_0^2}{m_{\text{eff}}} [2\alpha_0\alpha_1G/L - \alpha_1^2 - 2\alpha_0\alpha_2] z' = 0. \quad (34)$$

The condition for axial stability is

$$G/L > \alpha_1/2\alpha_0 + \alpha_2/\alpha_1, \quad (35)$$

which can be met with sufficient gain.

Equation (33) assumes that the error voltage  $v'$  is not coupled to  $\rho'$  and that the feedback is ideal with no phase shift. In a practical implementation of active DEP levitation, deviations from such ideal behavior would be expected.

By setting  $v' = 0$  and  $V(t) = V_0 \cos \omega t$ , the parametric stability of Eqs (30) and (31) may be considered. But in the inertially dominated and the heavily damped limits, stability is impossible to achieve for  $K > 0$ .

## Experiment

### Force measurement

Most attempts to measure the dielectrophoretic force and thus check the validity of Eq. (3) involve the use of electrode structures with well-known electrostatic field solutions. Jones and Bliss<sup>5</sup> used wedge-shaped electrodes to measure forces on small gas bubbles in insulating liquid dielectrics. Pohl and Pethig<sup>15</sup> describe experiments with an isomotive electrode structure which features a DEP force that is independent of position within the cell. (See Figure 3.) Within the accuracy of measurement, the experimental results are consistent with DEP theory.

### Levitation

DEP levitation makes possible some interesting applications of dielectrophoresis in terrestrial and extra-terrestrial environments. Veas and Schaeffer levitated small droplets of one liquid suspended in another<sup>4</sup> using a cusped field. Jones and Bliss<sup>5</sup> levitated both air bubbles and liquid droplets in dielectric liquids. Jones and Kallio<sup>12</sup> extended the measurements to various liquids, solid particles, and glass microballoons using the simple electrode geometry shown in Figure 4.

The matter of electrode shape has been pursued further by Jones and McCarthy<sup>16</sup>, who show that the effectiveness of a DEP levitation cell is very sensitive to electrode shape, as shown in normalized plots of the DEP force versus axial particle position in the cell. (Refer to Figure 5.) This observed sensitivity is consistent with the analytical work of Pohl and Pollock.<sup>17</sup>

### Frequency-Dependent Effects

Jones and Kallio<sup>12</sup> attempted to verify the theory concerning variable-frequency levitation of semi-insulating particles using ac and dc electric fields. The results are shown in Table 2.

Some variable frequency DEP levitation experiments using very small cells to levitate 50  $\mu\text{m}$  solid particles<sup>18</sup> and biological materials<sup>19</sup> in aqueous media have also been reported.

### Dielectric Constant Measurement

The use of DEP levitation for measurement of dielectric constant was reported in 1978<sup>6</sup>. All measurements are made with respect to a well-characterized standard dielectric liquid. A small gas bubble is levitated at a fixed position in the cell and the required voltage is noted. Then, the known liquid properties (mass density, dielectric constant) are used to calculate a geometric constant for the cell. The unknown is then introduced to the cell. In the case of an unknown liquid, a gas bubble is again levitated at the same position, or in the case of an unknown solid particle, the particle itself is levitated at the same position. The new voltage is noted and used in an analytic expression to compute the unknown dielectric constant.

Table 2. Results of some ac and dc levitation experiments.

Sphere	Liquid	$f_c$ (Hz)	$\tau_1$ (s)	Successful Levitation?	
				ac <sup>a</sup>	dc
Polystyrene	Transformer oil	0.02	18	No	No
Polystyrene	Silicone fluid		240	Yes	
Polystyrene	Corn oil		0.55	Yes	
Polystyrene	Castor oil		0.40	Yes	Yes
Polyvinyl acetate	Transformer oil		18	No	No
Polyvinyl acetate	Silicone fluid		240	No	
Polyvinyl acetate	Corn oil	0.7	0.55	No	No
Polyvinyl acetate	Castor oil		0.40	Yes	
Glass microballoon	Transformer oil	7	0.18	Yes	No
Glass microballoon	Corn oil	4	0.55	Yes	No
Solid glass	Corn oil		0.55	No	
Solid glass	Castor oil		0.40	No	

<sup>a</sup>  $f > 45$  Hz for all ac experiments.

Loomans and Jones<sup>20</sup> have investigated certain size-dependent phenomena (principally elongation) that have an effect on the accuracy of this DEP dielectric constant measurement scheme. They found up to 0.5% discrepancy in the volume normalized DEP force between small (<200  $\mu\text{m}$ ) and large ( $\sim 1200$   $\mu\text{m}$ ) diameter bubbles levitated in a cusped electrostatic field. (See Figure 6.)

#### Bubble and Particle Control

Appropriate design of electrodes permits the manipulation of bubbles and particles suspended in dielectric liquids. Figure 7a illustrates one periodic electrode structure that can be used for the conveyance of bubbles or particles. Depending on how the "bubble ladder" is connected, bubbles, etc., are collected and held at various locations between the rings. If the rings are connected to multiple-phase ac voltage, a synchronous pumping and delivery of the bubbles or particles should be possible. Another simple means of conveyance for bubbles and particles is shown in Figure 7b. Four electrode rods of alternate polarity are arranged parallel, forming a two-dimensional null along the axis. Bubbles or any particle with  $\kappa_2 < \kappa_1$  are attracted to this null and, therefore, can be conveyed along the axis of the bubble conduit using buoyancy or other means.

#### Work to be Done

Active feedback levitation of particles with  $\kappa_2 > \kappa_1$  has not been demonstrated yet. Such a demonstration would greatly extend the capabilities of DEP levitation. No zero-gravity demonstrations of DEP phenomena have been attempted. Experimental verification of zero-gravity levitation of bubbles, fluid droplets, or particles at a null in an electrostatic field is needed to evaluate the dielectrophoretic effect in extra-terrestrial applications.

#### Conclusion

Dielectrophoresis offers some unique capabilities for the control and manipulation of small uncharged gas bubbles, liquid droplets, and solid particles suspended in liquid media. Investigators have successfully levitated and controlled various particles (up to 1 mm in diameter) in dielectric fluid media using intense electric fields. Using more modest electric fields, levitation experiments have been extended down to small particles (<50  $\mu\text{m}$ ) in aqueous media. The limit on dielectrophoresis imposed by Joule heating is most harmful in large electrode geometries or in highly conducting liquids, where electric fields of sufficient strength for DEP cannot be imposed. Charge relaxation produces significant frequency-dependent effects on the dielectrophoretic force, which can be used to characterize the electrical and dielectric properties of unknown solid and liquid media.

In applications not requiring stable levitation, dielectrophoretic forces can be used for separation, agglomeration, collection of bubbles, droplets, and particles with no real restrictions on relative dielectric constants. But a fundamental electrostatic theorem, which permits local three-dimensional field intensity minima, while excluding such maxima, imposes the condition  $\kappa_2 < \kappa_1$  for stable static levitation. This condition must be generalized for the dispersive case (see Table 1). However, active feedback may be used to levitate particles when  $\kappa_2 > \kappa_1$ .

## Applications

The study of bubbles, droplets, and particles suspended in liquid media is important in many fields of science and technology. Dielectrophoretic phenomena, since they represent an important case of interactions of electric fields with these small multi-phase systems, merit attention. Some general categories of DEP experiments of at least potential interest in the weak gravitational environment of space are discussed below.

- Zero-gravity hydrodynamics - Levitation of bubbles and droplets in space provides the opportunity to study reduced and zero gravity hydrodynamics. DEP levitation might afford unique opportunities to observe the dynamics of uncharged dielectric liquid droplets and bubbles.
- Multi-phase separations - Some preliminary work on using nonuniform electric fields to separate constituents in gas/liquid and solid/liquid systems in zero gravity has been reported. New space manufacturing processes which require separation could benefit from DEP techniques.
- Biology in space - New opportunities for biological experimentation on living cells exist in reduced gravity. DEP levitation can be used to position cellular materials in vitro and to perform certain dielectric measurement diagnostics.
- Electrochemical experiments - Limited experience exists in the study of solid particles in aqueous media using DEP levitation. Using variable-frequency techniques, the dispersive nature of double layers in electrolytes may be investigated using certain types of small particles.
- High-voltage engineering - DEP levitation affords a means to study solid/liquid/gas interactions in the presence of strong electric fields. Bubbles and particulate impurities are known to be important in the breakdown of dielectric liquids. Experience with liquid insulants in zero gravity is very limited. Thus, dielectrophoretic levitation may be a useful investigative tool in extra-terrestrial, high-voltage engineering applications.
- Dielectric measurements - The dielectric constant measurement scheme described elsewhere in this paper offers a unique opportunity for the nondestructive evaluation of solid dielectric particles from power to audio frequencies and rf. Simple  $\epsilon'$  measurements on liquids have already been demonstrated.

Other applications of dielectrophoretic effects, in general, and DEP levitation, in particular, may be envisioned. For example, processing and ultrasonic cleaning of small spherical particles, such as laser targets, might be possible using DEP levitation. Levitated particles can be rotated to improve the uniformity of coating operations in wet processing.<sup>12</sup>

Dielectrophoretic phenomena offer unique means to control and manipulate small, uncharged gas bubbles, liquid droplets, and solid particles suspended in liquid media. In the reduced gravitational environment of space, these nonuniform electrostatic field effects can be used to provide a controllable body force which is localized and tailored to requirements by proper electrode design. A better understanding and appreciation of dielectrophoresis will enhance the basic investigations of drops and bubbles and may open some new opportunities for space processing of materials.

## Acknowledgments

This paper is based on work performed for the National Bureau of Standards and for the Laser Program at Lawrence Livermore Laboratory. Their support is gratefully acknowledged.

## References

1. Pohl, H.A., "The Motion and Precipitation of Suspensoids in Divergent Electric Fields," J. Appl. Phys. 22 (1951) 869.
2. Pohl, H.A., and Hawk, I., "Separation of Living and Dead Cells by Dielectrophoresis," Science, 152 (1966) 647.
3. Benguigui, L. and Lin, I.J., "Dielectrophoretic Filtration of Nonconductive Liquids," Separation Science and Technology, to appear.
4. Veas, F., and Schaeffer, M.J., "Stable Levitation of a Dielectric Liquid in a Multiple-Frequency Electric Field," Proceedings of Int'l Symposium on Electrohydrodynamics, Massachusetts Institute of Technology, March-April 1969, pp. 113-115.

5. Jones, T.B., and Bliss, G.W., "Bubble Dielectrophoresis," J. Appl. Phys., 48 (1977) 1412.
6. Kallio, G.A., and Jones, T.B., "Dielectric Constant Measurements Using Dielectrophoretic Levitation," IEEE Trans. Industry Applic., IA-16 (1980) 69.
7. Garton, C.G., and Krasucki, Z., "Bubbles in Insulating Liquids: Stability in an Electric Field," Proc. Royal Soc. (London), A280 (1964) 211.
8. Jones, T.B., and McCarthy, M.J., "Deformation of Liquid Droplets and Gas Bubbles in Electric Fields," May 1976, unpublished.
9. Holmes, L.M., "Stability of Magnetic Levitation," J. Appl. Phys., 49 (1978) 3103.
10. Jones, T.B., "Cusped Electrostatic Fields for Dielectrophoretic Levitation," J. Electrostatics, 11 (1981) 85-95.
11. Benguigui, L. and Lin, I.J., "More About the Dielectrophoretic Force," 1981, unpublished.
12. Jones, T.B. and Kallio, G.A., "Dielectrophoretic Levitation of Spheres and Shells," J. Electrostatics 6 (1979) 207.
13. Lamb, H., Hydrodynamics (Dover, New York, 1945) art. 92.
14. Levich, V.G., Physicochemical Hydrodynamics, (Prentice-Hall, Englewood Cliffs, N.J. 1962) art. 70.
15. Pohl, H.A., and Pethig, R., "Dielectric Measurements Using Nonuniform Electric Field (Dielectrophoretic) Effects," J. Phys. E. 10 (1977) 190.
16. Jones, T.B., and McCarthy, M.J., "Electrode Geometries for Dielectrophoretic Levitation," J. Electrostatics 11 (1981) 71-83.
17. Pohl, H.A., and Pollock, K., "Electrode Geometries for Various Dielectrophoretic Force Laws," J. Electrostatics 5 (1978) 337.
18. Bahaj, A.S., and Bailey, A.G., "Dielectrophoresis of Small Particles," Proceedings of IEEE-Industry Applications Society 1979 Annual Meeting, Cleveland, Ohio, October 1979, pp. 154-157.
19. Kaler, K., and Pohl, H.A., "Dynamic Dielectrophoretic Levitation of Living Individual Cells," Proceedings of IEEE-Industry Application Society 1979 Annual Meeting, Cleveland, Ohio, October 1979, pp. 214-217.
20. Jones, T.B., and Loomans, L.W., "Size Effect in Dielectrophoretic Levitation," 1981, in preparation.

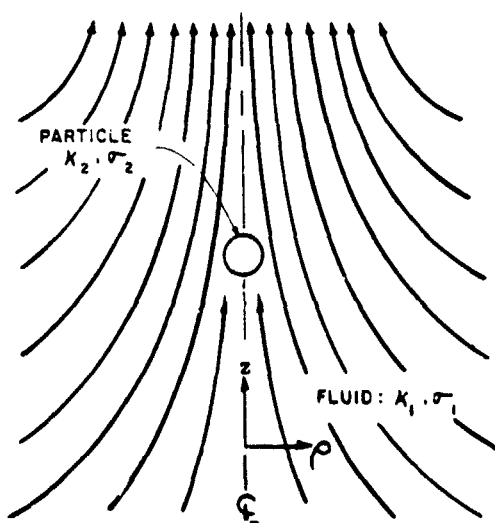


Figure 1. Axisymmetric cusped electrostatic field for passive dielectrophoretic levitation. ( $K_2 < K_1$ )

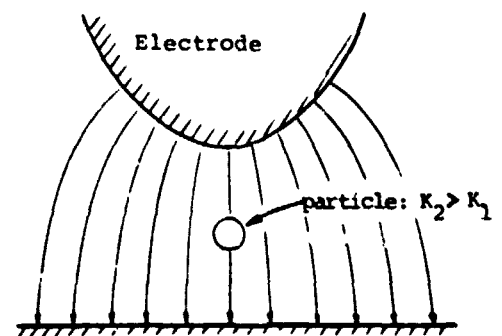


Figure 2. Axisymmetric electrostatic field for active feedback dielectrophoretic levitation.

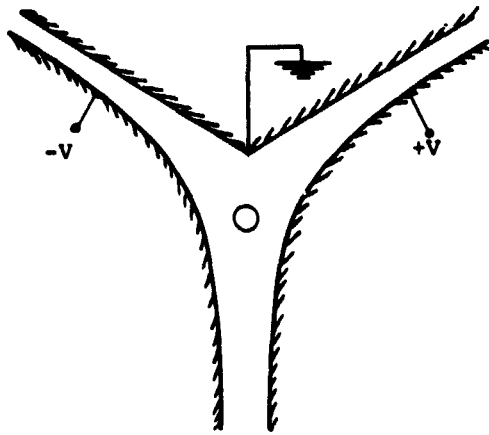


Figure 3. Isomotive electrode structure of Pohl and Pethig [15].

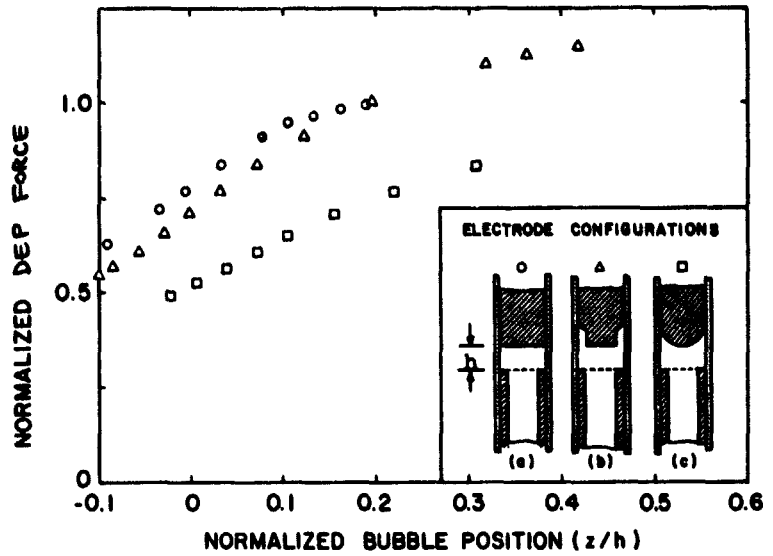


Figure 5. Typical normalized DEP force data for various electrode geometries.

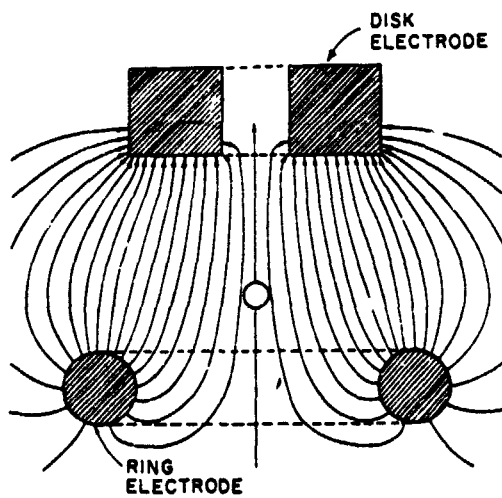


Figure 4. Cusped levitator geometry employing ring and disk electrodes.

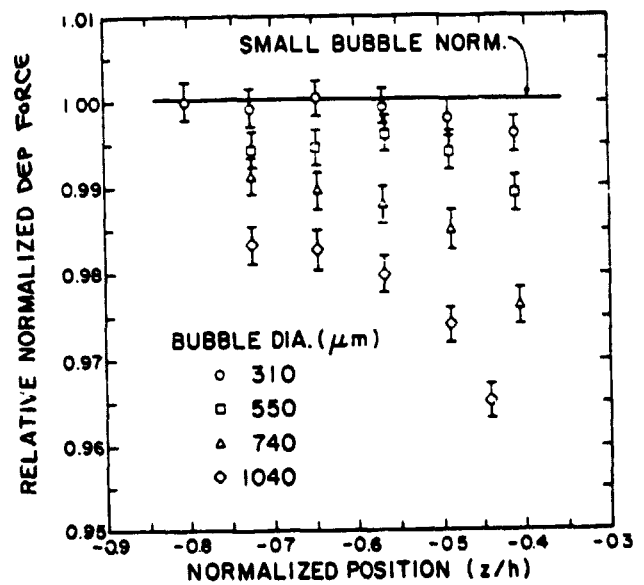


Figure 6. Normalized DEP force data versus position for bubbles of various sizes.

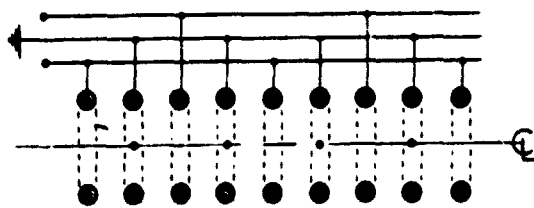
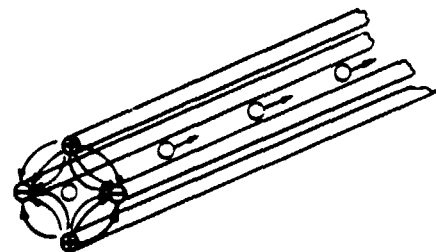


Figure 7. a) Periodic electrode structure for synchronous DEP bubble or particle transport.



b) DEP bubble/particle conduit.

## The motion of bubbles inside drops in containerless processing

N. Shankar, P. Annamalai, Robert Cole and R. Shankar Subramanian

Department of Chemical Engineering, Clarkson College of Technology  
Potsdam, New York 13676Abstract

A theoretical model of thermocapillary bubble motion inside a drop, located in a space laboratory, due to an arbitrary axisymmetric temperature distribution on the drop surface is constructed. Typical results for the stream function and temperature fields as well as the migration velocity of the bubble are obtained in the quasistatic limit.

The motion of bubbles in a rotating body of liquid is studied experimentally, and an approximate theoretical model is developed. Comparison of the experimental observations of the bubble trajectories and centering times with theoretical predictions lends qualified support to the theory.

Introduction

With the advent of the Space Shuttle, orbital processing of materials over extended periods of time will become realizable in the near future. The near free fall environment aboard orbiting spacecraft is particularly attractive for containerless operation. For instance, materials may be melted while suspended, and cooled without contacting a container. It has been suggested that certain high technology glasses which are difficult or impossible to make on earth because of container-wall-induced heterogeneous nucleation can be made in a free fall environment.<sup>1,2</sup> Other applications for containerless processing include the measurement of physical properties of highly reactive melts, and the preparation of ultrapure materials which are easily contaminated by containers.

In many of the above applications, it is likely that gas bubbles will be formed in the melts processed in space. For instance, in the manufacture of glasses, bubbles are formed due to the liberation of gaseous products from chemical reactions. The removal of such bubbles is essential to the preparation of a useful final product. At Clarkson, with financial support from NASA, experiments are being designed for flight aboard NASA rockets and the Space Shuttle on the subject of surface tension gradient driven motion of gas bubbles in glass melts and model fluids. The experiments will involve the photographic observation, under reduced gravity conditions, of the motion of, and the interaction among, bubbles in a liquid drop which is spot-heated. They are described in detail elsewhere.<sup>3,4</sup>

Another topic to be addressed, in our free fall experiments, is the centering of gas bubbles inside a liquid drop. Such centering plays an important role in the process currently employed for the production of uniform hollow glass shells (microballoons) used in inertial confinement fusion research.<sup>5</sup> Typically, a collection of gel particles is dropped into a vertical tube furnace. The particles melt and gas bubbles form. At some point, these bubbles coalesce into a large bubble which centers itself inside the molten glass drop. At the bottom of the furnace, fairly uniform shells are obtained.<sup>5</sup> In view of the conditions of operation in the production process, it is quite difficult to isolate a single particle, and follow its time-temperature history carefully. Thus, there is considerable uncertainty at this time concerning the mechanisms which might be operative in centering the bubble inside the molten liquid drop in the furnace. The sphericity and wall-thickness uniformity of the hollow glass shells obtained is crucial to the success of the fusion process wherein the shells are filled with a Deuterium-Tritium mixture and an implosion is achieved by irradiation with a laser pulse or an ion beam.<sup>6</sup>

In the near free fall conditions aboard the Shuttle, a bubble can be introduced into a liquid drop and various centering mechanisms such as rotation, oscillation, expansion/contraction, etc., which have been proposed to date, can be studied. Manipulation of the drop and bubble system may be achieved using acoustic fields.<sup>7,8</sup>

In this presentation, some of our ground-based research on the motion of bubbles inside drops will be described. Theoretical work has been performed on thermocapillary bubble migration inside a drop, and is being reported in the literature.<sup>9,10</sup> More details will be given in (11). Experimental work is under way on the behavior of bubbles placed inside a rotating liquid body. Some of this work is being reported in the literature<sup>12</sup> and details may be found in (13).

### Thermocapillary motion of bubbles inside drops

A bubble placed inside a drop in the absence of gravity will move if a non-uniform temperature field is induced and maintained on the drop surface. This motion will be a direct consequence of the tangential stresses at both the drop surface and the bubble-liquid interface caused by the variation of surface tension with temperature. Such stresses will induce motion in the liquid shell due to viscous traction, and cause the movement of the bubble. In fact, a gas bubble placed in a quiescent liquid body with a non-uniform temperature field will propel itself toward the warmer regions in the liquid by causing motion of the liquid in its vicinity. The problem of the isolated bubble has been examined in the past, and both theoretical<sup>14,15</sup> and experimental<sup>14,16</sup> results are available.

In the present problem, several variations may be posed. When the prescribed temperature field is axially symmetric (as obtained perhaps by spot-heating the drop), and when the bubble is located along this symmetry axis, the velocity and temperature fields in the liquid shell will possess axial symmetry. Furthermore, we restrict attention to the quasi-static limit wherein the unsteady accumulation terms as well as the convective transport terms are ignored in comparison to the molecular transport terms in the governing conservation equations. In this case, the equations of conservation of momentum and energy are linear, and the powerful principle of superposition can be used to construct solutions.<sup>17-19</sup> The general solutions presented in (18,19) may be specialized to the boundary conditions applicable to our problem in a straightforward, but tedious manner. Details are presented elsewhere.<sup>9-11</sup>

In view of the linearity of the governing equations, the resulting motion of the bubble may be studied conveniently by decomposing the arbitrary temperature field into spherical harmonics. The scaled migration velocity ( $U$ ) of the bubble has been calculated as a function of reduced bubble size  $\kappa$  (Bubble radius/Drop radius) and the scaled distance between the drop and bubble centers  $D$  (scaled using drop radius) for the first three Legendre modes of the surface temperature field. As expected, in all these cases, the bubble moves towards the nearest warm pole. For a  $P_1$ -mode surface temperature field, for a fixed  $\kappa$ , the velocity of the bubble  $U$  increases with decrease in  $D$ , and reaches a maximum when the bubble reaches the center of the drop. For higher modes,  $U$  first increases from its value of zero at  $D = 0$  for increasing  $D$ , but ultimately decreases as the bubble approaches the drop surface. For all modes, for fixed  $D$ , the velocity of the bubble increases with  $\kappa$ , for a wide range of values of  $\kappa$ .

A typical set of results for the isotherms and streamlines induced by a  $P_1$ -mode surface temperature field is presented in figure 1. Here, due to the symmetry of the fluid flow, a bubble placed anywhere on the symmetry axis will move toward the warm pole along the symmetry axis. However, for the  $P_2$  and higher modes of the surface temperature field, a bubble located at the center of the drop will not move. Any displacement of the bubble from the drop center will result in the motion of the bubble to the nearest warm pole (not shown). Detailed results on the motion of the bubble are given elsewhere.<sup>9-11</sup>

We also might note here that a simple approximation can be constructed for the bubble velocity for relatively small bubble size. This approximation, presented in (9,10) involves the calculation of the streaming velocity of the fluid in the drop at the location of the bubble center in the absence of the bubble using results available in the literature.<sup>20</sup> Then, the thermocapillary migration velocity of an isolated bubble in a quiescent liquid subjected to the temperature gradient existing in the drop at the location of the bubble center (but in the absence of the bubble) is computed from (14). The two are added to give the desired approximation. As shown in (9,10) this approximation is quite good for relative bubble radii of up to a tenth of the drop radius, and for even larger values when the bubble is close to the center of the drop.

### Bubble motion in a rotating liquid

A gas bubble in a rotating liquid body will experience buoyancy toward the axis of rotation due to the radial acceleration field quite analogous to upward buoyancy due to earth's gravity.<sup>21-24</sup> Relatively small bubbles, introduced into highly viscous liquids rotating at small angular velocities, will migrate principally in the radial direction when viewed in a reference frame rotating with the liquid. Coriolis deflection under these conditions will be a small secondary effect.

In an effort to investigate this bubble centering mechanism, we have performed experiments using a spherical thin-walled glass shell approximately 70 mm in diameter. The shell is filled with a Dow-Corning DC-200 series silicone oil through a hole on the surface of the sphere, leaving a small air bubble (~2 mm diameter) in the liquid, and sealed using a piece of gum-tape. The bubble is initially located at the highest point in the liquid, a position dictated by gravity. The shell is then rotated about a horizontal axis with the aid of a D.C. motor. The bubble spirals in toward the rotation axis on the equatorial plane of the

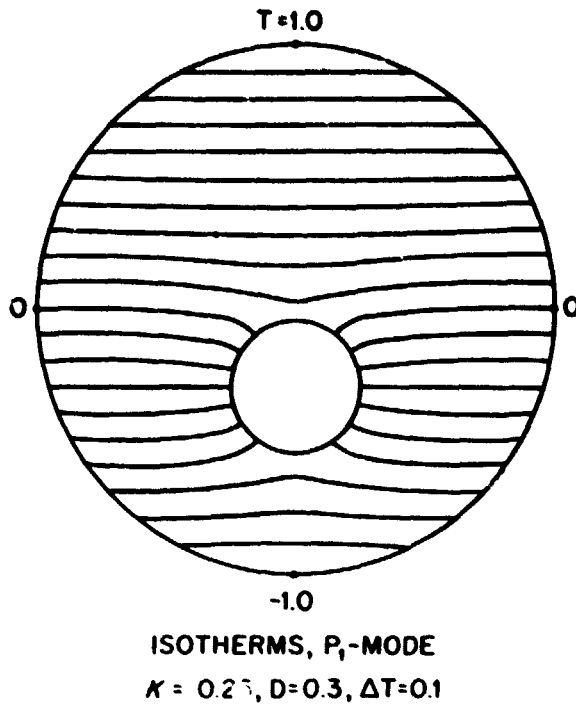


Figure 1a. Isotherms for the eccentric bubble system for a P<sub>1</sub>-mode temperature field on the drop surface, κ = 0.25, D = 0.3.

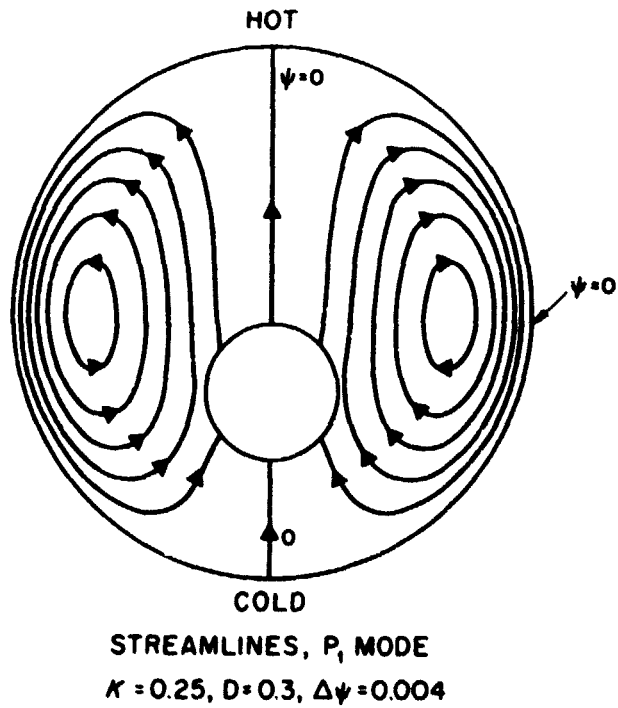


Figure 1b. Streamlines for the eccentric bubble system for a P<sub>1</sub>-mode temperature field on the drop surface, κ = 0.25, D = 0.3.

shell, and the process is recorded using a high speed motion picture camera, or a video camera depending on the rotation rate of the sphere for the experimental run. More details may be found in (12,13).

In Figure 2, experimental data are shown for a typical run. The radial position of the bubble, scaled by the shell radius, and corrected for optical displacement effects, is plotted against time, and the migration of the bubble to the rotation axis may be seen clearly. An approximate theoretical description of the migration process has been developed<sup>12,13</sup> and the prediction from theory may be seen to be in reasonable agreement with the data shown in Figure 2. The effects of secondary flows during spin-up and gravity on the bubble migration process have been discussed elsewhere.<sup>12</sup>

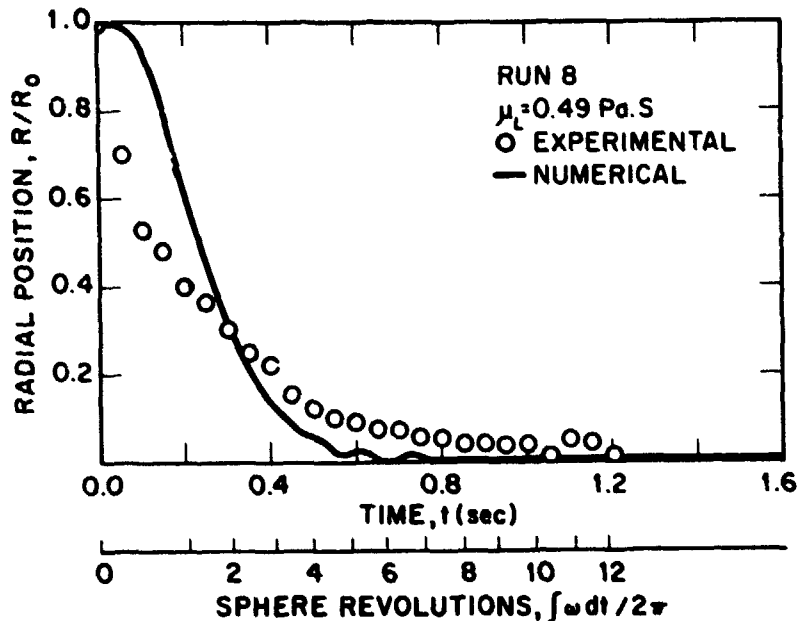


Figure 2. Bubble migration towards the rotation axis as a function of time (upper scale) and of cumulative sphere revolutions (lower scale) for Run 8.

#### Conclusions

Some potential mechanisms for the migration of gas bubbles in liquid bodies under reduced gravity conditions have been presented and discussed. Theoretical predictions indicate that thermocapillary migration may be used to move bubble to the surface of a liquid drop, and experimental data suggest that rotation of a drop containing bubbles is a useful mechanism for moving bubbles to the center of a drop. Both of the above mechanisms, being independent of gravity, may be effectively used to manage gas bubbles in space processing.

#### Acknowledgments

This work was supported by the Materials Processing in Space Program Office of the National Aeronautics and Space Administration through a contract (NAS8-32944) from the Marshall Space Flight Center to Clarkson College of Technology. We are grateful to the Dow-Corning Corporation for donating the DC-200 series silicone oils used in this study.

#### References

1. Weinberg, M. C., Glass Industry, p. 22, March 1978 .
2. Nielson, G. F., and Weinberg, M. C., "Outer Space Formation of a Laser Host Glass," J. Non-crystalline Solids 23, 43. 1977.
3. Subramanian, R. S. and Cole, R., "Experiment Requirements and Implementation Plan (ERIP) for Physical Phenomena in Containerless Glass Processing," NASA Marshall Flight Center, Document 77FR010, August 1979.
4. Annamalai, P., Shankar, N., Cole, R., and Subramanian, R. S., "Bubble Migration Inside a Liquid Drop in a Space Laboratory," Appl. Sci. Res., in press. 1982.

5. Nolen, R. L., Downs, R. L., Miller, N. J., Elmer, M. A., Doletzky, N. E. and Solomon, D. E., "Inertial Confinement Fusion," Optical Society of America, Washington. 1978.
6. Woerner, R. L., Draper, V. F., Koo, J. C., and Hendricks, C. D., Conference on Inertial Confinement Fusion, Digest of Technical Papers, Optical Society of America, Washington. p. 32. 1980.
7. Whymark, R. R., "Acoustic Field Positioning for Containerless Processing," *Ultrasonics*, pp. 251-261. November 1975.
8. Wang, T. G., Saffren, M. M., and Elleman, D. D., in "Proceedings of the International Colloquium on Drops and Bubbles" (Ed. D. J. Collins et al.), Pasadena, CA, pp. 266-299. 1974.
9. Shankar, N., Cole, R., and Subramanian, R.S., "Thermocapillary Migration of a Fluid Droplet Inside a Drop in a Space Laboratory," *Int. J. Multiphase Flow* 7, (6) 581-594. 1981.
10. Shankar, N., and Subramanian, R. S., "The Slow Axisymmetric Thermocapillary Migration of an Eccentrically Placed Bubble Inside a Drop in a Space Laboratory," submitted to *J. Fluid Mech.*
11. Shankar, N., Ph.D. thesis in Chemical Engineering, Clarkson College of Technology, in progress.
12. Annamalai, P., Subramanian, R. S., and Cole, R., "Bubble Migration in a Rotating, Liquid-Filled Sphere: Application to the Formation of Hollow Glass Laser Fusion Targets," submitted to *Phys. Fluids*.
13. Annamalai, P., "Bubble Motion in a Rotating Liquid," M.S. Thesis, Clarkson College of Technology. 1979.
14. Young, N. O., Goldstein, J. S., and Block, M. J., "The Motion of Bubbles in a Vertical Temperature Gradient," *J. Fluid Mech.* 6, 350. 1959.
15. Subramanian, R. S., "Slow Migration of a Gas Bubble in a Thermal Gradient," *AIChE J.* 27 (4), 646. 1981.
16. Hardy, S., *J. Colloid Interface Sci.* 69, (1), 157. 1979.
17. Happel, J., and Brenner, H., *Low Reynolds Number Hydrodynamics*, Prentice Hall, Englewood Cliffs, New Jersey. 1965.
18. Jeffery, G. B., *Proc. Roy Soc. London* A87, 109. 1912.
19. Stimson, M., and Jeffery, G. B., *Proc. Roy. Soc. London* A111, 110. 1926.
20. Drago, A. L., in proceedings of the International Colloquium on Drops and Bubbles, (D. J. Collins et al., Ed), Jet Propulsion Laboratory, California, pp. 208. 1974.
21. Clifton, J. V., Hopkins, R. A., and Goodwin, D. W., "Motion of a Bubble in a Rotating Liquid," *J. of Spacecraft* 6, 215. 1969.
22. Schrage, D. L., and Perkins, Jr., H. C., "Isothermal Bubble Motion Through a Rotating Liquid," *J. Basic Engg. Trans. ASME*, 187. March 1972.
23. Siekmann, J., and Johann, W., "On Bubble Motion in a Rotating Liquid Under Simulated Low and Zero Gravity," *Ingenieur Archiv* 45, 307. 1976.
24. Siekmann, J., and Dittrich, K., "Note on Bubble Motion in a Rotating Liquid Under Residual Gravity," *J. of Non-linear Mechanics* 12, 409. 1977.

## Acoustically Induced Oscillation and Rotation of a Large Drop in Space

Nathan Jacobi, Arvid P. Croonquist, Daniel D. Elleman, and Taylor G. Wang

Jet Propulsion Laboratory, California Institute of Technology  
Pasadena, California 91109

### Abstract

A 2.5 cm diameter water drop was successfully deployed and manipulated in a triaxial acoustic resonance chamber during a 240 sec low-gravity SPAR rocket flight. Oscillation and rotation were induced by modulating and phase shifting the signals to the speakers. Portions of the film record were digitized and analyzed. Spectral analysis brought out the  $n = 2, 3, 4$  free oscillation modes of the drop, its very low-frequency center-of-mass motion in the acoustic potential well, and the forced oscillation frequency. The drop boundaries were least-square fitted to general ellipses, providing eccentricities of the distorted drop. The normalized equatorial area of the rotating drop was plotted vs a rotational parameter, and was in excellent agreement with values derived from the theory of equilibrium shapes of rotating liquid drops.

### Introduction

This report describes an experimental study which is contributing to the understanding of containerless processing of molten materials in space. This study was performed on a 2.5 cm diameter water drop successfully deployed and manipulated in a triaxial acoustic resonance chamber during a 5 min SPAR (Space Processing Applications Rocket) flight. Three aspects of containerless processing technology in space are of particular interest: stability, oscillation, and rotation of a molten sample. Stability studies will help us determine the effect of residual g-jitter on the positioned sample, as well as the focusing requirement of the optics. Oscillation studies will enable us to measure the surface tension of the sample, as well as to better understand induced mixing currents within a liquid melt. Rotation studies will demonstrate the feasibility of degassing and shaping melts. In addition, a rotating sample can even out the nonuniformity of the temperature environment.

With these broad objectives in mind, the primary objectives of this flight were to: (1) Study the center-of-mass motion in an acoustic chamber. The initial velocity and position of the drop due to the retraction of the injectors gave the drop energy to oscillate in the acoustic potential well throughout most of the experiment. Effects of g-jitter on this motion can be observed from the film record and accelerometer telemetry. (2) Determine the rotation capability of the acoustic chamber. The torque on the drop generated by the acoustic field slowly rotates the drop up to 2 rps. The rate of spin-up establishes the rotation capability of the chamber on a liquid drop. (3) Study the drop shape change due to rotation. The shapes of the drop in near rigid-body rotation from this experiment are compared with existing equilibrium shape calculations. If rotation is to be used as a method of shaping liquid melts, it is important to determine the deviation between calculated and observed shapes. (4) Study the frequency response and damping mechanisms of drop oscillations for both free and forced oscillations. The initial perturbation of the drop shape generated by the drop injection system is allowed to damp down with the acoustic field on. The time required for the positioned liquid drop to approach its quiescent state can be determined from the film record.

### Apparatus and Operation

A schematic drawing of the payload is shown in Fig. 1. The heart of the apparatus is a triaxial acoustic resonance chamber which is used to position and control large liquid drops in low-g environments. The chamber itself is nearly cubical, with inside dimensions of 11.43 x 11.43 x 12.70 cm. Three acoustic drivers are fixed rigidly to the center of three mutually perpendicular faces of the chamber. During operation of the chamber, each driver excites the lowest-order standing wave along the direction that it faces. In the resonant mode, the acoustic pressure is maximum at the nodes of the velocity wave (i.e., at the walls) and minimum at the antinodes (the center). There is a tendency for introduced liquids and particles to be driven toward the antinodes, where they collect and remain until excitation ceases.

Rotation of the sample requires that two dimensions of the chamber, the x and y, be of the same length and that the x and y drivers be driven at the same frequency with a phase separation of 90°. For non-rotation applications, the two axes can be driven at 0° or 180° with respect to one another. However, at these phase shifts, interference patterns

are produced in the chamber that seriously distort the shape of the drop. In order to alleviate this problem, the acoustic fields are turned on and off in a cyclic manner so that when the x axis acoustic field is on the y acoustic field is off, and when the x is off the y is on. This complementary modulation of the x and y axes is done at a frequency that is high compared to the frequencies of the lowest normal modes of the drop.

The acoustic chamber was located in the rocket payload so that the z axis of the chamber was parallel to the center line of the rocket (Fig. 1). The bulk of the data from this experiment was obtained with a 16 mm cine camera, run at 48 frames per second. The camera was directed along the z axis; in addition, two mirrors gave nearby orthogonal views along the x and y axes. The sound intensity at each wall, the deployment system condition, camera and lighting status, and the frequency of the z-axis signal were monitored, telemetered to the ground station and recorded in real time.

This type of acoustic resonance chamber was designed by Wang et al.<sup>1</sup> for levitation and space processing applications. More details and the results of analysis of a previous SPAR flight can be found in Jacobi et al.<sup>2</sup>

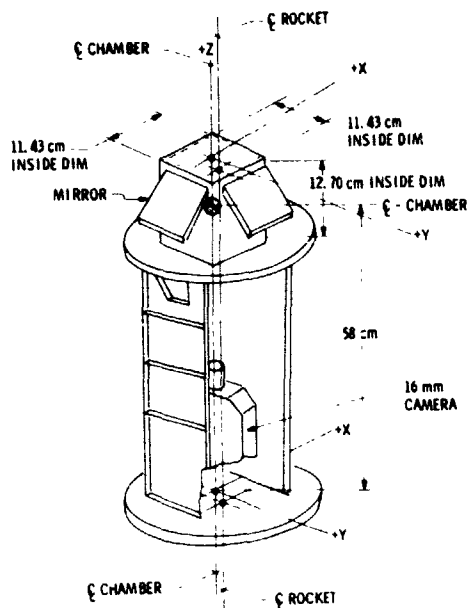


Fig. 1. Schematic drawing of the SPAR payload showing the acoustic chamber, cine camera, and mirrors.

Data Analysis

The timing for the various phases of this flight experiment is presented in Table 1. The following five time sequences were identified for analysis.

- (a) Free oscillation (127-145 sec). When the fluid injectors were retracted, the drop was held in position by the acoustic field. Free oscillations (excited by the retracting injectors) damped out, and the drop moved back and forth in the acoustic potential well. This part was used to observe free oscillations, to measure the radius of the drop, and to study its center-of-mass motion.

Table 1. Sequence of Events

Clock Time (sec after lift-off)	Event
85	Camera on
90	Complementary modulation on
105	Fluid delivered through injector
117	Fluid delivery off
127	Fluid injectors extracted
127-145	Free oscillation
145	z modulation on
145-265	Forced oscillation
265	z modulation off
265-300	Drop relaxation
300	Complementary modulation off; 90 phase shift
300-330	Induced rotation
330	90° phase shift off; complementary modulation on
330-360	Coasting
365.5	Drop hits wall

## BLACK AND WHITE PHOTOGRAPH

- (b) Forced oscillation (145-147 sec). As the acoustic pressure along the z axis was modulated at a low frequency, the resulting oscillations of the drop were very regular for three seconds.
- (c) Combined oscillation and rotation (147-265 sec). The regular behavior of the drop's response to the z axis modulation quickly developed an unexpected twist: to the large amplitude oscillation was added rotation of the drop. This sequence is the most difficult and intriguing one to interpret. The acoustic forces and torques on a strongly deformed drop at an arbitrary position are poorly understood.
- (d) Relaxation of the drop (265-300 sec). With the complementary modulation of the x and y axes on, the drop relaxed prior to being spun up. The information in this sequence was similar to that in sequence (a).
- (e) Spin-up of the drop (300-330 sec). With a phase difference of  $90^\circ$  between the x and y pressure amplitudes, a torque was generated on the drop which caused it to rotate the z axis. Deformed shapes were observed, which can be compared with theoretical predictions of the equilibrium shape of a rotating liquid drop.

The strategy used for the data analysis of the 16 mm cine film record consisted of preliminary analysis performed on a Vanguard Motion Film Analyzer and a more detailed study of fully-digitized boundaries of selected frames (provided by JPL's Image Processing Laboratory) using a small computer. A sample cine frame is shown in Fig. 2a, from the forced oscillation sequence. Figure 2b shows the computer-digitized boundaries for the frame in the preceding photograph. Both the "raw" data and a quadratically-smoothed boundary are shown for each of the three views. It must be noted that, despite the satisfactory appearance of the original photograph, some irregularities do appear in the digitized and smoothed versions. These may be due to overlap with the speaker ports, specular or back reflections, or to a peculiarity in the digitization algorithm. It is a persistent feature throughout the film. Table 2 shows the frame sequences that were digitized and the frame densities. The total number of frames processed was 1826, with typically 90 to 150 points per boundary. The boundary data were recorded in the form of 3-digit integers, thus placing a limit upon the resolution of the digitization.



Fig. 2a. Typical frame from the 16 mm record which shows three orthogonal views of the drop undergoing forced oscillation ( $t = 147.0$  sec).

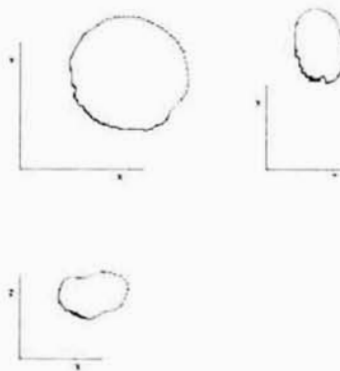


Fig. 2b. Digitized boundaries of the drop images shown in a. The points are "raw" data and the lines are their quadratically-smoothed description.

Table 2. Digitized Frames		
Time (sec)	Event	Density
127.1--130.4	Free oscillation	1/1
130.4--144.6	Free oscillation	1/3
144.6--147.1	Forced response: regular	1/1
147.1--170.4	Forced response: rotation	1/3
263.7--300.4	Free oscillation	1/4
300.4--333.7	Rotation	1/5

It was felt that prior to the automatic processing of relatively large amounts of data, it would be useful to investigate some of the interesting features on a Vanguard

Motion Film Analyzer. These measurements provided some insight into what might be expected from a more detailed analysis. Three topics were handled with this simple technique. As the drop moved periodically in the acoustic potential well, the frequency of the motion was measured and compared with a theoretical prediction approximating the acoustic potential well by an equivalent harmonic oscillator potential. These frequencies are correlated with the acoustic force and with the pressure level in the chamber. The two lowest normal mode frequencies,  $f_2$  and  $f_1$ , were identified. With a knowledge of the surface tension, measured shortly before the flight, these measurements were used to infer the volume of the drop. The ratio of the minor to major axes was measured before, during, and after the rotation sequence. While there was significant scatter in the results, the ratio was close to 1.0 prior to rotation, and showed a measurable change when the drop was spun up.

While some of the main results will be described on the following pages, more details concerning the analysis of this flight can be found in the report by Wang et al.<sup>3</sup>

Numerical tests. As another preparatory step to the data analysis, it was decided to investigate numerical test cases involving the recovery of a known signal in the presence of various amounts of noise. The first of two such experiments was designed to recover the coefficients of the normal modes of a perturbed boundary, a situation which is encountered when analyzing the oscillatory motion of a drop. The boundary was represented in the form

$$\frac{r(\theta)}{R} = 1 + \sum_n a_n P_n(\cos \theta) + bN, \quad (1)$$

where  $a_n$  are preassigned values, and  $b$  is the noise amplitude. The problem was to recover  $a_n$  in the presence of noise, by either direct numerical integration around the boundary, using the orthogonality of the Legendre polynomials, or by least squares techniques which avoided the approximation involved in numerical integration. The results were similar for both approaches, with somewhat better accuracy provided by the least squares analysis.

The second numerical experiment was designed to determine the ratio of the major to minor axis of a general perturbed ellipse, a situation encountered when a drop is distorted either by rotation or oscillation. In this case the coefficients of a general ellipse

$$ax^2 + 2bxy + cy^2 + 2dx + 2ey + 1 = 0 \quad (2)$$

in the presence of noise, were determined by a least squares approach. The coefficients  $a$ ,  $b$ ,  $c$  determine the principal axis of the ellipse

$$\text{tg } 2\alpha = \frac{2b}{a - c} \quad (3)$$

and the ratio of axes is given by

$$\text{ratio} = \left( \frac{a \sin^2 \alpha + c \cos^2 \alpha - b \sin 2\alpha}{a \cos^2 \alpha + c \sin^2 \alpha + b \sin 2\alpha} \right)^{1/2} \quad (4)$$

This ratio was also determined by a direct "min-max" approach, where extremal radius vectors from an approximate center are found. This approach was found to be noise-limited, and impractical for useful data reduction.

#### Center-of-Mass Motion

A large water drop moves in an acoustic potential well determined by the acoustic force components

$$F_i = \frac{5\pi}{6} \frac{P_i^2}{\rho_a c^2} k_i a^3 f(2k_i a) \sin 2k_i x_i \quad (5)$$

where  $p$  is the acoustic pressure,  $\rho_a$  is the density of air,  $c$  is the speed of sound,  $k_i = \sqrt{L_i}$  is the wave number, and  $f(2k_i a)$  is a shape factor

$$f(2k_i a) = \frac{\frac{\sin 2k_i a}{2k_i a} - \cos 2k_i a}{\frac{1}{3}(2k_i a)^3} \xrightarrow{k_i a \rightarrow 0} 1 - \frac{1}{10}(2k_i a)^2 \quad (6)$$

This expression for the force was recently verified by laboratory measurements and analysis by Leung et al.<sup>4</sup> For small displacements from the center  $\sin 2k_i x_i \sim 2k_i x_i$ , resulting in a harmonic oscillator well in which the frequency of oscillation will be

$$\omega_{cm}^2 = \frac{5}{4} f(2k_i a) \frac{k_i^2 p_i^2}{\rho_d \rho_a c^2} \quad (7)$$

where  $\rho_d$  is the drop density.

The oscillation frequency of the center-of-mass motion was determined from the film in two ways. First, the center-of-mass motion was crudely studied on the Vanguard, and a center-of-mass frequency was determined by averaging over several cycles. At 265 sec, the sound pressure level was decreased from 148 to 145 dB, which corresponds to a decrease by a factor of 2 in the force and of  $\sqrt{2}$  or 0.71 in the frequency. The corresponding ratios of observed frequencies along the three axes were 0.81, 0.84, and 0.80. Secondly, the center-of-mass coordinates of the digitized boundaries were determined, and then Fourier transformed. A sample is shown in Fig. 3, where (a) shows two periods of the oscillation of one coordinate, and (b) shows the corresponding power spectrum. Typically observed frequencies were  $\sim 0.15$  Hz, while the value predicted from Eq. (7) is  $\sim 0.14$ . Because there is a change in elevation between JPL (where the package was calibrated) and White Sands Test Range (where it was sealed prior to launch), there were some changes in the acoustic parameters involved. An estimate showed that the theoretical value of 0.14 Hz should be modified to  $\sim 0.16$  Hz. If the nonharmonicity of the acoustic potential well were taken into account, a reduction of several percent is expected in the value of the center-of-mass frequency.

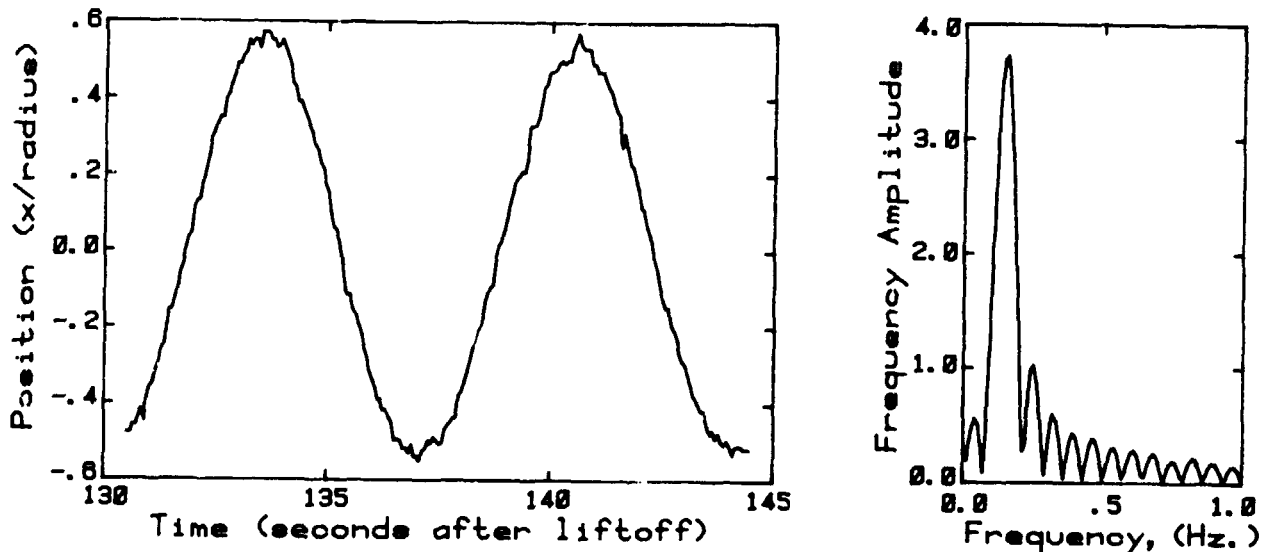


Fig. 3. Study of the center-of-mass motion of the drop in the acoustic potential well:

- (a) sinusoidal behavior in the time domain
- (b) a single peak in the frequency domain.

#### Rotation

For the thirty seconds of induced rotation (1600 frames on the film), every fifth frame was digitized. The expectation was that the drop's appearance in the main view, for which the line of view coincided with the axis of rotation, would be circular, while in the side views it would appear circular initially and become gradually more and more

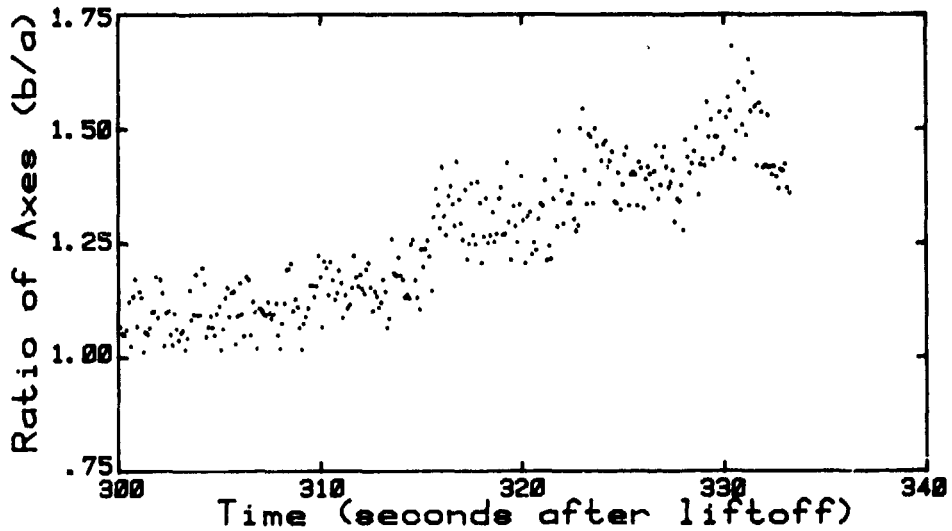


Fig. 4. Ratio of the major and minor axes during the sequence when the acoustic torque was acting on the drop (300 to 330 sec). The view is perpendicular to the axis of rotation. From this ratio a value of  $\beta$  was obtained. For example,  $b/a = 1.5$  corresponds to  $\beta = 0.42$ .

elliptical. These frames were analyzed by the least squares ellipse analysis (see Eqs. 2-4 above). The expected features showed up. While the  $a/b$  ratio of the main view remained constant, the same ratio for a side view gradually increased from 1.0 at the onset of rotation to roughly 1.5 at the end (Fig. 4). Using the theoretical results of Chandrasekhar<sup>5</sup>, Ross<sup>6</sup>, and Brown<sup>7</sup>, we were able to relate the observed  $a/b$  ratio to the rotational parameter

$$\beta = \left( \frac{\Omega}{\omega_2} \right)^2 \quad (8)$$

where  $\Omega$  is the angular velocity of the rotating drop, and  $\omega_2$  is the lowest mode oscillation frequency. The observed  $a/b$  ratio at the end of the rotation sequence corresponds to  $\beta \sim 0.3$ . This value, in turn, implies a rotation rate of 8.92 radians/sec, or 1.42 rps. Thus, although we could not directly determine the angular velocity for lack of tracer particles, we were able to infer it using these theoretical relations. Also, note that the value of  $\beta$  reached is very close to the first bifurcation point ( $\beta = 0.313$ ), at which the theory of equilibrium shapes of a rotating drop predicts possible transition from axially symmetric to non-axially symmetric equilibrium shapes.

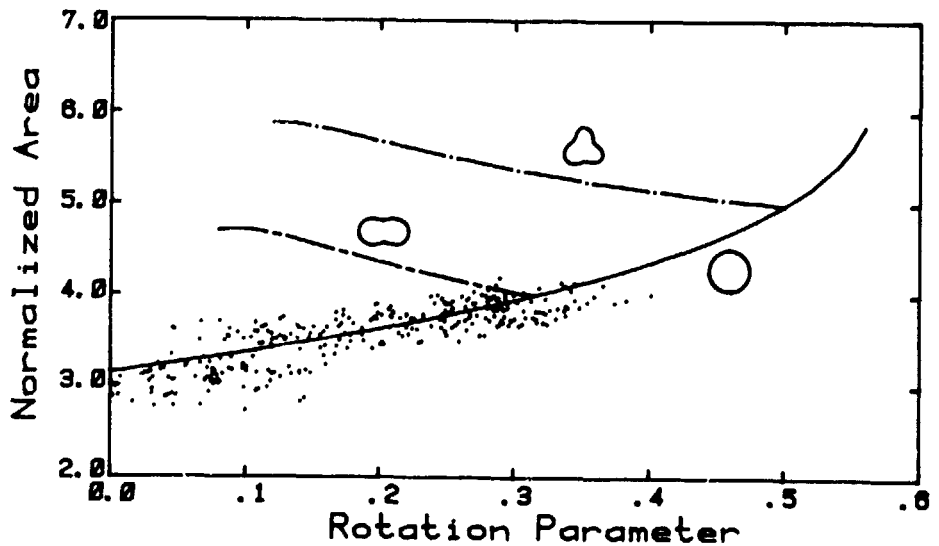


Fig. 5. Comparison of the experimental points and theoretical curves (Brown<sup>7</sup>) relating the equatorial area to the angular velocity. All quantities are normalized:  $A = \text{Eq. Area} / (\text{Resting Radius})^2$  and  $\beta = \text{Rot. Par.} = (\Omega/\omega_2)^2$ . The curve through the data represents the axisymmetric family of equilibrium shapes while the two side branches represent two- and three-lobed shapes.

The analysis was continued one more step. A relative equatorial area can be found from the product  $ab$  in the main view. A comparison of the theoretical and observed normalized equatorial areas is shown in Fig. 5 in which all boundary points were included in the analysis, showing excellent agreement with the theory. To the best of our knowledge, this is the first time that an observation has been made under conditions similar to those stipulated by the theory of equilibrium shapes of rotating drops. This obviously calls for an extension of such measurements to higher rotation rates. If a drop were spun in one direction and the torque quickly reversed, it might enable observation of the nonaxially symmetric equilibrium shapes theoretically predicted.

#### Oscillation

The natural oscillation frequencies of a liquid drop are given in the linear approximation by

$$\omega_n^2 = n(n-1)(n+2) \frac{\sigma}{\rho_d a^3} \quad (9)$$

where  $\sigma$  is the surface of the drop. The oscillation frequencies can be determined by analyzing both free oscillation data (as was done in Ref. 2) and forced oscillation data. When the drop oscillated, the reflections of the photo lamps showed that motion; using the time information on the edge of the film and advancing the film through a certain number of cycles, a rough value of the frequency of these oscillations could be obtained. The frequencies  $f_2 = 2.48 \pm .03$  and  $f_3 = 4.67 \pm .05$  Hz were obtained from the early sequence (127-145 sec) and  $f_2 = 2.54 \pm .03$  from the latter (265-300 sec). The frequencies expected for an 8.6 cc water drop with a surface tension of 71 dynes/cm are  $f_2 = 2.74$  Hz and  $f_3 = 5.31$  Hz. Frequencies were also determined by the peaks of the power spectrum of vertical and horizontal chords on the digitized data. Such a sample is shown in Fig. 6, where the power spectrum shows the mode  $n = 2$ , as well as traces of the modes  $n = 3, 4$ . At the time of this writing the full boundaries are being analyzed to provide the coefficients  $a_n(t)$  of Eq. (1). The Fourier transform of the latter is expected to provide the corresponding frequencies.

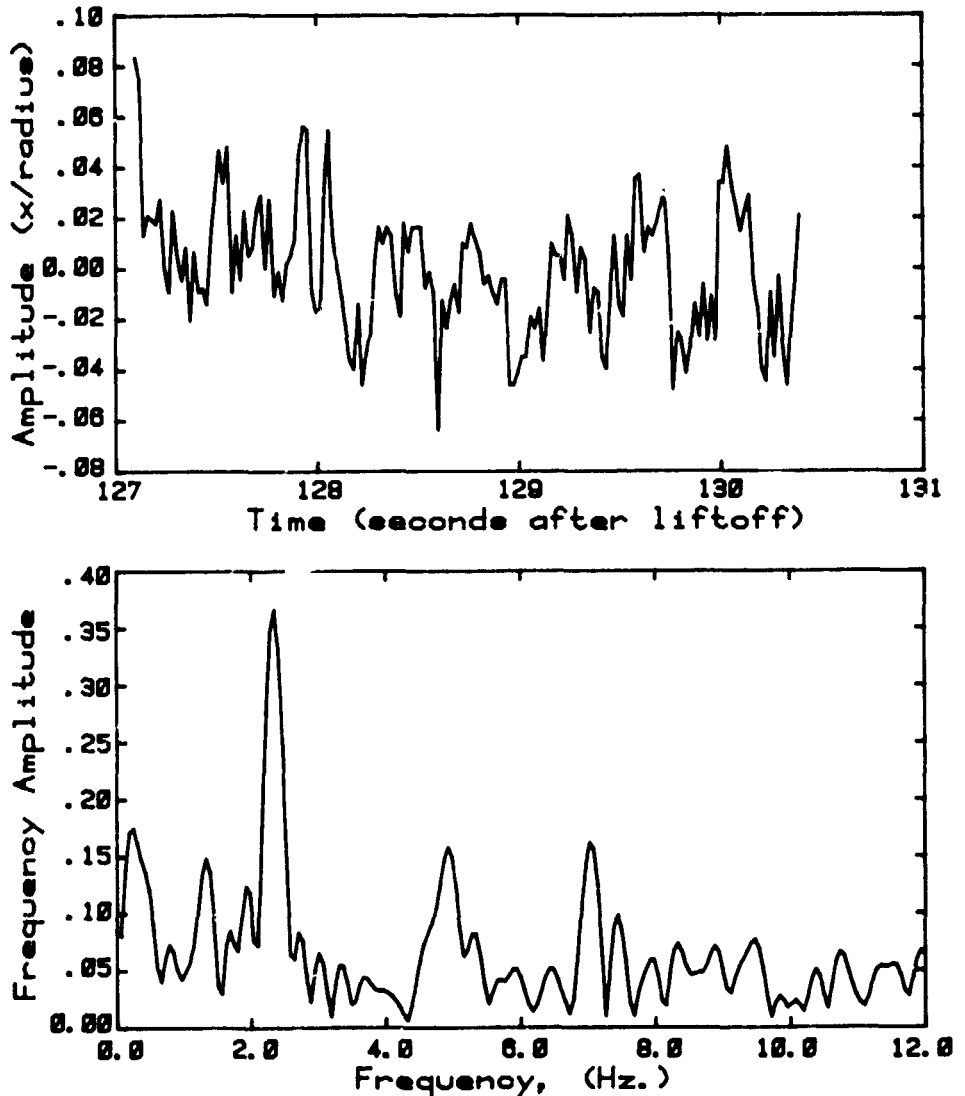


Fig. 6. Study of the drop's natural oscillations:  
 (a) difference between vertical and horizontal oscillations.  
 (b) frequency spectrum of data shown in (a).

During the forced oscillation sequence, the amplitude modulation of the acoustic pressure field along the z axis was swept from 2.3 to 2.9 Hz over a two-minute period, so as to contain the expected resonant frequency, 2.6 Hz, with a sufficient safety margin. The drop began oscillating in the  $n = 2$  normal mode during the first few seconds, as intended. However, as the amplitude became very large, the regularity deteriorated very quickly and rotation set in. The coefficient  $a_2(t)$  in Eq. (1) was determined by direct numerical integration, and by a vertical-horizontal chord method. The results are described in Ref. 3, but it can be generally stated that the cause of the rotational stability which developed two seconds into the forced oscillation sequence is not well understood at the present time. The acoustic field in which the drop finds itself is fairly complicated. Its components along each axis are modulated: there was amplitude modulation along the z axis, and complementary modulation along the x and y axes. In addition, the drop was undergoing a continuous low-frequency center-of-mass motion in this complex potential field.

#### Conclusions

The objectives of this experiment were achieved. The drop was deployed and acoustically manipulated as planned.

There is no satisfactory understanding of the initially strong oscillation seen during the forced oscillation sequence (at 2.3 Hz rather than 2.5 Hz) and the subsequent highly irregular motion which appears to be a superposition of oscillation and rotation.

During the rotation sequence of this experiment, the first bifurcation point between axisymmetric and triaxial shapes was reached in only thirty seconds of applied torque. Since equilibrium probably had not been reached, this means that spending more time on the rotation sequence or increasing the torque by using a higher sound pressure in future experiments might take the drop beyond the first bifurcation point. In particular, such an experiment would show whether non-axially symmetric equilibrium shapes are excited beyond the first bifurcation point.

#### Acknowledgements

The authors are grateful to P. Rayermann and J. Brown for assistance in data processing and programming; to R. Selzer and R. Ramage of the Image Processing Laboratory at JPL for digitizing the data; and to R. Irigoyen, J. Conley, L. Robinson, and K. Tarver for their valuable assistance in all phases of this experiment. This paper presents the results of one phase of research carried out at the Jet Propulsion Laboratory, California Institute of Technology, under contract with the National Aeronautics and Space Administration.

#### References

1. T. G. Wang, M. M. Saffren, and D. D. Elleman, Acoustic Chamber for Space Processing, AIAA paper 74-155 (1974).
2. N. Jacobi, R. P. Tagg, J. M. Kendall, D. D. Elleman, and T. G. Wang, Free Oscillations of a Large Drop in Space, AIAA paper 79-225 (1979).
3. T. G. Wang, D. D. Elleman, N. Jacobi, and A. P. Croonquist, Containerless Processing Technology Experiment Report, SPAR VI, Experiment 76-20 (May 1981).
4. E. Leung, N. Jacobi, and T. G. Wang, Acoustic Radiation Force on a Rigid Sphere in a Resonance Chamber, JASA, in press (December 1981).
5. S. Chandrasekhar, The stability of a rotating liquid drop, Proc. Roy. Soc. **A286**, 25 (1965).
6. D. K. Ross, The shape and energy of a revolving liquid mass held together by surface tension, Aust. J. Phys. **21**, 823 (1968).
7. R. Brown, The shape and stability of three-dimensional interfaces, Ph.D. thesis, U. of Minnesota (1979).

## Mechanisms of droplet combustion

C. K. Law

Department of Mechanical and Nuclear Engineering, Northwestern University  
Evanston, Illinois 60201

Abstract

The fundamental physico-chemical mechanisms governing droplet vaporization and combustion are discussed. Specific topics include governing equations and simplifications, the classical  $d^2$ -Law solution and its subsequent modification, finite-rate kinetics and the flame structure, droplet dynamics, near- and super-critical combustion, combustion of multicomponent fuel blends/emulsions/suspensions, and droplet interaction. Potential research topics are suggested.

1. Introduction

Research on the gasification, oxidation, and dynamics of fuel droplets commands both practical and fundamental interest to energy and combustion science. On the practical aspect one recognizes that petroleum oil constitutes a significant share of the world energy supply. Since these fuel oils are usually introduced into the combustor as sprays of droplets, it is reasonable to expect that the collective gasification of individual droplets would intimately influence the bulk spray vaporization and oxidation characteristics, which in turn determines the combustor performance. On the fundamental aspect droplet combustion is a problem involving complex chemically-reacting multicomponent two-phase flows with phase change, rich in physical and chemical phenomena typically of interest to the study of aerothermochemistry.

Figures 1a to 1c show some possible droplet combustion modes. In Fig. 1a the fuel droplet is motionless in a stagnant, gravity-free, oxidizing environment of infinite extent. The lack of either forced or natural convection implies that spherical symmetry exists. The basic mechanisms leading to the complete gasification of the droplet are heat and mass diffusion due to the existence of temperature and concentration gradients, the radial convection because of the continuous transfer of mass from the droplet surface to the ambient, and chemical reaction in the flame region. The burning is of the diffusion-flame type in which the outwardly-diffusing fuel vapor and the inwardly-diffusing oxidizer gas approach the reaction zone in approximate stoichiometric proportion. Reaction between them is rapid and intense, implying that the reaction zone is thin and very little reactants can leak through the flame. The chemical heat generated at the flame is transported both outward and inward to heat up the approaching oxidizer and fuel gases in order to achieve ignition. The rest of the inwardly-transported heat is used for droplet heating and to effect liquid gasification.

In the presence of either forced and/or natural convection, a non-radial relative velocity exists between the droplet and the surrounding gas. The shear stress exerted by the gas flow on the surface induces a recirculatory motion within the droplet (Fig. 1b). For higher rates of external convection, flow separation occurs close to the rear stagnation point, creating wake regions both inside and outside of the droplet (Fig. 1c). The presence of the non-radial convection generally enhances the transport rates and thereby the gasification rate, although for sufficiently intense flows the envelop diffusion flame can be extinguished, leading to significant reductions in the gasification rate. It is clear that fluid motion can have strong influence on the combustion process.

The bulk parameters of interest in droplet combustion studies include the droplet gasification rate, the flame location and temperature, the droplet drag, ignition and extinction limits, and the extent of pollutant formation such as that of  $\text{NO}_x$ . The droplet diameters of interest are typically between 10  $\mu\text{m}$  and 100  $\mu\text{m}$ ; gasification of smaller droplets can be considered to be instantaneous during the period between spray injection and active combustion, while large droplets either tend to breakup or cannot achieve complete gasification during the available residence time. Droplet breakup also limits its maximum Reynolds number,  $Re$ , to about 100 for typical surface tension values of hydrocarbon fuels,  $Re$  being defined as the ratio of the characteristic inertia to viscous forces. It may also be noted that it is frequently desirable for the droplets within a spray to have a distribution of sizes and velocities in order to achieve an optimum spatial distribution through penetration as well as a controlled rate of gasification and thereby chemical heat release.

The basic spherically-symmetric, pure-component, droplet combustion model was formulated in the fifties. This model has since been termed the  $d^2$ -Law because it predicts that the

square of the droplet diameter decreases linearly with time. In subsequent years the basic understanding of this model has been extensively revised while other aspects of droplet combustion have also been investigated. Extensive reviews of these developments can be found in Refs. 1 to 3.

The purposes of the present paper are to familiarize the reader with the influence and modeling techniques of chemical reactions in droplet processes, to briefly review current understanding of the basic physico-chemical mechanisms governing droplet combustion, and to suggest potential areas of research. In the next section some frequently-invoked assumptions during droplet combustion modeling are stated and a set of simplified governing equations presented. The  $d^2$ -Law is then derived, and its limitations and subsequent modifications in light of experimental results discussed. This is followed by special topics on finite-rate kinetics, droplet dynamics, high-pressure combustion, multicomponent droplet combustion, and droplet interaction. In Section 9 potential areas of research are suggested.

## 2. Assumptions and simplified governing equations

The general equations governing droplet combustion are those of heat, mass, and momentum conservation, in both the gas and liquid phases, and their coupling at the interface. Auxiliary relations needed are the equations of state and those describing chemical reactions and interfacial phase change. The chemical reactions of interest are usually those of fuel vapor decomposition and oxidation in the gas phase. For very high boiling point fuels, their pyrolysis in the liquid phase may also be of relevance. These equations, for general combustion problems, can be found in the text by Williams.<sup>4</sup>

We shall instead study in the following a simplified system which illustrates the basic diffusive-convective-reactive nature of droplet combustion. The major assumptions are as follows.

- (A1) Diffusion being rate-limiting, although second-order diffusion, that is the Soret and Dufour effects, are neglected.
- (A2) Isobaric processes because of the low Mach number flow.
- (A3) Gas-phase quasi-steadiness. Because of the significant density disparity between liquid and gas, the liquid possesses much inertia such that its properties at the surface, for example the regression rate, temperature, and species concentrations change at rates much slower than those of the gas-phase transport processes. Thus the gas-phase processes can be treated as steady, with the surface boundary variations occurring at longer time scales.
- (A4) Constant gas-phase transport properties. A single binary diffusion coefficient,  $\delta$ , is used for all pairs of species. The specific heat  $C_p$ , the thermal conductivity coefficient  $\lambda$ , and the product  $\rho\delta$ , are assumed to be constants, where  $\rho$  is the density.

With the above assumptions, the gas-phase governing equations are

$$\text{Continuity} \quad \nabla \cdot (\rho \underline{u}) = 0 \quad (1)$$

$$\text{Species} \quad \nabla \cdot (\rho \underline{u} Y_i - \rho \delta \nabla Y_i) = \dot{w}_i, \quad i=1,2,\dots,N \quad (2)$$

$$\text{Energy} \quad \nabla \cdot (\rho \underline{u} C_p T - \lambda \nabla T) = \dot{q} \quad (3)$$

$$\text{State} \quad p = \rho (R \bar{O} / \bar{W}) T \quad (4)$$

where  $T$  is the temperature,  $p$  the pressure,  $\bar{W}$  an average molecular weight,  $\underline{u}$  the velocity,  $Y_i$  the mass fraction of species  $i$ ,  $\dot{w}_i$  the chemical production rate of  $i$ ,  $\dot{q}$  the chemical heat generation rate, and  $N$  the total number of species.

For each of the equations represented by Eqs. (2) and (3), the first and second terms on the LHS respectively represent convective and diffusive transport, while the RHS is the chemical source/sink term. From chemical kinetics it is well known that the oxidation of a fuel species leading to the formation of products occurs through a complicated sequence of intermediate reactions with a myriad of intermediate species. Thus, for example, the term  $\dot{w}_i$  represents the sum of the mass rates of production and destruction, per unit volume, of species  $i$  from all of the reaction steps.

The adoption of such a detailed kinetic scheme yields immensely complicated expressions for  $\dot{w}_i$  and invariably necessitates the use of numerical solutions. Furthermore, except for the simplest hydrocarbon fuels, the detailed oxidation kinetics of the heavier ones are largely unknown. Thus frequently it is both necessary and useful to approximate the detailed kinetics as a one-step overall reaction between the fuel,  $F$ , and oxidizer,  $O$ , as



where  $\sigma_O$  is the stoichiometric mass coefficient of the oxidizer per unit mass of fuel consumed, and  $Q$  is the associated heat release. The consumption rate of  $F$  can then be expressed as

$$\dot{w}_F = - A \rho_O^a \rho_F^b \exp\left(-\frac{E}{R^* T}\right) \quad (6)$$

which shows that the overall reaction rate is proportional to the concentrations of the reactants and is dependent on the temperature through the Arrhenius factor characterized by an activation energy  $E$ . The exponents  $a$  and  $b$  are the empirically determined reaction orders with respect to the fuel and oxidizer, while  $A$  is the frequency factor which is a measure of the collision frequency between the reactants. Since  $\rho_i = Y_i \rho$ , Eq. (6) can also be expressed as

$$\dot{w}_F = - A \rho^{(a+b)} Y_O^a Y_F^b \exp\left(-\frac{E}{R^* T}\right) \quad (7)$$

Finally, recognizing that in any given reaction the rate of chemical heat release as well as the rates of creation and destruction of all species must be stoichiometrically related, we have

$$\dot{w}_O = \sigma_O \dot{w}_F$$

and (8)

$$\dot{q} = - Q \dot{w}_F$$

for the reaction given by Eq. (5).

Equations (2) and (3) are now well defined. It is clear that the highly non-linear nature of the reaction rate term, which also strongly couples the  $Y_i$  and  $T$  variations, introduces challenging mathematical difficulties and interesting physical phenomena to the problem.

Considerable simplification in the analysis results if one adopts the Shvab-Zeldovich Formulation, which requires

(A5) Unity Lewis number, or  $Le = \lambda / C_p \rho \delta = 1$ .

Thus a linear combination of Eqs. (2) and (3) eliminates the reaction term from all but one of the  $(N+1)$  equations. In particular, if we define a coupling function

$$\Gamma_i = \frac{Y_i}{\sigma_i} + \frac{C_p T}{Q} \quad (9)$$

where  $\sigma_F = 1$ , then Eq. (2) can be replaced by

$$\Gamma_i\text{-Conservation} \quad \nabla \cdot (\rho u \Gamma_i - \rho \delta \nabla \Gamma_i) = 0 \quad i=O, F \quad (10)$$

which shows that  $\Gamma_i$  is a conserved scalar during the chemical reaction of Eq. (5). Physically  $\Gamma_i$  represents the sum of the thermal and chemical energies which remains constant when heat and mass are transported at equal rates.

The problem is thus simplified to the solution of the chemically-inert Eq. (10) together with Eq. (3). Sometimes it is possible to first solve for  $\Gamma_i$  such that  $Y_i$ , and thereby Eq. (3), become only a function of  $T$ . The problem is decoupled.

To demonstrate this methodology and be more specific in our discussions, let us further assume

(A6) Spherical symmetry, implying the absence of natural or forced convection.

Then the governing equations become

$$\text{Continuity} \quad \frac{d\bar{m}}{dr} = 0 \quad (11)$$

$$r_i\text{-Conservation} \quad \bar{m} \frac{d\Gamma_i}{dr} - \frac{d}{dr} (\bar{r}^2 \frac{d\Gamma_i}{dr}) = 0 \quad i=O,F \quad (12)$$

$$\text{Energy} \quad \frac{\bar{m}}{r^2} \frac{d\bar{T}}{dr} - \frac{1}{r^2} \frac{d}{dr} (\bar{r}^2 \frac{d\bar{T}}{dr}) = D\bar{T}^{-(a+b)} Y_O^a Y_F^b \exp \left\{ -\frac{E}{R^0} \left( \frac{1}{T} - \frac{1}{T_r} \right) \right\} \quad (13)$$

where  $r$  is the radial co-ordinate,  $s$  indicates the surface,  $\bar{m} = (\rho u r^2) / (\rho \delta r_s)$ ,  $\bar{r} = r/r_s$ ,  $T = C_p T/Q$ ,

$$D = \left\{ \frac{r_s^2}{\rho \delta} \right\} \left\{ A \left( \frac{C_p \rho \bar{w}}{Q R^0} \right)^{(a+b)} \right\} \exp \left( -\frac{E}{R^0 T_r} \right)$$

is the ratio of the characteristic flow time to the characteristic reaction time, and  $T_r$  is a characteristic temperature in the reaction zone.

Equation (11) shows that

$$\bar{m} = \text{constant} \quad (14)$$

implying that the mass flow rate is a constant as it should be.

Equations (12) and (13) are to be solved subject to the boundary conditions

$$\text{At } \bar{r} = \infty: \quad Y_O = Y_{O\infty} \quad (15)$$

$$Y_F = 0 \quad (16)$$

$$\bar{T} = \bar{T}_\infty \quad (17)$$

$$\text{At } \bar{r} = 1: \quad dY_O/d\bar{r} = \bar{m} Y_O \quad (18)$$

$$dY_F/d\bar{r} = -\bar{m}(1-Y_F) \quad (19)$$

$$d\bar{T}/d\bar{r} = \bar{m}L/Q \quad (20)$$

$$\bar{T} = \bar{T}_s \quad (21)$$

where  $L$  is the latent heat of gasification. Equations (18) and (20) respectively state that oxidizer does not penetrate into the surface, and that all the heat conducted to the droplet is used for gasification. Equations (15) to (21) constitute seven boundary conditions to solve for the three second order differential equations, Eqs. (12) and (13), together with the burning rate parameter  $\bar{m}$ .

Solving Eq. (12), we have

$$\left( \frac{Y_O}{\sigma_O} + \bar{T} \right) = \left( \frac{Y_{O\infty}}{\sigma_O} \right) e^{-\bar{m}/\bar{r}} - \beta (1 - e^{-\bar{m}/\bar{r}}) + \bar{T}_\infty \quad (22)$$

and

$$(Y_F + \bar{T}) = (1 - \beta) (1 - e^{-\bar{m}/\bar{r}}) + \bar{T}_\infty \quad (23)$$

where

$$\beta = \frac{C_p (T_\infty - T_s) + L}{Q}$$

Thus the problem is reduced to the solution of Eq. (13) for  $\bar{T}$ , with  $Y_O$  and  $Y_F$  given by Eqs. (22) and (23).

### 3. The $d^2$ -Law and its modifications

A particularly simple solution exists if we make the following assumption.

- (A7) Reaction proceeds with an infinitely fast rate at an infinitesimally-thin flame located at  $\tilde{r}_f$ , implying that both reactants are totally consumed there.

Thus we have

$$Y_O = Y_F = 0, \quad \tilde{T} = \tilde{T}_f, \quad \text{at } \tilde{r} = \tilde{r}_f \quad (24)$$

Furthermore, since there is now no leakage of the reactants through the flame, the oxidizer concentration is identically zero in the inner region to the flame. Thus, in particular, at the droplet surface we have

$$Y_O = 0 \text{ at } \tilde{r} = 1 \quad (25)$$

Applying Eqs. (24) and (25) to Eqs. (22) and (23), we obtain three equations from which the three parameters of practical interest, namely the burning rate  $\tilde{m}$ , the flamefront standoff ratio  $\tilde{r}_f$ , and the flame temperature  $\tilde{T}_f$ , can be solved as

$$\tilde{m} = \ln(1+B) \quad (26)$$

$$\tilde{r}_f = \frac{\tilde{m}}{\ln(1+Y_{O_\infty}/\sigma_O)} \quad (27)$$

and

$$\left\{ \frac{C_p(T_f - T_\infty)}{Y_{O_\infty}/\sigma_O} \right\} + \{L + C_p(T_f - T_s)\} = Q \quad (28)$$

$$\text{where } B = \frac{C_p(T_\infty - T_s) + (Y_{O_\infty}/\sigma_O)Q}{L} \quad (29)$$

is a transfer number representing the ratio of the "driving force" for vaporization to the "resistance" to vaporization. The chemical source term,  $(Y_{O_\infty}/\sigma_O)Q$ , is usually much greater than the thermal term,  $C_p(T_\infty - T_s)$ . Equations (26) to (28) show that  $\tilde{m}$ ,  $\tilde{r}_f$ , and  $T_f$  are constants for a given fuel-oxidizer system.

Finally, further assume that

- (A8) Fuel vaporization rate at surface is equal to fuel consumption rate at flame  $\dot{m} = 4\pi\rho_l r_s^2$ .

Then

$$-\frac{d}{dt} \left( \frac{4}{3} \pi \rho_l d_s^3 \right) = \dot{m} \quad (30)$$

which is simply

$$\frac{d(d_s^2)}{dt} = -K \quad (31)$$

with

$$K = \frac{8\rho\delta}{\rho_l} \ln(1+B) \quad (32)$$

where  $\rho_l$  is the liquid density. The parameter  $K$  is known as the evaporation or burning rate constant.

Integrating Eq. (31) yields

$$d_s^2 = d_{s0}^2 - Kt \quad (33)$$

which forms the basis of the  $d^2$ -Law.

Setting  $d_s = 0$ , we obtain the total burning time as

$$\tau = \frac{d_{s0}^2}{K} \quad (34)$$

Equation (34) shows that  $\tau$  varies quadratically with the initial droplet size, hence demonstrating the basic principle of atomization in order to achieve rapid gasification.

It is also of interest to note that in Eq. (28) we have expressed  $T_f$  in such a way as to illustrate the fact that it is just the adiabatic flame temperature for the stoichiometric reaction between the liquid fuel and the oxidizer-inert mixture. That is, the amount of heat release,  $Q$ , by burning unit mass of fuel is used (a) to gasify the fuel and heat the fuel vapor from  $T_s$  to  $T_f$ , and (b) to heat  $(Y_{O_2}/\rho_0)^{-1}$  amount of the oxidizer mixture from  $T_s$  to  $T_f$ .

Figure 2a shows the  $d^2$ -Law temperature and concentration profiles, which are typical of diffusional burning.

Because of its simplicity, the  $d^2$ -Law has been extensively used in modeling droplet and spray combustion. In particular, the qualitative behavior of Eq. (33) has been found to be largely correct while the burning rate constant can generally be predicted to within a factor of two, allowing for the uncertainty in selecting transport property values.

However, experiments<sup>5,6</sup> on spherically-symmetric droplet combustion reveal certain qualitatively different behaviors, indicating the existence of serious weaknesses in the  $d^2$ -Law. Figure 3 shows that, immediately after ignition, there exists a short period during which  $d_s^2$  practically does not change. Furthermore, rather than a constant,  $\bar{r}_f$  increases significantly after ignition. In a low- $Y_{O_2}$  environment the increase persists until burnout, while in a high- $Y_{O_2}$  environment  $\bar{r}_f$  levels off toward the latter part of the droplet lifetime.

Both of these deviations are consequences of initial conditions which are not included in the  $d^2$ -Law. The initial slow rate of surface regression is primarily due to the need to heat up the initially cold droplet to a temperature hot enough to sustain steady burning; frequently this temperature is close to the liquid's boiling point under the prevailing pressure. During this period most of the heat generated is used for droplet heating instead of gasification, thereby resulting in a slow surface regression rate. The droplet also expands as it is heated up, hence compensating for the reduction in the droplet size from gasification.

Since active droplet heating and intense gasification are somewhat mutually exclusive, droplet heating is mostly over in about the first 10% of the droplet lifetime. For the remaining period  $d_s^2$  should vary approximately linearly with time. During multicomponent droplet combustion or high-pressure combustion the droplet heating period can be considerably longer, as will be discussed later.

To model droplet heating one may simply include in the latent heat of vaporization,  $L$ , an additional amount representing the heat conducted into the droplet interior. This amount can then be determined by solving the temperature distribution within the droplet.<sup>7,8</sup>

The observed behavior of  $\bar{r}_f$  can be explained by the fact that the fuel vapor present in the region between the droplet and the flame continuously change as the droplet and flame sizes change.<sup>6</sup> The significance of this variation can be appreciated by considering a droplet immediately after it is ignited. At that instant the amount of fuel vapor present in the inner region should be of the same order as the amount present in the droplet vicinity before ignition. Since this amount is very small because of the low droplet temperature, the flame initially must lie close to the droplet surface. With subsequent gasification the fuel vapor present in the inner region increases and larger flames can be supported. Therefore only part of the fuel vaporized during this period is consumed at the flame, the rest is being accumulated in the inner region as the flame expands. This amount may also become depleted toward the latter part of the droplet lifetime.

It is reasonable to expect that the accumulated amount is significant because although the gas density is low compared with the liquid density, the flame size can be substantial such that volume effect dominates. Furthermore the fuel vapor is accumulated at the expense of the finite droplet mass. Indeed it is easy to demonstrate<sup>6</sup> that the amount of the fuel vapor present, as given by results of the  $d^2$ -Law, is of the same order as the droplet mass.

The existence of this accumulation process implies that mass conservation is actually violated in  $d^2$ -Law. Rather, overall mass conservation for the fuel vapor should read,

- Gasification rate at droplet surface
- = Consumption rate at flame
- + Accumulation/Depletion rate in the inner region

(35)

The last term is absent in the  $d^2$ -Law.

When the accumulation process is included in the formulation<sup>6</sup>, then the experimentally observed behavior of  $\bar{r}_f$  is predicted. The result that  $\bar{r}_f$  does approach a constant value for burning in high  $Y_{O_2}$  environments can also be explained by its relatively smaller flame size, which requires less fuel vapor for accumulation.

An important practical implication of fuel vapor accumulation is that since the fuel gasification rate is not equal to the fuel consumption rate, adoption of the  $d^2$ -Law in spray modeling may result in grossly erroneous estimates of the bulk chemical heat release rate. In particular, in a low-oxidizer environment some fuel vapor is still left behind upon complete droplet gasification, as shown in Fig. 4.

#### 4. Finite-rate kinetics and the flame structure

It is perhaps somewhat remarkable that because of the basic diffusive nature of droplet combustion, much can be learned by making the flame-sheet approximation without having to consider the detailed reaction kinetics. There are, however, certain phenomena in which the chemical reaction rate can be of the same order as the diffusion rate in parts of the flow field. They can only be described by allowing for finite-rate kinetics and thereby resolving the flame structure. Important examples are the determination of the ignition/extinction limits and the combustion of monopropellant droplets.

To resolve the flame structure, it is necessary to solve Eq. (13) with the reaction term, which is governed by the Damköhler number  $D$  and the activation energy  $E$ . For reactions of interest to combustion  $E$  usually assumes a large value, of the order of 20 to 100 kcal/mole. Thus the Arrhenius factor  $\exp(-E/RT)$  is a very sensitive function of temperature. It assumes the maximum value at the location of the maximum temperature in the flow field. However, by moving slightly away from this location, the slight decrease in the temperature can significantly reduce the magnitude of the Arrhenius factor and thereby effectively freeze the chemical reaction.

Thus the flow field can be considered to consist of a narrow reaction region separating two broad chemically-frozen regions in which fuel and oxidizer diffuse toward each other. Furthermore, since the gradients of the flow properties are very steep within the narrow reaction region, diffusion dominates over convection and therefore balances the reaction term. On the other hand in the frozen regions diffusion balances convection. Finally, since reaction proceeds at a finite rate, the reactants cannot be completely consumed within the flame and therefore may leak through it. This leakage represents incomplete fuel utilization and in severe cases can lead to extinction. The general temperature and concentration profiles are shown in Fig. 2b.

A solution of Eq. (13) usually yields an S-shaped multi-valued curve when a relevant parameter, say  $\bar{m}$ , is plotted versus  $D$  (Fig. 5). This S-curve can be interpreted as follows.

For  $D = 0$ , the flow is chemically frozen everywhere and we retrieve the pure vaporization state. By gradually increasing  $D$  along the lower branch, weak chemical reaction is possible leading to slight increases in  $\bar{m}$ . However, with continuous increase in  $D$  a value  $D_I$  will be reached beyond which the only possible solution lies on the upper branch. Thus at  $D_I$  the system changes abruptly from the lower to the upper branch, which represents all the possible burning states. In particular as  $D \rightarrow 0$  we retrieve the flame-sheet solution. Therefore this lower turning point can be identified as the ignition state and  $D_I$  an ignition Damköhler number. Similarly if we continuously decrease  $D$  along the upper branch, then beyond  $D_E$  steady burning ceases to be possible and only the lower branch has solutions. Therefore the upper turning point can be identified as the extinction state and  $D_E$  an extinction Damköhler number.

Physically, the non-existence of solutions implies that the chemical reaction rate cannot balance the heat transport rate. Thus for the lower branch, beyond  $D_I$ , the chemical heat is generated so fast in the reaction region close to the hot, oxidizing, ambience that they cannot be transported away in a steady manner. This leads to an increase in the reaction zone temperature and thereby further increase in the reaction rate, culminating in the runaway event of ignition. This feed-back mechanism proceeds extremely rapidly because of the highly temperature-sensitive Arrhenius kinetics.

Similarly, for the upper branch, the effects of the finite reaction rate are that the flame is broadened and both fuel and oxidizer can now leak through the flame zone. Thus with excessive leakage the chemical heat release cannot keep up with the heat transported

away from the flame zone, leading to a precipitous drop in the flame temperature and thereby extinction.

Equation (13) has been formally solved using the newly-developed technique of large activation energy asymptotic technique.<sup>9,10</sup> The diffusive-reactive and diffusive-convective regions are separately solved and matched, using the ratio of the thermal energy in the reaction region to the activation energy as the small parameter of expansion. The S-curve is reproduced and explicit expressions derived for the ignition and extinction states. These criteria are useful in assessing the combustibility of a given droplet-oxidizer system.

Finite-rate kinetics is also essential in the study of monopropellant droplet combustion. Unlike conventional hydrocarbon fuels which burn through diffusion flames, a monopropellant contains both fuel and oxidizer. Thus after gasification the outwardly-transported gas is a premixed combustible, which will eventually burn as a premixed flame. While a detailed discussion of the structure of premixed flames is outside the scope of this paper, it may be noted that studies<sup>4</sup> have shown that for large droplets the burning resembles that of one-dimensional premixed flame, with

$$\frac{d(d_s)}{dt} - \text{constant} ,$$

while for small droplets the burning resembles that of the conventional fuel droplet, with

$$\frac{d(d_s^2)}{dt} - \text{constant} .$$

## 5. Droplet dynamics

The heat and mass transfer processes of the spherically-symmetric droplet combustion discussed so far are closely influenced by the droplet dynamics, and vice versa. As mentioned previously, while increasing non-radial convection generally increases the gas-phase transport rates and thereby the burning rate, there exists an upper limit in the convection intensity at which the flame can be blown off, that is extinguished. Various semi-empirical correlations have been proposed for the burning rate augmentation due to convection, such as<sup>2</sup>

$$\frac{K}{K_{s.s.}} = \left\{ 1 + \frac{0.278 \text{ Re}^{1/2} \text{ Pr}^{1/3}}{(1+1.232/\text{RePr}^{4/3})^{1/2}} \right\} \frac{\ln(1+B)}{B} \quad (36)$$

where  $K_{s.s.}$  is the spherically-symmetric result. Systematic theoretical and experimental investigation on the blow-off of the droplet flame have also been conducted. In particular criteria governing the blow-off limits have been determined.<sup>11</sup>

Combustion can influence the droplet drag and therefore its dynamics in three essential ways. The outward mass flux at the droplet surface reduces friction drag but increases pressure drag because of early separation. The net result is as yet unclear. The existence of the interfacial velocity, especially after the droplet has been substantially heated up, may delay separation and hence reduce both the friction and pressure drag. Finally, the significant elevation of the temperature in both the gas and liquid phases, and the increase in the gas density because of the presence of the high-molecular-weight fuel vapor, can all greatly influence the fluid properties and therefore the drag coefficient. The above factors have not been systematically investigated.

In the section on multicomponent fuels we shall further show that the existence of internal motion may qualitatively influence the combustion characteristics of multicomponent droplets.

## 6. Near- and super-critical combustion

Because of the enhanced combustion efficiency and intensity under high pressure, internal combustion engines operate under elevated pressures frequently in excess of the thermodynamic critical pressure of the liquid fuel. For example, while the critical pressures of diesel fuels are of the order of 20 atm, the pressure within diesel engines can range from 40 atm at the end of the compression stroke to twice that value at the peak combustion pressure. While these values seem to indicate that the droplet should undergo supercritical combustion early in its lifetime, considerations of the finite droplet heating rate and the dissolution of the permanent gases, which can raise the critical pressures of the fuel to the range of 40 to 60 atm, render it possible that the droplet actually attains criticality after it is mostly vaporized.

At elevated pressures various aspects of low-pressure droplet combustion need to be revised. The elevation of the liquid boiling point lengthens the droplet heating period and thereby its lifetime. The overall chemical reaction rate generally increases with pressure, hence making extinction more difficult but favoring the formation of such pollutants as  $\text{NO}_x$  and soot. As the critical state is approached, gas-phase compressibility becomes important, while the reduced surface tension enhances internal circulation and favors droplet deformation and breakup. The gas-phase quasi-steady assumption breaks down as the gas and liquid densities become comparable. Finally, at the critical state the distinction between gas and liquid vanishes and the phenomena of interest cease to belong to the area of droplet combustion.

### 7. Multicomponent droplet combustion

Much of the earlier studies on droplet combustion used pure fuels. However, recent developments in engine design and fuel formulation indicate that multicomponent effects will become progressively more important in the utilization of liquid fuels. Combustion processes within engines will be more tightly controlled to further improve efficiency and reduce emissions. The synthetic fuels derived from coal, tar sand, and oil shale will have more complex composition as well as higher and wider boiling point ranges. There also exists considerable interest in the utilization of such hybrid fuels as water/oil emulsions, alcohol/oil solutions and emulsions, and coal-oil mixtures. The widely different physical and chemical properties of the constituents of these hybrid fuels necessitates consideration of multicomponent effects in an essential way.

To understand heterogeneous multicomponent fuel combustion, either as a droplet or in some other forms (e.g. pool burning), the following three factors have to be considered.

- (i) The relative concentrations and volatilities of the liquid constituents, as would be expected.
- (ii) The miscibility of the liquid constituents. This controls the phase change characteristics. For example the partial vapor pressure of a miscible fuel blend can be greatly modified when it is emulsified with even a small quantity of water and changes into an immiscible mixture.
- (iii) The intensity of motion within the liquid. This influences the rate with which the liquid components can be brought to the surface at which gasification takes place.

The third point requires further amplification. First, it is obvious that no matter how volatile a liquid element is, it cannot gasify unless it is exposed at the droplet surface either through the passive mode of surface regression, or the active modes of diffusion and internal circulation. However, liquid-phase mass diffusion is an extremely slow process; its rate being one to two orders slower than that of surface regression. Therefore with it being the dominant active mode of transport, it is reasonable to expect that both the volatile and non-volatile liquid elements in the core of the droplet will be "trapped" during most of the droplet lifetime. Under this situation the relative volatilities of the individual components obviously cannot be the dominating factors in effecting gasification. On the other hand, in the presence of internal circulation, liquid-phase mass transport is facilitated such that the relative volatilities exert much stronger influence on the individual gasification rates.

Thus the combustion characteristics of a multicomponent droplet can be discussed in the two extreme rates of internal mixing, namely (a) a diffusion limit in which there is no motion within the droplet interior such that diffusion is the only active transport mode, and (b) a (somewhat artificial) distillation limit in which it is assumed that mixing occurs so fast that the states within the droplet interior are perpetually uniformized. Let us first discuss the combustion of miscible fuel blends in these two limits.

Because of diffusional resistance, it is reasonable to expect that the composition of the droplet inner core is practically not influenced by the surface gasification and therefore remains close to its initial value. However, since the volatile component has a relatively lower concentration at the surface, therefore there must exist a thin surface layer through which the composition rapidly changes<sup>12, 13</sup>, as shown in Fig. 6. Furthermore, overall mass conservation requires that the fractional gasification rate of the  $i$ th species must be equal to its initial mass fraction. Therefore it is reasonable to expect that after the initial droplet heating period, a  $d^2$ -Law behavior should prevail for the droplet size history, as shown in Fig. 7.

The diffusional stratification of the concentration can lead to the occurrence of an interesting disruptive combustion phenomenon termed micro-explosion.<sup>13</sup> It is reasoned that since the droplet surface has a higher concentration of the non-volatile, high-boiling-point, component, and since the droplet temperature is controlled by its composition at the

surface, therefore the droplet can be heated to a high temperature. However, the droplet inner core is concentrated with the volatile, low-boiling-point, component. It is therefore possible that the inner core mixture can be heated to its limit of superheat and homogeneously nucleates. The subsequent internal pressure build-up is tremendous and causes the droplet to explode violently.

It has also been predicted that micro-explosion can occur only for an optimum range of mixture concentration; the non-volatile component is needed to drive up the droplet temperature while the volatile component is needed to facilitate homogeneous nucleation.<sup>14,15</sup> Furthermore, since the boiling point increases significantly with pressure while the homogeneous nucleation temperature is extremely insensitive to pressure variations, at least for pressures not close to critical, it is also suggested<sup>13</sup> that increasing pressure enhances the occurrence of micro-explosion. This is an attractive consideration for application in internal combustion engines.

The occurrence of micro-explosion and its compositional dependence have been experimentally verified<sup>16</sup>, although the pressure dependence has not been experimentally investigated.

The possible occurrence of micro-explosion offers interesting potential in the flexibility with fuel atomization. That is, fine atomization need not be the primary concern with designing the spraying process. In fact, it may be advantageous to have somewhat larger droplets which possess sufficient inertial for penetration into the combustor interior in order to achieve optimum charge distribution. Upon penetration, rapid gasification can then be effected through micro-explosion.

In the distillation limit<sup>17</sup> the perpetual uniformization of the droplet composition implies that the volatility-differentials should be the controlling factor. The gasification of the components should occur approximately sequentially according to their relative volatilities. Thus for components with sufficiently different volatilities a plot of  $d_s^2$  versus time should yield approximately linear segments of different slopes separated by sharp transition periods, during which the droplet temperature increases (Fig. 7). Such behavior has been experimentally verified. The droplet lifetime may or may not exceed that of the diffusion limit. It is also obvious that in the absence of diffusional stratification micro-explosion will not occur in this limit. Thus enhanced mixing, say in the form of internal circulation generated by external convection, tends to inhibit micro-explosion.

It may also be noted that the distillation limit is an artificial one. Recently more rigorous analyses<sup>18</sup> allowing for internal circulation show that the distillation limit can never be approached and that diffusional stratification prevails even under intense external convection. On the other hand experiments on droplet combustion subjected to either natural and/or forced convection do show distillation-like behavior even with mild convective intensity.<sup>3</sup> As of now no satisfactory explanation exists for this disagreement.

Next we discuss the combustion of water-in-oil (W/O) emulsions, which have been tested in a variety of combustors including the diesel engine, the gas turbine, and furnaces and boilers.<sup>19</sup> The results generally indicate a reduction in soot and  $\text{NO}_x$  emissions while those of CO and unburned hydrocarbons are somewhat increased. Change in the combustor efficiency on the basis of oil consumption is less clear; slight improvements and degradation have been reported depending on the state and type of the combustor, the testing procedure, and the properties of the emulsions used.

The main differences between an W/O emulsion and a miscible fuel blend is that the water micro-droplets do not diffuse and that the immiscibility property can significantly influence the phase equilibrium relation at the droplet surface. For example under equilibrium vaporization, which implicitly requires a distillation mode of internal transport, each immiscible component will vaporize independent of the presence and quantity of the other component. This implies that the boiling point of the emulsion is limited by the lower of the boiling points of these components. Thus the attainable temperature and the associated vapor pressure of a high-boiling-point oil can be greatly suppressed by adding only a small quantity of water. Micro-explosion obviously is not possible. On the other hand, in the absence of significant internal motion, it has been found<sup>20,21</sup> that micro-explosion again occurs and is actually more violent than that for a miscible fuel blend. This is reasonable because of the large amount of the superheated mass available within the water micro-droplets.

Finally we discuss the combustion of coal-oil-mixtures (COM), which offers a promising technology for coal utilization by mixing finely crushed coal in oil and then directly burn the coal-oil mixture in such stationary burners as furnaces and boilers. The concept is attractive in that it enables the direct substitution of oil by coal, that the crushing and mixing processes involved in its preparation are more economical than the energy-expensive coal-liquefaction and gasification processes, and that the mixture is still pumpable and

hence can be readily used in the conventional oil-fired combustors with minimum hardware modification.

The combustion characteristics of COM droplets again depend intimately on the extent of internal circulation. Internal bubbling and disruptive combustion should be facilitated because, with coal particles serving as potential heterogeneous nucleation sites, the droplet does not need to reach the high temperature required to initiate homogeneous nucleation. However, the intensity of explosion will be milder because of the reduced amount of superheat available.

Experimentally, sporadic, mild fragmentations have been observed for a suspended coal/diesel droplet burning in the quiescent, normal atmosphere.<sup>16</sup> The fragmentation becomes explosive with the addition of less than 5% water. However, these fragmentations can be completely suppressed<sup>22</sup> by increasing the extent of external convection produced either by upward blowing of hot gas or simply letting the COM droplet fall through a hot furnace. Therefore in the absence of fragmentation, all the coal particles originally present in the COM droplet are concentrated into a large coal particle agglomerate<sup>22</sup>, which requires a long burning time and is expected to be a serious problem with COM utilization in combustors with short residence times.

### 8. Droplet interaction

In the practical situation within a spray, any given droplet is surrounded by and therefore interacts with the rest of the droplet ensemble. Since the characteristic droplet separation distance can be of the same order as the flame size<sup>3</sup>, the intensity of interaction can be quite strong. In particular, for sufficiently short separation distances, the droplets will burn as a merged flame instead of individually.

To study interaction effects, it is necessary to solve Eqs. (3) and (10), together with the momentum conservation equation, for the three-dimensional flow configuration. If we make the thin-flame approximation and also assume weak convection, then the analysis simplifies to that of the Laplace Equation, of which many solution procedures exist. In the presence of convection, special solutions<sup>23-25</sup> have also been obtained.

Experimentally it has been demonstrated<sup>22</sup> that interaction reduces the droplet burning rate because of the competition for oxygen.  $d^2$ -Law behavior obviously does not hold because of droplet regression and therefore the continuous variation of the droplet surface separation distance. The presence of buoyancy, however, can significantly increase the burning rate because of the synergistically-enhanced convective transport between droplets.<sup>26-28</sup>

The case of strongly convective situation is of special interest because of the influence of wake regions on neighboring droplets.<sup>29</sup> Another area of active research on droplet interaction is the Leidenfrost Phenomenon<sup>29</sup>, in which the droplet gasifies over a hot surface and exhibits a non-monotonic behavior in its lifetime with increasing surface temperature.

### 9. Concluding remarks

Presently the fundamental mechanism governing low-pressure, spherically-symmetric, single-component droplet combustion can be considered to be reasonably well understood. However, quantitative prediction of the burning characteristics is still inadequate, primarily as a result of transport property variations. This becomes serious during intense burning because the elevated flame temperature not only causes dissociation, but also introduces greater temperature and compositional variations in the transport properties. It would be of interest to conduct a numerical simulation of such a process, using realistic transport properties but simplified reaction schemes, and compare the predictions with the existing experimental data. Caution should be exercised in assessing the initial conditions which affect the droplet heating and fuel vapor accumulation processes.

The dynamics of a vaporizing droplet, with various intensities of interfacial mass flux, and the coupled problem of droplet vaporization under external convection, have not been adequately explored. Systematic studies assuming low, intermediate, and moderately high Reynolds number flows are all needed.

A detailed study of the droplet internal motion and transfer processes could also resolve the issue that while theoretical analysis on convective multicomponent droplet combustion shows non-uniform droplet concentration persists throughout the droplet lifetime, experimental results seem to indicate a batch distillation mode with the concentration perpetually uniformized.

The phenomenon of micro-explosion has potential to improve charge preparation and deserves further study. For miscible fuel blends the dependence of micro-explosion on the fuel composition and internal motion is sensitive and should be characterized. For W/O emulsions, emulsion stability, the optimum water droplet sizes, and the effect of pressure are the important problems.

High-pressure near-critical and super-critical combustion is a fertile area of research. The primary question here is whether the droplets can reach criticality before they have been substantially gasified. Many of the assumptions in modeling low-pressure droplet combustion break down near the critical state. The attainment of micro-explosion and coal-particle agglomeration also depends on whether criticality is reached before these events take place.

In view of the recent interest to conduct combustion experiments in the gravity-free Space-Lab environment, a candidate experiment is that of the combustion and micro-explosion of multicomponent droplets. This experiment cannot be easily and perfectly conducted on earth using conventional techniques. For example the suspension technique cannot be used because the suspension fibers can serve as heterogeneous nucleation sites to induce artificial micro-explosion. Freely-falling droplets experience forced convection and therefore internal circulation, whose intensity also continuously varies because of the changes in the droplet velocity and size. Finally, the presence of natural convection also induces internal motion. Thus only in a gravity-free environment can a stationary and convection-free experiment involving an unsuspended droplet be conducted.

Recent advances in computational techniques also allow the possibility of studying certain aspects of droplet combustion which are not easily amenable to analytical solutions. One example is the effects due to variable transport property values as just mentioned. The influence is especially strong in the liquid phase. For convective combustion numerical solution is also useful because of the lack of spherical symmetry, the presence of the complex flows, and the fact that relevant Reynolds numbers frequently are in the analytically difficult range of 1 to 100. During high pressure combustion much of the conventional assumptions describing droplet combustion break down (e.g. gas-phase quasi-steadiness and compressibility) such that numerical solutions again may be necessary. Finally, studies on droplet interaction may also find numerical approach useful because of the lack of symmetry in the problem.

#### Acknowledgments

The support of the author's work on droplet and spray combustion over the past few years by the Division of Basic Energy Science of the Department of Energy, and the Heat Transfer Program of the National Science Foundation, is appreciatively acknowledged. This review was prepared while the author was on sabbatical leave at the Sandia National Laboratories, Livermore, under the sponsorship of Associated Western Universities, Inc., and the Department of Energy.

#### References

1. Williams, A., "Combustion of Droplets of Liquid Fuels: A Review," Combust. Flame, Vol. 21, pp. 1-31, 1973.
2. Faeth, G. M., "Current Status of Droplet and Liquid Combustion," Prog. Energy Combust. Sci., Vol. 3, pp. 191-224, 1977.
3. Law, C. K., "Recent Advances in Droplet Vaporization and Combustion," to appear in Prog. Energy Combust. Sci., 1982.
4. Williams, F. A., Combustion Theory, Addison-Wesley, Reading, 1965.
5. Okajima, S. and Kumagai, S., "Further Investigation of Combustion of Free Droplets in a Freely Falling Chamber Including Moving Droplets," Fifteenth Symposium (International) on Combustion, the Combustion Institute, Pittsburgh, PA, pp. 401-417, 1975.
6. Law, C. K., Chung, S. H., and Srinivasan, N., "Gas-Phase Quasi-Steadiness and Fuel Vapor Accumulation Effects in Droplet Burning," Combust. Flame, Vol. 38, pp. 173-198, 1980.
7. Law, C. K., "Unsteady Droplet Combustion with Droplet Heating," Combust. Flame, Vol. 26, pp. 17-22, 1976.
8. Law, C. K. and Sirignano, W. A., "Unsteady Droplet Combustion with Droplet Heating - II. Conduction Limit," Combust. Flame, Vol. 28, pp. 175-186, 1977.
9. Linan, A., "The Asymptotic Structure of Counterflow Diffusion Flames for Large Activation Energy," Acta Astronautica, Vol. 1, pp. 1007-1039, 1974.
10. Law, C. K., "Asymptotic Theory for Ignition and Extinction in Droplet Burning," Combust. Flame, Vol. 24, pp. 89-98, 1975.
11. Wu, X., Law, C. K., and Fernandez-Pello, A. C., "A Unified Criterion for the Convective Extinction of Fuel Particles," to appear in Combust. Flame, 1981.
12. Landis, R. B. and Mills, A. P., "Effects of Internal Diffusional Resistance on the Vaporization of Binary Droplets," Paper B7.9, 5th International Heat Transfer Conf., Tokyo, Japan, 1974.

13. Law, C. K., "Internal Boiling and Superheating in Vaporizing Multicomponent Droplets," AICHE J., Vol. 24, pp. 626-632, 1978.
14. Law, C. K., Law, H. K., and Lee, C. H., "Combustion Characteristics of Coal/Oil and Coal/Oil/Water Mixtures," Energy, Vol. 4, pp. 329-339, 1979.
15. Law, C. K. and Law, H. K., "A d<sup>2</sup>-Law for Multicomponent Droplet Vaporization and Combustion," AIAA Preprint No. 81-0264, to appear in AIAAJ., 1982.
16. Lasheras, J. C., Fernandez-Pello, A. C., and Dryer, F. L., "Experimental Observations on the Disruptive Combustion of Free Droplets of Multicomponent Fuels," Combust. Sci. Tech., Vol. 22, pp. 195-209, 1980.
17. Law, C. K., "Multicomponent Droplet Combustion with Rapid Internal Mixing," Combust. Flame, Vol. 26, pp. 219-233, 1976.
18. Lara-Urbanejo, P. and Sirignano, W. A., "Theory of Transient Multicomponent Droplet Vaporization in a Convective Field," Eighteenth Symposium (International) on Combustion, the Combustion Institute, Pittsburgh, PA, pp. 1365-1374, 1981.
19. Dryer, F. L., "Water Addition to Practical Combustion Systems - Concepts and Applications," Sixteenth Symposium (International) on Combustion, the Combustion Institute, Pittsburgh, PA, pp. 279-295, 1977.
20. Law, C. K., "A Model for the Combustion of Oil/Water Emulsions," Combust. Sci. Tech., Vol. 17, pp. 29-38, 1977.
21. Lasheras, J. C., Fernandez-Pello, A. C., and Dryer, F. L., "On the Disruptive Burning of Free-Droplets of Alcohol/n-Paraffin Solutions," Eighteenth Symposium (International) on Combustion, the Combustion Institute, Pittsburgh, PA, pp. 293-305, 1981.
22. Miyasaka, K. and Law, C. K., "Combustion and Agglomeration of Coal-Oil Mixtures in Furnace Environments," Combust. Sci. Tech., Vol. 24, pp. 71-82, 1980.
23. Labowsky, M., "A Formalism for Calculating the Evaporation Rates of Rapidly Evaporating Interacting Particles," Combust. Sci. Tech., Vol. 18, pp. 145-151, 1978.
24. Umemura, A., "A Unified Theory of Quasi-Steady Droplet Combustion," Eighteenth Symposium (International) on Combustion, the Combustion Institute, Pittsburgh, PA, pp. 1355-1363, 1981.
25. Ray, A. K. and Davis, E. Y., "Heat and Mass Transfer with Multiple Particle Interactions - Part I: Droplet Vaporization," Chem. Eng. Comm., Vol. 6, pp. 61-79, 1980.
26. Feedoseeva, N. V., "Combustion of a System of Liquid Fuel Drops," Adv. in Aerosol Phys., No. 2, pp. 110-118, 1972.
27. Feedoseeva, N. V., "Interaction of Two Vigorously Evaporating Drops in the Absence of Convection," Adv. in Aerosol Phys., No. 3, pp. 27-34, 1973.
28. Miyasaka, K., and Law, C. K., "Combustion of Strongly-Interacting Linear Droplet Arrays," Eighteenth Symposium (International) on Combustion, the Combustion Institute, Pittsburgh, PA, pp. 283-292, 1981.
29. Tamura, Z. and Tanasawa, Y., "Evaporation and Combustion of Drop Contacting with a Hot Surface," Seventh Symposium on Combustion, Butterworth, London, pp. 509-522, 1959.

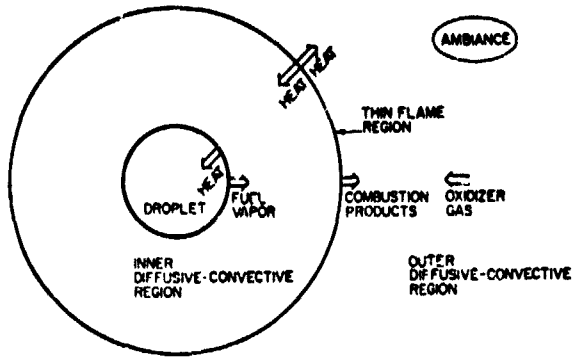


Figure 1a. Schematic showing spherically-symmetric droplet combustion.

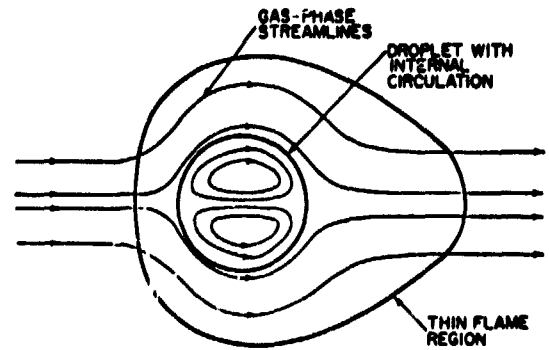


Figure 1b. Schematic showing convective droplet combustion without flow separation.

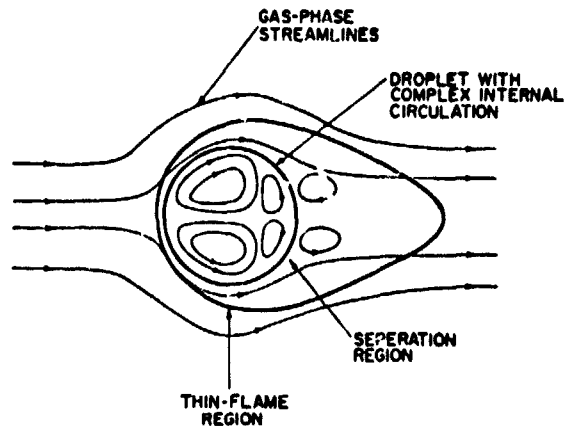


Figure 1c. Schematic showing convective droplet combustion with flow separation.

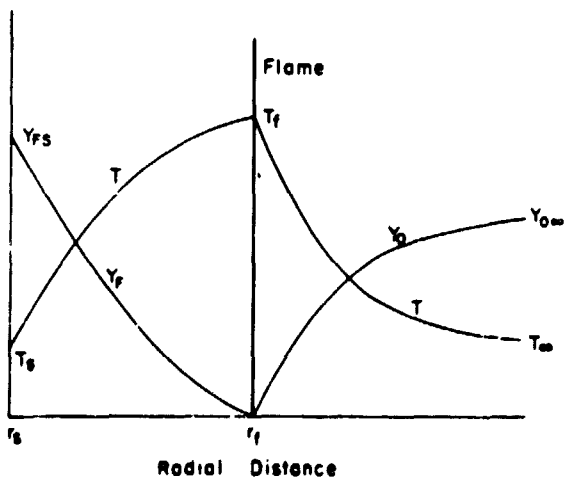


Figure 2a. Temperature and concentration profiles during droplet combustion in the flame-sheet limit.

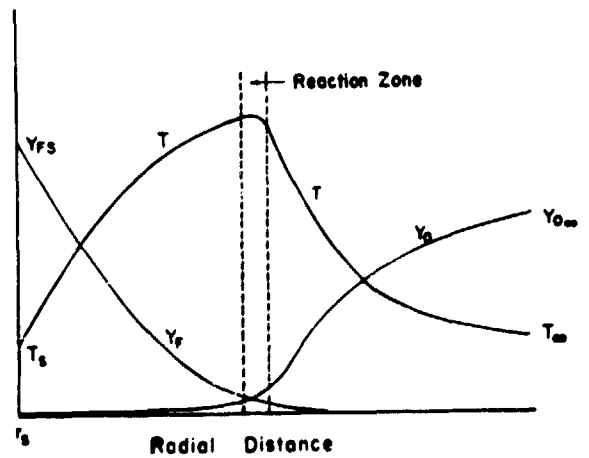


Figure 2b. Temperature and concentration profiles during droplet combustion with finite rate kinetics.

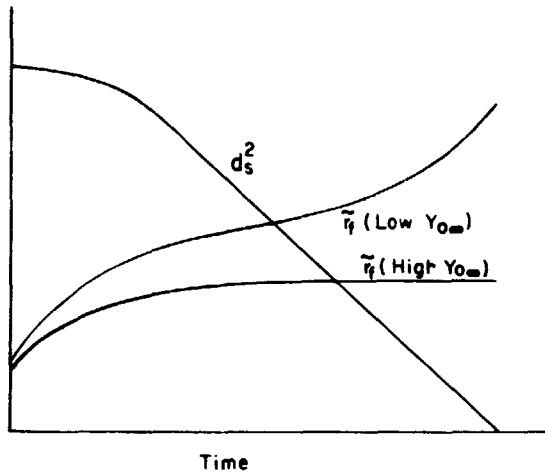


Figure 3. Experimental results on the temporal variations of diameter-squared,  $d_s^2$ , and flame-front stand-off ratio,  $\bar{r}_f = r_f/r_s$ , during spherically-symmetric combustion.

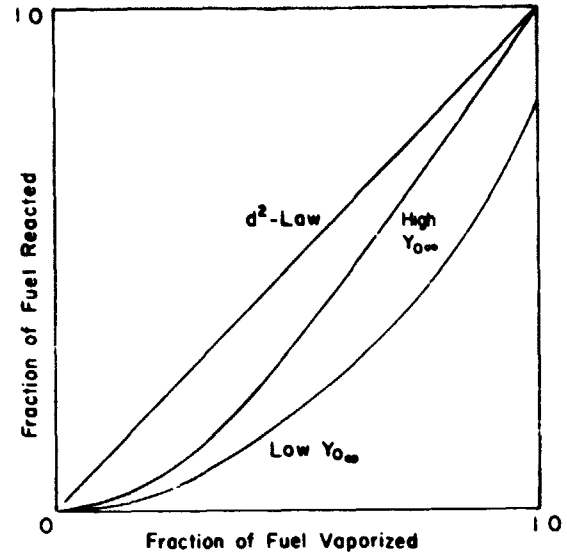


Figure 4. Fractional amount of fuel reacted as function of fractional amount vaporized, illustrating the importance of fuel vapor accumulation.

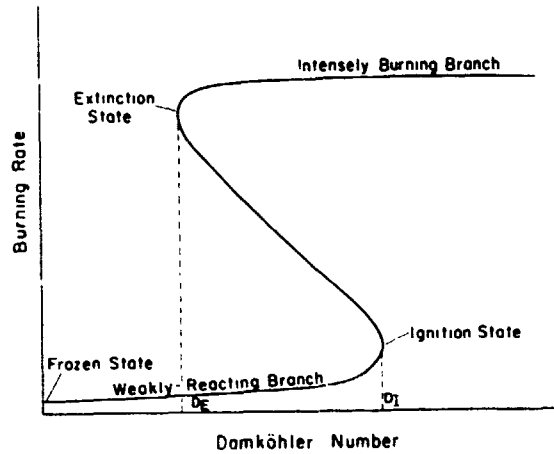


Figure 5. S-shaped response curve representing all possible solutions of quasi-steady droplet burning with finite reaction rate.

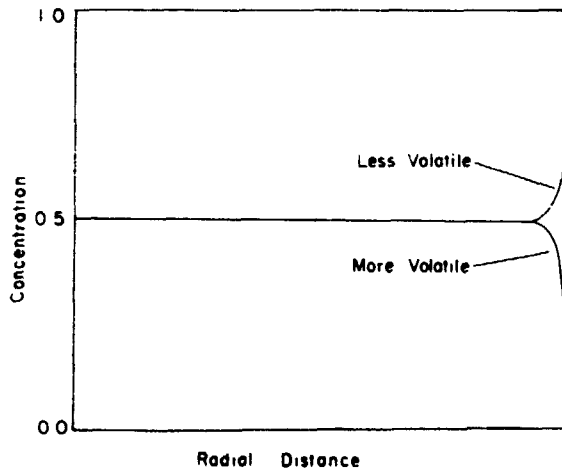


Figure 6. Droplet concentration profile for a bi-component droplet with initially equal concentrations.

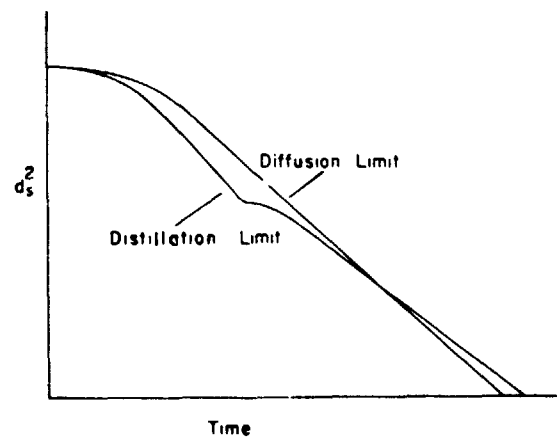


Figure 7. Temporal variation of the droplet surface area in the two limits of internal mass transport.

A numerical study of drop-on-demand ink jets

J. FICOM

International Business Machines Corporation, Research Laboratory,  
 5600 Cottle Road, San Jose, California 95193

Abstract

A discussion is given of ongoing work related to development and utilization of a numerical model for treating the fluid dynamics of ink jets. The model embodies the complete nonlinear, time dependent, axi-symmetric equations in finite difference form. An earlier work treated continuous jets in which periodic boundary conditions allowed study of local capillary instability to drop formation in a moving reference frame. The present study includes the jet nozzle geometry with no-slip boundary conditions and the existence of a contact circle. The contact circle is allowed some freedom of movement, but wetting of exterior surfaces has not yet been addressed. The principal objective in current numerical experiments is to determine what pressure history, in conjunction with surface forces, will lead to clean drop formation.

I. Introduction

Recent experimental fluid drop studies related to ink jet printer design have provided an extensive input to guide development of a comprehensive numerical model for treating surface tension driven flows. As a consequence, a full nonlinear model now provides feedback of fundamental interest regarding the appropriate interaction of forces for drop formation. The system of numerical programs is lengthy and complex but seems adaptable to many problems involving drops and bubbles.

In a previous study, we considered the so-called "continuous jet", where equally spaced drops are produced in a continuous stream.<sup>1</sup> An "infinite jet" model, assuming periodic boundary conditions for a single drop region, provided information on drop stream control through suitable harmonic disturbances. Of general interest beyond practical matters of ink jets is that these numerical solutions gave the complete intervening behavior between Rayleigh's inviscid capillary jet<sup>2</sup> (initial solution) and Lamb's oscillating drop after breakup<sup>3</sup> (final solution).

The present study has the added complication of flow from a nozzle, controlled by a pressure history intended for the release of a single drop. A contact circle is now involved with the uncertainty of what constitutes a rigorous treatment of such a boundary. Further uncertainty exists regarding the pressure history, produced by a transducer, since the small scale of the jet precludes measurement of even peak pressures. Fortunately the parameter  $R/W$  (Reynolds number / Weber number) is in a range that is amenable to numerical approximation, and it therefore seems possible that numerical experimentation will shed light on the existing uncertainties.

Currently, the numerical programs are operational with contact circle treatment such that no wetting is permitted, as is generally the case with analytic treatment of pendant drops. Motion of the contact circle occurs when negative pressures (relative to ambient) are applied at the nozzle entrance and fluid is drawn inward from the free surface. Currently, a square wave history of uniform pressure at the nozzle inlet is employed to drive the jet. A positive pulse sufficient to produce the experimental drop size is followed by a negative pulse which serves to initiate detachment of a drop. The negative pulse is terminated when the net impulse returns to zero. At this stage, surface tension must carry the contraction to final detachment of the drop. The objective of the work is to establish quantitatively the conditions which provide optimum drop characteristics for high resolution printing.

In the following, we outline the numerical method which does not differ appreciably from reference 1. We then discuss a series of results which have thus far been confined to parameters of interest in ink jet hardware development. Concluding remarks point up those aspects of the work where numerical solution has provided practical insight into the behavior of the flows.

II. Numerical Method

The geometry we consider is easily visualized from an examination of output graphics of Fig. 1. A nozzle section of unit radius with inlet on the left is assumed to be connected to a cylindrical chamber with radius large compared to the nozzle. In Fig. 1 the nozzle section is five units in length. (Note that tick marks on plot axes define finite difference mesh distances). Only a small additional annular region is needed in the geometry since drops generally will be limited to sizes on the order of the nozzle diameter and wetting of the outlet facing is not currently permitted. Axi-symmetry is assumed and hence the calculation region involves only the upper half of the views in the output graphics. The lower half is added for esthetic purposes in the plotting programs.

The initial solution is impulsive with a prescribed uniform pressure at the circular cross section of the inlet. At the initial instant ( $t=0$ ) the outlet meniscus is flush with the nozzle facing, this being the

equilibrium configuration in the absence of wetting. Taking the ambient pressure as zero at this free surface we begin with a linear axial pressure gradient in the nozzle section. The flow velocities are initially zero. The calculation proceeds by explicit time differences with all succeeding time steps following the same prescription which we will now outline for a first step.

Because we here use a vorticity streamfunction formulation our first aim is to provide appropriate boundary conditions for the latter. This is rather complex since indeed none of the boundaries except the axis of symmetry can be treated simply especially since we want a time varying pressure at the inlet and also wish to provide for entrance flow from a chamber. We begin in a somewhat roundabout way by computing the velocity fields through the momentum equations. In axis-symmetric form these equations are

$$\begin{aligned} \frac{\partial u}{\partial t} + \frac{\partial u^2}{\partial z} + \frac{1}{r} \frac{\partial uv}{\partial r} &= - \frac{\partial P/\rho}{\partial z} - \frac{\nu}{r} \frac{\partial}{\partial r} (\omega r) \\ \frac{\partial v}{\partial t} + \frac{\partial uv}{\partial z} + \frac{1}{r} \frac{\partial v^2}{\partial r} &= - \frac{\partial P/\rho}{\partial r} + \nu \frac{\partial \omega}{\partial z} \end{aligned} \quad (1)$$

Here  $u$  is the axial velocity ( $z$  direction) and  $v$  is the radial velocity ( $r$  direction).  $P$  is the pressure,  $\rho$  is the fluid density and  $\nu$  the fluid viscosity. We choose to express the diffusion terms as vorticity gradients because the vorticity ( $\omega$ ) is always available to simplify the calculation. However, we currently are expressing the diffusion in the axial velocity equation in terms of  $u$  because accuracy in the nozzle boundary layer seems to require it.

A small forward integration in time of (1) leads to flow because of the pressure gradient in the nozzle. Now by integrating the first of (1) over a fluid (control) volume of the nozzle we may obtain the uniform streamfunction value at the nozzle boundary relative to a zero streamline at the axis. That is, the time derivative of the streamfunction  $Q$  at the nozzle surface becomes

$$\left( \frac{dQ}{dt} \right)_{r_0} = \frac{1}{z_0} \int_0^{r_0} r (u_L^2 - u_R^2 + P_L - P_R) dr - \frac{\nu r_0}{z_0} \int_0^{r_0} \omega_{r_0} dz \quad (2)$$

where we have deleted terms that do not contribute. In (2) L and R refer to left and right cross sections of the cylindrical control volume which initially includes the entire fluid region.  $z_0$  is the length of the nozzle and  $r_0$  its radius.

We can, of course, have the control volume continue to be all of the fluid region even when a drop is forming but then (2) becomes a more difficult expression. Also, if the free surface draws inward the control volume, as expressed in (2), must be shortened by revising  $z_0$  and excluding some of the fluid near the outer edge of the outlet.

Thus far we still do not know the boundary conditions for  $Q$  at the entrance of the nozzle or at the free surface. For the latter we integrate the expressions

$$\frac{\partial Q}{\partial z} = -rv \quad \text{and} \quad \frac{\partial Q}{\partial r} = ru \quad (3)$$

singly or in combination, beginning at the axis of symmetry outward to the surface. This provides for  $Q$  at points on the surface at roughly mesh length distances. It is necessary, however, to define the free surface as a set of particles generally 5 to 10 per mesh distance. At these surface particles  $Q$  is given through interpolation among those given above and the value previously obtained at the nozzle boundary.

Finally, two conditions are provided at the inlet. If flow is inward we simulate flow from a large chamber by requiring uniform inflow. This effectively requires the boundary layer at the nozzle surface to begin at the inlet. With  $Q$  already known at the nozzle boundary, a mean velocity  $u$  may be obtained using the second of (3) for the entire inlet cross section. Reversing the procedure we obtain  $Q$  at inlet mesh points.  $Q$  is not linear in the axis-symmetric case.

For reverse flow we assume that flow into the chamber will be the same as in the immediately adjacent region inside the nozzle or

$$\frac{\partial Q}{\partial z} = 0$$

there.

At this point we are not yet ready to solve internal streamfunction values, we need yet to know the vorticity in the interior. Using the time dependent equation

$$\frac{\partial \omega}{\partial t} + \frac{\partial u \omega}{\partial z} + \frac{\partial v \omega}{\partial r} = \nu \left[ \frac{\partial^2 \omega}{\partial z^2} + \frac{\partial}{\partial r} \left( \frac{1}{r} \frac{\partial \omega r}{\partial r} \right) \right] \quad (4)$$

we increment the vorticity forward in time as we had done the velocities. This is of course meaningless for the first time step because the vorticity field is null. At the second time step and all following vorticity will derive from the no-slip nozzle surface and to a lesser extent from the free surface.

Internal streamfunction values are now obtained by simultaneous solution at all net points of the equation

$$\frac{\partial^2 Q}{\partial z^2} + r \frac{\partial}{\partial r} \left( \frac{1}{r} \frac{\partial Q}{\partial r} \right) = -r\omega . \quad (5)$$

This is followed by resetting the velocities using (3) and the after thought determination of vorticity at the nozzle surface using

$$\omega_b = - \left( \frac{\partial u}{\partial r} \right)_b$$

The redundancy of the above may be questioned but our objective thus far is to provide for more options on how solution is to be carried out both for convenience and accuracy. Solution of (5) is of necessity by iteration rather than direct because of the time varying fluid region. Convergence is of course enhanced if in the course of getting surface streamfunction values through (3) one fills in internal points. The difference in the final outcome from (5) relates to truncation errors in (3), particularly in the nonlinear terms. One in fact would find that strict use of (3) only would leave in doubt what value to give the streamfunction at the nozzle surface because each integration upward along  $z$ =constant lines would give a different error.

With the streamfunction given at "Lagrangian" free surface points we may evaluate the normal and tangential velocities there. That is

$$u_\tau = \frac{1}{r} \frac{\partial Q}{\partial \eta} \quad \text{and} \quad u_\eta = - \frac{1}{r} \frac{\partial Q}{\partial \tau} \quad (6)$$

where  $\tau$  is tangential and  $\eta$  is normal. The second of these is readily obtained from particle  $Q$  values, the first through a nearest approach method relative to selected interior points followed by interpolation. We require surface points or particles to carry with them coordinate information, local arc lengths and angles (relative to the axis of symmetry). Using the angle we may obtain  $u$  and  $v$  for the particles through a rotational transformation.

Updating the surface configuration with

$$\frac{dz}{dt} = u \quad \text{and} \quad \frac{dr}{dt} = v , \quad (7)$$

we proceed to determine new local arc lengths along the surface and new angles. Thus

$$\begin{aligned} \delta\tau^2 &= \delta z^2 + \delta r^2 \\ \text{and} \quad \alpha &= \tan^{-1} \frac{\delta r}{\delta z} . \end{aligned} \quad (8)$$

It is now easy to obtain surface pressures. Relative to ambient "zero" pressure they are given by

$$\left( \frac{P}{\rho} \right)_s = \sigma \left( \frac{\cos \alpha}{r} - \frac{\partial \alpha}{\partial \tau} \right) + \nu \frac{\partial u_\eta}{\partial \eta} , \quad (9)$$

where  $\sigma$  is the surface tension coefficient. The first term on the right expresses the destabilizing curvature around the axis of symmetry, the second, the stabilizing curvature in the  $r$ - $z$  plane and the last term the pressure contribution from local deformation. For the last term we again use a closest approach method for evaluation relative to selected interior points. However, a local continuity expression

$$\frac{\partial u_\eta}{\partial \eta} + \frac{\partial u_\tau}{\partial \tau} - u_\eta \frac{\partial \alpha}{\partial \tau} + \frac{v}{r} = 0 \quad (10)$$

could probably be used.

At this stage we may iterate a Poisson's equation for the pressure. That is

$$\frac{\partial^2 P/\rho}{\partial z^2} + \frac{1}{r} \frac{\partial}{\partial r} \left( r \frac{\partial P/\rho}{\partial r} \right) = -G \quad (11)$$

where

$$G = \frac{\partial^2 u^2}{\partial z^2} + \frac{2}{r} \frac{\partial uv}{\partial r \partial z} + \frac{1}{r} \frac{\partial v^2}{\partial r} \quad (12)$$

The boundary condition for the pressure is known everywhere except at the nozzle surface where the condition on the derivative is

$$\left( \frac{\partial P}{\partial r} \right)_b = v \left( \frac{\partial \omega}{\partial z} \right)_b \quad (13)$$

G is required at only interior points.

Obtaining the vorticity at the free surface has been somewhat of a problem. In terms of surface quantities we write

$$\omega = \frac{\partial u_\eta}{\partial \tau} + \frac{\partial u_\tau}{\partial \eta} + u_\tau \frac{\partial \alpha}{\partial \tau} \quad (14)$$

Unfortunately in a stationary reference frame this is subject to large errors because in a spherical drop (for example) large numbers must effectively cancel to produce a small real vorticity. To overcome this we define velocities relative to a mean for each contiguous part of the fluid so that (14) is evaluated in terms of disturbance quantities.

Scaling to permit nondimensional calculation is the same as with the earlier capillary instability problem.<sup>1</sup> The reference length is the nozzle radius  $r_0$ . The reference velocity is the capillary wave velocity

$$v_0 = \left( \frac{\sigma}{\rho r} \right)^{1/2} \quad (15)$$

giving a time scale

$$t_0 = \left( \frac{\rho r^3}{\sigma} \right)^{1/2} \quad (16)$$

This leads to use of the single parameter, Reynolds number over Weber number

$$\frac{R}{W} = \left( \frac{\sigma r}{\rho v^2} \right)^{1/2} \quad (17)$$

Thus the above equations are made dimensionless by replacing  $v$  by  $W/R$  wherever it appears and replacing  $\sigma$  by 1.0.

### III. Results

During the development of the numerical program there was constant reference to experimental work that was being conducted in the development of ink jet hardware.<sup>4</sup> Unfortunately because of the small size of the jet the crucial measurement of driving pressure could not be made. Lacking this knowledge, along with uncertainty concerning the numerical program itself, made convergence to a successful method very difficult. A failure to obtain a solution comparable to experiment could mean being outside the range of pressure values appropriate for drop formation or could mean there was a fundamental problem in the numerical program. The program is quite complex and the running times are by no means short. Unlike experiments which can be conducted in rapid succession to achieve a certain operating behavior, the numerical experiments took too much time for many wrong guesses. Now, however, we are quite close to experiment and the model has shown evidence of being adequate. We will perhaps never know the exact character of the pressure that drives the jet but once having achieved agreement in jet characteristics, here demonstrated in a quantitative visual form, we are in a

position to understand most properties of interest in the flows. Even now, however, one must be mindful of limitations of the approximate solution since unlimited grid resolution is of course impossible.

To illustrate the numerical solutions we have chosen a case which gives the most interesting overall results achieved by the time of this writing. Figures 1, 2 and 3 show a sequence of four solutions each in consecutive times for  $R/W=5$ . The pressure history is one which begins with a suction (negative pressure) followed by a positive pressure and then a negative pressure again. The second negative pressure terminates when the net impulse is zero. While not necessary, a very small residual positive pressure rather than zero was maintained for the remainder of the running time of this case. The square wave pressure at the inlet and times (both in nondimensional units) are as in Table 1.

Table 1

t	P/p
0 - 0.21	-60.0
0.21 - 0.82	+80.0
0.82 - 1.43	60.0
1.43 -	+ 1.0

The nondimensional times for the plots illustrated are given in Table 2.

Table 2

Fig.	Time	Plot Interval Q	QMAX	QMIN	Plot Interval P	PMAX	PMIN
1-1	0.25	0.03125	0.0	-0.52	4.0	80.0	-2.9
1-2	0.68	0.125	2.03	0.00	4.0	93.3	0.2
1-3	1.03	0.0625	1.97	0.00	4.0	7.5	-84.0
1-4	1.64	0.0625	0.99	-0.17	0.5	7.1	-3.0
2-1	2.05	0.03125	0.78	-0.08	0.25	4.5	-0.4
2-2	2.52	0.03125	0.66	-0.07	0.25	4.2	0.0
2-3	2.97	0.03125	0.60	-0.06	0.125	4.2	0.7
2-4	3.57	0.03125	0.53	-0.05	0.25	7.6	0.0
3-1	4.18	0.03125	0.53	-0.05	1.0	17.1	-1.2
3-2	4.52	0.03125	0.53	-0.05	1.0	20.7	-0.4
3-3	4.67	0.03125	0.54	-0.05	2.0	48.6	0.6
3-4	5.03	0.03125	0.52	-0.03	2.0	35.9	0.6

In all figures the streamfunction is plotted as solid lines. Negative streamlines include tick marks. This is manifested as tick marked lines for flow to the left (reverse flow in the nozzle) where the boundary layer vorticity is predominantly negative. The vorticity vector (positive) is outward in upper half plane and inward in the lower half. The center line is the streamline  $Q=0$  as discussed previously. Where this line appears it is a solid line without tick marks. There are also tick marks on the solid boundaries of the nozzle but since these are rectilinear they are distinguishable from streamlines. As mentioned before, the tick mark spacing on the rectilinear lines show the grid spacing. This is only roughly true on curved streamlines.

Pressure "isobars" are plotted as dashed lines with shorter dashes for negative pressures. The zero pressure line also has long dashes.

One can use the above information and Table 2 to determine contour values throughout the plots. In some places this is difficult but knowing the maximum and minimum values helps and greater detail is probably of little use. Because of limited plotting area, say in the contracted neck of the jet, the isobars are difficult to distinguish as negative or positive. They are of course positive there because of the high surface pressure. Also it should be noted that in the axi-symmetric case streamlines are not uniformly spaced for a uniform flow velocity. This is the reason for the gap in streamlines along the central axis where a tube of flow involves little true flow because its cross sectional area is small, yet the flow velocity may be high.

Beginning with Fig. 1 and referring to Table 1 we note that the time is in the period where the inlet pressure is positive but flow is still into the chamber because of fluid inertia from the initial suction period. The left most isobar at the inlet is +80 (see Table 2) while the lowest pressure is at the concave meniscus surface and is -2.9. As a reference it is of interest that, in nondimensional units, a drop of unit radius has a surface pressure of +2.0. One unit of pressure being provided by each component of the surface tension. Here in the first plot the stable component of the surface tension is such as to restore the

flush status of the meniscus at the face of the nozzle. Acting along with the positive inlet pressure the flow direction is soon reversed.

In the second plot of Fig. 1 the toroidal circulation at the inlet is because of flow bending inward from the simulated large chamber preceding the nozzle. The pressure is negative at points just inward from the circulation where the flow rate is high while at the center line the deformation causes a pressure exceeding the inlet pressure. The meniscus surface has a pressure near unity.

In the next plot a drop is forming through forward motion even though the inlet pressure has been reversed. Note the short dashed lines of pressure (negative) and a zero pressure in the contracted region of the incipient drop. Again the inlet toroidal circulation is still producing a pressure lower than the applied inlet pressure but now more negative than the -60 units there. The circulation is in the process of spreading and dying out.

In the last plot of Fig. 1 only remnants of the inlet circulation remains and a separation streamline now divides flow forward in the drop with predominantly reversed flow in the nozzle. Note that reversed flow begins in the boundary layer of the nozzle. At the time of the last plot of Fig. 1 the pressure cycle is past. The remaining motion of the jet is passive except for the minor influence of the small positive (unit pressure) hereafter present at the inlet. The highest pressure is at the forward most point of the jet and is a result of local deformations only.

In Fig. 2 the progress of the jet is observed at four succeeding stages. In the first of these there is evidence of local reverse circulation at the meniscus region tending to remove the concave curvature. This and the continuing flow into the chamber are because of the stabilizing surface tension in this region. At the same time the destabilizing surface tension component is causing higher pressures at the contraction although at this stage contraction is dominated simply by mass depletion due to the forward and backward flow. These processes continue to the time of the last plot of Fig. 2 where the surface tension pressure at the contraction is becoming an influence on local behavior. The meniscus region has been pushed outward to be convex partly because of the local high pressure and partly from inertial motion from the earlier restoring pressure. Also the taper of the connecting shank to the drop is no longer linear. This further indicates the influence of the surface tension pressure at the contraction.

In Fig. 3 we continue toward drop break off and include two plots following breakoff. Note that a restoring pressure of the meniscus portion drives fluid into the chamber to a small extent so that the outward bulge is diminished between the first and second plot of Fig. 3. Also we note that a second contraction is occurring just behind the drop.

Drop break off was here preset to occur when only one mesh distance ( $1/20$  of the nozzle diameter) remained. At this point the mechanics of the numerical program requires a zero radius and local angles consistent with a break. The break is assumed to be locally spherical so that the two components of surface tension are the same. This eliminates the singularity of the unstable component which takes on the value of the stabilizing component.

Two separate problems are solved simultaneously after breakup. The meniscus converges here to a spherical surface of unit radius because of the residual unit pressure at the inlet. The drop portion of the jet proceeds toward a state where a drop plus a satellite exist because of the contraction behind the main drop.

#### IV. Concluding Comments

We are interested here in summarizing those things learned from the numerical model thus far. In some cases the information was partially known from experiment and matters were clarified and/or confirmed by the model. In other cases the information from the model gave insight thus far unobtainable experimentally.

1. The peak pressure magnitudes for driving the jet are now obtainable. These, of course, depend on nozzle losses but can be fairly well estimated for an initial trial calculation.
2. The pressure history to drive the jet is nearly a symmetric one for clean drop formation with a net zero impulse for a single drop. The negative phase of the pressure history is essential to drop break off in the range of parameters here studied.
3. Uniform pressure at the inlet cross section and ignored wetting of the outer facing of the nozzle are reasonable simplifying assumptions that do not affect comparison with experiment.
4. In the range of parameters here studied, the meniscus is very overdamped as is the drop. Experimental meniscus oscillations presumably relate to chamber or chamber to nozzle transition characteristics. The latter can be studied with the present model.
5. The flow fields throughout the history of drop generation may be analyzed in almost complete detail from the numerical results and, internal flows, usually not visible experimentally, may here be studied.

References

1. Fromm, J. E., "Finite Difference Computation of the Capillary Jet, Free Surface Problem," Lecture Notes in Physics 41, 188-193, Seventh International Conference on Numerical Methods in Fluid Dynamics, Springer-Verlag, Berlin 1981.
2. Rayleigh, J. W. S., The Theory of Sound, Vol. 2, p. 351, Dover. 1945.
3. Lamb, H., Hydrodynamics, p. 450, Dover. 1945.
4. Lee, F. C., Mills, R. M.; Falke, F.E., "Drop-on-Demand Ink Jet Printing at High Print Rates and High Resolution," to be published.

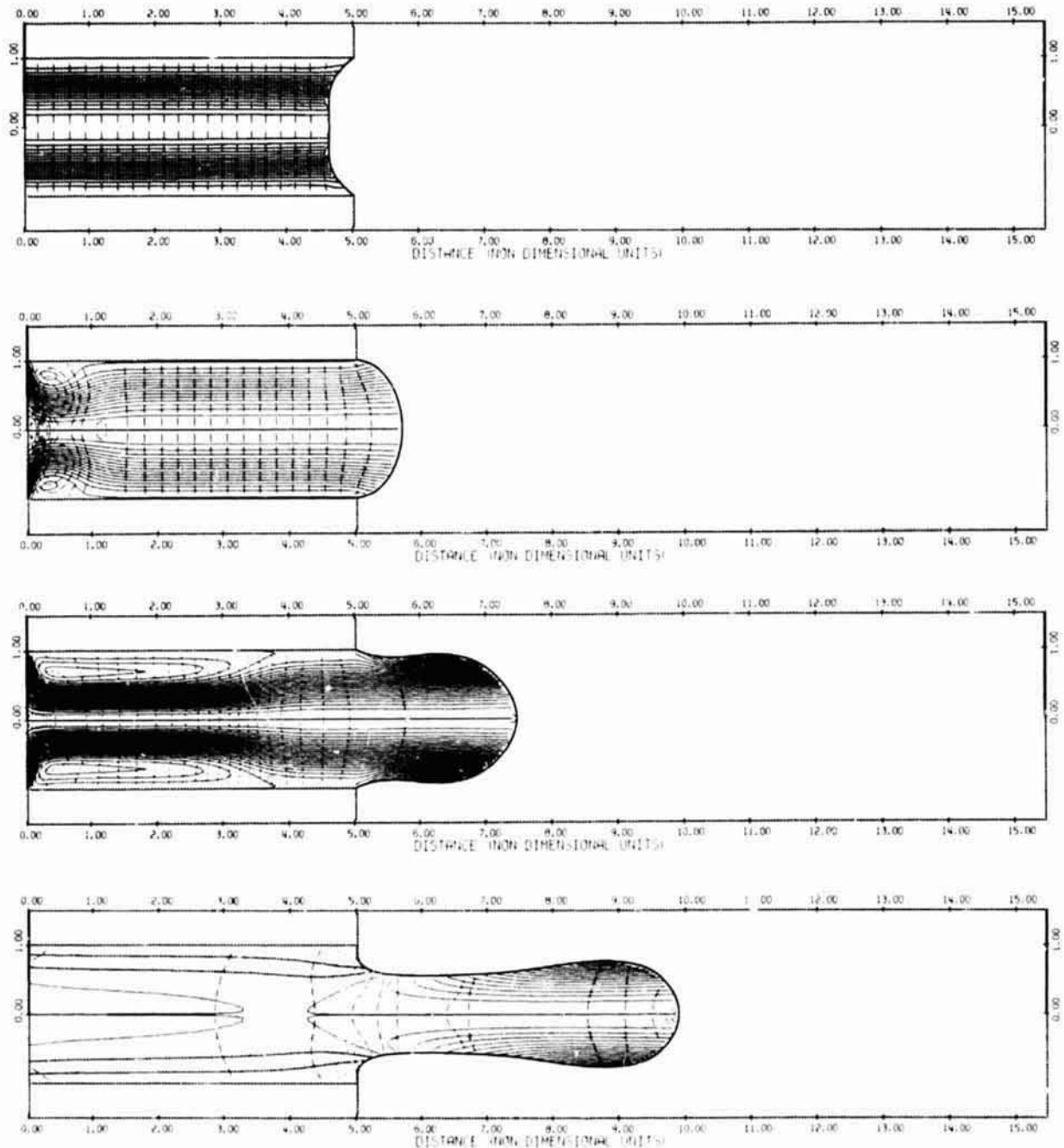


Figure 1. Computer graphical output for numerical solution of jet drop formation. See Table 2.

ORIGINAL FIGURES  
OF POOR QUALITY

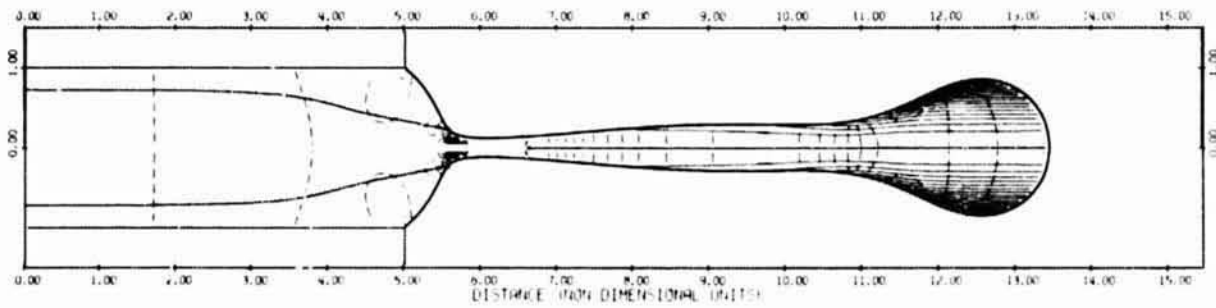
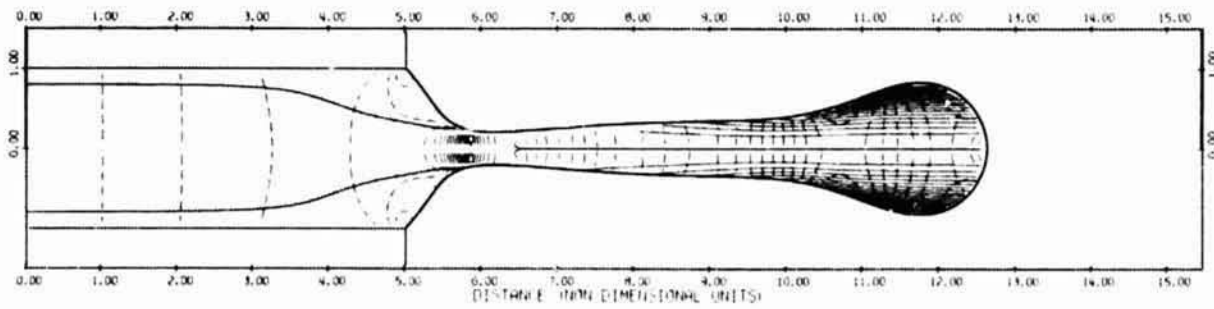
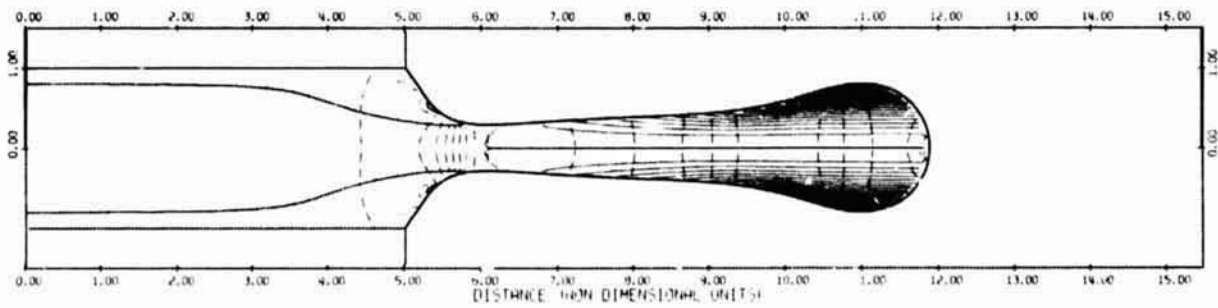
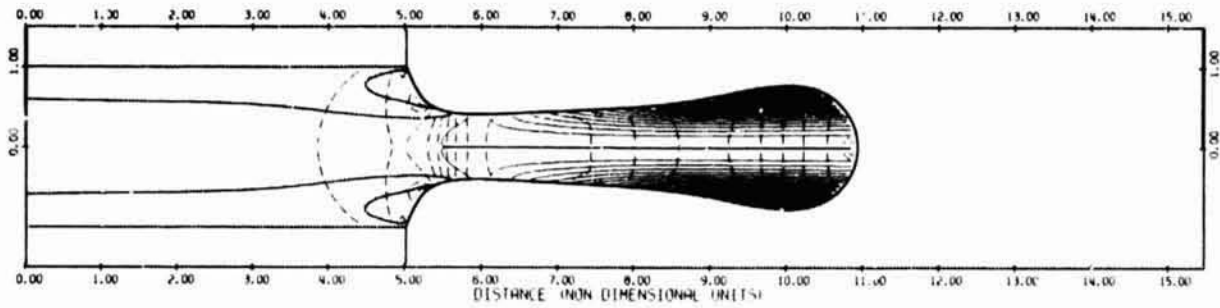


Figure 2. Continuation of Fig. 1.

ORIGINAL PAGE IS  
OF POOR QUALITY

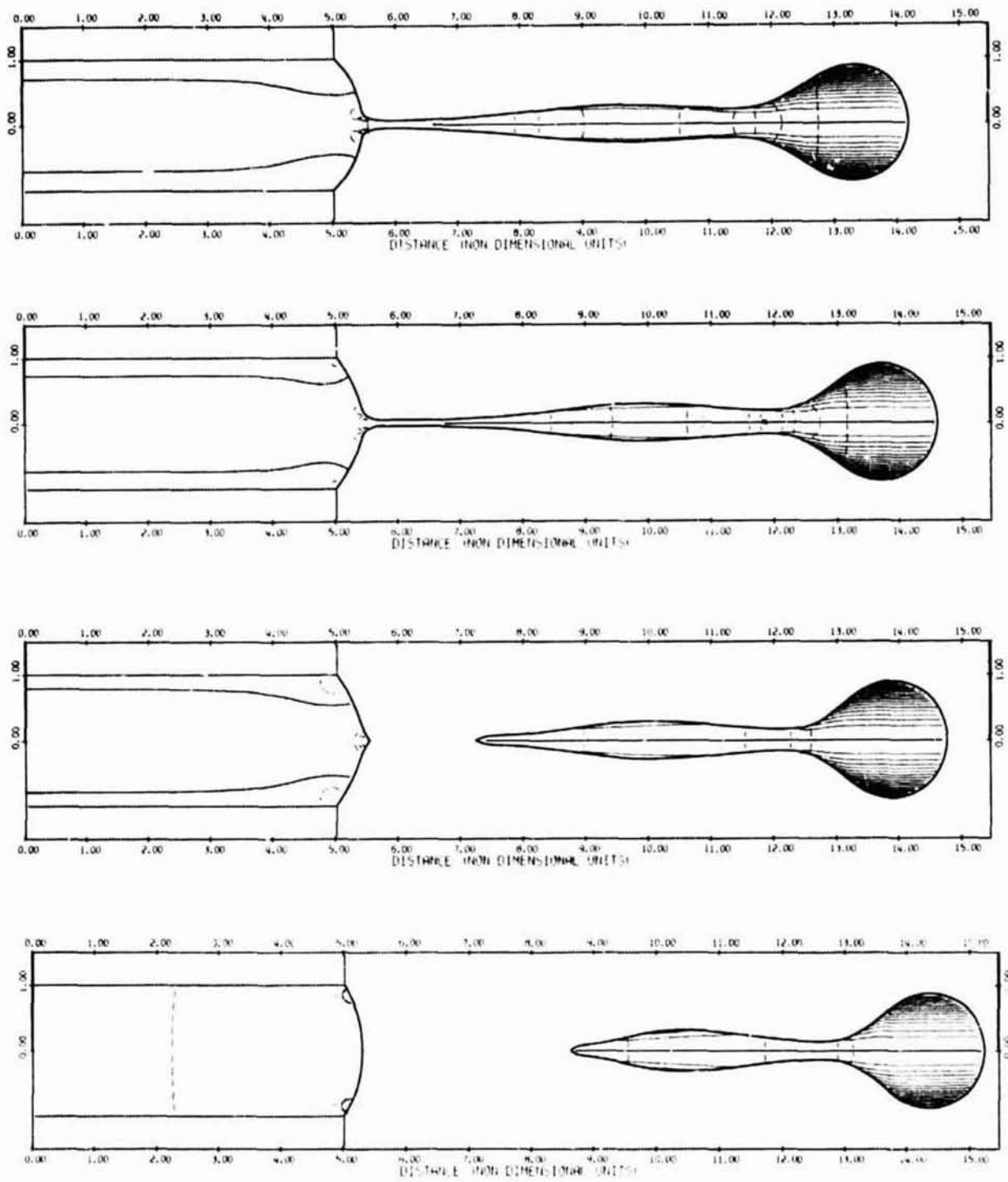


Figure 3. Continuation of Fig. 1.

Electrohydrodynamic (EHD) Stimulation of Jet Breakup

Joseph M. Crowley

Dept. of Elec. Eng., Univ. of Illinois, Urbana, Illinois  
and Xerox Corporation, Rochester, New York

Abstract

Electrohydrodynamic (EHD) excitation of liquid jets offers an alternative to piezoelectric excitation without the complex frequency response caused by piezoelectric and mechanical resonances. In an EHD exciter, an electrode near the nozzle applies an alternating Coulomb force to the jet surface, generating a disturbance which grows until a drop breaks off downstream. This interaction can be modelled quite well by a linear, long wave model of the jet together with a cylindrical electric field. The breakup length, measured on a 33  $\mu\text{m}$  jet, agrees quite well with that predicted by the theory, and increases with the square of the applied voltage, as expected. In addition, the frequency response is very smooth, with pronounced nulls occurring only at frequencies related to the time which the jet spends inside the exciter.

Introduction

Most of the existing ink jet printers based on jet breakup use acoustic excitation of the jet to introduce the disturbance which eventually grows to form ink drops. With a single jet, this method works very well, since the breakup point can be controlled through a feedback loop which alters the amplitude of the excitation. The extension of this technique to multiple jet printers presents some difficulties, however, since the jets interact with the acoustic waves set up in the exciter, causing variations in the breakup length.

Excitation based on electrostatic forces appears to offer more promise for multiple jet printers, since the excitation is applied via electrodes which are placed downstream of the nozzle, allowing individual control of individual jets. Although droplet production by electric excitation has been known for some time, there has been no work reported which offers a theoretical model of this process, or which describes systematic measurements of the breakup length with EHD excitation. The present paper is intended to fill this gap.

A Simple Theory of EHD Excitation

A detailed analysis of the EHD exciter has been undertaken, and will be presented elsewhere<sup>1</sup>. In the course of that work, a simple model was developed, which will be used here to describe the exciter used in the experiments. The geometry of the jet is defined by Figure 1, which shows a liquid jet entering an electrode. The jet has a radius  $R$ , and moves with a velocity  $U_0$ .

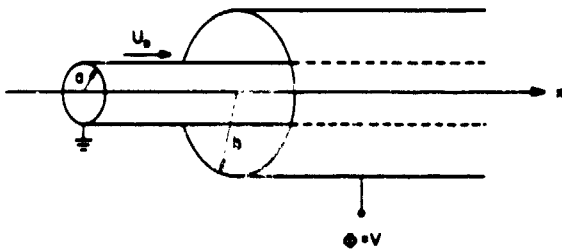


Figure 1  
A Liquid jet entering an electrode

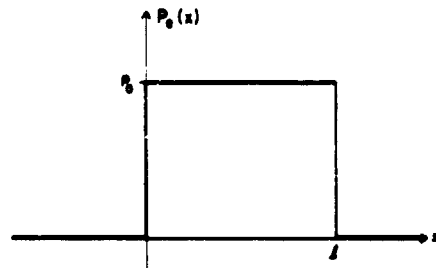


Figure 2  
Electric pressure in the step exciter

This particular electrode is shown as a cylinder, but it can have any shape, since the theory assumes only that the electric field at the surface of the jet can be calculated.

Theoretically, the jet is modelled by the long wave approximation<sup>2</sup>, in which the disturbance is assumed to be much longer than the jet radius, and the axial velocity and pressure are assumed to be constant across any section of the jet. With these assumptions, the momentum equation for motion in the axial direction can be written as

$$\frac{\partial U}{\partial t} + U \frac{\partial U}{\partial x} = - \frac{1}{\rho} \frac{\partial p}{\partial x} \quad (1)$$

while Conservation of Mass for a round jet gives

$$\frac{\partial R}{\partial t} + U \frac{\partial R}{\partial x} + \frac{R}{2} \frac{\partial U}{\partial x} = 0 \quad (2)$$

The pressure in the momentum equation consists of contributions from the surface tension of the jet and also from the electric field at its surface.

#### The Inertial Limit

The surface tension term is well known in the fluid mechanics of jets; it leads to growth of the disturbance into drops. Inside the exciter, which is usually only a fraction of a wavelength long, the droplet growth is very small, so the effects of surface tension will be neglected here. The electric pressure can be most easily obtained by using the Maxwell stress tensor at the surface of the jet. Since the jet is assumed to be a good electrical conductor, the electric field will be normal to the surface of the jet, which implies that no electric shear forces can be exerted<sup>3</sup>. The only electrical force corresponds to a (negative) pressure, given in terms of the field strength at the jet surface as

$$p(r, x, t) = - \frac{1}{2} \epsilon E^2 \quad (3)$$

For example, if the electrode surrounding the jet is assumed to be a circular cylinder of radius  $b$ , at a voltage  $V(x, t)$ , then the normal electric field at the surface of the jet will be

$$E = \frac{V(x, t)}{a \ln(b/a)} \quad (4)$$

so that the electric pressure is given by

$$p = - \frac{\epsilon V^2(x, t)}{2a^2 \ln^2(b/a)} \quad (5)$$

#### Linearization

In most of the growth region the amplitude of the waves is usually quite small, so that the equations may be further simplified by linearization. If we define

$$U = U_0 + u, \quad u \ll U_0 \quad (6)$$

$$R = a + \delta, \quad \delta \ll a \quad (7)$$

and neglect all second order terms, the equations of motion for small disturbances on the jet reduce to

$$\frac{\partial u}{\partial t} + U_0 \frac{\partial u}{\partial x} = - \frac{1}{\rho} \frac{\partial p}{\partial x} \quad (8)$$

$$\frac{\partial \delta}{\partial t} + U_0 \frac{\partial \delta}{\partial x} + \frac{a}{2} \frac{\partial u}{\partial x} = 0 \quad (9)$$

These equations have been written in terms of the convective derivative of the surface displacement, defined by

$$\delta' = \frac{\partial \delta}{\partial t} + U_0 \frac{\partial \delta}{\partial x} \quad (10)$$

In the inertial approximation, the use of this surface velocity simplifies the resulting equations.

The electric pressure depends on the electric field at the surface of the jet, and this field will usually change as the jet expands and contracts. Thus perturbations in radius will lead to perturbations in the electric pressure, which in turn depend on the detailed structure of the field near the jet. Like the surface tension term, the perturbation electric field mainly influences the growth rate of the droplet disturbance. Its effect is usually much less than that of the surface tension, so it will also be neglected, as the surface tension was. The equation of the jet then becomes

$$\left( \frac{\partial}{\partial t} + U_0 \frac{\partial}{\partial x} \right) \delta' = \frac{a}{2\rho} \frac{\partial^2 p}{\partial x^2} \quad (11)$$

The linear response of the jet will generally be expressed in terms of its response to a sinusoidal pressure variation. For each term in the Fourier series, the driving pressure is most conveniently written in terms of complex amplitudes as

$$p = \text{Re}[\tilde{p}(x) e^{i\omega t}] \quad (12)$$

The response to this drive can likewise be written as

$$\delta = \text{Re}[\tilde{\delta}(x) e^{i\omega t}] \quad (13)$$

so that the equation of motion for the exciter (Equation 12) reduces to an ordinary differential equation for the complex amplitude of the radial velocity

$$\left( i\omega + U_0 \frac{d}{dx} \right) \tilde{\delta}' = \frac{a}{2\rho} \frac{d^2 \tilde{p}}{dx^2} \quad (14)$$

There are several ways to solve this equation, but since we will be dealing with singular spatial functions such as the impulse and step, the easiest solution is that which uses the Laplace transform in  $x$ . With the definition of the Laplace transform as

$$\tilde{\delta}(x) = \int \hat{\delta}(s) e^{sx} dx \quad (15)$$

and

$$\tilde{p} = \int \hat{p}(x) e^{sx} dx \quad (16)$$

the equation can be transformed into

$$(i\omega + U_0 s) \hat{\delta}' = \frac{a}{2\rho} s^2 \hat{p} \quad (17)$$

which can be inverted to find the response as soon as the spatial distribution of electric pressure is known.

### Constant Pressure Exciter

The simplest practical exciter is a cylindrical electrode of length  $l$ . The entire exciter is driven from a single voltage source, for example  $V_0 + V_1 \sin(\omega t)$ , so that the same pressure is applied throughout. For this exciter,  $p$  has the spatial form shown in Figure 2. with a time varying magnitude of

$$p(t) = -\frac{\epsilon}{2a^2 \ln^2(b/a)} \left[ \left( V_0^2 - \frac{V_1^2}{2} \right) + 2V_0 V_1 \sin \omega t + \frac{V_1^2}{2} \sin 2\omega t \right] \quad (18)$$

This pressure has components at DC,  $\omega$ , and at  $2\omega$ , but since the equation is linear, each component can be treated separately. For the component at  $\omega$ , the electric pressure has the form

$$\bar{p} = p_0 = \frac{\epsilon V_{\text{eff}}^2}{2a^2 \ln^2(b/a)} \quad (19)$$

where  $V_{\text{eff}}$  is the effective (RMS) value of the voltage, which in this case is  $2V_0 V_1$ . For this exciter, the Laplace transform of the drive is

$$\hat{p} = -p_0 \left( \frac{1 - e^{-sl}}{s} \right) \quad (20)$$

giving the radial velocity at the exit as

$$\hat{\delta}'(x) = -\frac{ap_0}{2\rho U_0} \left[ \Delta(x) + \frac{i\omega}{U_0} e^{-\frac{i\omega x}{U_0}} - \Delta(x-l) - \frac{i\omega}{U_0} e^{-\frac{i\omega(x-l)}{U_0}} \right] \quad (21)$$

The response has an impulse ( $\Delta$ ) in velocity because the jet quickly contracts as it enters the exciter and expands as it leaves. These impulses have no effect downstream, since they vanish as soon as the jet has passed the entrance or exit. For practical purposes, then, the velocity of the jet at the exit of the exciter can be written as

$$\hat{\delta}' = \frac{i\omega ap_0}{2\rho U_0^2} \left( 1 - e^{-\frac{i\omega l}{U_0}} \right) e^{-\frac{i\omega x}{U_0}} \quad (22)$$

The velocity has an exponential delay term which can be analyzed more conveniently by extracting a factor corresponding to the center of the exciter, using the relation

$$1 - e^{-\frac{i\omega l}{2}} = e^{-\frac{i\omega l}{2}} 2i \sin \frac{\omega l}{2} \quad (23)$$

The velocity response then has the magnitude

$$|\hat{\delta}'_0| = \frac{ap_0}{\rho U_0^2} \left| \sin \frac{\omega l}{2U_0} \right| \quad (24)$$

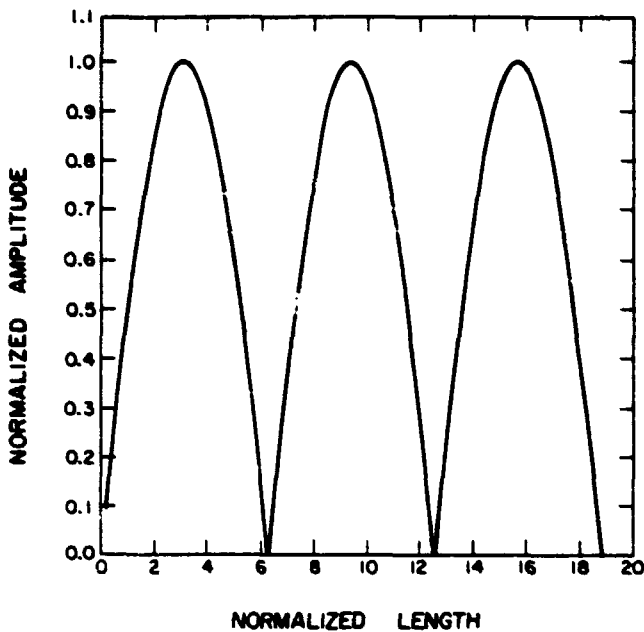


Figure 3  
Exciter output versus length

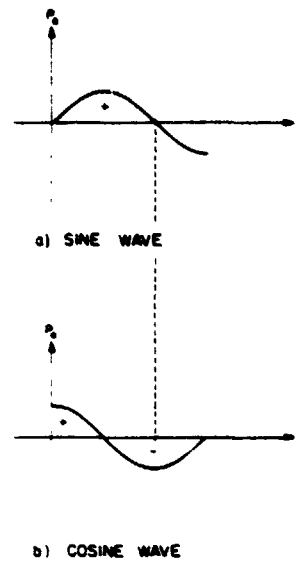


Figure 4  
Force variation within the exciter

which is shown in Figure 3 as a function of exciter length.

The nulls and peaks which occur in the response are caused by the alternation of electric pressure while the jet is inside the exciter. If the pressure is sinusoidal, as shown in Figure 4a, the net impulse given to the jet over one period of excitation will be zero, since the jet is influenced by equal and opposite half cycles. Thus if the jet is within the exciter for a whole period of excitation, (i.e., the exciter is one wavelength long), the response will show a null. On the other hand, there will be a peak for lengths which are one half wavelength long. While this effect is easy to see from Figure 4a, some care must be used in interpreting such diagrams, since they may suggest erroneous nulls, depending on the choice of phase at the inlet. For example, if the sinusoidal force were chosen to be a cosine, as in Figure 4b, it would be easy to infer that the null would occur when the exciter is only one half wavelength long. This is not true, because the cosine is one special choice from all of the phases which occur during a complete cycle.

Because of the peaks and nulls in the frequency response, the output of the exciter can not be increased indefinitely simply by increasing the length of the exciting electrodes. Instead, an optimum length, which may be fairly small by macroscopic standards, must be selected to achieve maximum output. This explains why the electrodes used in earlier work on EHD excitation were usually not very efficient.

#### Downstream Response

The approximate surface displacement far downstream is given by<sup>1</sup>

$$s = \frac{\delta'_0}{2\mu U_0} e^{\mu x} \quad (25)$$

where

$$(\mu a)^2 = \alpha^2 \left( \frac{\omega a}{U_0} \right)^2 \left[ 1 - \left( \frac{\omega a}{U_0} \right)^2 \right] \quad (26)$$

The breakup length can be determined by extrapolating the downstream response to the point of breakup,  $l_b$  to give the breakup length equation,

$$\xi_B = \frac{1}{\nu} c_n \left( \frac{2a_0 U_0}{\delta_0^2} \right)$$

(27)

Thus the breakup length can be calculated as soon as the exciter output is known.

## Experiments

### Apparatus

Several experiments were performed in order to test the predictions of the EHD exciter theory. The nozzle and associated apparatus were mounted on a specially designed frame which allowed adjustment and positioning suitable for the experiments. The fluid used in most of these experiments had a density of 1030 kg/m<sup>3</sup> and a surface tension of 39 mN/m. The jet formed by the nozzle had a radius of 16.5  $\mu$ m. Its velocity was determined by measuring the wavelength of the disturbance at a known frequency.

The exciter electrodes used in most of these experiments consisted of steel plates of various nominal thicknesses (3-7 mil, or 75-175  $\mu$ m) through which holes were drilled. The holes ranged in nominal diameter from 3-7 mils (75-175  $\mu$ m). Microscopic examination of the electrodes revealed that the holes were essentially straight sided, although occasional burrs could be seen.

### Procedure

Since the electrodes consisted of a single piece of metal, they had to be in position before the jet was turned on to avoid splashing and electrical shorting between exciter and ground. As a compromise between speed and complexity, we first located the approximate axis of the jet by focussing a microscope on the nozzle orifice along the nozzle axis. The electrode, mounted on a three axis micromanipulator, was then moved into position so that the desired exciter hole appeared to be on the nozzle axis, as seen through the microscope. The microscope was then removed to the side, where the jet and hole would both be visible at an oblique angle, and the jet turned on. The original electrode placement was usually within a few mils of the desired placement, could be quickly adjusted to center the electrode and allow the jet to stream through unhindered.

The jet was then turned off to allow the electrode to be cleaned by wiping with absorbant paper towels. Upon restarting, the jet always went through the hole cleanly, without splashing or blocking, even for the 3 mil hole, once the initial centering procedure had been carried out. In most cases, the jet would restart cleanly even if the electrode had not been wiped clean.

Several arrangements were used to provide different voltage levels. An operational amplifier could be connected directly to the electrodes, giving voltage up to 150V. In order to increase the voltage, the output of the operational amplifier was often connected to either a wide band or a narrow band transformer. The secondary winding of the transformer furnished higher AC voltages than the amplifier, and additional increases in the effective voltage could be achieved by connecting the secondary in series with a DC power supply. With this arrangement, peak voltages up to 800V were obtained. This voltage was not limited by breakdown in the exciter, but by the available power supplies and amplifiers.

In carrying out the experiments, the jet was turned on and the voltages adjusted to the desired value. The position of the breakup was then measured by a micrometer which moved a long focal length microscope to the breakup point while the phase of the viewing strobe was slowly rolled. The breakup position can be measured very precisely (+10  $\mu$ m) with this technique if the jet is quiet. At very long breakup lengths (>4 mm), the natural breakup of the jet caused the breakup point to vary erratically. Lateral movement of the electrode varied the breakup point, probably by increasing the electric field strength at the surface of the jet. This effect was used to center the jet before each measurement, since the point of minimum excitation should correspond to a centered jet.

## Frequency Response

The simple theory presented above predicts maxima and minima in the frequency response of the exciters. In order to test these predictions, frequency sweeps were performed on a number of exciters. The easiest feature of the response to check is the null which occurs when the frequency corresponds to an entire wavelength of the disturbance inside the jet at any time. Figure 5 depicts the frequency response for an electrode which is 7 mils (178  $\mu\text{m}$ ) thick.

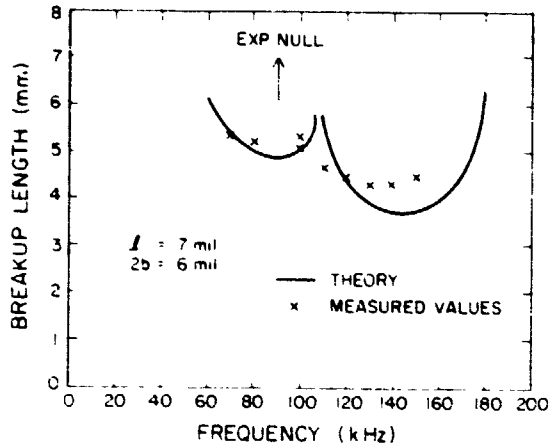


Figure 5  
Frequency response for a 7 mil exciter

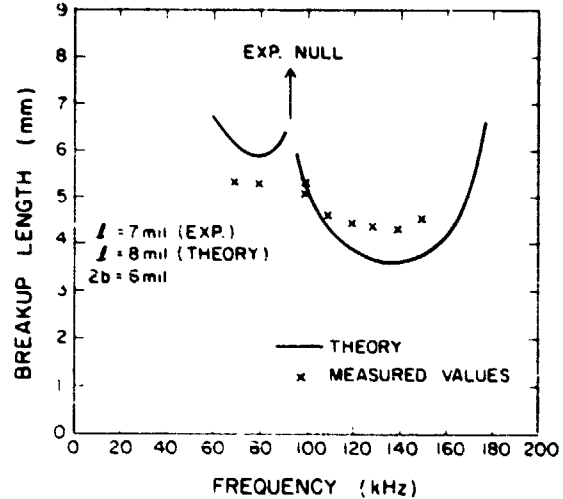


Figure 6  
Same thickness, but 8 mil theory

For this length, the null is expected at 108 kHz. Since this null occurs near the maximum growth rate of the jet, it could be observed experimentally by varying the frequency to produce the longest apparent breakup length. This null frequency (shown in Figure 5.3 by an arrow) is lower than expected from theory by approximately 15%. Reasonable variations in the fringing length and jet velocity could not account for the discrepancy, but increasing the effective length of the exciter from 7 to 8 mils gave better agreement, as shown in Figure 6. This extension in length might be justified by the presence of burrs at either end of the hole, since such burrs were often observed in microscopic examination of the holes. Another possibility is the effect of fringing in extending the effective length of the electrode beyond the physical limits of the conductor.

This exciter exhibits the predicted null in the frequency response, but does not test the exciter at the thickness which is expected to give the shortest breakup length. Since short breakup length is desired in practical printers, the frequency response of a shorter (3 mil or 76  $\mu\text{m}$ ) electrode was also measured. The results of this measurement, along with the predictions of the theories, are shown in Figure 7.

Just as in the earlier measurements, the theory predicts both the magnitude and the shape of the frequency response quite well ( $\pm 0.2$  mm or 10%) whether the fringing fields are included or not, although the fringing approximation seems to give better results at the shortest breakup lengths. To appreciate this agreement, it should be kept in mind that the theory, which rests on the fundamental equations of electrostatics and fluid mechanics, contains no adjustable parameters. The breakup length is predicted only in terms of geometrical measurements, applied voltage, and material properties.

## Voltage response

Compared to acoustic excitation, EHD excitation is often relatively weak, so that the magnitude of the drive is extremely important in practice. The theory presented above predicts that the excitation pressure is proportional to the square of the effective voltage, so that a relatively large increase in the excitation may be obtained by increasing the voltage at which the exciter operates. This prediction was tested experimentally by varying both the AC and DC voltage levels over a wide range, and measuring the breakup length.

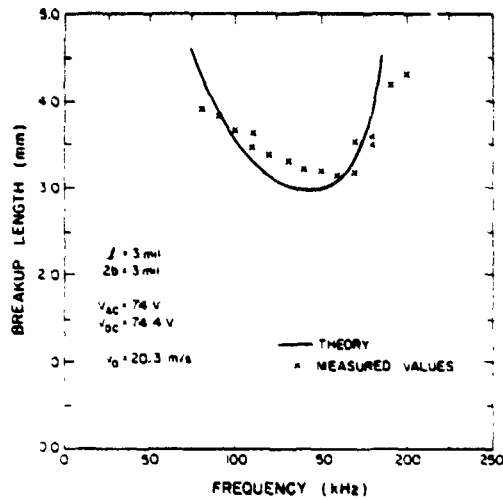


Figure 7  
Frequency response for a 3 mil thickness

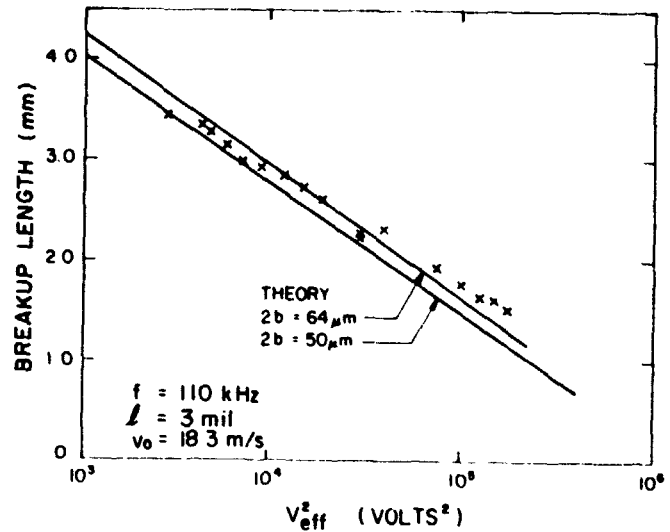


Figure 8  
Breakup length versus effective voltage

Since the breakup length depends logarithmically on the excitation, a plot of breakup length against the logarithm of the effective voltage should give a straight line. Experimental values of breakup length are plotted in this way in Figure 8, along with the predictions of the simple theoretical model. Both the magnitude and slope of the breakup length follow the predictions well, although the slope of the line appears to be somewhat flatter than expected. These results give us some confidence in extrapolating the design to even higher voltages to achieve a shorter breakup length if necessary, although these lengths are already comparable to those used in acoustic excitation.

#### Acknowledgments

The experimental work described here was carried out at the laboratories of the Xerox Corporation at Webster, New York, on occasional visits. Its success is due in large measure to the active cooperation of several people, especially Thomas Warren, in seeing that the necessary equipment was set up and working, and that help was always available when needed.

#### References

1. Crowley, J. M., "The Theory of Electrohydrodynamic Droplet Generators," to be published
2. Lee, H. C., "Drop Formation in a Liquid Jet," IBM Journal of Research and Development, July, 1974, pp.364-369
3. Melcher, J. R., Field Coupled Surface Waves, MIT Press, Cambridge, Mass., 1963

## The stress system generated by an electromagnetic field in a suspension of drops

M. Emin Erdoğan

Istanbul Teknik Üniversitesi, Makina Fakültesi, Gümüşsuyu, İstanbul, Turkey

### Abstract

This paper deals with the calculation of the stress generated in a suspension of drops in the presence of a uniform electric field and a pure straining motion, taking into account that the magnetohydrodynamic effects are dominant. It is found that the stress generated in the suspension depends on the direction of the applied electric field, the dielectric constants, the viscosity coefficients, the conductivities and the permeabilities of fluids inside and outside the drops. The expression of the particle stress shows that for fluids which are good conductors and poor dielectrics, especially for larger drops, magnetohydrodynamic effects tend to reduce the dependence on the direction of the applied electric field.

### Introduction

The study of a flow system in which the electric field and the velocity field effect each other is called electrohydrodynamics. The applications of electrohydrodynamics are numerous: cryogenic fluid management in the zero-gravity environment of space, formation and coalescence of solid and liquid particles, electrogasdynamic high voltage and power generation insulation research, physicochemical hydrodynamic, heat, mass and momentum transfer, electrofluid dynamics of biological systems, and atmospheric and cloud physics.<sup>1-5</sup> In nature and industry we are quite often concerned with the properties of a fluid in which small particles are suspended and carried about by the motion of the ambient fluid. If the average distance between the particles is small compared with the characteristic length of the motion of the suspension, one can regard the suspension as a homogeneous fluid. The problem is to determine the rheological properties of this equivalent fluid from the knowledge of the properties of the ambient fluid. The macroscopic properties of the suspension will be referred to as bulk properties. When the suspension is dilute, the suspending fluid Newtonian the particles rigid spheres, and the particle Reynolds number sufficiently small, the suspension can be described in bulk as a Newtonian fluid with an effective viscosity  $\mu^* = \mu (1 + 2.5 c)$ , provided only that the particles are not subjected to an externally applied force or couple. For the more general case, the non-isotropic structure of the suspension usually results in a non-Newtonian form for the bulk stress tensor.<sup>6</sup> The formulation of the problem of determining the stress in a suspension of particles is not straight-forward, partly due to the fact that the bulk stress in a suspension is not obvious. Bulk stress and other bulk properties are defined in terms of ensemble averages of the actual quantities. This is shown by Batchelor<sup>6</sup> to be equivalent to defining bulk properties in terms of volume averages provided that the averaging volume is chosen to contain many particles and is such that the statistical properties of the suspension are uniform over it.

In the case of a dilute suspension, which means that the flow near any one particle is independent of all the other particles, the contributions to the bulk stress from the various particles are linearly additive. The contributions may be classified in three groups: : The first is a purely isotropic contribution, the second is the contribution of the deviatoric stress and the third represents the contribution to the bulk stress due to the presence of the particles. The stress in third type of contribution is termed as "particle stress" and only the deviatoric part of it is significant.

Non-Newtonian behavior of a suspension can occur in general in the following cases:<sup>7</sup> (i) Non-spherical particles can cause some directional properties.<sup>6,8</sup> (ii) The effect of weak Brownian motion.<sup>9</sup> (iii) The effect of a couple on a particle is to rotate and to generate an antisymmetric part of the particle stress tensor.<sup>8,10</sup> (iv) The effect of the shape of a deformable particle gives rise to non-linear stress.<sup>11</sup> (v) Surface tension at the boundary of a fluid particle or elasticity of a solid particle can cause time-dependent effects and the suspension exhibits visco-elastic properties.<sup>11,12</sup> (vi) In the case of sufficiently large size, the inertia forces cannot be neglected in the relative motion near one particle and the particle stress depends non-linearly on the bulk velocity gradient.<sup>13</sup>

In this paper an expression is found for the particle stress tensor of a suspension of drops in an electric field. It is assumed that the suspension is dilute, suspending fluid Newtonian, the drops spheres and the particle Reynolds number sufficiently small. The explicit form of the stress tensor depends on the electromagnetic properties of the drops and their surroundings; therefore, the flow due to a single drop is needed in determining the

particle stress of a suspension. For this reason, consideration is given first to the flow due to a drop in the presence of an electric field in a pure straining motion.

Experimentally and theoretically it has been shown by Taylor<sup>14</sup> that a circulation can occur in a drop and its surrounding in the presence of a uniform electric field. This flow field set up is due to the surface charge and the tangential electric field stress over the surface of the drop. The flow field outside the drop given in<sup>14</sup> is very similar to a system in which the field carries a uniform current.<sup>15,16</sup> In such a case the flow field is produced by the rotational Lorentz force due to the distorted electric current and the associated magnetic field. For fluids which are poor conductors the magnetic effects are negligible, and for fluids which are good conductors and poor dielectrics, or for larger drops the magnetohydrodynamic effect may be dominant.<sup>17</sup>

Following the general arguments given in<sup>18</sup> and <sup>19,20</sup> the pressure and the velocity in the fluid outside the drop and inside the drop which is embedded in a pure straining motion are determined. Since the governing equations are linear in terms of velocity and the electric field, the effects in the cases of a drop in an electric field in the absence of a pure straining motion and a drop in a pure straining motion without an electric field can be superimposed.

Since it is assumed that the suspension is dilute, the flow near one drop is independent of other drops and so we may use the results obtained for one drop to evaluate the integral in the particle stress. The expression of the particle stress has two terms, one with an applied electric field and the other without electric field. The term which depends on electric field presents a directional effect, and this makes the suspension a non-Newtonian fluid. This shows that the suspension of drops in an electric field cannot be represented by a viscosity that is independent of the rate-of-strain. The viscosity depends on the direction of the applied electric field.

The first term of the particle stress shows the effect in the absence of an applied electric field, and the second term denotes the additional effect due to the applied electric field. The second term contains two parts: one is due to the absence of the magnetic effect in the fluid outside the drop and the other is due to the presence of the magnetic effect. When the magnetohydrodynamic effect is absent, the expression of the particle stress reduces to that of given in.<sup>21</sup>

#### The expression of the bulk stress

In order to establish the relation of the bulk stress to the velocity and stress distributions in the fluid near individual particles, the expression for the bulk stress in the suspension as a volume integral is used. The average volume  $V$  is chosen to contain many particles and is such that the statistical properties of the suspension are uniform over it. The hydromechanical bulk stress in the suspension is

$$\Sigma_{ij} = \frac{1}{V} \int \sigma_{ij} dV .$$

since the effect of inertia forces in the relative motion near a particle is neglected. The Maxwell bulk stress tensor may be defined in a similar manner. The bulk velocity gradient is given by

$$\frac{\partial U_i}{\partial x_j} = \frac{1}{V} \int \frac{\partial u_i}{\partial x_j} dV ,$$

where  $\sigma_{ij}$  and  $u_i$  are the actual values of the hydromechanical stress and velocity at any point  $x$  in the suspension, whether it be in the ambient fluid or inside a particle. The surface and the volume of a typical particle in  $V$  will be denoted by  $A_0$  and  $V_0$  respectively.

Assuming that the ambient fluid is Newtonian with the viscosity  $\mu$  the hydromechanical bulk stress may be written as

$$\Sigma_{ij} = \frac{1}{V} \int_{V-\Sigma V_0} \left\{ -p\delta_{ij} + \left( \frac{\partial u_i}{\partial x_j} + \frac{\partial u_j}{\partial x_i} \right) \right\} dV + \frac{1}{V} \sum \int_{V_0} \sigma_{ij} dV , \quad (1)$$

where the summation is over all the particles in  $V$ . The bulk velocity gradient becomes

$$\frac{\partial U_i}{\partial x_j} = \frac{1}{V} \int_{V-\Sigma V_0} \frac{\partial u_i}{\partial x_j} dV + \frac{1}{V} \sum \int_{A_0} u_i n_j dA \quad (2)$$

where  $n$  is an outward unit normal to  $A_0$ . Neglecting inertia effects, the following can be written :

$$\int_{V_0} \sigma_{ij} dV = \int_{A_0} \sigma_{ik} x_j n_k dA \quad (3)$$

With the addition (2) and (3), the expression (1) becomes

$$\begin{aligned} \Sigma_{ij} = & -\delta_{ij} \frac{1}{V} \int_{V-\Sigma V_0} p dV + \mu \left( \frac{\partial u_i}{\partial x_j} + \frac{\partial u_j}{\partial x_i} \right) \\ & + \frac{1}{V} \Sigma \int_{A_0} \left\{ \sigma_{ik} x_j n_k - \mu (u_i n_j + u_j n_i) \right\} dA \end{aligned} \quad (4)$$

The volume  $V-\Sigma V_0$  is wholly occupied by ambient fluid and the volume  $V_0$  must be regarded as including the interfacial layer; and the surface  $A_0$  will be regarded as a surface just outside of the interfacial layer. The first term in the expression for  $\Sigma_{ij}$  in (4) is a purely isotropic contribution, the second is the deviatoric stress and the third represents the contribution to the bulk stress due to the presence of the particles. The third term in (4) is called the "particle stress" and is denoted with  $\Sigma_{ij}^{(p)}$ .

It is assumed that the suspension of particles is force-free and couple-free. Since the exertion of a couple on the particles by external means generates an antisymmetric contribution to the bulk stress, the bulk stress in the absence of a couple exerted on particles thus becomes a symmetrical tensor.

When the ratio of the convection of charge to the conduction current, which is referred to as the electric Reynolds number, is much smaller than unity, the influence of the electric stresses on the fluid is included in the model, but there is no reciprocal effect of the motion on the fields. A similar situation for the magnetic field can be considered with no effect of the motion on the magnetic field; and the electric current density is thus given by its electrostatic form. For this reason, in this paper, in view of the absence of the reciprocal effect of the motion on the electromagnetic field, the hydromechanical bulk stress in the suspension is considered alone.

#### Governing equations

The magnetic induction in the fluid in and out of the drop is not negligible because of dynamic currents are not small enough. It is assumed that the influence of the electric stresses on the fluid is included in the model, but there is no reciprocal effect of the motion on the fields. Therefore, the appropriate laws of electrodynamics are essentially those of electrostatics for the electric field and the electric current density, except for the magnetic induction field. Under the conditions considered here, the governing equations of electrohydrodynamics are<sup>2,2</sup>:

$$\nabla \cdot \mathbf{E} = 0, \quad (5)$$

$$\nabla \cdot \mathbf{E} = 0, \quad (6)$$

$$\mathbf{J} = \sigma \mathbf{E} \quad (7)$$

$$\nabla \times \mathbf{H} = \mathbf{J} \quad (8)$$

$$\nabla \cdot \mathbf{H} = 0 \quad (9)$$

$$\nabla p = \mu \nabla^2 \mathbf{u} + \chi \sigma \mathbf{E} \times \mathbf{H} \quad (10)$$

$$\nabla \cdot \mathbf{u} = 0 \quad (11)$$

where  $\mathbf{E}$ , is the electric field intensity,  $\mathbf{J}$  the electric current density,  $\mathbf{H}$  the magnetic field,  $\sigma$  the electric conductivity,  $\mathbf{u}$  the velocity,  $p$  the pressure,  $\mu$  the viscosity,  $\chi$  the permeability. Throughout the paper MKS units are used. Because of the absence of fluid motions the term  $\sigma \chi \mathbf{u} \times \mathbf{H}$  in (7) and the term  $\sigma \chi (\mathbf{u} \times \mathbf{H}) \times \mathbf{H}$  in (10) are omitted.

The boundary conditions to be applied at the interface of a drop in an electric field are the following<sup>2,2</sup>

$$n \times \{E\} = 0 \quad (12)$$

$$n \cdot \{\sigma E\} = 0 \quad (13)$$

$$n \cdot \{u\} = 0 \quad (14)$$

$$n \times \{u\} = 0 \quad (15)$$

$$n \times \{\sigma + t + h\} = 0 \quad (16)$$

$$n \cdot \{\sigma + t + h\} + T \left( \frac{1}{R_1} + \frac{1}{R_2} \right) = 0 \quad (17)$$

where  $\sigma$  is the viscous stress,  $t$  and  $h$  are the electric part and magnetic part of the Maxwell stress tensor, respectively, and  $\{A\}$  denotes the jump of  $A$  across the interface.  $T$  is the surface tension, and  $R_1$  and  $R_2$  are the radii of curvature of the surface, these radii are taken as positive when the corresponding center of curvature lies on the side of the interface to which  $n$  points.

Under the conditions considered here, the electric field  $E$  and  $H$  and the velocity field  $u$  can be determined independently by equations (5)-(11) and then, they can be related by the boundary conditions (12)-(17).

#### A drop in an electric field

We consider a drop or bubble, assuming that its shape is spherical with radius  $a$ . The distance between electrodes and the drop measures to many radii thus causing the electric field far from the drop to be uniform. An appropriate spherical polar coordinates are defined with the origin at the center of the drop and the symmetry axis in the direction of the applied field. There are four boundary conditions for the electric field intensity: (i)  $E$  is finite inside the drop, (ii) the tangential component of the electric field is continuous across the surface of the drop; (iii) there is no surface current; and (iv)  $E$  tends to  $E_0$  as  $|x|$  tends to infinity. Subject to these boundary conditions, equations (5)-(7), (12) and (13) give for the electric field outside the drop

$$E = E_0 \left( 1 + \frac{1-\alpha}{2+\alpha} \frac{a^3}{r^3} \right) - 3 \frac{1-\alpha}{2+\alpha} \frac{a^3 (E_0 \cdot x) x}{r^5} \quad (18)$$

where  $r = |x|$ , and for that inside the drop

$$\bar{E} = \frac{3}{2+\alpha} E_0 \quad (19)$$

where  $\alpha = \bar{\sigma}/\sigma$ . A symbol with a bar is used for the quantities of the medium inside the drop and a symbol without a bar is used for those of the medium outside the drop. The expression in equation (19) shows that the electric field inside the drop is uniform.

Since there is no applied magnetic field, equations (8) and (9) give for the magnetic field outside the drop

$$H = -\frac{1}{2} \sigma \left( 1 - 2 \frac{1-\alpha}{2+\alpha} \frac{a^3}{r^3} \right) x \times E_0 \quad (20)$$

and for that inside the drop

$$\bar{H} = -\frac{3\bar{\sigma}}{2(2+\alpha)} (x \times E_0) \quad (21)$$

The circulation in and round the drop is responsible for the electric surface force density and the magnetic force density which are related to the Maxwell stress tensor. Expression of  $t$  and  $h$  over the surface of the drop are needed. The tangential and normal component differences of  $t$  across the surface of the drop are

$$n \times \{t\} = \frac{9\bar{E}}{(2+\alpha)^2} (\alpha\beta - 2) (n \times E_0) (n \cdot E_0) ,$$

$$n \cdot \{t\} = \frac{9\bar{E}}{2(2+\alpha)^2} \left[ E_0^2 (1-\beta) + (E_0 \cdot n)^2 (\beta + \alpha^2\beta - 2) \right] ,$$

where  $\beta = \epsilon/\bar{\epsilon}$  is the ratio of the permittivities. The tangential and normal component differences of  $h$  across the surface of the drop are

$$n \times \{h\} = 0 \quad ,$$

$$n \cdot \{h\} = \frac{9a^2 \sigma^2}{8(2+\alpha)^2} (\bar{\chi} - \chi)(n \times E_0)^2 \quad ,$$

The flow considered in this paper is governed by equations (10) and (11). The boundary conditions for the velocity are: (i)  $u$  is finite inside the drop and tends to zero as  $|x|$  tends to infinity; (ii)  $u \cdot n = 0$  and  $\bar{u} \cdot n = 0$  at the interface; (iii) the tangential component of the velocity across the drop is continuous; (iv) tangential electric stress and tangential magnetic stress and tangential viscous stress are in balance at the interface.

Following the general arguments given in<sup>18</sup> and<sup>19</sup> the pressure and the velocity in the fluid outside the drop<sup>23</sup> can be written as

$$\frac{P - P_0}{\mu} = b_{jj} R(r) + b_{kj} x_k x_j Q(r) \quad , \quad (22)$$

$$u_i = b_{jj} x_i f(r) + b_{ij} x_j g(r) + b_{kij} x_k x_j x_i h(r) \quad (23)$$

where

$$b_{ij} = E_{\alpha i} E_{\alpha j} \quad , \quad b_{ij} = b_{ji} \quad , \quad b_{ii} = E_{\alpha i}^2 \quad ,$$

and the expressions for  $R, Q, f, g$  and  $h$  are given in the appendix. Using the same reasoning as for outside the drop, the pressure and the velocity inside the drop<sup>23</sup> can be written as

$$\frac{P - \bar{P}_0}{\bar{\mu}} = b_{jj} \bar{R}(r) + b_{kj} x_k x_j \bar{Q}(r) \quad , \quad (24)$$

$$\bar{u}_i = b_{jj} x_i \bar{f}(r) + b_{ij} x_j \bar{g}(r) + b_{kij} x_k x_j x_i \bar{h}(r) \quad , \quad (25)$$

where the expression for  $\bar{R}, \bar{Q}, \bar{f}, \bar{g}$  and  $\bar{h}$  are given in the appendix.

The balance of the normal stresses on the interface of the drop is given by equation (17). Since it is assumed that the interface of the drop is to be spherical the last term in equation (17) is replaced by  $-2T/a$ . In order to find out whether the drop will become oblate or prolate under conditions where equation (17) is not quite satisfied, the Taylor technique<sup>14</sup> is employed and it is assumed that a stress  $F_0 \cos^2 \theta [x_i (E_{\alpha i} n)^2 / E_0^2]$  is applied normally to the surface of the drop, which is necessary to keep it spherical. Replacing  $T$  in the modified form of equation (17) it is found that

$$P_0 - \bar{P}_0 = \frac{\bar{\mu} U (3+2\gamma)}{a} + \frac{9\bar{\epsilon} E_0^2 (1-\beta)}{2(2+\alpha)^2} - \frac{2T}{a} - \frac{3\sigma^2 a^2 E_0^2}{2(2+\alpha)^2} - \frac{9\sigma^2 a^2 E_0^2}{2(2+\alpha)^2} (\chi + \bar{\chi}) \quad ,$$

$$F_0 = \frac{\bar{\epsilon} E_0^2}{(2+\alpha)^2} \left\{ \frac{9}{2} \left[ \beta(1+\alpha)^2 - 2 + \frac{2}{5} \frac{(3+2\gamma)(\alpha\beta-1)}{\gamma+1} \right] - \frac{3\chi\sigma^2 a^2}{40\bar{\epsilon}} \left[ \frac{7-2\alpha-5\alpha^2}{\gamma+1} + 14 - 4\alpha - (25 + 15 \frac{\bar{\chi}}{\chi}) \alpha^2 \right] \right\}$$

where  $\gamma = \mu/\bar{\mu}$ . The expression of  $F_0$  has been given in<sup>17</sup> (an arithmetic error in equation (30) in<sup>17</sup> is corrected, and 44 is replaced by 14). The equilibrium geometry depends on  $F_0$ , namely the functional relation which is given by  $\alpha, \beta, \gamma, \chi, \bar{\chi}, \sigma$  and  $a$ . For a detailed discussion the reader may be referred to.<sup>17</sup>

#### A drop in an electric field in a pure straining motion

Since the governing equations are linear in terms of the velocity and electric field, the effects in the case of a drop in an electric field without a linear velocity at infinity and that of a drop embedded in a pure straining motion in the absence of a uniform electric field at infinity can be superimposed. Following the general arguments given in the previous paragraph the pressure and the velocity in the fluid outside the drop can be written as

$$\frac{P-P_0}{\mu} = b_{ij} R(r) + h_{kj} x_k x_j Q(r) + B \frac{e_{kj} x_k x_j}{r^3}, \quad (26)$$

$$u_i = b_{ij} x_j f(r) + b_{ij} x_j g(r) + b_{kij} x_k x_j x_i h(r) + e_{ij} x_j G(r) + e_{kij} x_k x_j x_i H(r) \quad (27)$$

and inside the drop as

$$\frac{\bar{P}-\bar{P}_0}{\mu} = b_{ij} \bar{R}(r) + b_{kij} x_k x_j \bar{Q}(r) + \bar{B} e_{kj} x_k x_j, \quad (28)$$

$$\bar{u}_i = b_{ij} x_j \bar{f}(r) + b_{ij} x_j \bar{g}(r) + b_{kij} x_k x_j x_i \bar{h}(r) + e_{ij} \bar{G}(r) + e_{kij} x_k x_j x_i \bar{H}(r), \quad (29)$$

where  $k, Q, f, g, h, \bar{R}, \bar{Q}, \bar{f}, \bar{g}, \bar{h}, B, G, H, \bar{B}, \bar{H}$  are given in the appendix. Although a similar discussion to that given in the previous paragraph for the shape of the drop can be done, this is beyond the scope of this paper.

#### The particle stress in a dilute suspension

By the expression dilute suspension it is meant that the flow near one particle is independent of all the other particles. However, a simple model<sup>4</sup> illustrates how surprisingly close the spheres are for concentrations which are numerically quite small. The relation (4) shows that for a dilute suspension the different particles in the volume  $V$  of suspension make linearly additive contributions to the particle stress and the particle stress obtained under these conditions is correct to the order of  $c$  (where  $c$  is the concentration of particles by volume). Thus, the results obtained in the previous section may be used to evaluate the third term in equation (4). However, some necessary modifications must be made. The velocity, pressure and stress in the fluid will be written as

$$u_i = e_{ij} x_j + u'_i, \quad p = P + p', \quad \sigma_{ik} = -P \delta_{ik} + 2\mu e_{ik} + \sigma'_{ik},$$

where  $P$  is a constant and  $u'_i, p', \sigma'_{ik}$  are the disturbance quantities resulting from the presence of the particle. The particle stress becomes

$$\Sigma_{ij}^{(p)} = \frac{1}{V} \int_{A_0} \{ \sigma'_{ik} x_j n_k - \mu (u'_i n_j + u'_j n_i) \} dA, \quad (30)$$

since only the deviatoric part of the particle stress is significant, the term  $-P \delta_{ij}$  and similar terms are omitted.

Inserting equations (26) and (27) in equations (30) and using the well-known identities

$$\int n_i n_j dA = \frac{4\pi a^2}{3} \delta_{ij},$$

$$\int n_i n_j n_k n_l dA = \frac{4\pi a^2}{15} (\delta_{ij} \delta_{kl} + \delta_{ik} \delta_{jl} + \delta_{il} \delta_{jk}),$$

in which the integration is carried over the surface of a sphere of radius  $a$ , the following equation is obtained

$$\Sigma_{ij}^{(p)} = c \left[ \frac{\gamma(2\gamma+5)}{\gamma+1} \mu e_{ij} + \frac{27(1-\alpha\beta)\gamma}{5(2+\alpha)^2(1+\gamma)} (1-\lambda\Phi) \bar{E}_{ij} \bar{E}_{ij} \right], \quad (31)$$

in this equation

$$\Phi = \frac{\gamma+1}{9\gamma(1-\alpha\beta)} \left[ \frac{1}{2} + \frac{(1-\alpha)(7+5\alpha)}{4(1+\gamma)} \right], \quad \lambda = \frac{\chi \sigma^2 a^2}{\xi}, \quad \alpha = \frac{\sigma}{\sigma'}, \quad \beta = \frac{\xi}{\xi'}, \quad \gamma = \frac{\mu}{\mu'}, \quad c = \frac{\Sigma V}{V}$$

Since only deviatoric part of the particle stress is significant, an isotropic term in the expression for the particle stress is not considered. If  $\lambda$  goes to zero equation (31) reduces to that given in.<sup>21</sup> The first term of the particle stress, given by equation (31), shows the effect in the absence of an applied electric field, and the second term denotes the additional effect due to the applied electric field. The second term of the particle stress contains two parts: one is due to the absence of the magnetic effect in the fluid outside the drop and the other is due to the presence of the magnetic effect. Since it is assumed that the fluid outside the drop is more conductive than inside the drop, the conductivity ratio  $\alpha$  is very much smaller than unity, and the fluid outside the drop is poor dielectric in comparison to that inside the drop, the dielectric ratio  $\beta$  is very much smaller than unity, then  $\phi > 0$  and the magnetic effect works to reduce the dependence of the particle stress on the direction of the applied electric field.

#### Acknowledgment

The author is indebted to Mrs. Noyan Özgüç who did the typing with patience.

#### Appendix

$$R(r) = -\frac{\chi\sigma^2 r^2}{4\mu} - \frac{A}{3r^3}, \quad Q(r) = \frac{\chi\sigma^2}{4\mu} + \frac{A}{r^3} - \frac{\chi\sigma^2}{\mu} \frac{1-\alpha}{2+\alpha} \frac{a^3}{r^3} - \frac{\chi\sigma^2}{2\mu} \frac{(1-\alpha)^2}{(2+\alpha)^2} \frac{a^6}{r^6},$$

$$A = -\frac{6a^2}{E_0^2} U + \frac{3\chi\sigma^2 a^3}{4\mu} \frac{(1-\alpha)(5+\alpha)}{(2+\alpha)^2}, \quad U = \frac{\alpha E_0^2 \bar{E}}{\mu (2+\alpha)^2 (4+\gamma)} \left[ -\frac{9}{40} (\alpha\beta-1) + \frac{\chi\sigma^2 a^3}{E} \frac{(1-\alpha)(7+5\alpha)}{40} \right],$$

$$f(r) = \frac{U}{\alpha E_0^2} \left[ \left( \frac{a^3}{r^3} - \frac{a^5}{r^5} \right) + \frac{U^*}{U} \left( \frac{a}{r} - \frac{5+\alpha}{2+\alpha} \frac{a^3}{r^3} + 2 \frac{1-\alpha}{2+\alpha} \frac{a^4}{r^4} + \frac{1+2\alpha}{2+\alpha} \frac{a^5}{r^5} \right) \right],$$

$$g(r) = -\frac{2U}{\alpha E_0^2} \left[ \frac{a^5}{r^5} + \frac{U^*}{U} \left( \frac{a}{r} - \frac{1-\alpha}{2+\alpha} \frac{a^4}{r^4} - \frac{1+2\alpha}{2+\alpha} \frac{a^5}{r^5} \right) \right],$$

$$h(r) = \frac{U}{\alpha^2 E_0^2} \left[ \left( 5 \frac{a^7}{r^7} - 3 \frac{a^5}{r^5} \right) - \frac{U^*}{U} \left( \frac{a^3}{r^3} - 3 \frac{5+\alpha}{2+\alpha} \frac{a^5}{r^5} + 8 \frac{1-\alpha}{2+\alpha} \frac{a^6}{r^6} + 5 \frac{1+2\alpha}{2+\alpha} \frac{a^7}{r^7} \right) \right], \quad U^* = \frac{\chi\sigma^2 a^3 E_0^2}{8\mu} \frac{1-\alpha}{2+\alpha}$$

$$\bar{R}(r) = \left[ \frac{7U}{\alpha^2 E_0^2} - \frac{9\sigma^2 \bar{X}}{4\mu(2+\alpha)^2} \right] r^2, \quad \bar{Q}(r) = \frac{21U}{\alpha^2 E_0^2} + \frac{9\sigma^2 \bar{X}}{4\mu(2+\alpha)^2},$$

$$\bar{f}(r) = \frac{U}{\alpha E_0^2} \left( \frac{r^2}{a^2} - 1 \right), \quad \bar{g}(r) = \frac{U}{\alpha E_0^2} \left( 3 - 5 \frac{r^4}{a^4} \right), \quad \bar{h}(r) = \frac{2U}{\alpha^2 E_0^2},$$

$$B = -\frac{2\gamma+5}{\gamma+1} \alpha^2, \quad \bar{B} = \frac{21\gamma}{2(\gamma+1)\alpha^2}, \quad G = i - \frac{\alpha^6}{(\gamma+1)r^6}, \quad H = \frac{B}{2r^6} + \frac{5\alpha^6}{2(\gamma+1)r^7}, \quad \bar{G}_z = \frac{3\gamma}{2(\gamma+1)} + \frac{5\bar{B}}{24} r^3, \quad \bar{H}_z = -\frac{2\bar{B}}{24}$$

#### References

1. Melcher, J.R., Review of IUTAM-IUPAP, Symposium on electrohydrodynamics, *J. Fluid Mech.* Vol. 40, pp. 541-655, 1970.
2. Melcher, J.R., *Electrohydrodynamics*, Proc. 13th Theor. and Appl. Mech. Congress, Springer-Verlag, pp. 240-253, 1972.
3. Jones, T.B., Electrostatically enhanced heat transfer in liquids-A review, *Advances in Heat Transfer*, Vol. 14, pp. 107-148, 1978.
4. Shercliff, J.A., Thermoelectric magnetohydrodynamics, *J. Fluid Mech.*, Vol. 91, pp. 231-251, 1979.
5. Shercliff, J.A., Thermoelectric magnetohydrodynamics in closed containers, *Phys. Fluids*, Vol. 22, pp. 635-640, 1979.
6. Batchelor, G.K., The stress system in a suspension of force-free particles, *J. Fluid Mech.*, Vol. 41, pp. 545-570.
7. Batchelor, G.K., *Suspension Mechanics-The Fluid Dynamicist's Gateway to Rheology*, Proc. 1970 Heat Transfer and Fluid Mechanics Institute (Ed. T. Sarkaya; Stanford University Press, 1970).

8. Leal, L.G. On the effect of particle couple on the motion of a dilute suspension of spheroids, J.Fluid Mech., Vol. 46, pp.395-416, 1971.
9. Leal, L.G. and Hinch, E.J., The effect of weak Brownian rotations on particles in shear flow, J.Fluid Mech., Vol.46, pp.685-703, 1971.
10. Hall, W.F. and Busenberg, S.N., Viscosity of magnetic suspensions, J.Chem.Phys., Vol.51, pp.137-144, 1969.
11. Goddard, J.D. and Miller, C., Nonlinear effects in the rheology of dilute suspension, J.Fluid Mech., Vol.28, pp.657-73, 1967.
12. Roscoe, R., On the rheology of a suspension of viscoelastic spheres in a viscous liquid, J.Fluid Mech., Vol.28, pp.273-293, 1967.
13. Goldsmith, H.L. and Mason, S.G., The microrheology of dispersions, Rheology, Theory and Applications, Vol.4 (Ed.F.R.Eirich), Academic Press, pp.85-250, 1967.
14. Taylor, G.I., Studies in electrohydrodynamics, I. The circulation produced in a drop by an electric field, Proc.Roy.Soc., Vol.A 291, pp.159-166, 1966.
15. Sozou, C., Flow induced by the presence of a nonconducting ellipsoid of revolution in fluid carrying a uniform current, J.Fluid Mech., Vol.42, pp.124-138, 1970.
16. Chow, C.V. and Halat, J.A., Drag of a sphere of arbitrary conductivity in a current carrying fluid, Phys.Fluids, Vol.12, pp.2317-2322, 1969.
17. Sozou, C., On fluid motions induced by an electromagnetic field in a liquid drop immersed in a conducting fluid, J.Fluid Mech., Vol.51, pp.585-591, 1972.
18. Batchelor, G.K., An Introduction to Fluid Dynamics, Cambridge University press, 1967.
19. Erdoĝan, M.E., Circulation of fluid in and round a drop by an electric field, Bull. Tech. Uni.Ist., Vol.24, pp.1-18, 1971.
20. Erdoĝan, M.E., Two-dimensional drop in the presence of a electric field, Archives of Mechanics, Vol.29, pp.197-204, 1977.
21. Erdoĝan, M.E., The stress system in a suspension of drops in an electric field, Z.angew. Math.Phys., (ZAMP), pp 213-220, 1972.
22. Melcher, J.R. and Taylor, G.I., Electrohydrodynamics, A review of the role of interfacial shear stress, Annual Review of Fluid Mechanics, Vol.1, pp.11-146, 1969.
23. Erdoĝan, M.E. The stress system generated by an electromagnetic field in a suspension of drops embedded in a pure straining motion, Ins.Nuclear Energy, N.19, pp-1-12, 1972.
24. Green, J.T., Properties of suspensions of rigid spheres, Ph.D.dissertation, University of Cambridge, 1971.

C-2

Hydrodynamic Performance of an Annular Liquid Jet:  
Production of Spherical Shells

James M. Kendall

Jet Propulsion Laboratory  
Pasadena, CA 91109

Abstract

An annular jet flow of liquid surrounding a flow of gas at its core is extremely unstable. Axisymmetric oscillations arise spontaneously, and grow with such rapidity along the axial dimension that a pinch-off of the liquid and an encapsulation of the core gas occurs within as few as four jet diameters. The shells which result thereby may be described as thick-wall bubbles, for which van der Waals forces are unimportant. A description is given here of the fluid dynamic processes by which the shells are formed, and of means for preserving and promoting the geometrical symmetry of the product. The forming of metallic shells is mentioned.

Introduction

The investigation described here follows from considerations put forward by Messrs. T. G. Wang and D. D. Elleman of this Laboratory for the production of rigid, impermeable shells for various applications. They had noted during zero-G flights of the NASA KC-135 aircraft that free-floating drops of water containing a gaseous bubble spontaneously assumed a spherical and concentric form, suggesting that if the liquid were to solidify in such state there might result a product of some utility. They proposed a means for the mass-production of liquid shells within the laboratory, based upon the periodic cutting-off of lengths of a gas-core liquid jet, with concurrent sealing of the free ends by any of several methods which seemed promising. This author's earliest attempt to generate a suitable jet flow for evaluating the technique revealed immediately that the hollow jet was sufficiently unstable that the formation of shells needed no inducement.

Fig. 1 illustrates this. The upper figure there pertains to a 4.0-mm jet of water which accelerated downward under action of gravity. The three component photographs were obtained at stations separated axially by 1.0 m each, so that the observation extended over 2.0 m, or more than 500 diameters. The flow within the nozzle was intentionally rendered slightly periodic in order to stimulate the wave growth evident at the second and third stations on account of the well-known Rayleigh instability.<sup>1</sup> An important feature of the Rayleigh analysis, and of an experiment such as this, is that disturbances extending over a wide range of wave numbers are unstable, and that the growth of even the most unstable of these is quite slow, requiring hundreds of diameters for pinch-off under the present conditions. No single wave number is favored to the exclusion of all others. By contrast, the lower figure shows the same nozzle, except that a coaxial flow of air had been provided at the center of the jet. Again, there existed an axial growth of axisymmetric waves, but these grew to such magnitude that pinch-off, accompanied by encapsulation of the core gas, is to be observed at a station approximately four diameters from the nozzle. Most importantly, no perturbation was supplied in this case, yet the frequency stability of the cyclic process was exceedingly uniform, resulting in a corresponding uniformity in mass of the individual shell specimens. It is the formation of these which is the subject of the study to be described.

The work has been motivated jointly by scientific interest in the fluid motion, and by the potential utility of a method for the mass-production of rigid shells of high quality. One application for these concerns fusion target technology. There, it is sought to produce metallic shells of high precision and strength, and preferably composed of a metal of high average atomic number. Hendricks<sup>2</sup> has described some of the truly remarkable accomplishments of a program for the manufacture of multi-layer target shells.

Apparatus and techniques

Experiments have been carried out employing a number of different nozzles and operating fluids. Fig. 2 shows, on the left, the general configuration of a typical nozzle, other designs having differed from this principally with regard to dimensions and to mechanical details of alignment. Typical flow settings for this nozzle are included. Other nozzles incorporated nozzle exit diameters of 0.3, 0.66, and 2.0 mm. The principal features are the central tube through which the gas supply is introduced, the contour of the interior surface of the liquid-flow channel, and the passageway of liquid flow defined by the clearance between the gas tube and nozzle aperture. The performance was relatively insensitive to the gas-tube wall thickness and to the axial position of the gas-tube terminal end, but radial

ORIGINAL PAGE IS  
OF POOR QUALITY

alignment was moderately important. On the right is shown the smallest nozzle tested, a millimeter scale being included. Water and glycerin served as the working liquids in performance tests, and liquid metals were also used as noted later. Test gasses included compressed air, helium, nitrogen and Freon-12. Liquid flow regulation was accomplished through adjustment of the free-surface elevation, or by gas-pressurization of the reservoir. The required pressure was equal to the sum of the pressure drop through the nozzle due to viscosity, plus the Bernoulli term. Gas flow control was accomplished by providing a fine capillary tube ahead of the gas supply tube in order to raise the supply pressure to a value easily measured and regulated.

Gas flow rates were determined by measurement of the pressure imposed upon the capillary resistor, the flow through which in turn had been calibrated against a wet test meter. Liquid flow rates were measured by capturing the stream of shells in a graduated cylinder for a precise duration. The frequency of shell production was determined stroboscopically or by measurement of the frequency of light-beam interruption. Shell diameters were measured optically under stroboscopic illumination using a traversing-mount telescope. Heat transfer to freely-falling shells was determined by measuring the temperature difference between that of heated water within the reservoir and that of shells captured at various distances below the nozzle exit.

### Results

#### Shell formation.

Both the gas and the liquid issued from the nozzle in steady motion, but, because of instability, the flow became strongly periodic within a short distance from the nozzle exit. Fig. 3 shows four phases of the cyclic motion through which shells were formed. There, the velocity of the gas was three times that of the liquid. It is important to recognize that the volume flow rate of the gas therefore exceeded, by the same factor, the rate at which new volume was generated within the hollow core by the downward flow of liquid. The first frame depicts the free-surface configuration at the instant at which the liquid had sealed the core. On account of the larger volume rate of the gas, the gas of necessity produced a radial displacement of the cylindrical surface of the liquid, as in the second frame. The bulbous feature became progressively larger and more spherical, and was at the same time convected downward on a neck of liquid emerging from the nozzle, as in the third and fourth frames. The neck then collapsed under action of surface tension, completing the formation of a gas-filled nodule. Successive nodules of encapsulated gas produced in this manner were temporarily interconnected by a filament of liquid which broke subsequently, setting free the individual shells. None of the fill gas escaped.

A notable feature of this action is that the frequency stability of the process, estimated by stroboscopic observation, appeared to exceed one part in  $10^3$ . The motion was sufficiently definite that an attempt to alter the frequency by sinusoidal perturbation of the fill gas was unsuccessful. Moreover, even the details of the breakage of the filament were stationary; instantaneous oscillation waveforms induced upon the shells by the energy release, evident in figures described below, remained constant in appearance when viewed in stroboscopic light, and the ejection of satellite droplets, whenever present, was similarly constant. The motion was highly deterministic.

#### Analysis.

No analysis adequate to explain the shell formation process is known to be available at present. D. Weihs of Technion, Haifa, Israel (private communication) has performed a linearized, parallel-flow, analysis of a hollow jet and shown that, as in Rayleigh instability, a range of wave lengths is unstable. This result is in contrast with the present observation that a single frequency of oscillation is dominant. Evidently, a numerical analysis such as that described by Fromm<sup>3</sup> will be required.

It may be appropriate here to consider the relative importance of various forces, and to present an analysis of a limiting case. The forces and stresses to be considered include the following:

Dynamic pressure of the gas,	$\rho_g v_g^2/2$
Dynamic pressure of the liquid,	$\rho_l v_l^2/2$
Viscous stress of the liquid,	$\mu_l v_l/r$
Capillary pressure,	$\sigma/r,$
Hydrostatic pressure,	$\rho_l g/r$

ORIGINAL MANUSCRIPT  
OF PAPER QUANTITY

Here,  $\rho$  denotes density,  $V$  denotes velocity,  $\mu$  denotes viscosity,  $\sigma$  denotes interfacial tension,  $G$  is gravity, and  $r$  is the jet radius. Subscripts  $g$  and  $l$  denote gas and liquid. A number of these stresses are generally or conditionally unimportant, as will be shown. On the basis of the formation cycle of Fig. 3, the forces which seem to be predominant are those of capillary pressure and of liquid dynamic pressure, and even the latter may be regarded as of secondary magnitude because the principal component of motion amounts to a uniform translation of the liquid. The motions with respect to this average one give form to the cycle, but do not induce substantial pressures.

The most important forces are evidently those due to capillary pressure. Accordingly, a static analysis has been made and found to provide a useful prediction of the shell diameter and of the formation frequency. Fig. 4 shows an idealization of the configuration present in the third frame of Fig. 3, consisting of a cylindrical neck joined to a spherical bulb. The reason that the spherical and cylindrical regions remain distinct is described below. The pressure required to support the cylinder against collapse is given by

$$p_c = \frac{2\sigma}{r_c},$$

where  $p_c$  and  $r_c$  are the pressure within, and the average radius of the cylinder. The factor, 2, accounts for the presence of the interior and exterior surfaces. The corresponding pressure for the sphere is

$$p_s = \frac{4\sigma}{r_s}.$$

The higher factor here results from the compound curvature of the spherical surface. It is to be noted that  $r_c$  is independent of time, whereas  $r_s$  is an increasing function of time. As the sphere fills, the pressure therein falls, and when the radius attains a value twice that of the cylinder the pressure becomes less than that required to prevent collapse of the cylinder. Therefore, according to this analysis, when the sphere attains a diameter twice that of the jet, its growth will be terminated by a sealing-off of the core. The frequency of formation may then be estimated in terms of the prevailing gas flow rate and the volume of each shell. It is to be noted that although the instability and shell formation process are surface-tension-driven, this parameter does not appear in the expression for the expected diameter.

This prediction of diameter was tested through measurement of the shell diameter and formation frequency as a function of flow rate. Fig. 5 presents this result in dimensional units. There, the measured diameter may be compared with the value expected from static analysis, shown as a horizontal line. Estimates of the interior and exterior radii of the surfaces were incorporated in forming the latter value, rather than the average. The measured shell diameters exceed the predicted value by approximately 10 percent, and do not fully verify the expected constancy in diameter. Nevertheless, the static analysis appears to have some merit. Also shown is the formation frequency, which possesses a one-third power dependence upon the flow rate. One important consequence of the frequency variation is that a measure of control may be gained over the wall thickness of the shells on account of the constancy of the liquid flow rate. Further control is to be had through adjustment of the dimension of the annular passageway of liquid flow.

Dynamic forces were responsible for preserving the demarkation between the spherical and cylindrical regions of the flow, since this could not have been maintained statically. It is believed that the abrupt change in surface curvature propagated in wave-like manner upward against the downflow of the jet, but with a velocity less than that of the liquid. An estimate of the wave speed has been made by considering the liquid to constitute a membrane, with transverse curvature being neglected. The wave speed,  $V_w$ , would be given by  $(2\sigma/\rho_l\delta)^{1/2}$ , where  $\delta$  is the thickness of the layer, as in Fig. 4. The ratio of liquid velocity,  $V_l$ , to this velocity is then

$$\frac{V_l}{V_w} = \left[ \frac{\rho_l V_l^2 \delta}{2\sigma} \right]^{1/2},$$

a number found to exceed unity substantially in all successful tests, thereby indicating that a "supersonic" jet velocity is required for maintaining the spherical and cylindrical regions as distinct. For the case of small liquid velocities the bubble remained attached to the nozzle and grew to a diameter several times that of the orifice before bursting.

ORIGINAL PAGE IS  
OF POOR QUALITY

**Further Experiments.**

A number of experiments were carried out with the intention of exploring the regimes of operation and of assessing the relative importance of various forces and stresses. One such stress was the dynamic pressure of the gas. The expected unimportance of this quantity was verified by the finding that the bubble formation frequency and geometry were independent of gas composition for equal rates of flow of the gasses, Freon 12, nitrogen, and helium, which span a density range 30:1. Also, the effect of the viscosity of the liquid, which may be characterized in terms of the Reynolds number,  $\rho_1 v_1 r / \mu_1$ , was examined. It was found for the case of glycerin as the test liquid within the 4.0-mm nozzle that the formation process was changed little from that for water, which possesses 500-fold less viscosity. It is believed that Reynolds numbers in excess of  $10^2$  are adequate to ensure operation similar to that described.

It was pointed out that surface tension did not appear in the expression for shell diameter. This was tested by operating the 4.0-mm nozzle at constant flow of distilled water, to which was added in transient manner a surfactant (Kodak Photo-Flo). Fig. 6 compares the formation process before and after the addition of surfactant. Stroboscopy indicated that the frequency of formation diminished in consequence by approximately one percent, and an increase in diameter of one-third that amount must have occurred, but was not easily detectable. The most apparent difference in the two streams of the figure is a lesser degree of surface-wave activity upon the shells in the presence of surfactant. The waves were induced by the breakage of the interconnecting filament, and the energy released thereby must have been reduced by the lowering of the surface tension. The surfactant may have contributed to a damping of the motion as well as to the reduction in initial wave amplitude. As a general observation, the addition of surfactant improved the apparent quality of shells observed at a station one or two meters below the nozzle exit.

The effect of gas flow rate upon shell diameter and formation frequency was described above, and it was indicated that the gas volumetric flow rate must exceed that at which the liquid flow generates new volume within the core for successful operation. Fig. 6 shows the progression in flow geometry as the gas flow rate was increased for a constant liquid velocity. The three settings are characterized there in terms of the ratio of the gas-to-liquid velocities. For a ratio slightly above unity, shown in the first frame, a relatively long time interval was required to accumulate sufficient gas to form a shell, and the axial spacing between shells was large. It was found in this case that the configuration of the cylindrical neck was steady in time, that the motion of seal-off was confined to a region several diameters below the nozzle, and that the diameter of the shells was somewhat less than twice that of the nozzle. For a ratio of velocities near optimal, as in the center frame, the motion was as described previously, with the diameter being twice that of the nozzle. The third frame shows that for a high flow rate the shells exhibited the same 2:1 diameter ratio, but were produced at sufficiently short intervals as to remain interconnected for considerable distance, whereupon erratic coalescence was observed. The thinness of the shell wall may be seen.

As a further test of the range of operation, the liquid rate was increased four-fold with respect to that of the former figure, and the gas rate was advanced to approximately three times that of the liquid, or near optimal. The result is shown in Fig. 8, wherein the two frames at the right were obtained at higher magnification than that on the left, and differ only with regard to the phase of the cyclic motion. As seen, the water surface had assumed a very irregular form, and this is believed to have been due to an onset of fluid turbulence within the gas flow. The Reynolds number of the flow within the supply tube amounted to 5000, approximately, a value for which a turbulent condition is to be expected. Apparently, the unsteadiness of the turbulence induced capillary waves upon the free surface of the liquid. Even though this additional complexity was present, the shell-formation cycle remained similar to that shown before, with the shell diameter having been twice that of the nozzle.

As a test of nozzle geometry, the 4.0-mm nozzle was operated with air tubes whose diameters were as small as 1.2 mm. The spacing interval between nodules was large, as in the first frame of Fig. 7, because the gas flow was restricted. The interconnecting filament contained much of the liquid, and this was transferred to the shells upon breakage, rendering the walls thick.

**Shell Symmetrization.**

An important goal of the work was to produce rigid shells possessing a high degree of symmetry. Two aspects of this matter were considered. First, it was necessary to prevent the specimens from becoming distorted during the time interval following formation and preceding solidification. In particular, the shells were launched by the jet with a certain velocity, and tended to gain additional velocity by gravitational acceleration. The air resistance was found to produce a strong decentering force upon the captured gas, resulting in a localized

## ORIGINAL QUALITY OF POKK QUALITY

thinning of the wall, and terminating in rupture. This type of distortion and failure were particularly severe for large shells, for which the dimensionless parameter characterizing gravitational effects,  $\rho_1 Gr^2/\sigma$ , was also large.

Control over this problem was gained by constructing a drop tower in the form of a vertical wind tunnel configured such that the airflow within it accelerated downward with a 1.0-G value. With proper placement of a shell generator therein, the specimens experienced no relative air velocity, and no decentering force. Fig. 9 shows a 7.0-mm  $H_2O$  shell photographed in free-fall in this tunnel at a location 2.0 m below the nozzle. The exterior surfaces of the shells were found to be spherical to within one percent. The white line appearing within the image circumference in Fig. 9 was determined through use of a ray-tracing program to represent the location of the interior surface of the shell. The wall thickness was thereby indicated to amount to ten percent of the radius and to be uniform to within ten percent. In the absence of the downflow, the shells ruptured before reaching this station of observation. As a means for determining whether the reduction in relative airflow would prevent the freezing of molten metal specimens, measurements were made of the temperature-loss of hot water shells. The heat transfer rate was found to exhibit a fairly sharp minimum when the airflow acceleration was adjusted to a 1.0-G value, but to retain more than half the rate prevailing when the mismatch was substantial. Although solidification of metal specimens has not been attempted here, difficulty on account of the magnitude of the heat transfer is not expected for the case of moderate shell sizes.

A second aspect of shell symmetrization concerned the promotion of centering by means of shell vibration. Theoretical and experimental studies on shell dynamics are given by Saffren, Elleman, and Rhim<sup>4</sup>. Included there are numerical results for shell vibration frequencies for the case of inviscid liquids, together with experimental results showing that such vibration has the beneficial effect of inducing a centering of the interior surface with respect to the exterior one. Also, Lee, Feng, Elleman, and Wang and Young<sup>5</sup> show that the centering force attainable by means of forced oscillation is very strong. The present studies do not yet include results on centering by stimulated oscillation, but an observation of possible interest was made for the case in which surfactant was added to water. As mentioned, the initial level of shell oscillation induced by breakage of the liquid filament was greatly diminished then, and vibration was not detectable by eye at stations a few centimeters below the nozzle. Nevertheless, the centering of the surfaces was judged to equal that of the distilled water case.

### Production of metal shells.

As indicated, metal shells may find application in inertial-confinement fusion technology. Such shells must be dimensionally precise, smooth, and strong. It has been shown here that the hollow-jet instability produces shells of great dimensional uniformity, that surface tension produced sphericity, and that forces not directly identified resulted in a concentricity of the surface. Work has been initiated on the use of liquid metals to form shells, and various aspects of this have been described by Kendall, Lee, and Wang<sup>6</sup>. The most successful results to date were obtained by Lee, who used a nozzle similar to that shown in Fig. 2. The metal employed was an alloy of gold, lead, and antimony which may, with adequate cooling rate, be solidified in the amorphous state. Certain properties of this metal, including that of surface smoothness, have been described by Lee, Kendall, and Johnson<sup>7</sup>.

Fig. 10 shows two shell specimens formed of this metal. The radiograph indicates that the wall thickness uniformity was good. The wall was sufficiently thin that the average density of this specimen was less than that of water. The SEM photograph on the right shows a shell which was broken at the time of recovery, thereby making visible the wall thickness and a portion of the interior surface. The cooling rate in this experiment was insufficient to attain the amorphous state, and surface imperfections are clearly evident on that account. Most liquid metal tests have involved tin or lead, rather than the alloy, and these have been found to model the flow of the alloy fairly well. Tin shells with diameters between 0.75 and 2.0 mm have been produced. A problem yet to be circumvented concerns the formation during solidification of an exterior surface protrusion at each of the locations from which a filament of liquid had been attached. This defect is apparently due to material properties or to heat transfer, and is not of fluid-dynamic origin.

### Acknowledgments

This work represents one phase of research carried out at the Jet Propulsion Laboratory, California Institute of Technology, under Contract NAS 7-100 of the National Aeronautics and Space Administration. E. W. Miles and M. E. Lucero performed many of the observations reported here. G. E. Tennant fabricated the nozzle components. J. R. Gatewood provided extremely valuable advice on materials and techniques for the metal shell experiments.

ORIGINAL PAGE  
BLACK AND WHITE PHOTOGRAPH

References

1. Lamb, H. "Hydrodynamics," 6th ed., Dover Publ. Co.
2. Hendricks, C. D., "Inertial Confinement Fusion Targets," Second International Colloquium on Drops and Bubbles, Monterey, CA, November 1981.
3. Fromm, J., "A Numerical Study of Drop-On-Demand Ink Jets," Second International Colloquium on Drops and Bubbles, Monterey, CA, November 1981.
4. Saffren, M., Elleman, D., and Rhim, W.-K., "Dynamics of Compound Drop Systems," Second International Colloquium on Drops and Bubbles, Monterey, CA, November 1981.
5. Lee, M. C., Fang, I-An, Elleman, D. D., Wang, T. G., and Young, A. T., "Generation of a Strong Core Centering Force in a Submillimeter Compound Droplet System," Second International Colloquium on Drops and Bubbles, Monterey, CA, November 1981.
6. Kendall, J. M., Lee, M. C., and Wang, T. G., "Metal Shell Technology Based upon Hollow Jet Instability," J. Vacuum Sci. and Tech., Mar. 1982 (to be published).
7. Lee, M. C., Kendall, J. M., and Johnson, W. L., "Spheres of the Metallic Glass  $Au_{55}Pb_{22.5}Sb_{22.5}$  and their Surface Characteristics," Applied Phys. Letters, Mar. 1982 (to be published).

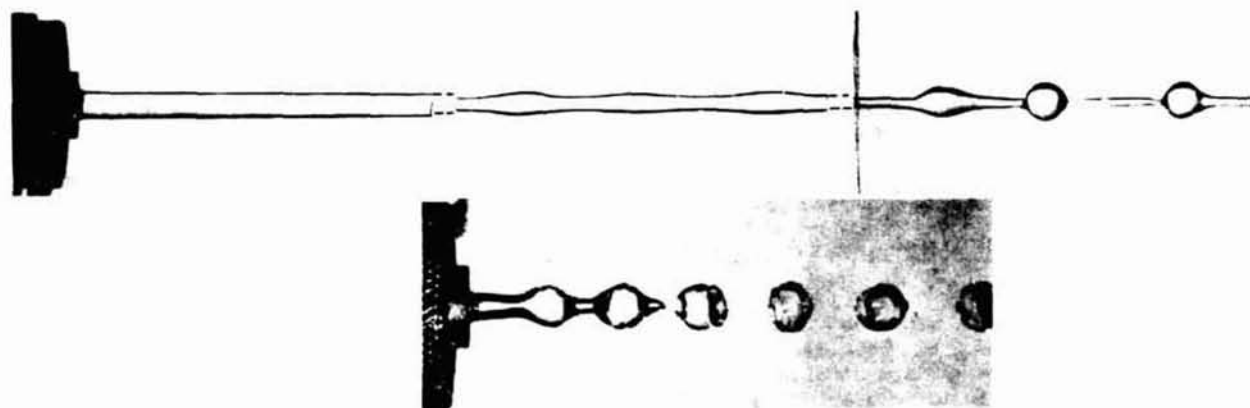


Fig. 1. Flow of water from a 4.0-mm nozzle; drops are produced by Rayleigh instability. Photographs obtained with 1.0-m axial spacing (upper). Same condition except for gas flow at core; shells are produced (lower).

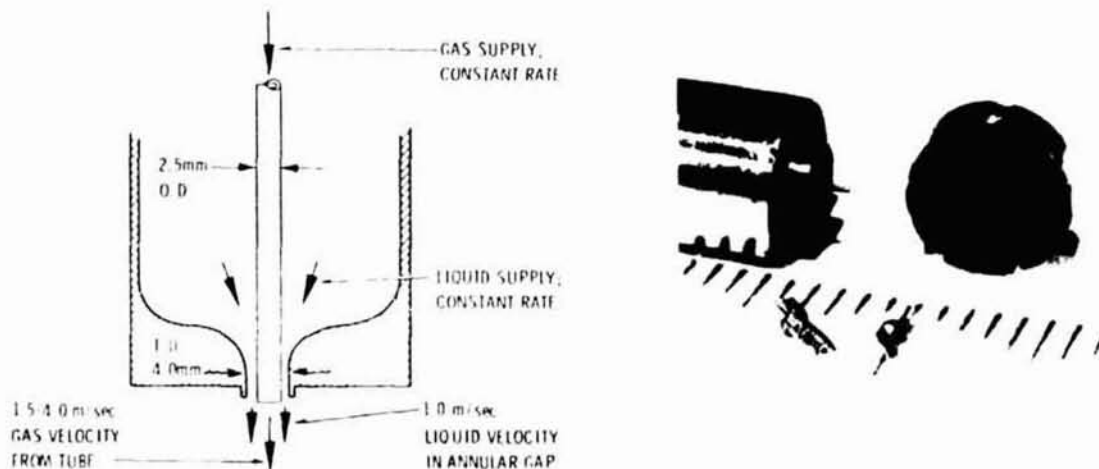


Fig. 2. Nozzle schematic, with typical flow conditions indicated (left). Photograph of a small nozzle, disassembled (right).

ORIGINAL PAGE  
BLACK AND WHITE PHOTOGRAPH

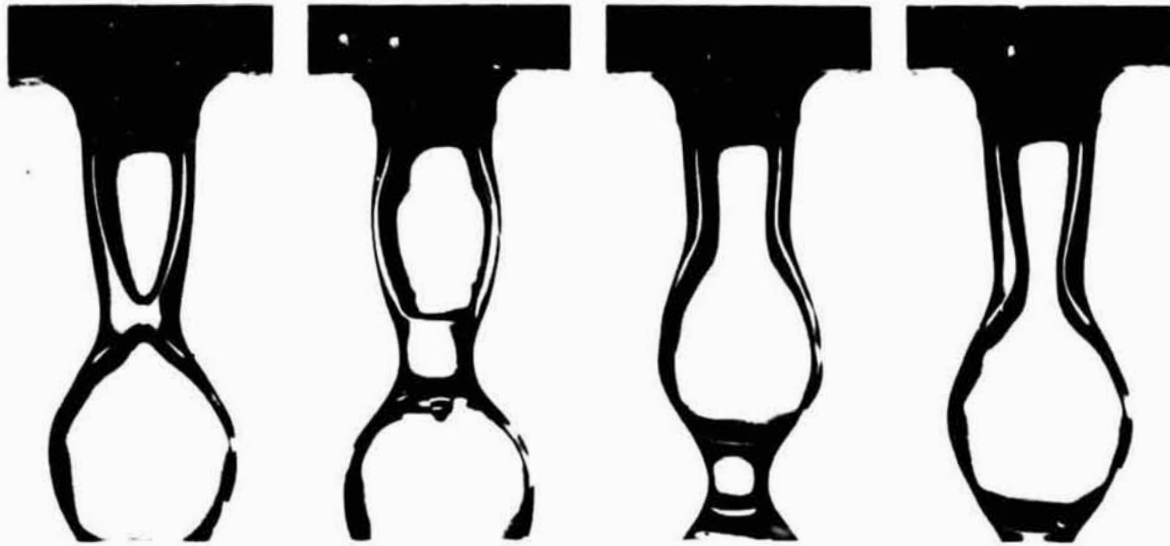


Fig. 3. Shell formation cycle.

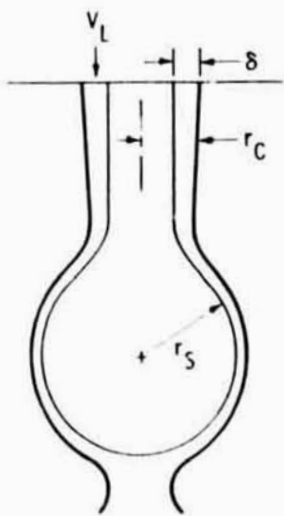


Fig. 4.

Idealization of liquid surface configuration.

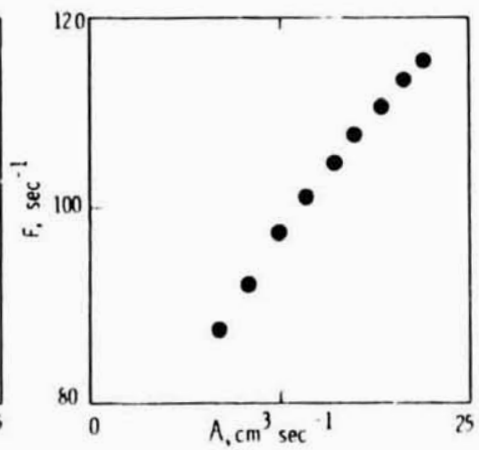
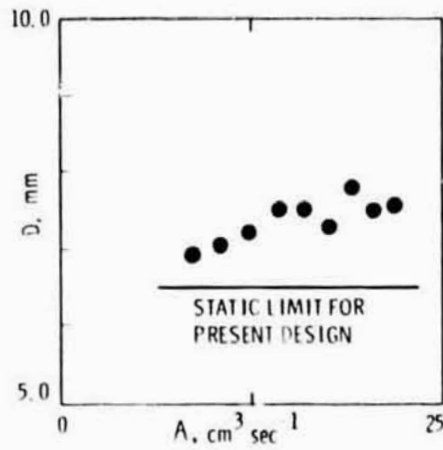


Fig. 5.

Shell diameter (left) and formation frequency (right) versus fill-gas flow rate for a 4.0-mm nozzle.

ORIGINAL PAGE  
BLACK AND WHITE PHOTOGRAPH

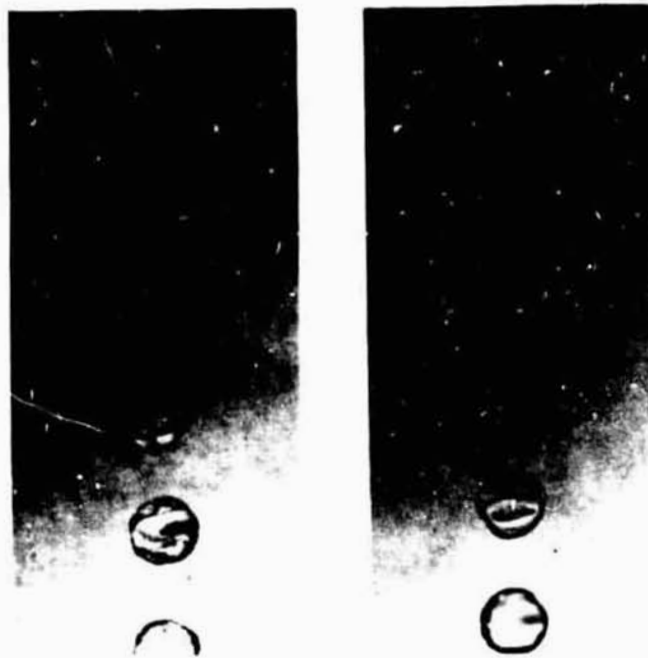


Fig. 6. Flow of distilled water from a 4.0-mm nozzle (left); same with surfactant (right).

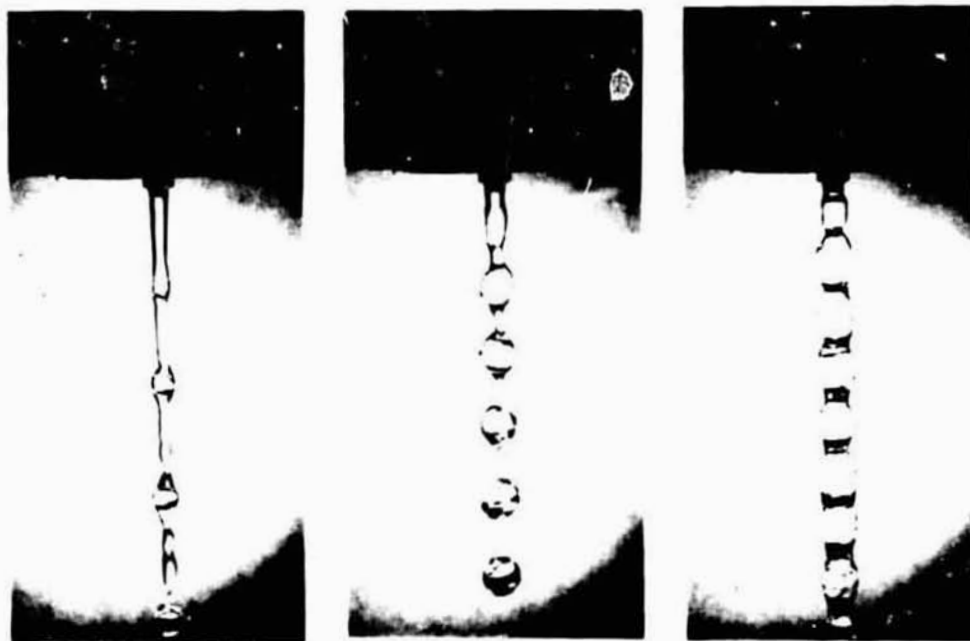


Fig. 7. Flow of water from a 4.0mm nozzle at  $V_1 = 1.09$  m/sec.  $V_g/V_1 = 1.4$  (left), 4.2 (center), and 12.6 (right).

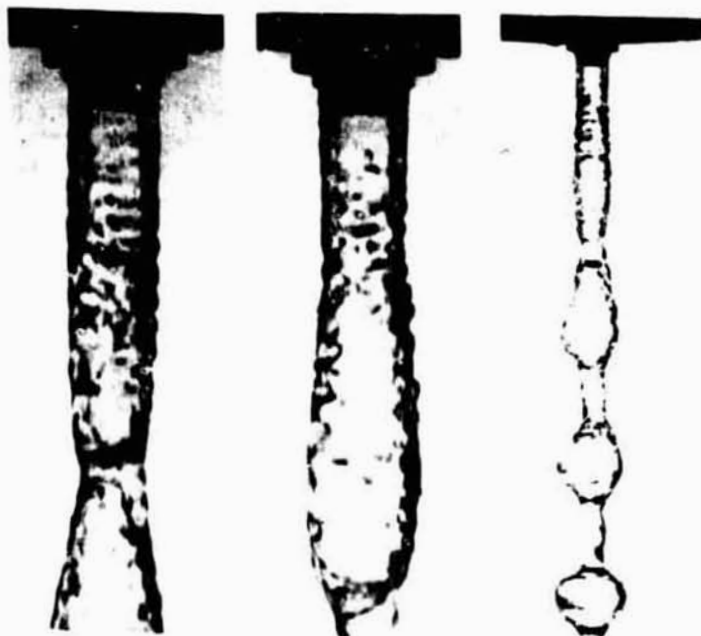


Fig. 8.

High velocity water flow from a 4.0-mm nozzle;  $V_1 = 4.75$  m/sec;  
 $V_2/V_1 = 3.0$ ; close-up view for two phases of motion (left,  
center); distant view (right).



Fig. 9.

7.0-mm diam. water shell with  
surfactant; in free-fall.

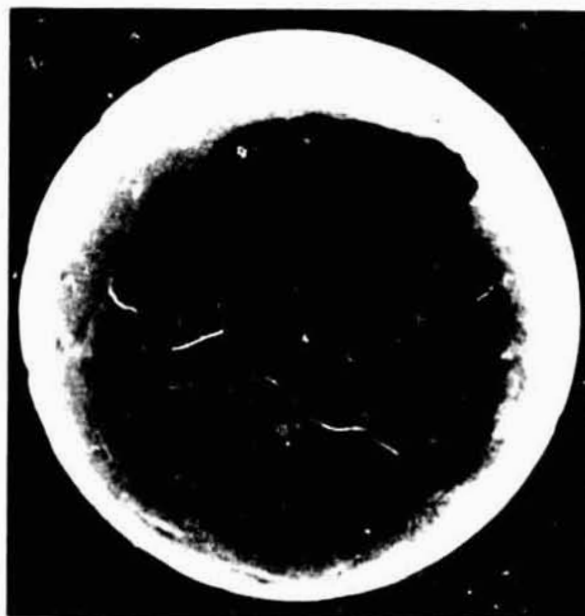
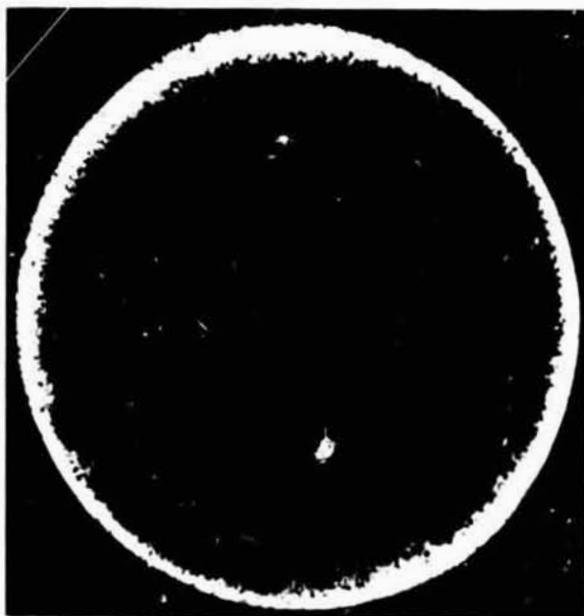


Fig. 10. Radiograph of an undamaged 1.5-mm gold alloy shell (left); SEM photo-  
graph of similar shell except portion of surface is missing (right).

Inertial Confinement Fusion Targets\*

Charles D. Hendricks

Lawrence Livermore National Laboratory  
 Mail Stop L-482, P. O. Box 5508, Livermore, California 94550

Abstract

Inertial confinement fusion (ICF) targets are made as simple flat discs, as hollow shells or as complicated multilayer structures. Many techniques have been devised for producing the targets. Glass and metal shells are made by using drop and bubble techniques. Solid hydrogen shells are also produced by adapting old methods to the solution of modern problems. Some of these techniques, problems and solutions are discussed. In addition, the applications of many of the techniques to fabrication of ICF targets is presented.

Introduction

In the most simple, straight forward direct driven case, an ICF target may be a simple ball on a stalk, fiber network, or film support as shown in Figure 1. In a more complicated case the fuel is inside a hohlraum designed to contain thermal x-rays produced by interaction of the driver beam with the outer shell. To simplify the presentation, in the remainder of this paper I will only discuss direct driven ICF targets.



Figure 1. Ball-on-Stalk.

The fabrication of laser fusion targets presents a set of unique problems in material science, chemistry, physics, optics and microscopic mechanical techniques. As target designs have evolved from simple disks of plastic, metals or glass to multilayer spherical shells, our techniques for glass sphere production, polymer and metallic layer deposition, mechanical assembly and characterization have also evolved.

Our early metallic disk targets were prepared by means of two primary techniques. Some of the disks were deposited on thin plastic films by evaporation through a small (100-150  $\mu\text{m}$ ) hole in a mask. Others were made by a cookie cutter technique, punching the disks from a thin metal foil. More recently we have made disks by masking and etching a silicon wafer to leave a flat topped, circular set of posts onto which is

\* Work performed under the auspices of the U. S. Department of Energy by the Lawrence Livermore National Laboratory under contract number W-7405-ENG-48.

ORIGINAL PAGE  
BLACK AND WHITE PHOTOGRAPH

evaporated a metal layer of correct thickness. The disks are then removed from the top of the cylindrical posts by using a microscopic vacuum chuck. Disks have also been made of a low density ( $\rho = 0.05-0.07$  gm/cc) cellulose acetate foam by slicing from an extruded foam cylinder. For use as a target, a disk is mounted on edge on the tip of a few micrometer diameter drawn glass fiber whose base fits in a holder for insertion into the laser target chamber.

ICF targets consisting of hollow-spherical glass shells have been used extensively at many laboratories. Initially the shells were obtained commercially in batches which were produced primarily for plastic fillers and other industrial uses. Even with the relaxed specifications of early targets, it was a difficult and time consuming task to find one which was good enough to use.

Quite naturally, the manufacturers were not particularly interested in surface quality or uniformity of the sphere walls. To find a suitable target, we often sorted through  $10^9-10^{11}$  glass shells! Because of the inefficiency of the sorting techniques and lack of availability of spheres which met our stringent specifications even after the sorting process, we decided to make our own high quality glass shells.

A liquid drop method developed at Lawrence Livermore National Laboratory (LLNL) has allowed us to improve the quality and yield of glass shells until we find that 90 to 99 out of 100 meet the much more severe requirements of today's targets instead of the 1 in  $10^9$  to  $10^{11}$  which satisfied some of our earlier less critical needs. To achieve such phenomenal yields, very uniform liquid drops of an aqueous solution of glass forming chemicals are generated and introduced into a vertical tube furnace as shown in Figure 2.

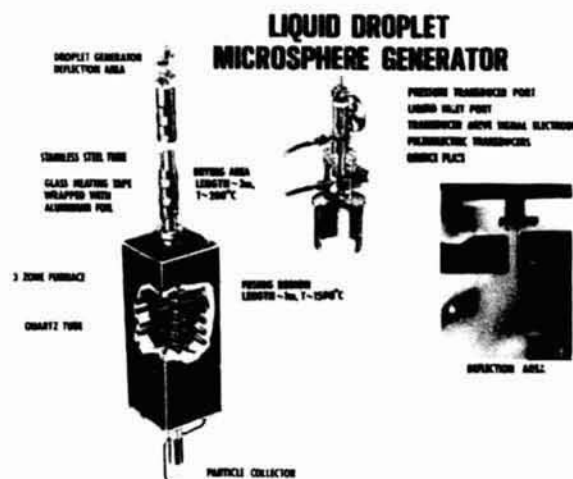


Figure 2. Liquid Droplet Microsphere Generator.

The aqueous solution of glass forming chemicals (e.g. sodium silicate, boric acid, sodium hydroxide, potassium hydroxide, etc.) is forced through an orifice to form a cylindrical jet. A capillary wave launched onto the jet by means of a piezo-electric transducer induces the jet to break up into a series of uniform drops. The solvent (water) is evaporated from the drops in a vertical column at about  $350^{\circ}\text{C}$ , leaving dry particles which continue into a higher temperature region of the furnace to form glass spheres. Water of hydration and gases evolved from the chemical constituents expand in the molten glass spheres and form the glass into very uniform hollow shells. Instead of a yield of one in  $10^9$  or  $10^{11}$ , our process yields the 99 out of 100 which meet the criteria for target use. This means a surface which is smooth to  $100\text{\AA}$  and a wall thickness which does not vary by more than 1% of its average value. Surface tension of the glass in the low viscosity state makes the liquid into essentially perfect spheres.

The uniformity and reproducibility of the initial droplets are important to the process from several points of view.

Some of these are:

1. Equal mass of glass in every shell.
2. Repeatability allows variation of parameters to experimentally optimize the process.
3. Reproducible injection into furnace.

The droplet process allows us some optimization of a slightly different process for producing the glass spheres. One of the earliest processes for producing hollow glass spheres commercially involved introducing dry particles of mixed glass materials into a gas flame. As the material fused in the flame, gases evolved from the components formed small bubbles whose walls became thin as expansion occurred. The internal bubble walls perforated and after a few milliseconds or less, one relatively internal large bubble was formed of all the smaller bubbles. The single bubble continued to expand and a hollow shell was formed. The glass flame was short and the glass shells cooled quickly on emerging from the flame and were literally scooped off the chamber floor, bagged and marketed in large quantities.

Preparation of the dry particles to be put into the flame (or other high temperature device, e.g. vertical tube furnace) varied with particular manufacturers. The glass forming materials could be mixed into a slurry, dried, pulverized, sieved and otherwise manipulated to gain some uniformity of size. Another method involved dissolving the chemicals in water (and often included a decomposable gas former such as urea) and spray drying to form the dry particles which were then put into a flame or furnace for sphere production.

The liquid drop generation technique allows us to produce first a set of uniform dry particles which can subsequently be introduced into a furnace or flame for fusing and forming into glass shells. Many variations of the basic theme are possible and are useful in specific circumstances.

The reasons for the almost perfect centering of inner and outer surfaces, i.e. uniform wall thickness, are not completely clear for any of these techniques. The most probable mechanism is that variations in the temperature profile seen by the glass shells during the forming process provide variations in internal pressure in the shells which tend to pump the walls and induce flow in the glass which leads to centering. That pressure variations may indeed lead to the centering mechanism, is substantiated to some extent by the work of Taylor Wang, Dan Elleman, and their colleagues on bubble centering in liquid shells.

It should be pointed out that a large fraction of the fly-ash from large coal fired power plants consists of small, hollow glassy shells.

Experimental results indicate that for shell sizes up to about 3 mm, gravitational and aerodynamical forces do not appear to cause asphericity or decentering of inner and outer surfaces in vertical tube furnaces. Some analyses predict problems from these forces at even smaller sizes. A possible explanation of the absence of irregularities in the spheres may be that the spheres rotate and, indeed, may move up, down and sideways as well in the turbulent atmosphere of the furnace. Our observations extend only to spheres up to 3 mm size range. Larger shells may also not be disturbed by asphericity or decentering. At this time we have no data for larger sizes.

After the spheres are collected from the furnace, they are washed and filled with a mixture of deuterium and tritium (DT). These gases diffuse rapidly through the glass walls if the spheres are at a temperature of a few hundred degrees Celsius (e.g. 350°C). At lower temperatures the gas will not diffuse back out of the spheres over periods of several months to several years.

Spheres whose walls vary in thickness by more than 1-2% and whose surfaces have peak-to-valley roughness variations of more than a few hundred (100-300) Angstroms are of little interest for use as targets. Targets which are simple bare balls can sometimes be lower quality spheres than our canonical high quality shells.

Other direct driven targets are also of interest and require other techniques for production. Multiple layer coatings of various materials must be applied to the surface of gas or metal spheres to produce a complete target. We must produce metal shells which have the same high quality walls and surfaces as our present glass shells. The coatings, which may be CH or CF polymers, polymers with a few atomic percent of a high atomic number material distributed molecularly throughout the polymer, or layers of copper or beryllium or other materials should be very high quality. Layer thickness variation and surface irregularities should be kept to the few hundred to the thousand Angstrom range.

ORIGINAL PAGE  
BLACK AND WHITE PHOTOGRAPH

Some of our targets are glass shells coated with fluorocarbon polymers (like Teflon) or hydrocarbon polymers (like polyethylene) or metallic layers such as copper, gold, silver or platinum. After the glass shells are filled with DT, the coatings are applied by sputtering, plasma activated polymerization, chemical vapor deposition, electro-deposition or other suitable processes. Specks of dust, surface weathering, or other irregularities as small as a few tens of Angstroms initiate or seed irregular growth patterns in the coatings during the deposition processes. Unless the substrate spheres are virtually perfect and absolutely clean, it is very difficult to produce high quality coated shells. Figure 3 shows coating irregularity which originated on a defect or microscopic dirt speck on the surface of the glass sphere.

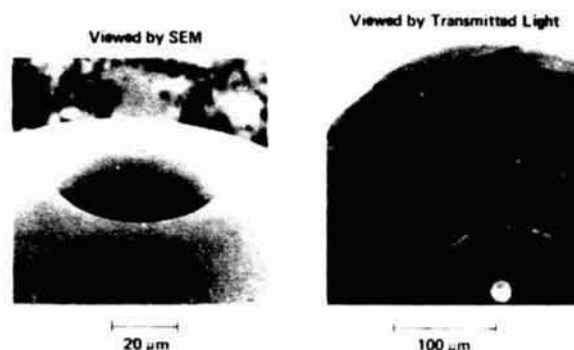


Figure 3. Thick Hydrocarbon Coating Defect.

Of course, we must maintain the surface quality of the coatings at the  $100 \text{ \AA}$  smoothness level for thin coatings and at about  $1\%$  of the thickness for thick coatings.

To avoid introducing damage sites by contact with supporting surfaces during the coating processes, we have developed a molecular beam levitation (MBL) technology which uses gas at very low pressure flowing through a collimated hole structure. The spheres are placed above the structure and the impact of the molecules on the spheres transfer sufficient momentum to levitate a steel sphere as large as a  $3/8$  inch diameter. The system is operated at a pressure low enough that sputtering and various beam coating processes can be accomplished. The levitation process is sufficiently gentle that multishell assemblies in which inner spheres are suspended concentrically by means of a thin web ( $\approx 200 \text{ \AA}$  thick Formvar) can be overcoated to produce a seamless outer shell. A levitated sphere is shown in the MBL in Figure 4.

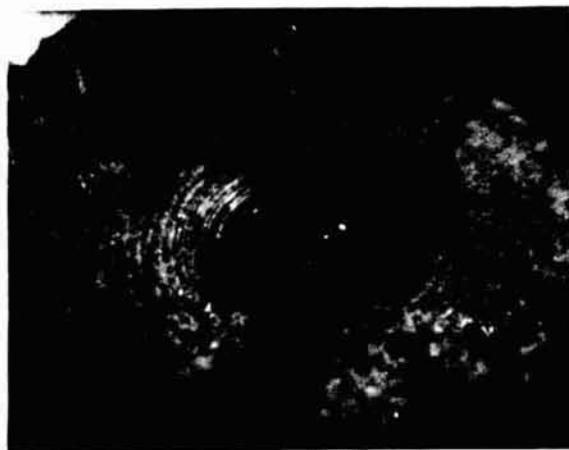


Figure 4. Levitated Spherical Shell.

A second technique for producing the outer shell is that of assembling two hemishells around the inner sphere (Figure 5). Techniques for making and assembling hemishells

ORIGINAL PAGE  
BLACK AND WHITE PHOTOGRAPH

into spherical shells have been developed to a relatively successful state. Utilizing single-point diamond tools and high precision air-bearing spindle lathes, we make machined hemishells with 250-300 Å surface finishes. To avoid assembly problems, we have also machined step joints into the edges of the shells as shown in Figure 6. The spheres are assembled around DT filled, coated glass shells to form double shell targets.



Figure 5. Double Shell Target Assembly



Figure 6. Mating Polystyrene Hemishells.

A number of directly driven targets for future reactor applications require metal spheres as containers for the DT fuel. Metal spheres have been produced by a number of techniques including annular jet techniques (e.g. copper, woods alloy, tin) and by deposition on and leaching out of spherical mandrels, and by machine lapping methods. It is not anticipated that fusion targets will become less difficult to produce or that the critical parameters will be relaxed in the near future. The techniques used to characterize the targets (optical interferometry, microradiography, electron and ion beam techniques) are, in some cases, in the development stages. A great deal of research remains to be done just on measurement techniques.

Some target designs contain one or more layers of solid DT fuel. Conceptually, in a paper design, such layers are easy to put in a target. Experimentally it may be very difficult to produce such targets. Many of the details of cryogenic targets we have down cold. However, there are still many problems to be solved before high quality cryogenic targets can be irradiated in the laser target chamber.

At each step of the target fabrication process it is imperative to have accurate data on the geometry of the spheres, the coatings, supporting films, DT fill, hemishells and the assembled target. To make all these measurements we have developed a highly sophisticated set of characterization systems and analytical techniques and apparatus.

Transparent shells, walls and surfaces are measured to a few hundred Angstroms accuracy with lateral resolution of about 2 micrometers or better. Transmission interferometry provides an excellent tool for characterization of transparent spheres and shells. Total 4π characterization of a glass shell can take up to 5 hours if done manually looking through an interference microscope. To reduce the time necessary for a complete 4π characterization of a sphere, we have developed an automated sphere characterization system which measures the sphere and plots a contour map to a height accuracy of about 200 Å with a lateral resolution of about 2 micrometers in about 5 minutes.

For detailed surface analysis and analytical studies we rely heavily on Scanning Electron Microscopy and Auger microprobes. Information on chemical composition of surfaces as well as on surface contours is thus made available to material scientists who are concerned with coating, sphere formation, and other materials problems.

Targets for economical energy production in the future are yet to be fully developed. However, in several areas we have made significant progress toward high rate, low cost production of reactor class targets.

Techniques for producing fully cryogenic targets and for levitating and transporting targets of all types have been developed. We are continuing our efforts toward determining the building blocks for a target factory (figure 7).

ORIGINAL PAGE IS  
OF POOR QUALITY

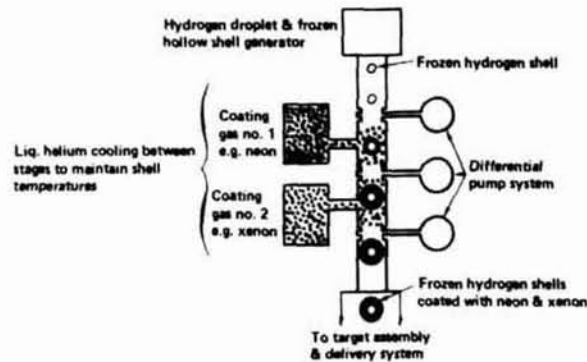


Figure 7. Multilayer Cryogenic Reactor Target Production.

As new target designs are generated and more powerful and energetic lasers are built, new targets must be produced. We are continuing the research and development which will allow us to respond to the continuing challenges in the field of target fabrication in inertial confinement fusion.

As further experiments are done with more energetic and powerful driver beams, our understanding of target designs should improve and our target fabrication tasks will change -- but they are not likely to become easier!

#### DISCLAIMER

This document was prepared as an account of work sponsored by an agency of the United States Government. Neither the United States Government nor the University of California nor any of their employees, makes any warranty, express or implied, or assumes any legal liability or responsibility for the accuracy, completeness, or usefulness of any information, apparatus, product, or process disclosed, or represents that its use would not infringe privately owned rights. Reference herein to any specific commercial products, process, or service by trade name, trademark, manufacturer, or otherwise, does not necessarily constitute or imply its endorsement, recommendation, or favoring by the United States Government or the University of California. The views and opinions of authors expressed herein do not necessarily state or reflect those of the United States Government thereof, and shall not be used for advertising or product endorsement purposes.

OMMIT TO P. 96

Colliding droplets: A short film presentation\*

C. D. Hendricks

University of California, Lawrence Livermore National Laboratory  
P. O. Box 5508, Livermore, California 94550

Abstract

A series of experiments were performed in which liquid droplets were caused to collide. Impact velocities to several meters per second and droplet diameters up to 600 micrometers were used. The impact parameters in the collisions vary from zero to greater than the sum of the droplet radii. Photographs of the collisions were taken with a high speed framing camera in order to study the impacts and subsequent behavior of the droplets. The experiments will be discussed and a short movie film presentation of some of the impacts will be shown.

A series of experiments was set up to study collisions of liquid drops with variable impact parameter, drop diameter and drop velocity. Several materials were studied although water was the primary liquid for many experimental reasons and as a result of our then current interests in cloud physics and meteorological phenomena.

Two drop generators were arranged to project drops toward a region in the focal plane and field of view of a high speed framing camera. Drops were produced by each generator at rates of a few thousand per second. By electrically charging and deflecting some of the drops from each generator, single drop-pair collisions were obtained without aerodynamic effects from preceding drops. The drops were spaced sufficiently far apart that the aerodynamic disturbances from a pair of colliding drops had completely disappeared before the succeeding pair of drops arrived.

High framing rate photographs were taken of droplets of several sizes and velocities. Drops with two diameters (120 and 600 micrometers) and several impact velocities (1, 3, 5 and 7 meters/second) were of particular interest. Figure 1 is a series of frames of a collision between two 120 micrometer drops. It is interesting to note that collisions between successive pairs of drops were reproducible enough that a strobe light synchronized with the droplet production frequency could be used to study the impact and subsequent composite drop behavior in detail.

DISCLAIMER

This document was prepared as an account of work sponsored by an agency of the United States Government. Neither the United States Government nor the University of California nor any of their employees, makes any warranty, express or implied, or assumes any legal liability or responsibility for the accuracy, completeness, or usefulness of any information, apparatus, product, or process disclosed, or represents that its use would not infringe privately owned rights. Reference herein to any specific commercial products, process, or service by trade name, trademark, manufacturer, or otherwise, does not necessarily constitute or imply its endorsement, recommendation, or favoring by the United States Government or the University of California. The views and opinions of authors expressed herein do not necessarily state or reflect those of the United States Government thereof, and shall not be used for advertising or product endorsement purposes.

ORIGINAL PAGE  
BLACK AND WHITE PHOTOGRAPH

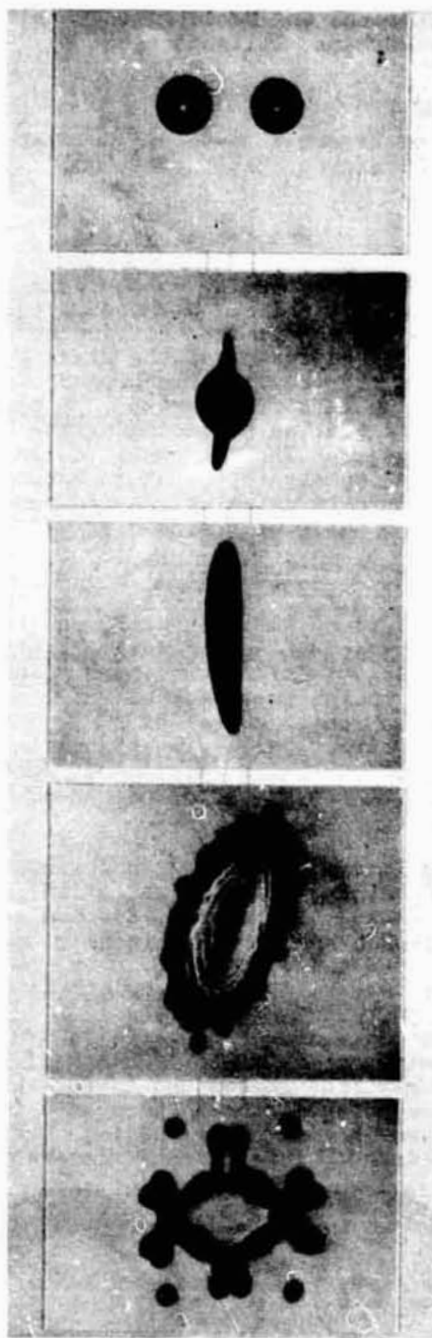


Figure 1 A series of frames of a collision  
between two 120 micrometer drops.

\* Work performed under the auspices of the U. S. Department of Energy by the Lawrence Livermore National Laboratory under contract number W-7405-Eng-48.

81  
D3  
N82 23431

Behavior of liquid hydrogen inside an ICF target<sup>1</sup>

K. Kim and L. Mok

Department of Electrical Engineering, University of Illinois  
Urbana, Illinois 61801

T. Bernat

Lawrence Livermore National Laboratory  
Livermore, California 94550

Abstract

The configuration of liquid hydrogen inside a spherical glass shell ICF target has been studied both theoretically and experimentally. Because of the zero contact angle between the  $D_2$  liquid and glass substrate and the limited wetting surface that is continuous, the liquid hydrogen completely covers the interior of the glass shell, resulting in the formation of a void at the center. For this reason, the present problem distinguishes itself from that for a sessile drop sitting on a flat surface. A theory has been formulated to calculate the liquid hydrogen configuration by including the London-dispersion force between the liquid and the substrate molecules. The net result is an augmented Bashforth-Adams equation appropriate to a spherical substrate, which is considered to be the major contribution of the present work. Preliminary calculations indicate that this new equation accurately models the liquid hydrogen behavior inside a spherical microshell.

Introduction

In the inertial confinement fusion (ICF) research, one of the important tasks is to find an optimum target design which can achieve sufficiently high fuel density with minimum compression energy input. Various target designs have been proposed. Among them is a cryogenic target, which consists of a hollow uniform shell of liquid or solid DT (Deuterium, Tritium mixture) condensed onto the inner surface of a glass microballoon (GMB). Mason<sup>4</sup> has theoretically predicted that such targets will give higher fusion yields. Recently, from the preliminary results of their target implosion experiment, Henderson and his coworkers<sup>5</sup> have noted that neutron yields are enhanced by a factor of ten or more when a cryogenic DT target is used instead of a gas DT target.

Because of this preliminary finding (which needs further investigation), the cryogenic targets are currently attracting a fair amount of attention. Several techniques have been developed to fabricate these targets.<sup>3,13</sup> However, difficulties have been encountered, especially in conjunction with producing and maintaining a uniform liquid layer inside the GMB. Some researchers have obtained a liquid spheroid on one side of the GMB, whereas others have produced a continuous liquid layer, more often with one side thinner than the other.

Shown in Figure 1 are the micrographs of a  $D_2$ -filled GMB target, 320  $\mu\text{m}$  in diameter, 15  $\mu\text{m}$  in thickness, and filled with approximately 700 atm of  $D_2$  gas at room temperature. Figures 1a and 1b are, respectively, the shadow and interference micrographs of the target at room temperature. The corresponding pictures taken at a temperature ( $\sim 25$  K) below the liquefaction point of  $D_2$  are shown in Figures 1c and 1d. The interference micrographs were obtained using a home-made Mach-Zehnder interference microscope.



Figure 1. Pictures of a  $D_2$ -filled glass microshell, 320  $\mu\text{m}$  in diameter and 15  $\mu\text{m}$  in thickness, filled with approximately 700 atm of  $D_2$  gas at room temperature. Figure 1a. Shadow micrograph at room temperature; Figure 1b. Interference micrograph at room temperature; Figure 1c. Shadow micrograph of the target with a continuous liquid- $D_2$  layer at a cryogenic temperature; Figure 1d. Interference micrograph of the same target in Figure 1c.

One distinct feature exhibited by Figure 1 is that the liquid D<sub>2</sub> formed inside the GMB spreads out and completely wets the entire substrate. The net result is a continuous liquid layer having a gas void inside of it. This situation is particularly interesting, not only because it is unique (note that one cannot achieve the same situation with a sessile drop sitting on a flat surface), but also because it offers a promising possibility for fabricating a uniform layer of DT-condensate inside an ICF target.

Presented in this paper is an in-depth study of the behavior of a liquid inside a spherical microshell (SMS). First, a physical model is formulated to predict the liquid profile inside the SMS. These theoretical predictions are then compared with the experimental results obtained for a GMB containing liquid hydrogen. It is hoped that this study will result in a reliable scheme for producing and maintaining a uniform layer of DT-condensate inside a cryogenic ICF target.

### Theories for the profile of liquid inside a spherical microshell

For the convenience of presentation, we first formulate a simple theory applicable to a liquid contained in a spherical substrate. Then, after showing that the theory is incapable of describing a continuous liquid layer wetting the entire substrate - namely, that it is only appropriate to a liquid layer having a well-defined line of contact between the substrate, liquid, and vapor, it is extended by including the van der Waals attraction between the liquid and the substrate molecules. This latter theory, as will be shown, does have the properties appropriate for describing a continuous liquid layer and, therefore, constitutes a major contribution of the current work.

### Profile of liquid with contact line inside a spherical microshell

Following Gibbs<sup>14</sup>, we calculate the minimum energy configuration of the liquid enclosed in an SMS using the calculus of variations. Consider a coordinate system shown in Figure 2a where the thick solid line represents the inner surface of the GMB. For the moment, we consider the gravitational force and the interfacial tensions at the liquid-vapor, liquid-solid and solid-vapor interfaces as the major forces contributing to the energy of the system. Providing that the profile of the liquid-vapor interface is symmetric about the  $\tilde{y}$ -axis, the total energy of the system can, therefore, be expressed as the sum of the following terms.

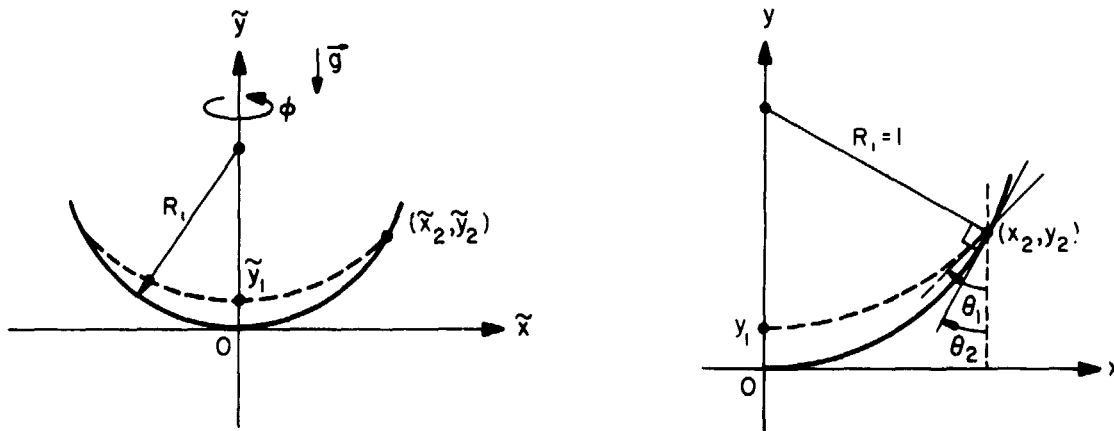


Figure 2. (a) Cylindrical coordinate system employed for the description of a spherical target. (b) The cylindrical system shown above redefined in dimensionless units.

$$E_g = \rho g \int_{V_L} \tilde{y} \, dv = 2\pi \int_{\tilde{y}_1}^{\tilde{y}_2} \frac{1}{2} \rho g y [R_1^2 - (\tilde{y} - P_f)^2 - \tilde{x}^2] \, d\tilde{y} \quad (1)$$

$$E_{LV} = \gamma_{LV} \int_{S_{LV}} ds = 2\pi \int_{\tilde{y}_1}^{\tilde{y}_2} \gamma_{LV} \tilde{x} [1 + (\tilde{x}')^2]^{1/2} \, d\tilde{y} \quad (2)$$

$$E_{SL} = \gamma_{SL} \int_{S_{SL}} ds = 2\pi \int_{\tilde{y}_1}^{\tilde{y}_2} \gamma_{SL} R_i d\tilde{y} \quad (3)$$

$$E_{SV} = \gamma_{SV} \int_{S_{SV}} ds = \text{Constant} - 2\pi \int_{\tilde{y}_1}^{\tilde{y}_2} \gamma_{SV} R_i d\tilde{y} \quad (4)$$

where  $\rho$  is the density of liquid;  $g$  is the gravitational acceleration;  $V_L$  is the volume of the liquid;  $\gamma_{LV}$ ,  $\gamma_{SL}$ , and  $\gamma_{SV}$  are the interfacial tensions at the liquid-vapor, solid-liquid and solid-vapor interfaces ( $S_{LV}$ ,  $S_{SL}$ , and  $S_{SV}$ ), respectively;  $R_i$  is the inner radius of the SMS; and  $\tilde{x} = d\tilde{x}/d\tilde{y}$ .

The variations are now subject to the constraint of the enclosed liquid volume, which is constant for a given temperature and gas fill pressure (e.g.,  $P_0$  pressure) of the SMS. (Note that the thermal energy of the system, which is also a constant at a given temperature, is uniquely determined once the liquid volume is specified, and, therefore, not specifically considered.) The expression of the liquid volume in this case is

$$V_L = \text{Constant} + 2\pi \int_{\tilde{y}_1}^{\tilde{y}_2} \frac{1}{2} [R_i^2 - (\tilde{y} - R_i)^2 - \tilde{x}^2] d\tilde{y} \quad (5)$$

Combining Eqs. (1) through (5), and carrying out the mathematics required to arrive at the Euler equation<sup>13</sup>, one obtains

$$\frac{\tilde{x}''}{[1 + (\tilde{x}')^2]^{3/2}} - \frac{1}{\tilde{x}[1 + (\tilde{x}')^2]^{1/2}} = - \frac{\rho g \tilde{y} + \lambda}{\gamma_{LV}} \quad (6)$$

where  $\tilde{x}'$  and  $\tilde{x}''$ , respectively, denote the first and second derivatives of  $\tilde{x}$  with respect to  $\tilde{y}$ , and  $\lambda$  is the usual Lagrange multiplier resulting from the constraint of constant liquid volume. The absence of the solid-liquid and solid-vapor interfacial tensions,  $\gamma_{SL}$  and  $\gamma_{SV}$ , in Eq. (6) was to be expected since the corresponding interfacial energy terms,  $E_{SL}$  and  $E_{SV}$ , depend only on the two end points  $\tilde{y}_1$  and  $\tilde{y}_2$ , which remain unchanged during the process of calculus of variations.

Letting

$$x = \frac{\tilde{x}}{R_i} \quad , \quad y = \frac{\tilde{y}}{R_i} \quad , \quad \alpha = \frac{\lambda R_i}{\gamma_{LV}} \quad \text{and} \quad \beta = \frac{\rho g R_i^2}{\gamma_{LV}} \quad (7)$$

the dimensionless form of Eq. (6) is obtained as

$$\frac{x''}{[1 + (x')^2]^{3/2}} - \frac{1}{x[1 + (x')^2]^{1/2}} = -(\alpha + \beta y) \quad (8)$$

Two end-point conditions are needed to close this equation. They are

$$1. \quad x' = \infty \quad \text{at} \quad x = 0 \quad (9a)$$

$$2. \quad x(y) = [1 - (y - 1)^2]^{1/2} \quad \text{at} \quad y = y_2 \quad (9b)$$

The first condition simply states that the liquid profile is symmetric about the  $\tilde{y}$ -axis. The second condition is the so-called transversality condition<sup>15</sup> - that is, at  $y = y_2$  the liquid-vapor interface lies on the inner surface<sup>16</sup> of the SMS. It is easy to verify that the second condition gives rise to Young's equation<sup>18</sup> for the contact angle,  $\theta$ , i.e.,

$$\cos \theta = \cos (\theta_1 - \theta_2) = \frac{\gamma_{SV} - \gamma_{LS}}{\gamma_{LV}} \quad (10)$$

The definitions of the angles  $\theta_1$  and  $\theta_2$  are given in Fig. 2b.

Note that Eq. (6) is reduced to the equation derived earlier by Bashforth and Adams for a sessile drop<sup>17</sup> if the origin of the coordinate system is shifted to  $x = 0$  and  $y = y_1$ , and the normalization variable is replaced by the radius of curvature at the origin. So, we henceforth, refer to Eq. (6) (or Eq. (8)) as the Bashforth - Adams equation. The original derivation was based on the force balance at the liquid-vapor interface, i.e., a direct application of the Young-Laplace equation.<sup>18</sup>

For the case of a sessile drop, the reader is referred to the work of D. N. Staicopolus for a complete numerical solution of the Bashforth-Adams equation<sup>19</sup>. An approximate analytical solution of a similar equation has been worked out by P. Concus for calculation of the equilibrium meniscus in a vertical right circular cylinder.<sup>20</sup>

In the current analysis, a direct integration of Eq. (8) subject to a given contact angle is carried out using numerical methods. Before presenting the numerical solution, however, certain points must be clarified:

1. The liquid-vapor interfacial tension is assumed to be constant throughout the calculations regardless of the position and curvature of the interface. This assumption is justified because the radii of curvature of interest in the present case are in the range of 0.01 cm, which is several magnitudes larger than the case studied by Tolman,<sup>21</sup> Kirkwood and Buff,<sup>22</sup> and Benson and Shuttleworth.<sup>23</sup> These authors have found that the surface tension of a small droplet decreases with increasing curvature. Tolman estimated that a 4 per cent drop in the surface tension would occur if the diameter of a droplet was in the order of  $10^{-6}$  cm;
2. The liquid is assumed to be incompressible, and the effect of the vapor pressure on the liquid-vapor surface tension is neglected;
3. The contact line is assumed to be ideal. An ideal contact line means that two mathematically defined surfaces meet together. Thus, the line should be infinitesimal and no liquid film exists beyond the line. In conjunction with this, we note that the validity of Young's equation for the contact angle has long been claimed by Gauss<sup>24</sup> and Gibbs<sup>14</sup> and more recently by Johnson,<sup>25</sup> and Goodrich.<sup>26</sup> For arguments advocating its invalidity, however, the reader is referred to a recent paper by G. J. Jameson and M. C. G. del Cerro.<sup>27</sup>

Numerical solutions of the Bashforth-Adams equation (Equation (8)) satisfying the end-point conditions Equation (9) have been obtained. Figure 3 shows a set of typical solutions obtained for the liquid deuterium enclosed in a GMB for different values of contact angle. The GMB target chosen was 67  $\mu\text{m}$  in inner radius, of 3  $\mu\text{m}$  thickness, and was assumed to be at a uniform temperature of 24 K. For ease of comparison with the experimental results, which is to be made in the future, the room-temperature  $\text{D}_2$ -fill pressure of the target was chosen to be 110 atm. This fill pressure, along with the dimensions and temperature of the target, allows one to determine the amount of liquid deuterium inside the target using the equation of state.<sup>28</sup>

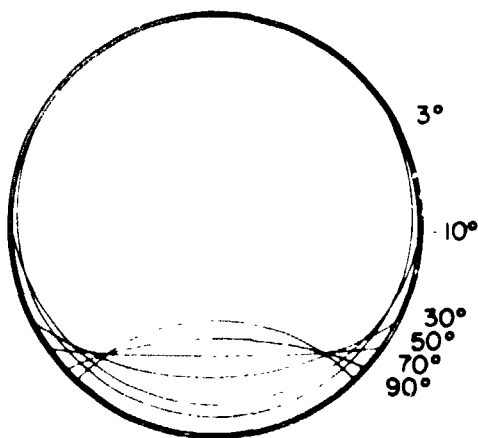


Figure 3. Numerical solutions of the Bashforth-Adams equation for various contact angles. The inner radius of the GMB is 67  $\mu\text{m}$ , the wall thickness is 3  $\mu\text{m}$ , and the temperature is 24 K. The liquid enclosed is deuterium and the fill pressure is 110 atm at room temperature.

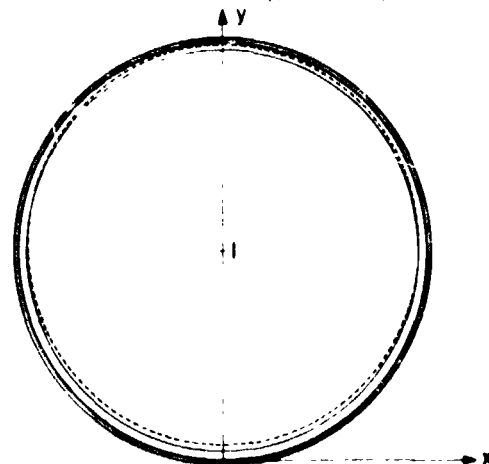


Figure 6. Numerical solutions of the augmented Bashforth-Adams equation. The solid line is for  $B_{SL} = 4.277 \times 10^{-58}$  erg-cm<sup>58</sup> and the broken line is for  $B_{SL} = 4.277 \times 10^{-58}$  erg-cm<sup>58</sup>. The volume of liquid deuterium is  $1.208 \times 10^{-7}$  cm<sup>3</sup> and the temperature is 28 K. The inner radius of the SMS is 67  $\mu\text{m}$  and the wall thickness is 3  $\mu\text{m}$ .

As clearly seen from Figure 3, the location of the contact line between liquid, solid, and gas rises as the value of the input contact angle (one of the end-point conditions, Equation (9)) is decreased. This is simply because of the fact that the smaller the contact angle, the larger is the area wet by the liquid. For zero contact angle, it is, therefore, believed that the liquid will wet the entire target substrate, resulting in a continuous liquid layer. In this case, there will be a gas bubble inside the target completely surrounded by the liquid--a situation not possible in the case of a sessile drop sitting on a flat surface.

Although different input values of the contact angle were used at the same temperature to produce the results in Figure 3, in reality, there can only be one correct contact angle corresponding to a given temperature. Since this correct contact angle is not theoretically available as a function of temperature for the current problem, it must be measured experimentally. Good and Ferry measured the contact angle between liquid hydrogen and a few different materials and reported that it was zero for all the materials studied.<sup>29</sup> Neither the details of the experimental arrangement nor the ranges of the observation temperatures were, however, included in their report. Considering the difficulties involved in maintaining a stable cryogenic environment and, in particular, the difficulties in creating and verifying an isothermal environment, it might perhaps not be totally unreasonable to suggest that the work of Good and Ferry be re-examined, or even redone using carefully designed, more modern equipment for all liquid hydrogen temperatures.

Assuming now that the contact angles of liquid hydrogen and, according to what of liquid deuterium are zero, it is most probable that the liquid deuterium condensed in an SMS exists in the form of a continuous layer.<sup>12,13</sup> It is for this reason that we now go back to the Bashforth-Adams equation and see if it can adequately give rise to a continuous liquid layer solution.

Profile of a continuous liquid layer inside a spherical microshell

Let us now consider a situation where the liquid inside an SMS forms a continuous layer, i.e., no liquid-vapor-solid contact line. The coordinate system used in this case is shown in Figure 4a. Following the same procedures previously used, and considering only the terms pertaining to the gravitational force and the liquid-vapor interfacial tension, one can easily derive a differential equation, which is identical to Eq. (8). The boundary conditions are, however, different. Since the gravitational force is chosen acting parallel to the y axis, the profile of the vapor void (or the bubble) should also be symmetric about the y axis. Therefore, the boundary conditions for the bubble are

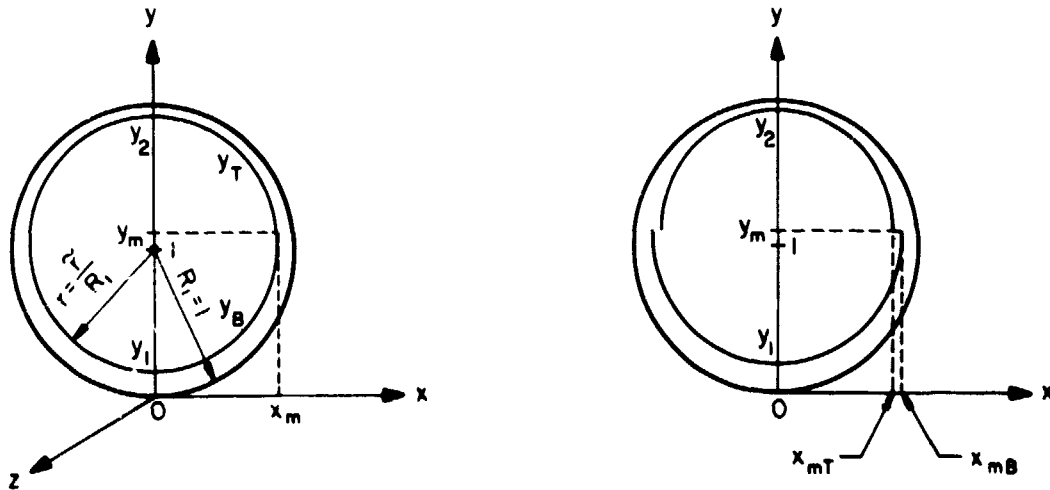


Figure 4. (a) Coordinate systems used in the continuous liquid layer case. At  $x = x_m$  and  $y = y_m$ ,  $x'$  is equal to zero. (b) Numerical solution of Bashforth-Adams equation with one boundary condition satisfied, i.e., at  $x = 0$ :  $x' = \infty$ . Note that  $x_{mB} > x_{mT}$  at  $x' = 0$ .

$$\begin{aligned}
 (1) \quad x' &= \infty & \text{at } x &= 0, \quad y = y_1 \\
 (2) \quad x' &= \infty & \text{at } x &= 0, \quad y = y_2
 \end{aligned}
 \tag{11}$$

Before finding the numerical solutions of Equations (8) and (11), it is worthwhile to study Equation (8) somewhat more carefully. Upon integration, Equation (8) gives rise to

$$x' = \frac{\pm [x^2 - \int_0^x \bar{x}(\alpha + \beta y_{B,T}) d\bar{x}]^{\frac{1}{2}}}{\int_0^x \bar{x}(\alpha + \beta y_{B,T}) d\bar{x}} \quad (12)$$

where  $y_{B,T}$  denotes the two values of  $y$  corresponding to a single value of  $x$ : in the region where  $x'$  is positive,  $y_B$  is used, with B denoting the "Bottom"; and in the region where  $x'$  is negative,  $y_T$  is used, with T representing the "Top". From Equation (12) one finds that where  $x' = 0$ , that is, when  $x$  takes on the maximum value,  $x_m$ , the values of  $x$  are given by

$$x_{mB} = \int_0^{x_{mB}} \bar{x}(\alpha + \beta y_B) d\bar{x} \quad , \quad \text{and} \quad (13a)$$

$$x_{mT} = \int_0^{x_{mT}} \bar{x}(\alpha + \beta y_T) d\bar{x} \quad , \quad (13b)$$

where the subscripts "B" and "T" again refer to "Bottom" and "Top," respectively. Because  $\alpha$  and  $\beta$  are constants and  $y_B \neq y_T$ , Equation (13) implies that one has two different values of  $x$  at  $x' = 0$ . Referring to Figure 4b, since  $y_T$  is always larger than  $y_B$ , one deduces that

$$x_{mB} > x_{mT} \quad (14)$$

This deduction is clearly physically contradictory because no bubble can exist if there is a discontinuity in the liquid-vapor interface. Consequently, there will be no solution to Equation (8) which can satisfy the bubble boundary conditions Equation (11).

The numerical solutions of Equation (8) indeed illustrate this point.<sup>30</sup> Only one of the two boundary conditions Equation (11) is satisfied, i.e., either  $x'_B = \infty$  at  $x = 0$ , but  $x'_T = \infty$  at  $x \neq 0$ ; or  $x'_T = \infty$  at  $x = 0$ , but  $x'_B \neq \infty$  at  $x = 0$ . It is obvious that some forces acting on the bubble that are different from the gravitational force and liquid-vapor interfacial tension are left out of the theory hitherto considered.

There are several types of forces among molecules and atoms<sup>31</sup>: the attractive forces are primary (chemical) bonds, metallic bonds, and secondary (physical) bonds, whereas the repulsive forces are Born repulsions. Primary bonds and metallic bonds are usually strong, and are the basic forces responsible, for example, for forming different stable substances on earth. Secondary bonds are the long-range but weak attraction forces among atoms and molecules and are generally called van der Waals forces.

In fact, van der Waals forces are a collective term for the four different forces, namely, the Debye induction force between a permanent dipole and a neutral molecule,<sup>32</sup> the Keesom orientational force between two freely rotating permanent dipoles,<sup>33</sup> the London-dispersion force due to electron fluctuations around nuclei,<sup>34</sup> and the Margenau force arising from the dipole-quadrupole interaction.<sup>35</sup> Since the liquid of our interest is deuterium or deuterium-tritium mixture and they are nonpolar neutral molecules, only the London-dispersion force is considered. The Born repulsion force is also neglected because it is inverse twelfth power of distance and thus quickly dies out as the distance is increased. The typical effective distance of the Born repulsion force is about 7 Å.

Two approaches are widely used to calculate the total attraction energy of the London-van der Waals type between two macroscopic bodies. One is London-Hamaker's approach<sup>36,38</sup> in which the additivity of the London-van der Waals forces is assumed. The other is Lifshitz's macroscopic approach<sup>37</sup> in which the attraction energy is directly calculated from the imaginary parts of the complex dielectric constants of the media, especially their far ultraviolet portions.<sup>38</sup> Lifshitz's approach is thought to be better than that of London and Hamaker, especially in the case where the separation distance between two macroscopic bodies is large. This is mainly due to the additivity assumption and the intrinsic characteristics of the dispersion forces.

The London-van der Waals forces are electromagnetic-like forces, so they will be subject to retardation, i.e., at large separations the forces will be reduced because the finite time required for their propagation causes a phase difference between the electronic oscillations of the interacting molecules. Because of this retardation effect, the attraction energy calculated by London-Hamaker's approach will be over-estimated for molecules with large separations.<sup>39</sup> When the retardation effect is put into the calculation, as Casimir

and Polder,<sup>40</sup> and Overbeck<sup>41</sup> did, the two approaches usually have differences within an acceptable range.<sup>39,42,43</sup>

To avoid the mathematical difficulties and the scarcity of the data required of the Lifshitz's macroscopic approach, the London-Hamaker's approach is adopted. The nonretarded London-van der Waals forces are considered first. The effects of retardation then follow.

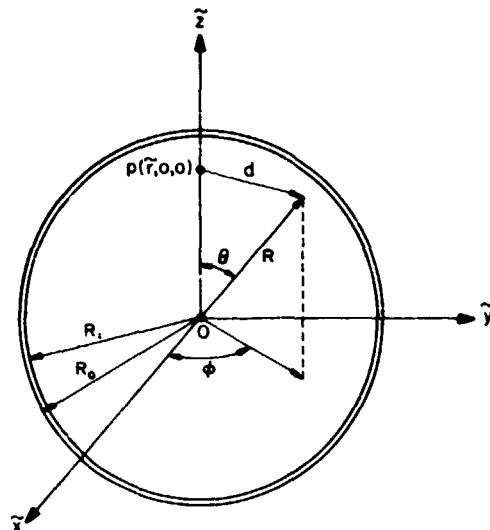


Figure 5. Spherical coordinate system used in the calculation of the London-van der Waals attraction energy between the liquid molecule at  $p(\bar{r}, 0, 0)$  and the spherical substrate with inner radius equal to  $R_1$  and outer radius equal to  $R_0$ .

The coordinate system used is shown in Figure 5. The energy due to the London-van der Waals forces of a liquid molecule at the point  $p(\bar{r}, 0, 0)$  is then expressed as

$$E_p(\bar{r}) = N_s \int_{V_s} dv U(d) \quad (15)$$

where the London potential  $U(d) = -B_{SL}/d^6$  with  $B_{SL}$  denoting the London constant between the solid (substrate) and liquid molecules;  $d$  is the distance between the substrate and liquid molecules;  $N_s$  is the number density of the substrate molecules; and  $V_s$  is the volume occupied by the substrate. Noting the azimuthal symmetry of the system, application of the cosine rules enables one to rewrite Equation (15) as

$$E_p(\bar{r}) = -2\pi B_{SL} N_s \int_{R_1}^{R_0} R^2 dR \int_{-1}^{+1} du \frac{1}{[R^2 + \bar{r}^2 - 2\bar{r}Ru]^3} \quad (16)$$

where  $u = \cos \theta$ .

After straightforward integration, Equation (16) becomes

$$E_p(\bar{r}) = \frac{+4\pi}{3} B_{SL} N_s \left[ \frac{R_0^3}{[R_0^2 - \bar{r}^2]^3} - \frac{R_1^3}{[R_1^2 - \bar{r}^2]^3} \right] \quad (17)$$

The total energy due to the London-van der Waals forces between the liquid and the solid wall is then

$$E_{LVDW} = N_L \int_{V_L} dv E_p(\bar{r}) \quad (18)$$

where  $N_L$  is the number density of the liquid and  $V_L$  is the volume occupied by the liquid.

In terms of the normalized cylindrical coordinate system defined in Figure 4a, Equation (18) is

$$E_{LVDW} = 2\pi N_L \int_{y_1}^{y_2} dy \int_0^x x dx E_p(r) \quad (19)$$

where

$$E_p(r) = \frac{4}{3R_i^3} \pi B_{SL} N_s \left[ \frac{R_e^3}{(R_e^2 - r^2)^3} - \frac{1}{(1 - r^2)^3} \right]$$

$$r = \sqrt{x^2 + (y - 1)^2}$$

$$R_e = \frac{R_o}{R_i}$$

Following the same mathematical procedures previously used (i.e., the calculus of variations), one obtains

$$\frac{x''}{[1 + (x')^2]^{3/2}} - \frac{1}{x[1 + (x')^2]^{1/2}} = -[a + by + \bar{A} D(x, y)] \quad (20)$$

where

$$\bar{A} = \frac{4 - B_{SL} N_s N_L}{3 \gamma_{LV} R_i^2}$$

$$D(x, y) = \frac{R_e^3}{(R_e^2 - r^2)^3} - \frac{1}{(1 - r^2)^3}$$

and the rest of the symbols are as defined in Equation (7). This equation is similar to the Bashforth-Adams equation Equation (8), except that an extra term resulting from the London-van der Waals energy is added. For this reason, we name Equation (20) as the "Augmented Bashforth-Adams equation."

Integrating Equation (20) once and applying the bubble boundary conditions Equation (11), one has

$$\beta V_v + 2\pi \bar{A} \int_0^{x_m} x [D_T(x, y_T) - D_B(x, y_B)] dx = 0 \quad (21)$$

where  $V_v$  is the specific volume of the vapor void, or the bubble (i.e., the actual volume of the void divided by  $R_i^3$ ), the subscript T denotes the upper (top) portion of the bubble where  $x' > 0$ ; and the subscript B denotes the lower (bottom) portion of the bubble where  $x' < 0$ . From Equation (21), one can easily see that as  $\beta$  approaches zero and/or  $\bar{A}$  approaches infinity,  $[D_T(x, y_T) - D_B(x, y_B)]$  will take on a value which is vanishingly small. Or, putting it in another way, at either or both of these two limits, the thickness of the liquid layer is uniform, or the bubble is a complete sphere. In practice, however, the values of  $\bar{A}$  and  $\beta$  are finite and, therefore, the thickness of the liquid layer at the bottom of an SMS is always larger than that at the top.

The numerical solutions of Equation (20) satisfying the bubble boundary conditions Equation (11) are plotted in Figure 6. Note that there is only one unique solution for each set of parameters used. The SMS chosen is 67  $\mu\text{m}$  in inner radius, 3  $\mu\text{m}$  in thickness, and contains liquid  $D_2$  of volume  $1.208 \times 10^{-7} \text{ cm}^3$ . The calculations are done for two different values of the London constant  $B_{SL}$ . As expected, larger  $B_{SL}$  produces a liquid layer more uniform in thickness. This effect is more clearly demonstrated by Figure 7 in which both the top and bottom thicknesses of the liquid layer are plotted as a function of  $B_{SL}$  for two different values of liquid  $D_2$  volume. That a larger  $B_{SL}$  is required to support a thicker uniform layer is clearly shown in the figure, which is consistent with the competing nature of the gravity and the van der Waals attraction.

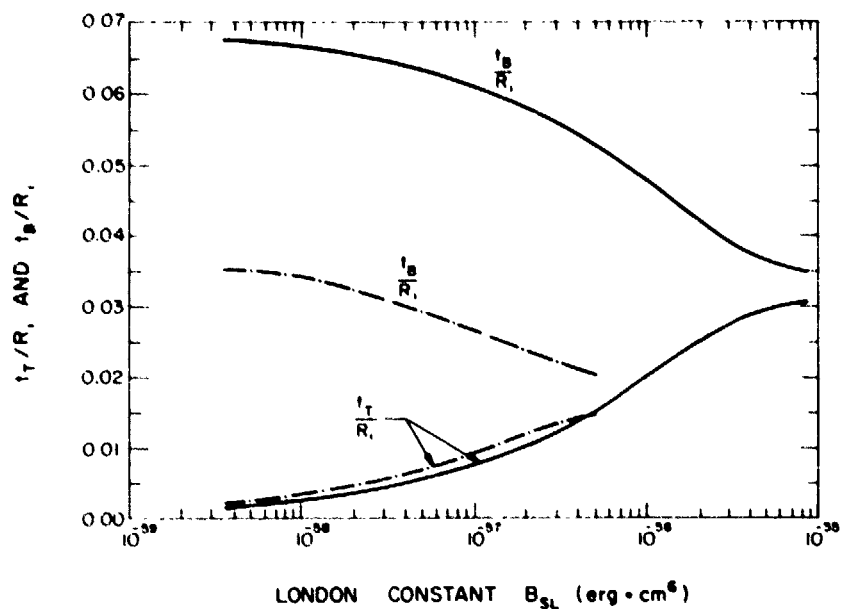


Figure 7. Equilibrium top and bottom thicknesses of liquid deuterium layer inside an SMS at 28 K. The target has inner radius of  $67 \mu\text{m}$  and wall thickness of  $3 \mu\text{m}$ . The broken lines are for the liquid volume of  $6.47 \times 10^{-7} \text{ cm}^3$  and the solid lines are for  $1.208 \times 10^{-7} \text{ cm}^3$ .

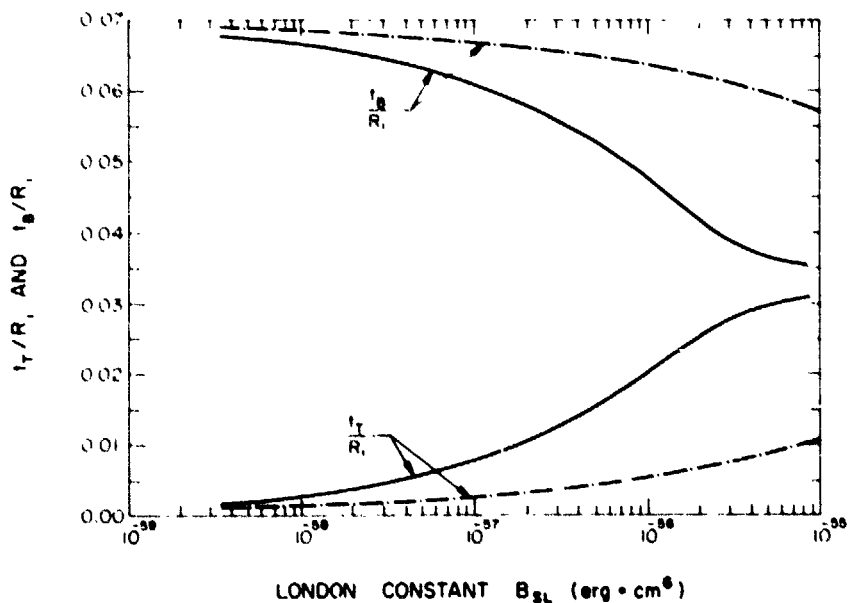


Figure 8. Comparison of equilibrium top and bottom thicknesses of liquid deuterium layer for nonretarded (solid lines) and retarded (broken lines) London-van der Waals forces. The inner radius of the SMS is  $67 \mu\text{m}$  and its wall thickness is  $3 \mu\text{m}$ . The volume of liquid deuterium is  $1.208 \times 10^{-7} \text{ cm}^3$  and the temperature is 28 K.  $\lambda_c$  used in the calculation of retarded London-van der Waals forces is  $10^5 \text{ cm}$ .

Since the wall thickness of the SMS and the thickness of the liquid layer are generally in the order of 1  $\mu\text{m}$ , the retardation effect of the London-van der Waals forces could be significant as pointed out by Casimir and Polder.<sup>40</sup> To include such a retardation effect, a correction function has been introduced into the London potential by Overbeck:

$$U(d) = - \frac{B_{SL}}{d^6} f(p) \quad (22)$$

where  $p = 2 \pi d / \lambda_c$  with  $\lambda_c$  being the characteristic wavelength of the electronic oscillation of atoms; and

$$f(p) = \begin{cases} 1.01 - 0.14 p, & \text{for } 0 < p < 3 \\ 2.45 p^{-1} - 2.04 p^{-2}, & \text{for } 3 < p < \infty \end{cases}$$

Unfortunately, this formula is not easily applicable to our case since two separate functions are involved in two different ranges. Schenkel and Kitchener<sup>44</sup> have found an approximation for  $f(p)$  for the range,  $1 < p < \infty$ . According to these authors, the deviation in the values of  $f(p)$  is less than 5% within this range. The Schenkel-Kitchener approximation is

$$f(p) \approx \frac{2.45}{p} - \frac{2.17}{p^2} + \frac{0.59}{p^3} \quad (23)$$

Replacing the London-potential  $U(d)$  in Equation (15) with this approximation (Equations (22) and (23)) and carrying out the straightforward, yet tedious, integration, one obtains a lengthy expression for the retarded London-van der Waals attraction energy between a liquid molecule at point  $p(r,0,0)$  and the entire substrate of thickness of  $(R_0 - R_1)$  (see Figure 5).<sup>30</sup>

This expression has been used in conjunction with the Augmented Bashforth-Adams approach to determine the retardation effect of the London-van der Waals forces. Plotted in Figure 8 are the equilibrium top and bottom layer thicknesses of the liquid deuterium inside an SMS of inner radius 67  $\mu\text{m}$  for various strengths of the London constant. The temperature of the SMS is 28 K and the volume of the liquid deuterium is  $1.208 \times 10^{-7} \text{ cm}^3$ . As expected, the thickness of the top liquid layer is smaller than the case where the retardation effect is not included.

Note that the Augmented Bashforth-Adams equation Equation (20) with the retarded London-van der Waals energy term is only good within the range  $1 < p < \infty$ . This range might be extended down to  $p = 0.5$ , with a slightly larger error, as pointed out by Schenkel and Kitchener.<sup>44</sup> In general,  $\lambda_c$  is in the order of  $10^{-5} \text{ cm}$ , so that  $p = 0.5$  corresponds to  $d \approx 100 \text{ \AA}$ . Consequently, as long as the top liquid layer thickness (i.e. the smaller thickness) is larger than 100  $\text{\AA}$ , the error in the solution of this equation will be negligible.

Finally, it must be pointed out that the liquid-vapor interfacial tension has been assumed to be constant throughout the calculations, which might turn out to be an important source of error.

### Conclusion

An "Augmented Bashforth-Adams" equation, Equation (20), appropriate to a spherical substrate, has been derived for the first time by including the London-dispersion force as the two-body interaction force between the liquid and substrate molecules. This was prompted by a proof presented in this work that the Bashforth-Adams equation, Equation (8), has no solution subject to the boundary conditions Equation (11) required of a continuous liquid layer. The choice of the London-dispersion force was specifically motivated by the desire to describe the liquid hydrogen behavior inside a spherical microshell ICF target, and was justified by the fact that liquid hydrogen consists of nonpolar neutral molecules.

Considering the fact that most of the previous work on the thin-film phenomena, of which a wealth of literature<sup>27,45</sup> exists, has only dealt with either plane- or cylinder-like geometries, the principal contribution of the present work is to have formulated a theory appropriate to a spherical substrate.

It is hoped that with this work headway has been made toward an active investigation of the thin-film phenomena involving spherical geometry, not only for its own scientific merit, but also for a very interesting practical application - namely, the ICF target research.

### Acknowledgment

One of us (KK) would like to thank Chun Huh of Exxon Production Research for many useful suggestions.

### References

1. Work supported by USDOE under LLNL Subcontract 8320003.
2. R. J. Mason and R. L. Morse, Nuc. Fusion 15, 935 (1975).
3. R. J. Mason and R. L. Morse, Phys. Fluids 78, 814 (1975).
4. R. J. Mason, Nuc. Fusion 15, 1031 (1975).
5. T. M. Henderson, et al., Laser Interaction and Related Plasma Phenomena, ed. H. J. Schwarz and H. Hora (Plenum Publishing Corp., New York, 1977), Vol. 4A.
6. T. M. Henderson et al., Advances in Cryogenic Engineering (Plenum Press, New York, 1975), Vol. 21.
7. E. R. Grilly, Rev. Sci. Instrum. 48, 148 (1977).
8. J. R. Miller, Advances in Cryogenic Engineering, (Plenum Press, New York, 1978), Vol. 23.
9. T. M. Henderson, et al., Advances in Cryogenic Engineering (Plenum Press, New York, 1978), Vol. 23.
10. K. Kim, B. J. Smoot, R. L. Woerner and C. D. Hendricks, Appl. Phys. Lett. 31, 282 (1979).
11. K. Kim and H. Rieger, Appl. Phys. Lett. 37, 425 (1980).
12. J. Fanning, L. Mok, K. Kim and T. P. Bernat, Bull. Am. Phys. Soc. 25, 933 (1980).
13. T. P. Bernat and K. Kim, Proc. ICF Conf., OSA/IEEE, San Diego, CA (Feb. 1980).
14. J. W. Gibbs, Trans. Connecticut Acad. Arts Sci. 3, 343 (1877).
15. See, for example, F. B. Hildebrand, Methods of Applied Mathematics, (Prentice-Hall, Inc., New Jersey, 1965), 2nd edition, p. 139.
16. T. Young, Phil. Trans. Roy. Soc. London 95, 65 (1805).
17. F. Bashforth and J. C. Adams, An Attempt to Test the Theory of Capillary Action (Cambridge University Press and Deighton, Bell and Co., 1892).
18. P. S. de Laplace, Mechanique Celeste, Suppl. au X Livre, Courcier, Paris, 1805.
19. D. N. Staicopolus, J. Colloid Sci. 18, 793 (1963); 17, 439 (1962); 23, 453 (1967).
20. P. Concus, J. Fluid Mech. 34, 481 (1958).
21. R. C. Tolman, J. Chem. Phys. 17, 333 (1949).
22. J. G. Kirkwood and F. P. Buff, J. Chem. Phys. 17, 338 (1949).
23. G. C. Benson and R. Shuttleworth, J. Chem. Phys. 19, 130 (1951).
24. K. F. Gauss, Werke (Göttingen, 1877), Vol. 5, pp. 287-292.
25. R. E. Johnson, J. Phys. Chem. 63, 1655 (1959).
26. F. C. Goodrich, Surface and Colloid Science, ed. Matijevic (1969), Vol. 1.
27. G. J. Jameson and M. C. G. del Cerro, J. Chem. Soc. Faraday Trans. I, 72, 883 (1976).
28. P. C. Souers, "Cryogenic Hydrogen Data Pertinent to Magnetic Fusion Energy," Lawrence Livermore National Laboratory, Report UCRL-52628 (1979).
29. R. J. Good and G. V. Ferry, Adv. Cryo. Eng. 8, 306 (1963).
30. L. Mok, K. Kim, and T. P. Bernat (To be published).
31. F. Z. London, Trans. Faraday Soc. 33, 8 (1937)
32. P. Debye, Phys. Z. 21, 178 (1920).
33. W. H. Keesom, Phys. Z. 22, 129 (1921).
34. F. Z. London, Phys. Z. 63, 245 (1930).
35. H. Margenau, Phys. Rev. 38, 747 (1931).
36. H. C. Hamaker, Physica 4, 1058 (1937).
37. E. M. Lifshitz, Sov. Phys. JETP 2, 73 (1956).
38. H. Kupp, "Particle Adhesion Theory and Experiment," Advances in Colloid and Interface Science (Elsevier Publishing Co., Amsterdam, 1967), p. III.
39. J. Gregory, "The Calculation of Hamaker Constants," Advances in Colloid and Interface Science (Elsevier Publishing Co., Amsterdam, 1969), p. 396.
40. H. B. G. Casimir and D. Polder, Phys. Rev. 73, 360 (1948).
41. J. Th. G. Overbeck, Colloid Science, ed. H. R. Kruyt (Elsevier Publishing Co., London, 1952).
42. T. D. Blake, J. Chem. Soc. Faraday Trans. I, 192 (1975).
43. A. Sheludko, "Thin Liquid Films," Advances in Colloid and Interface Science (Elsevier Publishing Co., Amsterdam, 1967), p. 390.
44. J. H. Schenkel and J. A. Kitchener, Trans. Faraday Soc. 56, 161 (1960).
45. For a recent review, see, for example: K. K. Mohanty, H. T. Davis, and L. E. Scriven, Proc. 3rd Int. Conf. Surface Colloid Sci., Stockholm, Sweden, Aug. 20-25, 1979.

Generation of a Strong Core-Centering Force  
in a  
Submillimeter Compound Droplet System\*

Mark C. Lee, I-an Feng, Daniel D. Elleman and Taylor G. Wang  
Jet Propulsion Laboratory, California Institute of Technology  
Pasadena, California 91109

and

Ainslie T. Young  
Los Alamos National Laboratory, University of California  
Los Alamos, New Mexico 87545

Abstract

By amplitude-modulating the driving voltage of an acoustic levitating apparatus, a strong core centering force can be generated in a submillimeter compound droplet system suspended by the radiation pressure in a gaseous medium. Depending on the acoustic characteristics of the droplet system, it has been found that the technique can be utilized advantageously in the multiple-layer coating of an inertial confinement fusion pellet.

Introduction

One of the important areas of research pertinent to the fabrication physics of inertial confinement fusion targets involves the investigation of various physical mechanisms that generate bubble-centering forces during the formation stage of fusion pellets. Theoretically, the strength of this force is proportional to the frequency of the normal mode oscillation of the compound-droplet system<sup>1</sup>. This frequency is given by

$$f = \frac{1}{2\pi} \sqrt{\frac{\sigma l(l+1)(l-1)(l+2) [\epsilon^{l+\frac{1}{2}} - \epsilon^{-(l+\frac{1}{2})}]}{\rho R_0^3 [(l+1) \epsilon^{l+\frac{1}{2}} + l \epsilon^{-(l+\frac{1}{2})}]}} \quad (1)$$

for a rigid-cored compound-droplet system of an inviscid fluid.  $\sigma$  and  $\rho$  are the surface tension and density of the fluid, respectively.  $R_0$  is the radius of the compound drop,  $\epsilon$  is the ratio of  $R_0$  to the radius of the core and  $l$  is any positive integer with the fundamental frequency corresponding to  $l = 2$ . In Fig. 1, Eq. (1) is plotted for the fundamental oscillation frequency ( $l = 2$ ) versus  $R_0$ . It is interesting to note that, for the two core sizes chosen in the figure, there is an optimal  $R_0$  at which the oscillation frequency reaches a maximum. This value of  $R_0$  can be regarded as the most efficient radius of the compound-droplet system to generate the core-centering force.

It is most convenient to generate and study this core-centering force using an acoustically-levitated submillimeter compound-droplet system. First, the oscillation can be excited easily by amplitude modulation of the carrier voltage of an acoustic levitating apparatus at the appropriate normal mode frequency of the compound droplet system. Second, for a submillimeter compound-droplet system, the core-centering force is very strong indeed. In comparison, the force is only barely observable for drop systems 5 mm or larger.

Experimental Apparatus

An acoustic apparatus has been specifically developed to handle samples of submillimeter sizes in a gaseous medium. This apparatus consists of an acoustic levitation device, deployment devices for small liquid and solid samples, heat sources for sample heat treatment, cold gas cooling system, acoustic alignment devices and data acquisition instrumentation. The levitation device includes a spherical aluminum dish 12" in diameter and 0.6" in thickness, 130 pieces of PZT transducers attached to the back side

\*The research described in this paper was carried out by the Jet Propulsion Laboratory, California Institute of Technology, under contract with the National Aeronautics and Space Administration.

of the dish and spherical concave reflector situated in the vicinity of the center of curvature of the dish. In Fig. 2, the underside of the focusing radiator is shown. In operation, the transducers are driven in phase at one of the resonant frequencies of the radiator. Figure 3 gives the top view of the hemispherical dish. At the center is the reflector for the production of the levitating force. A liquid sample atomizer is shown at the left. In Fig. 4, this device is shown in greater detail. It consists of an acoustic stepped-horn and two PZT transducers pre-stressed to 5000 psi for high power operation. It is supported by a knife edge at the step. A liquid drop placed at the tip of the horn can be transported to the levitating position through an atomization process. The focusing radiator levitating device operates at 75, 105 and 163 kHz, respectively. It has been demonstrated that a sample with a specific gravity as large as 19.3 can be levitated in this apparatus. The lateral positional wandering of the sample in the force well is estimated at less than 5% of the dimension of the sample size used.

#### Compound Droplet System

To create a compound droplet system, a solid sphere is first positioned in the acoustic field at the tip of a vacuum chuck and allowed to drift into the force region upon vacuum release. Liquid material is deployed by first atomizing the material into a fine mist in the vicinity of the force well. The mist is driven by the acoustic force, depositing it onto the surface of the sphere forming a compound droplet system. A typical droplet system has a dimension of about 250  $\mu\text{m}$  diameter for the core and 100  $\mu\text{m}$  thick shell for the liquid layer.

Usually, a compound droplet formed in this manner is not designed to be neutrally buoyant. The gravitational force will manifest itself in two ways: 1. Depending on the relative specific gravity between the core and the fluid, the core will be off-centered, float to the top or sink to the bottom of the liquid shell, and 2. The gravity will deform the droplet to an approximately oval shape (Fig. 5). The second effect could be minimized significantly by increasing the surface tension of the fluid and/or reducing the size of the droplet. It has been observed that the percentage deformation between the two axes is less than 5% for a pure water droplet of typical 500  $\mu\text{m}$  in size. The first effect, on the other hand, is omnipresent, as long as the experiment is performed terrestrially in a one-g environment.

#### Core-centering Force

The core-centering force has been observed in a compound-drop system of 1 cm or larger in a neutral buoyancy tank, where three liquids of comparable specific gravity are present. The core-centering force, in this case, is rather weak because of the size of the drop and the particular set of boundary conditions involved. In this report, we will present results of a strong core-centering force generated acoustically in a submillimeter compound droplet system suspended by the radiation pressure in a gaseous medium.

To generate such a core-centering force, the liquid shell is set into oscillation at one of its natural normal modes. To accomplish this, an amplitude modulation at appropriate frequency is applied to the carrier driving voltage of the focusing radiator levitating apparatus. When the frequency of the amplitude modulation is tuned into the natural oscillation frequency of the compound droplet system, a large amplitude oscillation of the liquid shell is produced driving the core to the center of the system in a fraction of a second. For a typical sized droplet used in the experiment, a modulating frequency between 500 to 1000 Hz is required. Using a water-coated glass-microballoon system, it can be further verified that this is a very strong force indeed in view of the fact that the ratio of specific gravities between the water and the core is approximately five. In Fig. 6, a glass microballoon coated with a layer of water is shown to be centered by this force.

An experimental technique to quantify this force has been devised. A promising method is to generate a secondary oscillation of the core in the presence of the core-centering force. From the frequency of the core oscillation, a force constant  $k$  can be measured, thus the core-centering force can be obtained from  $f = -kx$ , where  $x$  is the displacement of the core from the center position in the presence of the core-centering force.

#### Summary and Concluding Remarks

In summary, we have demonstrated an acoustic technique for generation of a strong core-center force for a submillimeter compound-droplet system. Centering forces of this general nature are important in understanding the physics of, for instance, the formation of glass pellets. The application of this kind of force, for example, can be very advantageous in the multiple-layer coating of an inertial confinement fusion pellet<sup>3</sup>.

ORIGINAL PAGE  
BLACK AND WHITE PHOTOGRAPH

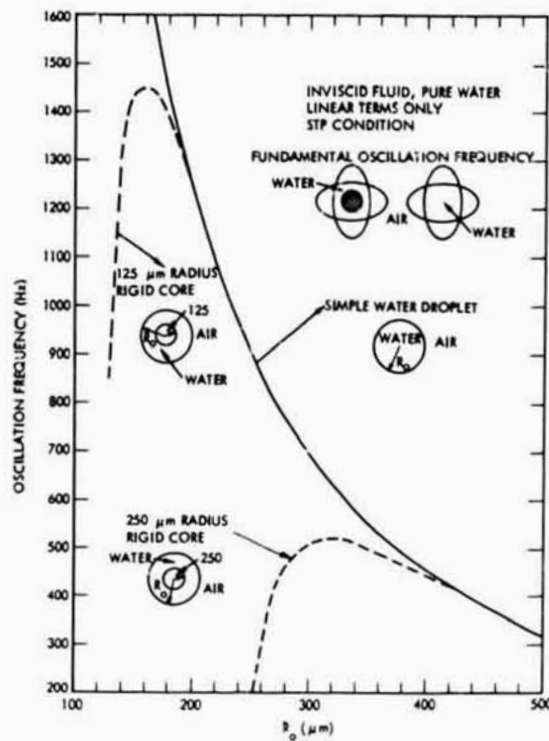


Figure 1. Frequency of normal mode oscillation as a function of the radius of a compound droplet system. The core is rigid and  $l = 2$ .

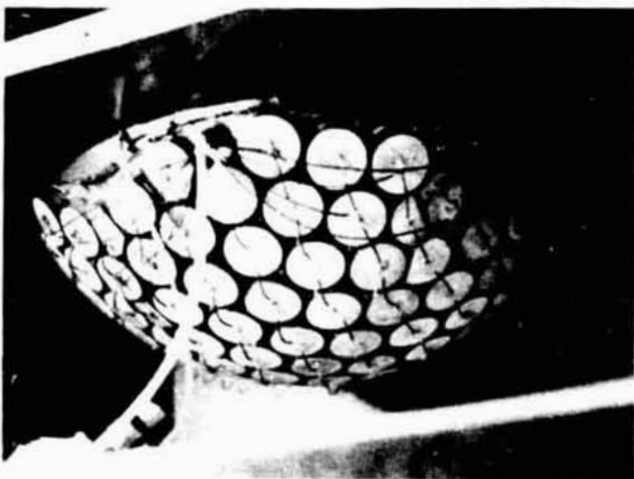


Figure 2. The underside of the focusing radiator acoustic levitation apparatus.

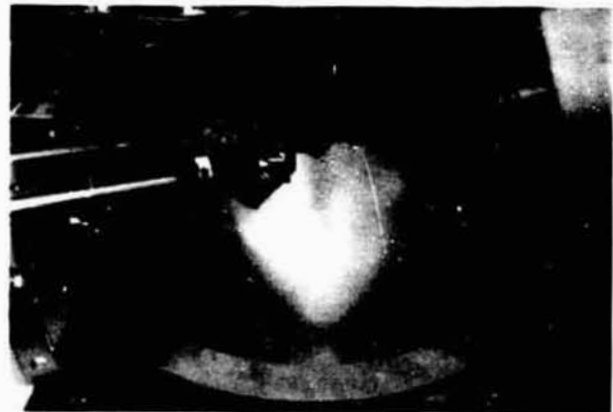


Figure 3. The top view of the focusing radiator acoustic levitation apparatus. The reflector is situated at the vicinity of the focal point. The liquid sample atomizer is at the left.

ORIGINAL PAGE  
BLACK AND WHITE PHOTOGRAPH

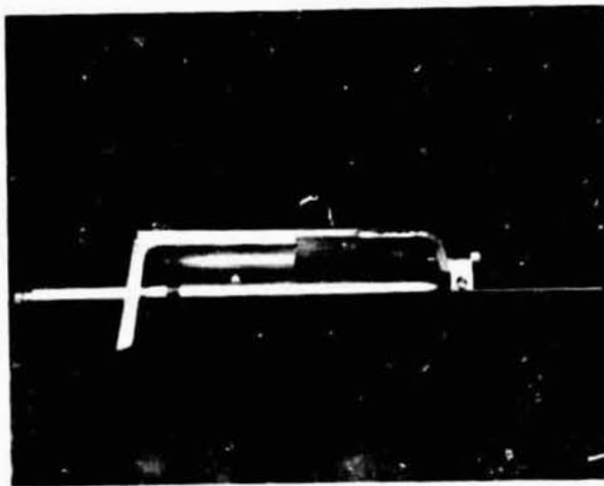


Figure 4. The stepped-horn acoustic atomizer for liquid sample deployment.

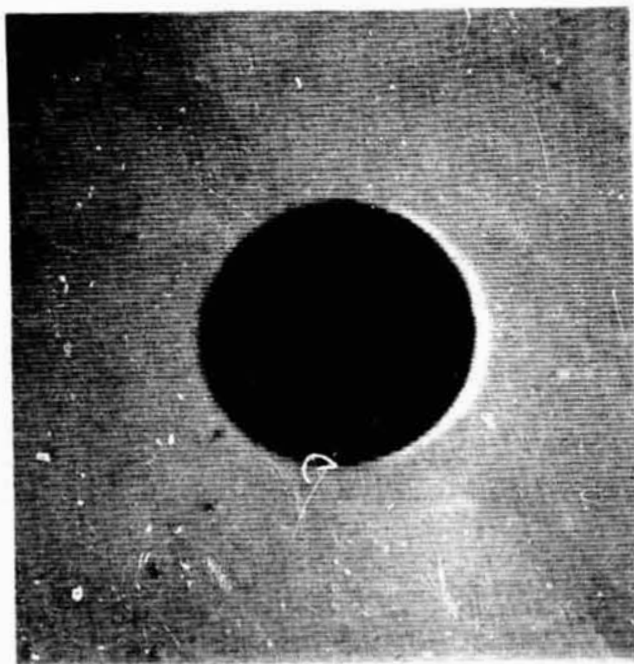


Figure 5. A glass microballoon immersed in water. The buoyancy force pushes the glass microballoon upward.



Figure 6. A water-coated glass microballoon with a strong core-centering force on.

#### References

1. Saffren, M. M., Elleman, D. D., and Rhim, W-K., Dynamics of Compound Drop Systems, Proceedings of the Second International Colloquium on Drops and Bubbles, Monterey, CA., Nov. 19-21, 1981 (to be published).
2. Lee, M. C., Application of an Ultrasonic Focusing Radiator for Acoustic Levitation of Submillimeter Samples, Proceedings of IEEE Ultrasonic Symposium, Chicago, Illinois, Oct. 14-16, 1981 (to be published).
3. Lee, M. C., Feng, I., Elleman, D. D., Wang, T. G, and Young, A. T., Coating of Glass Microballoon Using an Acoustic Technique, Journal of Vacuum Science and Technology, March/April, 1982.

Dis \* N82 23433

Holographic studies of the vapor explosion of vaporizing  
water-in-fuel emulsion droplets

Stephen A. Sheffield

Sandia National Laboratories  
Division 2513, P. O. Box 5800, Albuquerque, New Mexico 87185

C. F. Hess and J. D. Trolinger

Spectron Development Laboratories, Inc.  
3303 Harbor Boulevard, Suite G-3, Costa Mesa, CA 92626

Abstract

Holographic studies have been performed which examine the fragmentation process during vapor explosion of a water-in-fuel (hexadecane/water) emulsion droplet. Holograms were taken at 700 to 1000 microseconds after the vapor explosion. Photographs of the reconstructed holograms reveal a wide range of fragment droplet sizes created during the explosion process. Fragment droplet diameters range from below 10 microns to over 100 microns. It is estimated that between ten thousand and a million fragment droplets can result from this extremely violent vapor explosion process. This enhanced atomization is thus expected to have a pronounced effect on vaporization processes which are present during combustion of emulsified fuels.

Introduction

Water has long been observed to have a beneficial effect on combustion of liquid fuels but a complete understanding of the mechanisms by which this enhancement occurs is just beginning to emerge. Water-in-fuel emulsions are being used or considered for use in many combustion applications where particulate pollution is a problem because of the potential of decreased particulate emissions and enhanced combustion. Although a number of studies have been carried out to determine the physical processes involved in the combustion of emulsified fuels, primarily phenomenological explanations have resulted. The present experiments are part of a larger program designed to quantify the phenomena which have been observed and understand the enhancement process.

The first enlightening experiments were performed by Ivanov, et al.<sup>1</sup> of the Soviet Union in the late 1950's. They showed that water/oil emulsion droplets burned disruptively when suspended on a quartz fiber (called a sting) and ignited. This disruptive burning process was called a "microexplosion." In 1976, Dryer and coworkers<sup>2,3</sup> performed similar experiments at Princeton University and from their observations suggested that the water in the oil matrix was superheating. Near the limit of superheat, the water homogeneously nucleates rapidly to produce a vapor-phase explosion. The limit of superheat for water is approximately 260°C so their concept was that paraffinic fuels with a boiling point above this, when emulsified with water, should lead to a vapor explosion while those with boiling points below would not vapor explode. This means that hexadecane (boiling point 287°C) emulsions should vapor explode while tetradecane (252°C) emulsions should not. However, their early observations of burning emulsion droplets suspended on a quartz sting indicated dodecane (216°C) emulsions microexploded. They felt the sting was probably a source of nucleation sites that led to premature water nucleation. In order to eliminate the sting nucleation problems, free droplet studies were necessary.

Recently, studies by Lasheras, Dryer, et al.<sup>4,5</sup> have been carried out in which free emulsion droplets were injected into the hot combustion products streaming out of a flat flame burner. Vapor explosions were observed using droplets of hexadecane/water and tetradecane/water emulsions but not in dodecane/water emulsions. These results correlated very nicely to a theoretical prediction by Avedesian<sup>6,7</sup> which predicted tetradecane/water emulsions should be on the edge of failure to undergo vapor explosion because the fuel boiling point is very close to the superheat limit for the system.

The above mentioned studies have been primarily phenomenological with respect to the processes occurring during the vapor explosion because of the difficulties in photographing a free droplet. Two recent studies by Sheffield, Baer and Denison<sup>8,9</sup> using emulsion droplets levitated above a hot plate have shown that a number of very interesting processes take place during the heatup and vapor explosion process. Surface tension induced circulation occurs inside the droplet and the small water droplets coalesce to form larger water globules during the heatup process. Then the large globules settle to the bottom of the droplet just prior to the vapor explosion. The explosion process was clearly shown to be

very violent, producing fragment velocities ranging from 30 to 90 meters per second. However, instrumentation was not adequate to resolve fragment sizes in these experiments.

The holography experiments described in this paper were carried out for the purpose of visualizing the explosion fragments to determine the extent of the fragmentation process. Droplet fragments from less than 10 to over 100 microns in diameter have been clearly identified at times 700 to 1000 microseconds after the vapor explosion starts. These experiments will be discussed in detail in terms of the experimental setup, experimental observations, and their correlations with previous results.

### Experimental Setup

A water-in-fuel emulsion consists of a heterogeneous mixture with the fuel as the matrix, water as the dispersed phase, and a surfactant which is used to stabilize the material. In this study, the fuel was n-hexadecane ( $C_{16}H_{34}$ ). The surfactant was a mixture of Span 80 and Tween 80<sup>10</sup> to give an HLB number of about 5.5 which results in a fuel soluble surfactant and produces a relatively stable water-in-fuel emulsion. Emulsions were made by mixing 29% water, 69% n-hexadecane, and 2% surfactant (by volume) in a domestic blender for several minutes. The resulting emulsion has a milky color with the dispersed water drops a few microns in diameter.

The free droplet experiment adopted in the present study uses the Leidenfrost phenomenon<sup>11</sup> to levitate a droplet above a heated surface. This experiment consists of placing an ~2 mm diameter droplet of emulsion on a heated metal surface using a small syringe to form the drop. The plate temperature is maintained above the Leidenfrost temperature of the fuel so that fuel evaporation causes the droplet to levitate about 10 to 50 microns above the plate<sup>12</sup>. A slight 50 mm diameter spherical indentation in the highly polished plate stabilizes the droplet in one area during its heatup period so that it can be easily photographed. The heated plate was maintained at temperature by using a laboratory hot plate.

For these particular experiments, the plate was replaced by a stainless steel substrate machined to the shape of a truncated cone 25 mm diameter at the base and 12 mm diameter at the top, which was highly polished with a spherical indentation in it. This substrate was placed on a laboratory hot plate and maintained at a temperature of about 500°C. An insulation sheet 25 mm thick with a cutout to accommodate the cone shaped substrate was placed over the hot plate during each experiment to eliminate any hologram noise which might be generated by a large amount of natural convection induced turbulence in the 30 cm hot plate region surrounding the exploding droplet. The holocamera, Model HTC-5000 built by Spectron Development Laboratories, has a pulsed ruby laser light source which is switched by a Pockels cell to give a 10 to 20 nanosecond pulse between 700 and 1200 microseconds after the holocamera is triggered. The low end of this delay is controlled by the amount of time it takes the flash lamp to pump the ruby rod to a sufficiently energetic state that a reliable laser pulse can be obtained when the laser pulse is allowed to escape by triggering the Pockels cell. A schematic of the experimental setup is shown in Figure 1. Notice that the holography system consists of a reference beam which travels approximately the same distance as the information beam. The information beam passes through the explosion regime and then interferes with the reference beam on the film plane and exposes the glass holographic plate producing the hologram. Two lenses which are not shown on the figure were inserted in the information beam at the proper places to position the image of the droplet explosion behind the holographic plate to simplify the reconstruction. By properly choosing these lenses, magnification of the explosion was obtained in some of the experiments.

Triggering of the holocamera was accomplished by passing a helium-neon laser beam close to the side of the droplet and into a photo detector setup that was designed to send out a trigger signal when the beam was interrupted. Since the beam was near the bottom of the droplet, it was interrupted when the vapor explosion produced the early jetting to the side. A trigger signal then went to the holocamera. Between a settable delay of 700 to 1000 microseconds after the holocamera was triggered, the Pockels cell was triggered, providing the laser pulse required to produce the hologram. Since the laser pulse width was limited to 10 to 20 nanoseconds, a stop action hologram of the explosion process was produced. Resolution of the holograms was a few microns with this configuration so fragment droplets of a few microns were detectable.

Reconstruction of the explosion images was accomplished by expanding a helium-neon laser beam and orienting the developed holographic plate in the expanded beam so that the three dimensional image was formed off at an angle from the main beam as shown in Figure 2. Pictures were then taken of the image using macrophotography techniques to provide the desired magnification. An Olympus OM-2 camera was used to take the pictures.

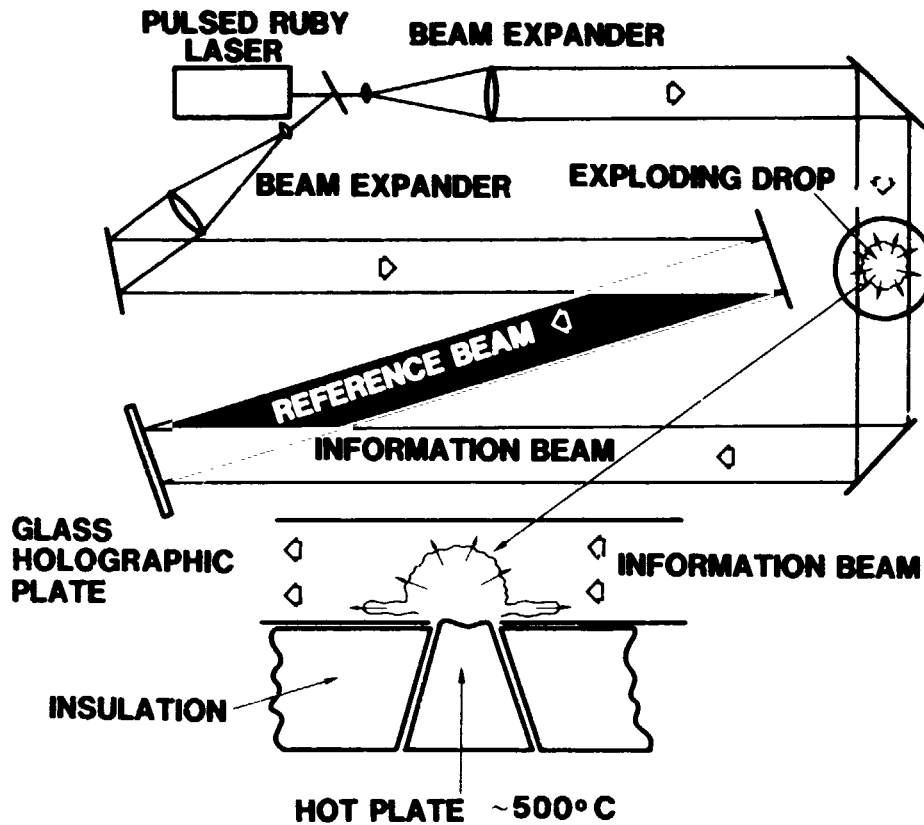


Figure 1. Exploding droplet holography experimental setup.

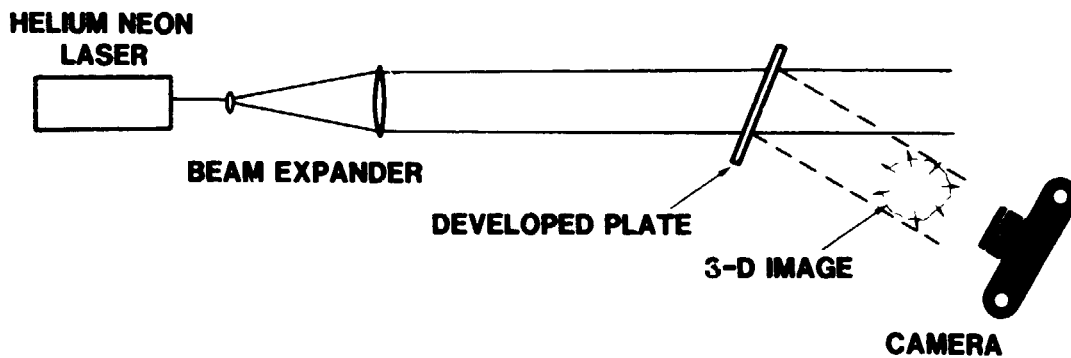


Figure 2. Holographic image reconstruction setup.

## Results and Discussion

Over 30 holograms of exploding droplets were taken during this study. Some explosions were obviously less violent than others probably due to premature heterogeneous nucleation of the water before it reached the superheat limit. Three representative holograms were picked for close study and several photographs of the reconstructed images were made. In Figures 3, 4, and 5, respectively, fragmentation is shown 700, 875, and 1000 microseconds after the holocamera was triggered. It was possible to make only one hologram of each droplet explosion so these figures represent three different explosions with the accompanying differences between them one might expect.

Figure 3 clearly shows the nature of the fragmentation process with a jet visible near the plate, moving out parallel to the plate. Other parts of the droplet liquid are in the form of ligaments in the process of breaking up to form droplets. The lower left enlargement shows a ligament that has nearly completed the breakup process. The next two enlargements, moving clockwise around the center picture, show a common area; only the position of the camera focus has been changed to show the three dimensionality of the hologram image. Some droplets which are in focus in one enlargement are out of focus in the other. The enlargement in the top-right corner was made in an area that appears to have only a few droplets in the center picture but the enlargement shows a large number are actually present. The same is true for the lower-right enlargement. From the scale it is clear that the ligaments and a few droplets are larger than 100 microns in size, but a large number are substantially smaller.

Figure 4 shows a droplet explosion 875 microseconds after the holocamera was triggered. Although this explosion looks considerably different from the one shown in the previous figure, many droplets with a wide range of sizes are discernable. No ligaments appear in this explosion, however. The jet on the left side is visible but the one on the right seems to have already disappeared, perhaps, as a result of the explosion venting more to the right side than the left during the early part of the process. This phenomenon has been observed in high speed framing camera pictures in earlier testing.

Figure 5 shows a droplet explosion 1000 microseconds after the holocamera triggered. Again the remains of the jets are visible near the plate. The lower-left enlargement contains part of the jet, but droplets are not clearly discernable in this area of the picture, so they are apparently on the order of the resolution of the hologram, around 1 to 5 microns. Other drops in the center picture and the enlargements range from about 10 to 100 microns in size. Most of the ligaments appear to have already broken up because there are only a few small ones present throughout the picture. The top-left enlargement shows an area where very few droplets are discernable in the central picture, but many drops are clearly observable in the enlargement, some in the 10 micron range. Again this figure shows, in a graphic way, the tremendous fragmentation that results from the vapor explosion.

Although this experimental setup represents a somewhat non-physical situation as far as simulating a combustion environment is concerned, it does provide a needed visualization of the explosion process. The jetting near the substrate is due to the asymmetric confinement and heating provided by the substrate. It is felt, however, that the explosion upward is quite representative of what one might expect in a combustion environment. The small droplets formed in the jets by the rapid venting provide an interesting comparison to those formed in the less violent upward explosion.

Droplets formed in the jet are on the order of a few microns which means they could vaporize in a few hundred microseconds<sup>13</sup> unless the atmosphere around them was saturated with fuel vapor as is probably the case at the late times of the holograms. This correlates nicely with high speed framing camera pictures which show the jets disappearing. For comparison purposes a sequence taken at 40,000 frames per second has been included as Figure 6. It shows the jet disappearing in frame 5, about 200 microseconds after the explosion starts. In this sequence, the side jets are moving out at about 90 m/s and the droplet is exploding upward at between 30 and 70 m/s. The droplets visible in the holograms, which are much later in time than the film sequence, have moved about 30 mm in 1000 microseconds (average velocity of 30 m/s). As expected, the droplets are slowing down due to drag as they move out. It is estimated that the drop velocity should be reduced to the surrounding gas velocity in 10 to 20 mm of travel<sup>13</sup> so the true droplet velocity is probably slower than the calculated average velocity at these late times. Based on this, one would expect the diameter of the sphere of influence of the explosion to be about 30 to 60 mm or about 15 to 30 or more initial droplet diameters in these experiments.

Pictures of the holograms in Figures 3 through 5 clearly show that a large number of fragment droplets are formed. No attempt has been made to carefully count all the drops in each picture because this only represents a small slice of the whole explosion volume. If one assumes a 2 mm droplet is reduced to a monodisperse group of 50 micron diameter fragments, one drop would produce over 50,000 fragment droplets. If the fragment diameter

ORIGINAL PAGE  
BLACK AND WHITE PHOTOGRAPH

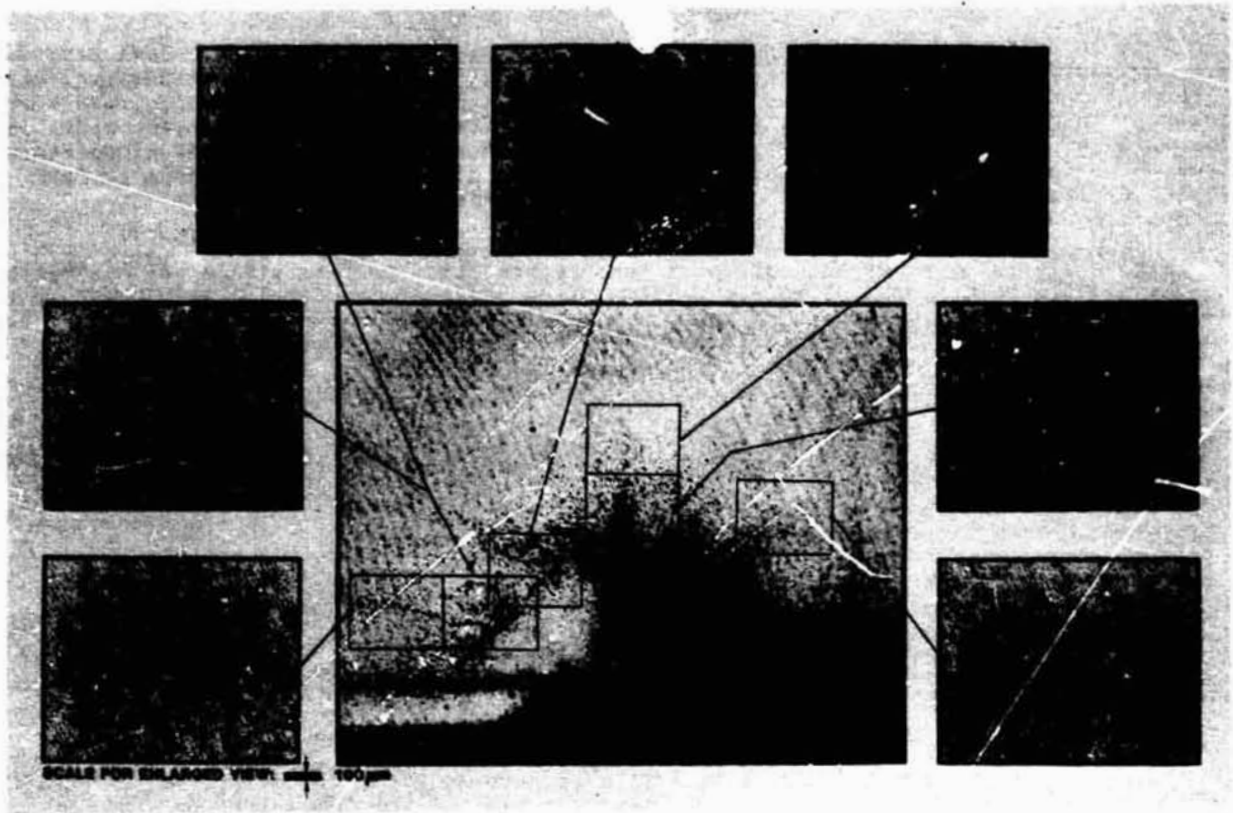


Figure 3. Picture of image of droplet explosion 700 microseconds after holocamera was triggered.



Figure 4. Picture of image of droplet explosion 875 microseconds after holocamera was triggered.

ORIGINAL PAGE  
BLACK AND WHITE PHOTOGRAPH

was 30 microns, one drop would produce 300,000 fragment droplets. In this case we have a distribution of sizes from too small to measure in the jets (probably a few microns in diameter) to over a hundred microns. An average size is probably between 30 and 50 microns which indicates there are on the order of tens of thousands to hundreds of thousands of fragments from one drop exploding. An estimate of the number of drops visible in one picture led to about 4000 drops. Since this is only a slice of the whole volume, one would expect to have 10 to 100 times this many in the entire explosion, again leading to the same estimate as above. We have estimated that the lower and upper limits on numbers of fragments formed are ten thousand and a million, respectively.



Figure 5. Picture of image of droplet explosion 1000 microseconds after holocamera was triggered.

#### Conclusions

Time resolved holography has been shown to be an extremely useful experimental technique to study the vapor explosion of a vaporizing water-in-fuel emulsion droplet. It has led to some very graphic pictures of the droplet fragmentation which results from the explosion. Fragment sizes from less than 10 to larger than 100 microns are visible with the average probably in the 30 to 50 micron range. In the early time holograms (700 microseconds), ligaments that are breaking up are visible, while at the later times (1000 microseconds) the ligament breakup is nearly complete. Estimates based on the average size and the number of drops visible in the pictures of the holograms indicate that lower and upper limits for the numbers of fragments are ten thousand and a million. The typical number is probably between 50,000 and 300,000, indicating the very violent nature of the vapor explosion.

The distances that the fragments have traveled after the explosion lead to an average velocity of 30 m/s compared to between 30 and 70 m/s when the explosion first starts, indicating a drag induced reduction in velocity. The sphere of influence of the explosion is estimated to be about 15 to 30 original droplet diameters.

#### Acknowledgements

We would like to thank Tim Wilmot and Fred Mason for helping in the experimental setup and operation and Robert Nichols for taking pictures of the holograms and putting together the collages.

ORIGINAL PAGE -  
BLACK AND WHITE PHOTOGRAPH

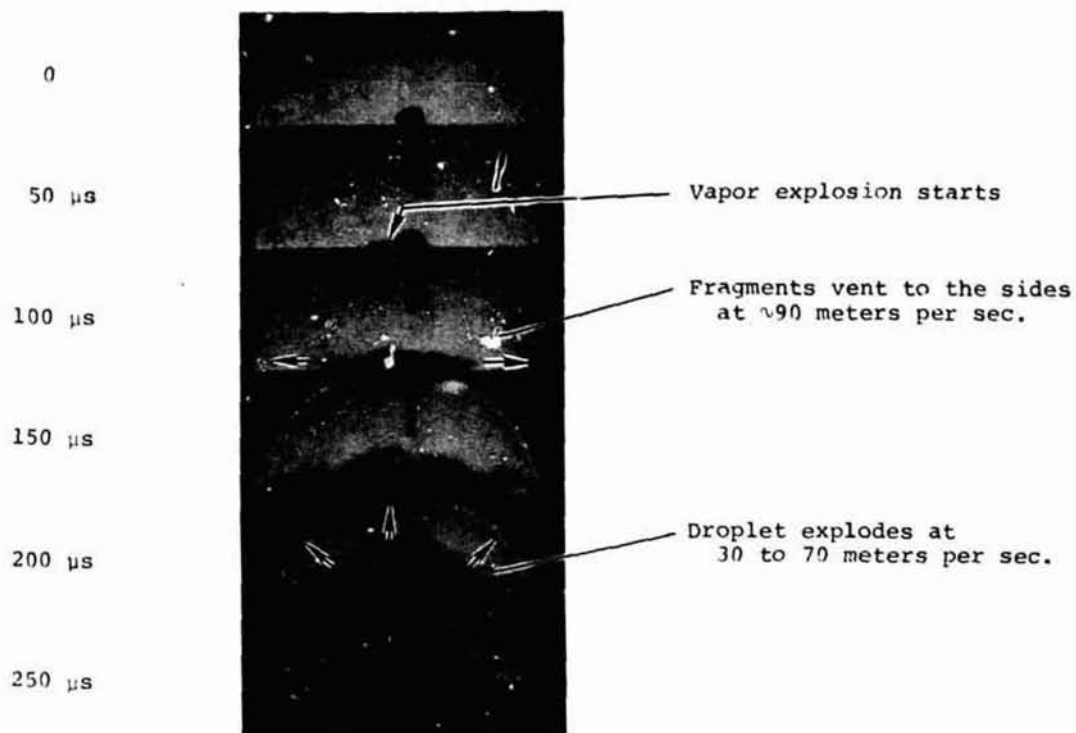


Figure 6. High speed framing camera sequence of a droplet explosion. Droplet was backlit with an expanded laser beam. Frames are 50 microseconds apart.

References

1. Ivanov, V. M. and Nefedov, P. I., Experimental Investigation of the Combustion Process of Natural and Emulsified Liquid Fuels, Trudy Instituta Goryachikh Iskopayemykh, Vol. 19, pp. 35-45, 1962; Translated as NASA TTF-258. 1965.
2. Dryer, F. L., Water Addition to Practical Combustion Systems - Concepts and Applications, Sixteenth Symposium (International) on Combustion, the Combustion Institute, pp. 279-295. 1977.
3. Dryer, F. L., Rambach, G. D., and Glassman, I., Fundamental Concepts on the Use of Emulsions as Fuels, Aerospace and Mechanical Sciences Report No. 1271, Princeton University. 1976.
4. Lasheras, J. C., Fernandez-Pello, A. C., and Dryer, F. L., Initial Observations on the Free Droplet Combustion Characteristics of Water-in-Fuel Emulsions, Combustion Science and Technology, Vol. 21, pp. 1-14. 1979.
5. Lasheras, J. C., Kennedy, I. M., and Dryer, F. L., An Initial Study of the Effects of Alcohol and Water Addition on the Burning of Isolated Distillate Fuel Droplets, presented at the Spring Meeting of Western States Section, the Combustion Institute, April 21-22, 1980, University of Calif., Irvine, Calif.
6. Avedesian, C. T., and Andres, R. P., Bubble Nucleation in Superheated Liquid-Liquid Emulsions, Jnl. of Colloid and Interface Science, Vol. 64, pp. 438-453. 1978.
7. Avedesian, C. T., Superheating and Nucleation of Water in Hydrocarbons and of Hydrocarbon Mixtures, Ph.D. Thesis, Dept. of Mechanical and Aerospace Engineering, Princeton University, 1980.
8. Sheffield, S. A., Baer, M. R., and Denison, G. J., Observations of Vaporizing Water-in-Fuel Emulsion Droplets, presented at the 1980 Technical Meeting, the Eastern Section of the Combustion Institute, Nov. 12-14, 1980, Princeton, New Jersey.
9. Baer, M. R., Sheffield, S. A., and Denison, G. J., Circulation and Coalescence Within a Vaporizing Emulsified Fuel Droplet, presented at the 1980 Technical Meeting, the Eastern Section of the Combustion Institute, Nov. 12-14, 1980, Princeton, New Jersey.
10. Obtained from ICI United States Inc., Specialty Chemicals Division, Wilmington, Delaware 19897.
11. Gottfried, B. S., Lee, C. J., and Bell, K. J., The Leidenfrost Phenomenon: Film Boiling of Liquid Droplets on a Flat Plate, Int. J. Heat Mass Transfer, Vol. 9, pp. 1167-1187. 1966.

12. Kistemaker, J., The Spheroidal State of a Waterdrop, the Leidenfrost Phenomenon, Physica (Netherlands), Vol. 29, pp. 96-104. 1963.
13. Baer, M. R., Sandia National Laboratories, private communication.

Droplets generated from a new 'ogee' shaped,  
liquid, air-shear, electrostatic nozzle

I.I. Inculet, T.E. Base and G.S.P. Castle  
Faculty of Engineering Science  
The University of Western Ontario  
London, Ontario, Canada, N6A 5B9

## ABSTRACT

A series of experimental tests was carried out on an 'OGEE' shaped planform, liquid air-shear electrostatic nozzle. Liquid was ejected from the upper surface of the nozzle and was then dispersed and atomized efficiently by a high speed air flow passing over the nozzle and by the effect of two very strong coherent air vortices generated by the 'OGEE' shaped nozzle surface. Initial test results which are presented in the paper show the nozzle to perform far superior to a similar delta wing shaped nozzle design which is used extensively in various industrial applications.

## INTRODUCTION

The air shear nozzle is used in many spray applications which require relatively large quantities of finely atomized liquid droplets. It consists of an orifice which introduces a liquid into a high velocity air stream. The atomization results from the mechanical disruption of the liquid stream by the air shear and pressure forces<sup>1</sup>. A number of different geometries have been used for the nozzle ranging from simple open tubes to aerodynamically shaped nozzles. One commonly used geometry is a delta wing shaped planform nozzle with a raised lip along its trailing edge (See Figure 1.) In a previous investigation<sup>2</sup> the atomization pattern of this nozzle was studied in order to optimize the positioning of an induction electrode for electrostatic charging of the droplets. In the course of this investigation it was discovered that contrary to expectations, the majority of the atomization took place off the open surface of the nozzle rather than the raised lip. This observation led to further experimentation to determine the influence of the aerodynamic shape on the effectiveness of atomization. It led to the development of the new OGEE shaped liquid air shear nozzle shown in Fig. 2 (Patent Pending). In what follows a description of the theory of operation along with experimental results are presented for both the delta wing and OGEE nozzles with and without electrostatic charging.

## AIR FLOW CHARACTERISTICS AS APPLIED TO AIR SHEAR NOZZLE DESIGN

The OGEE air shear nozzle, as shown in Fig. 2, has a slender wing airfoil planform shape. The particular shape used is called an 'OGEE' wing according to the resemblance to a leading edge of a wave like form similar to the letter 's'. The characteristics of slender wings are well described by Hoerner<sup>3</sup>. The essential flow regime generated by a slender wing at an angle of incidence to the approaching flow consists of two, strong, coherent vortices circulating with opposite rotational sense. These vortices start at the apex of the nozzle and are continually shed from the sharp 's' shaped leading edge to proceed downstream and pass over the trailing edge. The two vortices pass over the trailing edge of the nozzle at a position ranging from 90% to 70% of the semi span measured from the nozzle centre line. This depends on the angle of incidence and the ratio of the semi span to the length. The height of the vortex cores above the wing increases with an increase in the angle of incidence. In the design of an air-shear nozzle the angle of incidence and span to length ratio has to be chosen such that the vortices shed from the leading edge have a trajectory passing near the region where liquid will be released into the flow. One advantage of using a slender wing shaped nozzle instead of a more conventional straight wing of higher aspect ratio is that in the case of a slender wing the coherent vortex pattern is fully developed before the flow reaches the trailing edge whereas for a straight wing, the flow is not fully developed until at least several wing spans downstream of the trailing edge. In the final design, the vortices pass over the upper surface of the nozzle and increase the divergence of the liquid flow emitted from the upper surface. The effect of the two vortices also creates a very low pressure or high suction which improves the liquid flow and droplet atomization. The effect of the circulation and rotation of the vortices also improves the mass transfer of the liquid droplets after the two-phase flow has passed downstream of the trailing edge of the nozzle. A physical advantage of the 'OGEE' shaped planform nozzle compared with the delta wing shaped nozzle is that geometrically a larger liquid jet can be achieved for the same length, span and thickness of nozzle.

## INDUCTION CHARGING WITH AIR SHEAR NOZZLES

The geometry of the air shear nozzle described above is ideally suited for induction charging since the atomization takes place over the open face of the nozzle. Thus by placing an insulated plane electrode opposite the nozzle face and by ensuring that the liquid has adequate conductivity and is connected to ground, induction charging of the droplets will take place at the moment of atomization. The advantages of combining electrostatic charging in droplet spraying are well known<sup>4</sup> and when compared with simple mechanical atomization include:

1. The production of smaller more uniformly sized droplets, since electrostatic surface charge counteracts surface tension forces,
2. More uniformly dispersed droplets on account of the mutual repulsion caused by their like charges,
3. More effective deposition of the charged droplets on target surfaces, due to the attraction by induced space charge image.

In the previous work with the delta wing shaped nozzle<sup>2</sup> the size and shape of the induction electrode was investigated along with the value of optimum induction field to maximize the charge to mass ratios.

#### EXPERIMENTAL RESULTS

The experiments were carried out using a commercially available air blast sprayer of the Kinkelder type as used in agricultural spraying. For the purpose of these tests, the spray heads were modified to allow induction charging<sup>4</sup>. This modification consisted of replacing the cast aluminum spray heads with identically shaped fibreglass heads having conductive induction electrodes embedded flush with the inside surface at points opposite the air shear nozzles. The electrodes were connected via an imbedded high voltage cable to a self regulating H.V. power supply rated 15 kV open circuit. The power supply was fed from a 12 V DC battery. The complete spray system is shown in Fig. 3. With this arrangement it was possible to test the air shear nozzles under fixed conditions with the only difference being the presence or absence of induction charging (i.e.: induction voltage switched on or off).

Figure 4 shows an example of the type of atomization produced with a single OGEE nozzle mounted in the spray head. This photograph illustrates the back flow of liquid caused by the vortices induced by the OGEE nozzle and the resulting atomization. Normally five nozzles were mounted in the head during the tests.

The droplets were sampled using microscope slides coated with viscous polybutene. The slides were mounted behind a mechanical shutter having a 1 cm diameter opening. This allowed the slide to be exposed to the cloud of droplets for brief exposures ( $\approx$  0.5 second). The viscous polybutene trapped the droplets intact and when covered with a slide cover immediately after sampling, allowed particle analysis to be done up to 2 or 3 days after the test without any change in the sample. The particles were counted and sized manually using a microscope equipped with a squared graticule.

The spray pattern was sampled with the shutter mounted at a right angle to the spray flow at a distance of 3 m from the heads. Droplet charges were measured by collecting samples of the spray in a shielded metallic container connected as a Faraday pail. Thus by measuring the accumulated charge for a given mass of droplets, the average charge to mass ratio was calculated.

Table I, gives a summary of the results obtained for one set of conditions. A similar pattern of results was found for different flow rates for both the liquid feed and the entrainment air.

TABLE I  
RESULTS OF TESTS ON THE 'OGEE' SHAPED PLASTIC NOZZLE AND A DELTA WING SHAPED METAL NOZZLE

	'OGEE' Shaped Plastic Nozzle		Delta Wing Metal Nozzle	
	Voltage 'On'	Voltage 'Off'	Voltage 'On'	Voltage 'Off'
Mean diameter of droplet ( $\mu\text{m}$ )	51	61	69	70
Standard deviation of diameters measured ( $\mu\text{m}$ )	37	32	48	61
Charge to mass ratio ( $\mu\text{C/g}$ )	6.2	N/A	5.8	N/A
Air speed (m/s)	85	85	85	85
liquid flow rate = $10^{-2}$ kg/s/nozzle				

#### DISCUSSION

One of the most significant findings in the course of this development was the observed backflow of the liquid over the top surface of the OGEE nozzle. The flow visualization studies clearly showed that when the liquid emerged from the upper surface of the nozzle the initial motion was upstream due to the separated flow near the centre of the nozzle. This greatly improved the mechanical atomization of the liquid since it was more readily entrained by the two strong coherent vortices. In addition, the upstream motion produced a larger area of atomization giving better exposure to the inducing electric field for the combined mechanical-electrostatic atomization.

As seen from Table I, the OGEE generated droplets offered considerable improvement over the delta wing nozzle. Comparing the two conditions i.e. with and without electrostatic charging it is seen that:

- a) the droplets generated with the OGEE are smaller in diameter; 13% in the case of pure mechanical atomization, 26% in the case of mechanical-electrostatic atomization.
- b) the droplets generated with the OGEE are more uniform; the standard deviation is 48% smaller in the case of mechanical atomization, 23% smaller in the case of mechanical-electrostatic atomization.
- c) the number of droplets generated with the OGEE is greater: considering that the liquid flow rates were the same in all cases and that mass is proportional to the cube of diameter the average number of OGEE generated drops is 147% greater than the delta generated drops for the mechanical atomization, and 245% greater for the mechanical-electrostatic atomization.
- d) the mechanical-electrostatic atomization produced in the OGEE nozzle is superior to all other conditions in terms of minimum particle size, uniformity of particle size, maximum number of droplets for a given liquid flow rate and charge to mass ratio.

#### CONCLUSIONS

Due to the improved atomization it is believed that the new nozzle described here will have superior characteristics for both industrial and agricultural applications where large concentrations of reasonably uniform, small sized droplets are required. Also being an air shear nozzle it retains the advantages of having a relatively large diameter clog free feed allowing substantial liquid flow rates.

#### ACKNOWLEDGEMENTS

The authors gratefully acknowledge the National Science and Engineering Research Council of Canada for their support of this project.

#### REFERENCES

- <sup>1</sup>Fisher, R.W., Menzies, D.R. and Hikichi, A., "Orchard Sprayers", Ontario Ministry of Agriculture and Food, Publication 373, 1976.
- <sup>2</sup>Inculet, I.I. and Castle, G.S.P., "Development and Testing of an Electrostatic Sprayer for Use in Orchards", Report of AERD Program File 0752.01843-9-0907, Engineering and Statistical Research Institute, Research Branch, Agriculture Canada, Ottawa, 1980.
- <sup>3</sup>Hoerner, S.F., Borst, H.V., "Fluid Dynamic Lift", publ., L.A. Hoerner, N.J., 1975.
- <sup>4</sup>Inculet, I.I., Castle, G.S.P., Menzies, D.R., and Frank, R., "Deposition Studies With a Novel Form of Electrostatic Crop Sprayer", Journal of Electrostatics, Vol. 10, May 1981, pp.65-72.

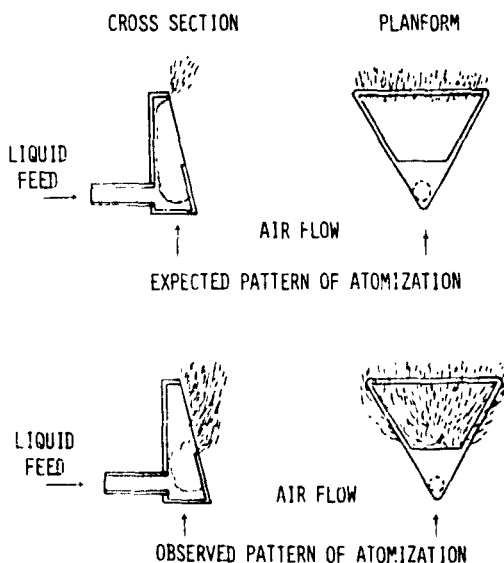


FIGURE 1. DELTA WING SHAPED AIR SHEAR NOZZLE

ORIGINAL PAGE  
BLACK AND WHITE PHOTOGRAPH

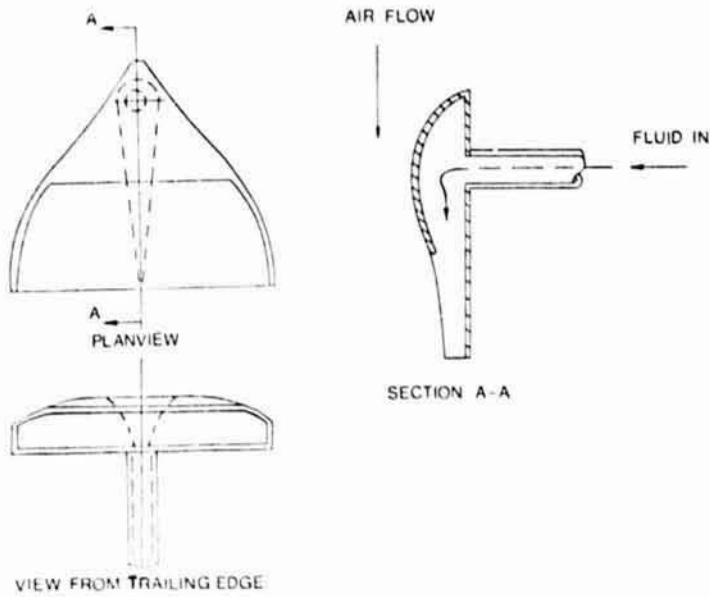


FIGURE 2. THE OGEE AIR SHEAR NOZZLE.



FIGURE 4. LIQUID ATOMIZATION FROM A SINGLE OGEE NOZZLE MOUNTED IN THE SPRAY HEAD (ENTRAINMENT AIR VELOCITY 85 M/S).

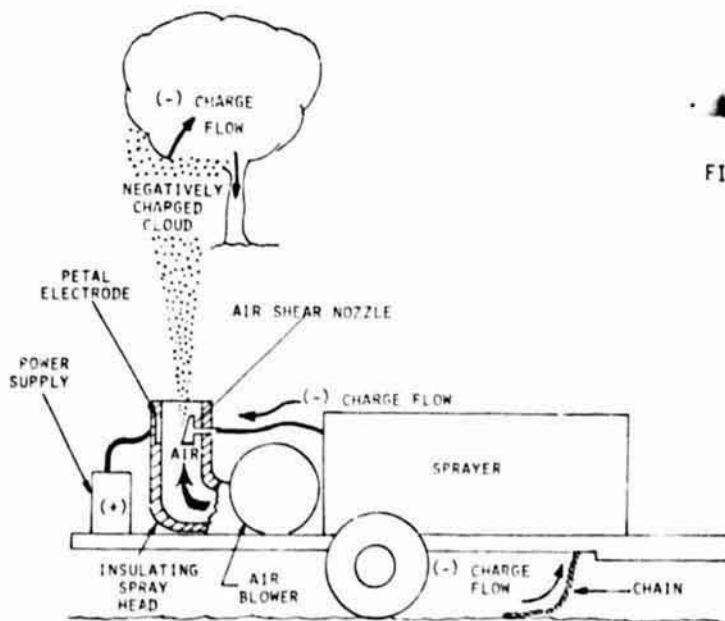


FIGURE 3. THE ELECTROSTATIC SPRAY SYSTEM.

## Liquid drop technique for generation of organic glass and metal shells\*

C. D. Hendricks

University of California, Lawrence Livermore National Laboratory  
Post Office Box 5508, Livermore, California 94550Abstract

We have for several years utilized the technique of capillary wave synchronization of the break-up of single and multiple component jets to produce uniform sized liquid drops and solid particles, and hollow liquid and solid shells. The technique has also been used to encapsulate a number of liquids in impermeable spherical shells.

Highly uniform glass shells have been made by generating uniform drops of glass forming materials in an aqueous solution, subsequently evaporating the water, and then fusing and "blowing" the remaining solids in a high temperature vertical tube furnace. Experimental results will be presented and the critical problems in further research in this field will be discussed.

Drop generation from a liquid stream has been experimentally observed since man's beginning. In recent times more precise techniques have been developed and used in such diverse fields as electric propulsion of spacecraft, cloud physics, high speed printing, magnetic confinement, fusion reactor fueling and inertial confinement fusion target fabrication. Other uses which are perhaps more common but less well known in the physics and engineering communities are encapsulation of one fluid inside another and generation of gas filled soluble capsules for study of blood pressure in the heart and other parts of the circulatory system.

In the time span from 1966 to 1981 our work has included liquid drop, solid particle and hollow shell generation from many different liquids from hydrogen to gold and including many organic and inorganic materials. A very brief chronology of our work is shown in Figures 1-10. Building on the work of Rayleigh, we developed techniques to produce very uniform drops with a wide range of sizes and materials.<sup>1</sup> Figure 1 shows a "solid" jet of liquid on which a capillary wave has been launched to initiate generation of uniform drops. Figure 2 shows a jet of water into which air has been injected.<sup>2</sup> The composite jet generated hollow shells of water around individual air bubbles. By the mid-1960's, we were interested in encapsulating fluids inside impermeable shells. Some of our first encapsulations were liquids such as silicone and organic oils in alginate shells. We were interested in multiple layers and built tri-axial systems as shown in Figure 3. However, a simple double tube concentric system was sufficient for the single shell encapsulation. An aqueous solution (Fluid #1) of sodium or potassium alginate was passed through the outer part of the system. Fluid #2 was the liquid to be encapsulated, e.g. an oil with Flame Red dye dissolved in the oil or other fluid including gases such as air. In the double concentric system, the inner tube and Fluid #3 were not present. Controlled, driven break-up of the two component jet formed highly concentric capsules. The capsules were passed through a mist or fine spray of calcium, magnesium or zinc chloride solution or into a bath of such solutions. Rapid change of the sodium or potassium alginate to calcium, magnesium or zinc occurred. The latter compounds are relatively insoluble in water and formed a "skin" on the capsule. Subsequent drying of the particles resulted in a thin walled spheroid containing the encapsulated fluid.

Further experiments resulted in the generation of spheres of polymeric materials, water shells with air as the inner fluid, copper, and more recently gold. Epoxy resins and appropriate hardners can be dissolved in solvents such as acetone, MEK or methylchloride. If the resin and curing agent are dissolved separately in dilute solutions, mixing does not result in curing of the epoxy. However, if droplets of the mixed solution are formed, allowed to pass through a heated column and the solvents evaporated, the resin and hardner react to form a normal, cured epoxy shell or solid bead (depending on temperature, rate of transport, etc.).

An apparatus (Figures 4 and 5) to produce copper shells from molten copper was constructed and operated and produced the spheres shown in Figure 6. The high temperature parts of the apparatus (copper reservoir, gas injection tube, orifices, etc.) were quartz. The apparatus was filled with hydrogen gas to reduce the formation of oxides. All the copper was run through the quartz system before cooling was allowed because of differences in expansion coefficients of copper and quartz. Copper will wet clean high temperature quartz and will shrink enough to pull pieces out of the quartz as it cools.

Hollow hydrogen shells were produced in the early 1970's by initiating bubbles in jets of liquid hydrogen.<sup>3</sup> The shells were frozen and had diameters of over a hundred micrometers and wall thicknesses of about ten micrometers. Solid spheres of hydrogen were also produced using some of the same techniques to launch capillary waves on a liquid hydrogen jet for control of jet break-up to generate uniform drops. The hydrogen spheres (hollow and solid) have both immediate and potential use in the magnetic confinement and inertial fusion programs. Figure 7 shows hollow hydrogen shells produced from jets of liquid hydrogen.

As the laser fusion program developed during the early 1970's it became necessary to produce glass shells with exceptionally smooth surfaces and uniform walls.<sup>4</sup> A solution of glass forming chemicals in water was used to form a cylindrical jet which was then caused to break into uniform drops. The drops passed vertically downward into a hot column. In the upper portion the solute was evaporated at about 550°C to leave dry particles. In the lower part of the column, the temperature was increased to 1200<sup>o</sup>-1500°C and the particle fused to form hollow glass shells. The apparatus is shown in Figure 8. Recent development of the process allows production of high quality glass shells with 90-99% having uniform walls and smooth surfaces such as those shown in an interference microscope in Figure 9.

Silver spheres have been formed by a technique similar to that used for forming glass spheres.<sup>5</sup> A solution of silver nitrate was formed into drops which were allowed to fall through the low temperature-high temperature column. Figure 10 shows the spheres resulting from the process. Some are hollow and some are solid. The surfaces of the spheres are smooth to 0.1-0.5 micrometer.

We have found liquid drop techniques to be very useful in several diverse areas. For producing very uniform metallic, organic, inorganic and, in particular, glassy shells, the liquid jet method is the most reproducible and exceptionally useful of all the techniques we have studied.

#### References

1. J. M. Schneider and C. D. Hendricks, "Source of Uniform-Sized Liquid Droplets," Rev. Sci. Inst. 35, 1349 (1964).
2. R. J. Calliger, R. J. Turnbull and C. D. Hendricks, "Hollow Drop Production by Injection of Gas Bubbles into a Liquid Jet," Rev. Sci. Inst. 48, 846 (1977).
3. C. D. Hendricks and C. Foster, "Hollow Hydrogen Shells for Laser Fusion Targets," Phys. Soc. Series II, 19, 927 (1974). Also see Lawrence Livermore National Laboratory Report UCRL-78481 (1976).
4. C. D. Hendricks and J. Dressler, "Production of Glass Balloons for Laser Targets," Bull. Amer. Phys. Soc. Series II, 21, 1137 (1976).
5. "Metal Sphere Development," 1980 Laser Program Annual Report, Lawrence Livermore National Laboratory, UCRL-50021-80, p. 4-4, 4-6 (1980).

#### DISCLAIMER

This document was prepared as an account of work sponsored by an agency of the United States Government. Neither the United States Government nor the University of California nor any of their employees, makes any warranty, express or implied, or assumes any legal liability or responsibility for the accuracy, completeness, or usefulness of any information, apparatus, product, or process disclosed, or represents that its use would not infringe privately owned rights. Reference herein to any specific commercial products, process, or service by trade name, trademark, manufacturer, or otherwise, does not necessarily constitute or imply its endorsement, recommendation, or favoring by the United States Government or the University of California. The views and opinions of authors expressed herein do not necessarily state or reflect those of the United States Government thereof, and shall not be used for advertising or product endorsement purposes.

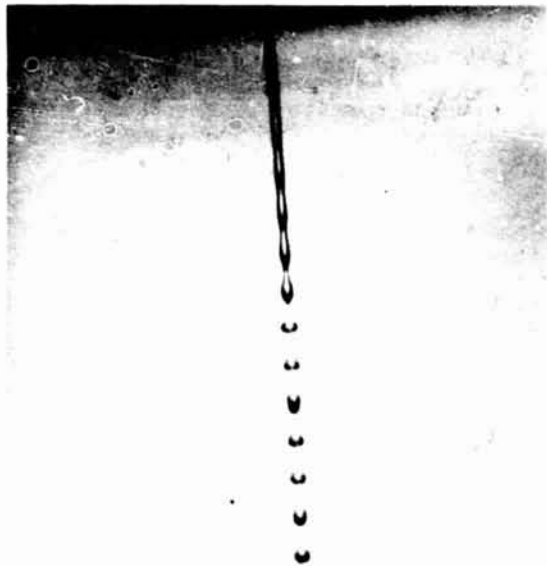


Figure 1 A typical liquid jet on which a capillary wave has been launched to synchronize break-up of the jet into uniform drops.



Figure 2 A water-air jet from which hollow spheres of water are being generated. The inner orifice can be moved axially to optimize the shell production. Gas flow rate, liquid flow rate, orifice diameters and drive frequency are important parameters. (1974)

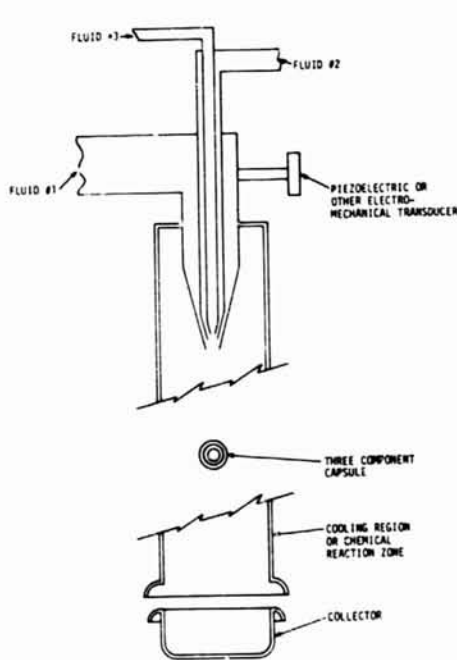


Figure 3 An apparatus designed to produce multilayer spheres. Encapsulation of one liquid in another can be accomplished by a double instead of a triple coaxial system. (ca 1966)

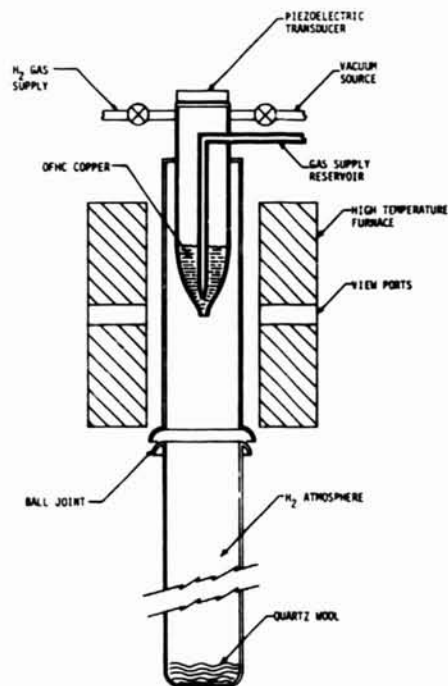


Figure 4 Schematic diagram of a system designed to produce hollow and solid spheres from high melting point materials such as copper. (1974)

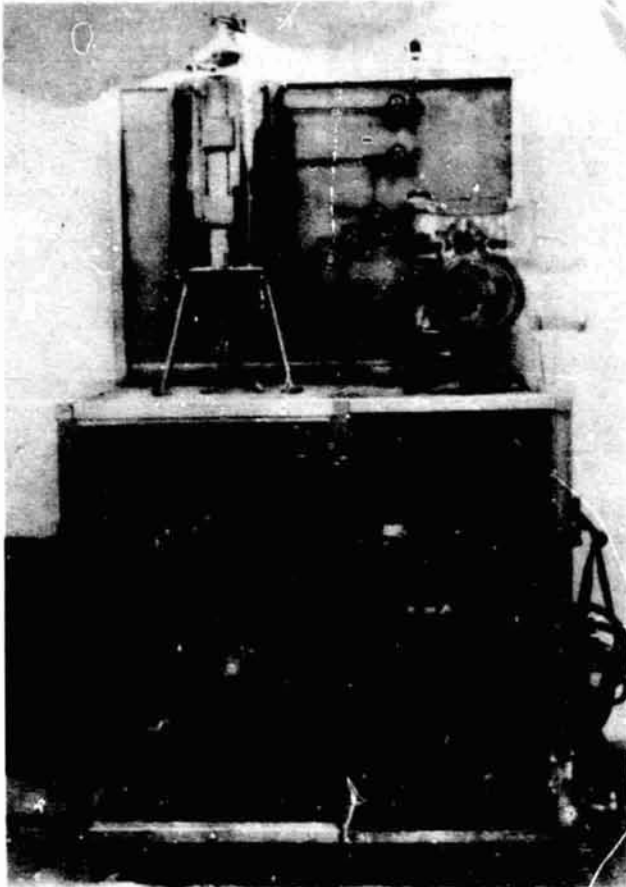


Figure 5 Photograph of an experimental system used to produce copper shells and solid spheres. (1974)

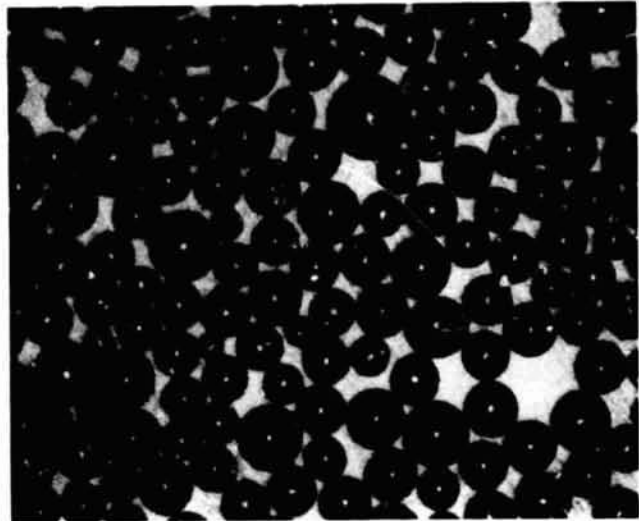


Figure 6 Copper sphere produced in the apparatus shown in Figure 5. (1974)

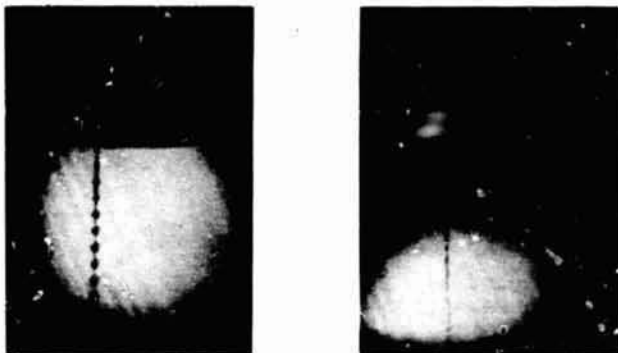


Figure 7 Hollow spheres produced from jets of liquid hydrogen. (1972)

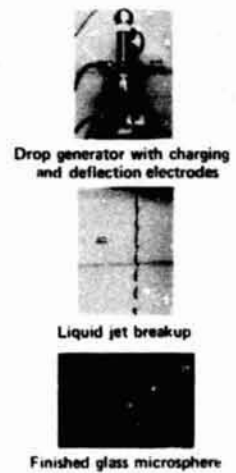
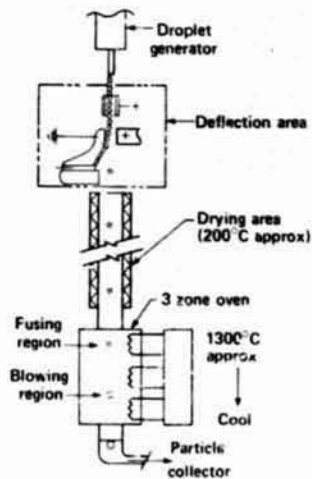


Figure 8 A system used to produce high quality glass shells. (1976)

ORIGINAL PAGE  
BLACK AND WHITE PHOTOGRAPH

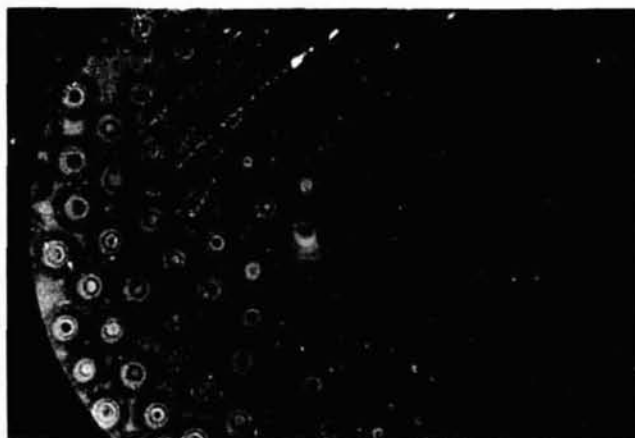


Figure 9 Interference microscope fringes in glass shells produced by liquid drop techniques. Perfectly uniform (surface, wall and sphericity) shells are indicated by circular fringe patterns.

METAL SPHERES, HOLLOW  
COMPOSITION: SILVER (AG, AT. NO. 47,  $\rho = 10.5$ )  
DIAMETER: UP TO 20  $\mu\text{m}$   
WALL THICKNESS: 5 - 10  $\mu\text{m}$   
SURFACE ROUGHNESS: PEAK-TO-VALLEY = .1 - .5  $\mu\text{m}$   
PROCESS: LIQUID DROP GENERATOR  
(1980)

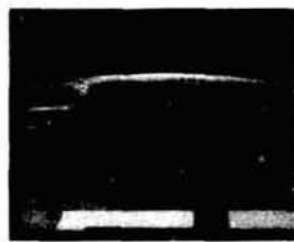


Figure 10 Silver spheres produced by liquid drop techniques. (1980)

\* Work performed under the auspices of the U. S. Department of Energy by the Lawrence Livermore National Laboratory under contract number W-7405-Eng-48.

Surface tension and contact angles: molecular origins and associated microstructure

H. T. Davis

Department of Chemical Engineering and Materials Science, University of Minnesota,  
151 Amundson Hall, 421 Washington Avenue S.E., Minneapolis, Minnesota 55455

Abstract

Gradient theory converts the molecular theory of inhomogeneous fluid into nonlinear boundary value problems for density and stress distributions in fluid interfaces, contact line regions, nuclei and microdroplets, and other fluid microstructures. The relationship between the basic patterns of fluid phase behavior and the occurrence and stability of fluid microstructures is clearly established by the theory. All the inputs of the theory have molecular expressions which are computable from simple models.

On another level, the theory becomes a phenomenological framework in which the equation of state of homogeneous fluid and sets of influence parameters of inhomogeneous fluids are the inputs and the structures, stress tensions and contact angles of menisci are the outputs—outputs that find applications in the science and technology of drops and bubbles.

Introduction

As witnessed by the papers presented at this colloquium, drops and bubbles, thin films and adsorbed layers, and contact angles are key actors in numerous natural and man-made processes. With our knowledge of and demands on these processes becoming more sophisticated, it is increasingly important to have a molecular level theory of structure and stress in interfaces. Although the formal statistical mechanical theory of inhomogeneous fluids at equilibrium has been developed rather extensively over the last two decades, the formal theory is presently intractable.<sup>1,2</sup> Far more powerful is gradient theory,<sup>2</sup> an approximation going back to Rayleigh<sup>3</sup> and van der Waals<sup>4</sup> which was rediscovered by Cahn and Hilliard<sup>5</sup> and was recently put into modern form by Rongiorno *et al.*<sup>6</sup> and Yang *et al.*<sup>7</sup> Successes in predicting the surface tension of polymer melts,<sup>8</sup> hydrocarbons and their mixtures,<sup>9</sup> and water<sup>10</sup> prove that the theory is useful for real fluids. In this paper, I outline the elements of gradient theory and describe applications that my Minnesota colleagues and I have made of the theory to fluid-fluid interfaces, fluids at solid surfaces, and drops and bubbles.

Gradient theory of microstructured fluids

A fluid microstructure is an inhomogeneous region in a fluid in which component densities vary appreciably over molecular distances. Any fluid is, of course, inhomogeneous because of the presence of gravity. However, the inhomogeneities that result from gravity are so weak that component densities vary negligibly over molecular distances. Similarly, the inhomogeneities induced by ordinary centrifugal fields and by the temperature and composition gradients involved in the usual transport situations are very weak. If the component densities vary sufficiently little over molecular distances, then the thermodynamic functions can be approximated locally by the corresponding functions for homogeneous fluid at the local composition. In fluid microstructures the effect of the local component density variations must be accounted for in the local thermodynamic functions.

In the absence of external fields and density inhomogeneities, the Helmholtz free energy density is  $f_0$ . From intermolecular interactions species  $i$  and  $j$  give to  $f_0$  a contribution of the order of  $a_{ij}n_i n_j$ ,  $n_i$  and  $n_j$  being component densities and  $a_{ij}$  a characteristic energy parameter. The factor  $1/2 n_i n_j$  is a measure of the number of interacting pairs. If the fluid is inhomogeneous at position  $r$ , then the number of interacting pairs in the vicinity of  $r$  should be corrected by some amount  $1/2 \delta n_i \delta n_j$ . An estimate of  $\delta n_i$  is  $r_{ij} \nabla n_i$ ,  $r_{ij}$  the range of the intermolecular force between  $i$  and  $j$  and  $\nabla n_i$  the gradient of  $n_i$  at  $r$ . It follows heuristically then that the local Helmholtz free energy density of inhomogeneous fluid is  $f_0(n) + \sum_{i,j} \frac{1}{2} c_{ij} \nabla n_i \cdot \nabla n_j$  plus terms higher order in gradients of component densities;  $f_0(n(r))$  is the Helmholtz free energy density of homogeneous fluid at the local composition  $n(r) = \{n_1(r), n_2(r), \dots, n_\nu(r)\}$  and the terms involving density gradients are the Helmholtz free energy density of the inhomogeneity. The quantity  $c_{ij}$  is proportional to  $a_{ij} r_{ij}^2$ , the proportionality factor arising from appropriate molecular averaging. If an external conservative potential  $u_e^i(r)$  is present, then to the local free energy density is added  $\sum n_i u_e^i$ . Putting together the pieces of this heuristic argument, one gets the gradient theoretical formula for the Helmholtz free energy  $F$  of inhomogeneous fluid:

$$F = \int_V [f_0(n) + \sum_{i,j} \frac{1}{2} c_{ij} \nabla n_i \cdot \nabla n_j + \sum_i n_i u_i^1] d^3r \quad (1)$$

If the density gradients are macroscopic, e.g., caused by gravity or ordinary centrifugal fields, then  $\nabla n_i$  is of the order of  $n_i/L$ ,  $L$  being the dimension of the system. In this case the quantity  $c_{ij} \nabla n_i \cdot \nabla n_j$  is negligible since it is of the order of  $(r_{ij}/L)^2$  compared to the local value of the homogeneous fluid free energy density  $f_0$ . Thus, it is appropriate to identify  $\sum_{i,j} \frac{1}{2} c_{ij} \nabla n_i \cdot \nabla n_j$  as the free energy density of fluid microstructure.

Van der Waals introduced the one-component version of Equation (1) in his theory of liquid-vapor interfaces and Cahn and Hilliard<sup>5,11</sup> used a binary regular solution version of the equation in connection with interfacial structure and spinodal decomposition of sub-cooled homogeneous solution. In the modern statistical mechanical version of the theory,<sup>2,6,7</sup> Equation (1) is derived from a formal component density expansion of the exact free energy of inhomogeneous fluid. Expressions are obtained which relate the local "influence parameters"  $c_{ij}$  of inhomogeneous fluid to the fluid radial distribution functions of homogeneous fluid at local component densities. The heuristic connection of the influence parameter  $c_{ij}$  to  $a_{ij}r_{ij}$  is justified by the rigorous statistical mechanical expressions.

In its modern version gradient theory is a very attractive description of inhomogeneous fluid: on the one hand the inputs  $f_0(n)$  and  $c_{ij}(n)$  can in principle be computed from the molecular theory of homogeneous fluid, but on the other hand if molecular theory is insufficiently developed for the fluids of interest semiempirical or empirical schemes can be used to deduce equations of state for  $f_0(n)$  and  $c_{ij}(n)$ . Along these lines it is encouraging that the molecular theoretical formulas for  $c_{ij}$  and some predictions<sup>12,13</sup> based on simple models imply that the influence parameters are often only weak functions of component densities. Similarly, the success of the theory with constant  $c_{ij}$  in predicting the surface tensions of hydrocarbon mixtures<sup>9</sup> and water<sup>10</sup> argues against appreciable density dependence of the influence parameters. The importance of this is that one can determine the values of influence parameters from limited experimental data. In all the applications I discuss below the influence parameters are held constant.

At equilibrium the grand potential,

$$\Omega \equiv F - \sum_i \mu_i \int_V n_i d^3r \quad (2)$$

is a minimum in a closed system. The chemical potential,  $\mu_i$ , plays the role of a Lagrange multiplier accounting for the constraint that  $N_i (= \int_V n_i d^3r)$  is fixed in a closed system. The density distributions  $n_i(r)$ ,  $i=1, \dots, v$ , that minimize  $\Omega$  must, according to the calculus of variations, obey the corresponding Euler equations

$$\mu_i = u_i^e + \mu_i^0(n) - \sum_j \nabla \cdot (c_{ij} \nabla n_j) + \sum_{j,k} \frac{1}{2} \frac{\partial c_{jk}}{\partial n_i} \nabla n_j \cdot \nabla n_k ; \mu_i^0 \equiv \partial f_0 / \partial n_i \quad (3)$$

$i=1, \dots, v$ . Boundary conditions appropriate for a given fluid microstructure must be assigned and the component densities of the microstructure determined by solving these nonlinear differential equations. Thus, gradient theory reduces the problem of determining equilibrium fluid microstructures to a nonlinear boundary value problem. Of course, once a microstructure solution has been obtained its stability has to be established by proving that it is a local minimum of the grand potential  $\Omega$ . Typically one solves nonlinear differential equations by discretization (e.g., finite difference or finite element) and iteration using the Newton-Raphson technique.<sup>14,15</sup> A byproduct of such a solution technique is that the matrix generated by the Newton-Raphson technique is the one required for stability analysis of the solution so obtained, i.e., the same algorithm generates the solution and the elements of stability analysis.

The pressure tensor is another quantity of interest in fluid microstructures. In homogeneous fluid, the pressure is isotropic, i.e., the number of lines of force passing through a small element of area from molecules lying on each side of element is independent of the orientation of the element. This is because the molecular population is identical in all directions in homogeneous fluid. This is not true in inhomogeneous fluid and so the isotropic pressure of homogeneous fluid,  $P_0(n)I$ , must be corrected to account for local component density variation.  $I$  is the unit tensor. Since the number of lines of force passing through the area element will depend on orientation, components of the pressure tensor are in general different in an inhomogeneous fluid, i.e., the pressure tensor  $\underline{P}$  is anisotropic. To second order in density gradients the general formula for the pressure tensor is of the form<sup>2</sup>

$$P = P_0(n)I + i \sum_{j=1}^v \{ \ell_{ij}^{(1)} n_i \nabla n_j + \ell_{ij}^{(2)} (\nabla n_i) (\nabla n_j) + [ \ell_{ij}^{(3)} n_i \nabla^2 n_j + \ell_{ij}^{(4)} (\nabla n_i) \cdot (\nabla n_j) ] I \} \quad (4)$$

where  $\ell_{ij}^{(1)}, \dots, \ell_{ij}^{(4)}$  are functions of the local composition  $n$ . The one component version of Equation (5) was first proposed by Korteweg.<sup>16</sup> The theoretical formulas for the  $\ell_{ij}^{(\alpha)}$  are much more complicated than that for the influence parameters.<sup>2</sup> Several simplified versions of the  $\ell_{ij}^{(\alpha)}$  have been investigated.<sup>13</sup> The simplest of these is obtained by assuming that the influence parameters are constant and that the  $\ell_{ij}^{(\alpha)}$  must be consistent with the constancy. The result is<sup>2</sup>

$$P = P_0(n)I - \frac{2}{3} i \sum_{j=1}^v c_{ij} \{ n_i \nabla n_j - \frac{1}{2} (\nabla n_i) (\nabla n_j) + \frac{1}{2} [ n_i \nabla^2 n_j - \frac{1}{2} (\nabla n_i) \cdot (\nabla n_j) ] I \} \quad (5)$$

Since  $f_0$  and  $P_0$  are related by the thermodynamic relation  $dP_0 = -d(f_0V)$ , at constant  $T, n_1^W, \dots, n_v^W$ , the gradient theory of stress given by Equation (5) requires exactly the same inputs as the gradient theory of the free energy.

In what follows the influence parameters are always assumed to be constant and either the van der Waals (VDW) equation of state or one of its empirically modified successors, the Peng-Robinson (PR) equation,<sup>17</sup> is used. Both equations can be summarized as

$$P_0(n) = \frac{nkT}{1 - nb} - \frac{n^2 a}{1 + \psi [2nb - (nb)^2]} \quad (6)$$

$\psi=0$  in the VDW equation and  $\psi=1$  in the PR equation.  $a$  and  $b$  are energy and volume parameters. For pure fluids the parameters are determined by the critical temperature and pressure for the VDW equation and these plus the acentric factor for the PR equation.<sup>17</sup> The recommended forms of  $a$  and  $b$  for mixtures is  $nb = \sum_i n_i b_i$  and  $n^2 a = \sum_i \sum_j n_i n_j a_{ij}$ , where  $b_i$  and  $a_{ii}$  are pure fluid parameters and  $a_{ij}, i \neq j$ , are mixture parameters to be determined by a fit of the equation to experimental data on two-component systems. The PR equation is quantitatively superior to the VDW equation but qualitatively both are quite similar, and so either serves equally well the purposes of this article.

#### Planar interfaces

The component density profiles,  $n_i(x)$ , of a planar interface are obtained by solving Equation (3) with  $u_i^i = 0$  and subject to the boundary conditions  $n(x = -\infty) = n^{(1)}$  and  $n(x = \infty) = n^{(2)}$ , where  $n^{(1)}$  and  $n^{(2)}$  denote the component densities in coexisting bulk phases 1 and 2. These component densities are of course determined by the usual equilibrium conditions  $P_0(n^{(1)}) = P_0(n^{(2)})$ ,  $\mu_i^0(n^{(1)}) = \mu_i^0(n^{(2)})$ ,  $i=1, \dots, v$ . Equation (3) can be solved analytically in the case of a one-component fluid but must be solved numerically in the multicomponent case.<sup>6, 9, 18</sup>

The density profile of a one-component liquid-vapor interface predicted with the VDW equation at the reduced temperature  $kTb/a = 0.197$  is shown in Figure 1. The density is

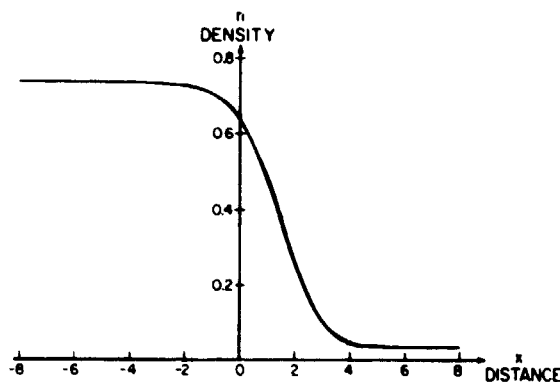


Figure 1. Density in units of  $b^{-1}$ , distance in  $\sqrt{c/a}$ .  $kTb/a = 0.197$ . Ref. 14.

given in units of  $b^{-1}$  and the distance in units of  $\sqrt{c/a}$ , a length of the order of magnitude of a molecular diameter. In a planar interface the normal pressure  $P_N$ , that is the component of pressure measured by a flat test surface lying in the interfacial plane, is constant in accordance with the condition of hydrostatic equilibrium ( $\nabla \cdot P = 0$ , or  $dP_N/dx = 0$  since  $P = P_N \mathbf{i}\mathbf{i} + P_T(\mathbf{j}\mathbf{j} + \mathbf{k}\mathbf{k})$ ,  $\mathbf{i}$  the unit vector along the x-axis). On the other hand, the transverse pressure  $P_T$ , the component of pressure measured by a flat test surface orthogonal to the interfacial plane, is not constrained by hydrostatic equilibrium and must take on whatever values forced on it by the density profile.  $P_T$  cannot be constant in the interface; otherwise, the interfacial tension, which is the difference between the normal and transverse pressures integrated across the interface, namely,

$$\gamma = \int_{-\infty}^{\infty} (P_N - P_T) dx, \quad (7)$$

would have to be zero.

From Equation (5) it follows that

$$P_T = \frac{2}{3} P_O(\eta) + \frac{1}{3} P_N. \quad (8)$$

This result, which has been derived from several approximations<sup>1,3</sup> to the coefficients in the gradient theoretical pressure tensor, is heuristically very suggestive. The density  $n(x)$  is uniform in a plane parallel to the interface, that is the pressure is isotropic in such a plane. The contribution to the transverse pressure from molecules lying near the plane is expected to be proportional to  $P_O(n(x))$ . Molecules lying further from the plane are distributed to maintain a constant normal pressure  $P_N$ . The contribution of the so-distributed molecules to the transverse pressure should be of same order of magnitude. Thus, it might be argued that  $P_T$  will be a linear combination of  $P_O(n)$  and  $P_N$ , the respective coefficients being 2/3 and 1/3 reflecting the fact that the dimensions of the interfacial plane are 2 and the normal direction is 1. It would be interesting to find a convincing derivation of Equation (8) from this point of view. An accounting of the lines of intermolecular force passing through a small element of area versus orientation of the element might be fruitful in pursuing this goal.

An important implication of Equation (8) is that the structure of the transverse pressure in the interface is determined by the equation of state of homogeneous fluid. The normal and transverse pressures corresponding to the profile in Figure 1 are shown in Figure 2. As expected there is a wide region in which the interface is under tension (i.e.,  $P_T < P_N$ ). Since tension is positive and equals the area under the curve  $P_N - P_T$  versus  $x$ , there must be a region in which  $P_T > P_N$ . There is however a small region of compression ( $P_T > P_N$ ) on the gas side of the interface. The correspondence between the van der Waals loops in the PVT phase diagram for homogeneous fluid is seen by comparing Figures 2 and 3. The normal pressure  $P_N$  is of course the liquid-vapor coexistence pressure, i.e.,  $P_N = P_O(n_l) = P_O(n_v)$ ,  $n_l$  and  $n_v$  the liquid and vapor densities, respectively. The region of compression in the interface arises from the region in which the pressure isotherm lies above the tie-lines, which locate the pressure  $P_N$ .

A significant feature of the theory is that the structure and stress in the interface are determined by the thermodynamic functions of homogeneous fluid in the metastable and unstable regions of the PVT diagram. It has usually been thought that in the unstable region of the phase diagram the thermodynamic functions are meaningless. Far from being meaningless, the behavior of these functions in this region is a determining factor of interfacial behavior. The gradient terms provide the necessary free energy to stabilize states that would be unstable in homogeneous fluid.<sup>7</sup>

As a critical point or a solution plait point is approached, the VDW loops in the pressure isotherm begin to flatten out and become symmetric about the tie-line, both patterns of which drive the tension towards zero. That tension goes to zero as a critical point is approached is well-known, but the mechanism of getting low tension by symmetrizing the VDW loops of the pressure isotherm is novel. Such an example is provided in Figure 4, in which is given density and pressure profiles of the liquid-liquid interface of carbon dioxide and decane.<sup>19</sup> The profiles were predicted with the PR equation using the mixture parameter values  $a_{12} = \sqrt{a_{11}a_{22}}$  and  $c_{12} = 0.9\sqrt{c_{11}c_{22}}$  and  $c_{ii}$  values fitted from pure fluid surface tension. The tension of the interface in Figure 4 is  $\gamma = 0.6$  dyn/cm.

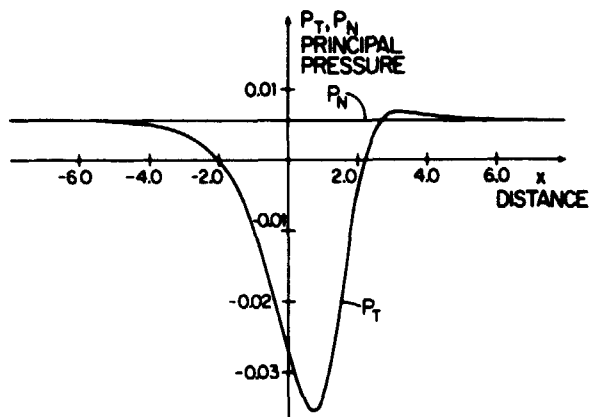


Figure 2. Principal pressures in a planar interface. VDW fluid. Pressure in units of  $a/b^2$ , distance in  $\sqrt{c/a}$ . Ref. 14.

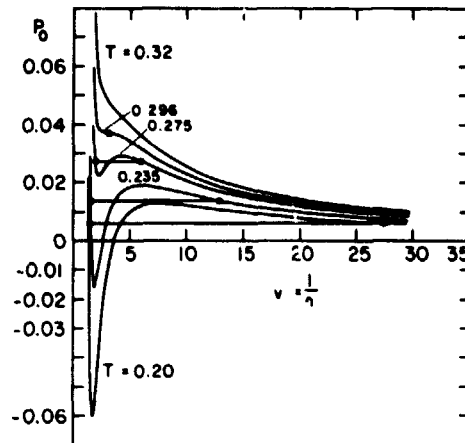


Figure 3. PVT phase diagram of a VDW fluid. Density in units of  $b^{-1}$ , temperature in  $a/kb$ . The liquid-vapor densities are indicated by points connected with constant-pressure tie-lines.

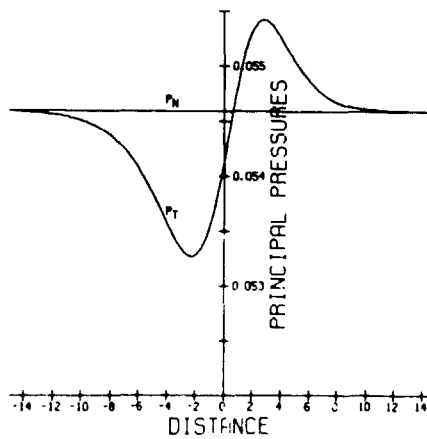
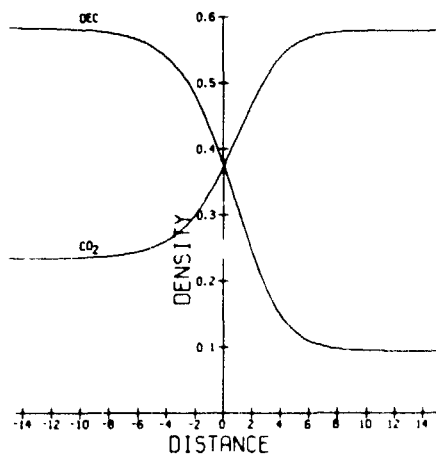


Figure 4. Density and principal pressure profiles of a  $\text{CO}_2$ -decane liquid-liquid interface of a PR fluid.  $kb/a = 0.148$ , density  $n_i$  in units of  $b^{-1}$ , distance in  $\sqrt{c/a}$ , pressure in  $a/b^2$ .  $a, b, c$   $\text{CO}_2$  values. Ref. 19.

### Contact angle, wettability, and film formation

The adsorption and wetting characteristics of fluids on solid surfaces and at fluid-fluid interfaces are of enormous practical interest in the design of detergents, lubricants, flotation and foaming agents, paints, capillary delivery devices, and the like. In spite of such practical importance, the molecular theory of adsorption and wetting is still a fledgling science, based most often on *ad hoc* models for various special situations. Gradient theory shows promise of giving a unified theoretical basis to the subject. In what follows, the theory is applied to adsorption and film formation at interfaces, three phase contact regions and the contact angle, and perfect wetting transitions.

Suppose a fluid-fluid interface contacts a flat solid wall as indicated in Figure 5. If the meniscus (a mathematical surface representing the position of the interface) is observed at some distance  $R$  lying far enough from the solid for bulk fluid phases to exist on each side of the surface but not far enough for gravitational distortion to affect it, then the observed contact angle  $\theta$  obeys Young's equation

$$\gamma_{\gamma\alpha} = \gamma_{\gamma\beta} + \gamma_{\alpha\beta} \cos\theta \quad (9)$$

$\gamma_{\gamma\alpha}$  and  $\gamma_{\gamma\beta}$  denote the tensions (or surface excess free energies) of fluid phases  $\alpha$  and  $\beta$  with solid phase  $\gamma$ .  $\gamma_{\alpha\beta}$  is the interfacial tension of the interface between fluids  $\alpha$  and  $\beta$ . The basis and meaning of Equation (9), which can be derived from a force balance on the hemicylinder whose cross-section is shown in dashed lines in Figure 5, has been discussed at length in a recent paper by Benner *et al.*<sup>15</sup>

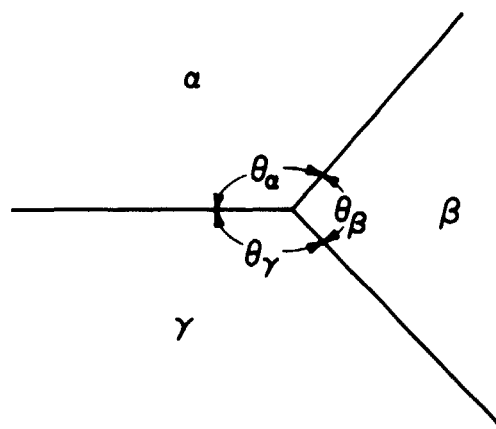
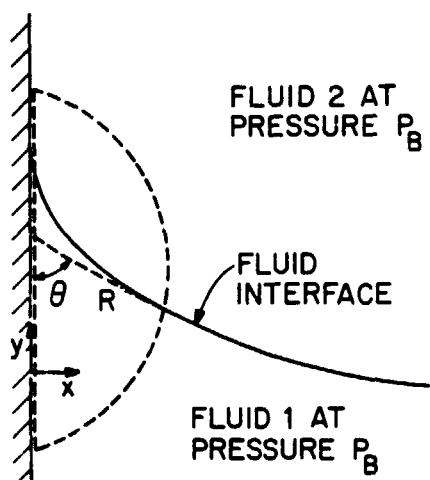


Figure 5. Angle of contact of fluid meniscus at a flat solid wall. Figure 6. Angles of contact of three fluid phases.

If all three phases are fluid, then the menisci define three dihedral angles (Figure 6) obeying the force balance

$$\frac{\gamma_{\alpha\beta}}{\sin\theta_\gamma} = \frac{\gamma_{\gamma\beta}}{\sin\theta_\alpha} = \frac{\gamma_{\gamma\alpha}}{\sin\theta_\beta} \quad (10)$$

A contact angle is not always observed when three phases are brought together. If either of the inequalities

$$\gamma_{\gamma\alpha} > \gamma_{\gamma\beta} + \gamma_{\alpha\beta} \quad \text{or} \quad \gamma_{\gamma\beta} > \gamma_{\gamma\alpha} + \gamma_{\alpha\beta} \quad (11)$$

then Equation (9) (or (10)) has no solution and the free energy of the system will decrease as the result of a thin layer of phase  $\beta$  (or phase  $\alpha$ ) intruding between phase  $\gamma$  and phase  $\alpha$  (or phase  $\beta$ ) as shown in Figure 7. The intruding phase is said to *completely or perfectly wet* the interface between the other two phases. The transition between contact angle and perfect wetting behavior occurs at conditions for which one of the inequalities in Equation (11) becomes an equality.

Perfect wetting is of course essential in applications involving spontaneous spreading of some fluid at an interface. Examples of perfect wetting are well-known. In the presence of air, most liquids perfectly wet on clean metal surfaces, water on quartz, some organic liquids on water, some organic liquids on some polymers, etc. Not so well-known is critical point wetting, a phenomenon hypothesized recently by Cahn.<sup>20</sup> He noted that according to critical point theory and experiment, as a critical point of phase  $\alpha$  and  $\beta$  is approached along a temperature, pressure, or chemical potential path, the interfacial tension approaches zero asymptotically as

$$\gamma_{\alpha\beta} = \gamma_{\alpha\beta}^0 \left| 1 - \frac{h}{h_c} \right|^{1.3}, \quad (12)$$

where  $h$  is the field variable (any thermodynamic quantity being the same in all coexisting phases),  $h_c$  its value at the critical point, and  $\gamma_{\alpha\beta}^0$  a scale factor. Cahn postulated that the difference  $|\gamma_{\gamma\alpha} - \gamma_{\alpha\beta}|$  will approach zero as the composition of the components in phases  $\alpha$  and  $\beta$  approach each other, i.e., it obeys the scaling law

$$|\gamma_{\gamma\alpha} - \gamma_{\alpha\beta}| = \gamma_{\alpha\beta\gamma}^0 \left| 1 - \frac{h}{h_c} \right|^{0.34} \quad (13)$$

sufficiently near the critical point. Since  $\gamma_{\alpha\beta}$  approaches zero faster than that postulated for  $|\gamma_{\gamma\alpha} - \gamma_{\alpha\beta}|$ , Cahn concluded that there will always exist a critical wetting value of the field variable,  $h_{cw}$ , not equal to  $h_c$ , at which one of the fluids will become perfectly wetting. The combination of Equations (9), (12) and (13) gives asymptotic formulas for the contact angle at a solid as  $h$  approaches  $h_{cw}$ , namely,

$$\cos\theta = \pm \left( \frac{\gamma_c}{\gamma_{\alpha\beta}} \right)^{0.74} = \pm \left| \frac{h_{cw} - h_c}{h_c - h} \right|^{0.96} \quad (14)$$

where  $\gamma_c$  is the value of  $\gamma_{\alpha\beta}$  at  $h = h_{cw}$ .

The practical significance of Cahn's theory is that one of a pair of fluids can always be made perfectly wetting in the presence in a third phase by adjusting field variables (e.g., by changing temperature or pressure or by adding some component) to get near a critical point.

To test the validity of Equation (13), an unverified hypothesis, and to understand the relation of  $\gamma_{cw}$  and  $h_{cw}$  to fluid and solid properties and interfacial structure, Teletzke *et al.*<sup>21</sup> studied with  $\gamma_{cw}$  gradient theory the behavior of a one-component fluid at a flat solid wall. Some results of this work are of interest here. The PR equation of state was used for the fluid and the wall was characterized by the wall-fluid molecule potential

$$u_e(x) = W \left[ \frac{1}{45} \left( \frac{d}{x} \right)^9 - \frac{1}{6} \left( \frac{d}{x} \right)^3 \right], \quad (15)$$

a choice appropriate for walls and fluids composed of molecules interacting with the 6-12 Lennard-Jones potential.  $x$  denotes the distance from the wall.  $W$  is a measure of the strength of the wall-fluid potential and  $d$  its range.

The gradient profile equation with constant influence parameter was solved for the density profile  $n(x)$  by the Galerkin technique using a finite element basis set. The solid-fluid tension can be computed as the area derivative of the free energy,  $\gamma = \partial F / \partial A$ , or, equivalently, from the pressure formula,  $\gamma = \int_0^\infty [P_0(n_B) - P_T] dx$ ,  $n_B$  being the bulk density of fluid far from the wall. The boundary conditions for the problem are  $n(x) \rightarrow 0$  as  $x \rightarrow 0$  and  $n(x) \rightarrow n_B$  as  $x \rightarrow \infty$ .

A PR fluid has an upper critical temperature  $T_c$  equal to 0.1704 in the units  $a/b$ .

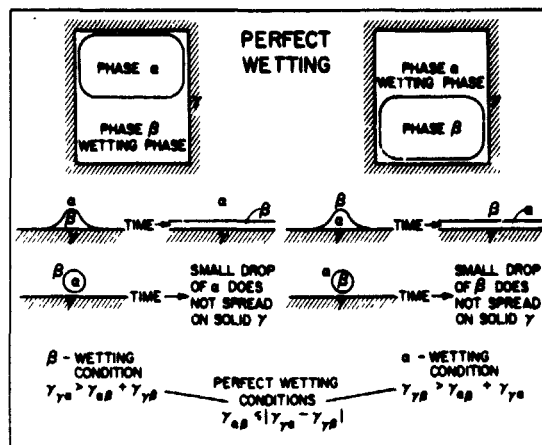


Figure 7. Conditions for perfect wetting by either phase  $\alpha$  or phase  $\beta$ .

Gradient theory predicts a critical-wetting temperature  $T_{cw}$  above which the liquid phase becomes perfectly wetting at the solid-vapor surface. An example is shown in Figure 8, for the solid-fluid parameters  $W = 6.4$  a/b and  $d = \sqrt{c/a}$ . Below  $T_{cw}$  a drop of liquid would not spread on the solid, but would form a contact angle. Above  $T_{cw}$  the drop would spread to form a perfectly wetting layer. The critical wetting temperature depends on  $W$  and  $d$ . At fixed  $d$ ,  $T_{cw}$  decreases with increasing  $W$ , i.e., as the strength of the solid-liquid potential increases perfect wetting occurs at lower temperature. At fixed  $W$ ,  $T_{cw}$  decreases with increasing range  $d$  of the wall potential, i.e., the longer the range of the potential the lower the temperature at which perfect wetting occurs.

Correspondingly, the characteristic tension  $\gamma_c \equiv \gamma_{LV}(T_{cw})$  decreases with increasing  $T_{cw}$  (and, therefore, with decreasing  $W$  or  $d$ ). If  $W$  and/or  $d$  are small enough, then  $T_{cw}$  is near the critical point and Equation (14) should hold if Cahn's hypothesis is true. This was indeed found to be true (although there is a small detail of mean-field versus correct scaling laws<sup>21</sup>). On the other hand, as  $W$  and/or  $d$  increase, the perfect-wetting temperature  $T_{cw}$  decreases and Equation (14) no longer holds. At sufficiently low temperature the interface is very sharp (narrow) and the Good-Girifalco formula<sup>23</sup>

$$\cos \theta = 2 \sqrt{\frac{\gamma_c}{\gamma_{LV}}} - 1 \quad (16)$$

ought to hold since it is based on a discontinuous interface approximation. This turns out to be the case. The dependence of  $T_{cw}$  and  $\gamma_c = \gamma_{LV}(T_{cw})$  on  $W$  and the dependence of  $\cos \theta$  on  $\gamma_{LV}(T)/\gamma_c$  for various values of  $W$  are shown in Figures 9 and 10 for the case  $d = \sqrt{c/a}$ . The

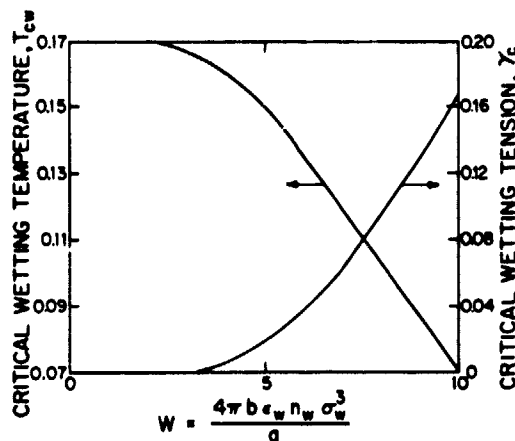


Figure 9. Variation of critical wetting temperature (units a/kb) critical wetting tension (units  $\sqrt{ac/b^2}$ ) with  $W$  (units a/b). Ref. 21.

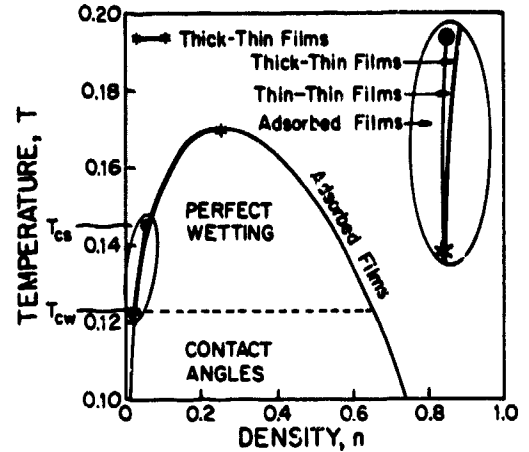


Figure 8. Phase and film diagram for a Peng-Robinson fluid. Temperature in units a/kb, density in  $b^{-1}$ . Ref. 21.

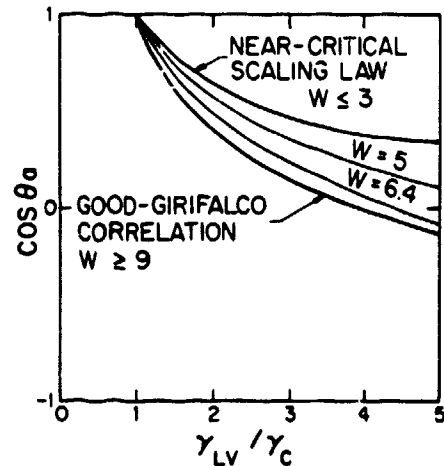


Figure 10. Contact angle versus  $\gamma_{LV}(T)/\gamma_c$  for various  $W$ . Ref. 21.

near-critical scaling law, Equation (14), holds for  $W \leq 3$ , the Good-Girifalco formula, Equation (16), holds for  $W \geq 9$ . In the intermediate range, neither formula holds.

Several years ago, Zisman<sup>24</sup> suggested that the contact angle correlates with the ratio  $\gamma_{LV}/\gamma_C$  but that  $\gamma_C$  was a characteristic only of the solid, not of the fluid phase. The implication of Figure 9 is that this is not so unless the reduced energy parameter  $Wb/a$  and length parameter  $d/\sqrt{c/a}$  are fixed in the series of fluids compared. As these ratios depend both on solid and fluid, it appears that Zisman's scaling worked because the fluid parameters  $b/a$  and  $\sqrt{c/a}$  were not very different for the systems compared.

Another thing gradient theory predicts is a first order transition of the adsorbed layer at the solid surface. In the temperature range  $T_{cw}$  to  $T_{cs}$  (Figure 8), as the bulk fluid density increases from zero towards the gas side of the phase diagram a composition is reached at which two adsorbed layers or thin-films of different thickness are predicted at the same equilibrium conditions. An example is shown in Figure 11. As the bulk density is increased beyond the thin-film coexistence curve the thin-film grows continuously into a thick thin-film to become finally a perfectly wetting layer of liquid when the liquid-vapor phase dome is reached. The temperature  $T_{cs}$  is a film critical point. Above  $T_{cs}$ , as bulk density increases from zero to the liquid-vapor coexistence curve an adsorbed layer grows continuously through thin-film states into a perfectly wetting layer of liquid phase. Below  $T_{cw}$  only submonolayer adsorption occurs with increasing density until at the liquid-vapor coexistence curve liquid appears as a drop with a contact angle. On the liquid side of the coexistence region only submonolayer adsorption occurs. A thin-film transition was predicted by Saam and Ebner<sup>25</sup> using an integral model free energy. Their thin-film coexistence curve is very similar to that of described here. The thin-film transition predicted by Cahn on the basis of a two-dimensional model of the solid is, however, qualitatively different.<sup>21</sup>

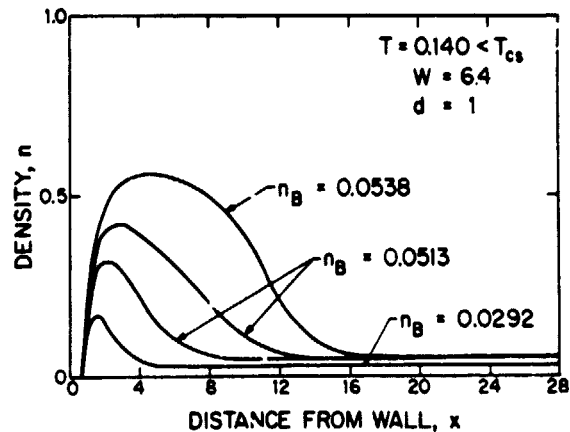


Figure 11. Density profile of fluid at a solid wall as a function of bulk fluid density. Ref. 21.

It should be emphasized that according to the theory the patterns of film and phase behavior of a one-component fluid at a solid wall are general. Sufficiently near a critical point of a pair  $\alpha$  and  $\beta$  of multicomponent coexisting fluid phases, either  $\alpha$  or  $\beta$  will become perfectly wetting at the interface formed by a third phase  $\gamma$  and the nonwetting fluid phase. The third phase  $\gamma$  can be solid or liquid. The critical point can be an upper or lower critical point. In approaching a critical point along any field variable  $h$ , e.g. temperature, pressure, or chemical potential of a component, there will be a critical wetting value  $h_{cw}$ , a finite distance from the critical point value  $h_c$ , at which one of the near-critical phases becomes perfectly wetting on a third phase. Outside but near the coexistence composition region of  $\alpha$  and  $\beta$ , a first order thin-film transition occurs with a coexistence curve lying between  $h_{cw}$  and  $h_{cs}$ ,  $h_{cs}$  being the film critical point.  $h_{cs}$  lies between  $h_{cw}$  and  $h_c$ . If  $h$  lies between  $h_{cw}$  and  $h_c$ , then sufficiently near the  $\alpha$ - $\beta$  coexistence region a thin-film formed between the third phase  $\gamma$  and, say, phase  $\alpha$  will thicken continuously into a layer of the perfectly wetting phase  $\beta$ .

An example of the structure and stress of a liquid-vapor interface at which a thin-film has almost grown into a layer of a second liquid phase is shown in Figure 12. This figure was taken from the work of Falls *et al.*<sup>19</sup> in which theory was applied with the PR equation to planar interfaces and spherical drops formed in carbon dioxide and decane mixtures. The transverse pressure profile is highly structured, looking like that of a liquid-liquid interface on the left and of a liquid-vapor interface on the right.

There is abundant evidence that the qualitative patterns of wetting transitions described here are correct<sup>26, 22, 27</sup> and the expected continuously thickening thin films have been observed by ellipsometry.<sup>28</sup> However, the predicted first order thin-film transition has not been verified experimentally, nor have the critical exponents of Equations (13) and (14) been established experimentally.

The theory of wetting transitions and film formation at flat surfaces requires solving only a one-dimensional density profile problem. However, if the structure and stress of

ORIGINAL PAGE IS  
OF POOR QUALITY

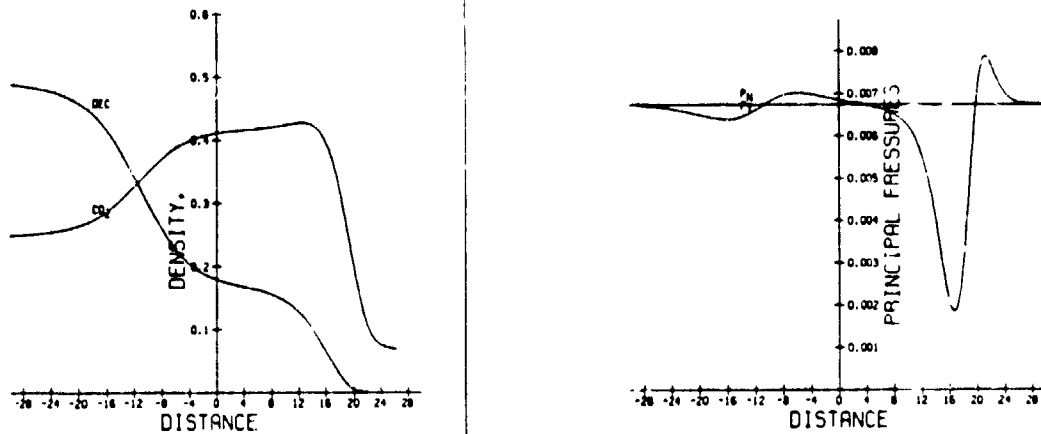


Figure 12. Density and pressure profiles of a thin-film at a liquid-vapor interface in CO<sub>2</sub> and decane. Density  $n_1$  in units  $b_1^{-1}$ , distance in  $\sqrt{c_{11}/a_{11}}$  and pressure in  $a_{11}/b_1^2$ . Component 1 is CO<sub>2</sub>.  $kTb_1/a_{11} = 0.148$ . Ref. 19.

the three phase contact region is desired, the problem becomes of necessity greater than one-dimensional, even if one phase is a flat solid. If a fluid-fluid interface contacts a flat solid the component densities depend on the distance  $x$  from the wall and the distance  $y$  parallel to the wall. Benner *et al.*<sup>15</sup> have recently studied the contact region of a one-component liquid-vapor interface at flat solid. The PR equation was used for the fluid and Equation (15) for the wall-fluid interaction potential. The space available here does not allow an extensive discussion of the paper. However, one interesting feature is that the stress state in the liquid-vapor interface is affected relatively far from the interface. An example of this is given in Figure 13. The principal pressure directions in the  $x$ - $y$  plane are indicated by crosses, the size of which indicates the magnitudes of the principal pressures in the  $x$ - $y$  plane. Far away from the solid and the liquid-vapor meniscus (defined as the position where  $n(x,y) = 1/2(n_1 + n_2)$  and indicated by the solid curve) the pressure components equal the bulk fluid value which is so small the corresponding crosses are almost invisible on the scale of Figure 13. At a planar liquid-vapor interface the normal pressure component ( $P_{11}$ ) would be constant and therefore the pressure crosses would appear as horizontal lines ( $P_{22}$  large,  $P_{11}$  small) in the interfacial zone. Instead, even to the far right of Figure 13, a distance of about 25 molecular diameters away from the wall, the normal pressure component is very large. And the principal stress pairs  $P_{11}$ ,  $P_{22}$  undergo four sign changes in going from the liquid to the vapor phase. Wild and wonderful patterns! Are they consequential? A major conclusion from the work of Benner *et al.* is that at a flat surface Young's equation is applicable outside the contact region (see Figure 5). The radius of the contact region is two or three times the thickness of the interfacial zone between the fluid phases.

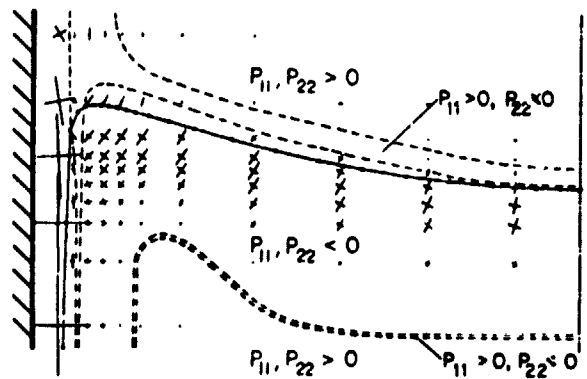


Figure 13. Principal pressure and components in a liquid-vapor interface near a wall.  $kTb/a = 0.1$ ,  $W = 6a/b$ . Width of region shown is  $25c/a$ . PR fluid. Ref. 15.

Spherical fluid microstructures

Visible examples of spherical microstructures are the drops and bubbles that occur in mists, foams, beverages, manufactured glass, and basalt lavas. Invisible examples are colloidal particles, vesicles, and micelles. The classical description of spherical structures is based on the Young-Laplace equation and the Kelvin equation expressing mechanical and chemical equilibrium between a bulk phase interior and a bulk phase exterior separated by an interface having the tension of a planar interface. In a sufficiently small spherical microstructure, however, the interior will not be bulk phase and the tension will not be that of a planar interface. Deviation from classical behavior might be consequential in nucleating fluids and micellar solutions, in which the equilibrium microstructures are tens of angstroms in diameter and, to mention a couple of examples receiving special attention at this colloquium, microdrops or microbubbles in microdrops and thin liquid layers on the inside of glass shells.

Gradient theory provides a molecular level theory of spherical structures which establishes the point at which the classical description breaks down and determines the structure, stress and mechanisms of stability of spherical microstructures. By way of example, I will outline some results of the recent investigations of Falls *et al.*<sup>14,19</sup> on one and two-component microdrops and microbubbles.

For spherical microstructures suspended in bulk fluid, the boundary conditions are  $\partial n_i / \partial r = 0$  at  $r=0$  and  $n_i(r) \rightarrow n_{iB}$  as  $r \rightarrow \infty$ ,  $n_{iB}$  being the bulk phase density of  $i$  in the suspending fluid. With these boundary conditions and constant influence parameters, Falls *et al.* have solved gradient theory for a one-component VDW fluid<sup>14</sup> and a two-component PR fluid.<sup>19</sup> Figure 14 illustrates their results for the density profiles  $n(r)$  of liquid-like microdrops suspended in a vapor phase. From the Young-Laplace and Kelvin equations, one expects the interior of the drop to be at higher pressure, and therefore higher density, than the saturated liquid density  $n_{l}^{eq}$ . This is seen to be true in Figure 14 for drops of radius larger than about four molecular diameters (the "radius" of the drop does not have a precise meaning for microdrops). However, for smaller drops, the interior density decreases with drop size and the density profile takes on a Gaussian-like shape with no interior bulk region. The loss of a bulk-like interior begins to occur when the radius of the drop is about equal to the thickness of the liquid vapor interface.

Because the interface is curved, the normal pressure profile  $P_N$  ( $P = P_N(r)\hat{r}\hat{r} + P_T(r)(\hat{I} - \hat{r}\hat{r})$ ) in a spherical fluid structure is not constant across the interface. Thus, the pressure profiles in a spherical interface are quite different from those in a planar interface at the same temperature (compare Figures 15 and 2). This leads one to expect strong deviations between the tension  $\gamma_\infty$  of a planar interface and the tension  $\gamma(R)$  of a microdrop of radius  $R$ . Similar deviations are expected for the Young-Laplace equation as classically applied, i.e.  $P_N(r=0) - P_N(r=\infty) = 2\gamma_\infty/R$ . From the thermodynamics of drops it follows that the appropriate radius  $R$  with which to describe the tension of the drop is the radius of the surface of tension.<sup>29</sup> This radius (which does not differ greatly from the value of  $r$  at which  $n(r) = 1/2(n(r=0) + n_B)$ ) and the corresponding tension  $\gamma(R)$  are predicted by gradient theory.<sup>14</sup> As illustrated in Table 1, the tension of the drop does differ from  $\gamma_\infty$  for small drops and the classical Young-Laplace equation does break down. However, what is remarkable is that already for drops fifteen molecules wide the drop interface has virtually the same tension as a planar interface and the classical Young-Laplace equation is accurate.

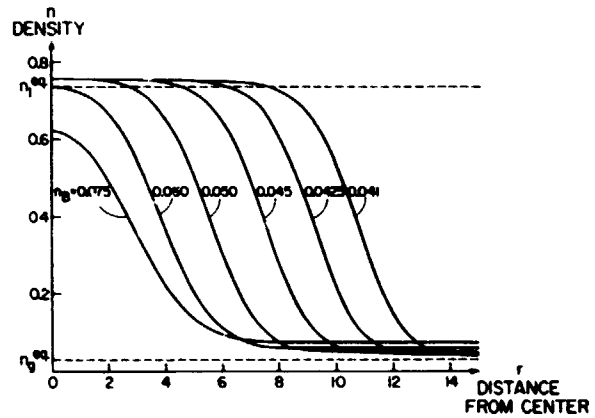


Figure 14. Density profiles of microspherical drops in a VDW vapor.  $kTb/a = 0.197$ , density in units of  $b^{-1}$ , distance  $r = \sqrt{c/a}$ .

Table 1. Microdrops in VDW vapor.  
 Radius R in units of  $\sqrt{c/a}$ .  
 $kTb/a = 0.197$ .

R	$\gamma(R)/\gamma_\infty$	$\frac{P_N(0) - P_N(\infty)}{(2\gamma_\infty/R)}$
2.56	0.79	-0.079
2.88	0.83	0.017
3.26	0.87	0.19
3.76	0.91	0.43
4.67	0.95	0.73
5.52	0.97	0.87
7.74	0.99	0.97
10.15	0.996	0.99

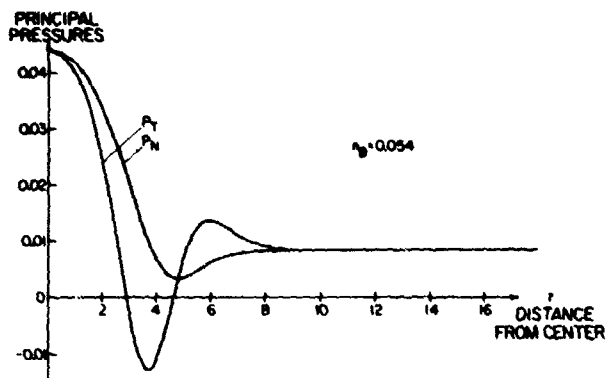


Figure 15. Principal pressure profiles of a microspherical drop in a VDW vapor. Pressure in units of  $a/b^2$ , density in  $b^{-1}$ , distance in  $\sqrt{c/a}$ .  $kTb/a = 0.197$ . Ref. 14.

The implication of the one-component studies just outlined is that microdrop curvature affects the interfacial structure and the interfacial tension very little once the drop radius is larger than 10 molecular diameters. In multicomponent systems this conclusion may or may not follow. Consider for example the bubble in liquid  $CO_2$  and decane shown in Figure 16 (from Falls *et al.*<sup>19</sup>). The radius of the bubble is only about 12 carbon dioxide diameters, but its component density profiles are almost identical to those of the planar liquid-vapor interface (indicated as a bubble with  $R=\infty$ ).

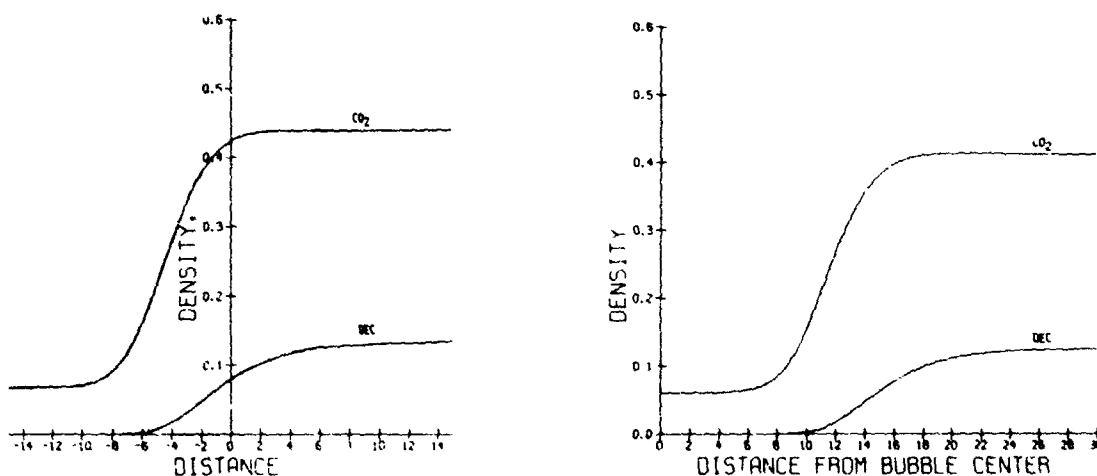


Figure 16. Density profiles in a planar liquid-vapor interface ( $R=\infty$ ) and in a bubble ( $R = 12$ ) in a  $CO_2$ -decane PR fluid. Density  $n_i$  in units of  $b_i^{-1}$ , distance in  $\sqrt{c_{i1}/a_{i1}}$ .  $kTb_1/a_{11} = 0.148$ . Ref. 19.

The tensions of the bubble and planar interface agree within 10%. Thus, this bubble behaves as expected from the one-component results.

However, as was discussed in the previous section (Figure 12), in a multicomponent fluid conditions can be such that a thin-film of an incipient third phase may be formed at an interface. These films are very sensitive to a change in a field variable. Curving an interface changes the chemical potential of the system (this follows from Kelvin's equation in the classical theory), and so it can be anticipated that under conditions of high adsorption or thin-film formation the interfacial structure and stress will be very sensitive to drop size. Comparison of the drop component density and pressure profiles of Figure 17 (from Falls *et al.*<sup>19</sup>) with the corresponding planar case, Figure 12, illustrates that this is

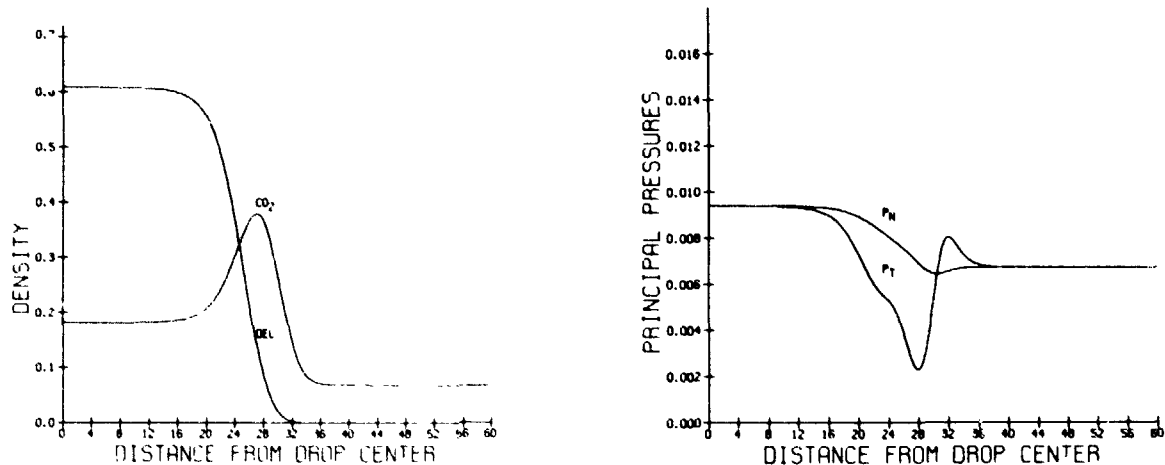


Figure 17. Density and pressure profiles of a drop in a CO<sub>2</sub>-decane PR fluid. Density  $n_i$  in units of  $b_i^{-1}$ ; pressure in  $a_{11}/b_1^2$ , distance in  $\sqrt{c_{11}/a_{11}}$ .  $kTb_1/a_{11} = 0.148$ . Ref. 19.

indeed the case. At this temperature, it has been estimated<sup>19</sup> from the theory that the drop structure will not begin take on the planar form until it is larger than 100 carbon dioxide molecules in radius. The important implication of this result is that *in regions of thin-film formation the interfacial composition can be greatly modified by curvature.* This fact might be quite important in the manufacture of objects with thin, uniform layers of a desired material.

Although space does not allow discussion, gradient theory predicts the work of formation of drops and bubbles, a quantity important to the theory of homogeneous nucleation. In fact, the theory was used by Cahn<sup>11</sup> to support his theory of spinodal decomposition. He showed that the barrier expected for the nucleation of microdrops is not there owing to the size dependence of the interfacial tension and that as a result a homogeneous material at the spinodal density can transform continuously into a multiphase system. In heterogeneous nucleation, it is likely that thin-film formation will be an important intermediate step in the process when conditions are right. These matters are ripe for future work.

#### Closing remarks

In closing, I would like to point out a few problems to which gradient theory might profitably be applied next.

1. Thin, uniform layers of fluid in a spherical solid shell. A fluid-solid potential will have to be introduced for shell. For uniform thin-films and thin layers of phase only spherically symmetric solutions need to be sought, so the problem remains one dimensional. By a different method Kim, Mok, and Bernat address this problem in their paper.
2. Fluid microstructure at rough or chemically heterogeneous solid surfaces. For this problem a two-dimensional solid-fluid potential will have to be introduced. Thus, the problem is two-dimensional.
3. Contact angles with rough or chemically heterogeneous solid surfaces. This involves the same solid-fluid potential as in Problem 2 and a fluid interface in the vicinity of

the solid and so is a three-dimensional problem. The problem will pose a challenge to computer-aided mathematics.

4. Drop shapes on inclined rough or chemically heterogeneous surfaces. This again is a three-dimensional problem and an even greater challenge than Problem 3.

#### Acknowledgement

I am grateful to the Department of Energy for financial support of this research and to my Minnesota colleagues for their roles in the research reviewed.

#### References

1. For example, see Percus, J. K., in The Equilibrium Theory of Classical Fluids, H. L. Frisch and J. L. Lebowitz, Eds., Benjamin, New York, 1966, pp. II33-II70.
2. For a recent review, see Lavis, H. T. and L. E. Scriven, Advances in Chemical Physics, to appear early in 1982.
3. Lord Rayleigh, Phil. Mag. **33**, 208 (1892).
4. Van der Waals, J. D. and Ph. Kohnstamm, Lehrbuch der Thermodynamik, Maas and Van Suchtelen, Leipzig, 1908.
5. Cahn, J. W. and J. E. Hilliard, J. Chem. Phys. **28**, 258 (1958).
6. Bongiorno, V., L. E. Scriven and H. T. Davis, J. Colloid and Interface Sci. **57**, 462 (1976).
7. Yang, J. M., P. D. Fleming III and J. H. Gibbs, J. Chem. Phys. **64**, 3732 (1976).
8. Poser, C. I. and I. C. Sanchez, J. Colloid and Interface Sci. **69**, 539 (1979).
9. (a) Carey, B. S., L. E. Scriven and H. T. Davis, Am. Inst. Chem. Eng. J. **24**, 1076 (1978); **26**, 705 (1980). (b) Carey, B. S., Ph.D. Thesis, University of Minnesota, 1979.
10. Guerrero, M. and H. T. Davis, Ind. Eng. Chem. Fundam. **19**, 309 (1980).
11. Cahn, J. W., J. Chem. Phys. **42**, 93 (1965).
12. McCoy, B. F. and H. T. Davis, Phys. Rev. A **20**, 1201 (1979).
13. Carey, B. S., L. E. Scriven and H. T. Davis, J. Chem. Phys. **69**, 5040 (1978).
14. Falls, A. H., L. E. Scriven and H. T. Davis, J. Chem. Phys. **75**, 3986 (1981).
15. Benner, R. E., L. E. Scriven and H. T. Davis, Royal Society of Chemistry's Faraday Symposium No. 16, "Structure of the Interfacial Region," Oxford University, 16-17 December 1981.
16. Korteweg, D. J., Archives Neerl. Sci. Exacts Nat. **6**, 1 (1904).
17. Peng, D. Y. and D. B. Robinson, Ind. Eng. Chem. Fundam. **15**, 59 (1976).
18. Sahimi, M., L. E. Scriven and H. T. Davis, 56th Annual Fall Technical Conference of SPE of AIME, San Antonio, TX, Oct. 5-17, 1981, SPE Reprint #10268.
19. From Falls, A. H., L. E. Scriven and H. T. Davis, J. Chem. Phys. (to be submitted).
20. Cahn, J. W., J. Chem. Phys. **66**, 3667 (1977).
21. Teletzke, G. F., L. E. Scriven and H. T. Davis, J. Colloid and Interface Sci. (to appear).
22. Teletzke, G. F., L. E. Scriven and H. T. Davis, 56th Annual Fall Technical Conference of SPE of AIME, San Antonio, TX, Oct. 5-17, 1981, SPE Reprint #10112.
23. Good, R. J. and L. A. Girifalco, J. Phys. Chem. **64**, 561 (1960); **61**, 904 (1957).
24. Zisman, W. A., Adv. in Chem. Series **43**, 1 (1963).
25. Saam, W. F. and C. Ebner, Phys. Rev. A **17**, 1768 (1978).
26. Moldover, M. R. and J. W. Cahn, Science **207**, 1073 (1980).
27. Teletzke, G. F., Ph.D. Thesis, University of Minnesota, 1979.
28. Kwon, O. D., D. Beaglehole, W. W. Webb, B. Widom, J. W. Cahn, M. R. Moldover and B. Stephenson (private communication).
29. Hill, T. L., J. Chem. Phys. **20**, 141 (1952); J. Phys. Chem. **56**, 526 (1952).

Large amplitude drop shape oscillations

E. H. Trinh and T. G. Wang

Jet Propulsion Laboratory, California Institute of Technology  
M.S. 183-901, 4800 Oak Grove Drive, Pasadena, CA.

Abstract

An experimental study of large amplitude drop shape oscillation has been conducted in immiscible liquids systems and with levitated free liquid drops in air. In liquid-liquid systems the results indicate the existence of familiar characteristics of nonlinear phenomena. The resonance frequency of the fundamental quadrupole mode of stationary, low viscosity Silicone oil drops acoustically levitated in water falls to noticeably lower values as the amplitude of oscillation is increased. A typical, experimentally determined relative frequency decrease of a 0.5 cm<sup>3</sup> drop would be about 10% when the maximum deformed shape is characterized by a major to minor axial ratio of 1.9. On the other hand, no change in the fundamental mode frequency could be detected for 1 mm drops levitated in air. The experimental data for the decay constant of the quadrupole mode of drops immersed in a liquid host indicate a slight increase for larger oscillation amplitudes. A qualitative investigation of the internal fluid flows for such drops has revealed the existence of steady internal circulation within drops oscillating in the fundamental and higher modes. The flow field configuration in the outer host liquid is also significantly altered when the drop oscillation amplitude becomes large.

Introduction

In this paper we report the outcome of a series of experiments aiming at determining the characteristics of large amplitude liquid drops shape oscillations. Two systems have been investigated in the present study: drops held stationary in an immiscible liquid host, and drops freely suspended in air. They have been made accessible to a controlled laboratory study through the technique of acoustic levitation<sup>1-3</sup>. Most of the experimental results presented here, however, deal with immiscible liquids systems.

Observations of the variations of the free decay frequency, the fundamental resonance frequency of a forced vibrating drop, the damping constant, and of the time distribution of the prolate and oblate configurations, have been made as functions of the oscillation amplitude. Visualization of the flow fields both inside and outside the oscillating drops suspended in liquid hosts has revealed a gradual appearance of a steady circulation not present for small amplitude oscillations.

Theoretical background

Theoretical analyses of small amplitude drop shape oscillations have been shown to be reasonably successful at describing the observed phenomena<sup>3</sup>. Recent linear treatments have included the normal mode approach<sup>4,5</sup>, as well as a solution to the initial value problem yielding the small time behavior<sup>6</sup>. The analytical solution of the complete nonlinear Navier-Stokes equations have not yet been made available, although results of numerical calculations suggest the appearance of various nonlinear effects as the vibration amplitude of liquid drops suspended in a gaseous medium is increased<sup>7</sup>. Among these predictions are a decrease in the free decay frequency and an unbalance in the time distribution of the prolate and oblate configurations characteristic of the fundamental mode.

On the basis of a linear treatment<sup>4,5</sup>, the steady-state frequencies for the oscillation modes of a liquid droplet immersed in an immiscible host liquid can be written

$$\omega_L = \omega_L^* - (\alpha/2) \omega_L^{* \frac{1}{2}} + \alpha^2/4 \quad , \quad \text{and} \quad \omega_L^* = \left[ \sigma L(L+1)(L-1)(L+2)/R^3 [L \cdot \rho_0 + (L+1) \cdot \rho_1] \right]^{1/2} \quad (1)$$

The subscripts i and o refer to the inner and outer fluids respectively.  $\rho$  designates the density,  $\nu$  the dynamic viscosity,  $\sigma$  the interfacial tension, and L refers to the mode number. The parameters  $\alpha$  and  $\gamma$  are characteristics of the fluids involved.<sup>5</sup>

The damping constant for small amplitude oscillations can be written as

$$\tau_L^{-1} = \frac{1}{2} \alpha \omega_L^{* \frac{1}{2}} + \frac{1}{2} \gamma - \frac{1}{2} \alpha^2 \quad . \quad (2)$$

According to these results no dependence on the oscillation amplitude for either the resonance frequency or the damping constant can be obtained, as they are valid only in the limit of small displacements of the drop surface.

BLACK AND WHITE PHOTOGRAPH

Photographs of experimentally obtained axisymmetric drop shape oscillations in the first three modes are reproduced in figure (1).

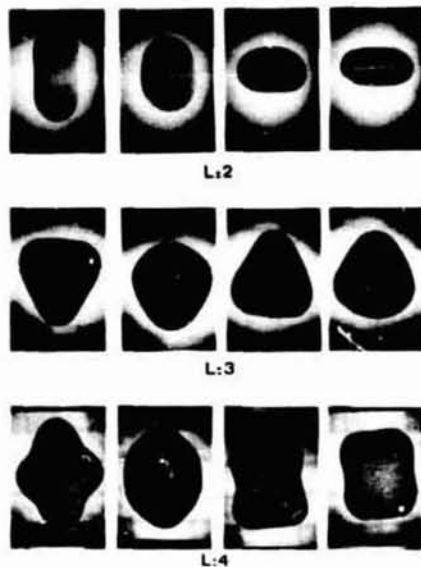


Figure 1 : Experimentally obtained resonance modes for shape oscillation of a 1cm<sup>3</sup> silicone oil drop in water.

Experimental technique

An acoustic standing wave established in a fluid-filled resonant cavity can be used to yield a stable positioning of a fluid sphere having different properties than the cavity fluid. This effect is the result of the action of acoustic radiation pressure forces, and can be obtained in liquids as well as in gases. Figure (2) illustrates such a system. This schematic representation is for a system involving a liquid drop trapped in a sound field established in an immiscible liquid host. In this particular case, the drop liquid has a higher compressibility and density than the host liquid, and is positioned near an acoustic pressure maximum.

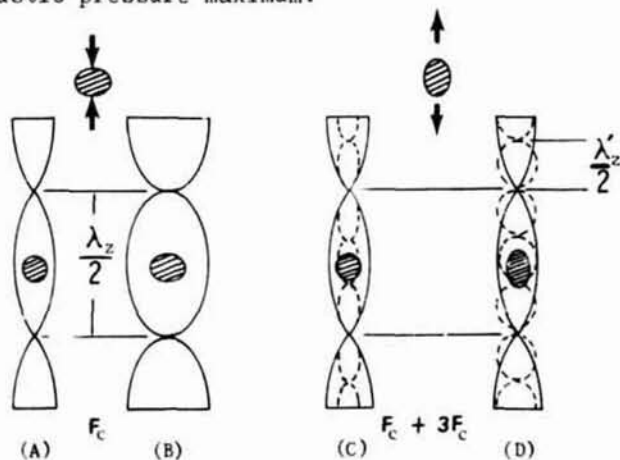


Figure 2 : Schematic representation of a liquid drop trapped in a standing wave. Figure 2b illustrates the action of the acoustic force deforming the drop into an oblate shape. Figure 2d shows the opposite action: the drop is elongated at the poles into a prolate configuration. In this work  $f_c = 22$  kHz.

The acoustic forces will also produce a deformation of the trapped drop when the acoustic pressure is increased (see figure 2a ). A low frequency modulation of this force is therefore possible through the modulation of the sound pressure. A steady-state drive of shape oscillations can then be obtained, and the successive drop resonances will be excited as the modulation frequency is varied.

In addition to the deformation shown where the drop is statically distorted into an oblate spheroid, the appropriate tailoring of the acoustic field distribution can provide static distortions into the prolate spheroidal shape. Hence, the opposite drive where the drop is pulled apart at the poles is also available (see figure 2c and 2d).

Figure (3) is a schematic diagram of the experimental apparatus. The necessary electronic instrumentation provides the required voltage drive to a piezoelectric transducer used to excite the acoustic standing waves. An optical detection system allows the monitoring of the shape of the drop. The analog signal thus obtained can be displayed on a CRT screen or can be plotted on a X-Y recorder as a DC signal proportional to the amplitude of oscillation. Resonance curves and free decay traces can be obtained in a straightforward manner. High speed cinefilms also provides the necessary data for the oscillation amplitude and the static equilibrium shapes.

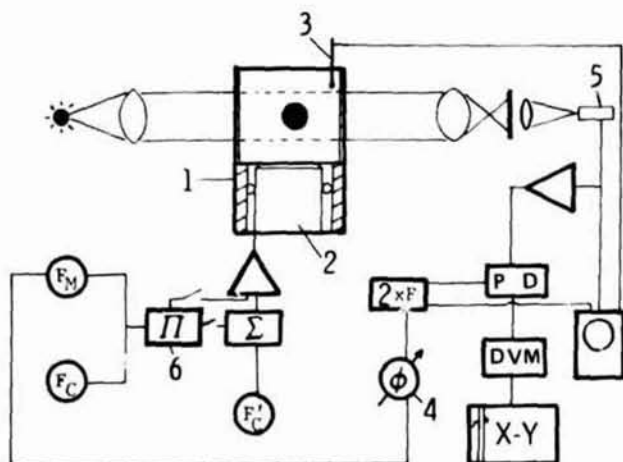


Figure 3 : The experimental apparatus. 1 is the acoustic cell, 2 is the piezoelectric transducer, 3 is a hydrophone, 4 is a variable phase shifter, 5 is a photodetector, 6 is a balanced modulator. The  $2xf$  frequency doubler supplies a reference signal with a determined phase relationship with respect to the hydrophone signal.

The voltage applied to the transducer terminals may be written

$$V_T = V_C \sin(2\pi f_c t) \cdot \cos(2\pi f_m t) \quad (3)$$

$f$  is the frequency of the high frequency standing wave (22 or 66 kHz in this case), and  $f_m$  is the modulation low frequency (from 2 to 15 Hz in this case for 1 cm diameter drops of oil in water). The acoustic pressure is proportional to this voltage for the linear operation of the transducer. The acoustic radiation pressure force is approximately proportional to the square of the acoustic pressure.

$$F_r \sim \langle P_{\text{acous}}^2 \rangle \sim \cos^2(2\pi f_m t) \quad (4)$$

The time average of this force is given by

$$\langle F_r \rangle \sim \langle \frac{1}{2}(1 + \cos 4\pi f_m t) \rangle \quad (5)$$

This includes a steady-state as well as a slowly varying force component at the frequency  $2f_m$ . The steady-state component induces a steady deformation of the drop shape.

#### Free decay frequency

Measurements of the free decay frequency in the immiscible liquid system as a function

of the initial oscillation amplitude were carried out by first exciting the drop into its first resonant mode. The modulated acoustic drive was then turned off and the decay phase observed. The free decay frequency was measured from both the oscilloscope traces and high speed motion picture films. The experimental uncertainty was within  $\pm 1\%$ .

In the axisymmetric case, and with the linear approximation, one might describe the deformation with the parameter

$$x(\theta, t) = r(\theta, t) - R_0 \quad (6)$$

where  $r(\theta, t)$  is the expression for the boundary of the drop, and  $R_0$  is the radius of a sphere of equal volume. A linear expansion would yield

$$x(\theta, t) \approx \sum_{n=2}^{\infty} \left[ x_n^{\text{static}} + x_n \cos(4\pi f_m t + \phi_n) \right] P_n(\cos\theta) \quad (7)$$

$P_n(\cos\theta)$  is a Legendre polynomial of order  $n$ . In this particular case where only the fundamental mode is excited, and for a reasonably high  $Q$  system ( $Q=15$ ), one has the approximations

$$x_2 \gg x_n \neq 2 \gg x_n^{\text{static}} \quad (8)$$

$x_n^{\text{static}}$  is the distortion produced by the static component of the acoustic force.

During free decay the drop deformation may be expressed as

$$x(\theta, t) \approx \sum_{n=2}^{\infty} \left[ x_n^{\text{static}} \cos(2 f_n' t + \phi_n') \exp(-b_n' t) + x_n \cos(2 f_n'' t + \phi_n'') \exp(-b_n'' t) \right] P_n(\cos\theta) \quad (9)$$

The term with the single prime refers to the decay of the static deformation, the double primed one to the decay of the oscillatory motion initially driven at the resonance frequency of the fundamental mode. In this particular case the time dependence of  $f_n'$ ,  $f_n''$ ,  $b_n'$ , and  $b_n''$  has been neglected. This has been justified by the experimental evidence.

Figure (4) reproduces some of the experimental results. The free decay frequency variations with the maximum oscillation amplitude prior to the decay phase are shown for a 0.5 and a 1 cm<sup>3</sup> drop of Silicone oil/CCl<sub>4</sub> mixture made almost neutrally buoyant with distilled water. A steady decrease can be observed with increasingly larger initial oscillatory motion.

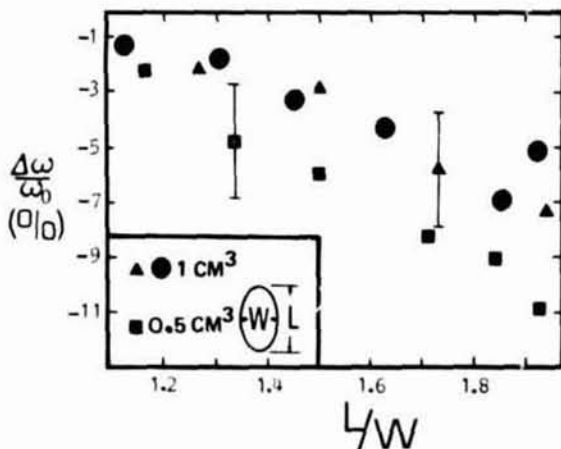


Figure 4 : Relative change in the free decay frequency as a function of the initial oscillation amplitude. The ratio  $L/W$  refer to the maximum deformation in the prolate shape during the steady-state forced oscillations prior to the free decay phase.

### Driven oscillations

The amplitude dependence of the fundamental resonance frequency for forced steady-state oscillations has been investigated both in the immiscible liquids system, and with drops suspended in air. The results are qualitatively different for the two systems, although the measurements made for a levitated drop in air are not as precise, and for significantly distorted drops due to the gravitational field.

Figure (5) is a plot of the relative frequency shift as a function of the oscillation amplitude for a 1 cm<sup>3</sup> drop of Silicone oil/CCl<sub>4</sub> mixture in distilled water. Qualitatively different results are obtained when the two opposite driving mechanisms are used. The oblate biased mechanism is based on a compression of the drop at the poles, while the prolate-biased drive consists in elongating the drop at the poles. The source of such a discrepancy has not yet been totally elucidated, but there are some indications that the interference of the acoustic fields on the drop motion might play an important role.

Figure (6) reproduces the results of measurements taken for drops of a mixture of glycerin and distilled water suspended in air. The equilibrium shape of the drops is oblate as indicated by the parameter ( $W/L$ )<sub>0</sub>. No change in the fundamental mode resonance frequency can yet be resolved within the experimental uncertainty ( $\pm 5\%$ ). These results have been obtained with an oblate-biased mechanism.

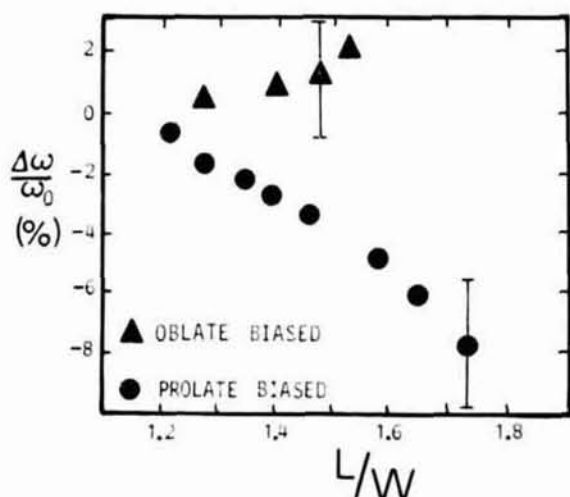


Figure 5: Amplitude dependence of the fundamental mode for forced oscillations for a liquid drop in H<sub>2</sub>O.

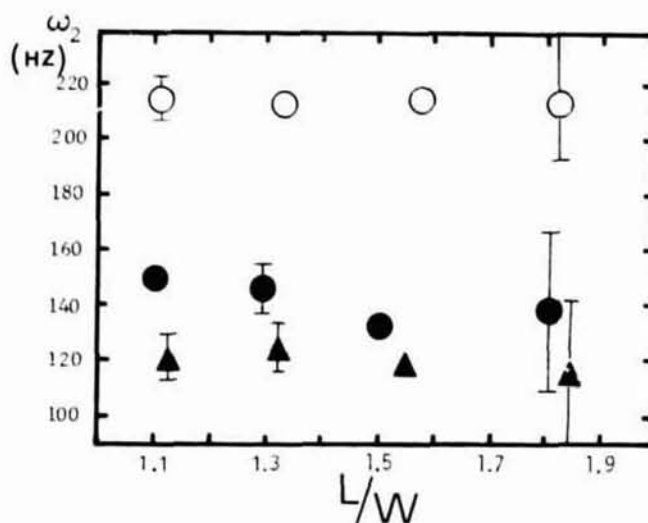


Figure 6: Amplitude dependence of the fundamental mode frequency for a drop levitated in air.  $\circ$   $R=0.097$  cm,  $\bullet$   $R=0.125$  cm,  $\blacktriangle$   $R=0.151$  cm. The static shape is oblate.  $(W/L)_0 \approx 1.2$ .

Decay constant measurement  $\approx 1.2$

Measurement of the dissipation rate of liquid drops oscillating in an immiscible liquid host has revealed a single value for the free decay constant for each initial oscillation amplitude. Figure (7) gives an example of such a decay process. The decrease to zero deformation is strikingly exponential, and is at a constant rate. This rate appears to vary for different initial oscillation amplitude, with a tendency for higher values for larger amplitudes. Figure (8) shows such results.

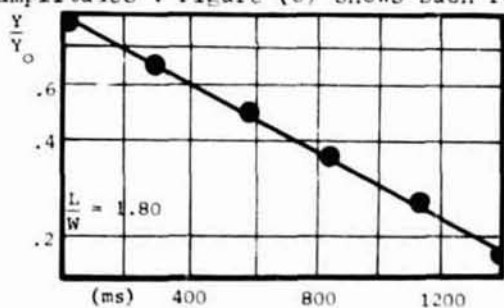


Figure 7: Time dependence of drop oscillation amplitude.

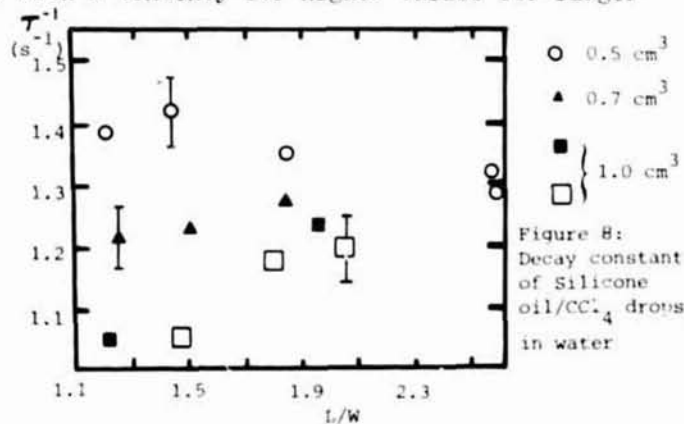


Figure 8: Decay constant of Silicone oil/CCl<sub>4</sub> drops in water

ORIGINAL PAGE  
BLACK AND WHITE PHOTOGRAPH

Time distribution of the prolate and oblate configurations

Immiscible liquids systems results suggest that the duration of the prolate configuration increases with the oscillation amplitude. Table (I) reproduces the results of measurements performed on drops with an oblate static equilibrium shape. The duration of the prolate configuration definitely shows an increase for larger amplitudes. Such an increase is also obtained when a static prolate shape is used.

Cycle number after termination of the steady drive	MAXIMUM OBLATE DISTORTION DURING OSCILLATIONS			
	W/L = 1.75		W/L = 1.31	
	$\frac{T_{oblate}}{T_{cycle}}$	$\frac{T_{prolate}}{T_{cycle}}$	$\frac{T_{oblate}}{T_{cycle}}$	$\frac{T_{prolate}}{T_{cycle}}$
1	0.51	0.49	0.51	0.49
2	0.53	0.47	0.53	0.47
3	0.54	0.46	0.55	0.45
4	0.57	0.43	0.60	0.40
5	0.60	0.40	0.64	0.36

Table I: Duration of the oblate and prolate cycles during the free decay of shape oscillations initially forced by acoustic forces. The static equilibrium shape is oblate. Larger amplitude oscillations increase the duration of the prolate phase.

Fluid flow fields

The visualization of the fluid flows fields revealed by suspended dye particles appropriately illuminated, has shown the gradual appearance of a steady circulatory motion superposed upon the oscillatory motion induced by the drop shape oscillations in liquid-liquid systems. Figure (9) shows photographs of such flow fields for small and large amplitude for both inner and outer liquids.

Figure 9: A. Streak patterns of suspended dye particles in a Silicone oil drop undergoing small amplitude oscillation in the L=2 mode. The drop is levitated in distilled water. ( $\Delta R/R \leq 0.05$ )  
B. Streak patterns for the same drop oscillating at higher amplitude. ( $\Delta R/R \approx 0.1$ ).

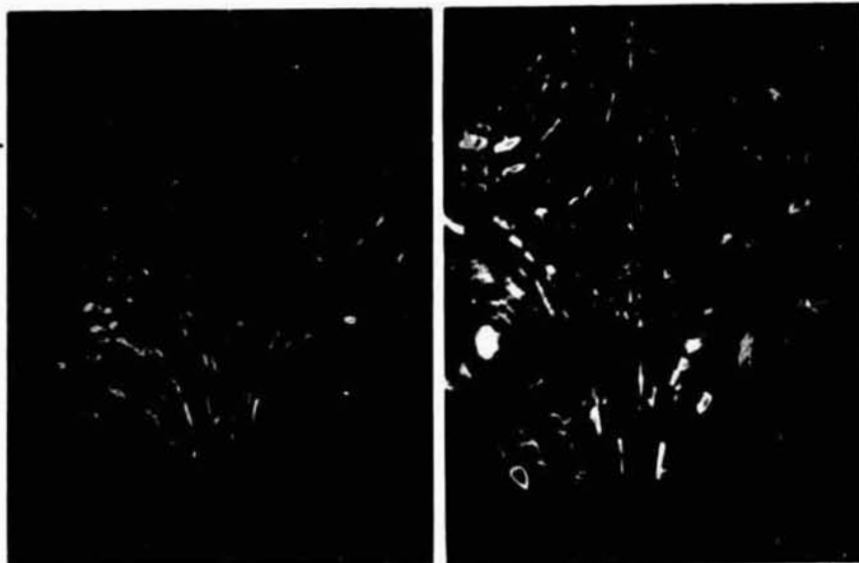


A

B

ORIGINAL PAGE  
BLACK AND WHITE PHOTOGRAPH

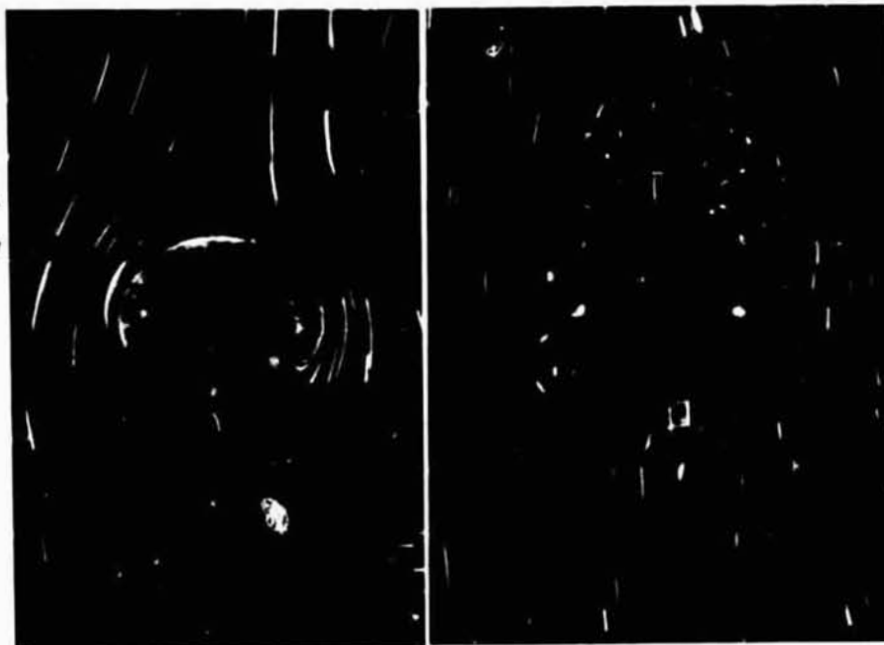
Figure 9: C. Same drop as in  
A and B, but the osci-  
llations are in the  
L=3 mode at small  
amplitude.  
D. L=3 oscillations  
at large amplitude  
( $\Delta R/R \approx 0.10$ ).



C

D

Figure 9: E. Flow pattern in  
the outer fluid with  
a stationary and  
still drop. The flow  
around the drop is  
caused by acoustic  
streaming, and is  
characterized by a  
Reynolds number of  
5.  
F. Flow pattern in  
the outer fluid for  
a drop oscillating  
in the L=2 mode at  
small amplitude.

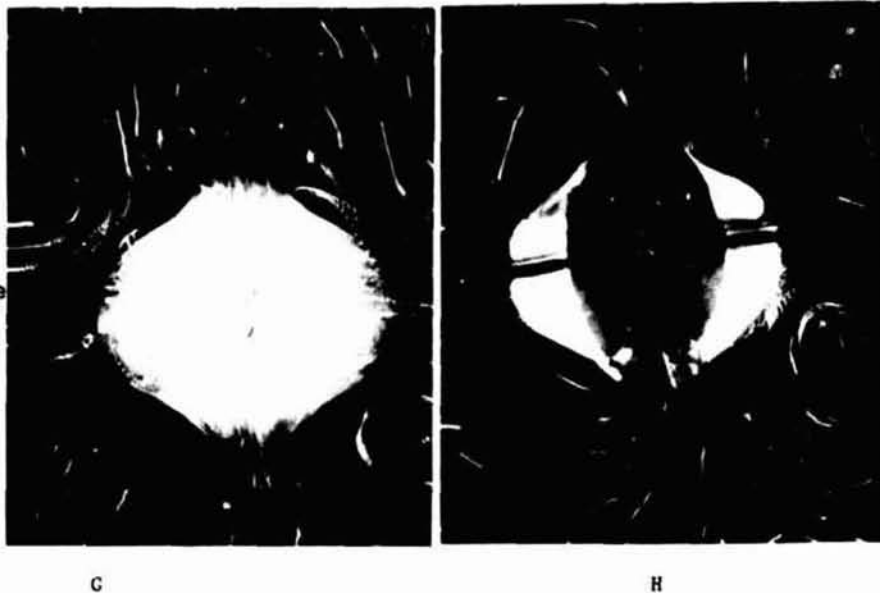


E

F

ORIGINAL PAGE  
BLACK AND WHITE PHOTOGRAPH

Figure 9: G and H.  
Flow pattern in the  
outer fluid with a  
drop oscillating in  
the L=2 mode at large  
amplitude.



Conclusion

The experimental observations gathered so far point to certain definite nonlinear characteristics of liquid-liquid systems. Both inertial and viscous effects have been shown to exist, and these must play an important role in causing these phenomena. The absence of theoretical information, however, has not allowed a further analysis.

The techniques using acoustic radiation pressure forces have been shown to allow the controlled experimental study of single drop phenomena. One must exercise caution, however, when interpreting the observations based on such a technique because of the unavoidable interaction between the acoustic fields and the drop motion.

Acknowledgement

The research described in this paper was carried out by the Jet Propulsion Laboratory, California Institute of Technology, under contract with the National Aeronautics and Space Administration.

References

1. T. Wang, M. Saffren, D. Elleman, "Drop dynamics in space", Proceedings of the First International Colloquium on Drops and Bubbles, Collins, Plessett, Saffren, Eds. 1974.
2. P. Marston, R. Apfel, "Acoustically forced shape oscillation of hydrocarbon drops levitated in water", J. Colloid and Interface Sci., vol. 68, pp 280-286, 1979.
3. E. Trinh, A. Zwern, T. Wang, "An experimental study of drop shape oscillations in liquid-liquid systems", J. Fluid Mechs., vol. 115, pp 453-475, 1982.
4. C. Miller, L. Scriven, "The oscillations of a fluid droplet immersed in another fluid", J. Fluid Mechs., vol. 32, pp 417-435, 1968.
5. P. Marston, "Shape oscillation and static deformation of drops and bubbles driven by modulated radiation stresses-Theory", J. Acoust. Soc. Am., vol. 67, pp 15-26, 1980.
6. A. Prosperetti, "Free oscillations of drops and bubbles: the initial value problem", J. Fluid Mechs., vol 100, pp 333-347, 1980.
7. B. Foote, PhD Thesis. University of Arizona, 1974.

## Bubble shapes in steady axisymmetric flows at intermediate Reynolds number

G. Ryskin and L. G. Leal

Department of Chemical Engineering, California Institute of Technology, Pasadena, CA 91125

Abstract

We consider the shape of a gas bubble which rises through a quiescent incompressible, Newtonian fluid at intermediate Reynolds numbers. Exact numerical solutions for the velocity and pressure fields, as well as the bubble shape, are obtained using finite difference techniques and a numerically generated transformation to an orthogonal, boundary-fitted coordinate system. No restriction is placed on the allowable magnitude of deformation.

Introduction

In spite of intensive investigation for more than 70 years, the theoretical problem of bubble and drop motion in an unbounded viscous Newtonian liquid, which may either be quiescent or undergoing some prescribed motion far from the bubble or drop, has remained essentially unsolved. The main difficulty, in addition to the usual nonlinearity of the equations of motion at finite Reynolds number, is that the bubble or drop shape is unknown and required as part of the solution of the problem. As a consequence, the boundary conditions at the bubble or drop surface are nonlinear, and, in addition, the solution depends on the prior history of the bubble or drop motion and interface shapes, even in the creeping motion limit.

This problem of bubble or drop motion in a viscous liquid, with an unknown boundary shape, is an example of the general class of so-called "free boundary" problems of fluid mechanics. Although a number of methods exist for this type of problem, which can be used to analyze the motion of bubbles or drops, all but purely numerical methods inevitably suffer from some restriction. Included is the asymptotic technique of "domain perturbations" which has been applied, for example, for buoyancy-driven motions of a drop at finite Reynolds,<sup>1</sup> and for a drop in a general linear "shear" flow,<sup>2</sup> but is restricted to small deformations from a known (or guessed) boundary shape. Boundary integral techniques are not restricted in the degree of deformation (and thus provide a powerful tool to study bubble and drop deformation<sup>3-5</sup>), but are only applicable in the limits of either creeping flow, or potential flow, where the governing differential equations are linear. For more general conditions, this leaves us with numerical methods which are not limited, in principle, either by the allowable degree of deformation or by linearity of the governing equations. Such methods have not been applied directly to the problem of calculating bubble or drop shapes in viscous flow so far as we are aware. However, in most other applications to free boundary problems in fluid mechanics, the numerical methods of choice have been based upon finite element formulations. At least in part, this has been a consequence of the loss of accuracy which occurs when finite difference techniques are applied in domains with boundaries that are not coincident with coordinate lines or surfaces. Thus, if one considers only the classical orthogonal coordinates, such as cylindrical, spherical, etc., the use of finite-difference methods is generally unacceptable for free boundary problems. The present paper explores the alternative possibility of finite-difference solutions based on a numerical method of constructing a system of orthogonal, boundary-fitted coordinates, for the problem of streaming flow past a bubble. We do not claim or intend to imply "superiority" in any sense over other possible numerical approaches to the same problem. Indeed, the methods described here are not at a sufficiently advanced stage of development for such comparisons to be meaningful, even if one were philosophically inclined to make them!

A detailed description of the methods of orthogonal mapping will soon appear in the *Journal of Computational Physics*,<sup>6</sup> and a more detailed description of methods and results for the application to the motion of a bubble or drop in a viscous fluid is presently in preparation. Here, we simply outline the method of solution and present two examples of the solution for streaming flow past a bubble at finite Reynolds number as an illustration of its application.

Orthogonal Mapping

The idea which we pursue is thus to obtain orthogonal boundary-fitted coordinates for the domain exterior to a bubble whose shape is unknown, though smooth and generally nonspherical. In the present development, the unknown shape is generated via an iterative procedure starting from some initial guess. At each step, with the boundary shape specified, mapping functions for the boundary-fitted coordinates are generated numerically, the equations of motion are then solved in the transform domain and the normal stress balance at the bubble surface is used to generate an improved shape. We restrict ourselves to steady, axisymmetric configurations and discuss the mapping problem in 2D, with the axisymmetric boundary shape generated by rotation about the axis of symmetry which is thus required to be a coordinate line for the transform coordinates.

In the remainder of this section, we outline a method of obtaining the desired coordinate transformation. From a mathematical point of view, we require a pair of functions  $x(\xi, \eta)$  and  $y(\xi, \eta)$  which map points of the physical domain onto a unit square,  $0 \leq \xi, \eta \leq 1$ , in the transform domain, with lines of constant  $\xi$  and  $\eta$  being orthogonal. For convenience, we designate the bubble surface as  $\xi = 1$ , and the upstream and downstream

axes of symmetry as  $\eta = 1$  and  $\eta = 0$ , respectively, with  $\xi \rightarrow 0$  corresponding to infinity. There has, of course, been a great deal of recent research aimed at the problem of obtaining numerically generated coordinate mappings. Included in this work are methods based on the solution of a pair of elliptic equations for the mapping functions,<sup>7</sup> conformal mapping,<sup>8</sup> direct integration of "Cauchy-Riemann"-type equations as an initial value problem starting from a boundary<sup>9,10</sup> and other methods of orthogonal mapping which are equivalent to conformal mapping with less restrictive constraints on the ratio of the diagonal components of the metric tensor (the latter are, in fact, most closely related to the present approach).<sup>11-13</sup> Limitations of space prevent a detailed review of this prior work. However, in general, the resulting coordinate systems are either nonorthogonal,<sup>7</sup> ill-conditioned in the sense of extreme sensitivity to boundary shape and/or (the possibility of) highly nonuniform spacing of coordinate lines (conformal mapping,<sup>8</sup> some types of "orthogonal mapping"<sup>11,12</sup>) or only suitable in some local subdomain (integrations of Cauchy-Riemann equations<sup>9,10</sup>).

The present objective is a numerically generated mapping which is applicable in the whole domain, automatically orthogonal and free of the usual sensitivity problems of conformal mapping. Our basis is conventional tensor analysis, yielding equations for  $x(\xi, \eta)$  and  $y(\xi, \eta)$  which are coordinate invariant. These equations follow almost trivially from the observation that a Cartesian coordinate  $x$  (or  $y$ ) is a linear scalar function of position, so that  $\text{grad } x$  (or  $\text{grad } y$ ) is constant and

$$\text{div grad } x = 0 \quad (1)$$

The latter is nothing more than the covariant Laplace equation for  $x$ . When expressed in terms of the desired (but as yet unspecified)  $\xi, \eta$  coordinates, it becomes

$$g^{ij} x_{;ij} = 0 \quad (2)$$

in which  $g^{ij}$  is the  $ij$  component of the metric tensor and ";" denotes regular covariant differentiation. Although the solutions of Eq. (1) (and the similar equation for  $y$ ) will not generally yield orthogonal coordinates, we further specify that

$$g_{ij} = 0 \quad \text{for} \quad i \neq j \quad (3)$$

and

$$g_{11} = h_\xi^2, \quad g_{22} = h_\eta^2 \quad (4)$$

with the  $h_\xi, h_\eta$  being "scale" factors for the  $\xi, \eta$  system. In this case, the equations governing the transformation (mapping) functions become

$$\frac{\partial}{\partial \xi} \left( f \frac{\partial x}{\partial \xi} \right) + \frac{\partial}{\partial \eta} \left( \frac{1}{f} \frac{\partial x}{\partial \eta} \right) = 0 \quad (5a)$$

$$\frac{\partial}{\partial \xi} \left( f \frac{\partial y}{\partial \xi} \right) + \frac{\partial}{\partial \eta} \left( \frac{1}{f} \frac{\partial y}{\partial \eta} \right) = 0 \quad (5b)$$

with

$$f(\xi, \eta) \equiv h_\eta / h_\xi \quad (6)$$

and the solution of these equations, subject to appropriate boundary conditions (which we shall discuss in the next section), will yield orthogonal coordinates for any  $f$ , which can thus be chosen freely. It may be noted that conformal mapping corresponds to the restrictive choice  $f(\xi, \eta) = 1$ , for all  $\xi, \eta$ .

In general, the "most appropriate" choice of  $f$  depends on the type of mapping required. The problem of direct mapping with fixed boundary shape and a specified distribution of coordinate nodes along the boundary is discussed elsewhere.<sup>6</sup> Here, we consider only the mapping problem in which the boundary shape is unknown and required as part of the solution of the overall problem. In this case,  $f(\xi, \eta)$  can be specified directly as a function of  $\xi, \eta$ , with the form for  $f$  chosen so as to yield desired properties of the transform coordinates (e.g. nonuniform spacing of coordinate lines in some region of the domain).

#### The fluid dynamics problem — basic formulation

Let us now return to the problem of uniform streaming flow past a bubble. In this case, we adopt the very simple form for  $f$ ,  $f(\xi, \eta) \equiv \pi \xi$ . In addition, we introduce a relatively simple modification of the mapping procedure outlined above to take care of the fact that infinite values of the mapping functions  $x$  and  $y$ , corresponding directly to an infinite domain, cannot be generated numerically. To avoid this difficulty, we simply calculate the mapping from the unit square in the  $\xi, \eta$  plane to an auxiliary finite domain, which is then transformed to the physical domain by a conformal inversion.

Now, one great advantage of orthogonal coordinates, in addition to avoiding inaccuracy of numerical approximation in nonorthogonal coordinates, is that physical components of vectors and tensors can be used instead of covariant or contravariant ones. The governing Navier-Stokes equations, plus boundary conditions, can thus be expressed in a straightforward manner in terms of the resulting boundary-fitted coordinates

$\xi, \eta, \phi$ , obtained by rotation of the two-dimensional coordinates given by  $x(\xi, \eta)$  and  $\sigma(\xi, \eta)$  (where  $x$  is parallel to the axis of symmetry and  $\sigma$  is the distance to this axis along a normal through the point of interest). If we introduce the streamfunction  $\psi$ , and use standard expressions for the invariant differential operators in general orthogonal curvilinear coordinates, the Navier-Stokes equations are

$$\frac{1}{h_\xi h_\eta} \frac{\partial \psi}{\partial \eta} \frac{\partial}{\partial \xi} \left( \frac{\zeta}{\sigma} \right) - \frac{1}{h_\xi h_\eta} \frac{\partial \psi}{\partial \xi} \frac{\partial}{\partial \eta} \left( \frac{\zeta}{\sigma} \right) = \frac{2}{Re} L^2(\zeta \sigma) \quad (7)$$

$$L^2 \psi + \zeta = 0 \quad (8)$$

where  $\zeta$  is the vorticity,  $Re = \frac{d \rho v_\infty}{\mu}$ ,  $d$  is the equivalent diameter of the bubble and

$$L^2 \equiv \frac{1}{h_\xi h_\eta} \left\{ \frac{\partial}{\partial \xi} \left( \frac{f}{\sigma} \frac{\partial}{\partial \xi} \right) + \frac{\partial}{\partial \eta} \left( \frac{1}{f \sigma} \frac{\partial}{\partial \eta} \right) \right\} \quad (9)$$

The streamfunction at infinity, for a uniform streaming flow, takes the form

$$\psi_\infty = \frac{1}{2} \sigma^2 \quad (10)$$

Thus, to avoid dealing with large (or infinite) numbers, we actually solve for

$$\psi^* = \psi - \psi_a \quad (11)$$

where  $\psi_a$  is the potential flow solution for flow past a spherical bubble with the given form  $\psi_\infty$  at infinity, i.e.

$$\psi_a = \frac{1}{2} \sigma^2 (1 - \xi^3) \quad (12)$$

Now, Eqs. (4) and (5), rewritten in terms of  $\psi^*$ , are to be solved for  $\psi^*$ ,  $\zeta$  and the bubble shape subject to the boundary conditions

$$\psi^* \text{ is bounded, } \zeta = 0; \quad \text{at infinity (i.e. } \xi = 0) \quad (13)$$

$$\psi^* = 0, \quad \zeta = 0; \quad \text{at } \eta = 0, \eta = 1 \quad (\text{symmetry axis}) \quad (14)$$

and, at the bubble surface,

$$\psi^* = 0 \quad (\text{zero normal velocity}) \quad (15)$$

$$\zeta + 2\kappa_{(n)}^{(\xi\eta)} u_s = 0 \quad (\text{zero tang. stress}) \quad (16)$$

$$-\frac{3}{4} C_D x - p_d + \tau_{nn} + \frac{4}{We} \left( \kappa_{(n)}^{(\xi\eta)} + \kappa_{(n)}^{(\xi\phi)} \right) = 0 \quad (\text{normal stress balance}) \quad (17)$$

The first term in (16) is the hydrostatic pressure;  $C_D$  is the drag coefficient;  $p_d$  is the dynamic pressure

$$p_d = \frac{1}{2} \rho v_\infty^2 - \frac{4}{Re} \int \frac{1}{\sigma h_\xi} \frac{\partial}{\partial \xi} (\sigma \zeta) h_\eta d\eta \quad (18)$$

$u_s$  is the surface velocity;  $\tau_{nn}$  is the normal component of viscous stress at the surface,  $We = \frac{d \rho v_\infty^2}{\gamma}$ ;  $\gamma$  is the surface tension, and  $\kappa_{(n)}^{(\xi\eta)}$  and  $\kappa_{(n)}^{(\xi\phi)}$  are normal curvatures in two perpendicular directions.

#### Numerical scheme

In order to solve Eqs. (7) and (8) of the preceding section, together with Eqs. (5a) and (5b) for the mapping functions  $x(\xi, \eta)$  and  $\sigma(\xi, \eta)$ , we used a uniform  $41 \times 41$  grid in the domain,  $0 \leq \xi, \eta \leq 1$ . The computations were carried out using single precision arithmetic on a VAX-11 computing system, which has a round-off error of  $O(10^{-6})$ . Thus, with an  $O(h^2)$  finite-difference scheme, this mesh size represents the practical limits of resolution in order that truncation error be comparable to this round-off error divided by  $h^2$  (when computing second derivatives).

The numerical scheme itself must be fast, highly stable and applicable to elliptic equations of quite general form. In the work reported here, we adopt the ADI scheme of Peaceman and Rachford and treat all equations of the problem (i.e. the equations of motion for  $\zeta$  and  $\psi$ , and the two mapping equations for  $x$  and  $\sigma$ ) as "quasi-time-dependent", by writing them in the standard form

$$\frac{\partial w}{\partial t} = q_1 \frac{\partial^2 w}{\partial \xi^2} + q_2 \frac{\partial^2 w}{\partial \eta^2} + q_3 \frac{\partial w}{\partial \xi} + q_4 \frac{\partial w}{\partial \eta} + q_5 w + q_6 \quad (19)$$

with  $\partial/\partial t$  representing a "fictitious" (or artificial) time derivative as required by ADI. An optimal value of the iteration parameter (i.e. time step) was determined<sup>14</sup> to be  $O(h)$ .

Boundary conditions for Eqs. (3), (5) and (6) are straightforward [see Eqs. (13)-(16) plus Ref. 6], with the exception of conditions at the bubble surface. Here, the necessary boundary values of vorticity are calculated indirectly from the boundary condition (16) on tangential stress using a natural extension of the method for a solid boundary suggested by Dorodnitsyn and Meller<sup>15</sup> and Israeli<sup>16</sup> and utilized previously for a spherical drop.<sup>17</sup> At each new iteration, say  $n$ , the new value of the boundary vorticity  $\zeta^n$  is determined from its previous value and the previous value of the tangential stress, as

$$\zeta^n = \zeta^{n-1} + \beta \left( -2\kappa \frac{(\zeta\eta)}{(n)} u_s^{n-1} - \zeta^{n-1} \right) \quad (20)$$

where the optimal  $\beta$  was found (by trial and error) to be approximately 0.2. When the solution has converged, of course, the tangential stress will be zero. Boundary conditions for  $x(\xi, \eta)$  and  $\sigma(\xi, \eta)$  at  $\xi = 1$  must also be discussed briefly. Both  $x$  and  $\sigma$  cannot be specified directly at  $\xi = 1$  if the condition  $g_{12} = 0$  is satisfied (i.e. the coordinates are to be orthogonal) as the problems for  $x$  and  $\sigma$  are then overdetermined. We would, on the other hand, like to approach the final solution for bubble shape iteratively starting from some initial guess. This involves incrementing the bubble boundary to create a new shape at each iteration, based upon the normal stress imbalance at the interface at the preceding iteration. However, in view of the restriction on simultaneous specification of  $x$  and  $\sigma$ , the necessary small displacement of the bubble boundary must be carried out indirectly rather than specifying increments in  $x(1, \eta)$  and  $\sigma(1, \eta)$  directly. This is accomplished by changing the mapping itself (rather than the position of the bubble surface) via incremental changes in the scale factor  $h_\xi$  of the mapping, i.e.

$$h_\xi^{(n+1)} \Big|_{\xi=1} = h_\xi^{(n)} \Big|_{\xi=1} \left( \frac{4\tau}{(\text{vol})^n} \right)^{1/3} + \beta_G \Delta^n \quad (21)$$

where  $\Delta^n$  is the normal stress imbalance at iteration  $n$ ,

$$\Delta = -\frac{3}{4} C_D x - p_d + \tau_{nn} + \frac{4}{We} \left( \kappa \frac{(\zeta\eta)}{(n)} + \kappa \frac{(\zeta\phi)}{(n)} \right). \quad (22)$$

The incremented  $h_\xi \Big|_{\xi=1}$  is then used to generate "equivalent" boundary conditions for

$$\frac{\partial x}{\partial \xi} \Big|_{\xi=1} \quad \text{and} \quad \frac{\partial \sigma}{\partial \xi} \Big|_{\xi=1} \quad (23)$$

The normal stress difference,  $\Delta$ , has to be normalized before it is used in (21) for changing the bubble shape because of the indeterminacy due to incompressibility ( $\Delta$  contains an integration constant); this indeterminacy is removed by requiring that the volume of the bubble remain constant.

The overall solution algorithm may thus be schematically represented as follows:

- (1) Start with an initial guess of the shape. Here we choose a spherical shape, i.e. a circle in a plane through the axis of symmetry. Hence, with  $f(\xi, \eta) = \pi\xi$  as indicated earlier, the mapping is initially  $x = \xi \cos \eta$  and  $y = \xi \sin \eta$ , corresponding to polar coordinates in the plane through the axis of symmetry.
- (2) For the given bubble shape and coordinate mapping, compute a new approximation for the dynamic fields ( $\psi$  and  $\tau$ ) by advancing the solution of the Navier-Stokes equations one iteration (i.e. one ADI time step).
- (3) Calculate the normal stress terms at the bubble surface, and if the condition (17) is not satisfied, increment the bubble shape by a small amount by incrementing  $h_\xi(1, \eta)$  using Eq. (21), and obtaining corresponding boundary conditions for  $\partial x/\partial \xi \Big|_{\xi=1}$  and  $\partial y/\partial \xi \Big|_{\xi=1}$ .
- (4) Calculate a new orthogonal mapping fitting the new bubble shape by solving Eqs. (5a,b) with appropriate boundary conditions (in practice we do only one ADI iteration on the mapping equations).
- (5) Repeat this process starting with step (2) until convergence is achieved.

### Results

We consider two cases here of streaming flow past a bubble.

Case A:  $Re = 2.47$ ,  $We = 4.00$

Case B:  $Re = 100.$ ,  $We = 2.00$

The final bubble shape is depicted for Case A in Fig. 1, where we show a portion of the final coordinate mesh and the upper half of the bubble boundary in the plane through the axis of symmetry. The flow is from left to right. The corresponding streamlines and lines of constant vorticity are shown in Figs. 2 and 3. It may be noted that the bubble shape is in qualitative agreement with available experimental results.<sup>18</sup> Indeed, the drag coefficient calculated here is 9.17, whereas the measured value at the same Reynolds number but somewhat larger  $We$  was 9.37. It may be noted that the drag coefficient was found experimentally<sup>18</sup> to be insensitive to  $We$  for large  $We$ . The streamlines and lines of constant vorticity for Case B are shown in Figs. 4 and 5, from which the bubble shape can also be discerned. Again, the flow is from left to right. It is thus evident that the bubble is actually flattened to a greater degree in the front and is more rounded at the rear. Shapes of this general type have been previously observed experimentally for similar values of  $Re$  and  $We$ ,<sup>19</sup> although a shape which is rounded in the front and flattened at the rear, which will occur for larger Reynolds number or larger Weber number, i.e. smaller surface tension, is much more common. Each example required about an hour of CPU time on a VAX-11 computer, starting from the irrotational flow past a sphere as an initial guess in both cases. The cost is thus on the order of \$10.

#### Acknowledgments

This work was supported by a grant from the fluid mechanics program of the National Science Foundation.

#### References

1. Taylor, T. D. and Acrivos, A., "On the Deformation and Drag of a Falling Viscous Drop at Low Reynolds Number", *J. Fluid Mech.* **18**, 466-476 (1964).
2. Cox, R. G., "The Deformation of a Drop in a General Time-Dependent Fluid Flow", *J. Fluid Mech.* **37**, 601-623 (1969).
3. Youngren, G. K. and Acrivos, A., "On the Shape of a Gas Bubble in a Viscous Extensional Flow", *J. Fluid Mech.* **76**, 433-442 (1976).
4. Miksis, M., Vanden-Broeck, J.-M. and Keller, J. B., "Axisymmetric Bubble or Drop in a Uniform Flow", *J. Fluid Mech.* **108**, 89-100 (1981).
5. Rallison, J. M., "A Numerical Study of the Deformation and Burst of a Viscous Drop in General Shear Flows", *J. Fluid Mech.* **109**, 465-482 (1981).
6. Ryskin, G. and Leal, L. G., "Orthogonal Mapping", submitted to *J. Comp. Phys.*
7. Thames, F. C., Thompson, J. F., Mastin, C. W. and Walker, R. L., "Numerical Solutions for Viscous and Potential Flow about Arbitrary Two-Dimensional Bodies Using Body-Fitted Coordinate Systems", *J. Comp. Phys.* **24**, 245-273 (1977).
8. Fornberg, B., "A Numerical Method for Conformal Mapping", *SIAM J. Sci. Stat. Comput.* **1**, 386-400 (1980).
9. Starius, G., "Constructing Orthogonal Curvilinear Meshes by Solving Initial Value Problems", *Numer. Math.* **28**, 25-48 (1977).
10. Davies, C. W., "An Initial Value Approach to the Production of Discrete Orthogonal Coordinates", *J. Comp. Phys.* **39**, 164-173 (1981).
11. Pope, S. B., "The Calculation of Turbulent Recirculating Flows in General Orthogonal Coordinates", *J. Comp. Phys.* **26**, 197-217 (1978).
12. Hung, T.-K. and Brown, T. D., "An Implicit Finite-Difference Method for Solving the Navier-Stokes Equation Using Orthogonal Curvilinear Coordinates", *J. Comp. Phys.* **23**, 343-353 (1977).
13. Mobley, C. D. and Stewart, R. J., "On the Numerical Generation of Boundary-Fitted Orthogonal Curvilinear Coordinate Systems", *J. Comp. Phys.* **34**, 124-135 (1980).
14. Ames, W. F., "Numerical Methods for Partial Differential Equations", Barnes and Noble, New York, 1969.
15. Dorodnitsin, A. A. and Meller, N. A., "Approaches to the Solution of Stationary Navier-Stokes Equations", *U.S.S.R. Comput. Math. & Math. Phys.* **3**(2), 205-217 (1968).
16. Israeli, M., "A Fast Implicit Numerical Method for Time Dependent Viscous Flows", *Stud. Appl. Math.* **49**, 327-349 (1970).
17. Rivkind, I. Ya. and Ryskin, G., "Flow Structure in Motion of a Spherical Drop in a Fluid Medium of Intermediate Reynolds Numbers", *Fluid Dyn.* **11**, 5-12 (1976).
18. Bhaga, D. and Weber, M. E., "Bubbles in Viscous Liquids: Shapes, Values and Velocities", *J. Fluid Mech.* **105**, 61-85 (1981).
19. Clift, R. C., Grace, J. R. and Weber, M. E., "Bubbles, Drops and Particles", Academic Press, 1978.

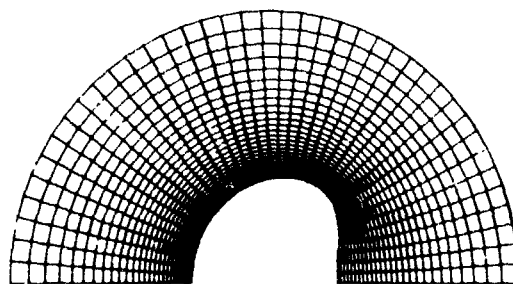


Figure 1. Coordinate mesh for Case A.

ORIGINAL PAGE IS  
OF POOR QUALITY

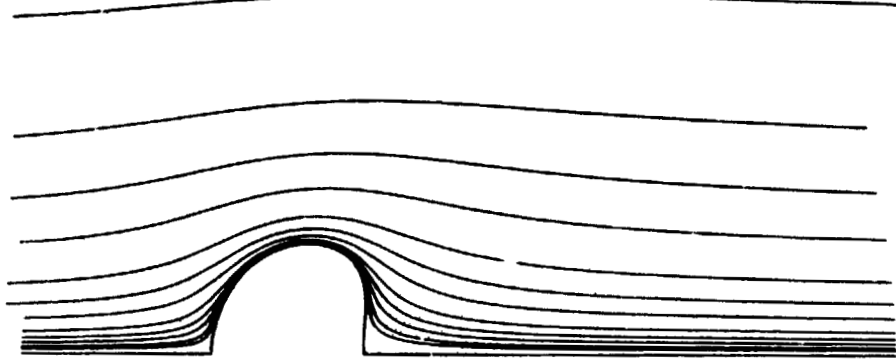


Figure 2. Streamlines for Case A.

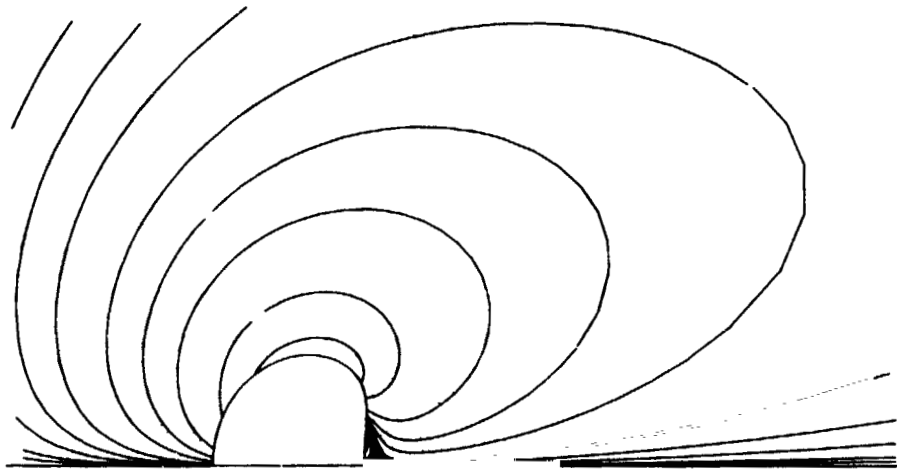


Figure 3. Lines of constant vorticity for Case A.

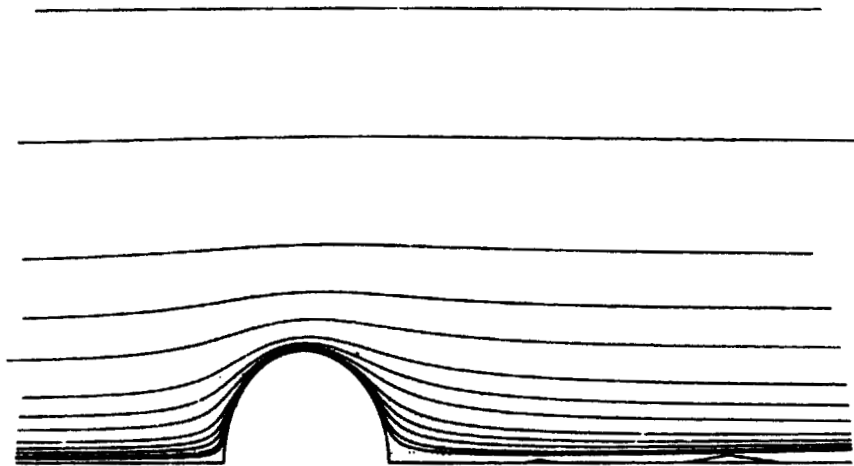


Figure 4. Streamlines for Case B.

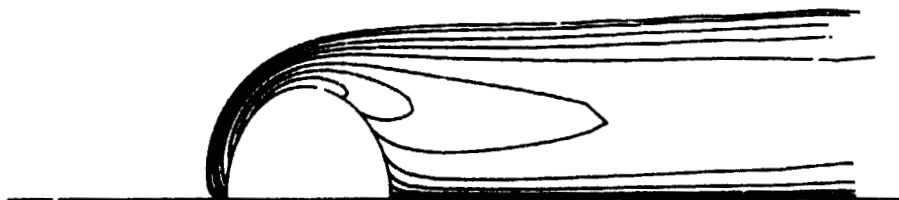


Figure 5. Lines of constant vorticity for Case B.

The production of drops by the bursting of a bubble  
at an air liquid interface

J.S. Darrozès and P. Ligneul  
Université Paris VI, Campus Univ. Bat 502 Orsay, Orsay, FRANCE 91405

Abstract

This work describes the fundamental mechanism arising during the bursting of a bubble at an air-liquid interface. A single bubble is followed from an arbitrary depth in the liquid, up to the creation and motion of the film and jet drops. Several phenomena are involved and their relative order of magnitude is compared in order to point out the dimensionless parameters which govern each step of the motion. Furthermore, this study is completed by high speed cinematography. The characteristic bubble radius which separates the creation of jet drops from cap bursting without jet drops is shown to be  $a = (\sigma/\rho g)^{1/2}$ . The corresponding numerical value for water is 3 mm and agrees with experimental observations.

Introduction : physical mechanisms description

The burst of gas bubbles on a liquid interface leads to a mass transfer in stratified two-phase flows which is of great importance in many fields such as ocean-atmosphere exchanges, aerosol generation, boilers, degazeification processes, etc... The physical mechanisms of such a phenomenon are still not wellknown. The burst occurs during a few tens of microseconds and involves many physico-chemical effects. The film cap draining is due to gravity and surface tension and its thickness (in the range of 0.5 to  $10^{-3}$  micrometers) may be small enough to produce non negligible intermolecular forces which depend on the impurities contained in the liquid phase. The film cap breakage generates an aerosol which is usually split into two distinct families which are the "film drops" and the "jet drops".

. The film drops are created by the tearing of the interfacial cap which propagates from an initial hole at a very high speed (8 m/s). Due to the tangential motion of the liquid film, some drops are ejected horizontally and the others are blown vertically by the air which was initially inside the bubble. Another possible mechanism is the sudden shattering of the whole cap which bursts into droplets in any direction. Film drops are very small (1 - 20  $\mu\text{m}$ ) and their number increases with the initial bubble diameter  $\phi_b$  (about 100 when  $\phi_b = 2$  mm, and 1000 when  $\phi_b = 6$  mm). They are ejected up to a height in the order of 10 to 20 mm above the free surface level.

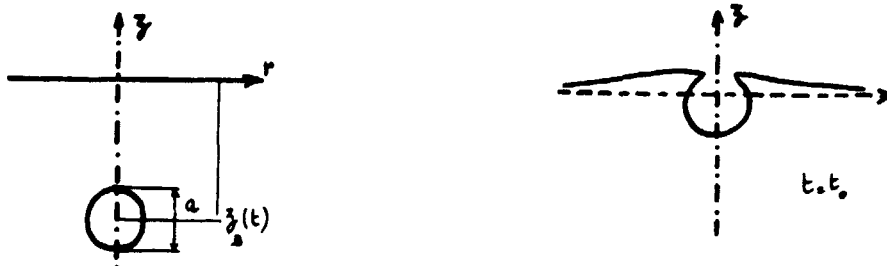
. The jet drops are produced by the very fast motion of the bubble bottom interface which is in a state of non-equilibrium when the film cap breaks. Instantaneously, gravity and surface tension act to create a strong interface deformation and give rise to the formation of a jet in the upward direction. Because of instabilities, the liquid jet is fragmented into several drops (from 1 to 5 depending on the bubble diameter  $\phi_b$ , in the range 6 mm to 0.1 mm). For values of  $\phi_b$  less than 2 mm, the ejection height of jet drops may reach 100  $\phi_b$  above the free surface level.

These two families lead to a transfer in the gas of two different kinds of chemical substances, namely the surfactants spread on the free surface (film drops) and the particules in suspension or dissolved inside the liquid (jet drops).

The aim of this paper is to consider a dimensional analysis of aerosol production in order to reach a better understanding of the phenomena involved during the bursting of the bubble. The notion of dimensionless parameters, characteristic times and predominant mechanisms may be used to define simplified experimental studies and to search for approximate analytical solutions. In what follows, several effects are analyzed :

- underwater bubble rising - film drainage - cap tear propagation
- film drops ejection - free surface motion after film cap rupture.

Underwater bubble rising



The dimensionless form of equations governing the relative liquid flow past the bubble is written with the characteristic bubble size  $a$ , the pressure variation  $\rho a g$  (involving the liquid density  $\rho$  and the acceleration  $g$  gravity) and an unknown characteristic time  $\tau$  which leads to the reference velocity  $a/\tau$ . The bubble motion is obtained from the fundamental dynamic law :

$$F = \iint_{ab} \left[ -p_{loc.} + \frac{2\nu}{g\tau a} \underline{D} \cdot \underline{n} \right] \cdot \underline{n} ds = 0 \quad (1)$$

in which the symmetric part  $\underline{D}$  of the velocity gradient  $\underline{\nabla v}$  and the local pressure  $p_{loc.}$  are given by the Navier-Stokes equation :

$$\frac{d^2 z_B}{dt^2} + \frac{dv}{dt} + \nabla(p_{loc.} - z) \frac{g\tau^2}{a} = \frac{\nu\tau}{a^2} \Delta v \quad (2)$$

The bubble shape is deduced from the normal stress equilibrium

$$p_i = p_{loc.} + \frac{p_a}{\rho g a} + z_B(t) - \frac{2\nu}{g\tau a} (\underline{D} \cdot \underline{n}) \cdot \underline{n} + \frac{4\sigma}{\rho g a^2} C \quad (3)$$

$\underline{n}$  is the unit normal vector,  $p_i$ ,  $C$ ,  $\nu$  and  $\sigma$  respectively stand for the internal bubble pressure, the mean curvature, the dynamic viscosity and the surface tension coefficient.

The local pressure is defined by the relation

$$p = \frac{p_a}{\rho g a} + z_B(t) + p_{loc.}$$

in which, for the most part, the constant  $p_a/\rho g a$  is much greater than unity.

It is easily seen, from equation (2), that high Reynolds number flows correspond to the characteristic time evolution  $\tau_g = (a/g)^{1/2}$ , and situations dominated by viscous effects are scaled by the reference time  $\tau_v = \nu/g$ . The relative Reynolds number :

$$R_r = a^3 g / \nu^2 = (a/a_1)^3 \quad (4)$$

leads to a characteristic length  $a_1 = (\nu^2/g)^{1/3}$  ( $\sim 50 \mu m$  for water). In equation (3), another length  $a_2 = 2(\sigma/\rho g)^{1/2}$  ( $\sim 6 \text{ mm}$  for water) is defined from the dimensionless number :

$$\Sigma = 4\sigma/\rho g a^2 = (a_2/a)^2 = (\tau_g/\tau_s)^2 \quad (5)$$

The new characteristic time  $\tau_s = \rho a^3/4\sigma$  concerns the interface vibrations due to the surface tension. Depending on the bubble diameter  $a$ , the following situations occur.

.  $a \gg a_2$ ,  $R_r \gg 1$ , motions due to surface tension are frozen, but the bubble can oscillate with instationary terms of equation (3) (bubble wake for instance) on the time scale  $\tau_g$ .

.  $a_1 \ll a \ll a_2$ ,  $R_r \gg 1$  but the non stationary terms in equation (3) are negligible and the bubble keeps its spherical shape.

.  $a \ll a_1$ ,  $R_r \ll 1$  and the comparison between the last two terms of equation (3) leads to a new length  $a_3 = \rho \nu^2/2\sigma$  ( $\sim 5 \cdot 10^{-3} \mu m$  for water). Bubble diameters less than  $a_3$  will not be considered in this paper. Therefor surface tension is the dominant phenomenon and deformations cannot occur. We will write  $\pi = a_3/a = \rho \nu^2/2\sigma a$  (always less than unity for water).

The characteristic velocities of the rising motion are  $(ag)^{1/2}$  when  $a > a_1$  and  $\frac{1}{18} \frac{a^2 g}{\nu}$  (stokes drag) when  $a < a_1$ .

#### Film draining

There are two fundamental mechanisms which cause the film draining, when the bubble arrives on the free surface. First, the gravity which creates the bubble motion and inertia terms (when  $a > a_1$ ) increases the local pressure  $p_a$  on the free surface. On the relative stagnation point, this increase is of the order of  $\rho g a$ . Secondly, the free surface curvature leads to a pressure increment in the order of  $4\sigma/a$ . Comparison between both phenomena

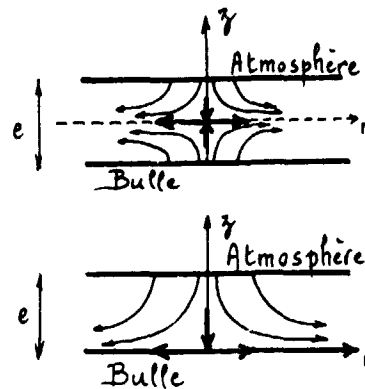
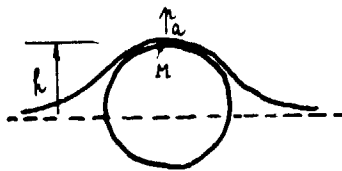
is given by the value of  $\Sigma = 4\sigma/\rho a^2$  introduced in the last paragraph. Consequently, for bubble diameters larger than  $a_2$ , the effect of gravity is predominant, and for  $a_1 \ll a \ll a_2$  the surface tension plays the most important role.

A very crude analysis for  $\Sigma \ll 1$  shows that (from the continuity equations) the liquid pushed up by the rising of the bubble (order  $\frac{\pi}{4} a^2 \sqrt{ag}$ ) must be evacuated through the lateral surface of a cylinder ( $\pi a h \sqrt{ag}$ ). This balance gives an order of magnitude of the height below the free surface which must be reached by the bubble top before undergoing a non negligible free surface deformation. When  $a_1 \ll a \ll a_2$ , the characteristic bubble rising velocity  $\sqrt{ag}$  has not the same order of magnitude as the characteristic velocity due to the surface tension pressure drop :  $(4\sigma/\rho a)^{1/2}$  and the same crude analysis leads to :

$$\frac{\pi}{4} a^2 \sqrt{ag} = 2 \pi a h (\sigma/\rho a)^{1/2} \text{ and } h = \frac{a}{4\Sigma^{1/2}} \ll a$$

For very small bubble ( $a_3 \ll a \ll a_1$ ), the same trivial argument gives :

$$h = a \pi^{1/2} \ll a$$



The characteristic draining time is easily deduced from the above considerations, and from the volume to be drained ( $\sim \frac{\pi a^3}{16}$  when  $\Sigma \ll 1$  ;  $\frac{\pi a^3}{4\Sigma^{3/2}}$  when  $a_1 \ll a \ll a_2$  ; and  $2 \pi a^3 \pi^{3/2}$  when  $a \ll a_1$ ). One obtains respectively for each situation  $\tau_d = \tau_g/4$ ,  $\tau_g/2\Sigma$ ,  $\sqrt{2} \tau_V \pi^{1/4} R_T$ . As an example in each case, one obtains respectively for  $a = 1$  cm, 1 mm and 10  $\mu$ m, the following values :  $\tau_d = 0.07$  s, 4 ms and 0.5 ms, in water. The end of drainage in the first two cases is governed by viscous effects when the Reynolds number based on the film thickness  $e$  is of order unity i.e.  $e \sim \nu/(ag)^{1/2}$  when  $\Sigma \ll 1$  and  $e \sim \nu(\rho a/\sigma)^{1/2}$  when  $\Sigma \gg 1$ . These limiting thicknesses in water are respectively 3  $\mu$ m and 0.3  $\mu$ m when  $a = 1$  cm and  $a = 1$  mm. At this stage, it is necessary to be very careful about the boundary conditions to be written on the film boundaries. For very dirty liquids, Haberman and Morton have shown that a vanishing velocity condition must be considered. In any case, one must take into account the influence of Van der Waals intermolecular forces which are, for a clean liquid, given under the form of a non isotropic tension in the normal direction to the film. Its value for a thickness  $e$  is (Sheludko):

$$\tau = \frac{4 \cdot 10^{-21}}{e^3} \text{ (MKSA units)}$$

this influence is non-negligible when the pressure gradient is of the same order :

$$a > a_2 (\Sigma \ll 1), \rho g \sim \frac{4 \cdot 10^{-21}}{e^4} \text{ and } e \sim \frac{5 \cdot 10^{-6}}{(\rho g)^{1/4}} = 0.5 \mu\text{m}$$

$$a < a_2 (\Sigma \gg 1), \frac{\sqrt{2}\sigma}{a^2 \Sigma^{1/4}} \sim \frac{4 \cdot 10^{-21}}{e^4} \text{ and } e \sim 10^{-5} a^{1/2} \text{ M.K.S.A. (0.3 } \mu\text{m when } a = 1 \text{ mm).}$$

These orders of magnitude for the film thickness is in agreement with the experimental evaluations.

### Cap tear propagation



Assuming that a hole is created instantaneously, the driving force is due to surface tension and leads to a characteristic velocity :  $v_f = (\sigma/\rho e)^{1/2}$ . If the characteristic thickness  $e \sim 1 \mu\text{m}$  is admitted, it follows that in water ( $\sigma \sim 0.07$ ) the tear propagates with a velocity of 8 m/s which is exactly the value observed experimentally with a high speed camera. This evaluation is valid, only when the liquid flow inside the film is dominated by the inertia terms. This happens for a local Reynolds number greater than unity :

$$R_f = \frac{v_f e}{\nu} \gg 1 \rightarrow e \gg \frac{\rho \nu^2}{\sigma} (= 0.01 \mu\text{m})$$

So, it is obvious that the experimental study of cap tear breaking may be performed without any precaution because any other phenomenon is frozen with respect to cap tear propagation. This has been done in the movie presented at the end of this paper.

This experiment shows the cap tear of a large bubble ( $\phi_b = 4 \text{ cm}$ ) at rest on the free surface of ordinary drinkable water. The hole is created on the circle which delimits the bubble cap on the free surface. It is due to a much smaller bubble sticking to the larger one and which causes a point of weakness. Some papers (Vrij, Ivanov, ...) explain the film breaking by the non stable modes of capillarity waves, but this is probably true for bi-distilled water only.

### Film drops ejection

The very complex nature of film cap fragmentation is not investigated in this paper, but we will consider the behaviour of a film droplet assumed to have a size in the order of  $1 \mu\text{m}$

The blowing-out is due to the fact that the pressure level inside the bubble before breaking is larger than on the outside. The sudden pressure drop is of order  $\rho_a g$  when  $\Sigma \ll 1$  and  $a/a$  when  $\Sigma \gg 1$ . For high Reynolds number gas flows, this produces velocities of order  $(\rho_L g / \rho_G)^{1/2}$  or  $(\sigma/a \rho_G)^{1/2}$ . For each case, the gas Reynolds number is :

$$R_G = \left( \frac{\rho_L g}{\rho_G} \right)^{1/2} \frac{a^{3/2}}{v_G} \gg 1 \text{ if } a \gg 5 \mu\text{m} \text{ (air and water)}$$

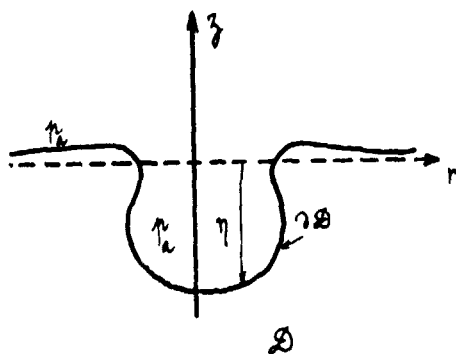
$$R_G = \left( \frac{\sigma a}{\rho_G \nu^2} \right)^{1/2} \gg 1 \text{ if } a \gg 0.1 \text{ \AA} \text{ (air and water)}$$

The characteristic time of a particule transport due to the viscous drag is  $\tau = \rho r^2 / \nu_G \rho_G$ , where  $r$  denotes the particule radius. For a micronic droplet this time is 1 millisecond, as a result, film drops follow instantaneously the air flow produced by the breaking. For bubble diameters : 1 cm, 1 mm, 10  $\mu\text{m}$ , the initial velocity of droplets are respectively : 10 m/s, 10 m/s and 100 m/s.

Experimentally, it is known that a 10  $\mu\text{m}$  bubble does not produce any film drops, but one can see that for most bubbles, there is a strong interaction between the cap tear propagation (8 m/s) and the air ejection (10 m/s). If the air flow is roughly supposed to be similar to a source flow, the velocity  $V_r$  at a distance  $r$  is given by  $V_r = V_1 (a/2r)^2$ . A numerical value of  $V_r$  with  $a = 1 \text{ mm}$  and  $r = 1 \text{ cm}$  is 2.5 cm/s (less than 1 km/h). This argument proves that film drops are immediately convected by the wind in ocean-atmosphere exchanges.

### Free surface motion after film cap rupture

It has been shown that film tear propagation occurs instantaneously with respect to the bubble rising velocity. This result is confirmed by Mac Intyre's visualisations and by the photographs given in the present paper. As a result, the curvature of the bubble is greater at the bottom than the sides. This causes stronger surface tension forces on the deepest part of the bubble interface and produces the jet when the surface tension phenomenon is not negligible with respect to the gravity effect.



The dimensionless equations governing the free surface motion are written assuming a potential flow ( $v = \nabla\phi$ ) for the liquid phase. It will be proved, later on, that inertia dominates the viscous terms. In a cylindrical coordinates system, the bubble diameter  $a$  is chosen as the reference length in the radial and vertical directions. The characteristic time  $T$  needed for the free surface  $z = \eta(r, t)$  to reach an altitude of order  $a$  is unknown at this stage.

$$\frac{\phi_0}{T} \frac{\partial \phi}{\partial t} + \frac{\phi_0^2}{2a^2} (\nabla\phi)^2 + \frac{\sigma}{\rho a} \left( \frac{z}{a} - C \right) = 0 \quad (5)$$

$$\frac{a}{T} \frac{\partial \eta}{\partial t} + \frac{\phi_0}{a} \left( \frac{\partial \eta}{\partial r} \cdot \frac{\partial \phi}{\partial r} - \frac{\partial \phi}{\partial z} \right) = 0 \quad (6)$$

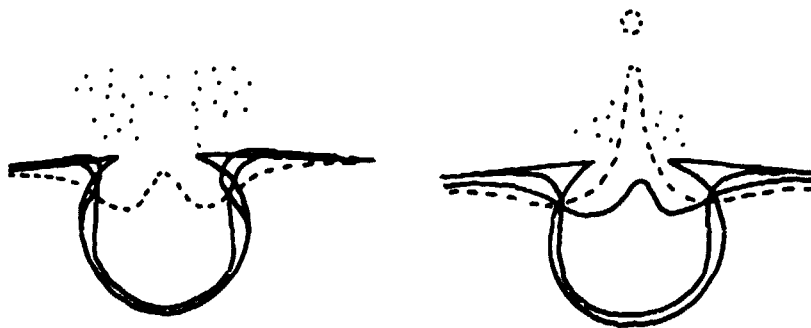
The reference potential  $\phi_0$  and the time  $T$  are obtained from the free surface boundary conditions. Equation (6) leads in any case to the relation  $\phi_0 = a^2/T$ . From equation (5), the characteristic time  $T$  depends on the comparison between  $\Sigma^{-1} = \rho g a^2/4$  (gravity) and the mean dimensionless curvature  $C$  which is of order unity.  $\Sigma \gg 1$ : surface tension is the dominant phenomenon and  $T = \rho a \phi_0 / \sigma = \rho a^3 / \sigma T$ . The characteristic time and velocity are respectively:

$$T = (\rho a^3 / \sigma)^{1/2} \text{ and } V = (\sigma / \rho a)^{1/2}$$

$\Sigma \ll 1$ : the free surface motion is governed by the gravity effect. One obtains respectively

$$T = (a/g)^{1/2} \text{ and } V = (ag)^{1/2}$$

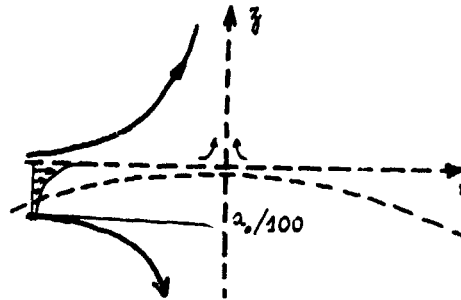
These results are valid only for high Reynolds number flows. When  $\Sigma \gg 1$  ( $a \ll a_2$ , 0.6 cm for water)  $R = aV/\nu = (a\sigma/\nu^2)^{1/2}$  which is larger than unity for bubble diameters larger than  $a = \nu^2/\sigma$  (0.01 m for water). When  $\Sigma \ll 1$ ,  $R = (a^3g/\nu^2)^{1/2}$  and the bubble diameter must be larger than  $a_1 = (\nu^2/g)^{1/3}$  (50  $\mu\text{m}$  for water). This condition is always fulfilled because  $a \gg 0.6$  cm.



The characteristic bubble diameter  $a_2 = (4\nu/\sigma)^{1/2}$  splits the possible free surface behaviours into two classes:

$a > a_2$  : the film cap rupture leads only to free oscillations of the free surface without jet, but many film droplets are blown into the atmosphere.

$a < a_2$  : the predominance of the surface tension effect leads to a strong driving force at the bottom of the bubble which produces a jet. Surface tension forces still act on the jet surface and cause pressure gradients along the jet axis, oriented from the smallest sections to the largest ones. The draining of the lowest sections due to this mechanism leads to the jet breaking into one or several drops.



The dimensionless equation (5) shows that the gravity effect becomes important for a dimensionless  $z$  of order  $\Sigma$ . So the jet top can reach an altitude of order  $a\Sigma$ . The experimental evaluation :  $100 a$ , given in the introduction corresponds to  $a = 0.6$  mm and an altitude of 60 cm. Dissipations due to viscous effects are given by the Reynolds number  $R = (a_0/\rho v^2)^{1/2} \sim 8.10$  for a 0.6 mm bubble diameter. In that case, the boundary layer on the free surface, in which viscous draining occurs has a thickness in the order of a hundredth of a bubble diameter.

#### Flow visualisation

The photographs given in this section have been obtained with a high speed camera HYCAM (7500 images per second in the present case). The first sequence represents a cap tear which propagates on a 4 cm bubble diameter, from a small bubble ( $\sim 1$  mm) which was initially attached to the large one on the free surface. One can observe that some droplets tangentially ejected by the tear motion have a much larger size than 1 micrometer.

The next two sequences show jet drops due to a 1 mm bubble diameter. In "JET N°1", the hole created instantaneously by the breaking of the film is shown. The jet thickness is of order 0.1 mm corresponding to velocities of order  $\sqrt{\sigma/\rho d_j} \sim 1$  m/s. The half-sphere in the upper part of each view is a liquid drop sticking on the end of a 1 mm cylindrical wire placed there to give an indication of the length scale. The "JET N°2" gives more details on the jet breaking mechanism. One can observe that the top drop has no motion during its growth, but its upward motion continues after its creation.

#### Concluding remarks

This paper is a first step in the study of aerosols created by bursting bubbles on an air-liquid interface. Jet drops have been studied and visualized in the past ; however a theoretical model for the prediction of the size and number of the drops would be useful for a better understanding of the jet breaking mechanisms.

Nevertheless, the lack of knowledge is more important for film droplets and a lot of experimental work will be necessary in order to visualize the film breaking and to predict the full size distribution of aerosols in a real industrial stratified two-phase flow figuration.

This study has been supported by a CNRS\* contract.

\* Centre National de la Recherche Scientifique (France).

ORIGINAL PAGE IS  
OF POOR QUALITY

References

Azhel, D. S. and TS LEE : "Acoustic resonance theory for the film cap of a gas bubble at a horizontal gas-liquid interface". Int. Conf. on momentum, Heat and mass transfer in two phase system. Dubrovnik, september 1970.

Blanchard, D.C. : "The Electrification of the Atmosphere by Particles from Bubbles in the Sea". Extr. de "Progress in Oceanography", Vol.1, pp. 73 & 202, Pergamon Press, 1963.

Blanchard, D.C. and Syzek, L.D. : "Concentration of Bacteria in Jet drops from Bursting Bubbles". Journal of Geophysical Research, Vol.77, n° 22, september 1972.

Detwiller, A. and Blanchard, D.C. : "Aging and Bursting Bubbles in Trace-Contaminated Water". Chemical Engineering Science, Vol.33, pp. 9-13, Pergamon Press, 1978.

Ivanov, I.B., Radoev, B., Manev, E. and Scheludko, A. : "Theory of the Critical Thickness of Rupture of Thin Liquid Film". Transactions of the Faraday Society, 66, n° 569, part.5, pp. 1262-1273, may 1970.

Kientzler, C.F., Arons, A.B., Blanchard, D.D. and Woodcock, A.H. : "Photographic Investigation of the Projection of Droplets by Bubbles Bursting at a Water Surface". Tellus, Vol.6, n° 1, pp. 1-7, february 1954.

McIntyre, F. : "Bubbles : A Boundary Layer "Microtome" for Micron-Thick Samples of a Liquid Surface". Journal of Physical Chemistry, Vol.72, n° 2, pp. 589-592, february 1968.

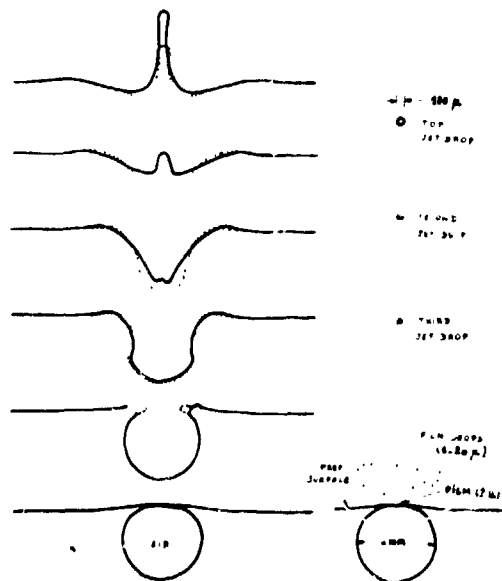
McIntyre, F. : "Flow Patterns in Breaking Bubbles". Journal of Geophysical Research, Vol.77, n° 27, pp. 5211-5228, september 1972.

McIntyre, F. : "Non-Lipid-Related Possibilities for Chemical Fractionation in Bubble Film Caps". J. R. O., pp. 515-527, 1974.

Quinn, J.A., Steinbrook, R.A. and Anderson, J.L. : "Breaking Bubbles and the Water-to-Air Transport of Particulate Matter". Chemical Engineering Science, Vol.30, pp. 1177-1184, Pergamon Press, 1975.

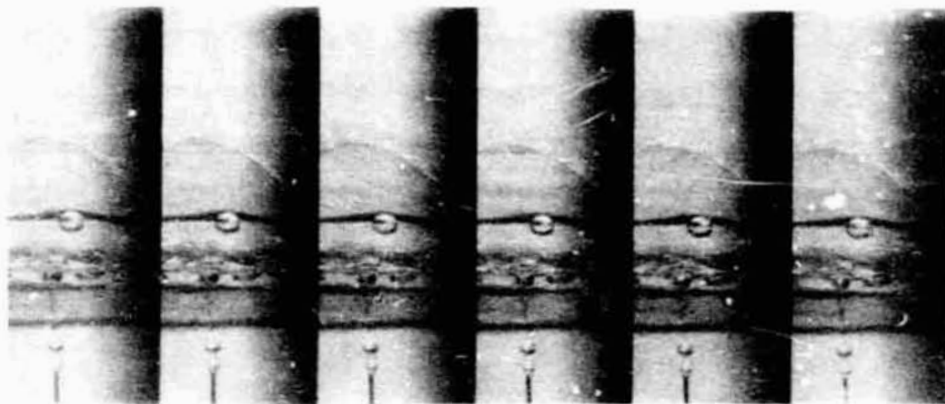
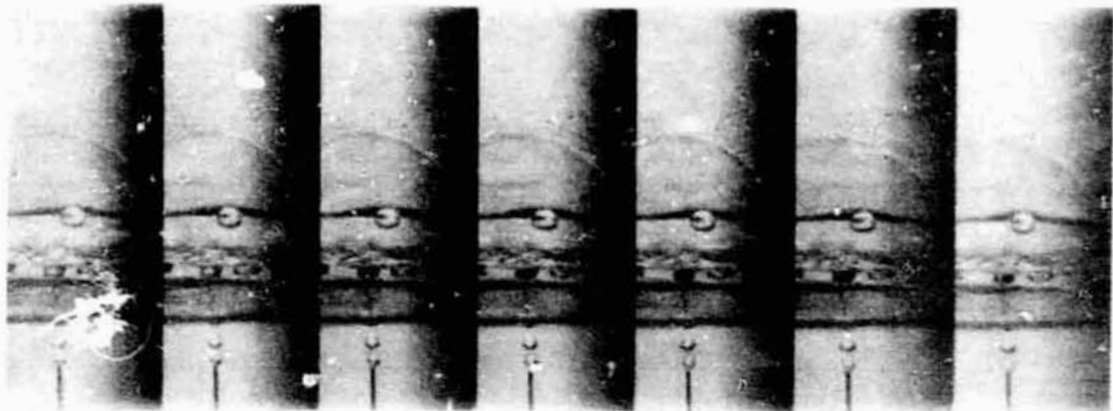
Scheludko, A. : "Thin Liquid Films". Advances in Colloid and Interface Science, t.1, pp. 391-464, 1967.

Toba, Y. : "Drop Production by Bursting of Air Bubbles on the Sea Surface, 2, Theoretical Study of the Shape of floating bubbles". J. Oceanogr. Soc. Jap., 15, 1, 1959.

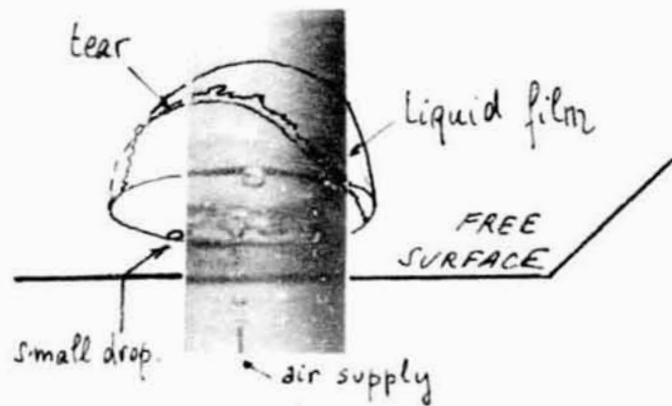


BUBBLE BURSTING AT AN AIR-LIQUID INTERFACE

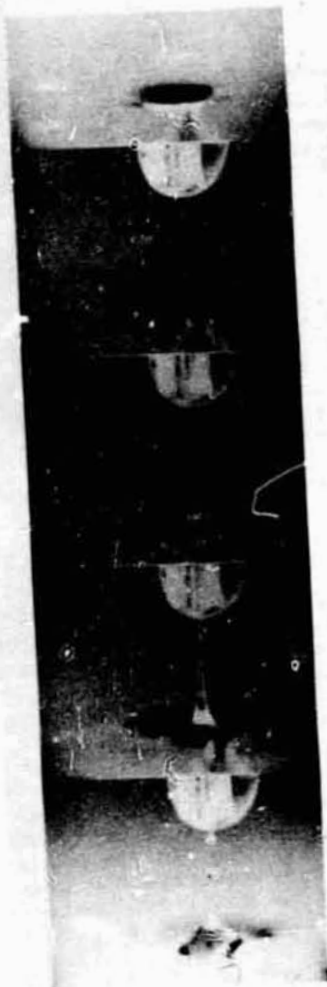
ORIGINAL PAGE  
BLACK AND WHITE PHOTOGRAPH



Film cap tear . 7.500 frames per second.



ORIGINAL PAGE  
BLACK AND WHITE PHOTOGRAPH



JET N:1



JET N:2

*Jet drops - 1.500 frames per second.*

**Resonances, Radiation Pressure, and Optical Scattering Phenomena of Drops and Bubbles**

P. L. Marston, S. G. Goosby,\* D. S. Langley, and S. E. LoPorto-Arione  
 Department of Physics, Washington State University, Pullman, Washington 99164

Abstract

Acoustic levitation and the response of fluid spheres to spherical harmonic projections of the radiation pressure are described. Simplified discussions of the  $l = 1, 2,$  and  $3$  projections are given. A relationship between the tangential radiation stress and the Konstantinov effect is introduced and fundamental streaming patterns for drops are predicted. Experiments on the forced shape oscillation of drops are described and photographs of drop fission are displayed. Photographs of critical angle and glory scattering by bubbles and rainbow scattering by drops are displayed.

Introduction

This paper summarizes research into resonance, acoustical, and optical properties of drops and bubbles. In addition to reviewing earlier work, models concerning tangential stresses, streaming, and the hexapole projection of the radiation pressure are given. These may be applicable to the enhancement of circulation in containerless conditions. New experiments are described. The methodology and notation are simplified from that in earlier papers to manifest the essential results. A review of research into optical properties of bubbles will be published separately<sup>1</sup> so that research is only briefly summarized (near the end of this paper) in a section which may be read independently of the others.

Acoustic Levitation

Experiments on a single drop with a stationary (or nearly so) center-of-mass are possible by counteracting gravitational buoyancy forces with forces due to acoustic radiation pressure. This technique has been particularly useful for obtaining physical properties of metastable liquids (for a review of this application see Ref. 2); however, the present paper is concerned with the mechanics of drops rather than the properties of the constituent fluid. The fluid in the drop is assumed to have a density  $\rho_i$ , sound speed  $c_i$ , and adiabatic compressibility  $\beta_i = (\rho_i c_i^2)^{-1}$ . It is assumed to be immiscible in the surrounding host fluid which has corresponding properties  $c_o, \rho_o,$  and  $\beta_o$ . The  $i$  and  $o$  diacritics refer to the inner and outer fluids, respectively. In the diagrams which follow, the  $z$  axis is chosen to be up, antiparallel to the acceleration of gravity. The incident acoustic wave (neglecting scattering) will usually be taken to have uniaxial flow parallel to the  $z$  axis. The time averaged stresses of the incident and scattered waves not only levitate the drop, they also change its shape.<sup>3</sup> These effects are roughly independent for small deformations and in this section the drop will be assumed to be spherical with a mean radius  $a$  with a center at  $z = 0$ .

To obtain sufficient radiation pressure forces to counteract buoyancy, the incident sound wave approximates a standing wave, which (for the case of uniaxial flow) has the following pressure  $p(z,t) = p_s \cos(kz + kh)\sin\omega t$  where  $k = \omega/c_s = 2\pi/\lambda$  and  $z = -h$  is the location of an adjacent velocity node. The average force vector  $\langle F \rangle$  of the fluid sphere due to the acoustic radiation pressure (which is second-order in  $p_s$ ) is<sup>4,5</sup>

$$\langle F \rangle = -2(\pi/3)a^3 p_s^2 k (\beta_i - \beta_o D) \sin 2kh, \quad D = (5q-2)/(2q+1), \quad (1a,b)$$

where  $\hat{z}$  is the  $z$  axis unit vector,  $q$  is  $\rho_i/\rho_o$ , and the effects of the viscosities of the inner and outer fluids have been neglected. The derivation of Eq. (1) assumes that both  $X \equiv ka \ll 1$  and  $X \ll X_m$  where  $X_m = a\omega/c_o$  and  $\omega$  is the lowest radial (or monopole) resonance frequency of the sphere. The latter requirement is due to the omission of the dynamical effects of resonance; in traveling waves these may be included by taking the appropriate case of an expression derived for elastic spheres (see discussion in Ref. 6 of Eq. 24). [It can be shown that the lowest non-zero root of  $(1-q)\tan X_i = X_i$  gives  $X_i = c_i X_m / c_o$ . Drops in liquids with  $|1-q| \ll 1$  have  $X_i \approx \pi/2$  and  $X_m \approx \pi c_i / 2c_o$ . Drops in air have  $q \gg 1$ ,  $X_i \approx \pi$  and  $X_m \approx \pi c_i / c_o$ . Gas bubbles have  $q \ll 1$  and  $X_m \approx (\beta_o/\beta_i)^{1/2} \ll 1$ .]

The cause of the term proportional to  $\beta_i$  is illustrated in Fig. 1. Assume that  $\beta_i \gg \beta_o$  and  $\rho_i \leq \rho_o$  so that  $\beta_i \gg \beta_o D$ . For  $0 < h \leq \lambda/4$ , as in Fig. 1,  $\langle F \rangle$  is directed downward

\*Present address: Naval Undersea Warfare Engineering Station, Keyport, WA 98345.

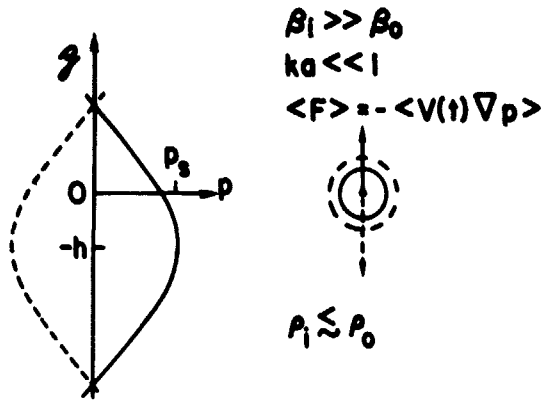


Fig. 1. The solid and dashed curves illustrate  $p$  of the incident wave for  $\omega t = \pi/2$  and  $3\pi/2$ , respectively. Quasi-static responses of the sphere and the associated instantaneous forces due to  $Vp$  are illustrated on the left.

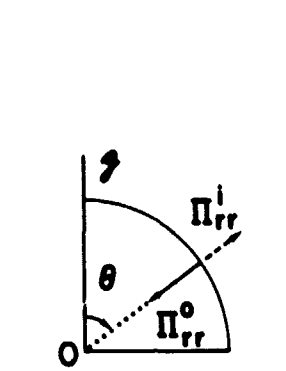


Fig. 2. Local mean stresses on a quadrant of the sphere's surface.

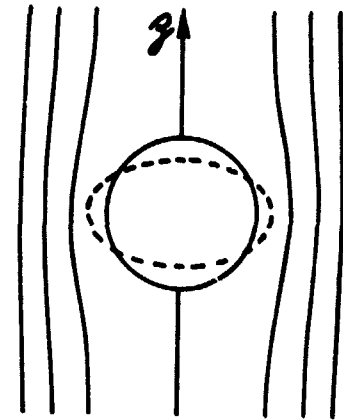


Fig. 3. Streamlines for inviscid low frequency flow past a sphere and (dashed) the favored deformation.

since the sphere's volume,  $V(t) = (4\pi a^3/3)[1 - \beta_0 p(0, t)]$ , is largest during that part of the cycle when  $(-Vp)$  is downward; conversely,  $\langle F \rangle$  is upward if  $\lambda/4 < h < \lambda/2$ . In a gravitational field  $g$ , there is an equilibrium position where  $\langle F \rangle = 24\pi a^3(\rho_1 - \rho_0)g/3$  provided  $p_s$  is sufficiently large. Equilibrium is slightly above a velocity node if  $\rho_1 < \rho_0$  and slightly below one if  $\rho_1 > \rho_0$ , provided  $\beta_0 D$  is negligible. For bubbles,  $\omega_0 = (3\beta_0 \rho_0 a^2)^{1/2}$  and if  $\omega > \omega_0$  the phase of the response is reversed from that shown in Fig. 1. The direction of  $\langle F \rangle$  is reversed so that the bubble is attracted to pressure nodes. There are ordinarily transverse pressure gradients which make the equilibrium unstable in this case.

For drops of hydrocarbon liquids in water,  $\beta_1 > \beta_0 D$  and the equilibrium position is close to a pressure antinode due to the phenomena illustrated in Fig. 1. Levitation apparatus often have a dependence of  $p_s$  transverse to the  $z$  direction which stabilizes the horizontal position. Typical designs<sup>2,4,8,9</sup> at ultrasonic frequencies require  $p_s \approx 2 \times 10^5$  Pa. The neglect, implicit in the derivations of Eq. (1), of viscous and thermal effects requires that the viscous ( $\delta_v^i$  and  $\delta_v^o$ ) and thermal ( $\delta_T^i$  and  $\delta_T^o$ ) penetration lengths be  $\ll a$ . These are given by  $\delta_v = (\nu/\omega)^{1/2}$  and  $\delta_T = (\chi/\omega)^{1/2}$  where, for the inner or outer fluid,  $\nu$  is the kinematic viscosity and  $\chi$  is the thermal diffusivity. For macroscopic drops the above conditions are satisfied and there is some experimental confirmation<sup>4,10</sup> of Eq. (1).<sup>11</sup> For microscopic objects, e.g., red blood cells, viscous corrections become significant.

For the levitation of liquid or solid spheres in air,  $(\beta_1 - \beta_0 D) \approx -\beta_0 5/2$  and Eq. (1) reduces to the well known expression first derived by King.<sup>12</sup> The sign of  $\langle F \rangle$  is reversed and equilibrium positions are near pressure nodes. Attraction to the velocity antinodes occurs because the average reduction in pressure due to the Bernoulli effect is strongest on that side of the drop. Equation (1) neglects harmonics generated from the nonlinearities of the equations-of-state. Harmonic effects can be significant in gases unless they are suppressed.<sup>13</sup>

### Multipole Projections of the Radiation Pressure

The radiation pressure on the surface of a compressible sphere is distributed nonuniformly. To describe the response of the sphere, it is convenient to use spherical harmonic (or "multipole") projections of the radial stress

$$R_{lm} = \int_0^{2\pi} d\phi \int_0^\pi (\Pi_{rr}^i - \Pi_{rr}^o) \bar{Y}_{lm}(\theta, \phi) \sin\theta d\theta, \quad \Pi_{rr}(\theta, \phi) = 2^{-1} [\beta \langle p_1^2 \rangle - \rho \langle v^2 \rangle] + \rho \langle v_r^2 \rangle \quad (2a, b)$$

where  $\theta$  is the polar angle illustrated in Fig. 2;  $\phi$  is the azimuthal angle;  $p_1, v$ , and  $v_r$  denote the total (incident + scattered) first-order pressure, velocity, and radial velocity;  $\langle \rangle$  denotes an average over an acoustic period; and the  $\bar{Y}_{lm}$  are real-valued spherical harmonic functions described in Ref. 14.\*\* Equation (2b) evaluated for the conditions at the inner side of the sphere's surface gives the radially outward force/area; evaluated at the

\*\*The notation is simpler than in Ref. 14 and 15 since we first consider unmodulated incident waves. Correct prescriptions for the  $\bar{Y}_{lm}$  with  $l \geq |m| \neq 0$  are given in footnote 4 of Ref. 14. Due to an error of transcription in Ref. 15, the sign of the  $\langle v_r^2 \rangle$  term was printed incorrectly in Eq. (M2).

outer side, it gives the inward force/area. Hence Eq. (2a) is the projection of the second-order radially outward force/area. Derivations of the stress tensor for Eq. (2b) are cited in Ref. 15. For incident waves characterized by uniaxial flows along the z axis,  $R_{lm} = 0$  for  $m \neq 0$  and the relevant  $Y_{lm}^0$  are just the ordinary  $Y_{lm}^0 = 0$  spherical harmonics:  $Y_{10}^0 = (4\pi)^{-1/2}$ ,  $Y_{11}^0 = (3/4\pi)^{1/2} \cos\theta$ ,  $Y_{20}^0 = (5/16\pi)^{1/2} (3\cos^2\theta - 1)$ , and  $Y_{30}^0 = (7/16\pi)^{1/2} (5\cos^3\theta - 3\cos\theta)$ . We retain the m subscript to allow for other incident waves.

For incident waves with no dependence on  $\phi$  (e.g., the uniaxial case mentioned), the continuity of  $v_r$  and  $p_1$  (both oscillate at frequency  $\omega$ ) at the boundary give the following local radiation stress on the sphere's surface<sup>14</sup>

$$\Pi_{rr}^i - \Pi_{rr}^o = \frac{(\beta_1 - \beta_0) p_1^2}{2} + \frac{d_1 \rho_0}{2} [qa^{-2} \langle (\frac{\partial \phi_1}{\partial \theta})^2 \rangle + \langle (\frac{\partial \phi_1}{\partial r})^2 \rangle] \quad (3)$$

where  $d_1 = q - 1$ ,  $\phi_1$  is the inner acoustic velocity potential and the derivatives are evaluated with the radial coordinate  $r = a$ ; Eq. (3) neglects viscous effects. Expressions for  $p_1$  at  $r = a$  and the  $\phi_1$  are derived in Ref. 5. If the incident wave is again the standing wave  $p(z, t) = p \cos(kz + kh) \sin \omega t$ , then Eq. (3) is applicable. From Fig. (2) we expect that  $\langle F \rangle = (4\pi/3) a^2 R_{10}$ ; indeed, a laborious computation of  $R_{10}$  reproduces Eq. (1) for the same conditions on  $X$  even though Eq. (1) was originally derived by a slightly different method of averaging.

To obtain those radiation stresses which favor the spheroidal (or "quadrupole") deformation of a compressible sphere, we used Eq. (3) and found that<sup>15</sup>

$$R_{20} = R_{20}' [1 + X^2 (\frac{d_2 b}{5} + \frac{q}{d_2^2} (1-b)) + O(X^4)] \sin^2 kh + R_{20}'' \cos^2 kh \quad (4)$$

$$R_{20}' = -\frac{3}{5} p_s^2 \beta_0 (5\pi)^{1/2} d_{1,2}^2, \quad R_{20}'' = p_s^2 \beta_0 (5\pi)^{1/2} \frac{X^2}{9d_3} (5d_{1,3}(2+d_3) + 3q - (2+q)b + O(X^2)) \quad (5a, b)$$

where  $d_1 = d/d_0$ ,  $d_2 = 1 + 2q$ ,  $d_3 = 2 + 3q$ , and  $b = \beta_1/\beta_0 = c^2/qc^2$ . It is assumed that  $X = ka \ll \epsilon_1$  and that  $X \ll X_m$ . A remarkable feature of Eq. (4) is that if  $q \neq 1$  and the sphere is not precisely centered on a velocity node, then  $\sin kh \neq 0$  and  $R_{20}$  does not vanish as  $X \rightarrow 0$  (that is as  $\lambda/a \rightarrow 0$ ). The reason for this is illustrated in Fig. 3. Assume also that  $\rho_1 \gg \rho_0$  (as for a drop in air) so that translational motion of the sphere is negligible. At the equator ( $\theta = 90^\circ$ ) the mean pressure is less than at the poles since the poles are stagnation points. Consequently, there is an outward directed stress on the equator which will tend to deform a drop into a nearly oblate spheroidal shape as has been observed.<sup>16</sup> The equilibrium shape is determined by a balance of  $R_{20}$  with stresses due to surface tension.<sup>14, 15</sup> The pressure distribution of oscillating incompressible potential flow<sup>15</sup> has been used to give an independent derivation of Eq. (5a) which does not even require that  $\rho_1 \gg \rho_0$ . This argument has also been extended to traveling waves, where as  $X \rightarrow 0$ ,  $R_{20} \rightarrow R_{20}'$  with  $p_s$  equal to the pressure amplitude of the incident wave. The only  $R_{lm}$  which do not necessarily vanish as  $X \rightarrow 0$  have  $l = 2$  or  $l = 0$ .

Compressible liquid drops (e.g., silicone oil or xylene) in water are attracted toward velocity nodes where the part of  $R_{20} \propto \sin^2 kh$  is small and  $R_{20}$  is dominated by  $R_{20}''$ . For these drops  $R_{20}'$ , and hence  $R_{20}$ , are negative numbers because  $(2+q)b$  dominates the other terms in the parentheses in Eq. (5b). The tendency is again to deform into an oblate spheroid but for a different reason than that depicted in Fig. 3; it appears that the attraction depicted in Fig. 1 of compressible fluids to the velocity node can also deform a drop. If a drop with  $\beta_1 > \beta_0$  is somehow constrained (e.g., with the radiation pressure of a second wave) to lie near a pressure node, the term of Eq. (4)  $\propto X^2 \sin^2 kh$  may be dominant if  $X^2$  is not too small. Then  $R_{20}$  is positive and the drop will tend to elongate. This is apparently due to the repulsion of highly compressible fluids from pressure nodes by the mechanism depicted in Fig. 1.

To obtain the hexapole projection, which favors a "pear" shaped deformation of a compressible sphere, we used Eq. (3) and found that  $R_{30} = -p_s^2 \beta_0 (\pi/7)^{1/2} X [(3qd_1/d_2 d_3) + O(X^2)] \sin 2kh$ . It is assumed that  $X \ll 1$  and that  $X \ll X_m$ . The dependences on  $kh$  and  $X$  differ from those of  $R_{20}$  but the periodicity in  $h$  may be argued from elementary considerations.

Equation (2) and these results for  $R_{20}$  and  $R_{30}$  neglect the previously mentioned harmonic effects<sup>13</sup> which are known to alter the  $\langle F \rangle$  exerted on spheres in air when the fundamental amplitude,  $p_s$ , is large. Harmonic effects should be negligible when the outer fluid is liquid or, if it is a gas and  $p_s$  is small.

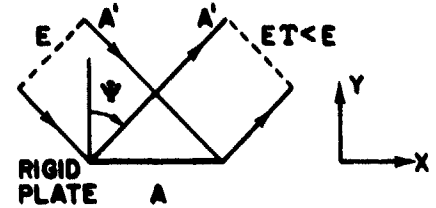


Fig. 4. Reflection of sound from a rigid plate produces tangential stresses.

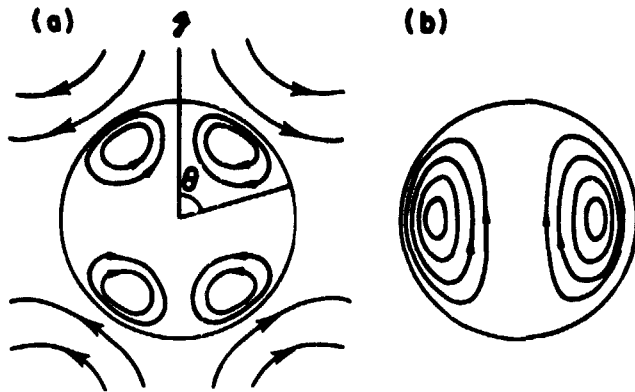


Fig. 5. Streaming patterns driven by projections of  $V \cdot T$  with (a)  $\ell = 2$ ,  $m = 0$ , and (b)  $\ell = 1$ ,  $m = 0$ .

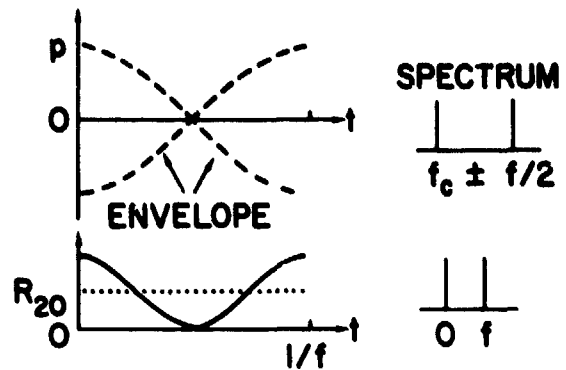


Fig. 6. An appropriate modulation of  $p$  gives equal oscillating and static terms in the  $R_{\ell m}$ .

### Tangential Radiation Stresses, the Konstantinov Effect, and Streaming

Let  $T = \hat{\theta} \Pi_{\theta r} + \hat{\phi} \Pi_{\phi r}$  denote the time-averaged tangential force vector per area of an infinitesimal region of surface on a compressible sphere. Here  $\hat{\theta}$  and  $\hat{\phi}$  denote the local unit vectors (at the surface point specified by  $\theta$  and  $\phi$ ) in the direction of increasing polar and azimuthal angles, respectively. The stress  $T$  is taken here to denote the total radiation stress due to the inner and outer (incident + scattered) acoustic waves. Marston has shown<sup>14</sup> that  $T$  vanishes if the first-order (or acoustic) flow is assumed to be adiabatic-inviscid (or "potential") flow. Viscous or thermal dissipation near the sphere's surface produces tangential stresses. The purpose of this section is to comment on these stresses and on the associated acoustic streaming.

The connection between dissipation and tangential stress is illustrated by the "thought experiment" shown in Fig. 4. A sound beam with a mean energy density  $E$  and area  $A'$  is reflected off a rigid plate of area  $A = A'/\cos\psi$ . The reflected beam has mean energy density  $TE$  where  $T < 1$ . The  $y$  coordinates at which these energy densities are specified are much greater than the viscous and thermal penetration lengths for the fluid,  $\delta_v$  and  $\delta_T$ . Attenuation due to any absorption in the bulk fluid (which leads in part to "volume" acoustic streaming) is neglected here so that  $T$  is associated with the losses localized within the region extending a few penetration lengths from the plate. The incident and reflected waves have pseudomomentum densities<sup>17</sup> of  $E/c$  and  $TE/c$  where  $c$  is the fluid's sound speed. Time rates-of-change of the incident and reflected pseudomenta (in their respective directions of propagation) are  $EA'$  and  $TEA'$ . The plate feels a tangential radiation force in the  $x$  direction equal to the rate of  $x$ -pseudomomentum loss,  $(1-T)EA'\sin\psi$ . Consequently the tangential radiation stress  $\Pi_{xy} = E(1-T)(A'/A)\sin\psi = (E/2)(1-T)\sin 2\psi$ . For an inviscid fluid,  $T = 1$  and  $\Pi_{xy} = 0$  at a rigid plate. An equation similar in form to this expression was derived by Borgnis<sup>18</sup> in a different context. He neglected the possibility of viscous and thermal boundary layers but attributed  $(1-T)$  as due to refracted waves within the (now elastic) reflector in an inviscid fluid. That interpretation would require that the refracted waves are absorbed within the plate. Also it neglects dissipation external to the plate.

A theory for the dependence of the intensity reflection coefficient  $T$  on the angle of incidence  $\psi$  was given by Konstantinov<sup>19</sup> for a rigid plate maintained at a fixed temperature. For the purpose of estimating the dependence of  $\Pi_{xy}$  on  $\psi$  and its maximum value  $\Pi_{xy}^1$ , our numerical tests show that the following approximation (Ref. 20, Eq. 1) to Konstantinov's  $T$  (see Ref. 19, Eq. 53) is applicable

$$T \approx (\psi_1^2 + \psi_2^2 - 2^{\frac{1}{2}}\psi_1\psi_2)/(\psi_1^2 + \psi_2^2 + 2^{\frac{1}{2}}\psi_1\psi_2) \quad (6)$$

where  $\psi_1 = (\pi/2) - \psi$  radians is frequently called the "grazing angle" and  $\psi_2 = \psi_v + \psi_T$  where  $\psi_v = k\delta_v$  and  $\psi_T = (\gamma-1)k\delta_T$ . Here  $\delta_v$  and  $\delta_T$  are the penetration lengths of the surrounding fluid as previously defined and  $\gamma$  is the ratio of specific heats at constant pressure and volume. There is a minimum  $T$  of  $(2^{\frac{1}{2}} - 1)^2 \approx 0.176$  which occurs for  $\psi_1 = \psi_2$ . Unless the acoustic frequency  $f = \omega/2\pi$  is quite large ( $\geq 1$  GHz), most fluids have  $\lambda \gg \delta_v$  and  $\lambda \gg \delta_T$  so that the minimum in  $T$  usually occurs for  $\psi$  near  $90^\circ$ . For most liquids  $\psi_v \gg \psi_T$  and the thermal boundary condition is not important.

In the following discussion of  $T$  and its influence on  $\Pi_{xy}$ , it should be remembered that for a given fluid,  $\psi_2 = \sqrt{\gamma}$ . Consider the cases of air and water at a temperature of  $20^\circ\text{C}$  and  $f = 1$  MHz: for air,  $\delta_v = 1.5 \mu\text{m}$ ,  $\delta_T = 1.8 \mu\text{m}$ , and  $\psi_2 = 2.4^\circ$ ; for water,  $\delta_v = 0.4 \mu\text{m}$ ,  $\delta_T = 0.15 \mu\text{m}$ , and  $\psi_2 = 0.10^\circ$ . Numerical computations give  $\Pi_{xy}^1 = \psi_2$  with  $\Pi_{xy} = 0.043 E$  when

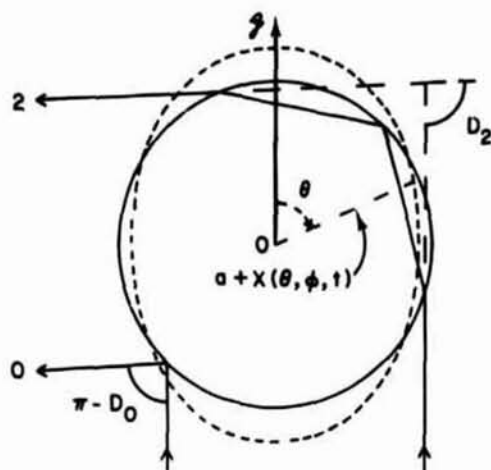


Fig. 7. Rays for a spherical drop of xylene in water which contribute to rainbow scattering. The dashed profile is when  $x_{lm}(t) > 0$ ,  $l = 2$ ,  $m = 0$ .



Fig. 8. Far-field scattering for: (a) the rainbow region of a xylene drop ( $a=200 \mu\text{m}$ ) levitated in water; and (b) the critical region of an air bubble ( $a=480 \mu\text{m}$ ) in water. In both cases the incident light had a wavelength (in water) of  $632.8 \text{ nm}/n_0$  where  $n_0 \approx 1.33$ . In (a) the scattering angle (denoted by  $D$  in Fig. 7) increases from left to right; the angular width of the photograph  $7^\circ$ . The coarse structure (broad vertical bands) is described by Airy's diffraction integral. In (b) the scattering angle ( $\phi$  in Fig. 11) decreases from left to right (with  $\phi_c$  near the left edge) and the width  $\approx 14^\circ$ . The coarse structure in (b) is due to critical diffraction and interference. The scattering plane and the incident electric field are perpendicular in (a) and parallel in (b).

$\psi_2 = 1^\circ$ . The  $\sin 2\psi$  factor in  $\Pi_{xy}$  causes  $\Pi_{xy}'$  to occur with  $\psi_1 > \psi_2$ . (The  $\psi_1$  associated with  $\Pi_{xy}'$  approaches  $6^\circ$  as  $\psi_2 \rightarrow 0$ ; it increases with increasing  $\psi_2$  with a slope of roughly 8 until  $\psi_2 = 1^\circ$  and more slowly thereafter.) The maximum in  $\Pi_{xy}$  is broad;  $\Pi_{xy}(\psi = 45^\circ) \approx 0.03 E$  when  $\psi_2 = 1^\circ$  and  $\Pi_{xy}(45^\circ)$  is roughly  $\propto \psi_2$ . For  $\psi \leq 70^\circ$ , Konstantin  $\Pi_{xy}$ 's  $T$  depends somewhat on  $\psi_0/\psi_1$ ; however, this dependence is not retained in Eq. (6) and in these estimates.

Herrey<sup>21</sup> has measured radiation stresses on a copper plate in water but did not detect tangential stresses for  $f = 1 \text{ MHz}$  and  $\psi \leq 50^\circ$ . It may be that for these  $\psi$  the experiment was not able to discriminate between the  $\Pi_{xy}$  and the much larger normal stress whose magnitude  $= 2E$  when  $\psi = 0$ . Second-order acoustic torques on a rigid surface caused by tangential stresses have been observed.<sup>22</sup>

It might appear that the expression for  $\Pi_{xy}$  does not allow for the momentum of fluid streaming near the surface. If the extent of the plate is lengthened, however, so that viscosity transfers the x-momentum of the second-order flow to the plate, the apparent  $\Pi_{xy}$  on the plate is still given by this expression. This may also be shown by considering the momentum flux across a control surface which encloses both the plate and the confined streaming. One procedure for describing how the first-order velocity  $v$  is coupled to the second-order velocity  $u$  is to consider the equation for the second-order vorticity:<sup>23</sup>

$$\left(\frac{\partial}{\partial t} - \nu \nabla^2\right) \nabla \times u = -\nu(S_E + S_R + S_T), \quad S_R = -\nu^{-1} \langle \nabla \times (v \times \nabla \times v) \rangle, \quad S_T = -\beta \langle \nabla \times (p_1 \nabla \times \nabla \times v) \rangle \quad (7a, b, c)$$

where  $S_E$  is Eckart's "volume" source of vorticity<sup>23</sup> which is negligible near the surface in comparison to the "surface" sources  $S_R$  and  $S_T$ . This procedure is useful for the description of streaming near rigid surfaces provided the Reynold's number (for  $u$ ) is small.

An approximation for  $u$  which should be useful near the fluid-fluid interface of a drop or a bubble was introduced by Marston.<sup>14</sup> It is to neglect the source terms in Eq. (7a) and to solve the resulting homogeneous vorticity equation subject to boundary conditions which include the tangential (T) and radial ( $R_{lm}$ ) radiation stresses on the interface. As reviewed subsequently, this procedure is particularly useful for describing the response to oscillating  $R_{lm}$  due to modulated sound. In this section the sound has no modulation and  $u$  is driven only by the T. By inspection of Eq. (7) and extension of the previous momentum arguments, this procedure should be useful if the spatial extent of the region of significant  $|\nabla \times v|$  is  $\ll a$ ; this will be so if  $\delta_\nu \ll a$  which is usually the case of interest. The resulting  $u$  can be written in a series which makes use of multipole projections  $(\nabla \cdot T)_{lm}$  of the tangential divergence of T [see Eq. (14) and Appendix B of Ref. 14]. As noted previously,<sup>15</sup> for steady flows the coupling coefficients in Ref. 14 were incorrect due to errors in the assumed boundary conditions (Ref. 14, Eq. C6 and C10). These errors have been corrected in the result given below. For incident acoustic waves with no  $\phi$  dependency  $\Pi_{\theta r} = 0$  and  $\Pi_{\theta r}$  is independent of  $\phi$ . This  $T(\theta)$  must be present because of the dissipation of sound present at interfaces separating real fluids.<sup>20</sup> Its description may be facilitated with methods developed for torques.<sup>22</sup>

Consider the particular case of  $\Pi_{\theta r} = B_2 \sin 2\theta$  where  $B_2$  is a constant. This  $\Pi_{\theta r}$  has  $(\nabla \cdot T)_{20} = 8(\pi/5)^{1/2} B_2/a$  and all other  $(\nabla \cdot T)_{lm} = 0$  as does the torque. The interface is

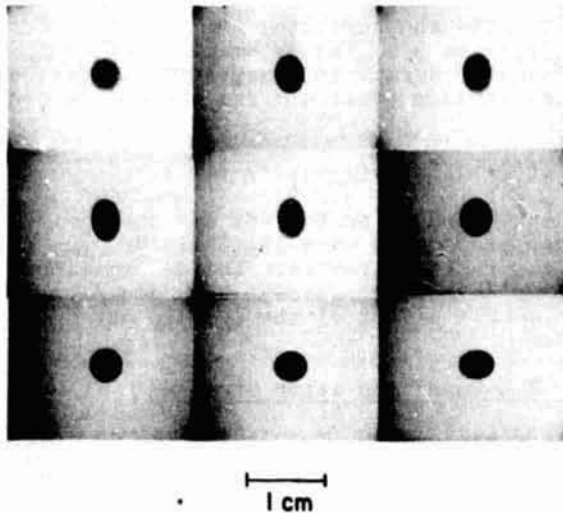


Fig. 9. A 2 mm radius drop undergoing forced quadrupole oscillations with  $f = 18$  Hz. Here and in Fig. 10, time increases from left to right and from top to bottom.

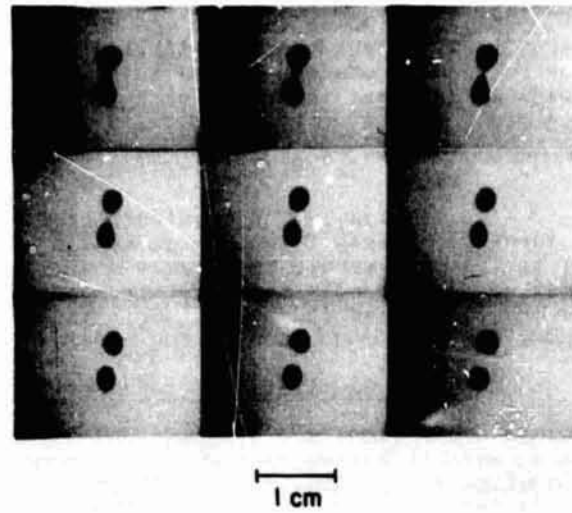


Fig. 10. A 1.7 mm radius drop splitting into two drops as a consequence of forced quadrupole oscillations with  $f = 24$  Hz. Here, and in Fig. 9, the  $z$  axis is vertical.

assumed to be ideal (free of surface viscosity) and the boundary conditions are continuity of normal and tangential velocities and the balance of forces. These give the following velocities inside (i), and outside (o), the sphere:  $u_o^i = (Gr/2)(5\tilde{r}^2 - 3)\sin^2\theta$ ,  $u_r^i = Gr(1 - \tilde{r}^2)(3\cos^2\theta - 1)$ ,  $u_\theta^o = Gr^{-4}\sin^2\theta$  and  $u_r^o = Gr^{-4}(1 - \tilde{r}^2)(3\cos^2\theta - 1)$  where  $\tilde{r} = r/a$ ,  $G = B_2 a / 5(\mu_i + \mu_o)$ , and  $\mu$  is the shear viscosity of the indicated fluid. Resulting streamlines are illustrated in Fig. 5(a). In addition to acoustic stresses, externally applied electric fields<sup>24</sup> can cause tangential stresses with this dependence on  $\theta$ . With an appropriate choice of material parameters, and  $B_2$ , we find that  $u$  and the radial stresses caused by  $u$  (described in the next section) agree with those predicted by Taylor's specialized method after correcting his algebraic errors.<sup>25</sup> The outer fluid is unbounded in this computation.

Consider now the case of  $\Pi_{\theta r} = B_1 \sin\theta$  where the only  $(\nabla \cdot T)_{\ell m} \neq 0$  has  $\ell = 1$  and  $m = 0$ . This stress is predicted to drive the following velocity field:  $u_\theta^i = G(2\tilde{r}^2 - 1)\sin\theta$ ,  $u_r^i = G(1 - \tilde{r}^2)\cos\theta$ ,  $u_\theta^o = (G/2)\tilde{r}^{-3}(1 + \tilde{r}^2)\sin\theta$ , and  $u_r^o = Gr^{-1}(\tilde{r}^2 - 1)\cos\theta$  where  $G = B_1 a / 3(\mu_i + \mu_o)$ . Interior streamlines are shown in Fig. 5(b); they are the same as those for small Reynolds number flow past a drop calculated by Hadamard and observed by Spells.<sup>26</sup> Far outside the drop, the streamlines are those for a Stokeslet, which is the creeping motion generated by a force concentrated at a point (see Fig. 5 of Ref. 27). This type of tangential stress will alter the net  $z$  directed force on a sphere from that given by Eq. (1).

For a large drop with  $\beta_i \ll \beta_o$  in an incident wave with  $X \gg 1$ , Eq. (6) and the considerations illustrated in Fig. 4 may be used to obtain the signs of  $B_1$  and  $B_2$ . If a traveling wave is incident from above, it is clear that  $B_1 > 0$  due to the Konstantinov effect. In a standing wave it is to be expected that  $B_2 > 0$  due to stress concentrations between  $\theta = 45^\circ$  to  $85^\circ$  in opposition with those between  $95^\circ$  to  $135^\circ$ ; however  $B_2$  should also depend on  $h$ . In either case,  $B_1 \propto p_s^2$  and  $B_2 \propto p_s^2$  unless the incident pressure amplitude  $p_s$  is large. [As with acoustic torques,<sup>22</sup>  $\Pi_{\theta r}$  may contain a term  $\propto p_s$  when the first order displacement amplitude  $(p_s / \rho c \omega) \geq \delta_v$ .] The total  $u$  will be the superposition of those driven by the individual  $(\nabla \cdot T)_{\ell m}$ .

#### Deformations Induced by Steady Radiation Stresses

Radiation stresses induce a mean displacement of the interface of a drop or bubble which is opposed by surface tension. The mean displacement (averaged over a period of the acoustic wave) of the interface from that of a sphere of radius  $a$  will be denoted as  $x(\theta, \phi, t)$  and may be described using the following spherical harmonic series:

$$x(\theta, \phi, t) = x_0(t) + \sum_{\ell=1}^{\infty} \sum_{m=-\ell}^{\ell} [\hat{x}_{\ell m} + x_{\ell m}(t)] \tilde{Y}_{\ell m}(\theta, \phi) \quad (8)$$

where  $\hat{x}_{\ell m}$  is a time-independent projection and  $x_{\ell m}$  is an oscillating one. The latter vanishes if the wave is not modulated and initial transients are allowed to decay. It will be assumed in this section that  $|x(\theta, \phi, t)| \ll a$  so that for drops the term<sup>14</sup>  $|x_0(t)|$  is much smaller than the largest  $|\hat{x}_{\ell m}|$ . The  $\ell = 1$  terms represent translations of the sphere's center which lead to the balance between  $\langle F \rangle$  and buoyancy. The terms representing static

deformations, the  $\hat{x}_{\ell m}$  with  $\ell > 1$ , are proportional to the radiation stresses on a sphere given by Eq. (2) (which neglect the deformation) provided the resulting  $|\hat{x}_{\ell m}| \ll a$ . [Corrections to the first-order scattering when  $X \ll 1$  will be  $O(\hat{x}_{\ell m}/a)$  or smaller and will induce only small changes in the stresses.] A balance of normal and tangential radiation stresses at an ideal interface with those due to the surface tension  $\sigma$  and the second-order flow gives

$$\hat{x}_{\ell m} = [a^2/\sigma(\ell-1)(\ell+2)] [R_{\ell m} - 3a(\nabla \cdot T)_{\ell m} \hat{r}/\ell(\ell+1)(2\ell+1)(\mu_0 + \mu_1)], \ell > 1, \quad (9)$$

where  $\hat{r} = \ell\mu_0 + (\ell+1)\mu_1$ . The magnitude of  $T$  can be estimated using Eq. (6) and the expression for  $\Pi_{xy}$ . Unless  $f$  is so high that  $\delta_V \ll \lambda$ , one expects to have  $|R_{\ell m}| \gg |a(\nabla \cdot T)_{\ell m}|$  for  $\ell > 1$  so that  $\hat{x}_{\ell m}$  should be largely determined by the radial stresses. The deformations  $\hat{x}_{\ell m}$  may easily exceed<sup>14</sup> the first-order particle displacements ( $p_S/\rho c\omega$ ); they are  $\approx p_S^2$  provided  $|\hat{x}_{\ell m}| \ll a$  and  $(p_S/\rho c\omega) \ll \delta_V$ . The most noticeable effect of the  $(\nabla \cdot T)_{\ell m}$  may be the second-order flow described in the previous section.

### Shape Oscillation Resonances Forced by Modulated Radiation Stresses

Second-order flows and deformations may be greatly enhanced by modulating the incident acoustic wave at a frequency so as to force shape oscillation resonance. The purpose of this section is to summarize the theory.<sup>14,15</sup> There is a slight change of notation from the previous sections:  $f_c$  will denote the frequency of the incident sound in the absence of modulation (typically  $f_c \geq 100$  kHz), and  $f$  (which is  $\ll f_c$ ) denotes the frequency of the shape oscillations. To drive the shape oscillations, the incident wave is a standing wave of the following form  $p(z,t) = -2p_c \sin(\omega_c t) \cos(\frac{1}{2}\omega_c t) \cos(kz+kh)$  where  $\omega_c = 2\pi f_c$ ,  $k = \omega_c/c_0$ ,  $\omega = 2\pi f$ , and  $z = -h$  is again the location of the adjacent velocity node with  $z = 0$  at the drop's center of mass. The factor  $(-2)$  is included only as a matter of convention.<sup>14,15</sup> That nonlinearities are essential to the generation of the low frequency shape oscillations is illustrated in Fig. 6. The upper part shows the modulation envelope and the spectrum of the incident sound which consists of two sidebands, each with an amplitude  $p_c$ , located at  $f_c - (f/2)$  and  $f_c + (f/2)$ . The wave at the carrier frequency  $f_c$  is suppressed, due to the modulation. From Eq. (2) it can be shown<sup>15</sup> that the radiation stresses vary in time such that  $R_{\ell m}(t) = \hat{R}_{\ell m}[1 + \cos(\omega t)]$  and this has a time dependence and spectrum illustrated in the lower part of Fig. 6. The radiation stress contains a static term and one which oscillates at the difference frequency of the sidebands. The constant  $\hat{R}_{\ell m}$  is given by the  $R_{\ell m}$  associated with a steady incident wave of frequency  $f_c$  and pressure amplitude  $p_S = p_c/\sqrt{2}$ . Consequently Eq. (4) and the result for  $R_{30}$  may be used here but with a simple substitution. For small  $p_c$ , the tangential stress  $T$  will also be proportional to  $p_c^2[1 + \cos(\omega t)]$ .

The theory for the response<sup>14,15</sup> is complicated by the nature of the boundary layer damping. In the present treatment we simplify the results by omitting the small deformation and flow induced by the oscillating part of  $(\nabla \cdot T)_{\ell m}$ . For incident waves with no dependence on  $\phi$ , all projections with  $m \neq 0$  vanish. Consequently the subscript  $m$  will be omitted. The oscillating parts of Eq. (8) are given by

$$x_\ell(t) = \tilde{x}_\ell \cos(\omega t - \xi), \quad \tilde{x}_\ell = \hat{x}_\ell \omega_\ell^{*2} / (U^2 + V^2)^{1/2}, \quad \tan \xi = V/U, \quad \ell > 1, \quad (10a,b,c)$$

$$\omega_\ell^* = [\sigma \ell(\ell+1)(\ell-1)(\ell+2)/a^3 \Gamma]^{1/2}, \quad U(\omega) = \omega_\ell^{*2} - \alpha \omega^{3/2} - \omega^2, \quad V(\omega) = \alpha \omega^{3/2} + \gamma \omega \quad (11a,b,c)$$

and the static parts,  $\hat{x}_\ell$ , are given from Eq. (9) by omitting the  $(\nabla \cdot T)$  term. In Eq. (11a)  $\omega_\ell^*$  is the natural frequency (neglecting viscosity) of the  $\ell$ th mode and  $\Gamma = \ell\rho_0 + (\ell+1)\rho_1$ . Here  $\alpha$  and  $\gamma$  are damping parameters [given by Eqs. (22) and (23) of Ref. 14] which are functions of  $\ell$ ,  $a$ ,  $\mu_1$ ,  $\mu_0$ ,  $\rho_1$ , and  $\rho_0$ ;  $\alpha$  is due to the damping of the boundary layer since it vanishes if either  $\rho_1\mu_1 \rightarrow 0$  or  $\rho_0\mu_0 \rightarrow 0$ . For drops surrounded by a liquid,  $\gamma$  is typically  $< \alpha\omega^{*2}$  but it is similar in magnitude to  $\alpha^2$ . It was assumed in the theory for  $\alpha$  and  $\gamma$  that the interface was ideal and thus free of surfactants.

From Eq. (10b),  $\tilde{x}_\ell$  depends both on the frequency and  $\ell$ th projection of the stress. As quantified below, when  $\omega$  is slightly less than  $\omega_\ell^*$ ,  $|\tilde{x}_\ell|$  is maximized; depending on the stress distribution, other modes may be driven but at lower (nonresonant) amplitudes. An example of a pure  $\ell = 2$  profile is shown in Fig. 7. It is convenient to omit the  $\ell$  subscript when possible in the following discussion. The phase delay of oscillations  $\xi$  is  $90^\circ$  when  $\omega$  is chosen to be the quadrature frequency  $\bar{\omega}$ . The prediction is that  $V(\bar{\omega}) = 0$  which gives  $\bar{\omega} = \omega^* - (\alpha/2)\omega^{*2} + \alpha^2/4$ . Due to the inertia of the boundary layer,<sup>14</sup>  $\bar{\omega} \neq \omega^*$ , unlike the case of ordinary damping. The mechanical  $Q$  of the  $\ell$ th mode is  $= \omega^{*2}/V(\omega^*)$  provided  $\mu_1$  and  $\mu_0$  are small enough to make this ratio somewhat larger than unity. [Evidently  $\bar{\omega} = \omega^*(1 - \frac{1}{2}Q^{-1})$  for liquid-liquid systems.] The response amplitude  $|\tilde{x}|$  is maximized when  $\omega = \bar{\omega}$ . At this maximum,  $\tilde{x} = Q\hat{x}$ , so the oscillations should be enhanced by a factor of  $Q$ . As  $\omega/\omega^* \rightarrow 0$ ,  $\tilde{x} \rightarrow \hat{x}$ ; however, as  $\omega/\omega^* \rightarrow \infty$ ,  $\tilde{x}/\hat{x} \rightarrow 0$ .

A matrix, Eq. (17) of Ref. 14, makes it possible to compute the oscillating part  $u$ . (The

total  $u$  also contains a static part driven by the static part of  $T$ .) In this matrix and in Eqs. (7), (9), (10), and (11), convection of momentum by the second order flow was neglected. This omission should have a negligible effect on the oscillations provided a Reynolds number  $R = \omega|\bar{x}|a/v_0$  and the static part of  $u$  are small.

### Observations of Forced Shape Oscillations and Rainbow Scattering from Drops

Three groups of experiments on forced resonance will now be summarized. The reader is encouraged to refer to the original papers<sup>3,8,9,28</sup> for details. The first and second made use of properties of scattered light,<sup>28</sup> to detect quadrupole ( $l = 2$ ) oscillation in which  $\bar{x}$  was a few  $\mu\text{m}$  and smaller. A profile of a drop and the relevant light rays are shown in Fig. 7. Most of the observations were done for drops of benzene and p-xylene in distilled water. The drops were levitated by a continuous acoustic standing wave with a typical frequency of 51 kHz which was  $\ll f_c$ . Their radii were in the range 150  $\mu\text{m}$  to 1.2 mm and the corresponding natural frequencies  $\omega^*/2\pi$  were predicted to be 1.1 kHz to 50 Hz.

In the first experiments,<sup>3</sup>  $f_c$  was typically 679 kHz. When  $\bar{x} = 0$ , the interference of rays labeled 0 and 2 in Fig. 7 produces a fine structure in the scattering visible to the eye via a telescope. This structure gives the closely spaced vertical fringes in Fig. 8(a). Conditions on the modulation leading to shape oscillations were mapped by making use of a blurring of the fringes induced by small  $\bar{x}$ . The conditions on  $\omega$  were consistent with the forcing of quadrupole resonance. Large  $\bar{x}$  leading to drop breakup were also observed.

The second group of experiments<sup>8,28</sup> gave quantitative resonance properties. These made use of photometric aspects of the coarse structure in the monochromatic rainbow scattering shown in Fig. 8(a). The "rainbow photometry" technique gave absolute measurements of  $\xi$  and relative measurements of  $\bar{x}$  with  $|\bar{x}| < 25 \mu\text{m}$  and  $0.5 \text{ mm} < a < 1.2 \text{ mm}$ . Here  $f_c = 217.5 \text{ kHz}$  and  $p_c \leq 70 \text{ kPa}$ . The results are summarized as follows. (i) The dependence of  $\xi$  on  $\omega$  is consistent with Eq. (10c) except that  $\alpha$  is larger than calculated and the inferred  $\sigma$  is 4% lower than expected. (ii) With the empirical  $\sigma$  and  $\alpha$ , the data give a dependence of  $\bar{\omega}$  on radius consistent with predictions. (iii)  $\bar{x}$  is maximized when  $\omega = \bar{\omega}$ . (iv) Provided  $h$  is held constant,  $\bar{x} = p_c$  as expected. (v) The empirical  $\alpha$  gave  $Q$  values which were 70% of the modeled values; however they are consistent with the presence of a film of impurities at the interface. (It is unfortunate that the drops were xylene<sup>8</sup> and benzene.<sup>3</sup> We have recently learned that these liquids almost always form nonideal interfaces with water.) (vi) Uncertainty in a conversion factor precluded the absolute measurement of  $\bar{x}$ ; however, the estimated  $|\bar{x}|$  are consistent with the  $R_{20}$  from Eq. (4). (vii) Empirical  $Q$  were typically = 7.

In the third group of experiments, Goosby<sup>9</sup> and Marston made hi-speed motion-picture photographs of drops undergoing forced shape oscillations. The drops consisted of a dyed silicone oil with  $v_1 = 2 \text{ cS}$  and  $\rho_1 = 0.88 \text{ gm/cm}^3$ . They were levitated by a 55 kHz wave in a water-filled resonator consisting of 50 mm x 75 mm glass microscope slides cemented along their long sides. A PZT disc (38 mm dia., 13 mm thick) drove both the 55 kHz wave and a modulated wave with  $f_c = 170 \text{ kHz}$ . Drops were levitated and  $f$  was adjusted to maximize  $|\bar{x}|$  for quadrupole oscillations apparent to the unaided eye. Figure 9 is taken from a sequence in which every third frame was printed giving a time interval between printed frames of 5.7 ms. Timing marks on the film revealed that  $\xi = 90^\circ \pm 9^\circ$  which agree with predictions. This is noteworthy because here  $|\bar{x}|/a = 0.4$  and the Reynolds number  $R = 180$ . For this measurement  $kh \ll 1$  and Eqs. (4) and (9) predict that  $\hat{x} < 0$ . The photographs and timing marks when combined with Eq. (10b) also give  $\hat{x} < 0$  with  $l = 2$  and  $m = 0$ .

As in Ref. 3, it was observed that oscillation amplitudes could be made large enough to fission the drop. Figure 10 shows the details of the fission process. The time interval between frames was 1.2 ms. This is a new acoustic technique for splitting drops since it relies on the modulation of the radiation pressure. Previous acoustic methods typically depended on transient cavitation to generate shock waves which could split drops.<sup>29</sup>

### The Physical Optics of Light Scattering from Bubbles

Unlike the case of scattering from drop-like objects, the physical optics of scattering from bubbles (where the refractive index of the scatterer  $n_1$  is less than that of the surroundings  $n_0$ ) has been explored only recently. This study has emphasized those angular regions of the scattering where diffraction corrects for divergences predicted by geometric optics.<sup>1</sup> These include glory or backscattering,<sup>30</sup> forward scattering,<sup>1</sup> and critical angle scattering.<sup>31,32</sup> The following is only a brief summary; the interested reader should consult Ref. 30-32 and papers cited therein. In this section,  $\phi$  denotes the scattering angle (Fig. 11),  $\lambda$  denotes the wavelength of light within the outer fluid,  $\theta_p$  denotes the local angle of incidence at the bubble's surface for a ray with  $p$  internal chords, and  $m \equiv n_1/n_0$ . Far-field scattering will be described which is that observed by a camera focused on  $\infty$ .

The critical scattering angle,  $\phi_c = 2 \arccos(m)$ , is where the surface reflected ray has an angle of incidence  $\theta_0 = \arcsin(m)$ . For  $\phi \leq \phi_c$ , geometric optics predicts that reflection

ORIGINAL PAGE  
BLACK AND WHITE PHOTOGRAPH

will be total, however models<sup>31</sup> and Mie theory<sup>32</sup> show that is not the case at  $\phi_c$  due to diffraction. For  $\phi < \phi_c (=83^\circ$  for bubbles in water) there is a coarse structure to the scattering due to this diffraction and to the interference with the  $p = 1$  ray. This structure (visible in Fig. (8b)) has an angular spacing which is typically  $\lesssim (\lambda/a)^{1/2}$  rad. Physical optics models of this structure<sup>32</sup> agree with Mie theory when  $a \geq 4\lambda$ . For a bubble and drop of the same size, each with  $a \gg \lambda$ , the bubble's coarse structure is broader than the rainbow's since the latter's quasi-period can be shown from Eq. 5 of Ref. 28 to be  $\lesssim (\lambda/a)^{2/3}$  rad. Other photographs of scattering by bubbles<sup>1,31</sup> reveal a fine structure due primarily to the interference of  $p = 0$  and  $2'$  rays. Its spacing is typically  $\lesssim 0.8 \lambda/a$  radians. Backscattering from bubbles in our model can easily exceed that from a perfectly reflecting sphere of the same size. It has a quasi-periodic structure which is especially regular for the cross-polarized scattering. Observations of this structure agree well with theory.<sup>30</sup> This structure is evident in Fig. 12 as the concentric rings centered in the  $\phi = 180^\circ$  direction and spaced at  $0.05^\circ$  intervals.

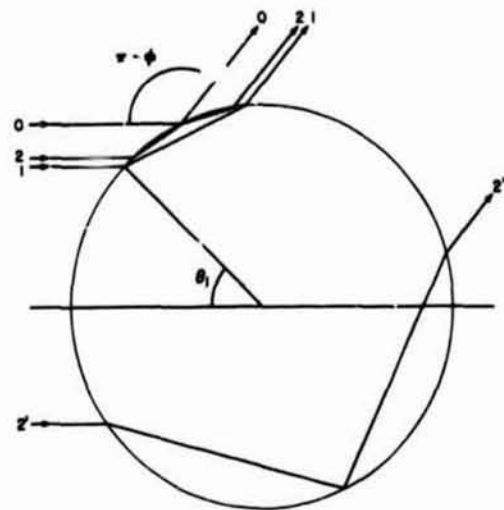


Fig. 11. Rays for a bubble in water.

Acknowledgments

We are grateful to R. E. Apfel for collaborating in the original studies<sup>3,8</sup> of shape oscillations. This work was supported by the Petroleum Research Fund (administered by the American Chemical Society), an M. J. Murdock Charitable Trust Grant of Research Corporation, and the Office of Naval Research. Marston is an Alfred P. Sloan Research Fellow.

References

1. P.L. Marston, D.S. Langley, and D.L. Kingsbury, in Proceedings of the IUTAM Symposium on the Mechanics and Physics of Bubbles in Fluids (at press).
2. R.E. Apfel, J. Acoust. Soc. Am. **70**, 636-639 (1981).
3. P.L. Marston and R.E. Apfel, J. Colloid Interface Sci. **68**, 280-286 (1979).
4. L.A. Crum, J. Acoust. Soc. Am. **50**, 157-163 (1971).
5. K. Yosioka and Y. Kawasima, Acustica **5**, 167-173 (1955).
6. T. Hasegawa, J. Acoust. Soc. Am. **61**, 1445-1448 (1977).
7. A.I. Eller, J. Acoust. Soc. Am. **43**, 170-171 (1968).
8. P.L. Marston and R.E. Apfel, J. Acoust. Soc. Am. **67**, 27-37 (1980).
9. S.G. Goosby, Photographs of Breakup of Drops Induced by Modulated Radiation Pressure, M.S. dissertation, Washington State University (1981).
10. R.E. Apfel, J. Acoust. Soc. Am. **59**, 339-343 (1976).
11. M.A. Weiser and R.E. Apfel, J. Acoust. Soc. Am. (submitted for publication).
12. L.V. King, Proc. Roy. Soc. **A137**, 212-240 (1934).
13. E. Leung, N. Jacobi, and T. Wang, J. Acoust. Soc. Am. (at press).
14. P.L. Marston, J. Acoust. Soc. Am. **67**, 15-26 (1980); (erratum at press).
15. P.L. Marston, S.E. LoPorto, and G.L. Pullen, J. Acoust. Soc. Am. **69**, 1495-1501 (1981).
16. R.R. Whymark, Ultrasonics **13**, 251-261 (1975); E. Trinh (private communication, 1981).
17. M.E. McIntyre, J. Fluid Mech. **106**, 331-347 (1981).
18. F.E. Borgnis, J. Acoust. Soc. Am. **24**, 468-469 (1952).
19. B.P. Konstantinov, Zhurnal Tekhnicheskoi Fiziki **9**, 226-238 (1939).
20. A.Y. Savelev, Sov. Phys. Acoust. **19**, 154-158 (1973).
21. E.M. Herrey, J. Acoust. Soc. Am. **27**, 891-896 (1955).
22. F.H. Busse and T.G. Wang, J. Acoust. Soc. Am. **69**, 1634-1638 (1981).
23. H. Medwin and I. Rudnick, J. Acoust. Soc. Am. **25**, 538-540 (1953).
24. G.I. Taylor, Proc. Roy. Soc. Lond. **A291**, 159-166 (1966).
25. J.R. Melcher and G.I. Taylor, Annu. Rev. Fluid Mech. **1**, 111-146 (1969).
26. K.E. Spells, Proc. Phys. Soc. **B65**, 541-546 (1952).
27. J. Lighthill, J. Sound Vib. **61**, 391-418 (1978).
28. P.L. Marston, Appl. Opt. **19**, 680-685 (1980).
29. M.K. Li and H.S. Fogler, J. Fluid Mech. **88**, 513-528 (1978).
30. D.S. Langley and P.L. Marston, Phys. Rev. Lett. **47**, 913-916 (1981).
31. P.L. Marston, J. Opt. Soc. Am. **69**, 1205-1211 (1979); **70**, 353(E) (1980).
32. D.L. Kingsbury and P.L. Marston, Appl. Opt. **20**, 2348-2350 (1981).

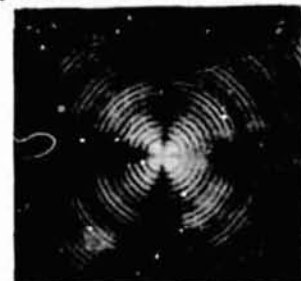


Fig. 12. Cross-polarized backscattering from a bubble in silicone oil with  $a^*$

## A numerical method for the dynamics of non-spherical cavitation bubbles

L. Guerri

Istituto di Matematica, Università di Pavia, 27100 Pavia, Italy

G. Lucca and A. Prosperetti

Istituto di Fisica, Via Celoria 16, 20133 Milano, Italy

Abstract

In this paper a boundary integral numerical method for the dynamics of non-spherical cavitation bubbles in inviscid incompressible liquids is described. A very efficient feature of this approach is that it involves only surface values of the velocity potential and its first derivatives, thus avoiding the problem of solving the Laplace equation in the entire domain occupied by the liquid. To illustrate the performance of the method the collapse of a bubble in the vicinity of a solid wall and the collapse of three bubbles with collinear centers are considered.

Introduction

The development of the study of the dynamics of non-spherical bubbles has been seriously hindered in the past by the lack of computational tools applicable to severe deformations of the spherical shape. Existing methods<sup>1-4</sup> are cumbersome to implement and require long execution times. These problems have prevented their widespread usage and common acceptance. In this study we shall present a much more efficient method based on the boundary integral approach<sup>5</sup> which can be implemented in a relatively small number of program instructions (500-600). It is flexible, precise, and requires short execution times (typically 3-5 minutes on a Univac 1100). The method is applicable to irrotational, incompressible, inviscid flow and we present an axisymmetric version of it. To illustrate the results obtainable in this way we consider the Rayleigh problem, one of the cases studied by Plesset and Chapman<sup>1</sup>, and the collapse of three bubbles with collinear centers.

Mathematical formulation

We consider the flow induced by one or more bubbles in a liquid occupying a domain  $\Omega$  bounded by the surface of the bubbles,  $S_b$ , rigid boundaries,  $S_r$ , and a "surface at infinity"  $S_\infty$ . In the hypotheses of inviscid irrotational flow the velocity field  $\underline{u}$  can be derived from a potential,  $\underline{u} = \nabla\phi$ , and the mathematical problem can be put in the form<sup>1</sup>

$$\nabla^2\phi = 0 \quad \text{in } \Omega, \quad (1)$$

$$\frac{\partial\phi}{\partial n} = 0 \quad \text{on } S_r, \quad (2)$$

$$\frac{d\phi}{dt} = \frac{1}{2}|\nabla\phi|^2 + \frac{P_\infty - P_b}{\rho} \quad \text{on } S_b, \quad (3)$$

$$\frac{d\underline{x}}{dt} = \nabla\phi \quad \text{on } S_b, \quad (4)$$

$$\phi \rightarrow 0, \quad p \rightarrow p_\infty \quad \text{on } S_\infty, \quad (5)$$

where  $p$  is the pressure,  $\rho$  is the density,  $\partial/\partial n$  is the normal derivative, and  $d/dt = \partial/\partial t + \nabla\phi \cdot$  is the convective derivative. The pressure in the bubble,  $P_b$ , and at infinity,  $P_\infty$ , are taken constant in this study, although this is by no means required by the method. Surface tension effects have been disregarded, but they can be included with relative ease.

The strategy of solution is in principle quite straightforward. Suppose that the position of the bubble surfaces  $S_b$  and the value of  $\phi$  on  $S_b$  are known at time  $t$ . Then Eq.(1) can be solved using the boundary conditions (2), (5), and the known  $\phi$  on  $S_b$ . From a knowledge of the potential it is then possible to evaluate the right-hand sides of (3) and (4), which allows

the computation of the new configuration of  $S_b$  and of the potential on it at time  $t+\Delta t$ . The cycle is then repeated.

The crucial step in this procedure is the solution of the potential problem. In the past this has been done by finite differences<sup>1,2,4</sup> or by singularity methods<sup>6,7</sup>. The first approach is wasteful because it requires that the potential be known over the entire domain  $\Omega$ , although only free surface values are needed. In addition, the position of  $S_b$  does not coincide with grid nodes in general, which leads to well-known problems of accuracy, coding, and others. The second method avoids the explicit solution of (1) because the assumed form for  $\phi$  already is a solution of the Laplace equation. However a certain amount of guessing is necessary, and it is not clear whether very extreme bubble deformations can be described satisfactorily with this approach. Our technique, based on the boundary integral, or boundary element, method<sup>5</sup>, retains the advantages of the singularity method while avoiding its disadvantages since it is based on an exact relation, Green's identity. This identity for a point  $\underline{x}$  belonging to  $S_b$  or  $S_r$  has the form<sup>5</sup>

$$\phi(\underline{x}) = \frac{1}{2\pi} \int_{S_b+S_r} \{ |\underline{x}-\underline{x}'|^{-1} \frac{\partial \phi}{\partial n'} - \phi(\underline{x}') \frac{\partial}{\partial n'} |\underline{x}-\underline{x}'|^{-1} \} ds' \quad (6)$$

In conditions of axial symmetry, which we assume, this relation can be simplified by carrying out the integration over the azimuthal angle explicitly with the result

$$\phi(\underline{x}) = \int_{\Gamma_b+\Gamma_r} \{ G(\underline{x};\underline{x}') \frac{\partial \phi(\underline{x}')}{\partial n'} - H(\underline{x};\underline{x}') \phi(\underline{x}') \} ds' \quad (7)$$

In this equation  $\underline{x}$  and  $\underline{x}'$  belong to a meridian (half)plane passing through the axis of symmetry and  $\Gamma_b$  and  $\Gamma_r$  are the traces on this plane of  $S_b$  and  $S_r$  respectively;  $s'$  is the arc length on these curves  $\Gamma$ . In the meridian plane we choose a Cartesian system of coordinates  $(r,z)$ , of which the  $z$ -axis coincides with the axis of symmetry. Then  $G,H$  have the form

$$G(r,z;r',z') = \frac{2r'}{\pi\sqrt{A}} K(m) \quad , \quad H(r,z;r',z') = \frac{2r'}{\pi} \frac{\partial}{\partial n'} \{ K(m) \sqrt{A} \} \quad , \quad (8)$$

where  $A = (r+r')^2 + (z-z')^2$ ,  $m=4rr'/A$ , and  $K$  denotes the complete elliptic integral of the first kind.

In the applications to be described in this paper the existence of the rigid boundary is accounted for by introducing a system of "image" bubbles. Therefore condition (2) will be implicitly satisfied and it is no longer necessary to indicate explicitly the rigid boundary  $S_r$  or  $\Gamma_r$ . Accordingly, we shall not carry these symbols along in the following equations and we shall denote  $\Gamma_b$  simply by  $\Gamma$ .

#### Numerical method

Since  $\phi$  is known on  $\Gamma$  from the previous time step, Eq.(7) can be regarded as an integral equation for  $\partial\phi/\partial n'$ . To solve it, we approximate the line  $\Gamma$  by a polygonal line consisting of  $n$  segments  $\Gamma_j$  on each of which  $\phi$  and  $\partial\phi/\partial n'$  are taken constants. (We have also made some numerical experiments assuming a linear variation of  $\phi$  obtaining virtually identical results). In this way we obtain from (7) a linear system

$$\sum_{j=1}^n a_{ij} w_j = b_i \quad , \quad i = 1, 2, \dots, n \quad (9)$$

where  $w_j = \partial\phi(\underline{y}_j)/\partial n'$  can be interpreted as the value of the normal velocity at the midpoint  $\underline{y}_j$  of  $\Gamma_j$  and

$$a_{ij} = \int_{\Gamma_j} G(r_1, z_1; r', z') ds' \quad , \quad b_i = \phi(\underline{y}_i) + \sum_{j=1}^n \int_{\Gamma_j} H(r_1, z_1; r', z') \phi(r', z') ds' \quad . \quad (10)$$

Here  $r_i, z_i$  are to be interpreted as the coordinates of the midpoint  $y_i$  of  $\Gamma_i$ . The integrals in (10) are performed numerically by a six-point Gaussian formula except for those over  $\Gamma_j = \Gamma_i$  for which the integrand has an (integrable) logarithmic singularity. A series expansion in the neighborhood of this singularity coupled with Simpson's formula over the rest of the interval is used in this case. The elliptic integrals are computed using the simple approximate formulae of Ref. 8. The tangential velocity along the bubble surface is computed to the same accuracy as the normal velocity as follows

$$v(y_i) = \frac{\phi(x_{i+1}) - \phi(x_i)}{|x_{i+1} - x_i|} \quad (11)$$

where  $x_{i+1}$  and  $x_i$  are the extrema of the segment  $\Gamma_i$ . The normal and tangential velocities computed in this way are then referred to the  $(r, z)$  system of coordinates and transported by linear interpolation from the midpoints to the extrema of the segments  $\Gamma_i$ .

At this point Eqs. (3) and (4) can be used to compute the advanced-time values of the positions of the vertices of the polygonal line and of the associated velocity potentials. For this purpose the following second-order formula is used

$$\phi_i(t_{n+1}) = (1-\tau^2) \phi_i(t_n) + \tau^2 \phi_i(t_{n-1}) + (1+\tau) \Delta t_n d\phi_i(t_n)/dt \quad (12)$$

where  $\tau = \Delta t / \Delta t_{n-1}$  and  $\Delta t = t_{n+1} - t_n$ . A similar relation is used to compute the new values  $r_i, z_i$  of the positions of  $x_i$ . The possibility of using higher order time integration formulae of this type is a distinctive advantage of the present method over finite-differences ones. This advantage stems from the fact that here it is possible to follow the individual trajectories of the vertices of the polygonal line during the entire calculation. The time step used in (12) is adjusted during the calculation so as to prevent excessive variations of  $\phi_i, r_i, z_i$  during a single step.

### Results

We shall present the results in terms of lengths and times made dimensionless with respect to  $R_0$ , the initial bubble radius, and  $t_0 = R_0 \{ \rho / (p_\infty - p_b) \}^{1/2}$ . The pressure inside the bubble and at infinity have been kept constant in all the examples discussed.

To test the reliability of the method and of the code we have first of all computed the collapse of a single spherical bubble in an unbounded liquid, the well-known Rayleigh problem. The calculation started to develop instabilities in the velocity for a bubble radius  $R = 1.411 \times 10^{-2}$ , radial velocity  $R = 483.7$ , at time  $t = 0.9162$ . It is well known that this spherical collapse is unstable. Therefore, the ability of the code to compute a decrease in radius by nearly two orders of magnitude with no smoothing techniques applied and within a maximum 1.8% deviation from sphericity is an indication of an excellent performance. The analytical result for the radial velocity for the value of the radius indicated above is  $R = 487.4$ , again in excellent agreement with the numerical result. Finally, the analytical value of the total collapse time is  $t_c = 0.91468$ , in very good agreement with the computed value, which practically corresponds to total collapse.

As a second test we have considered one of the cases studied by Plesset and Chapman<sup>1</sup>. Here the bubble collapses in the presence of a plane rigid wall, from which it is separated by a distance equal to half the initial radius at  $t=0$ . In the calculation the plane was simulated by introducing an image bubble equal and symmetrically located with respect to the real bubble. By taking advantage of the symmetry of the problem it is possible to maintain the number of unknowns in the system (9) equal to the number of segments of the real bubble. We show in Fig. 1 the bubble shapes at selected instants (heavy lines) and the trajectories of some of the points on the bubble surface (light lines). It is interesting to observe the very strong convergence of streamlines in the jet which evolves in the later stages of the collapse. The shapes of Fig. 1 agree with those of Ref. 1, but a more stringent comparison is afforded by the values of the velocity of the "north pole" of the bubble as computed by us (Fig. 2, upper line) and as given in Ref. 1 (Fig. 2, open circles). Although the comparison is good, some minor discrepancies exist the origin of which is not clear at the present time. It may be noted how-

ever from the shapes published by Plesset and Chapman<sup>1</sup> that some imprecision affects their method near the "north pole" of the bubble, where the tangent fails to be zero as it should. The lower line of Fig. 2 shows the time development of the velocity of the "south pole" of the bubble.

As a final example we consider the collapse of a system of three equal and equally spaced bubbles, with centers on the axis of symmetry. The evolution of the process is shown in Fig. 3 for initial bubble spacings of 0.5 (left), 0.2 (center), and 0.1 (right). Because of the symmetry of this situation only the upper bubble and the upper half of the middle bubble are shown in the figure. The collapse of the central bubble is strongly inhibited by that of the other two and its "poles" move very little. This effect of course increases with the proximity of the bubbles.

Finally, to give an idea of the computational requirements we present in Table 1 some information on the number of segments used (for all the examples this is the number of segments in the first quadrant of the (r,z) plane), the number of time steps, and the CPU needed for the calculation on a UNIVAC 1100/8. Note that we have not tried yet to optimize the method with respect to time step size and number of segments used. For instance, it is believed that the latter quantity, in the cases of Fig. 3, could be reduced substantially without appreciable loss of accuracy.

Table 1. Some details on the computation

Case	Number of segments	Number of time steps	CPU time (mins and secs)
Rayleigh problem	16	105	1 7
Figure 1	32	79	3 15
Figure 3, left	48	92	8 30
Figure 3, center	48	99	9 12
Figure 3, right	48	100	9 7

#### Conclusions

The boundary integral method described in the present study has proven to be a very efficient and accurate tool for the study of non-spherical bubble dynamics. It makes possible extensive investigations of non-spherical bubble behavior at a fraction of the effort and cost required by other methods. In addition to its value for specific problems, we think that this feature is particularly important in the present state of research in this field because in our opinion only numerical experiments can help develop the intuition necessary for further progress.

#### Acknowledgment

This study has been supported in part by Ministero della Pubblica Istruzione of Italy.

#### References

1. Plesset, M.S., and Chapman, R.B., "Collapse of an initially spherical vapour cavity in the neighborhood of a solid boundary," J. Fluid Mech., Vol. 47, pp. 283-290. 1971.
2. Chapman, R.B., and Plesset, M.S., "Nonlinear effects in the collapse of a nearly spherical cavity in a liquid," J. Basic Eng., Vol. 94, pp. 142-145. 1972.
3. Ivany, R.D., and Hammitt, F.G., "Cavitation bubble collapse in viscous compressible liquids-Numerical analysis," J. Basic Eng., Vol. 87, pp. 977-985. 1965.
4. Prosperetti, A., "On the dynamics of non-spherical bubbles," in Lauterborn, W. (Ed.) Cavitation and Inhomogeneities in Underwater Acoustics, Springer-Verlag 1980, pp. 13-22.
5. Jaswon, M.A., and Symm, G.I., Integral Equation Methods in Potential Theory and Elastostatics, Academic Press 1977.
6. Bevir, M.K., and Fielding, P.J., "Numerical solution of incompressible bubble collapse with jetting," in Ockendon, J.R., and Hodgkins, W.R. (Eds.) Moving Boundary Problems in Heat Flow and Diffusion, Clarendon Press 1975.
7. Blake, J.R., and Gibson, D.C., "Growth and collapse of a vapour cavity near a free surface," J. Fluid Mech., in press.
8. Hastings, C., Approximations for Digital Computers, Princeton University Press 1955.

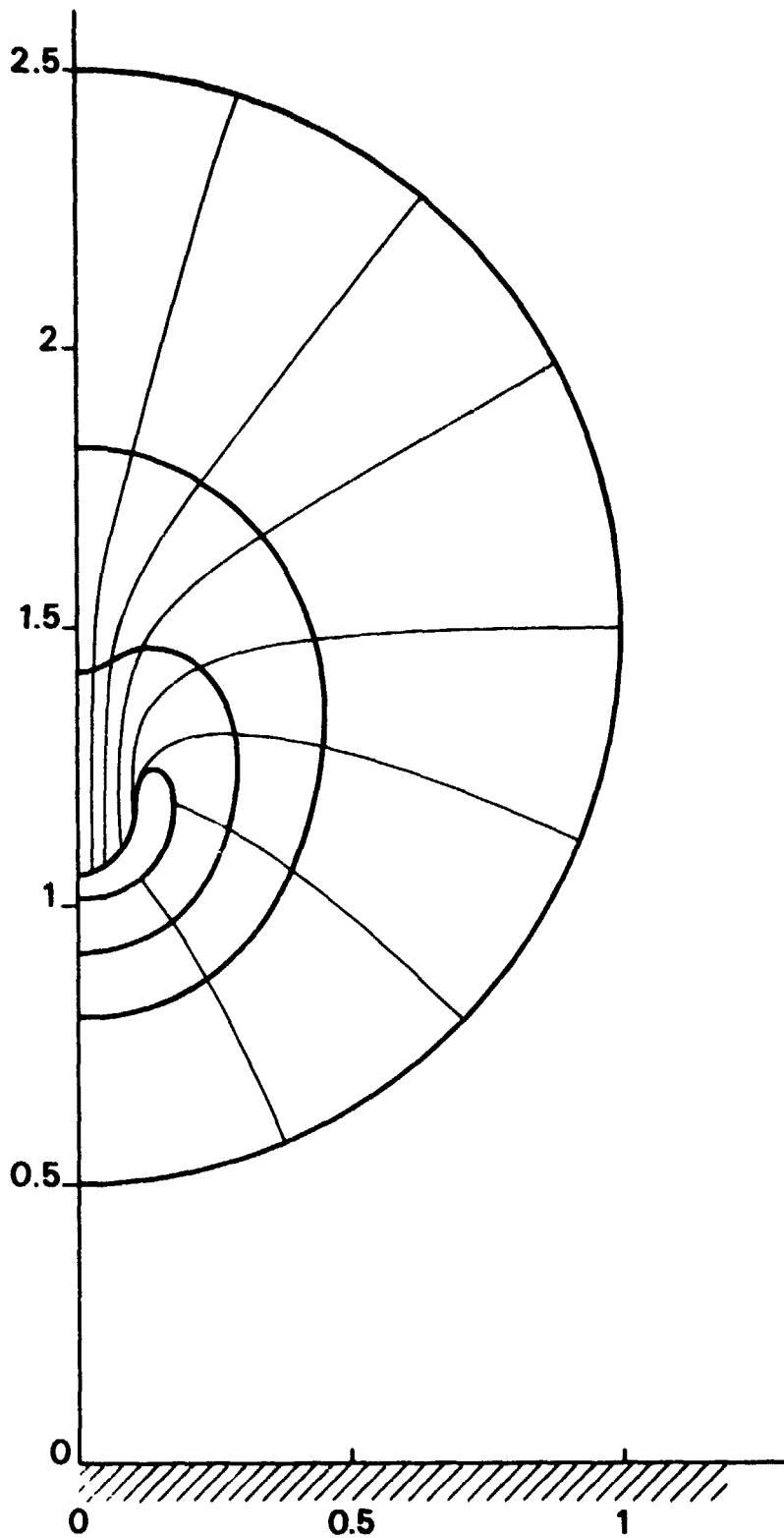


Figure 1. Collapse of an initially spherical bubble in the neighborhood of a solid plane from which it is separated by 0.5 times the initial radius. The shapes shown (heavy lines) are at  $t=0$ ,  $t=0.950$ ,  $t=1.010$ , and  $t=1.033$ . The collapse was completed during the time step after the last one shown. Light lines are particle trajectories.

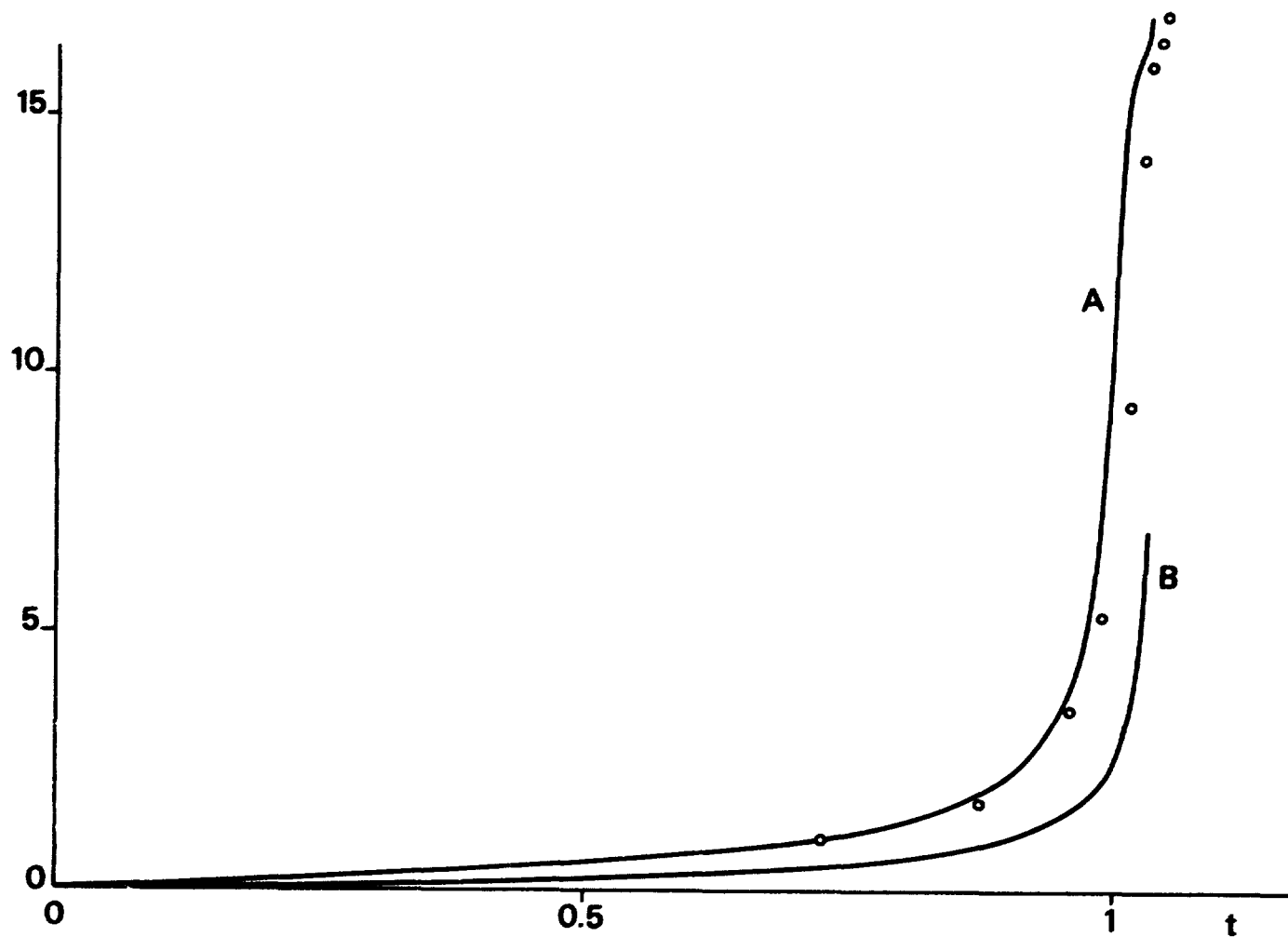


Figure 2. Comparison between the velocity of the "north pole" of the bubble of Fig. 1 (upper line) and the values given by Plesset and Chapman<sup>1</sup> (open circles). The lower line shows the velocity of the "south pole".

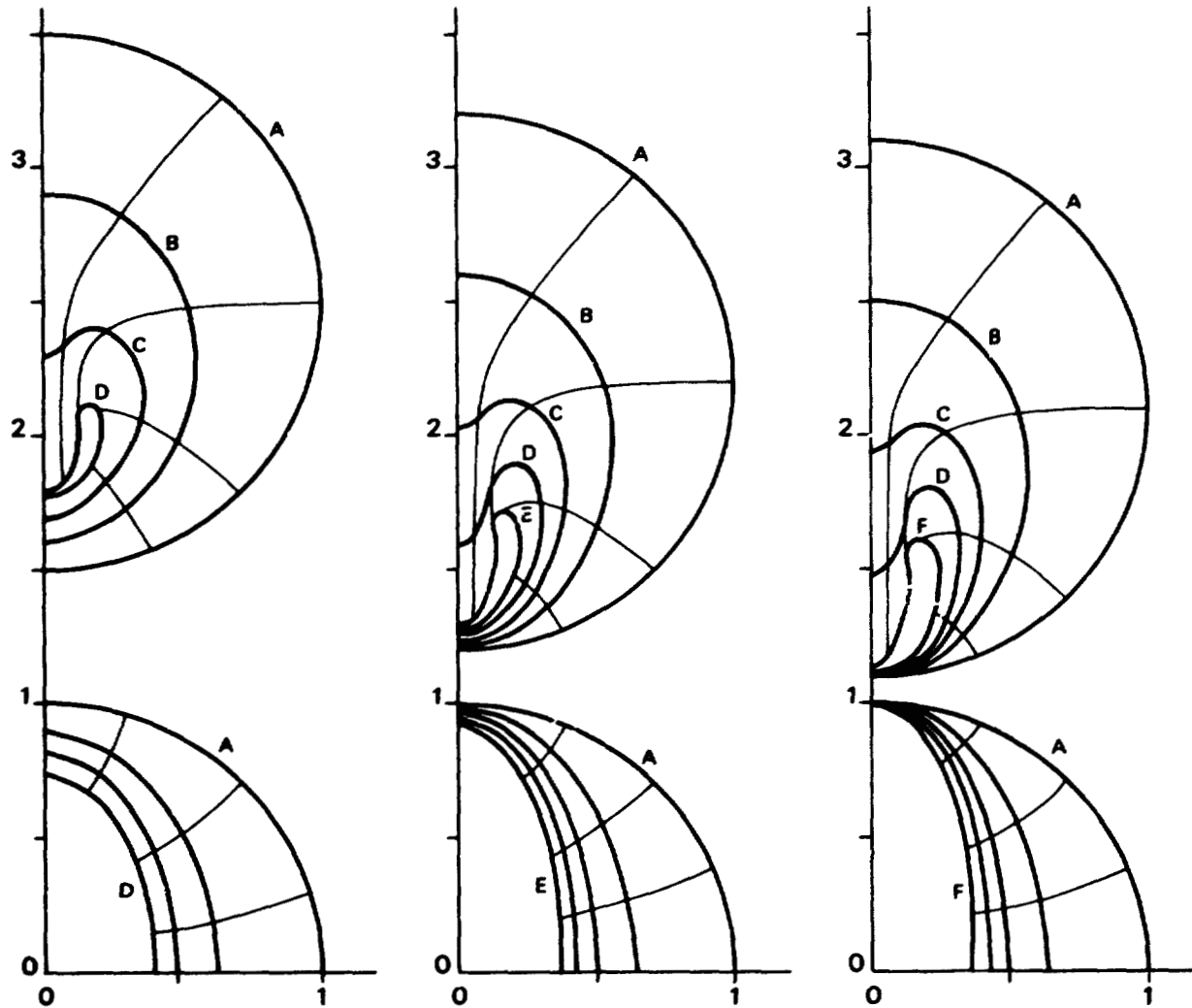


Figure 3. Collapse of three equal and equally spaced bubbles with collinear centers. The process is symmetric about the  $z=0$  plane. The initial bubble spacings are 0.5 (left), 0.2 (center), and 0.1 (right) times the initial radius. The shapes shown are for: A,  $t=0$ ; B,  $t=0.950$ ; C,  $t=1.063$ ; D,  $t=1.105$  (left and right),  $t=1.103$  (center); E,  $t=1.130$ ; F,  $t=1.135$ .

024  
N82 23442

Size distribution of Oceanic air bubbles  
entrained in sea-water by wave-breaking\*

François Resch

Université de Toulon, Château Saint Michel, 83130 La Garde, France

François Avellan

Ecole Polytechnique Fédérale de Lausanne, CH1015, Switzerland

Abstract

The determination of the size of oceanic air bubbles produced by whitecaps and wave-breaking is of great importance for predicting the production of liquid aerosols at the sea surface. These liquid aerosols are at the origin of most of the particulate materials exchanged between the ocean and the atmosphere. As no standard measurement techniques are presently available, a prototype has been especially designed and built using an optical technique. This technique is based on the principle of light scattering at an angle of ninety degrees from the incident light beam. The output voltage is a direct function of the bubble diameter. Calibration of the probe has been carried out within a range of 300  $\mu\text{m}$  to 1.2 mm. Bubbles are produced by wave-breaking in a large air-sea interaction simulating facility. Experimental results are given in the form of size spectrum.

Introduction

The production of marine aerosols, responsible for the transfer of large quantities (10<sup>10</sup> tons of salt per year) of materials from the ocean to the atmosphere, is governed by the bursting of air bubbles at the air-sea interface. These air bubbles are produced in bulk sea water by wave-breaking. After a variable life-span in water, the bubbles move up to the surface, burst and produce either jet drops or film drops or, most commonly, both simultaneously. The production of water droplets depends on the size of the generating air bubble. Consequently we have to determine the size-distribution, the concentration and the injection depths of this air bubble population in order to be able to predict the production of marine aerosols under varying wind conditions. This is of fundamental importance for our physico-chemical environment.

The physical mechanisms of bubble and drop production

When the wind speed is high enough, the waves become unstable and break. This leads to the presence of whitecaps at the sea surface and the penetration of air bubbles into bulk sea water. Although the mechanism by which these bubbles are introduced in water is not yet clear, it is thought that their presence might result principally from the three following processes: i) the formation of a roller at the wave crest engulfs a certain amount of air which is broken up in the water. This leads to the presence of larger bubbles close to the sea surface.

ii) the wave crest produces a plunging-like liquid jet which penetrates the sea water and leads to the production of bubbles of various sizes at various depths.

iii) the two-phase flow roller of the breaking wave slides down by gravity along the wave slope. This gravitational action combined with the horizontal shear stresses produced at the base of the roller introduces a large number of air bubbles near the throw of the wave, just as in the case of an hydraulic jump.

The injected bubbles are carried downwards by means of a water flow in one or a combination of the above patterns.

During their life-span in water (see figure 1), these air bubbles will be exposed to dynamic forces (drift currents, orbital movements), mass exchanges (growth or dissolution) and chemical reactions (collection of surfactants at their interface)<sup>2</sup>.

Owing to buoyancy forces, these bubbles return to the sea surface and break. This breaking leads to the formation of two families of droplets, the so-called "film drops" and "jet drops"<sup>3, 4</sup>.

\*Research done at the "Institut de Mécanique Statistique de la Turbulence". Laboratoire associé au CNRS, Université d'Aix-Marseille, 13003 Marseille, France.

Film drops are micronic in size. Their number is an increasing function of the generating bubble diameter. Jet drops are of a size approximate to  $1/10$  of the diameter of the generating bubble and their number is decreasing function of the size of the generating bubble. To date little is yet known about these two functions due to the large number of parameters involved.

It is to be noted that the bursting phenomenon is strongly dependent on the chemical composition of the interfacial microlayer.

To summarize, the production of marine liquid aerosols appears to result from a "cascade" or "chain" process<sup>5</sup> as schematically shown on Figure 2.

From the above description it appears evident that the determination of bubble characteristics such as size, injection depth and concentration, is of a particular importance.

### The measurement of bubble size

To date few investigators have tried to use various techniques to measure oceanic air bubble size. An acoustic technique was used by Medwin<sup>6</sup>, a trapping technique by Blanchard and Woodcock<sup>7</sup> and by Kolovayev, and a photographic method was used by Johnson and Cooke<sup>9</sup>. The results of these measurements have been carefully reviewed and compared by Wu<sup>10</sup>. The net result, however, is that more systematic measurements must be obtained by means of a reliable and proven technique.

After reviewing the various techniques available for detecting bubble size within the range 50  $\mu\text{m}$  to 5 mm, a local optical probe was selected.<sup>13</sup>

#### 1 - The principle of operation

The principle of operation of the optical probe is based on the measurement of the light flux scattered at an angle of ninety degrees from the incident light beam when a bubble is passing through the "sensing" volume. In the diameter range considered, the output signal, a direct function of the scattered flux, is proportional to the square of the bubble diameter. A simple calibration of the probe permits one to know the coefficient of proportionality.

#### 2 - Characteristics of the probe

The optical probe is schematically represented on Figure 3. The light source is made of a 2 mW He - Ne laser tube. The sensing volume, determined by the slit D1 and the diaphragm D2 approximately cylindrical in shape with a 500  $\mu\text{m}$  diameter and a 300  $\mu\text{m}$  height (see Figure 4). The light intensity should be uniformly distributed in this sensing volume. This is achieved by the presence of the two above-mentioned diaphragms D1 and D2.

It is important to mention that it is not the real bubble diameter  $d$  which is detected, but only the image of these diaphragms through the lenses in the bubble. This leads to an apparent diameter  $kd$  of the bubble, where  $k$  is independent of  $d$  and (here) of the order of  $1/20$ . This enables one to measure bubbles with a diameter larger than the "sensing" volume.

The laser source, the optical system, the photoamplifier and its associated electronics are gathered in a parallelepipedic waterproof stainless steel case of 5 cm x 10 cm x 30 cm (see Figure 4). A more detailed description of the probe is given by Avellan<sup>11</sup>.

#### 3 - Calibration of the probe

As mentioned above, calibration of the probe is necessary in order to convert the output signal voltage into bubble diameter. For this calibration, bubbles of a given and uniform diameter are produced by means of capillary glass-tubes in a unit especially built for this purpose (see Figure 5).

Special care was given so that the bubble completely crossed the "sensing" volume. A few thousand bubbles were so produced, their number carefully recorded and the total volume of air measured with a calibrated glass tube. It was then possible to relate the output voltage to bubble diameter. This was done for four different bubble sizes and, as expected, the output voltage is directly proportional to the square of the bubble diameter (see Figure 6).

### Experimental results

#### 1 - Data recording conditions and anticipated errors

Measurements were digitally recorded on magnetic discs and tapes through an analog to

digital converter combined with a mini-computer. In order to record only the presence of bubbles passing through the sensing volume of the probe, an hardware voltage amplitude threshold system was designed.

Side effect errors are possible when a bubble is only partially detected by the sensing volume. This error is an increasing function of the ratio of the bubble volume (based on the diameter  $k_d$ ) to the "sensing" volume. In a first approximation this error was neglected (the maximum value of  $k_d$  being  $\approx \frac{1}{20} \times 500 = 25 \mu\text{m}$  is to be compared with the  $300 \mu\text{m}/500 \mu\text{m}$  dimensions of the sensing volume).<sup>20</sup> A more complete statistical derivation has been developed by Avellan.

The error due the simultaneous passage of more than one bubble in the detecting volume  $V$  has also been disregarded. The concentration is so small that the probability of finding more than one bubble at the same time in the volume  $V$  is very low.

## 2 - Experimental conditions

Experiments were carried out in the large air-sea interaction facility of the "Institut de Mécanique Statistique de la Turbulence" (I. M. S. T., Marseille, France)<sup>12</sup>. Breaking waves were produced by both wind blowing (at 14m/s) and a wave generator. The probe was completely immersed in the water to a depth of few centimeters below the throw of the wave. Data were recorded during a three hour period. Approximately 500 bubbles were detected.

## 3 - Bubble size distribution

Voltage histogram and bubble size distribution are shown in Figure 7 and 8 respectively. They are normalized by the exact total number of bubbles detected, 517, and by the voltage window width, 156 mv. On the bubble size spectrum, confidence intervals have been reported. On the voltage histogram, larger bubbles, corresponding to values of voltage larger than 8 volts, were not taken into account as the photomultiplier gain was purposely limited.

## Discussion and Conclusions

These preliminary results show that such an optical probe can be used with success to determine the size spectra of oceanic air bubbles entrained in sea-water by wave-breaking.

The first obvious observation is that very large confidence intervals exist in the data plot. This is due to the overly small detecting volume for a two-phase flow configuration with a very small concentration of bubbles. If it looks advisable to limit, even to reduce, the recording time, it is then necessary to increase the detecting volume widely. With such a configuration, a factor of 1000 times larger for this volume, i. e. of 10 on the linear sizes would be suitable. This would allow ones not only to decrease the duration of the experiment and to limit the statistical uncertainties but would also drastically decrease the side effect error. In return, the coincidence effect could be increased, but could be easily taken into account during data processing.

It would also seem necessary to improve the resolution of the probe towards the smaller diameters, e. g. less than  $200 \mu\text{m}$ . This is presently being done by replacing the hardware voltage threshold system by a software one and by increasing the sensitivity of the photomultiplier. The software data acquisition control also allows one to record the time intervals between bubble appearance in the "sensing volume" which subsequently gives more information on the two-phase flow configuration.

Thanks to this first set of experimental results presented above, new additional experiments have been performed with the benefit of such improvements as on the probe characteristics and the data treatment. They were performed in the same simulating facility applying various wind conditions at various depths. They are presently under processing.

## Acknowledgments

The authors wish to acknowledge the contribution of the research and technical staff of the I. M. S. T. as well as the financial support given by the Centre National de la Recherche Scientifique and the Centre National pour l'exploitation des océans (grant n°80/2196).

## References

1. Resch F. J., Leutheusser H. J. and Alemu S. Bubbly two-phase flow in hydraulic jumps, Journal of the Hydraulics Division, A. S. C. E., 100, No HY1, Proc. Paper 10297, Jan., pp. 137-149, 1974.
2. Blanchard D. C. and Syzdek L. D., Concentration of bacteria in jet drops from bursting bubbles, J. Geophys. Res., 77, 5087-5099, 1972.

3. MacIntyre F., The top Millimeter of the ocean, Scientific American, 230, May 1974.
4. Blanchard D. C., The electrification of the atmosphere by particle from bubbles in the sea, Progress in Oceanography, 1, pp. 73-202. 1963.
5. Resch F. J., Echanges particulaires air-mer (au niveau de l'interface), Proceedings de l'Ecole Européenne d'Eté, Cahiers Jacques Fauchère. Université de Paris VI. 1981.
6. Medwin H., In situ acoustic measurements of bubble populations in coastal ocean waters, J. Geophys. Res., 75, 599-611. 1970.
7. Blanchard D. C. and Woodcock A. H., Bubble formation and modification in the sea and its meteorological significance, Tellus, 9, No2, pp. 145-158. 1957.
8. Kolovayev D. A., Investigation of the concentration and statistical size distribution of wind-produced bubbles in the near-surface ocean, Oceanology, Engl. Transl., 15, 659-661. 1976.
9. Johnson B. D. and Cooke R. C., Bubble populations and spectra in coastal waters : a photographic approach, J. Geophys. Res., 84, 3761-3765. 1979.
10. Wu J., Bubble populations and Spectra in near-surface ocean : summary and Review of Field Measurements. Journal of Geophys. Res., Vol 86, No C1, pp. 457-463. Jan. 1981.
11. Avellan F., Caractéristiques diphasiques des échanges particulaires à l'interface air-mer : étude météorologique. Thèse de Docteur-Ingénieur, I. M. S. T., Université d'Aix-Marseille.
12. Coantic M., Ramamonjariasca F., Mestayer P., Resch F. and Favre A., Wind water tunnel simulation of small-scale ocean-atmosphere interactions, J. of Geophys. Res., Vol 86, No C7, pp. 6607-6626. July 1981.
13. Resch F., Measurement techniques in the two-phase flow region of the air-sea interface layer, Proceedings of the dynamic flow conference, 1978.



Figure 1. Schematic representation of the air-sea particulate exchanges.

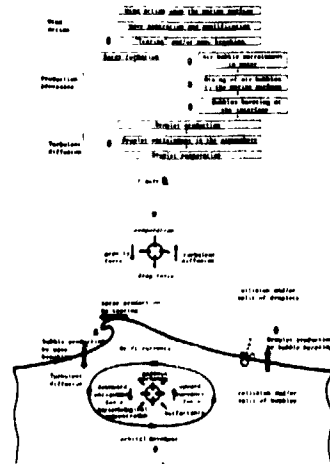


Figure 2. Physical mechanisms for the production of marine liquid aerosols.

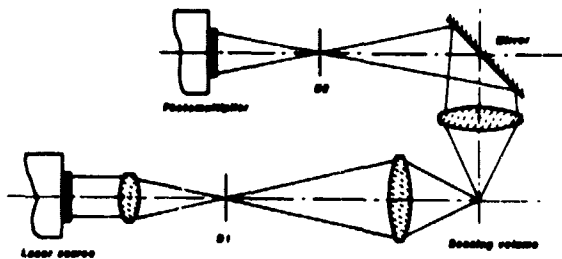


Figure 3. Schematic diagram of the optical part of the probe.

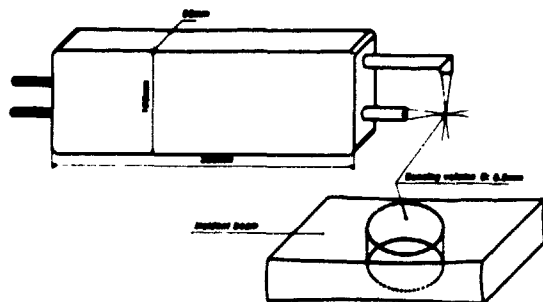


Figure 4. Optical probe with details of the sensing volume.

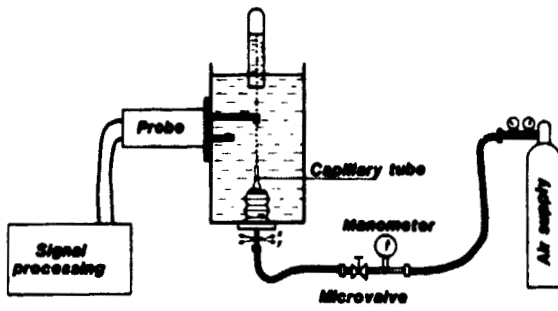


Figure 5. Calibration unit.

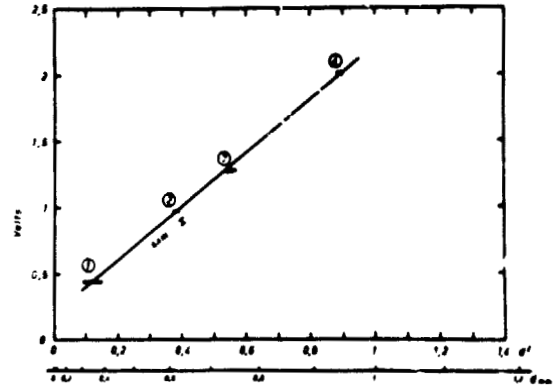


Figure 6. Calibration curve.

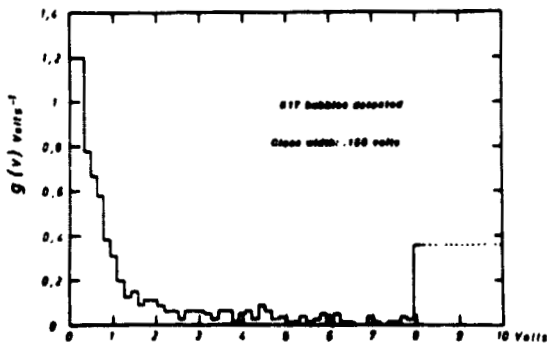


Figure 7. Normalized voltage histogram.

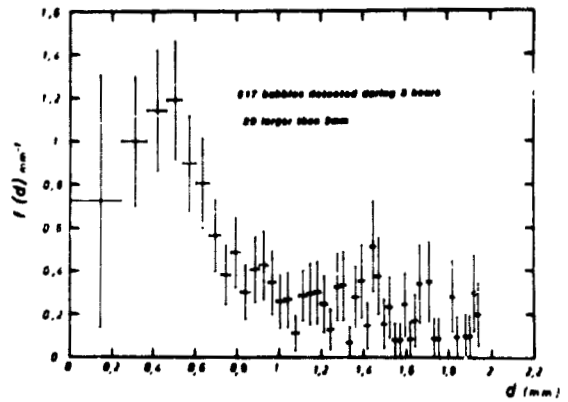


Figure 8. Normalized bubble size spectrum.

## Collapse of large vapor bubbles

James Tegart and Sam Dominick

Propulsion Section, Martin Marietta Denver Aerospace  
P. O. Box 179, Denver, Colorado 80201Abstract

The refilling of propellant tanks while in a low-gravity environment requires that entrapped vapor bubbles be collapsed by increasing the system pressure. Tests were performed to verify the mechanism of collapse for these large vapor bubbles with the thermodynamic conditions, geometry, and boundary conditions being those applicable to propellant storage systems. For these conditions it was found that conduction heat transfer determined the collapse rate, with the specific bubble geometry having a significant influence.

Introduction

The capability of refilling the storage tanks for liquid propulsion systems while a spacecraft is in earth orbit will yield a number of benefits. With refilling, the life of a spacecraft can be extended or a space-based vehicle could be reused for numerous missions. Methods of refilling a propellant tank while in low-gravity are currently being developed. This paper considers one aspect of tank refilling: the collapse of vapor bubbles that may become entrapped within the tank during filling.

Expulsion of liquid propellants from a tank under low-gravity conditions requires some means of ensuring that only liquid will be supplied to the engine. Capillary propellant management devices, using fine-mesh screen to orient liquid and exclude gas are the likely choice for the expulsion system, especially for cryogenic propellant applications. These devices are now being used for propellant expulsion on the Space Shuttle<sup>1</sup> and various communications satellites. In one configuration, the fine-mesh screen is used on channels mounted near the tank wall and encircling the tank. These channels form a flow passage from the bulk liquid, regardless of its orientation, to the tank outlet. Liquid flows through the screen in preference to gas, due to the capillary pressure differential developed at the pores of the screen.

During the filling of the tank, vapor bubbles can be entrapped within the channels of the capillary device if the screen becomes wetted before the vapor can escape. Vapor cannot be permitted to remain within the channels of the device since it could cause dryout of the screen and failure of the ability of the device to expel gas-free liquid. Such vapor bubbles can be eliminated by pressurizing the tank, making the liquid subcooled with respect to the vapor pressure and causing the vapor to condense. Collapse of the vapor bubble must occur within a reasonable length of time (preferably minutes) so that the refilling process can be completed and the subsequent mission for the spacecraft begun.

A survey of the analytical and experimental investigations of bubble collapse can be found in reference 2. Of the work surveyed, that of Florschuetz and Chao<sup>3</sup> seems the most comprehensive. It defines the regimes in which inertia, heat transfer, or both mechanisms determine the bubble collapse rate. For the case of heat transfer controlled collapse (of interest here) Florschuetz and Chao consider a solution based on the Plesset-Zwick temperature integral<sup>4</sup> to be an upper bound for the bubble size versus time curve and their "plane interface" solution to be an "approximate lower limit". However, Prigynakov<sup>5</sup> obtained a solution that "gives better agreement with experiments" and predicts a faster rate of collapse. Likewise, the analysis of Theofanous<sup>2</sup> predicts a faster collapse rate than Florschuetz and Chao and "improvements in the agreement are noted" when non-equilibrium effects were considered.

In applying any of the above theories to predict collapse times during tank refilling there are two concerns. One is that the collapse time for bubbles with volumes on the order of 100 cm<sup>3</sup> is desired, while the above theories have only been verified with tests of bubbles on the order of 1 cm<sup>3</sup>. The second concern is that bubbles in contact with the inside walls of the channels will be elongated in shape, while the existing theory is applicable only to spherical bubbles. An analytical and experimental investigation was therefore performed to determine the influence of bubble size and shape on the collapse time.

### Analysis

Florschuetz and Chao<sup>3</sup> define a dimensionless parameter,  $B_{eff}$ , to classify the mode of bubble collapse. For values of  $B_{eff}$  less than 0.05 heat transfer controls the collapse while values greater than 10 indicate inertia controls. An intermediate case exists between these values. The parameter is defined as

$$B_{eff} = \gamma^2 \left( \frac{\rho c \Delta T}{\beta L} \right)^2 \frac{\alpha}{r_i} \left( \frac{\rho}{\Delta P} \right)^{1/2} \quad (1)$$

(A list of symbols can be found at the end of this paper.)

Values of  $B_{eff}$  were calculated for typical conditions in a propellant tank and the range of conditions planned for the experiments, and it was established that in all cases  $B_{eff}$  is much less than 0.05 (on the order of 10<sup>-5</sup>), indicating that heat transfer will control the rate of bubble collapse.

The configuration of the bubble within the channel is as shown in Figure 1. Both screen and sheet metal surround the bubble on four sides with a vapor-liquid interface at each end. Under low-g conditions the liquid interface will have curvature, but a flat interface has been assumed here to simplify the analysis. It was assumed that the vapor bubble and liquid are initially in equilibrium and then the system pressure is instantaneously increased by some amount. The increase in pressure increases the saturation temperature of the vapor above the liquid temperature. This change in the thermodynamic condition results in condensation of the vapor and collapse of the bubble.

The change in the volume of the vapor bubble is dependent on the rate at which vapor condenses.

$$dV = \frac{1}{\rho_v} dm \quad (2)$$

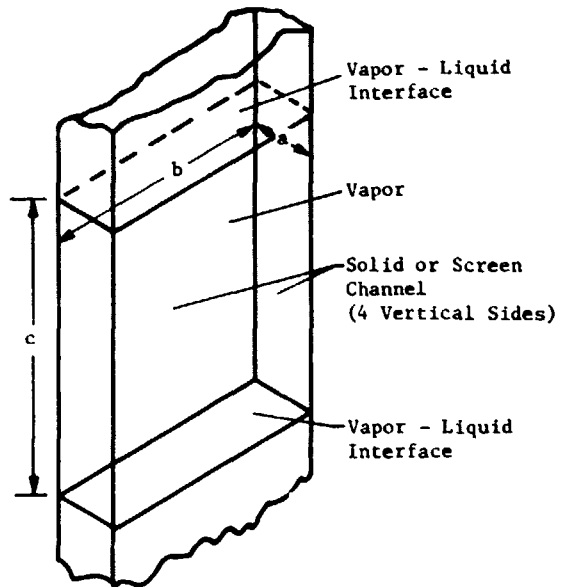


Figure 1. Bubble Geometry

The rate of condensation is dependent upon the rate at which heat is transferred from the vapor to the surrounding liquid.

$$dm = \frac{Q}{L} dt \quad (3)$$

Therefore

$$dV = \frac{1}{\rho_v} \frac{Q}{L} dt \quad (4)$$

The greater saturation temperature causes the vapor to condense on the liquid, creating a liquid film that is at the saturation temperature. Condensation continues based on the rate at which this heat can be conducted into the liquid. Convection heat transfer is negligible since the vapor temperature remains essentially unchanged during collapse. The unsteady heat conduction into a semi-infinite solid is given by <sup>6</sup>

$$Q = \frac{kA\Delta T}{\sqrt{\pi\alpha t}} \quad (5)$$

The conductivity is that of the liquid only since the contribution of the thin sheet metal and screen has a negligible effect on the heat transfer rate (this assumption will be discussed in more detail later). Then

$$\frac{dV}{A} = \frac{k\Delta T dt}{\rho_v L \sqrt{\pi\alpha t}} \quad (6)$$

which can be reduced to

$$\frac{dV}{A} = \sqrt{\frac{\alpha}{\pi}} Ja \frac{dt}{t} \quad (7)$$

where Ja, the Jacob number, is defined as

$$Ja = \frac{\Delta T_c \rho_l}{L \rho_v} \quad (8)$$

Based on the bubble geometry in Figure 1,

$$dV = ab \, dc \quad (9)$$

and

$$A = 2ab + 2bc + 2ac \quad (10)$$

After integration, the following equation is obtained for the collapse of the bubble from its initial length ( $c_i$ ) to any final length ( $c_f$ ).

$$t = \frac{\pi}{4Ja^2\alpha} \left[ \frac{ab}{2(a+b)} \ln \frac{(a+b)c_f + ab}{(a+b)c_i + ab} \right]^2 \quad (11)$$

For complete collapse of the bubble  $c_f$  equals zero. It was assumed that only the length of the bubble changes as it collapses, but there would be a transition to a spherical bubble when the length  $c$  approached the channel thickness,  $a$ . Based on the assumptions it would be expected that this equation would be most applicable to the collapse of larger bubbles and be least accurate for the collapse of smaller bubbles and the final stages of collapse of any bubble.

It is interesting to note that if a spherical bubble geometry is used in solving equation (7), then  $dV = dr$  and the time for a bubble to completely collapse from an initial radius ( $r_i$ ) is:

$$t = \frac{\pi r_i^2}{4Ja^2g} \quad (12)$$

This is the same result Florschultz and Chao<sup>3</sup> obtained for their plane interface solution. Priskyakov<sup>5</sup> obtained a similar result except that the coefficient was 16 instead of 4.

For a given bubble volume, equations (11) and (12) were used to calculate bubble collapse times. For larger bubbles the difference in geometry causes the rectangular shaped bubble to collapse about four times as fast as a spherical bubble of the same volume.

### Experiments

In order to verify the analytical model presented in the previous section and to investigate the influence of bubble geometry and the channel on bubble collapse, an experimental investigation was performed. The approach was to form a bubble within a channel, pressurize the container in which the channel was installed and monitor the collapse of the bubble. Since a stationary bubble can be formed and confined within the liquid by the channel, a one-g test closely represents the low-g conditions. The mechanism of the bubble collapse, conduction heat transfer, is independent of the g-level and only minor changes in the shape of the vapor bubble would be expected in low-g.

A transparent channel, to permit viewing of the vapor bubble, was fabricated from plastic. It had an inside cross-section of 2.5 cm by 7.6 cm and was 30.5 cm long. One side of the channel (see Figure 2) was a fine mesh screen having a 325 x 2300 (wires per inch in warp and shute directions) mesh, Dutch twill weave and an effective pore diameter of 7 microns. This screen was capable of retaining any size vapor bubble within the channel. The channel was installed vertically within a transparent plastic box (Figure 3).

Freon 11 (CCl<sub>3</sub>F) was selected as the test liquid. This Freon has a boiling point of 23.8°C at 1 atm so vapor bubbles could be easily created under ambient conditions. Liquid Freon 11 has the following properties at 20°C:  $\rho = 1.49 \text{ gm/cm}^3$ ,  $L = 43.1 \text{ cal/gm}$ ,  $c_p = 0.205 \text{ cal/gm}^\circ\text{C}$  and  $\alpha = 2.5 \times 10^{-4} \text{ m}^2/\text{hr}$ . The saturation curve is linear, having a slope of 0.32°K per kPa.

The test procedure was to fill the channel and container with liquid so the channel was completely filled and submerged, excluding all air from the channel. While maintaining the container at a higher pressure to inhibit boiling, the channel was vented to form the vapor bubble. If necessary, a vapor generator could be used to aid in forming a bubble of the desired initial size. The size of the bubble was monitored to ensure that the vapor was initially in equilibrium with the liquid. The initial temperature of the liquid, system pressure and bubble length were recorded.

A gaseous nitrogen pressurization system connected to the container was set to give a desired increase in system pressure. The valve that applied the pressure increase to the container had an opening time that was negligible in comparison to the typical collapse times of 1 to 11 seconds. A motion picture camera photographed the bubble collapse. The bubble length versus time was measured using a scale on the channel and the frame rate of the camera. A total of 99 tests were performed, primarily varying the initial bubble length and the amount of pressure increase.

For data correlation, the analytical model was adapted to the specific test conditions. The plastic walls of the channels influenced the modeling of the heat transfer, while the effect of the screen could be neglected. The plastic was 1.3 cm

ORIGINAL PAGE  
BLACK AND WHITE PHOTOGRAPH

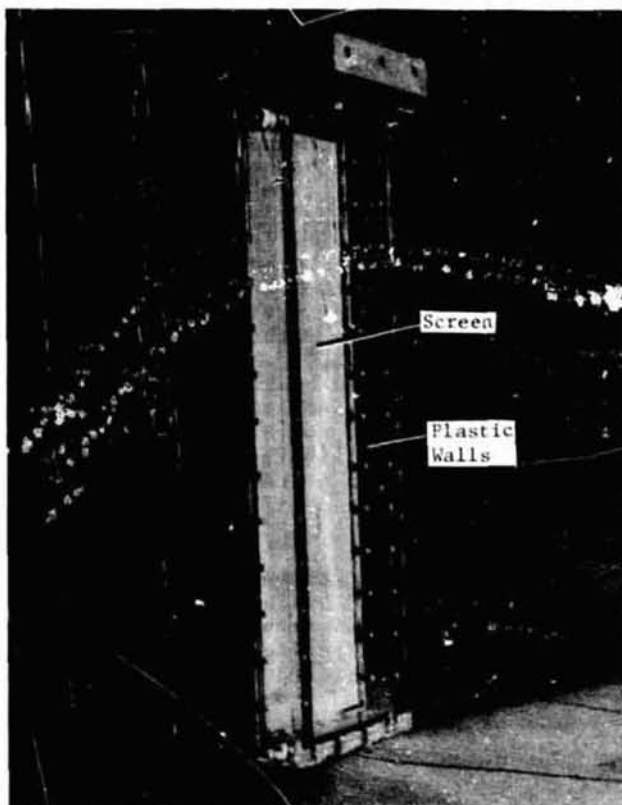


Figure 2. Channel Model

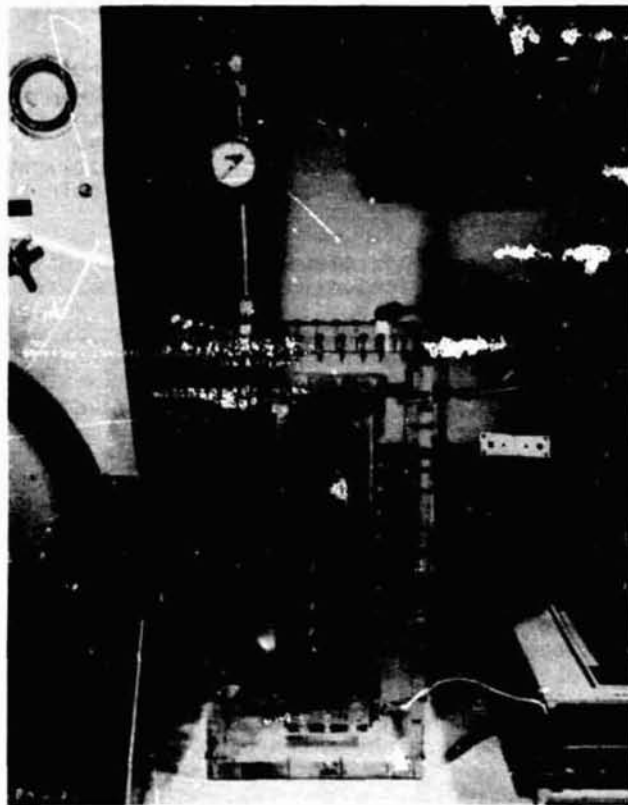


Figure 3. Test Apparatus

thick and had a diffusivity of  $4.5 \times 10^{-4} \text{ m}^2/\text{hr}$  (twice the value for the liquid), while the screen was 0.064 mm thick and had a diffusivity of  $1.5 \times 10^{-2} \text{ m}^2/\text{hr}$  (stainless steel). The thermal penetration thickness given by<sup>7</sup>

$$\delta_t = \sqrt{4\alpha t} \quad (13)$$

was used to evaluate the relative influence of the materials of the test article. For the vertical plastic walls the heat conduction occurred solely within the plastic so the liquid adjacent to the outside of the channel did not contribute to the heat transfer. The screen quickly reached the temperature of the surrounding liquid due to its thinness and high diffusivity, so its contribution to conduction perpendicular to its surface was negligible. Similarly, heat conduction parallel to the screen was shown to be negligible. Therefore, the heat transfer at the surfaces of the bubble were modeled as follows:

upper surface and 3 vertical sides - unsteady conduction into plastic, and screen surface and liquid surface - unsteady conduction into liquid

Equation (5) with the appropriate values for  $k$  and  $A$  was used for both cases.

From the film data it was established that the collapse of the bubble occurred as a rise in the liquid surface, changing only the length of the bubble, until small values of bubble length were reached. At bubble lengths less than one centimeter the bubble began to decrease in width and during the last stages of collapse the bubble reached a

spherical shape and then disappeared. The data correlation concentrated on the initial stages of collapse when only the length of the bubble was changing and the major change in volume occurred.

As previously discussed it was established that the screen had a negligible effect on the heat transfer into the liquid. However, another potential influence of the screen is the effect of its flow resistance on the collapse rate. Liquid must flow through the screen, filling the channel as the vapor condenses. An analysis determined that the pressure drop due to flow at the rate established by the bubble collapse had a negligible effect on the pressure of the liquid within the channel.

Preliminary correlations indicated that the bubble collapsed faster than predicted by equation (11) (including the above discussed modifications). Therefore a correlation coefficient,  $F$ , was applied to equation (5) for the heat transfer rate, giving a term  $F^2$  in the denominator of equation (11). It was found that the value of  $F$  that best correlated the collapse time of the bubbles typically ranged from 1.3 to 2.0. Neither the initial length of the bubble nor the change in system pressure appeared to have any effect on the variation in the value of  $F$ . Based on the excellent and more constant correlation obtained for the bubbles having long collapse times, a value of 1.4 for  $F$  was selected as giving the best fit. This means that the coefficient in equation (11) is increased to 8, placing the value midway between that of Florschuetz and Chao<sup>3</sup> with a coefficient of 4 and Prisyakov<sup>5</sup> with a coefficient of 16.

Figure 4 is an example of the correlation of a test in which the bubble had a long collapse time. A very close match between the calculated and measured collapse rate was obtained over the latter 10 seconds of the test. During the first 1.5 seconds of the test the bubble collapsed at a slower rate than predicted. This initial difference in the calculated and measured collapse rate becomes more evident in the shorter duration tests shown in Figures 5 and 6. Changing the heat transfer rate (through  $F$ ) only changed the point at which the curves for the calculated and measured collapse rate intersected and did not improve the match of their slopes.

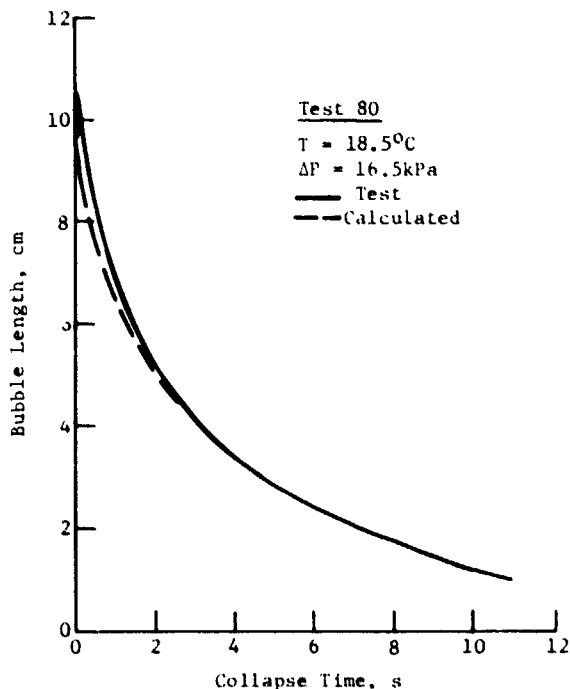


Figure 4. Correlation of Bubble Collapse, Long Collapse Time

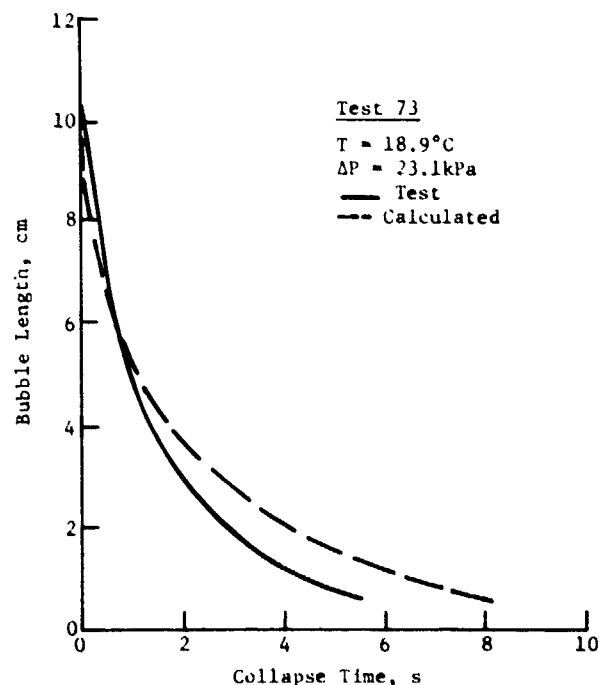


Figure 5. Correlation of Bubble Collapse Intermediate Collapse Time

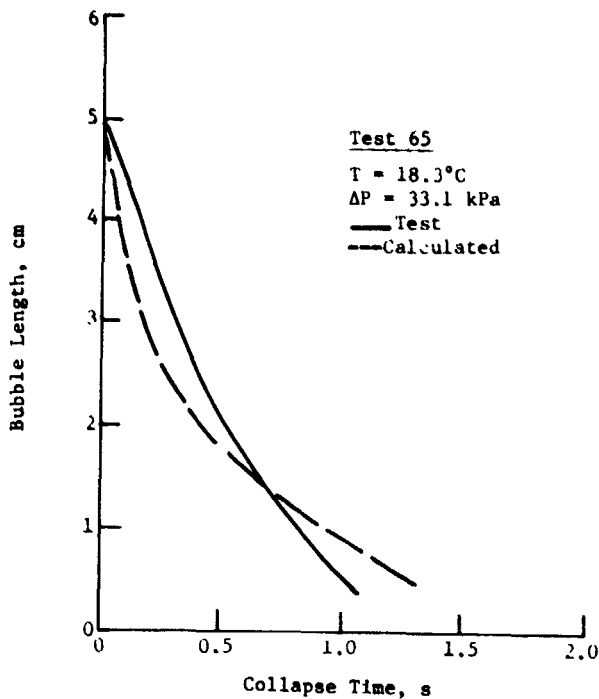


Figure 6. Correlation of Bubble Collapse, Short Collapse Time

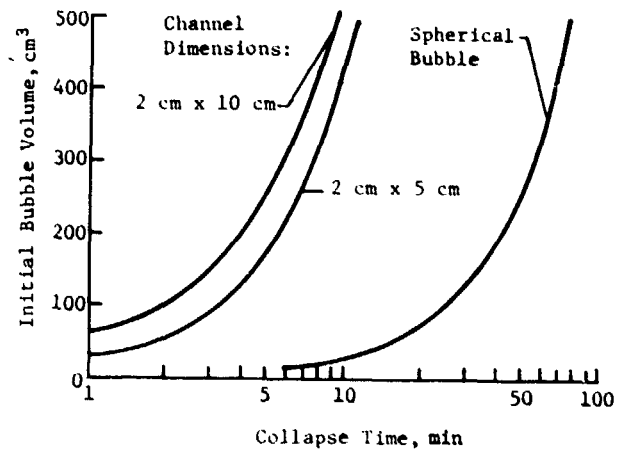


Figure 7. Collapse of Hydrogen Vapor Bubbles,  $T = 20.2^\circ\text{K}$ ,  $\Delta P = 50 \text{ kPa}$

### Conclusions

An analytical and experimental investigation of the collapse of a large vapor bubble inside of a channel has established that conduction heat transfer is the primary mechanism of collapse for the conditions of interest. It was found that the elongated shape of the bubble decreased the collapse time in comparison to a spherical bubble of the same volume. An analytical model, based on conduction heat transfer to the surrounding liquid, gave excellent correlation of those tests having a longer collapse time ( $\sim 10$  seconds).

It appears that there are two stages to the bubble collapse, based on the tests performed here. In the initial stage, lasting about 1.5 seconds, the rate of collapse was less than predicted by the heat transfer model. Apparently the inertia of the liquid, flowing into the channel through the screen to replace the condensed vapor, reduced the initial collapse rate. This effect made the correlation of the shorter duration tests less accurate.

During the later stage of collapse the rate was greater than predicted by the heat transfer model. This deficiency was corrected by the correlation coefficient which resulted in matching of the rates and times of collapse during that stage. This difference is typical of the variation noted in other bubble collapse analyses, as discussed in the introduction. When the collapse time is long, the influence of the initial phase became insignificant and the heat transfer model accurately predicted the collapse time.

A correlation coefficient of 1.4 was selected as giving the best fit to all the data. Based on the data, the following equation will accurately predict the longer collapse times and it will predict too long a time for short collapse periods.

$$t = \frac{\pi}{8Ja^2\alpha} \left[ \frac{ab}{2(a+b)} \ln \frac{ab}{(a+b)c_1 + ab} \right]^2 \quad (14)$$

When this equation is used to predict the collapse time of hydrogen vapor bubbles the result shown in Figure 7 is obtained. The saturation curve for hydrogen is non-linear and the change in saturation temperature with pressure becomes small at pressures above 100 kPa. For example, at 100 kPa a 50 kPa change in pressure causes the saturation temperature to change by only 1.5°K. Collapse times of many minutes, or even hours, are possible with hydrogen. Hydrogen presents a "worst-case" in comparison to other propellants for the problem of collapsing entrapped vapor bubbles during tank refill.

In comparison to the collapse time for a spherical bubble (based on Ref. 3), equation (14) yields a collapse time for an equal volume bubble in a channel that is about 10 times less. At these low collapse rates inertia effects should be negligible, so the assumptions applicable to equation (14) are justified for this application and reasonably accurate predictions of the collapse time should be expected.

#### List of Symbols

A	area
a,b,c	bubble dimensions
B <sub>eff</sub>	dimensionless group
c <sub>p</sub>	specific heat of liquid
F	correlation coefficient
Ja	Jacob number
k	thermal conductivity of liquid
L	heat of vaporization
m	mass
ΔP	difference between system pressure and vapor pressure
Q	rate of heat transfer
r	bubble radius
t	time
ΔT	difference between vapor saturation temperature and liquid temperature
V	volume
α	thermal diffusivity of liquid
ρ	liquid density
ρ <sub>v</sub>	vapor density
ρ̄ <sub>v</sub>	average vapor density
ψ	temperature difference correction factor (see Ref. 3)
δ <sub>t</sub>	thermal penetration thickness

#### References

- 1 Peterson, R. and Uney, P., Development and Qualification of the Space Shuttle Orbiter Reaction Control System Propellant Tank, AIAA Paper 78-1026, AIAA/SAE 14th Joint Propulsion Conference, Las Vegas, Nevada, July 1978.
- 2 Theofanous, T.G., et al, Nonequilibrium Bubble Collapse: A Theoretical Study, Chemical Engineering Progress Symposium Series, No. 102, Vol. 66, 1970, pp 37-46.
- 3 Florschuetz, L.W. and Chao, B.T., On the Mechanics of Vapor Bubble Collapse, Journal of Heat Transfer, May 1965, pp 209-220.
- 4 Plesset, M.S. and Zwick, S.A., The Growth of Vapor Bubbles in Superheated Liquids, Journal of Applied Physics, Vol. 25, No. 4, April 1954, pp 493-500.
- 5 Prismanyakov, V. F., Condensation of Vapour Bubbles in Liquid, Int. J. Heat Mass Transfer, Vol. 14, 1971, pp 353-356.
- 6 Carslaw, H.S. and Jaeger, J.C., Conduction of Heat in Solids, Oxford at the Clarendon Press, 1959.
- 7 Bird, R.B., Stewart, W.E., and Lightfoot, E.N., Transport Phenomena, John Wiley and Sons, Inc., 1960, p354.

## A New Droplet Generator

W.E. Slack

National Aeronautical Establishment  
National Research Council of Canada  
Ottawa, Canada, K1A 0R6

A new droplet generator developed for laboratory use at NAE is described. A loud speaker driven extractor needle is immersed in a pendant drop. Pulsing the speaker extracts the needle forming a fluid ligament which will decay into a droplet. The droplets are sized by stroboscopic photographs. The droplet's size can be changed by varying the amplitude of the speaker pulses and the extractor needle diameter. The mechanism of droplet formation is discussed and photographs of ligament decay are presented. The droplet generator works well on both oil and water based pesticide formulations. Current applications and results are discussed.

### Introduction

The NAE Droplet Generator is a device designed to produce and photographically record for subsequent sizing discrete droplets in a laboratory environment. It is also a useful instrument for observing the breakup or collapse of fluid ligaments.

### Description of the Droplet Generator

The droplet generator consists of a pendant drop generator, a droplet extractor, a photographic recording system and an electronic control system (Fig. 1).

#### Pendant Drop Generator

The source of fluid for the droplets is a pendant drop. A syringe pump drives a hypodermic syringe to supply fluid to a central port in a 6.35 millimeter (mm) diameter horizontal disc. It collects on this disc to form a pendant drop. The pendant drop is in the order of  $10^5$  times the size of the droplets produced and therefore the syringe pump does not need to be operated while generating droplets.

#### Droplet Extractor

The droplet extractor consists of a horizontal extractor needle which is connected by a drive shaft to the cone of an audio speaker. The needle drive shaft is supported in a bearing to maintain consistent needle tracking. By controlling the polarity and amplitude of electrical pulses to the speaker, the tip of the extractor needle can be driven into or pulled out of the pendant drop. Any audio speaker capable of taking continuous direct current loads and producing large cone deflections could be used. The speaker currently being used is a 25 watt 8 inch diameter speaker. With positive and negative pulses of 8 volts (6.5 watts), it produces an extractor needle movement of  $\pm 4.23$  mm (Fig. 2).

Power for the speaker is supplied by a dual variable voltage power supply. One half of the power supply provides the positive pulses to immerse the needle in the pendant drop while the other half provides the negative pulses to extract the needle. A conventional multimeter is used to set the amplitude of the pulses accurately.

The extractor needles are removable from the needle drive shaft and needles of various diameters, ranging in size from 98 microns ( $\mu\text{m}$ ) to 700 $\mu\text{m}$ , have been used.

#### Photographic Recording System

The droplet generator includes a photographic recording system to record photographic images of the droplets for subsequent sizing. The camera being used with the droplet generator is a conventional 35 mm Pentax Spotmatic with a motor drive film advance and a remotely operated shutter attachment. Since the droplets being photographed are small, considerable photographic magnification is required before they can be accurately sized. This requirement is met by using a 38 mm microscope objective lens in lieu of the conventional photo-optics and it is mounted on an appropriate extender tube to achieve a magnification of 10.

The formation of a droplet is a dynamic event and short photo exposures are required to obtain sharp droplet images. In addition there is a requirement for a high light level due to the extender tube. A strobotac and a stroboslave, operating in a single flash mode have been adequate. The strobes are aligned to bounce light off a white backdrop and provide a 3 microsecond ( $\mu\text{sec}$ ) exposure.

#### Droplet Generator Controller

The controller was developed specifically for the NAE Droplet Generator and its function is to control and sequence all the events associated with generating and photo-recording a droplet (Fig. 3). It can be operated in a "single droplet" mode or in a "continuous" mode

generating droplets at various preset rates of up to 3 droplets per second. The portion of the controller which operates the strobe lights contains an adjustable digital delay timer (1000 50 usec steps) to operate the lights at the appropriate instant.

### Operation of the NAE Droplet Generator

#### Adjusting the Extractor Needle Position

The criterion used to set the extractor needle position relative to the pendant drop is an arbitrary one but one which has provided consistent results. The needle is positioned vertically 1.0 mm below the pendant drop base so that it will enter the relatively flat side of the drop. It is positioned laterally so that the tip of the needle will be centered in the pendant drop when a full amplitude (8 volt) "IN" pulse is applied to the speaker.

#### Generating Droplets

For any given extractor needle a range of droplet sizes may be generated by varying the amplitude of the "IN" and "OUT" pulses to the speaker. The range of droplet sizes (Fig. 4) which can be expected is

$$D_n/3 \sim D_d < D_n$$

where  $D_d$  - diameter of the droplet

$D_n$  - diameter of the extractor needle

The time required to form a droplet varies considerably with changes in the "IN" and "OUT" pulse amplitudes and the delay timer must be set to photo record at the appropriate time.

### Applications of the Droplet Generator

The NAE Droplet Generator was developed specifically for biological applications. It is being used as a calibration tool in assessing aerial spray deposits and to treat insect larvae with specific dosages of pesticide. The droplet generator also appears to be suitable for studies on liquid ligament breakup or collapse.

#### Spread Factor Calibrations

For aerial spraying, it is customary to place sampling cards in the area to collect a sample of the pesticide. The cards retain the stains produced by the droplets and for subsequent pesticide accounting it is necessary to know the relationship between the size of the stain and the droplet that produced it. The droplet generator is used to produce and size droplets of the appropriate pesticide. The droplets are collected on sampling cards and the stains are sized by the NAE Flying Spot Scanner Analyzer. The computer outputs for the droplet and stain sizes are combined to produce a mathematical relationship between the size of a droplet and the size of the stain it will produce on a particular type of sampling surface. The mathematical relationships developed are typically

$$D_d = C + bD_s$$

where  $D_d$  - droplet diameter ( $\mu\text{m}$ )

$D_s$  - stain diameter ( $\mu\text{m}$ )

C - a constant

b - the slope of the curve

The slope confidence at the 90% interval is typically  $\pm 0.3\%$

#### Dispensing Minute Quantities of Fluid

The droplet generator can be used as a tool to dispense minute quantities of fluid (i.e. in the order of  $10^{-6}$  microlitres). It has been used to treat spruce budworm larvae with specific dosages of pesticide to determine required spray parameters for adequate insect control.

#### Studying Ligament Collapse

Figures 5, 6 and 7 are a series of photographs showing the formation of droplets. The process of forming a ligament and its collapse to form a droplet is extremely consistent. These photographic series are not high speed movies; they are, in each case, 20 photographs of 20 different droplets. In each case the photo exposure has been delayed by the time shown on each photograph.

Figures 5 and 7 show that with different combinations of "IN" and "OUT" pulse amplitudes the ligament may break free at one end first. In Figure 5 it breaks free from the needle first and the needle end of the ligament starts collapsing to form the droplet. This portion of the ligament starts moving towards the pendant drop. When the pendant drop end of the ligament finally breaks free, it too starts collapsing to form a droplet and this portion of the ligament moves away from the pendant drop. Since the needle end of the ligament started forming a droplet first, its mass is greater than the other portion of the

ligament and the resulting droplet has a horizontal velocity towards the pendant drop. Figure 7 shows the ligament breaking free from the pendant drop first and the resulting droplet is given a horizontal velocity away from the pendant droplet.

Figure 5 also shows that if the droplet contacts the pendant drop, both the droplet and the pendant drop distort but the droplet will bounce free from the elastic pendant drop surface. Figure 7 is an example of the droplet having sufficient horizontal velocity to overtake the extractor needle. Although the extractor needle is covered with fluid it cannot distort as the pendant drop did and the droplet is "captured" by the needle.

Figure 6 shows another phenomenon which is evident, to lesser degrees, in Figures 5 and 7; namely, the instability of a cylindrical liquid jet or ligament. In Figures 5 and 7 there is evidence that the ligament was trying to break up; however, each ligament did collapse into a discrete droplet before the break up could occur. In Figure 6 the separation of the ligament was delayed and the ligament did break up before it could collapse to form a single droplet.

These 3 figures show that varying the amplitude of the "IN" and "OUT" pulses varies the droplet formation process as well as the droplet size.

### Results with the Droplet Generator

#### Droplet Sizes Produced

The parameters which have a significant effect on the size of the droplets are:

- The diameter of the extractor needle
- The amplitude of the "IN" pulse to the speaker (i.e. the immersion depth of the needle in the pendant drop)
- The amplitude of the "OUT" pulse to the speaker (i.e. the velocity at which the needle is extracted from the pendant drop).

The viscosity of the fluid has very little effect on the size of the droplets produced.

Using extractor needles ranging from 98  $\mu\text{m}$  to 700  $\mu\text{m}$  has produced droplets ranging in size from 30  $\mu\text{m}$  to 800  $\mu\text{m}$ .

#### Droplet Size Consistency

Current applications of the NAE Droplet Generator have required the sizing of discrete droplets and the consistency of the droplet sizes has been of minor interest. Some tests have been carried out to determine the size consistency of the droplets and typical results are listed in Table 1.

TABLE 1

Droplet Size Consistency

Number of droplets sized	24
Mean drop diameter	179.34 $\mu\text{m}$
Range	5.3 $\mu\text{m}$
Standard deviation	1.20 $\mu\text{m}$

#### Accuracy of Droplet Sizing

The source of errors in sizing droplets and their estimated magnitude are listed in Table 2.

TABLE 2

Errors in Droplet Sizing

Source of Error	Magnitude of Error
Photographic magnification	$\pm 0.38\%$
Lens resolution	$\pm 0.9 \mu\text{m}$
Film resolution	$\pm 1. \mu\text{m}$
Measuring accuracy	$\pm 0.1 \mu\text{m}$

Tests to determine the error due to the sum of the last three items in Table 2 indicate an error of slightly over  $\pm 1. \mu\text{m}$ .

Figure 8 shows the optical layout for the droplet generator. An error in the distance from the lens to the droplet would induce a magnification error; however the optical depth of field is very limited and droplets which are off the focal plane sufficiently to produce a 0.38% error create a very badly out of focus image. If out of focus droplet images are deleted then the magnification error will be less than 0.38 percent.

ORIGINAL PAGE  
BLACK AND WHITE PHOTOGRAPH

SUMMARY

The NAE Droplet Generator is a device which will produce discrete droplets with fluids of various viscosities (i.e. heavy fuel oils or water). It has been used to generate droplets ranging in size from 30  $\mu\text{m}$  to 800  $\mu\text{m}$ . Images of the droplets produced are photographically recorded and can subsequently be sized to  $\pm 1.5 \mu\text{m}$ . Once the generator has been set to generate a specific size of droplet it will continue to produce droplets with a standard deviation of less than 1%.

The consistency of the droplet formation process also makes the generator a suitable instrument for observing fluid ligament break up or collapse.

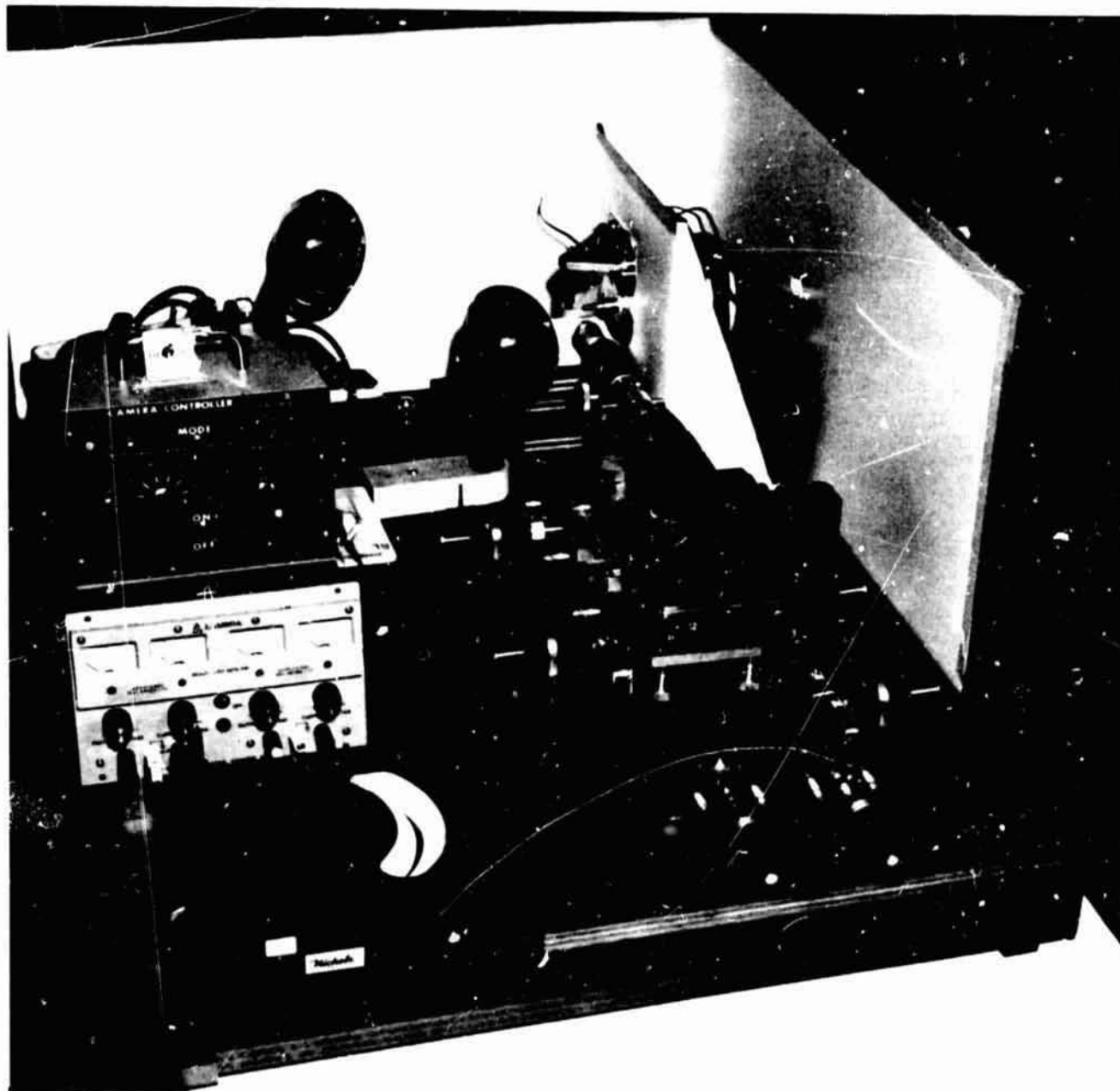


Figure 1: N A E droplet generator

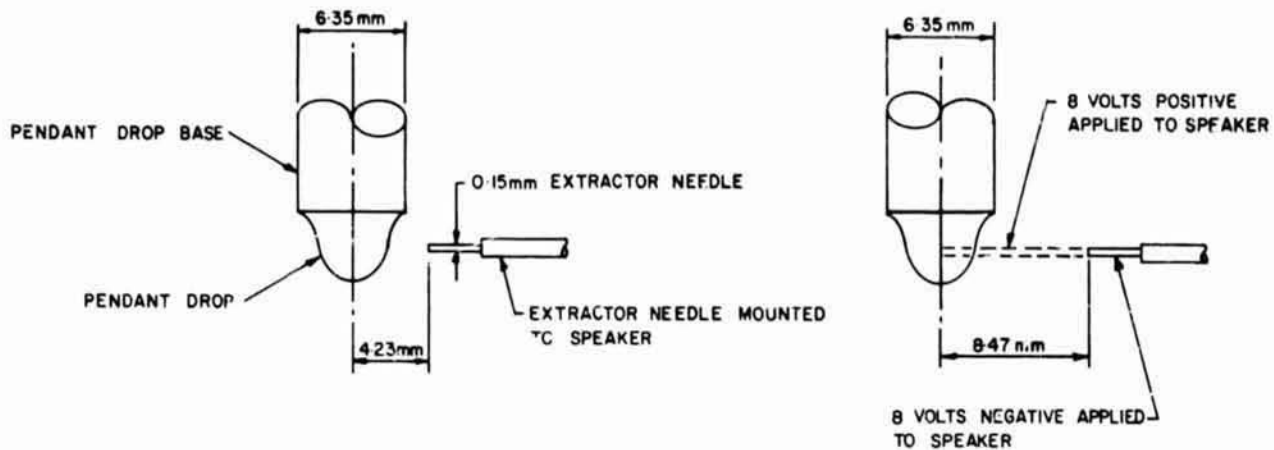


Figure 2: Pendant drop and droplet extractor

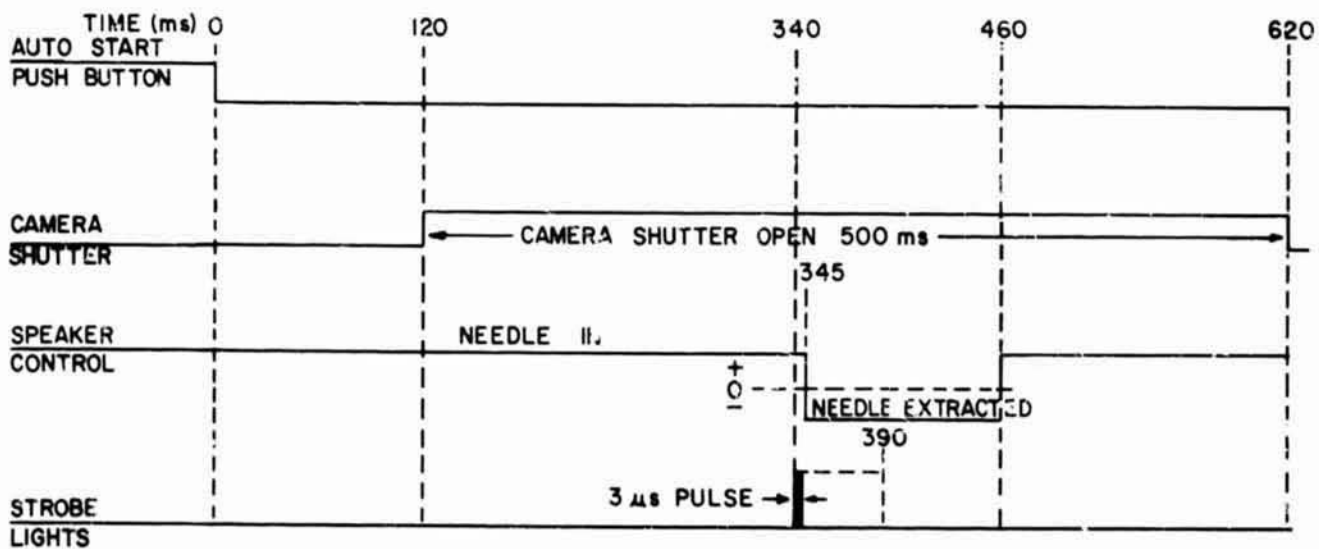


Figure 3: Droplet generator timing sequence

ORIGINAL PAGE  
BLACK AND WHITE PHOTOGRAPH

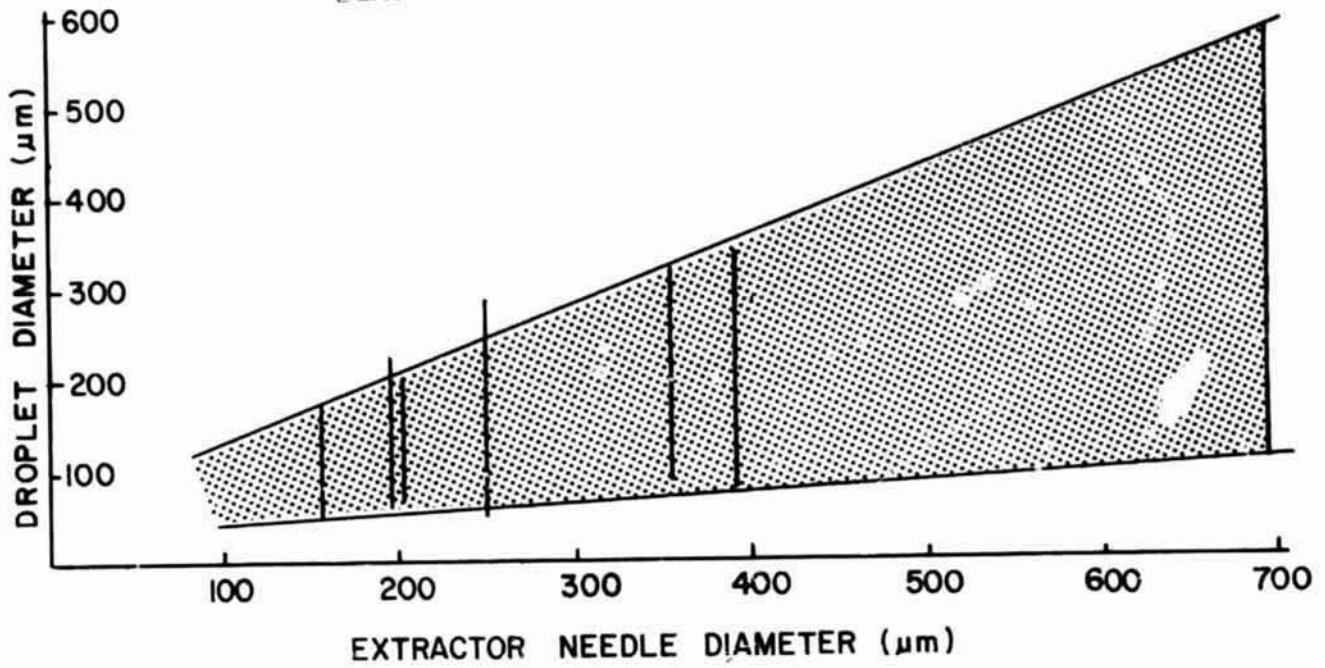


Figure 4: Droplet sizes vs extractor needle diameter

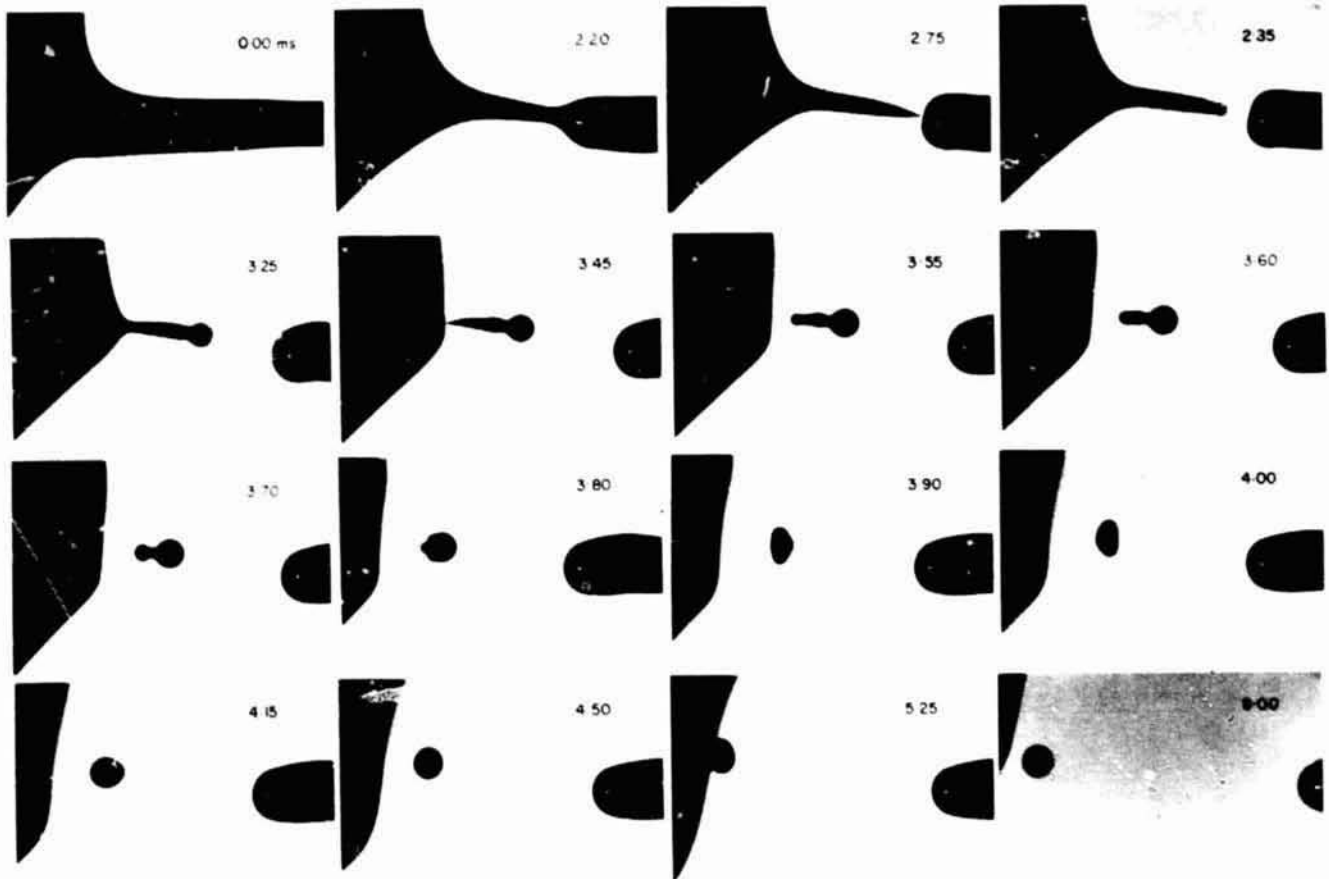
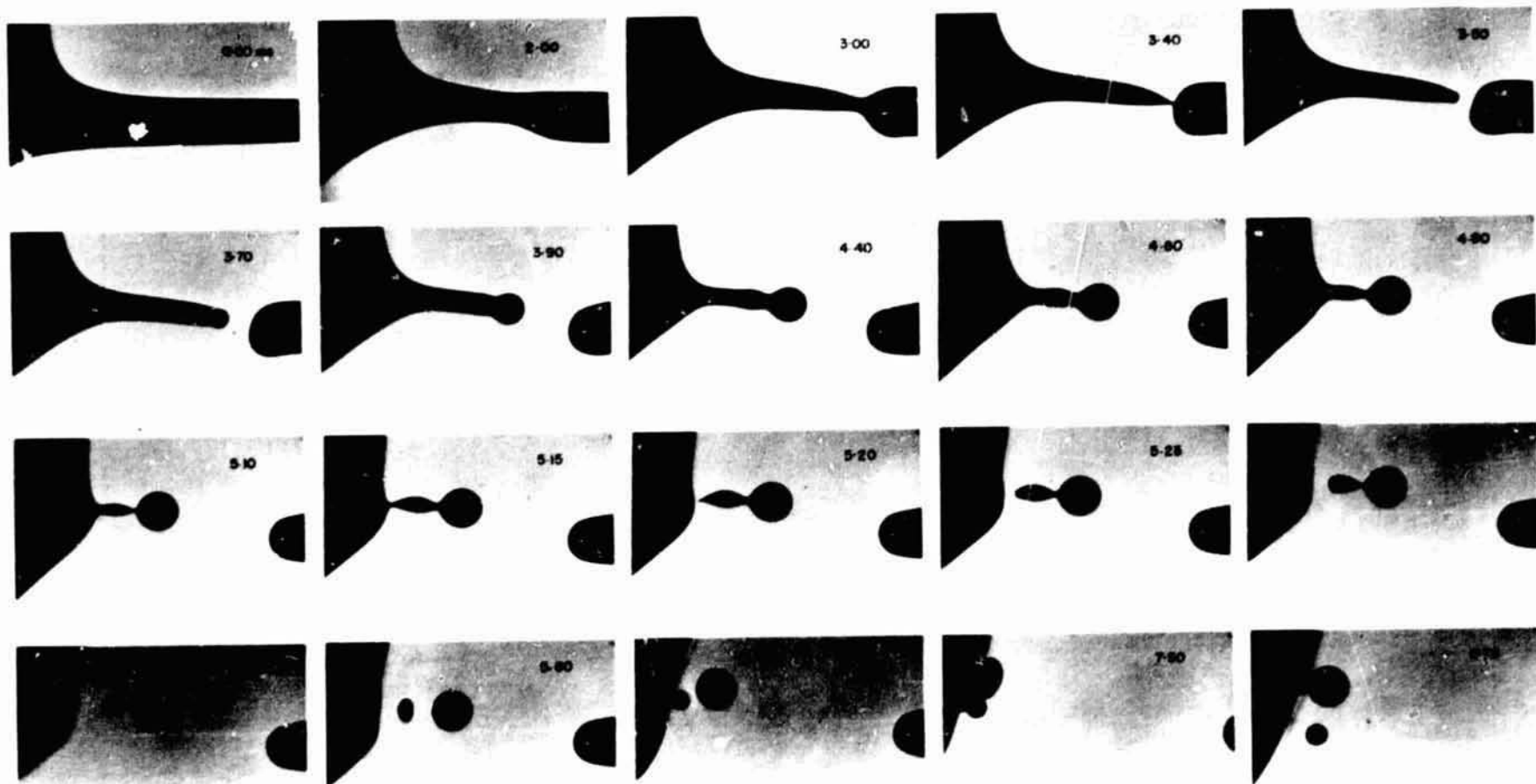


Figure 5: Ligament collapse to form a droplet



ORIGINAL PAGE  
BLACK AND WHITE PHOTOGRAPH

Figure 6: Ligament fission to form two droplets

ORIGINAL PAGE  
BLACK AND WHITE PHOTOGRAPH

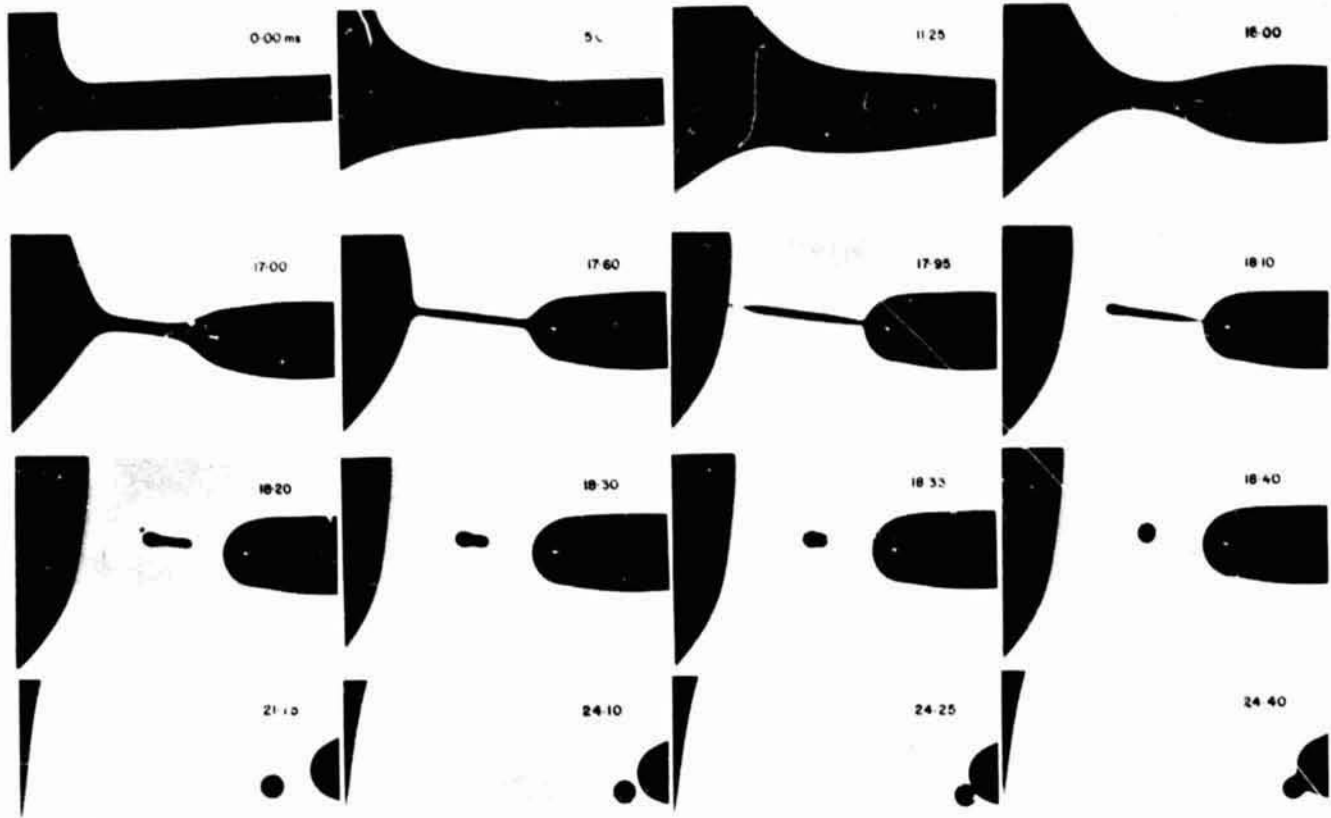


Figure 7: Needle-captured droplet

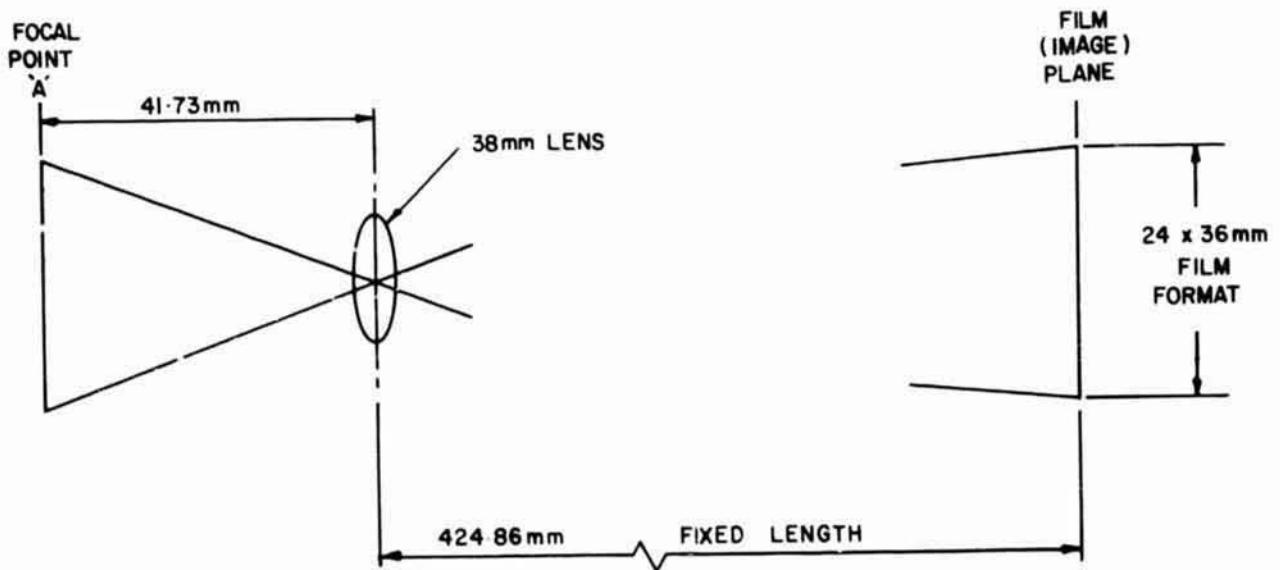


Figure 8: Photo-optical layout

## Non-axisymmetric shapes of a rotating drop in an immiscible system

T. G. Wang, R. Tagg, L. Cammack, and A. Croonquist

Jet Propulsion Laboratory  
 California Institute of Technology  
 4800 Oak Grove Drive  
 Pasadena, California 91109

Abstract

The non-axisymmetric shapes of a rotating drop in an immiscible system have been studied. Five basic families of shapes (axisymmetric, two-lobed, three-lobed, four-lobed, and toroidal) have been observed. The sequence (axisymmetric  $\rightarrow$  two-lobed  $\rightarrow$  three-lobed  $\rightarrow$  four-lobed  $\rightarrow$  toroidal) seems to be linked to increasing spin-up velocity. For the axisymmetric case, direct comparisons of experiments with the theory of a free rotating drop were surprisingly good — the equatorial area differs from theory by only 30%. Furthermore, the non-axisymmetric shapes are in good qualitative agreement with the theory, although the theory does not address the presence of an outer fluid.

Introduction

This paper describes the investigations of the dynamics of a rotating liquid mass under the influence of surface tension.

A large ( $\sim 15$ -cc) viscous liquid drop is formed around a disc and shaft in a tank containing a much less viscous mixture having the same density as the drop. This supporting liquid and the drop are immiscible. If the shaft and disc were not present, the drop would float freely in the surrounding medium and assume the shape of a sphere. With the drop attached and initially centered about the disc, the shaft and disc are set into rotation almost impulsively, reaching a final steady angular velocity within one-half to two revolutions. The drop deforms under rotation and develops into a variety of shapes depending on the shaft velocity. The process of spin-up, development, and decay (or fracture) to some final shape was common to all runs.

In this system, gravity is diminished at the expense of introducing a supporting liquid which is viscous and which may be entrained by the motion of the drop, thereby allowing angular momentum to be transferred from the drop. Nevertheless, comparison of this experiment's results to the theory of free rotating liquid drops is prompted by the fact that several novel families of drop shapes have been observed.

It is important to recognize that existing theory deals mainly with equilibrium shapes and their stability, while the drop in this experiment is undergoing a far more complicated process. The shape of a liquid drop spun on a shaft and supported by another liquid is very much a dynamical problem. A proper understanding of the results will only come with a dynamical analysis which succeeds in explaining the growth and decay with time of the various drop shapes.

Theory

The theory of the equilibrium shapes of rotating fluids began with investigations by Newton on the shape of the rotating earth, and the extensive theory that ensued was that of a free fluid held together by self-gravitation. An equilibrium figure for rotating liquid drops held together by surface tension was not demonstrated until more than seventy years later when Rayleigh<sup>(1)</sup> investigated droplets symmetric about the rotation axis (see also Appell<sup>(2)</sup>). The stability of the simple axisymmetric shapes awaited study by Chandrasekhar<sup>(3)</sup>.

Swiatecki<sup>(4)</sup> fits the problem of a liquid drop held together by surface tension into a broader scheme in which fluid masses may, in addition to having surface tension, be self-gravitating and/or possess a uniform density of electric charge. The astrophysical problem of the stability of rotating, self-gravitating stellar masses, and the problem of the fissionability of rotating, uniformly-charged "liquid drop" nuclei in nuclear physics, are thus unified with the problem of equilibrium shapes and stability of ordinary liquid drops.

Confining discussion to the case of surface tension forces only, it is necessary to define some of the parameters used to describe a free liquid drop in solid body rotation. The "free" drop is actually assumed to be contained within another fluid (for example, an atmosphere of gas) which rotates at the same angular velocity. The drop has density  $\rho_D$  and

ORIGINAL PAGE IS  
OF POOR QUALITY

rotates with angular velocity  $\Omega$ . The outer fluid has density  $\rho_F < \rho_D$ . The equilibrium shape of the drop must satisfy the equation: <sup>(5)</sup>

$$\Delta p_o + \frac{1}{2} \Delta \rho \Omega^2 r_1^2 = \sigma \nabla \cdot \hat{n}, \quad (1)$$

subject to the constraint that the drop have a fixed volume.  $\Delta p_o \equiv P_{D_o} - P_{F_o}$  is the difference in pressures on the axis of rotation inside and outside the drop,  $\Delta \rho = \rho_D - \rho_F$  is the density difference,  $r_1$  is the radius perpendicular to the axis of rotation and extending to the drop's surface,  $\sigma$  is the interfacial tension, and  $\hat{n}$  is normal to the surface ( $-1/2 \nabla \cdot \hat{n}$  is the local mean curvature).

If the density difference  $\Delta \rho$  is zero, the effect of rotation (i.e., the centrifugal term  $(1/2) \Delta \rho \Omega^2 r_1^2$ ) is completely removed and the shape satisfying Equation (1) would be a perfect sphere. In this experiment, however, the drop was rotated differentially with respect to the outer fluid, giving rise to the analogous centrifugal term  $(1/2) \rho (\Delta \Omega)^2 r_1^2$ ; this approach must suffer the effects of viscous drag and entrainment of the outer fluid. Some basis for comparison with the "free" drop system is preserved by making the outer fluid two orders of magnitude less viscous than the drop, and the experimental time short. Thus, a minimum amount of angular momentum transfers across the interface during the critical part of the experiment.

Returning to the free drop theory: Brown <sup>(5)</sup> rewrites Equation (1) in a dimensionless form

$$Ha_o = K + 2 \Sigma \left( \frac{r_1}{a_o} \right)^2, \quad (2)$$

where  $H \equiv 1/2 \nabla \cdot \hat{n}$  is the local mean curvature,  $a_o$  is the radius of a sphere having the same volume as the drop, and the parameters  $\Sigma$  and  $K$  are the rotational bond number and dimensionless reference pressure defined by:

$$\Sigma \equiv \frac{\Omega^2 \Delta \rho a_o^3}{8\sigma}, \quad (3)$$

$$K \equiv \frac{\Delta p_o a_o}{2\sigma}. \quad (4)$$

The axisymmetric and non-axisymmetric sequences excluding toroidal shapes may also be represented by a plot of the normalized equatorial area against  $\Sigma$ . (Figure 1).

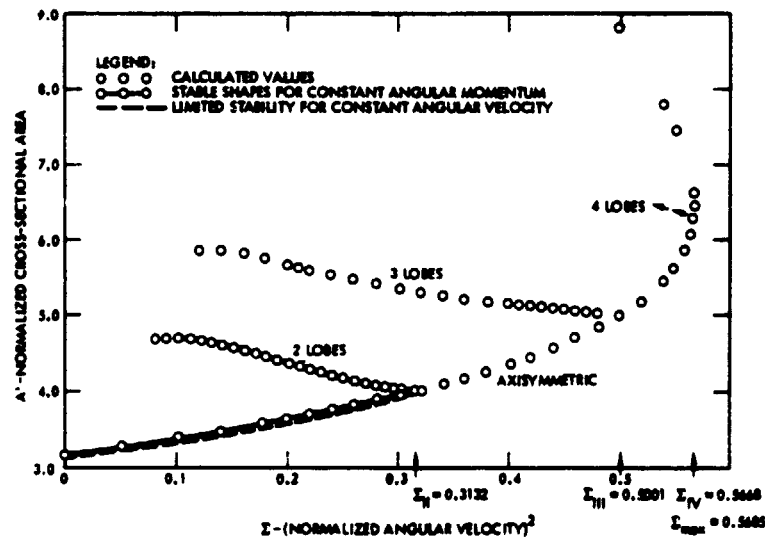


Figure 1. Calculated Equilibrium Shapes (from data reported by Brown <sup>(5)</sup>, supplemented by Chandrasekhar <sup>(3)</sup> and Ross <sup>(7)</sup>).

Experiment

The immiscible tank (see Figure 2) in which the drop is buoyantly supported and rotated consists of a Lucite cylinder which in turn is contained in a cubical outer tank. Cylindrical symmetry about the axis of rotation is thus obtained while lens-like distortion of the drop inside the cylindrical tank is minimized by the parallel-sided geometry of the outer tank and the water circulating between it and the inner tank.

The circulating water is pumped into the system from a constant-temperature bath with a 15-liter capacity. By this means we are able to control the temperature of the system to within  $.01^{\circ}\text{C}$  or better, such control is one of the most critical factors in the performance of the experiment.

The fluids we used in this experiment are silicone oil (Dow Corning 200,100 centistoke) for the drop, and a 3 to 1 water/methanol mixture for the host. The physical properties of the mixture are highly dependent on the temperature. Therefore, the equilibrium positions of the drop are extremely sensitive to the temperature gradient as shown in Figure 3.

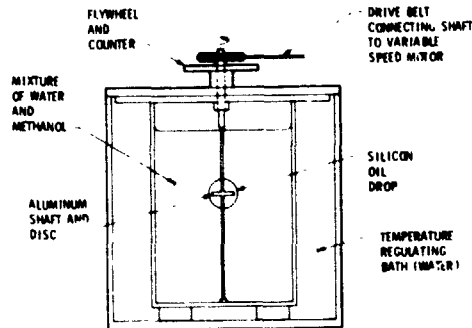


Figure 2. Immiscible System Apparatus

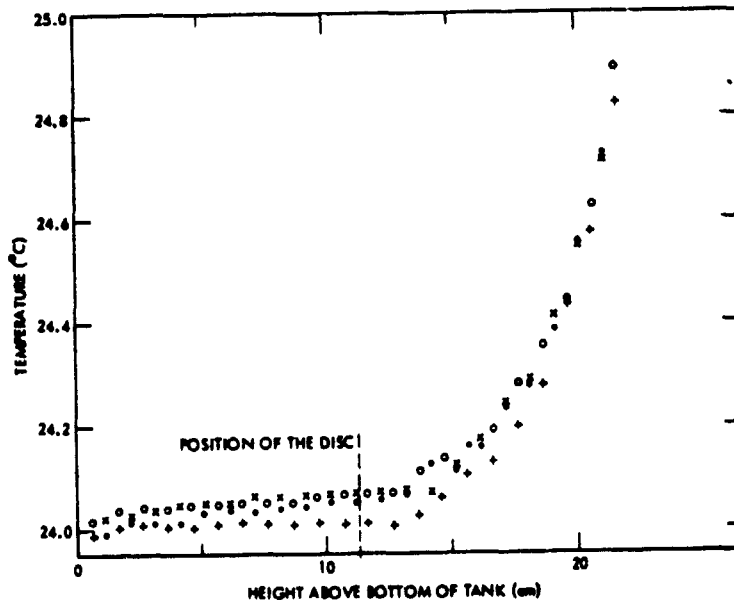


Figure 3. Temperature Profile of the Neutral Buoyancy Tank (Measurements made by Tom Chuh).

The shapes of rotating spheroids and the fluid flows are recorded on a camera (Milliken DBM-55) and digitized on a Vanguard Motion Analyzer. The flow visualization for inside the drop is accomplished by forming tracer particles out of the water/methanol mixture of different densities and vice versa for flow outside the drop.

### Results and Discussion

Five basic families of shapes are observed.<sup>(7,8)</sup> They are axisymmetric, two-lobed, three-lobed, four-lobed, and toroidal. Additionally, the off-axis single lobe is the final shape for all experimental runs except those in which the drop undergoes fracture. These shapes are shown in Figures 4-10.

Apart from the axisymmetric shapes at slow rotation rates, the three-lobed family was the easiest to obtain. This fact was due in part to the particular drop volumes and shaft dimensions used in this experiment. The ease with which three-lobed shapes are generated is nevertheless remarkable; even in an early, very crude 1/4-scale version of the experiment, three-lobed shapes were readily obtained.

Two-lobed shapes, which develop for slower shaft velocities ( $<2$  rps), may be harder to obtain because the decay processes which cause the drop to form into an asymmetric single lobe may set in before the drop can develop symmetric lobes. Four-lobed shapes, on the other hand, are obtained at generally higher shaft velocities ( $\sim 4$  rps) than the three-lobed shapes; when asymmetries develop in the drop at these angular velocities, fracture usually results.

During the decay of higher non-axisymmetric modes, one-lobe generally rotates faster than the others, eventually catching up and joining with the lobe preceding it. Thus, three converge into two and two into one. This is not surprising; the mass of the drop is never equally distributed among the lobes; so one lobe is smaller and suffers less drag by the surrounding fluid. The presence of drag is immediately apparent from the pinwheel appearance of all of the lobed shapes, with the lobes curving backwards against the direction of rotation.

A further effect, attributed to the motion of the outer fluid, appears in many runs in which two- and three-lobed shapes are produced; in the course of the drop's development, the drop rises and becomes sessile on top of the disc (i.e., it only contacts the upper surface of the disc and shaft). Three-lobes decay to two-lobes which are sessile (Figure 13) and often persist for many seconds before decaying to a single lobe (also sessile). This rising of the drop occurs even when the level of exact density matching is below the disc by, for example, two centimeters. Furthermore, above a rather well-defined shaft velocity midway in the range of velocities producing three-lobed shapes, a different effect occurs. The three-lobed drop still decays to a two-lobed one but with one lobe above the disc and the other below, i.e., the drop is tilted (Figure 14). This appears to be a very stable geometry which can persist for minutes.

Only a few instances of the toroidal shape have been observed with this system. Nevertheless, striking examples have been photographed of the formation of a torus and its subsequent highly symmetric fracture into three or four large drops and a corresponding number of small satellite drops (Figures 10 through 12). The sequence (axisymmetric - two lobed - three lobed - four lobed - toroidal) seems to be linked to increasing spin-up velocity.

ORIGINAL PAGE  
BLACK AND WHITE PHOTOGRAPH

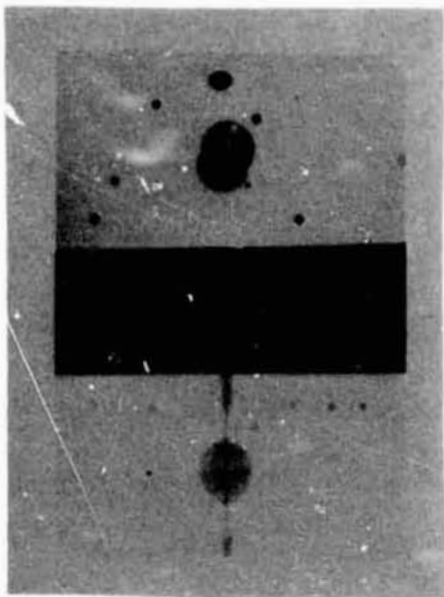


Figure 4. Drop At Rest. Note internal trace drops and external satellite drops.

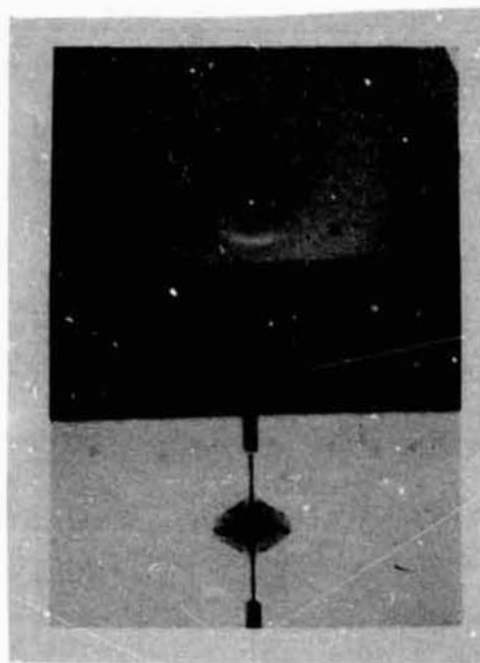


Figure 5. Axisymmetric Oblate Drop. (Shaft angular velocity = 0.8 rps).

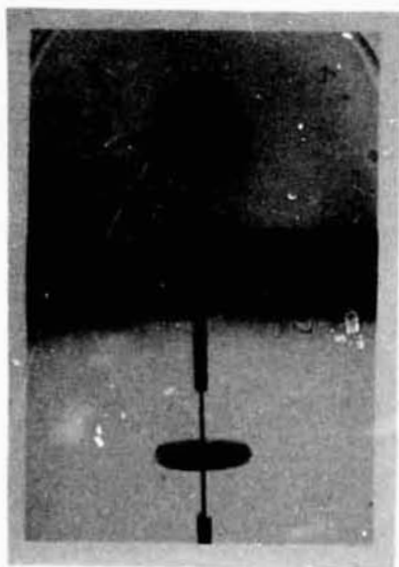


Figure 6. Axisymmetric Biconcave Drop (Shaft angular velocity = 1.3 rps), drop is still spinning up)

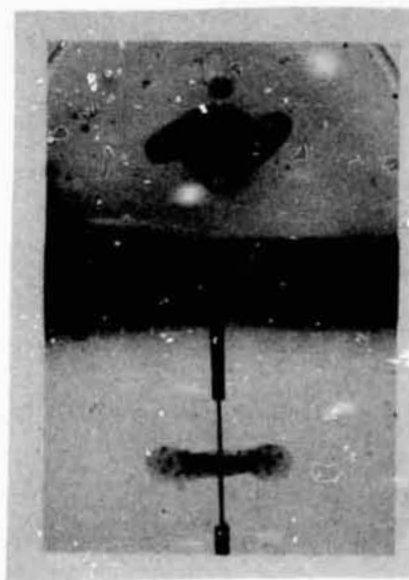


Figure 7. Two-lobed shape (Shaft angular velocity = 1.8 rps).

ORIGINAL PAGE  
BLACK AND WHITE PHOTOGRAPH

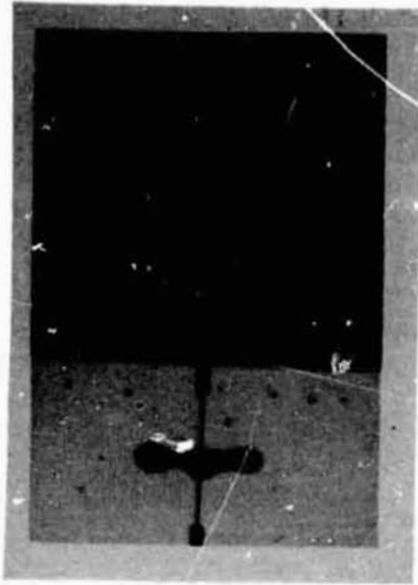


Figure 8. Three-lobed Shape  
(Shaft angular velocity = 2.0 rps)

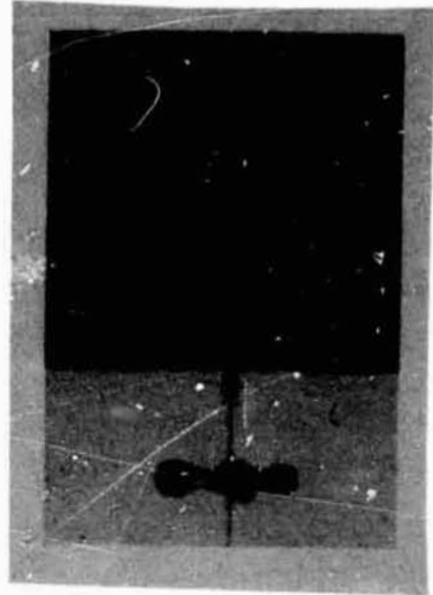


Figure 9. Four-lobed Shape  
(Shaft angular velocity = 3.6 rps)

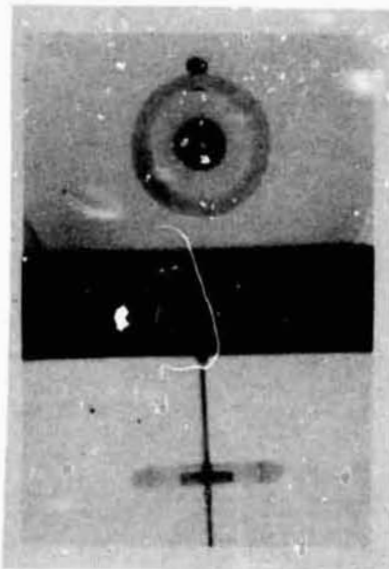


Figure 10. Torus (Shaft angular  
velocity = 4.8 rps)

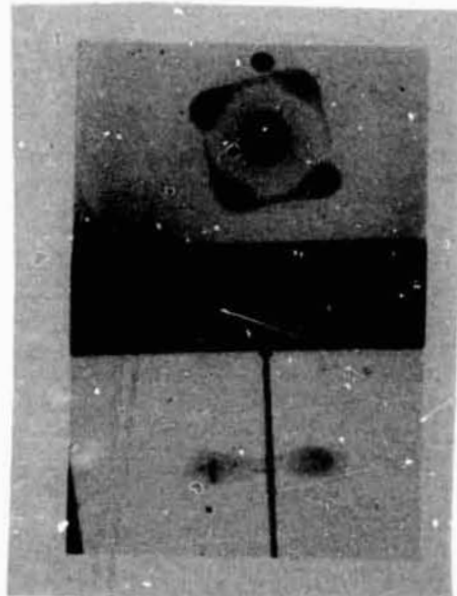


Figure 11. Break Up of Torus  
(Shaft is not rotating)

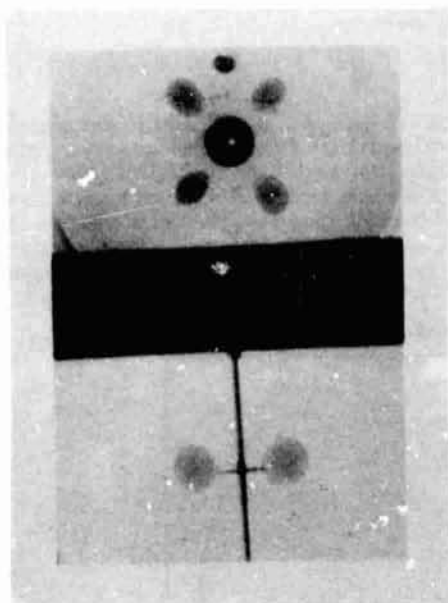


Figure 12. Break Up of Torus  
(Shaft is not rotating)



Figure 13. Single Lobe  
(Ultimate decay shape)

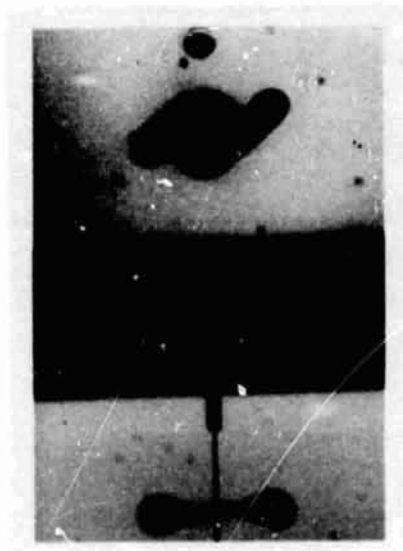


Figure 14. Sessile Two-Lobed  
Shape (The results of decay  
from a three-lobed shape; shaft  
is not rotating)



Figure 15. Tilted Two-Lobed  
Shape (Decay route for three-  
lobed shapes)

The comparisons between the shapes that we observed and the calculations by Brown<sup>(5)</sup>, Chandrasekhar<sup>(3)</sup>, and Ross<sup>(7)</sup> are given in the following section.

### A. Axisymmetric shape

The quantities which are determined for the axisymmetric shapes are  $a$ , the equatorial radius of the rotating drop, and  $\Omega$ , the drop's angular velocity. From a the normalized cross-sectional area  $A' = \pi a^2/a_0^2$  is calculated, while  $\Omega$  yields the dimensionless parameter  $\Sigma$ ,  $\rho$  is the density of the oil and  $\sigma$  is the interfacial tension between the oil and mixture.  $a_0$  is computed from the calculated drop volume. The experimental axisymmetric values are determined from the maximum drop deformation for a given rotation velocity. The experimental values are presented in Figure 16. As  $\Sigma$  increases, the axisymmetric shapes become less stable with respect to the  $n=1$  perturbation. Thus, no reliable data are available beyond the region where  $\Sigma = 0.4$ .

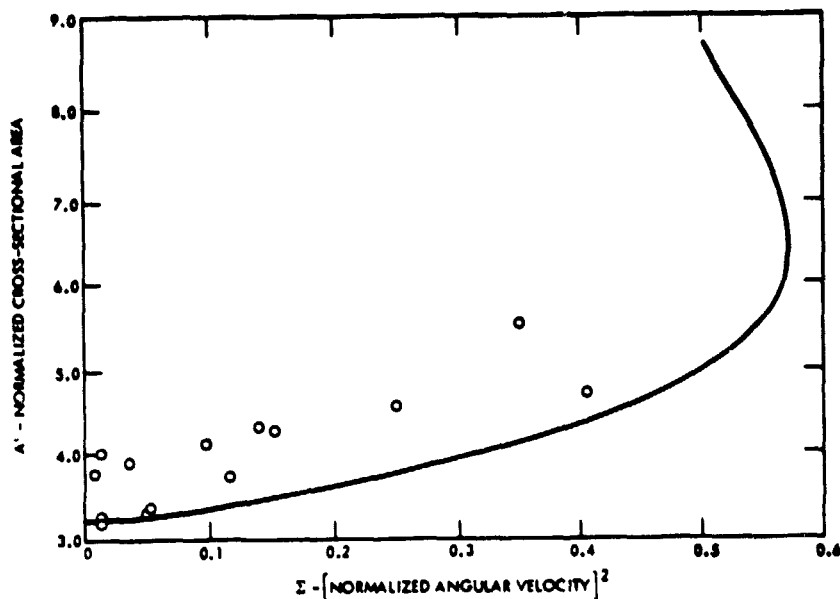


Figure 16. Experimental Results for Slowly Rotating Axisymmetric Drops. Theoretical Curve From Free Drop Calculations. 3,5,6

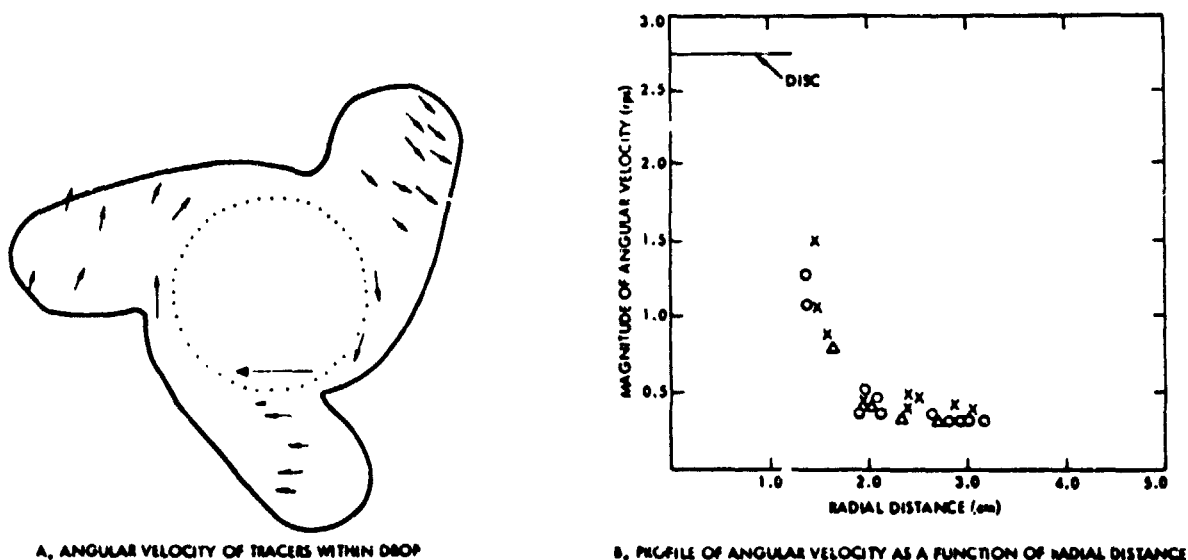


Figure 17. Angular Velocity Distribution for Three-Lobed Shape;  
Drop = 0.33 rps and Shaft = 2.74 rps

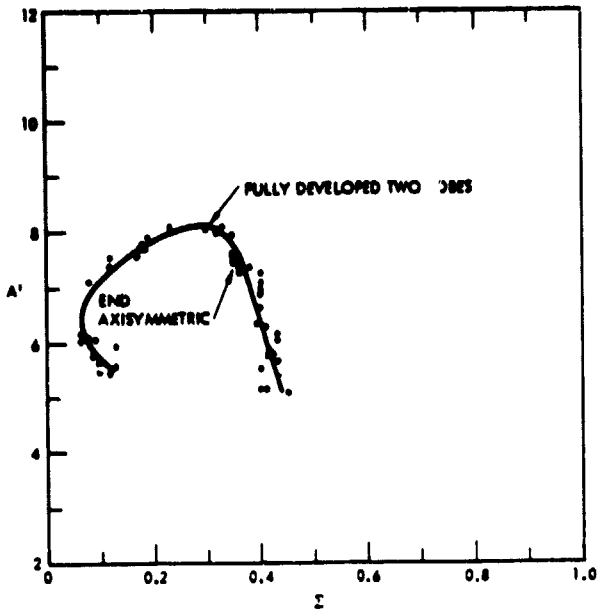


Figure 18.  $A'$  versus  $\Sigma$  for a Two-Lobe Run. ( $A'$  is the normalized equatorial area and  $\Sigma$  is proportional to the square of the angular velocity).

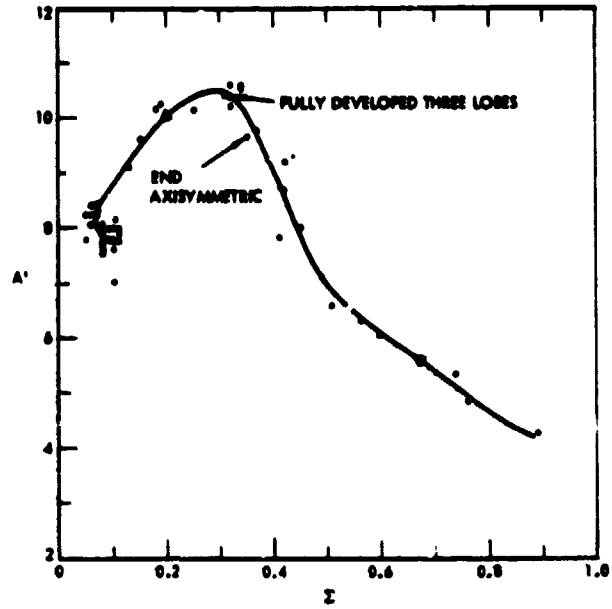


Figure 19.  $A'$  versus  $\Sigma$  for Three Lobe Run.

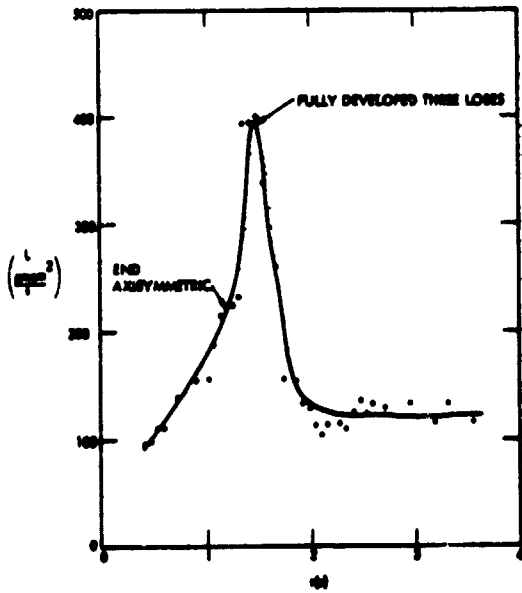


Figure 20.  $A'$  versus  $\Sigma$  for a Four Lobe Run.

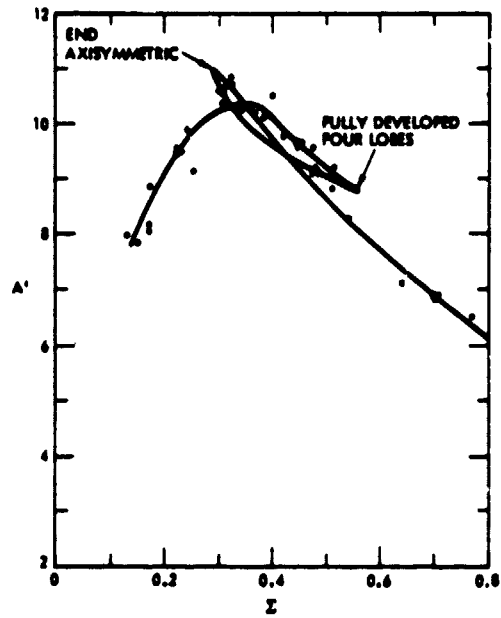


Figure 21. Angular Momentum versus Time for a Three Lobe Run.

### B. Non-axisymmetric shapes

Figure 17 shows velocity-profile data for a three-lobed shape. The existence of shear close to the disc is clearly demonstrated. It is also seen, that at a position away from the disc where 90 percent of the mass is located, a reasonably constant angular velocity exists. It is the measurement of this velocity which serves as the  $\Omega$  value for determining  $\Gamma$  for a given drop shape. However, the justification of this procedure is likely to break down during the initial spin up of the drop.

Figures 18-20 show graphs of the results of  $A/\omega$  versus  $\Gamma$  for the drops which developed to two-lobed, three-lobed, and four-lobed shapes.

The direction in which the  $A'$  versus  $\Gamma$  graphs was traveled, the time is indicated on each graph. In each run, the drop remains axisymmetric for a time prior to developing into its lobed shape.

By looking at the  $A'$ -versus- $\Gamma$  graphs of the three- and four-lobed runs, it can be seen that the curves occupy the same domain. This fact suggests the possibility that bifurcation points for the four-lobed and three-lobed shapes are close, and the three-lobed shape is more stable. As a result, the three-lobed shape occurred more frequently than the four-lobed shape.

The four-lobed curve of  $A'$  versus  $\Gamma$  has a rebound that is either nonexistent or not as profound in the three- and two-lobed runs.

In all runs, the angular momentum increases initially, reaches a peak, and then decreases. The shaft angular velocity is constant in the critical region, before and after the lobes have fully developed. (See Figure 21).

### CONCLUSIONS

Shapes of a rotating spheroid, have been observed and recorded in this experiment. These include the flattening of slowly rotating drops and the generation of toroidal and lobed shapes at higher rotation rates. Using data recorded on movie film, the development and decay of the rotating shapes were studied for the first time. The neutrally buoyant tracer droplets allowed us to study the dynamics of the behavior, the secondary flow generated by the rotation, the interaction between the drop and the host liquid, and the coupling between the shaft and disc and the drop.

For slowly rotating axisymmetric drops, direct comparisons of experiment with the theory of a free rotating drop were possible. The agreement was surprisingly good; the qualitative shape of the equatorial-area-versus- $\Gamma$  curves were similar, only differing from theory by 30%. This is remarkable because the theory does not address the presence of an outer fluid. The generation and study of axisymmetric equilibrium shapes for higher rotation rates is difficult, because of the presence of the more stable off-axis single lobed shape. This mechanism, axisymmetric shapes decay into single lobed shape, prohibited us from extracting from the data the exact location of the bifurcation points between families of equilibrium shapes.

When generating  $n \geq 2$  lobed drops in a controlled manner, primarily two- and three-lobed shapes were obtained. The latter had not been observed before. The study of equilibrium configurations of these lobed shapes is made difficult by the presence of the outer fluid; as soon as the lobes occur, the interaction between the drop and the host liquid increases significantly and generates large secondary flows. The accelerated transfer of angular momentum from the drop in the lobed configurations gives rise to decay routes in which one lobe slows and is absorbed by the one trailing it; this process continues until there is only an arm left. There were two exceptional types of decay in which either the whole drop would lift up (independently of the neutral buoyancy level) and become sessile on the disc, or would form a slanted drop; in both of these two cases, the shapes were very stable and long-lived. The behavior of lobed shapes was not easily compared to the free drop theory. The study of the angular velocities and momenta demonstrated that the development of the various lobed shapes takes similar paths, but no evidence was found for the location of branch points between axisymmetric and triaxial behavior.

At present, no framework exists for describing the dynamics of a drop rotating in another liquid. It is the authors' hope that the various phenomena observed and described in the course of this work will stimulate one.

#### REFERENCES

1. Rayleigh, Lord, "Equilibrium of Revolving Liquid Under Capillary Forces," *Phil. Mag.* 28, 161 (1914).
2. Appell, P., Traite de Mecanique Rationelle, Vol. 4, Pt. 1, Chapt. IX, Gauthier-Villars, Paris (1932).
3. Chandrasekhar, S., "The Stability of a Rotating Liquid Drop," *Proc. Roy. Soc. (London)*, 286, 1 (1965).
4. Swiatecki, W.J., "The Rotating, Charged or Gravitating Liquid Drop, and Problems in Nuclear Physics and Astronomy," *Ibid.*, p 52.
5. Brown, R., "The Shape and Stability of Three-Dimensional Interfaces," PhD Thesis, University of Minnesota (Minneapolis, MN, 1979).
6. Ross, D.K., "The Shape and Energy of a Revolving Liquid Mass Held Together by Surface Tension," *Aust. J. Phys.* 21, (1968), p. 823.
7. Tagg, R., Cammack, L., Croonquist, A., and Wang, T.G., "Rotating Liquid Drops; Plateau's Experiment Revisited," *Jet Propulsion Laboratory, Publication 80-66* (1980).
8. Tagg, R., and Wang, T.G., "The Shapes of Rotating Liquid Drops Neutrally Buoyant in Another Liquid," *Bull. Am. Physical Soc.* (1978).

## Fragmentation of Interstellar Clouds and Star Formation

Joseph Silk

Department of Astronomy, University of California  
Berkeley, California 94720Abstract

Two principal issues are addressed: the fragmentation of molecular clouds into units of stellar mass and the impact of star formation on molecular clouds. The observational evidence for fragmentation is summarized, and the gravitational instability described of a uniform spherical cloud collapsing from rest. The implications are considered of a finite pressure for the minimum fragment mass that is attainable in opacity-limited fragmentation. The role of magnetic fields is discussed in resolving the angular momentum problem and in making the collapse anisotropic, with notable consequences for fragmentation theory. Interactions between fragments are described, with emphasis on the effect of protostellar winds on the ambient cloud matter and on inhibiting further star formation. Such interactions are likely to have profound consequences for regulating the rate of star formation and on the energetics and dynamics of molecular clouds.

I. Introduction

We are far from understanding star formation. Observations are only beginning to probe the interiors of molecular clouds where star birth is occurring. Thus any attempt to present an overview of molecular clouds and star formation inevitably runs into immense gaps in our knowledge. Eventually, far infrared and millimetre wavelength maps will improve sufficiently to provide a much more coherent physical picture. For now, one can only speculate on the most probable processes that will occur and affect cloud evolution.

Gravitational instability is the process that we understand best, and much of the emphasis here will be on describing some of its ramifications in molecular clouds. There are important aspects of molecular clouds that will not be discussed here. These include formation and destruction, as well as the trigger mechanism by which collapse and star formation is initiated. My starting point will be a molecular cloud that is undergoing gravitational collapse. One might imagine that this is relevant to the cores of cold molecular clouds, as well as to clouds that have undergone sudden compression associated with passage of a shock front induced either by a nearby supernova or a collision with another cloud. However my intention is not to describe the grand design underlying molecular clouds and star formation, about which one can speculate at great length, but to focus on the physics of fragmentation. How do molecular clouds fragment into units of stellar mass? What are the observational indications and implications of fragmentation? These are the issues to be addressed here.

I commence by discussing the observational evidence for fragmentation in molecular clouds (§II). I then review the original argument by Jeans for gravitational instability, and indicate how this is modified for a uniform spherical cloud collapsing from rest (§III). Effects of finite pressure are considered, and the significance of the minimum Jeans mass for fragmentation is discussed. Next I discuss the role of magnetic fields in resolving the angular momentum problem and in making the collapse anisotropic (§IV). The consequences of anisotropic collapse for fragmentation theory are explored. Interactions between fragments are described, with emphasis on the interaction between newly formed protostars and the ambient cloud matter (§V). It is concluded that this interaction may have profound consequences for regulating the rate of star formation and the energetics and dynamics of molecular clouds.

II. Evidence for fragmentation

Molecular clouds are observed to contain smaller fragments. Cold clouds, such as the Taurus dark cloud, contain fragments with masses as small as  $\sim 1 M_{\odot}$ . The line widths of these fragments are often narrow, in some cases consistent with thermal support at  $T \sim 10\text{K}$ . Asymmetries in the overall profile of the Taurus cloud have been interpreted as evidence for systematic collapse or contraction (Myers 1981). Complexes near HII regions, while exhibiting broader line profiles, also contain fragments. At low resolution, such complexes as that near NGC 2264 contain fragments of  $\sim 100 M_{\odot}$  within a molecular cloud complex that has upwards of  $\sim 10^5 M_{\odot}$ . One might imagine that at higher resolution, finer structure would be seen: some tentative evidence for this comes from VLA observations of embedded HII regions (van Gorkom 1981). Evidently, fragmentation must have occurred into stellar masses at densities in the range  $10^3 - 10^5 \text{ cm}^{-3}$ .

Indirect evidence that strongly supports this conjecture comes from observations by Blaauw (1978), who studied the proper motions of O stars in a young expanding association. He found that the O star position vectors in a given subgroup could be traced back to encompass a minimum volume, which he identifies with that of the cloud out of which they formed. The star density at birth is about  $10^3 \text{ pc}^{-3}$ . An equal mass of gas in the same volume would be of mean density  $3 \times 10^4 \text{ cm}^{-3}$ . If there were a factor 10 more gas than stars at the formation epoch, as suggested by observations of the younger star formation regions near the Orion molecular cloud (Zuckerman and Palmer 1974), one infers an initial cloud density of  $3 \times 10^5 \text{ cm}^{-3}$ , similar to the

densities inferred in cold molecular cloud cores. Rapid dispersal of this gas could account for the positive energy of the O association.

A second piece of indirect evidence that supports the occurrence of fragmentation at densities comparable to those observed in molecular clouds comes from a resolution of the angular momentum problem encountered in theories of star formation in terms of the orbital angular momentum of wide binary pairs of stars. Magnetic braking enforces corotation at low densities, but must become ineffective at high densities in part because the field undergoes ambipolar diffusion relative to the neutral component. The specific orbital angular momentum of wide binaries (with periods  $< 10^2$  yr.) can be accounted for if angular momentum conservation first becomes effective at densities in the range  $10^3 - 10^6 \text{ cm}^{-3}$  (Mouschovias 1977). Prior to this, corotation should apply, with a specific angular momentum appropriate to that of a cloud undergoing differential rotation in the galactic gravitational field.

Additional evidence for this interpretation comes from two different observations. At least one isolated molecular cloud has recently been found to reveal evidence for undergoing magnetic braking (Goldsmith et al. 1981). Secondly, the mass function of binary secondaries with periods in the range  $10^2 - 10^6$  yr is indistinguishable from that of field stars, whereas that for shorter period binaries is much flatter (Abt and Levy 1976). This supports the viewpoint that such wide binaries formed by capture of field stars, whereas the close binaries formed by a different physical process, presumably by fission, that conserved the orbital angular momentum appropriate to an early phase of the collapse, presumably when magnetic braking first became ineffective.

One concludes that fragmentation into stellar mass units almost certainly has occurred at densities characteristic of molecular clouds.

### III. Gravitational instability and fragmentation

It was first demonstrated explicitly by Jeans that an infinite stationary uniform self-gravitating medium is susceptible to gravitational instability. Although Jeans' argument has since been shown to be technically incorrect, it is useful to review the result here. More sophisticated analyses in fact recover an identical criterion for instability. One finds that infinitesimal perturbations of the form  $\exp(i\omega t) \exp(ikr)$  grow at a rate given by the dispersion relation

$$\omega^2 = k^2 v_s^2 - 4\pi G\rho .$$

Hence perturbations of wavelength exceeding

$$\lambda_J \equiv \frac{2\pi}{k_J} = \pi v_s (G\rho)^{-1/2}$$

are unstable, those with  $\lambda \gg \lambda_J$  growing at a rate  $\sim [\exp(4\pi G\rho)^{1/2} t]$ .

While a similar result holds for any stationary self-gravitating system, the growth rate is drastically modified for perturbations of a cloud undergoing systematic collapse or expansion. In this case, the density  $\rho$  changes over an initial collapse (or expansion) time, which is also the time scale for the perturbation to grow. Consequently, the exponential growth rate changes to a secular growth rate. It is the convection by the principal flow of the background collapse that causes this effect. For a spherically symmetric uniform system undergoing collapse from rest, the free-fall time is

$$t_f = (3\pi/32G\rho_0)^{1/2} ,$$

where  $\rho_0$  is the initial density. The perturbation growth rate is

$$\delta \equiv \delta\rho/\rho = \delta_0 (t_f - t)^{-1}$$

in the linear regime, for density perturbations of initial amplitude  $\delta_0$  (Hunter 1962). Once  $\delta > 1$ , self-gravity becomes important for the fluctuations, and rapid growth ensues as may be demonstrated from an exact non-linear solution. However only if the initial amplitude is sufficiently large can we reasonably expect fluctuations to become large and the collapsing cloud to fragment.

What value is required for  $\delta_0$  in order for fragmentation to occur? Since the density increases in uniform spherical collapse as  $\rho = \rho_0(t_f - t)^{-2}$ , we infer that fluctuations are large when  $\delta \sim 1$ , or at a time given by  $t_f - t \sim \delta_0$ , just before collapse of the entire cloud at  $t_f$ . At this instant, the mean density has increased by a factor  $\rho/\rho_0 = (t_f - t)^{-2} = \delta_0^{-2}$ . Hence collapse by a factor  $10^4$  in density is necessary for perturbations of initial amplitude  $\delta_0 \sim 0.01$ .

This estimate assumes that the perturbations are always well above the instantaneous Jeans length. If they are not, growth can be suppressed (Figure 1). It is convenient to introduce the instantaneous Jeans mass defined by

$$M_J = \frac{\pi}{6} \rho \lambda_J^3 = \left(\frac{\pi^4}{6}\right) v_s^3 G^{-3/2} \rho^{-1/2} .$$

During the diffuse collapse phase, the cloud will remain approximately isothermal. Hence as the density increases,  $M_J$  will decrease. A fluctuation that is initially below the Jeans mass at the onset of collapse will eventually begin to grow when it first overtakes the Jeans mass. There is actually a minimum value for the Jeans mass, which effectively occurs when the collapse becomes adiabatic. This inevitably happens at a sufficiently high column density, when radiation trapping occurs and cooling is inhibited.

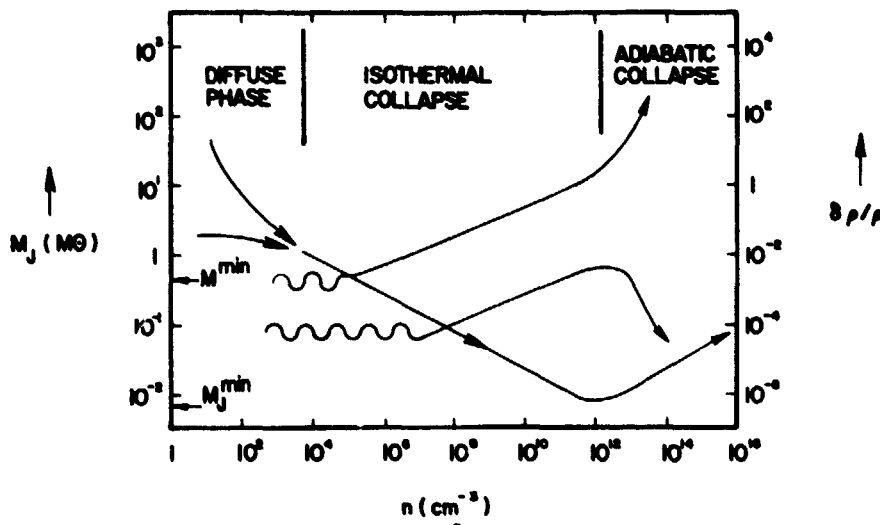


Figure 1. The fate of density fluctuations in a collapsing cloud. The Jeans mass (left ordinate) is shown as a function of density for spherical collapse using a silicate grain model. It attains a minimum value of  $\sim 0.007 M_{\odot}$  at a particle density of  $\sim 2 \times 10^{12} \text{ cm}^{-3}$ . The evolution of the density contrast (right ordinate) is illustrated for a fluctuation containing a mass  $M^{\text{min}}$  and for one of mass  $< M^{\text{min}}$  but  $> M_J$ .

Consider then a fluctuation of wavelength  $\lambda$  which only commences to grow at a time  $t_{\lambda}$  well into the collapse. In other words, at  $t_{\lambda}$ , the fluctuation mass  $M_{\lambda}$  first exceeds the Jeans mass. If the density contrast at this time is  $\delta_{\lambda}$ , fragmentation will occur at an epoch  $t_1$ , say, when the background density has increased by a factor  $(5/\delta_{\lambda})^2$ , according to a recent analysis of uniform spherical collapse (Tohline 1980). However a crucial assumption is that the collapse remains isothermal. In other words,  $\rho(t_1)$  must not exceed  $\rho(t_{\text{ad}})$ , where the epoch at which the collapse first becomes adiabatic is denoted by  $t_{\text{ad}}$ . Fragmentation will only be effective on mass scales larger than  $M_{\lambda}$ , since smaller scales will not have separated out by  $t_{\text{ad}}$ . If their density contrast is small at this stage, the fluctuations will not survive into the adiabatic collapse phase as distinct fragments. The minimum mass fragments to form will have just become non-linear at  $t_{\text{ad}}$ . If  $M_J^{\text{min}} = \rho(t_{\text{ad}})^{-1/2}$  denotes the minimum Jeans mass at  $t_{\text{ad}}$ , we infer that

$$\rho(t_{\text{ad}})/\rho(t_{\lambda}) > \rho(t_1)/\rho(t_{\lambda}) = (5/\delta_{\lambda})^2$$

and the minimum mass fragment is

$$M^{\text{min}} > (5/\delta_{\lambda}) M_J^{\text{min}}.$$

This simple result leads to a considerable difficulty in understanding star formation. In addition to the fact that collapse by a density enhancement factor of about  $10^5$  is required for fluctuations of amplitude 1 percent from the instant that they are first Jeans unstable, the minimum fragment mass becomes uncomfortably large. To see how this arises, let us briefly review the opacity-limited fragmentation argument that defines  $M_J^{\text{min}}$ .

The time evolution of a volume element in the uniform spherically collapsing cloud is defined by a locus in the temperature-density plane. The condition that the volume element be able to freely radiate away its thermal energy as it is compressed and its internal energy increases defines a relation between  $T$  and  $\rho$  that initially is almost isothermal:  $T = \rho^{1/8}$  is actually found to apply (Silk 1977a). Since the Jeans mass can be written

$$M_J = \text{constant} (\rho/\rho^0)^{3/2},$$

ORIGINAL PAGE IS  
OF POOR QUALITY

and the equation of state inferred for optically thin uniform spherical collapse is  $p = \rho^{9/8}$ , one sees that the Jeans mass decreases as  $M_J = \rho^{-5/16}$ . For exactly isothermal collapse, one would have  $M_J = \rho^{-1/2}$ .

At sufficiently high density, inhibition of cooling by radiation trapping qualitatively alters this result, since the effective equation of state now resembles  $p = \rho^{5/3}$ . This is inevitable, because the column density across a Jeans mass fragment is proportional to  $\rho^{1/2}$  and the optical depth eventually becomes large. The new equation of state in this adiabatic regime is derived by requiring that an isolated fragment be able to radiate away the gravitational energy acquired as it contracts. Since the cooling rate now depends on the fragment size, the evolution track in the (T,n) plane is mass-dependent. The Jeans mass now rises as  $M_J = \rho^{1/2}$ , and its minimum value occurs where the optical depth across a fragment is of order unity. Use of opacities corresponding to conventional grain models (graphite or silicates) and a solar abundance of heavy elements in grains yields a value  $M_{J}^{\min} = 0.005 M_{\odot}$  (Silk 1977a). There is a correction factor that should be incorporated due to the presence of neighbouring fragments which effectively decrease the solid angle over which an individual fragment can radiate freely (Smith 1977). This effect raises the minimum fragment mass by a factor  $\sim N^{1/6}$ , where N is the number of fragments in the cloud (Silk 1980).

Even in the absence of any heavy elements, opacity due to  $H^-$  formation is important. In this case, the minimum Jeans mass is  $\sim 0.3 M_{\odot}$  (Silk 1977b). A simple expression for  $M_{J}^{\min}$  that explicitly demonstrates the role of heavy elements is (Rees 1977, Silk 1977b)

$$M_{J}^{\min} = 20 M_{\odot} (kT/\mu c^2)^{1/4}.$$

Here  $M_{\odot} = (hc/G\mu)^{3/2} \sim 1 M_{\odot}$  is the Chandrasekhar mass and  $\mu$  is the mean molecular weight. Provided the heavy element abundance remains above  $\sim 10^{-3}$  that of the solar value, cooling occurs to below 10 K. However, at lower values, heavy element cooling is unimportant, and  $T \sim 10^4$  K is maintained by Ly $\alpha$  cooling.

The dilemma confronting fragmentation theory is now very apparent. With  $M_{\min} > 10^3 M_{J}^{\min}$  for  $\delta \sim 0.01$ , as expected in spherical collapse, it is not at all obvious how fragments of stellar mass can form. Fragments of primordial composition are entirely outside the conventional stellar mass range. Even for solar composition, stars of solar mass are excluded. Indeed, the fragments are likely to provide lower limits to the actual masses of the protostars that form. The various non-linear processes that one can imagine, including accretion of uncondensed matter and coagulation of fragments, will tend to increase the masses of fragments. This result led Tohline (1980) to conclude that Population III of primordial composition consisted not of stars but of very massive objects. Unfortunately, the little evidence one has is consistent with the notion that Population III consisted of stars, although practically all were considerably more massive than the sun. At least one halo star has been discovered with essentially zero metallicity ( $10^{-4.5} Z_{\odot}$  according to Norris [1981]), and presumably is a relic of population III.

Another consequence of the hierarchical opacity-limited fragmentation theory is that clouds fragment on a free-fall time-scale. There is considerable evidence that star formation is a much slower process. First, molecular clouds are relatively long-lived. Minimum estimates of lifetimes are  $\sim 10^7$  yr, and  $3 \times 10^7$  yr is probably more plausible given star formation efficiencies of order 10 percent, comparable to those observed in Taurus and Orion (Cohen and Kuhl 1979). Second, studies of the Hertzsprung-Russell diagram in open clusters indicate that low mass star formation proceeded on a longer time-scale than did massive star formation. In the case of the Pleiades, the nuclear turn-off age is  $7 \times 10^7$  yr, whereas there are many stars above the lower main sequence that must have been formed some  $2 \times 10^8$  yr ago (Stauffer 1980). A recent study of NGC 2264 (Strom 1981) concludes that the star formation rate increased with time as progressively more massive stars formed.

In order to attempt to reconcile fragmentation theory with star formation, two physical effects will be explored here. In §IV, the role of anisotropic collapse will be discussed. In §V, the interaction of newly formed protostars with uncondensed cloud matter will be considered.

#### IV. Anisotropic collapse and fragmentation

The envelope of a collapsing cloud will be more easily supported by the magnetic field, especially if it is somewhat tangled, than the cloud core. This is because the critical mass below which magnetic support is possible for a uniform spherical cloud (the "magnetic Jeans mass") is

$$M_{cr} = 6 \times 10^4 (B/10^{-6} g)^3 n^{-2} \xi M_{\odot},$$

where  $\xi = 0.3$  and  $B = n^{\kappa}$ , with  $1/3 < \kappa < 1/2$  (Mouschovias and Spitzer 1976; Mouschovias 1976). Consequently,  $M_{cr} = n^{-3(2/3-\kappa)}$ , and is reduced in the cloud core. In §II, evidence was cited that supports the occurrence of magnetic braking up to densities characteristic of molecular cloud cores. If angular momentum is conserved during collapse at densities greater than  $n_b$  and corotation with the galaxy is enforced at lower densities, the resulting specific angular momentum of a one solar mass fragment is  $j \sim 3 \times 10^{18} (n_b/10^6 \text{ cm}^{-3})^{-2/3} \text{ cm}^2 \text{ s}^{-1}$ . For the density range  $10^6 > n_b > 10^3 \text{ cm}^{-3}$ , one infers that  $10^{18.5} < j < 10^{20.5} \text{ cm}^2 \text{ s}^{-1}$ , and the corresponding range in periods of binary stars if formed with this amount of orbital angular momentum is  $10^{-1.5} - 10^{4.5}$  yr. This indicates that the angular momentum of molecular clouds resides in orbital angular momentum of wide binaries, provided that both fragmentation and magnetic braking have occurred at densities near  $n_b$ .

ORIGINAL PAGE IS  
OF POOR QUALITY

The collapse of cloud cores is accordingly likely to be anisotropic, contracting preferentially along field lines, since field decoupling will only occur gradually. Now the cloud, if cold, is highly Jeans unstable. The characteristic mass for gravitational instability is given by the Bonner-Ebert criterion, which takes account of the ambient pressure:

$$M_{BE} = 1.1(T/10K)^{3/2} (n/10^4 \text{ cm}^{-3})^{-1/2} M_{\odot}$$

Thus to decide whether fragmentation occurs, we see that spherical collapse may be an unrealistic assumption. A more plausible assessment of fragmentation may be given as follows.

Consider the collapse from rest of a cloud that is initially uniform, pressure-free and oblate spheroidal. For simplicity, only a small initial deviation from sphericity is assumed. The analysis of the growth of small density perturbations is similar to that for a uniformly collapsing sphere. The collapse of the spheroid is described by two scale factors:  $R(t)$  in the directions of two equal axes and  $Z(t)$  in the direction of the smallest axis. The position of any point in the spheroid is then given by  $r = r_0 R(t)$ ,  $z = z_0 Z(t)$ , where  $r$  and  $z$  are cylindrical coordinates and  $r_0$  and  $z_0$  refer to the initial position of the point. The density satisfies

$$\rho = \rho_0 (R^2 Z)^{-1},$$

where  $\rho_0$  is the critical density. Now the spheroidal cloud, even if very nearly spherical at the onset of the collapse, becomes progressively more flattened as the collapse continues (Lin, Mestel and Shu 1965). In fact, it collapses first along the  $z$ -axis into a thin pancake. What this implies is that in the final stages of the collapse,  $R(t)$  changes relatively slowly, while  $Z(t) \rightarrow 0$  (in practice, the thickness will be finite because the matter will possess a certain amount of thermal energy and pressure).

Recall that in uniform spherical collapse, a small density perturbation amplifies if its scale exceeds the Jeans length and results in fragmentation (that is to say,  $\delta\rho/\rho$  becomes large) shortly before the cloud itself has collapsed, in fact within a fraction  $1-\delta_0$  of an initial free-fall time. An interesting difference arises when we study the growth of perturbations in a spheroidal collapse. Density fluctuations that are predominantly aligned with the collapse ( $z$ ) axis do not become large, whereas fluctuations that are perpendicular to the collapse axis do amplify and separate out prior to the instant of pancaking. Self-gravity dominates the final evolution of oblate perturbations but is unimportant for prolate perturbations. The rate at which the oblate perturbations grow is found to be

$$\delta \sim \delta_0 Z^{-1}.$$

An interesting difference is now seen to arise from the one-dimensional nature of oblate spheroidal collapse. Because the density increases as  $\rho \propto Z^{-1}$  when  $Z \rightarrow 0$ , we see that the density enhancement achieved by the cloud at fragmentation ( $\delta \sim 1$  in the linear theory) is

$$\rho(t_f)/\rho_0 = Z(t_f)^{-1} = \delta_0^{-1},$$

in marked contrast to the result for spherical collapse. Inclusion of a finite initial pressure which acts to delay fluctuation growth modifies this result, but less severely than in the case of spherical collapse. This is because the retardation means that the entire growth occurs when the collapse is nearly one-dimensional, and the geometrical effects dominate the growth rate. If a fluctuation is first Jeans unstable with amplitude  $\delta_\lambda$  at an epoch  $t_\lambda$ , one finds that at fragmentation

$$\rho(t_f)/\rho(t_\lambda) \lesssim 2\delta_\lambda^{-1}.$$

Adopting the opacity-limited fragmentation result that fragments should have achieved density contrast of order unity prior to  $t_{ad}$ , one now infers that the minimum fragment mass

$$M^{\min} > (2/\delta_\lambda)^{1/2} M_J^{\min}.$$

for oblate spheroidal collapse. Since this result is valid even for initial flattenings  $z_0/r_0 \sim 0.8$ , one infers it is likely to apply in any realistic situation. The spherical collapse model is too highly idealized to be relevant, given any reasonable range of initial deviations from spherical symmetry as would be expected for plausible initial conditions at the onset of the collapse.

The implications for star formation are profound. For one expects the density fluctuation level to be at least  $\delta \sim 0.01$  over a wide range of scales. In primordial clouds, thermal instability associated with  $H_2$  cooling guarantees sizable fluctuations down to mass scales of a few  $M_{\odot}$ . In conventional molecular clouds, the complex history of a cloud, involving accumulation of debris from smaller clouds and evolving stars, suggests that fluctuations should be present down to scales of  $\sim 1 M_{\odot}$ . Moreover, the violent events inferred to be stirring up the interstellar medium (including supernova explosions and stellar winds) should also generate pressure fluctuations over a wide range of scales. These are able to penetrate  $\sim \delta_\lambda^{-1}$  wavelengths into a cloud before dissipating. Consequently, for a cloud of mass  $M_c$ , one expects the fluctuation level to be  $\delta_\lambda \sim (M_\lambda/M_c)^{1/3} > 0.01$  over stellar mass scales  $M_\lambda$ .

With  $M_{\text{min}} \sim 0.005 M_{\odot}$  in molecular clouds and  $0.3 M_{\odot}$  in primordial clouds, the preceding discussion implies that fragmentation is likely to be effective on scales as small as  $0.05 M_{\odot}$  (molecular clouds) to  $3 M_{\odot}$  (primordial clouds). The implications of this result for star formation are discussed below.

#### V. Interaction of protostellar winds with molecular clouds

Once protostars form of mass  $> 1 M_{\odot}$ , it seems likely that their energy input to the cloud will significantly inhibit continued fragmentation. It is this effect that provides promise of understanding the apparent longevity of molecular clouds in terms of their ability to survive many free-fall times. There is considerable evidence that protostellar winds provide an important energy input, at least into localized regions of molecular clouds. In what follows, I will summarize the evidence for this, and then attempt to make some global inferences about cloud evolution and star formation.

The most dramatic example of the interaction of a protostellar wind with a molecular cloud is L1551, which reveals a bipolar structure with a velocity spread of  $> 12 \text{ km s}^{-1}$  (Snell et al. 1980). There are associated Herbig-Haro objects whose measured proper motions project back to an infrared source at the center of the CO lobes. The total mass of high velocity gas is  $\sim 0.3 M_{\odot}$  over an extent of  $\sim 0.5 \text{ pc}$ . The luminosity of the central source is  $\sim 25 L_{\odot}$ , and is insufficient to drive the outflow by radiation pressure. Another source with similar parameters is NGC 1333 (Snell and Edwards 1981). Strong winds are also found around several much more luminous infrared sources, the best-studied example being IRc2 with a luminosity of  $> 10^4 L_{\odot}$  and  $10 M_{\odot}$  of gas moving at  $\pm 50 \text{ km s}^{-1}$ . Other examples are CepA (Rodriguez et al. 1980) and AFGL490 (Lada and Harvey 1981). Another interesting system is that of HH1 and HH2 (Jones and Herbig 1981), where measured proper motions indicate nearly collinear motions of filaments away from a centrally located T-Tauri like star at  $\sim 100 \text{ km s}^{-1}$ .

In general, bipolarity is not uncommon in pre-main-sequence objects (Calvet and Cohen 1978), and may be indicative of wind interactions with a central disk. Direct evidence for strong winds from pre-main-sequence stars has been obtained by Cohen et al. (1981), who discovered regions of extended free-free emission around several T-Tauri stars. If the outflow is spherically symmetric, a mass-loss rate  $\sim 10^{-6} M_{\odot} \text{ yr}^{-1}$  is inferred for T-Tauri, for example, although this may overestimate the actual mass loss rate if the wind is anisotropic.

One is tempted to try to relate wind input of energy to one of the great mysteries about molecular clouds, namely the origin of their supersonic line widths. Overall collapse provides an untenable explanation for the line widths, and one is left with a cloud model which consists of a number of supersonically moving clumps of gas. The outstanding questions are: what drives the clump motions and how are the clumps maintained for periods  $> 10^7 \text{ yr}$ ? A similar difficulty is encountered both in warm molecular clouds and in dark clouds.

The most natural explanation is that protostellar winds are continuously driving mass motions (Norman and Silk 1980). Cloud longevity can be understood if the winds are not disruptive, a plausible assumption for T-Tauri stars embedded in cold clouds. Now in a dense molecular cloud, a wind at  $< 200 \text{ km s}^{-1}$  will be radiative and approximately momentum conserving. One may crudely estimate the mean velocity dispersion acquired by an average volume element in a cloud of mass  $M_{\text{C}}$  containing  $M_{\star}$  in stars which have lost a fraction  $\Delta M_{\star}$  of their mass at some characteristic wind velocity  $V_{\text{W}}$  as

$$\langle \Delta v \rangle \sim \left( \frac{M_{\star}}{M_{\text{C}}} \right) \left( \frac{\Delta M_{\star}}{M_{\star}} \right) V_{\text{W}}$$

Evidently a substantial fraction of the cloud matter can be stirred up with  $\langle \Delta v \rangle \sim 1 \text{ km s}^{-1}$  if  $V_{\text{W}} \sim 200 \text{ km s}^{-1}$ ,  $M_{\star}/M_{\text{C}} \sim 0.1$  (as observed in dark clouds), and  $\Delta M_{\star}/M_{\star} \sim 0.1$ . For this to persist over  $2 \times 10^7 \text{ yr}$ , a considerable part of the cloud would have to be consumed in star formation: indeed, exhaustion of cloud material may lead to the formation of a T association. On the other hand, intervention of an external trigger, perhaps associated with a nearby supernova or expanding HII region, may change the cloud evolution in a manner that will now be outlined, and form an O association.

Let us suppose that the first stars to form are T-Tauri stars. These low mass stars develop winds which will sweep up shells of material. The final radius of such a shell is limited by the ambient cloud pressure  $p$  to

$$R = \left[ \frac{\dot{M} V_{\text{W}}}{4\pi p} \right]^{1/2} = 0.1 \frac{(\dot{M}/10^{-7} M_{\odot} \text{ yr}^{-1})^{1/2} (V_{\text{W}}/10^2 \text{ km s}^{-1})^{1/2}}{(n/10^3 \text{ cm}^{-3})^{1/2} (V_{\star}/1 \text{ km s}^{-1})} \text{ pc.}$$

where  $V_{\star}$  is the stellar velocity dispersion and  $\dot{M}$  the mean mass loss rate. The condition for such shells to grossly affect the cloud evolution and inhibit further fragmentation and star formation is that any pair of shells should intersect within the lifetime of the protostellar wind phase. This can be expressed as

$$\frac{1}{n_T \pi R^2 V_*} < \frac{M}{\dot{M}} \text{ or } n_T > 10 \frac{(V_*/1 \text{ km s}^{-1})(n/10^3 \text{ cm}^{-3})}{(V_w/10^2 \text{ km s}^{-1})} \text{ pc}^{-3}.$$

For comparison, one of the best studied dark cloud regions in Taurus-Auriga contains aggregates of between 4 (Jones and Herbig 1980) and 30 (Cohen and Kuhl 1979) T-Tauri stars  $\text{pc}^{-3}$  detectable at  $A_V < 4$ .

This demonstrates that wind-driven shells are likely to intersect. Shell intersection will result in the formation of supersonically moving clumps, since in general intersection occurs before the shells are in pressure balance. The characteristic clump masses are 0.1-1  $M_\odot$ , with sizes of  $\sim 0.1$  pc. They will only be weakly confined by ram pressure because of their low Mach numbers, and so will continuously replenish the interclump medium. However, new clumps will form, and clump collisions and accretion will result in their net growth. It seems likely that within a few collision times or crossing times, say  $10^6$  yr, a clump will have grown sufficiently to become Jeans unstable.

Let us speculate that in the absence of any external trigger, this results in further formation of low mass stars. In this manner, the process become self-perpetuating: low mass stars form, develop winds that sweep up shells, the shells intersect and form clumps, and the clumps coalesce and form more low mass stars. The process terminates either when the gas supply is exhausted, after  $> 10^7$  yr, or when an external trigger stimulates massive star formation that could catastrophically disrupt the cloud. An example of this would be a nearby supernova explosion that shocked the cloud, accelerating the rate of clump coalescence and providing enough energy input to also raise the Jeans mass substantially.

This scenario has a number of implications for cold molecular clouds. There should be embedded infrared sources with  $< 10 L_\odot$ , evidence for high velocity mass motions, an internal source of ultraviolet radiation that could affect dark cloud chemistry, and clumpiness on scales of 0.1-1  $M_\odot$ . Its principal virtue has been to make a direct connection between two distinct but more or less coincident time-scales: star formation is non-coeval in open clusters, apparently extending over a period  $> 10^7$  yr, and molecular clouds are long-lived, with lifetimes  $> 10^7$  yr and greatly in excess of free-fall time-scales. This provides the basis of our model, which asserts that such a fortuitous coincidence is really due to a direct physical coupling between molecular clouds and star formation. A major bonus is that the ongoing star formation provides a substantial momentum input into molecular clouds, leading to a natural interpretation of suprathermal line widths.

## VI. Conclusions

Molecular clouds undergo fragmentation at a density  $< 10^5 \text{ cm}^{-3}$ . Several lines of evidence lead to this inference, including the density of O associations at birth and molecular observations of nearby dark clouds. It is likely that deviations from sphericity induced by collapse along magnetic field lines play an important role in the fragmentation process. Anisotropic collapse enables smaller fragments to separate out before the increasing opacity inhibits any further fragmentation. Anisotropy has a dramatic effect on fragmentation because it limits the growth rate of the background density, whereas a fluctuation grows in density mostly because of its additional self-gravity, which is more or less independent of the background kinematics.

The smallest fragments to form and survive an initial free-fall time are not at the minimum Jeans mass but must be considerably larger, since they must have been able to attain a density contrast of order unity before the collapse becomes adiabatic. A highly simplified analysis suggests that the minimum mass fragments may be  $\sim 0.05 M_\odot$  in interstellar clouds; in primordial clouds, the minimum mass is likely to exceed  $\sim 3 M_\odot$ .

Once such fragments form and become protostars of mass  $> 1 M_\odot$ , they are likely to have a significant interaction with the rest of the cloud. After an initial free-fall time, only the innermost core of the cloud could have fragmented. One expects that a substantial fraction of the cloud will still be relatively diffuse at this stage, especially if magnetic support is important in the outer cloud envelope. The most effective mode of interaction is likely to be via stellar winds from pre-main-sequence stars. Observational evidence indicates that such winds may play an important role in stirring up molecular clouds.

Hence a plausible speculation is that the first strong protostellar winds can inhibit cloud collapse and fragmentation. Such winds are likely to interact and generate additional clumpiness in the cloud. Clumpiness enhances fragmentation, and it seems entirely possible that protostellar winds are self-sustaining. As some winds die away, new protostars form that are capable of providing a dynamically significant momentum input into the cloud. Only when the gas reservoir is depleted as a number of massive stars form would the star formation process terminate. In this way, one might be able to understand such issues as why star formation is non-coeval, why molecular cloud lifetimes are many free-fall times, and why clouds exhibit a clumpy structure and suprathermal linewidths.

This research has been supported in part by the U.S. National Science Foundation.

References

- Abt, H.A. and Levy, S. 1976, Ap. J. Suppl., 30, 273.  
 Blaauw, A. 1978, in Problems of Physics and Evolution of the Universe (Armenian Academy of Sciences: Yerevan), p. 101.  
 Calvet, N. and Cohen, M. 1978, M.N.R.A.S., 182, 687.  
 Cohen, M., Biegging, J.H., and Schwartz, P.R. 1981, Ap.J. (in press).  
 Cohen, M. and Kuhl, L.V. 1979, Ap. J. Suppl., 41, 743.  
 Goldsmith, P.F., Langer, W.D., and Young, J.S. 1981, Bull. A.A.S., 13, 508.  
 Hunter, C. 1962, Ap. J., 135, 594.  
 Jones, B. and Herbig, G. 1981, A.J. (in press).  
 Lada, C. and Harvey, P. 1981, Ap. J., 245, 58.  
 Lin, C.C., Mestel, L. and Shu, F. 1965, Ap. J., 142, 1431.  
 Myers, P. 1981, Ap.J., 242, 1013.  
 Mouschovias, T. 1977, Ap. J., 211, 147.  
 Mouschovias, T. 1976, Ap.J., 207, 141.  
 Mouschovias, T. and Spitzer, L. 1976, Ap. J., 210, 326.  
 Norman, C. and Silk, J. 1980, Ap. J., 238, 158.  
 Norris, J. 1981, private communication.  
 Rees, M.J. 1977, M.N.R.A.S., 176, 483.  
 Rodriguez, Ho, P. and Moran, J. 1980, Ap. J. Letters, 240, L149.  
 Silk, J. 1980, in Star Formation, 10th Saas Fee Advanced Course of the Swiss Society of Astronomy and Astrophysics, I. Appenzeller, J. Lequeux, and J. Silk (Geneva Observatory: Geneva). p. 131.  
 Silk, J. 1977a, Ap. J., 214, 152.  
 Silk, J. 1977b, Ap. J., 211, 638.  
 Smith, R.C. 1977, M.N.R.A.S., 179, 521.  
 Snell, R.L., and Edwards, S. 1981, preprint.  
 Snell R.L., Loren R.B., and Plambeck, R.L. 1980, Ap. J. Letters, 239, 21.  
 Stauffer, J. R. 1980, A.J., 85, 341.  
 Strom, S. 1981, presented at Star Formation Workshop, Aspen Center for Physics.  
 Tohline, J. 1980, Ap. J., 239, 417.  
 van Gorkom, J.H. 1981, private communication.  
 Zuckerman, B. and Palmer, P. 1974, Ann. Revs. Astronomy and Astrophysics, 12, 279.

N82 23447

Solidification of Carbon-Oxygen white dwarfs

by E. SCHATZMAN

Observatoire de Nice, B.P. 252 Nice Cedex 06007  
France

**Abstract.** During cooling, a hail of oxygen can fall in the center of a Carbon-Oxygen white dwarf. Consequences for white dwarfs evolution are considered. Formation of pulsars or type I Supernovae production can be the result of a difference in chemical composition.

The following report is divided into four sections: (1) elementary information on the internal structure of white dwarfs, (2) basic information on highly correlated plasmas, (3) implications for phase separation in the core of cooling white dwarfs, and (4) consequences for evolution of white dwarfs.

The present report can be considered as a continuation of a paper of Canal, Isern and Labay (1981).

(1) Internal structure of white dwarfs. We just recall a few properties of white dwarfs which are relevant to the present problem.

We describe a white dwarf as a non-rotating, spherical star, in hydrostatic equilibrium. The main problem concerns the equation of state,

$$P = P(\rho, T)$$

which, in the major part of the star cannot be distinguished from the equation of state of a Fermi gas at zero temperature,

$$P = P(\rho, 0)$$

The region where the departure from  $T = 0$  influences the structure is extremely small, and represent a mass  $\Delta M / M = 10^{-4.58} T_{\text{eff}}^{20/3}$

If we ignore the properties of the nuclei and introduce in the equations of hydrostatic equilibrium the general relativity corrections to the Newtonian theory of gravitation, we write

$$\frac{dP}{dr} = - \frac{GM}{r^2} \rho \frac{(1 + (P/\rho c^2)) (1 + (4\pi P r^3 / M c^2))}{(1 - (2GM/c^2))}$$

where the term  $(1 + (P/\rho c^2))$  represents the increase of inertial mass, the next term the increase in gravitationally attractive mass and the denominator term represents the change of the metric for Euclidian to non Euclidian.

The knowledge of the equation of state is necessary in order to solve the equation of hydrostatic equilibrium. At high densities we can write the relativistic equation of state,

$$P = K_2 (\rho / \mu_e)^{4/3}$$

with  $\mu_e = (A/Z)$  and

$$K_2 = 1.23 \cdot 10^{15}$$

At lower densities, the non relativistic equation of state (neglecting electrostatic interactions) is

$$P = K_1 (\rho / \mu_e)^{5/3}$$

with  $K_1 = 9.91 \cdot 10^{12}$ . The change from one equation of state to the other takes place for a density of about  $10^8$  g cm<sup>-3</sup>.

For the kind of white dwarfs we are considering, the transition from the non relativistic to the relativistic equation of state takes place at a mass  $\Delta M_{\text{rel}}$ :

$$\frac{\Delta M_{\text{rel}}}{M} = (4\pi R^4 / GM^2) (\rho / \mu_e)^{5/3} K_1 = 8 \cdot 10^{-5}$$

The mass radius relation for white dwarfs shows the existence of a maximum mass. For  $\mu_e = 2$ , we have the following properties of a white dwarf with the maximum mass :

$$M = 1.36557 M (\text{Sun})$$

$$R = 1066 \text{ km}$$

$$\rho_c = 1.92 \cdot 10^{10} \text{ g cm}^{-3}$$

A white dwarf of high density, close to the limiting mass (we should call it the Chandrasekhar-Kaplan limiting mass), has no other energy source than its internal thermal energy. As long as the inside of the white dwarf is fluid, the internal thermal energy is the sum of the thermal energy of the ions and of the thermal energy of the electrons,

$$U = (\rho / A m_H) \left( (3/2) k T + (3/4) \left( Z \pi^2 k^2 T^2 / m_e c^2 x \right) \right)$$

where  $x$  is related to the density by

$$\rho = (8 \pi / 3) (m_e^3 c^3 / h^3) (A m_H / Z) x^3$$

The corresponding cooling time scale is given by the heat balance condition.

Again, for the kind of stars which we are considering, close to the Chandrasekhar - Kaplan limit, we have for the characteristic cooling time

$$t = 10^{6.056} (T / 10^8)^{1/2} \text{ years.}$$

This is valid however only as long as the white dwarf has not reached the solid state. If we consider the ratio of the electrostatic energy to the thermal energy,

$$\Gamma = (Z^2 e^2 / a k T)$$

where

$$a = (3 Z / 4 \pi N_e)^{1/3}$$

is the ionic radius, the solidification takes place when

$$\Gamma = 160.$$

During cooling, the first point where solidification takes place is in the center of the star. Two quantities are important to consider : (1) the melting temperature inside the star ; (2) the Debye temperature inside the star. It turns out that the heat content of the electrons is much larger than the heat content of the ions.

When solidification takes place, the latent heat of solidification is liberated, and the consequence is a slowing down of the cooling. For the kind of stars which we are considering, this is completely negligible.

## 2. Highly correlated plasmas .

We have just seen that in a cold plasma, crystallization takes place when the ratio of the Coulomb energy to the thermal energy is about 160. We need not to consider in the following the quantum effects in the solid.

Let us consider now the case of a two component plasma, Carbon and Oxygen, which are the most abundant products of the late stages of stellar evolution.

There is a conjecture by Stevenson (1979) that an eutectic can exist, between Carbon and Oxygen, with the following characteristics :

$$\begin{aligned} X_O (\text{in number}) &= 0.332 \\ T_E &= 0.628 T_C (\text{melting of Carbon}) \\ &= 0.389 T_O (\text{melting of Oxygen}) \end{aligned}$$

with a density difference (Pollock and Hansel, 1974) :

$$\frac{\rho(\text{solid}) - \rho(\text{liquid})}{\rho} = 3 \cdot 10^{-4}$$

and with  $A(\text{Oxygen}) = 15.99468$  and  $A(\text{Carbon}) = 12.00000$ , we obtain :

$$\frac{\rho_0(\text{solid}) - \rho(\text{liquid})}{\rho} = \frac{3.10^{-4} - 3.24 \cdot 10^{-4} X}{1 - (X/4)} \quad ; X_C = X < 0.668$$

$$\frac{\rho_C(\text{solid}) - \rho(\text{liquid})}{\rho} = \frac{6.52 \cdot 10^{-4} - 4.07 \cdot 10^{-4} X}{(1 - (X/4))} \quad X > 0.668$$

As a consequence, we see that the density of the solid, either of pure carbon or of pure oxygen, is always larger than the density of the liquid.

During cooling, solid particles of Carbon, or solid particles of oxygen (according to the concentration) will appear and fall in the gravity field. When the chemical composition of the eutectic is reached, the solid particles of Carbon will be appreciably denser than the solid particles of Oxygen. In fact, we have:

$$(\Delta\rho/\rho) (\text{Carbon to Eutectic}) = 3.91 \cdot 10^{-4}$$

$$(\Delta\rho/\rho) (\text{Oxygen to Eutectic}) = 0.84 \cdot 10^{-4}$$

The argument of Stevenson is that, if the cooling is fast enough, the eutectic solidifies; if it is very slow, it will experience separation of Oxygen and Carbon. However, due to the large difference in the buoyancy forces, Carbon will settle faster.

### 3. Phase separation in white dwarfs.

We shall first consider the temperature excess of the condensing solid. Following the argument of Jeffreys (1918), and reproduced by Mason (1953), we assume the microscopic diffusion is the way by which the atoms join the growing crystal. We then have:

$$\rho(\text{solid}) R \frac{dR}{dt} = D (1-X) N_e (A/Z) m_H$$

Similarly, we write that the latent heat of crystallization, released on the crystal is carried away by thermal conductivity. We write,  $\lambda$  being the heat conductivity,

$$L R \frac{dR}{dt} = \lambda (T_S - T)$$

from which we derive the temperature excess:

$$T_S - T = \frac{D (1-X) \rho L}{\lambda}$$

$L$  is of the order of  $3 k T$  per ion. The microscopic diffusion coefficient is of the order of

$$D = a v_{th}$$

The thermal conductivity is large, heat being carried away by the relativistic electrons (Schwarzschild, White Dwarfs).

For  $\rho = 10^{10} \text{ g cm}^{-3}$ ,  $T = 10^8 \text{ K}$ , this gives

$$T_S - T = 1000 \text{ K} \ll T$$

Let us now consider the speed at which the crystals can fall inside the white dwarf. We consider that the force on the crystal is given by the Stokes formula. We then have:

$$-(GM/r^2) (4\pi a^3/3) (\rho_{\text{solid}} - \rho_{\text{liquid}}) = 6\pi \rho_S \nu a (dr/dt)$$

where  $\nu$  is the kinematic viscosity coefficient.

If we consider that the radius of the crystal,  $a$ , is time dependent,

$$(a^2/2) = D (1-X) t$$

we obtain,

$$(dr/dt) = - (16\pi/27) G \frac{\rho_{\text{solid}} - \rho_{\text{liquid}}}{\rho} (D/\nu) (1-X) t$$

we can write

$$r = r_0 \exp\left(-\left(t/\tau\right)^2\right)$$

and derive the time scale of the phase separation ,

$$\tau^2 = (27 / 8 \pi) (\rho / (\rho_{\text{solid}} - \rho_{\text{liquid}})) (1 / G \rho_{\text{liquid}}) (v / D) (1-X)^{-1}$$

The viscosity is due to the transfer of momentum to the ions . Therefore,  $v$  is of the order of  $D$  .  
With  $\rho = 2 \cdot 10^{10} \text{ g cm}^{-3}$ ,  $\Delta\rho / \rho = 3.9 \cdot 10^{-4}$ , we obtain ,

$$\tau = 6 \text{ sec}$$

With  $\Delta\rho/\rho = 0.84 \cdot 10^{-4}$ ,

$$\tau = 13 \text{ sec.}$$

We can consider that the cooling time is much longer than the crystallization time and the infalling time . Two cases have to be considered:

(1)  $X_C < 0.668$  : Oxygen is predominant .

Oxygen crystallizes immediately, as soon as the eutectic curve is reached. Carbon being soluble in oxygen, the temperature and the oxygen concentration decrease until the chemical composition of the eutectic is reached. The liquid, with the eutectic composition, which is left behind moves up and mixes with the liquid above, making it more rich in carbon. Further separation takes place until the whole solid oxygen corer is surrounded by the eutectic.

Due to the slow cooling, crystals of C and O will form, but we can expect Carbon to fall faster than Oxygen. The melting temperature will have a tendency to rise above the melting temperature of the eutectic, with a tendency of the mixture to solidify quickly. The most reasonable assumption is that the oxygen corer is surrounded by a solid eutectic.

(2)  $X_C > 0.668$  : Carbon is predominant .

We have a similar picture, but, instead of an oxygen core, we have a carbon core, surrounded by the solid eutectic.

#### 4. White dwarf evolution .

(a) thermal effects.

The infall of solid Oxygen (or solid Carbon) makes available a gravitational energy which is of the same order of magnitude as the internal heat content of the star, and larger than the latent heat which is made available during crystallization .

(b) role of accretion.

For a white dwarf, close to the Chandrasekhar - Kaplan limit, the capture of a small amount of matter can make the star unstable. Capture at an appreciable rate can take place when the white dwarf belongs to a binary system. The effect is a pressure increase in the core of the star.

Two cases have to be considered.

(i) the white dwarf has an oxygen core. In that case, electron capture on oxygen can take place.

The decrease in the number of free electrons per unit of mass generates instability . The star contracts about a speed which is sort of average between the free fall time and the characteristic time of electron capture, until it reaches dynamical instability .

What is expected is the formation of a neutron star. Mass ejection taking place at a later stage of collapse can lead to the escape of the star from the binary system. This could explain the large value of the space velocities of pulsars in the galaxy .

(ii) The white dwarf has a carbon core . In that case, dynamical instability would take place before electron capture . In fact the explosive reaction ,



would take place even before the star has begun to collapse. The present conjecture is that a thermal runaway would take place and the star would explode as a type I supernova.

## Bibliography

The theory of the internal structure of White dwarfs can be found in

S.Chandrasekhar : *Stellar Structure*, Chicago University Press, 1939

There are several monographies and review articles :

E.Schatzman , *White Dwarfs*, North Holland Publishing Comp. 1958

E.Schatzman , in *Handbuch d.Phys.* , Vol LI , 1958 , p.723

L.Nestel , in *Stars and Stellar Systems*, *Stellar Structure*, L.H.Aller and D.B.Mc Laughlin Ed., Chicago University Press, 1965, p.297.

A recent review paper is :

H.Van Horn , *Physics Today* 1979.

Recent developments on the theory of highly correlated plasmas can be found in :

Strongly coupled plasmas, Kalman G. and Cavini P. Ed. Plenum Press, N.Y. and London 1977 . See especially the papers by

Ichimaru S. p.189

Schatzman E. p.407

A colloquium , devoted to the problems of dense matter, includes many aspects of the properties of white dwarfs matter :

*Physique de la matière dense* , *Journal de Physique* , Tome 41 , C2 , 1980 . See especially the papers by

D.J.Stevenson , p.61

H.Van Horn , p.97.

The conductivity of degenerate matter has been studied by several authors . See especially :

A.Kovetz and G.Shaviv, *Astronomy and Astrophys.* 28, 315 , 1973.

Flowers E. and Itoh N. , *Astrophys. J.* 206 , 218, 1976.

The viscosity due to ions has been estimated by

H.Van Horn , in *Low Luminosity stars*, Kumar S. Ed. Gordon and Breach , N.Y. , London and Paris 1968, p.297.

Concerning the idea of non-explosive collapse, see :

R.Canal and E.Schatzman , *Astronomy and Astrophys.* 46, 229, 1976.

The colloquium :

*White dwarfs and degenerate stars*, I.A.U. Colloquium N° 53 , H.M.Van Horn and V.Weidemann Ed. See especially

R.Canal and J.Isern , p.52.

R.Mochkovitch , *Thèse de troisième Cycle*, 1980 (to be published )

The question of the effect of accretion on white dwarfs has been considered again during the I.A.U.

Symposium N° 93 :

*Fundamental problems in the theory of stellar evolution* , D.Sugimoto, D.Q.Lamb and D.N.Schramm Ed. Reidel 1981

ORIGINAL PAGE IS  
OF POOR QUALITY

## Drop processes in natural clouds

J. Latham

Physics Department, University of Manchester Institute of Science and Technology  
PO Box 88, Sackville Street, Manchester M60 1Qd, ENGLANDAbstract

Water drops are formed at cloud base by condensation upon nuclei and as they rise they grow by vapour diffusion in the slightly supersaturated environment of the clouds. Turbulent mixing between cloudy air and undersaturated air entrained from outside produces fluctuations in supersaturation, not linked to changes in vertical velocity, which cause broadening of the condensate spectrum and the rapid production of droplets large enough to engage in growth by coalescence. The probabilities of permanent union or the production of satellite droplets following the collision of a pair of raindrops is a sensitive function of several parameters. In some circumstances electrohydrodynamic bursting may influence the the properties of clouds.

1. Introduction

Liquid drops produced by natural processes in the Earth's atmosphere vary in size from around 0.1  $\mu\text{m}$  to 1 cm — a range of about twelve orders of magnitude in volume. This is not surprising that such drops are involved in a large number of physical processes and phenomena; some of which are of crucial importance to large-scale energy transport, the cleanliness of the atmosphere and the fertility of cultivated land. It would be beyond the scope of this short article to attempt a detailed review of each of these processes. Instead, they are treated, in Section 3, in a cursory manner which, it is hoped, will permit their range and their interdependence to be outlined; and one process — the diffusive mixing of dry and cloudy air, which is considered to be fundamental to the development of natural clouds — is selected for more comprehensive discussion, in the following section. This particular topic has been chosen in view of recent concentration of attention upon it by several groups of scientists.

2. The diffusive mixing of dry air with a population of cloud droplets

The sub-adiabatic liquid-water-contents generally observed within clouds from which ice is absent — or present only in insignificant quantities — are a consequence of the dilution of the clouds, during their growth, with environmental, undersaturated air. Recent work (Baker and Latham, 1979<sup>1</sup>; Baker, Corbin and Latham, 1980<sup>2</sup>; Telford and Chai, 1980<sup>3</sup>; Telford and Wagner, 1981<sup>4</sup>) has indicated that the non-uniform manner with which the environmental air mixes with the cloud gives rise to fluctuations in supersaturation — not linked to changes in updraught speed — which cause spectral broadening. A small fraction of the droplets move through the condensate spectrum to the coalescence stage of growth several times faster than predicted by classical descriptions of the entrainment process (for example, Warner (1973)<sup>5</sup>; Mason and Jonas, (1974)<sup>6</sup>; Lee and Pruppach (1977)<sup>7</sup>), in which the mixing between environmental and cloudy air at any level was assumed to be instantaneous and uniform. The droplet spectra predicted by Baker et al agreed well with those measured in cumulus by Warner (1969)<sup>8</sup>.

Baker et al did not specify the nature of the entrainment process but assumed that a volume of environmental air mixing instantaneously with cloudy air at a given level reduced the droplet population there by means of a combination of dilution and total evaporation of a fraction of droplets of all sizes. Telford and Chai assumed that outside air entrained into the cloud at its top became negatively buoyant as a result of droplet evaporation, and then descended, as a saturated stream, to mix with and thereby dilute cloud air at a lower level. The common consequence of both these mixing processes is a droplet spectrum identical in shape to that prior to mixing, but with reduced number concentrations in all size categories. Subsequent ascent of the mixed volume produces an enhancement in supersaturation as a consequence of reduced competition for water vapour; as a result, the droplets grow more rapidly than those in adiabatic regions of the cloud.

In neither of these studies was account taken of the finite rates at which cloudy and environmental air (or adjacent regions of cloud, with different properties) will mix. In this paper we present a model of the turbulent mixing of a spherical blob of droplet-free air, of original diameter  $\lambda_B$ , temperature  $T_B$  and supersaturation  $S$  ( $\leq 0$ ), and a cloud, represented by a spherical shell surrounding the blob of outer diameter  $\lambda_C$ , temperature  $T_C$ , supersaturation  $S$  ( $\geq 0$ ) and liquid water content  $L$ . The blob contains a distribution  $n(m_s)$  of cloud condensation nuclei, comprised of NaCl particles of mass  $m_s$  in equilibrium at the

relative humidity  $H = S + 1$ . This distribution is identical to that assumed to be contained within the droplets in the surrounding cloud, so that when turbulent mixing occurs at any level the total concentration of particles (droplets plus CCN) remains constant. The entire system is assumed to be moving upwards with a speed  $W$ .

The turbulent mixing of all properties transported is represented by diffusion with a single coefficient  $K$  determined on dimensional grounds from  $\lambda_B$  and  $\epsilon$ , the rate of dissipation of turbulent energy within the cloud:  $K = (\lambda_B^2 \epsilon)^{1/3}$ . If we assume that the turbulent motions transport energy, liquid-water, water-vapour and dry air simultaneously, we have

$$\frac{\partial h(R,t)}{\partial t} + W \frac{\partial h(R,t)}{\partial z} - K \nabla^2 h(R,t) = Q_h(R,t), \quad (1)$$

$$\frac{\partial \rho_1(R,t)}{\partial t} + W \frac{\partial \rho_1(R,t)}{\partial z} - K \nabla^2 \rho_1(R,t) = Q_1(R,t), \quad (2)$$

$$\frac{\partial \rho_v(R,t)}{\partial t} + W \frac{\partial \rho_v(R,t)}{\partial z} - k \nabla^2 \rho_v(R,t) = Q_v(R,t) \quad (3)$$

$$\frac{\partial \rho_a(R,t)}{\partial t} + W \frac{\partial \rho_a(R,t)}{\partial z} - k \nabla^2 \rho_a(R,t) = Q_a(R,t) \quad (4)$$

$$\frac{\partial n(r_i, R, t)}{\partial t} + W \frac{\partial n(r_i, R, t)}{\partial z} - k \nabla^2 n(r_i, R, t) = Q_n(r_i, R, t). \quad (5)$$

$\rho$ ,  $\rho_1$  and  $\rho_v$  are the densities of dry air, liquid water and water vapour, respectively;  $n(r_i, R, t)$  is the number density of droplets with radii in the interval  $(r_i, r_i + dr_i)$ ; and  $R$  is the radial vector. The energy term

$$h = [C_a \rho_a + C_1(\rho_1 + \rho_v)]T + \rho_v L_v, \quad (6)$$

where  $C_a$  and  $C_1$  are the specific heat of dry air and liquid water respectively and  $L_v (= 2.26 \text{ KJ g}^{-1})$  is an average value of the latent heat of vapourization of water. Equation (6) defines the temperature  $T$  in terms of the parameters of the problem.

The source terms  $Q$  are:

$$Q_h(R,t) = -[L_v Q_v(R,t) + \rho_a(R,t) g W(t)] \quad (7)$$

$$Q_v(R,t) = -4\pi \rho_w \sum_i n(r_i, R, t) r_i^2 \dot{r}_i(R,t) \quad (8)$$

$$Q_1(R,t) = -Q_v(R,t) \quad (9)$$

$$Q_n(r_i, R, t) = \frac{n(r_i, R, t)}{\rho_a(R,t)} \cdot Q_a(R,t) \quad (10)$$

$$Q_a(R,t) = -\rho_a(R,t) \cdot \left[ \frac{Q_T(R,t)}{T(R,t)} + \frac{g W(t)}{R_a T(R,t)} \right] \quad (11)$$

where  $\rho_a$  is the density of liquid water,  $g$  the acceleration due to gravity and  $R_a$  the gas constant per kilogramme of air.

$$Q_T(R,t) = \frac{Q_h(R,t)}{[C_a \rho_a(R,t) + C_1(\rho_1(R,t) + \rho_v(R,t))]} \quad (12)$$

The droplet growth equation is

$$\dot{r}_i(R,t) = \frac{D \rho_s(T)/\rho_w}{(r_i + a)} W \left[ S(R,t) - \frac{A}{r_i} + \frac{B m_s}{r_i^3} \right] \quad (13)$$

where

$$\rho_s(R,t) = 1.8 \times 10^9 \exp(-5400/T(R,t)) \quad (14)$$

is the saturation vapour density ( $\text{g m}^{-3}$ ),  $D$  is the coefficient of molecular diffusion ( $\text{cm}^2 \text{s}^{-1}$ ), the supersaturation  $S$  is expressed as a percentage,  $r_i$  is measured in micrometres,  $m_s$  in grammes, and the constants  $A$  and  $B$  possess the values  $0.115$  and  $1.4 \times 10^{13}$  respectively.  $a (= 5 \mu\text{m})$  is a characteristic length associated with the non-ideality in water condensation.

The rate of change of supersaturation

$$\dot{s}(R,t) = (100 + s(R,t)) \left[ \frac{Q_V(R,t)}{\rho_V(R,t)} - \frac{5.4 \times 10^3 Q_T(R,t)}{T^2(R,t)} - \frac{3.42 \times 10^{-2} W(t)}{T(R,t)} \right] \quad (15)$$

The precision of the foregoing equations could be increased, but such refinements were deemed unnecessary, in view of the very approximate relationship between this diffusion formulation and the mixing process within clouds. We note that the diffusivity representation is best applied to situations in which  $\lambda_B$  exceeds the characteristic spatial scale of the turbulent eddies. Although buoyancy gradients generated by evaporation will deform the volume under examination, we assume that spherical symmetry is preserved during the mixing process.

Figure (1) illustrates the predicted time variation of the fields of liquid-water-content,  $L$ , supersaturation,  $S$ , and temperature,  $T$ , resulting from the mixing of a blob of air of size  $\lambda_B = 100\text{m}$  and relative humidity 80% with a cloud of size  $\lambda_C = 200\text{m}$  and liquid water content  $L = 0.5\text{g m}^{-3}$ ,  $W = 0\text{ m s}^{-1}$ . In the first case illustrated (A,B,C) the cloud consists of droplets of radius  $3\mu\text{m}$  and in the second (D,E,F),  $r = 20\mu\text{m}$ . Since the turbulent energy dissipation rate  $\epsilon = 10^{-2}\text{m}^2\text{s}^{-3}$  the characteristic mixing times

$$\tau_{TC} = (\lambda_C^2/\epsilon)^{1/2} = 160\text{s} \quad (16)$$

$$\tau_{TB} = (\lambda_B^2/\epsilon)^{1/2} = 100\text{s} \quad (17)$$

We see, when  $r = 3\mu\text{m}$ , that evaporation of droplets carried by turbulence into the interior of the blob is a very rapid process - presumably because of the high surface/volume ratio of the droplets - so that the supersaturation rises from -20% to close on 0% in about 10s. The temperature difference (originally 2K) follows a similar pattern - since its changes are governed by evaporation when the latter is rapid - lagging just slightly behind the changes in  $S$ . Evaporation is confined more-or-less entirely to the region originally occupied by the blob. The liquid-water-content distribution takes considerably longer to level out, because evaporation inhibits its increase in the early stages of mixing, but nevertheless the gradient has been substantially reduced after 20 seconds, a period much less than the turbulent mixing times  $\tau_{TC}$  and  $\tau_{TB}$ .

Figure 1 shows that when the cloud consists of larger drops ( $r = 20\mu\text{m}$ ) the rate of increase of minimum supersaturation  $S$  towards zero is reduced - because evaporation is less effective - but is still essentially completed within 20 seconds. The temperature equalization curves again follow those of  $S$ , and there is a corresponding increase in the rapidity with which the gradient in  $L$  levels out. In this case turbulence distributed the undersaturation significantly into the cloud. Mixing is largely completed after 20s.

Figure (2) shows the time-development of the initially monodisperse spectrum ( $r=20\mu\text{m}$ ; the droplet concentration  $N = 15\text{ cm}^{-3}$ ;  $L = 0.5\text{g m}^{-3}$ ) at  $R = \lambda_B/2$ , the location of the original interface between the cloudy and undersaturated air ( $H = 80\%$ ),  $W = 0.0\text{m s}^{-1}$ . It is seen that the combination of evaporation and turbulent mixing introduces many new categories into the droplet size distribution.

Figure (3) presents the calculated spatial fields of  $L$  and  $S$ , at various times, for two different values of  $\epsilon$ , the turbulent energy dissipation rate,  $W = 0\text{ m s}^{-1}$ . In this case, the original spectrum, illustrated (A) in Figure 5, has a liquid water content  $L = 1.0\text{g m}^{-3}$ . It contains ten size classes (radii between 3 and  $12.5\mu\text{m}$ ) and is based on ones encountered in field studies on the summit of Great Dun Fell (Blyth et al (1980)). In this case  $\lambda_{TC} \sim 130\text{s}$  when  $\epsilon = 10^2\text{m}^2\text{s}^{-3}$  (A,B) and  $\lambda_{TC} \sim 270\text{s}$  when  $\epsilon = 10^3\text{m}^2\text{s}^{-3}$  (C,D); the corresponding values of  $\lambda_{TB}$  are 74s and 160s. When the mixing is rapid (A,B) the supersaturation becomes uniformly distributed within 20s, and gradients in  $L$  are eliminated well before 50s. With slower mixing the equalization of both  $L$  and  $S$  are slower, but are completed in times less than  $\tau_{TC}$ . In both cases undersaturations are created within the region occupied by the original cloud; a characteristic feature of the situations in which the cloud spectrum contains large drops - with correspondingly high values of evaporation time  $\tau_r$  (Baker et al, (1980)).

In figure 4 we present, for the cases covered by Figures 1 and 3, information on the rates at which the total amount of evaporation and the distribution of liquid water approach their final values.  $f$  (in curves A,B,C,D) is the ratio of the total evaporation that has occurred at time  $t$  (expressed, in Figure 4 as the dimensionless time  $t/\tau_C$ ) to that which has occurred when the cloud and blob are fully mixed. In curves E,F,G,H

ORIGINAL PAGE IS  
OF POOR QUALITY

$$f = 1 - \frac{(L_c - L_0)_t}{(L_c - L_0)_{t=0}} = 1 - \Delta L/L \quad (18)$$

where  $\Delta L = (L_c - L_0)_t$  is the difference, at time  $t$ , between the liquid water contents in the centre of the original blob ( $R=0$ ) and at the edge of the cloud ( $R=\lambda_c/2$ );  $L$  is the original liquid-water-content in the cloud.

The curves displayed in Figure 4 show clearly that: evaporation is completed long before the gradients in  $L$  are eliminated; uniformity in  $L$  is achieved - generally - in times much less than  $\tau_{rc}$ ; evaporation proceeds most effectively when droplets are small and mixing is fast. Further calculations (not illustrated) show that uniformity in  $S$  is achieved more quickly for increased values of  $L$ .

In Figure 5 we present various spectra resulting from the mixing with undersaturated air of a volume of cloud possessing an original liquid-water-content  $L = 0.5 \text{ g m}^{-3}$  and the size distribution (A) mentioned earlier,  $W = 0.0 \text{ m s}^{-1}$ . For the particular dimensions chosen ( $\lambda_c = 144 \text{ m}$ ,  $\lambda_B = 60 \text{ m}$ ) the final - well-mixed - value of  $L$ , if the humidity of the entrained air is 70% and the temperatures are as indicated, is  $0.32 \text{ g m}^{-3}$ . Curve B presents the classical spectrum, with  $L = 0.32 \text{ g m}^{-3}$ , which was obtained by the application of the droplet growth equation to all droplets in the original spectrum. All droplets have evaporated, so the peak radius has shifted substantially (whereas the peak concentration is virtually unchanged) and the reduction in radius is greater for the smaller droplets. Curve C,  $L = 0.32 \text{ g m}^{-3}$ , is obtained from our diffusive model, with  $\epsilon = 10^{-3} \text{ m}^2 \text{ s}^{-3}$ . This spectrum is seen to have a peak-radius only slightly below that of the original spectrum (A), but a substantially reduced peak-concentration. Thus the spectrum C, predicted from our model, lies between the classical spectrum B and the extreme inhomogeneous spectrum, but is very much closer to the latter - which is not shown since its similarity to B would cause confusion in presentation.

In Figure 6 we present three spectra resulting from the turbulent mixing of spectrum A - the same as in Figure 5 - with a blob of undersaturated air,  $W = 0 \text{ m s}^{-1}$ . The dimensions and temperatures, given in the legend, are the same for all three calculations. In B and C the relative humidity  $H = 70\%$  and the final water content  $L = 0.32 \text{ g m}^{-3}$ . In B,  $\epsilon = 10^{-3} \text{ m}^2 \text{ s}^{-3}$  and in C,  $\epsilon = 10^{-2} \text{ m}^2 \text{ s}^{-3}$ . Curves B and C are very similar, but B is more 'inhomogeneous' - smaller reduction in peak radius - consistent with the associated slower mixing in this case. Curve D ( $L = 0.18 \text{ g m}^{-3}$ ) was obtained with  $H = 40\%$  and  $\epsilon = 10^{-3} \text{ m}^2 \text{ s}^{-3}$ . This spectrum, although very different from one predicted by the classical description of mixing/evaporation (see, for example, Figure 4, Curve B), is substantially different from the equivalent 'extreme inhomogeneous' or 'dilution only' spectrum (again not shown), in which the shape of curve A would be preserved, and the mean radius would be the same as in A. This large departure from the extreme inhomogeneous spectrum may be attributed to the greater role of evaporation (relative to dilution) in producing the final spectrum (D).

In Figure 7 we show the effect of doubling the radius of all droplets in the spectrum A illustrated in Figure 5 and 6, whilst maintaining the liquid water content  $L = 0.5 \text{ g m}^{-3}$ ,  $W = 0 \text{ g m}^{-3}$ . The final spectrum (C) after evaporation and mixing is closer to the classical one B than in the earlier cases, presumably because for these large droplets the ratio of evaporation to mixing times,  $\tau_r/\tau_T$ , (Baker et al (1980)<sup>2</sup>) is no longer much less than unity.

In Figure 8 we attempt to examine, for a wide range of original conditions, the extent to which spectral changes resulting from turbulent mixing of undersaturated and cloudy air conform to the classical (homogeneous) picture or to the alternative extreme discussed by Telford and Chai, and by Baker et al. For ease of interpretation, these calculations were made with originally monodisperse spectra.

On the classical picture, to a first approximation, the concentration of droplets,  $N$ , in an originally monodisperse spectrum, is unchanged from the original value  $N_0$ , as entrainment reduces the liquid water content from  $L_0$  to  $L$ . On the extreme inhomogeneous picture,  $N$  is reduced in proportion to the reduction in  $L$ , (ie  $N = (L/L_0)N_0$ ). On the classical picture the water content is reduced in proportion to the reduction in the radius  $r$  (ie  $r^3 = (L/L_0)r_0^3$ , where  $r_0$  is the original radius). On the extreme inhomogeneous picture  $r$  is unchanged as  $L$  decreases. Thus we may define a parameter

$$\phi = (N/N_0)(L/L_0)/(R/R_0)^3 \quad (19)$$

which possesses a value  $\phi = 1$  for all  $L/L_0$  on the classical description of mixing and is given by  $\phi = (L/L_0)^2$  in the extreme inhomogeneous case.

These two extreme curves are plotted in Figure 8, together with individual values of  $\phi$  emanating from a variety of calculations, using the diffusive mixing model.

## ORIGINAL PAGE IS OF POOR QUALITY

The most important result is that, for all situations considered, the extreme inhomogeneous description of turbulent entrainment provides a much better approximation to reality than does the classical description. The departure from  $(L/L_0)^4$  can be quite substantial, however. We see from Figure 8 that this departure increases with decreasing  $\lambda_0$ , increasing H (at constant  $L/L_0$ ); decreasing L; decreasing  $\epsilon$ ; and (proportionately), decreasing  $L/L_0$ . All these tendencies are consistent with the basic ideas, advanced by Baker et al, that (1) the time constant ratio  $\tau_x/\tau_T$ , which equals zero in the extreme inhomogeneous case, increases with decreasing values of L and  $\lambda$  and with increasing  $\epsilon$  and H; and (2) that as  $(L/L_0)$  is reduced (by reducing H) the contribution of dilution to the overall reduction in water content is reduced.

### 3. Other processes

It is inappropriate, in an article of this limited length, to do other than to list further important processes, occurring in clouds, which involve drops. For a comprehensive and authoritative treatment of these the reader is referred to the excellent book of Pruppacher and Klett (1978). The processes include: condensation via heterogeneous nucleation; collision; coalescence; satellite drop production; electrohydrodynamic bursting; mechanical disruption; scavenging of particulate and gaseous pollutants; supercooling; freezing; accretion; secondary ice particle production; splashing; and lightning initiation by corona.

### Acknowledgements

Dr M B Baker, of the University of Washington, Seattle, USA, played the primary role in the development of the diffusive mixing model described herein. The special contribution of Dr M Guery is gratefully acknowledged.

### References

1. Baker M B & Latham J "The evolution of droplet spectra and the rate of production of embryonic raindrops in small cumulus clouds" J Atmos Sci, Vol 36, pp 1612-1615. 1979
2. Baker M B, Corbin R G & Latham J "The influence of entrainment on the evolution of cloud droplet spectra: I. A model of inhomogeneous mixing", Q J Roy Met Soc, Vol 106, pp 581-598. 1980
3. Telford J W & Wagner P B "Observations of condensation growth not determined by nuclei but by entity type mixing" (Preprint). 1981
4. Telford J W & Chai G K "A new aspect of condensation theory", PAGEOPH, Vol 118, pp 720-742. 1980
5. Warner J "The microstructure of cumulus cloud. Part IV, The effect on the droplet spectrum of mixing between cloud and environment", J Atmos Sci, Vol 30, pp 256-261. 1973
6. Mason B J & Jones P R "The evolution of droplet spectra and large droplets by condensation in cumulus clouds", Q J Roy Met Soc, Vol 100, pp 23-38. 1974
7. Lee I Y & Pruppacher H R, "A comparative study of the growth of cloud drops by condensation using an air parcel model with and without entrainment", PAGEOPH, Vol 115, pp 523-545. 1977
8. Warner J, "The microstructure of cumulus cloud. Pt 1, General features of the droplet spectrum", J Atmos Sci, Vol 26, pp 1049-1059. 1969.
9. Blyth A M, Choullarton T W, Fullerton G, Latham J, Mill C S, Smith M H & Stromberg I M, "The influence of entrainment on the evolution of cloud droplet spectra: II. Field experiments at Great Dun Fell", Q J Roy Met Soc, Vol 106, pp 821-840. 1980.
10. Pruppacher H R & Klett J D, Microphysics of Clouds and Precipitation, D Reidel (1978)

ORIGINAL PAGE IS  
OF POOR QUALITY

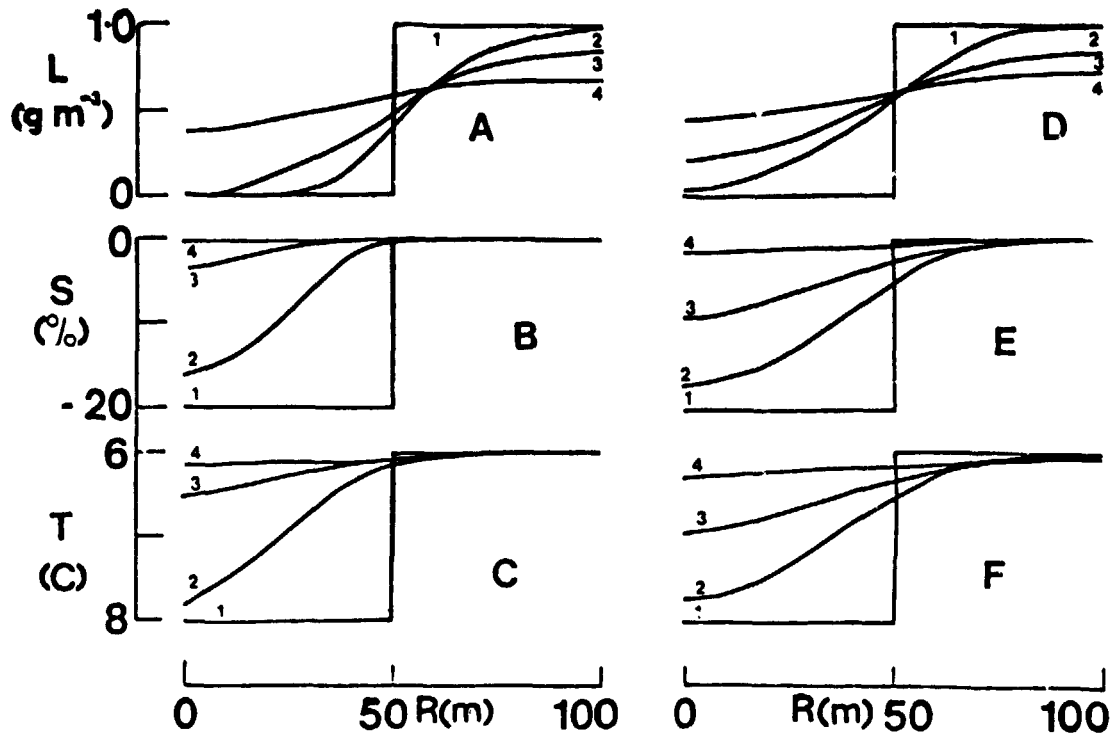


Figure 1: Calculated radial distributions of liquid-water-content,  $L$ , supersaturation  $S$  and temperature  $T$  at various times  $t$  during the turbulent mixing of a water cloud with a spherical blob of undersaturated air centrally embedded within it at  $t=0$ . Single category spectra.  $\lambda_b=100\mu\text{m}$ ;  $\lambda_c=200\mu\text{m}$ ;  $c=10^{-2}\text{m}^2\text{s}^{-3}$ ;  $m_s=10^{-16}\text{g}$ ;  $L=1.0\text{g m}^{-3}$ ;  $H=80\%$ ;  $T_b=281\text{K}$ ;  $T_c=279\text{K}$ . A, B, C:  $r=3\mu\text{m}$ ; D, E, F:  $r=20\mu\text{m}$ . 1,  $t=0$ ; 2,  $t=5\text{s}$ ; 3,  $t=10\text{s}$ ; 4  $t=20\text{s}$ .

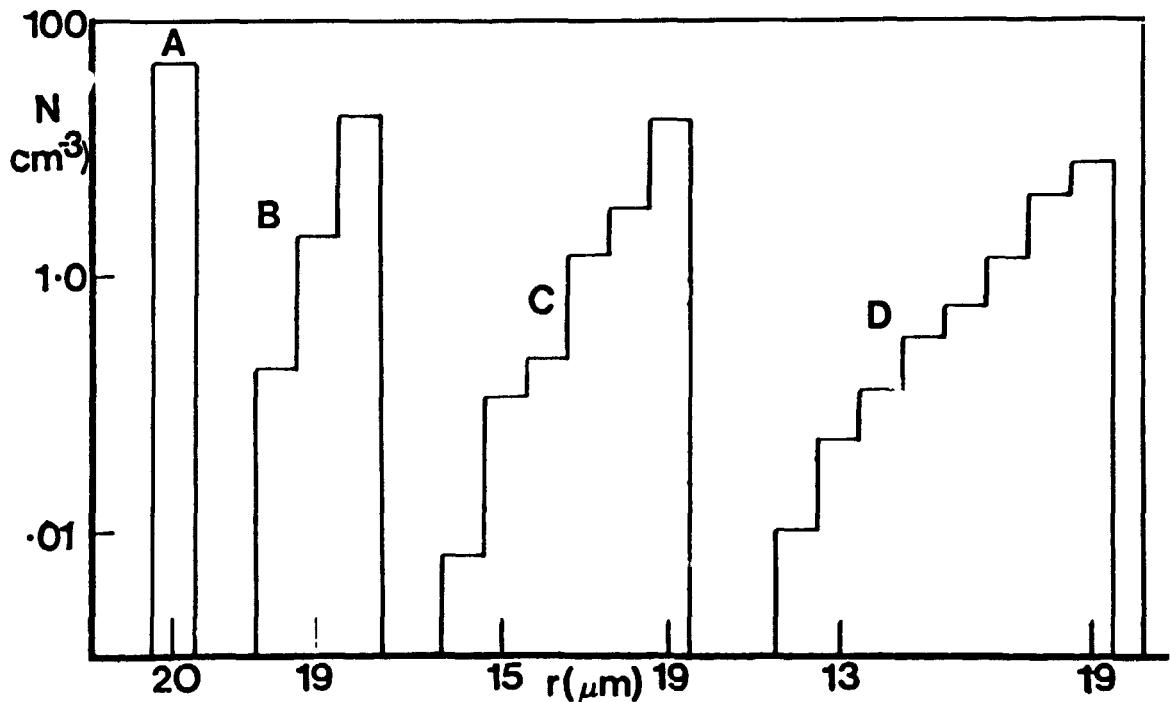


Figure 2: Calculated drop-size spectra at  $R=\lambda_B/2$  at various times  $t$  during the turbulent mixing of a water cloud with a spherical blob of undersaturated air centrally embedded within it at  $t=0$ . Single category spectrum.  $r=20\mu\text{m}$ ;  $\lambda_B=100\mu\text{m}$ ;  $\lambda_C=200\mu\text{m}$ ;  $c=10^{-2}\text{m}^2\text{s}^{-3}$ ;  $H=80\%$ ;  $T_b=281\text{K}$ ;  $T_c=279\text{K}$ . A,  $t=0$ ; B,  $t=5\text{s}$ ; C,  $t=10.2\text{s}$ ; D,  $t=12\text{s}$ .

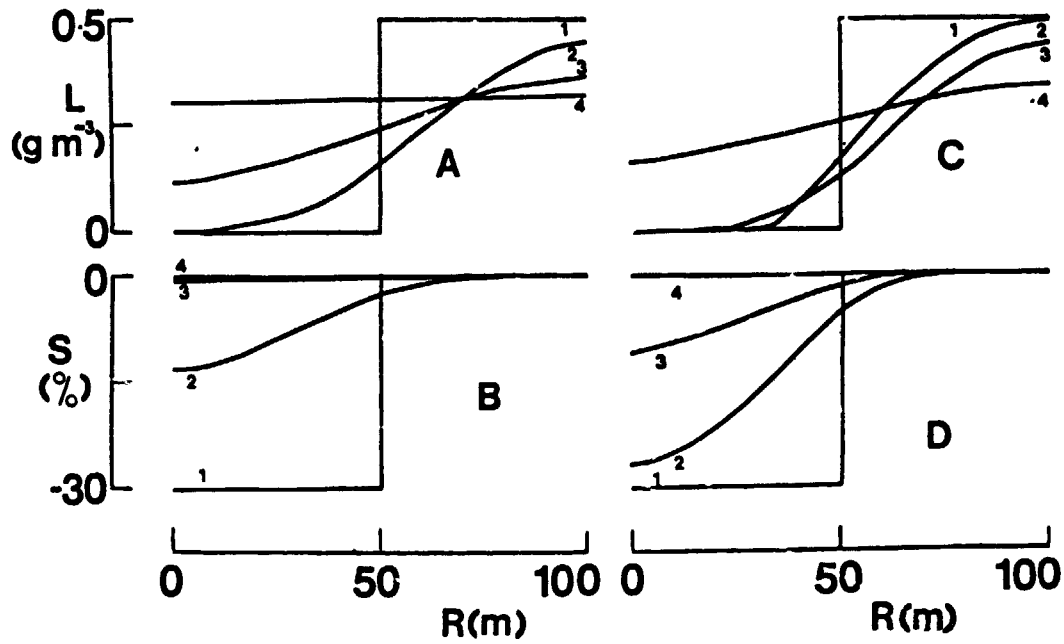


Figure 3: Calculated radial distributions of liquid-water-content,  $L$ , and supersaturation  $S$  at various times  $t$  during turbulent mixing of a water cloud with a spherical blob of undersaturated air centrally embedded within it at  $t=0$ . Ten category spectrum.  $\lambda_B = 60\text{m}$ ;  $\lambda_c = 144\text{m}$ ;  $m_s = 10^{-16}\text{g}$ ;  $L = 1.0\text{g m}^{-3}$ ;  $H = 70\%$ ;  $T_B = 281\text{k}$ ;  $T_c = 279\text{K}$ . A, B,  $\epsilon = 10^{-2}\text{m}^2\text{s}^{-3}$ ; C, D,  $\epsilon = 10^{-3}\text{m}^2\text{s}^{-3}$ . 1,  $t = 0.0\text{s}$ ; 2,  $t = 8\text{s}$ ; 3,  $t = 20\text{s}$ ; 4,  $t = 50\text{s}$ .

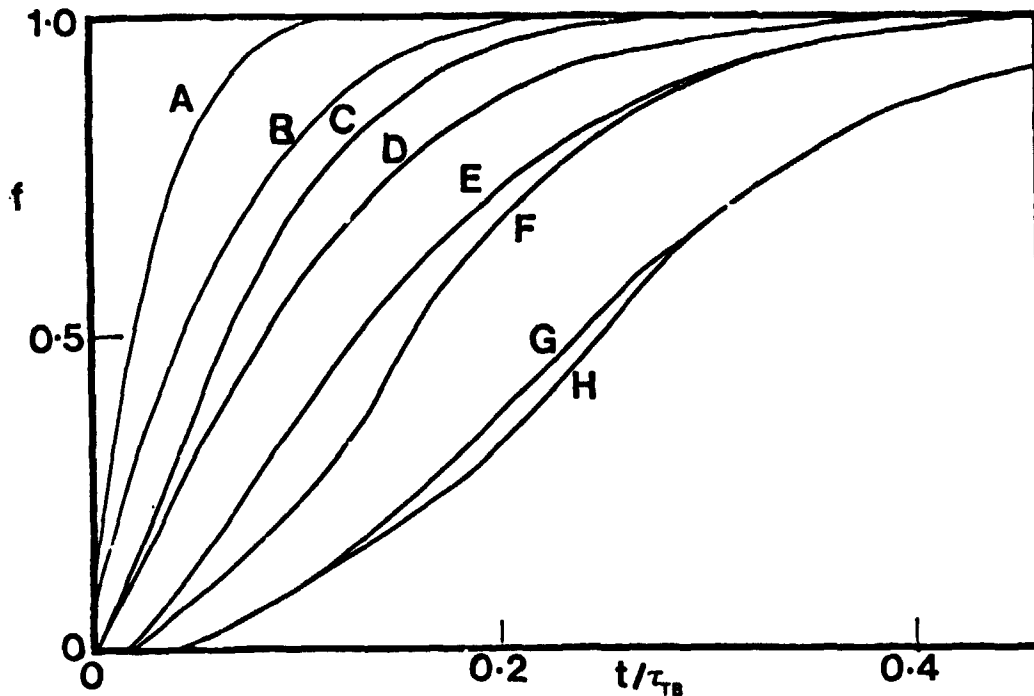


Figure 4: Calculated variation with dimensionless time  $t/\tau_B$  of the parameter  $f$  (defined in the text) which governs the rate at which the evaporative process and the redistribution of liquid water occurs, during the turbulent mixing of a water cloud with a spherical blob of undersaturated air centrally embedded within it. at  $t/\tau_B = 0$ ;  $m_s = 10^{-16} \text{m}$ ;  $T_B = 218 \text{K}$ ;  $T = 279 \text{K}$ ;  $\rho = 1.0 \text{g m}^{-3}$ .  
Curves A, D, E, F are for a single category spectrum,  $r = 3 \mu\text{m}$ ; (A,F),  $r = 20 \mu\text{m}$  (D,E).  
Curves B, C, G, H are for the 10-category spectrum (Figure 2). Curves A, B, C, D are for the evaporation; Curves E, F, G, H for liquid water (eqn 23).  
Curves A, D, E, F:  $\lambda_B = 60 \text{m}$ ;  $\lambda_C = 200 \text{m}$ ;  $\epsilon = 10^{-2} \text{m}^2 \text{s}^{-3}$ ;  $H = 70\%$ .  
Curves B, G  $\lambda_B = 60 \text{m}$ ;  $\lambda_C = 144 \text{m}$ ;  $\epsilon = 10^{-3} \text{m}^2 \text{s}^{-3}$ ;  $H = 70\%$ .

ORIGINAL PAPER  
OF POOR QUALITY

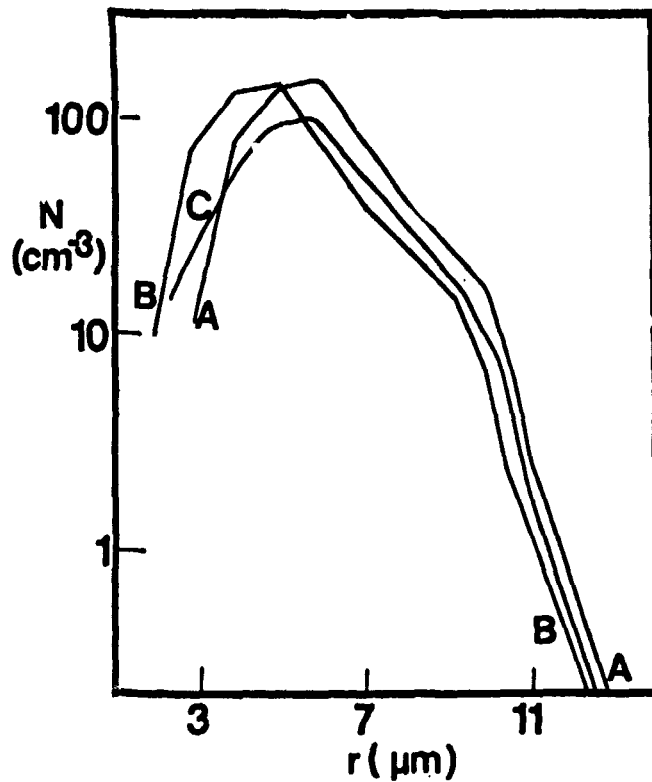


Figure 5: Droplet size distribution (C) calculated by application of the diffusive model to the mixing of a spherical blob of undersaturated air with a water cloud possessing the size distribution (A) at time  $t = 0$ . Spectrum B is calculated on the classical model of mixing. The liquid water content in A is  $0.5 \text{ g m}^{-3}$  and in B and C  $0.32 \text{ g m}^{-3}$ .  $\lambda_B = 60 \text{ m}$ ;  $\lambda_C = 144 \text{ m}$ ;  $c = 10^{-3} \text{ m}^2 \text{ s}^{-3}$ ;  $H = 70\%$ ;  $T_B = 281 \text{ K}$ ;  $T_C = 279 \text{ K}$ ;  $m_s = 10^{-18} \text{ g}$ .

ORIGINAL PAGE IS  
OF POOR QUALITY

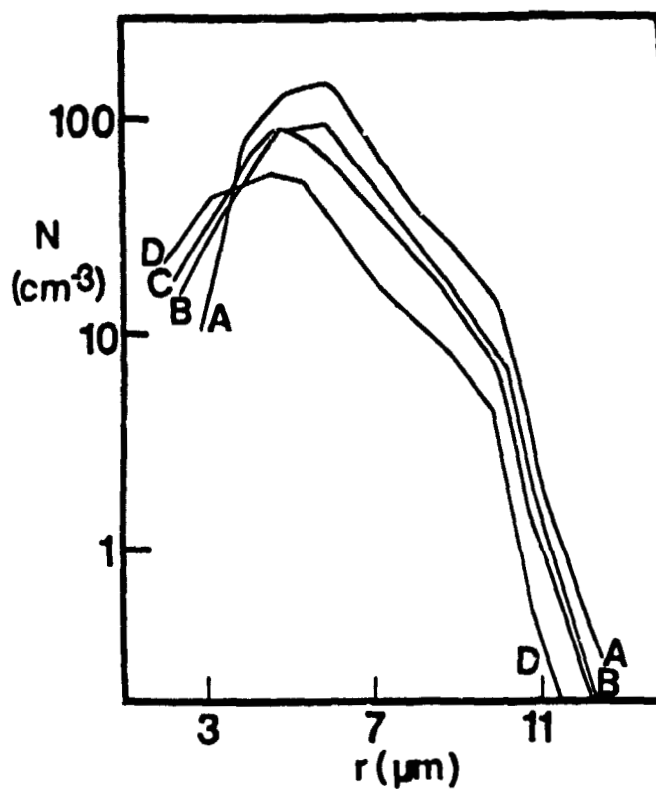


Figure 6: Droplet size distributions (B), (C) and (D) calculated by application of the diffusive model to the mixing of a spherical blob of undersaturated air with a water cloud possessing the size distribution (A) at time  $t=0$ .  $\lambda_B=60\mu$ ;  $\lambda_C=144\mu$ ;  $T_B=281K$ ;  $T_C=279K$ ;  $m_s=10^{-16}g$ ;  $L=0.5g\ m^{-3}$ ; B,  $e=10^{-3}m^2s^{-3}$ ,  $H=70\%$ ; C,  $e=10^{-2}m^2s^{-3}$ ;  $H=70\%$ ; D,  $e=10^{-3}m^2s^{-3}$ .

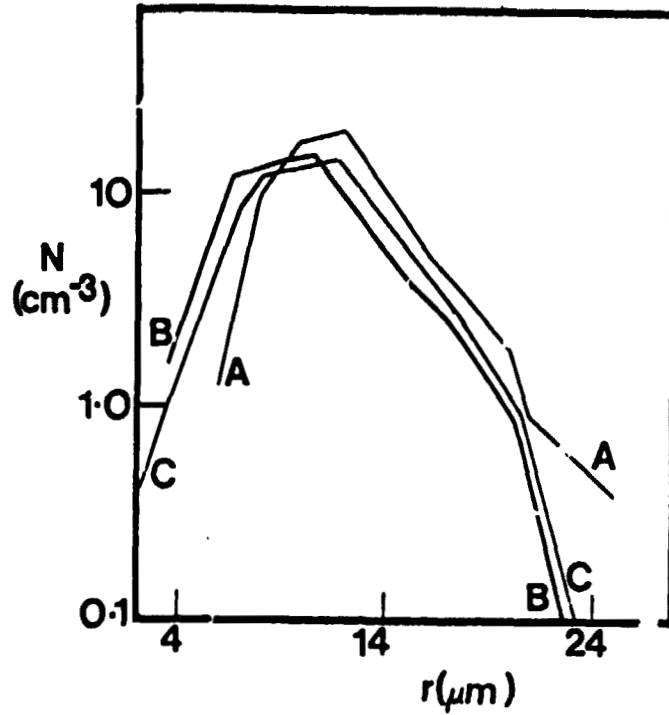


Figure 7: Droplet size distribution (C) calculated by application of the diffusive model to the mixing of a spherical blob of undersaturated air with a water cloud possessing the size distribution (A) at time  $t = 0$ . Spectrum (B) is calculated on the classical model of mixing. The liquid water content in A is  $0.5 \text{ g m}^{-3}$  and in B and C  $0.32 \text{ g m}^{-3}$ .  $\lambda_B = 60 \text{ m}$ ;  $\lambda_C = 144 \text{ m}$ ;  $c = 10^{-2} \text{ m}^2 \text{ s}^{-3}$ ;  $H = 70\%$   $T_B = 281 \text{ K}$ ;  $T_C = 279 \text{ K}$ ;  $m_w = 10^{-16} \text{ g}$ .

ORIGINAL PAGE IS  
OF POOR QUALITY

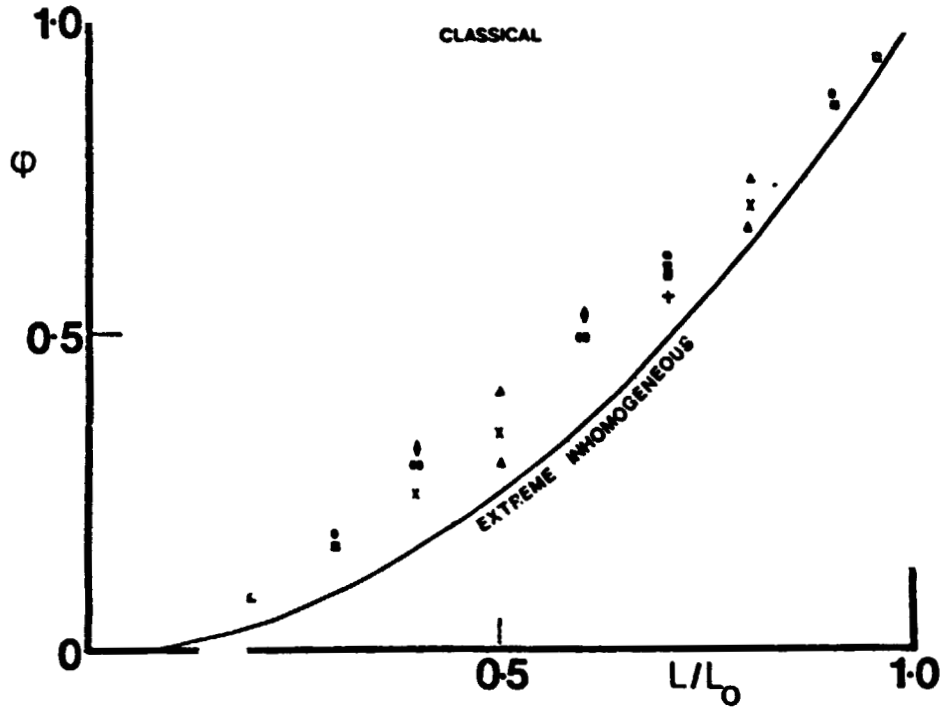


Figure 8: Values of the parameter  $\phi$ , defined by equation (24), calculated from the diffusive mixing model for various values of  $L/L_0$  and permutations of other parameters. Single category spectra. Except where indicated  $\lambda_B = 100\text{m}$ ;  $\lambda_C = 400\text{m}$ ;  $r = 10\mu\text{m}$ ;  $T_B = 281\text{k}$ ;  $T_C = 279\text{K}$ ;  $m_s = 10^{-16}\text{g}$ ;  $H = 80\%$ ;  $c = 10^{-2}\text{m}^2\text{s}^{-3}$ ;  $L = 1.0\text{g m}^{-3}$ . This permutation provides points (M).  
 (●),  $L = 0.5\text{g m}^{-3}$ ; ▲,  $\lambda_B = 20\text{m}$ ,  $\lambda_C = 80\text{m}$ ;  
 x,  $\lambda_B = 30\text{m}$ ;  $\lambda_C = 120\text{m}$ ; Δ,  $\lambda_B = 200\text{m}$ ,  $\lambda_C = 800\text{m}$ ;  
 ○,  $r = 30\mu\text{m}$ ; ●,  $r = 20\mu\text{m}$ ; +,  $c = 10^{-3}\text{m}^2\text{s}^{-3}$ ;  
 ▼,  $H = 70\%$ ; ●,  $H = 40\%$

A wind tunnel investigation of the shape of uncharged raindrops in the presence of an external, vertical electric field

H. R. Pruppacher, R. Rasmussen, C. Walcek

Department of Atmospheric Sciences, University of California, Los Angeles  
405 Hilgard Ave., Los Angeles CA 90024

P. K. Wang

Department of Meteorology, University of Wisconsin  
1110 W. Dayton St., Madison, WI 53706

Abstract

Results are presented of a recent wind tunnel experiment in which electrically uncharged water drops of 500 to 3000  $\mu\text{m}$  equivalent radius are freely suspended in the vertical air stream of the UCLA Cloud Tunnel. During this suspension the drops were exposed to external, vertical electric fields of 500 to 8,000 Volts/cm. The change in drop shape with drop size and electric field strength was noted and is discussed in the light of theoretical work cited in the literature which unfortunately does not take into account the effects of air flow past the drop. The wind tunnel study is documented here by stills from a 16 MM film record that demonstrates the shape of water drops in response to both hydrodynamic and electric forces.

Introduction

Cloud precipitation strongly affects the propagation of electromagnetic radiation. Much attention has been given to the dependence of the scattering of electromagnetic radiation of radar frequency on the size of the precipitation particle. Particle shape, however, also appears to be an important parameter. In particular, non-sphericity introduces asymmetry in the backscatter radiation field. This distortion forms the basis of new techniques for hail/rain discrimination, for the determination of raindrop size distribution, and for the determination of rainfall rates from radar observations.

To evaluate the radar data, the above mentioned techniques use the drop shapes experimentally derived from the wind tunnel measurements of Pruppacher and Beard<sup>1</sup> and from the theoretical model of Pruppacher and Pitter<sup>2</sup>. These drop shapes apply to equilibrium conditions only. It is further assumed that the drop is neither electrically charged nor embedded in an external electric field. In actuality, however, drops do not fall with a constant shape but rather undergo complex oscillations around their equilibrium shape. In addition, many clouds are electrically charged even in their early stages of development and, consequently, exhibit vertical and horizontal electric fields. Such electric fields cause the drops to be electrically polarized and therefore affect the equilibrium shape, as well as both the oscillation frequency and the oscillation amplitude of the drop. The electrically induced change in shape also affects the fall velocity of a drop. In addition, changes in the oscillatory motions may cause changes in the drop break-up behavior. All these effects, in turn, influence the drop size distribution and thus the rate of formation of precipitation inside a cloud.

In this report we concern ourselves exclusively with the effects of external, vertical electric field on drop shape. Several recent reports are available on this topic. Dawson and Warrender<sup>3</sup> studied experimentally the effect of a vertical, external electric field  $E_0$  on the terminal velocity  $V_\infty$  of electrically uncharged water drops in air which suffer a shape deformation due to the electric field. Generally,  $V_\infty$  was found to increase with the electric field strength. However, the velocity increase found was quite small. For drops of between 3 and 4 mm equivalent radius  $a_0$  (which is the radius of a sphere having the same volume as the distorted drop),  $V_\infty$  changed from 8.9 m/sec at  $E_0 = 0$  to 9.9 m sec<sup>-1</sup> at  $E_0 = 9$  kV/cm. These changes are smaller than those due to changes caused by the variation in air density and air viscosity which a drop experiences as it falls in the atmosphere<sup>4</sup>. Unfortunately, these velocity changes were not correlated to the corresponding shape changes of the drop, and only a few drop sizes were studied.

Billings and Holland<sup>5</sup> and Brazier-Smith et al.<sup>6</sup> studied experimentally and theoretically the effect of an horizontal, external electric field on the oscillation frequency of a water drop falling in air. For a given drop size  $a_0$ , the vibrational frequency was found to decrease with increasing  $E_0$  in a manner closely predictable by theory. Once again, only a few drop sizes were studied, and the turbulence in the wind tunnel used for

characterizing the vibration of the drops was not controlled. No studies of the frequency of drop oscillations were made for vertical electric fields.

Theoretical studies of the effects of an external electric field on the drop shape  $b/a$  (where  $a$  is the semi-axis perpendicular to the drop's fall axis, and  $b$  is the semi-axis along the drop's fall axis) were carried out by O'Konski and Thatcher<sup>7</sup>, Taylor<sup>8</sup>, Brazier-Smith<sup>9,10</sup>, Abbas and Latham<sup>11</sup>, and Richards and Dawson<sup>12</sup>. These studies showed that a water drop originally spherical becomes strongly prolate-spheroidally deformed in an external, vertical electric field. The deformations predicted by these theories appear to agree quite well with each other, in particular regarding the maximum stable drop deformation before break-up. The critical axis ratios predicted for break-up vary between  $b/a = 1.86$  (Taylor<sup>8</sup>) and  $b/a = 1.83$  (Brazier-Smith<sup>10</sup>). These estimates also agree with the value theoretically predicted by Abbas and Latham<sup>11</sup>. The various theories also indicate that the deformation parameter  $b/a$  can uniquely be expressed as an increasing function of the non-dimensional quantity  $X = E_0(a_0/\sigma)^{1/2}$ , where  $\sigma$  is the surface tension of water in air (Fig. 1).

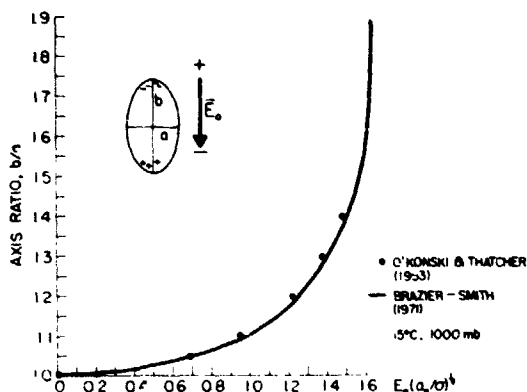


Figure 1. Variation of the theoretically predicted shape of a water drop in air with  $X = E_0(a_0/\sigma)^{1/2}$ , assuming that the drop's original shape is spherical, and that no hydrodynamic flow is present around the drop.

increasing drop size  $a_0$ . This behavior was verified by Wilson and Taylor<sup>15</sup>, Nolan<sup>16</sup>, Macky<sup>17</sup>, Ausman and Brook<sup>12</sup>, Dawson and Richards<sup>18</sup>, and by Griffiths and Latham<sup>14</sup>. In none of these studies, however, was a quantitative investigation made on the variation of  $b/a$  with  $E_0$  for various  $a_0$ . Instead, emphasis was placed on determining the critical electric field strength beyond which the drop would break up or show evidence of corona discharge. It was found that  $X = E_0(a_0/\sigma)^{1/2}$  had a value of 1.61 (Wilson and Taylor<sup>15</sup>), 1.51 (Macky<sup>17</sup>), 1.56 (Ausman and Brook<sup>12</sup>), and 1.81 (Griffiths and Latham<sup>14</sup>), for break-up or corona discharge. All experiments suffered from two serious deficiencies since, under the experimental conditions reported, (1) the drops did not reach terminal velocity and thus did not assume the hydrodynamically determined shape, and (2) the drops were forced to abruptly enter an electric field region created between two electrode plates causing non-equilibrium conditions between the drop and the environment.

A review and new wind tunnel results on the shape of water drops falling at terminal velocity in air in the absence of an external electric field have been given by Pruppacher and Beard<sup>1</sup> and Pruppacher and Pitter<sup>2</sup>. Their studies show that drops smaller than about 500  $\mu\text{m}$  radius can be considered as spheres. On the other hand, drops larger than 500  $\mu\text{m}$  are oblate-spheroidally deformed with an increasingly flattened lower side as the drop becomes larger. This causes the axis ratio  $b/a$  to be less than unity, with  $b/a$  decreasing as  $a_0$  increases. This behavior was found to be the result of an interaction between hydrodynamic forces, surface tension forces and hydrostatic forces. Thus, the actual drop shape in the absence of an external electric field is quite different from the spherical shape assumed by all previous theories on the effect of a vertical, external electric field on the drop shape.

Break-up of electrically uncharged drops was predicted for  $X = 1.625$  (Taylor<sup>8</sup>) and for  $X = 1.603$  (Brazier-Smith<sup>10</sup>), in agreement with the critical value of  $X$  computed by Abbas and Latham<sup>11</sup>. This correlation suggests that, for a given drop size and air pressure, the electric field required for a certain drop deformation, for drop break-up, and for the onset of corona discharge increases as the temperature decreases, i.e., as the surface tension increases. This trend has been experimentally verified by Ausman and Brook<sup>12</sup>. A different trend has been found with regard to air pressure. Griffiths and Latham<sup>14</sup> showed that the electric field strength required for onset of corona discharge on drops decreased with decreasing air pressure.

Electric charge appears to have a considerable effect on the electric field strength required for drop deformation. Abbas and Latham<sup>11</sup> showed that the correlation of  $b/a$  with  $X = E_0(a_0/\sigma)^{1/2}$  varies with the electric charge  $Q$  on a drop, shifting to smaller values as  $Q$  increases.

For electrically uncharged drops the correlation  $b/a$  vs.  $X = E_0(a_0/\sigma)^{1/2}$  suggests that the electric field strength  $E_0$  to achieve a certain drop deformation  $b/a$  decreases with

ORIGINAL PAGE  
BLACK AND WHITE PHOTOGRAPH

Present experimental set-up

A series of experiments in the UCLA Cloud Tunnel were undertaken to improve on previous experimental studies and to extend our present knowledge of the effect of an external electric field on the shape of water drops in air. The UCLA facility is a vertical wind tunnel which allows the free suspension of drops of equivalent radius  $a_0$  between 20  $\mu\text{m}$  and 3 mm in a vertical, low-turbulence air stream for long periods of time. In the present study, drops of equivalent radius between 500  $\mu\text{m}$  and 3000  $\mu\text{m}$  were suspended in the air stream between two metal screens acting as electrodes to create a vertical electric field. The screens, 6 cm x 6 cm, were separated by a distance of about 5 cm. The upper screen was charged to a positive electric potential; the lower to a negative electric potential. Electric fields between 500 Volts  $\text{cm}^{-1}$  and 8,000 Volts  $\text{cm}^{-1}$  were created. Computations based on the theoretical considerations of Smythe<sup>19</sup> indicate that, for the given electrode arrangement in our experimental set-up, the electric field is uniform and computable from  $E_0 = \Delta V/d$ , where  $d$  is the distance between the two electrodes and  $\Delta V$  is the potential difference between the two electrodes, with an error of less than 1% if the drop is kept inside an area around the wind tunnel axis of 10 mm x 10 mm. In most cases the drop was confined to this area. The drops studied were made from doubly distilled water and their size and shape documented photographically (Fig. 2). In each experiment, it was insured that

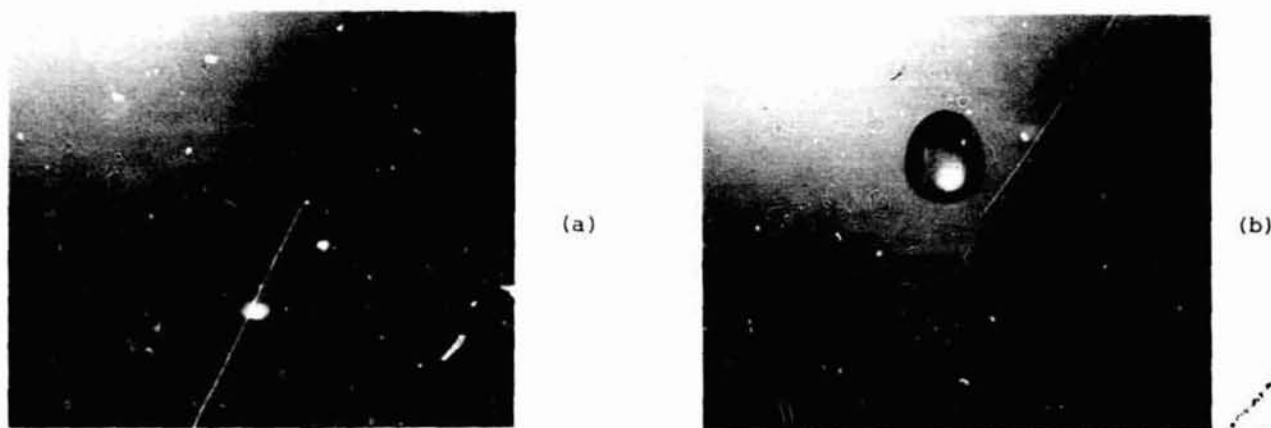


Figure 2. Water drops freely suspended in the vertical air stream of the wind tunnel;  $a_0 = 2.3$  mm. (a) No external electric field. (b) Vertical, external electric field;  $E_0 = 7.75$   $\text{kV cm}^{-1}$ .

the drops were electrically uncharged. For zero electric field, comparison was made with our previous studies on drop shape<sup>1,2</sup>. All experiments were carried out in an atmosphere of about 1000 mb air pressure and 15°C air temperature.

Results and discussion

The experimental results are summarized in Figs. 2 to 4. Figure 2 gives the variation of the drop shape  $b/a$  with equivalent drop radius  $a_0$  for various electric field strengths  $E_0$ . Comparison of the values for  $b/a$  for  $E_0 = 0$  with values previously obtained<sup>1,2</sup> shows satisfactory repeatability of our earlier results. We note further from this figure that the deformation caused by the electric polarization forces due to the electric field is strongly opposed by the hydrodynamic forces. The latter act to influence the drop to become oblate-spheroidally deformed, while the former attempt to deform the drop into a more spherical shape. Also notice that the larger the drop, the stronger the effect of the electric field. Extrapolation of our results to smaller drops suggests that electric field strengths smaller than 6  $\text{kV cm}^{-1}$  have a negligible effect on the drop shape if  $a_0 \leq 1$  mm. With increasing drop size, and with increasing field strength of the external electric field, the hydrodynamically caused deformation is counteracted with increasing efficiency. Thus, an external electric field of 3.2  $\text{kV cm}^{-1}$  begins to significantly affect the drop shape if  $a_0 > 0.15$  cm.

In Fig. 4 the variation of the drop shape  $b/a$  is plotted as a function of the electric field strength for different drop sizes. We note that, for drops of  $a_0 \geq 2$  mm, electric fields of  $E_0 \geq 1$   $\text{kV cm}^{-1}$  affect the drop shape  $b/a$ . This electric shape deformation increases with drop size. Since hydrodynamic forces also affect the drop more strongly the larger its size, a "cross-over" of the individual shape curve results. Thus, although large drops are most strongly oblate-spheroidally deformed for  $E_0 = 0$ , the deformation is efficiently counteracted with increasing field strength, resulting in a spherical and

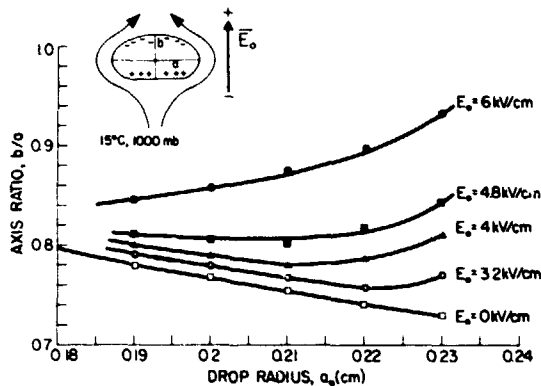


Figure 3. Present experimental results for the variation of the shape of a water drop falling at terminal velocity in air with equivalent drop radius  $a_0$  for various external electric field strengths.

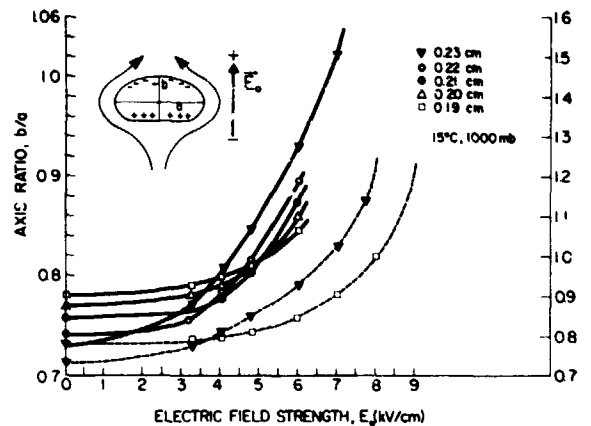


Figure 4. Present experimental results for the variation of the shape of a water drop falling at terminal velocity in air with electric field strength for various drop sizes. Solid line applies to left coordinate; dashed lines to right coordinate.

eventually a prolate-spheroidal drop shape. We further note that, at much lower values of  $E_0$  than those required for smaller drops which are originally less oblate-spheroidally deformed, a drop of  $a_0 = 0.23$  cm appears to require a limiting value of  $E_{0,crit} = 8$   $\text{kV cm}^{-1}$  for break-up; while a drop of  $a_0 = 0.19$  cm requires  $E_{0,crit} \approx 9$   $\text{kV cm}^{-1}$ . These latter findings are in good agreement with the observations of Ausman and Brook<sup>13</sup> and of Dawson and Richards<sup>16</sup>.

Figure 5 gives the variation of drop deformation with the quantity  $X = E_0(a_0/\sigma)^{1/2}$  for two drop sizes. We note from this figure that  $b/a$  is not a unique function of  $X$  for all  $a_0$ , as had been found on the basis of electrostatic theory cited in the literature which disregarded the flow around a drop. Instead,  $b/a$  vs.  $X$  is a function of  $a_0$  due to the significantly stronger oblate-spheroidal deformation of larger drops. However, we note that the dependence on  $a_0$  diminishes rapidly as  $X$  approaches the critical value for drop break-up. In fact, our experimental data suggest that for all drops break-up appears to occur as  $X$  approaches a value of about 1.6, as had been predicted by theory which does not take into account the flow around the drop.

Break-up of single large drops in the absence of an electric field proceeds via hydrodynamic forces acting on the drop's lower side (i.e., on the drop's upstream side). Our observations show that, in contrast, drop break-up in the presence of an external electric field proceeds via instabilities on the drop's upper side (i.e., on the drop's downstream side).

Our observations suggest that for low external, vertical electric fields the hydrodynamic forces dominate initially; and that the effect of the electric forces is small and confined to the downstream side of the falling drop where the flow field is weak. However, as the electric field grows in intensity, the percentage contribution of the electric field to the drop deformation increases rapidly. Thus, for a drop of  $a_0 = 0.23$  cm and for an electric field of  $E_0 = 4$   $\text{kV cm}^{-1}$  (7.75  $\text{kV cm}^{-1}$ ),  $b/a = 1.07$  (1.45), if the drop is stagnant and there is assumed to be no flow past it (see Fig. 1). For the case of drop deformation due only to hydrodynamic flow ( $E_0 = 0$ ), we find  $b/a = 0.73$ , in accordance with our previous results. For the case of both electric field and flow affecting the drop shape  $b/a = 0.81$  (1.14) for  $E_0 = 4$   $\text{kV cm}^{-1}$  (7.75  $\text{kV cm}^{-1}$ ) (see Fig. 4). These

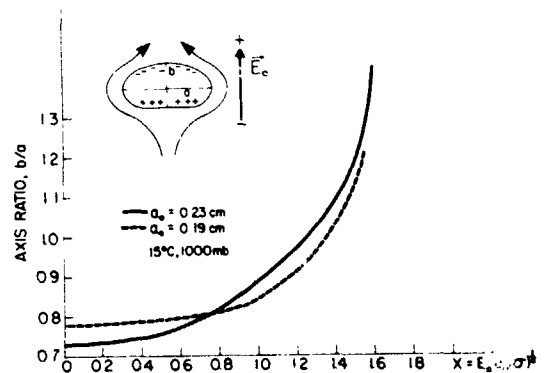


Figure 5. Present experimental results for the variation of the shape of a water drop falling at terminal velocity in air with  $X = E_0(a_0/\sigma)^{1/2}$ , for different drop sizes.

numbers suggest that the percentage deviation of the shape ( $b/a$ ) flow only from the shape ( $b/a$ ) flow + field increases from 10% to 36% as the field grows from  $4 \text{ kV cm}^{-1}$  to  $7.75 \text{ kV cm}^{-1}$ , thus indicating the rapidly reduced effect of the flow on the final drop shape as the electric field grows. Eventually, as the field approaches breakdown value, the hydrodynamic forces completely lose their effect on the drop's downstream side. The critical value, then, of  $X = E_0(a_0/\sigma)^{1/2}$  for drop disintegration is the same as for no flow conditions, i.e., approximately 1.6.

No quantitative studies have yet been undertaken by us to verify results published in the literature on the effect of an external electric field on the oscillation frequency and amplitude of large drops. Qualitatively, we found that the amplitude of oscillation was reduced with increasing strength of an externally applied vertical electric field. Our studies on drop variations also indicate that, during a vibration cycle, the concave impression on the upstream (i.e., the bottom) side of the drop - induced by hydrodynamic forces (see Pruppacher and Pitter<sup>2</sup>) - remains a present feature on the drop's lower side, even when the drop is exposed to an external electric field.

Also, no quantitative studies have yet been undertaken by us to verify the results published in the literature on the effect of temperature, pressure, and the presence of electric charges on the drop deformation in an external electric field. Such studies are planned for future experiments.

#### References

1. Pruppacher, H. R., and K. V. Beard, 1970: A wind tunnel investigation of the internal circulation and shape of water drops falling at terminal velocity in air. Quart. J. Roy. Meteor. Soc., 96, 247-256.
2. Pruppacher, H. R., and R. L. Pitter, 1971: A semi-empirical determination of the shape of cloud and rain drops. J. Atmos. Sci., 28, 86-94.
3. Dawson, G. A., and R. A. Warrender, 1973: The terminal velocity of raindrops under vertical electrical stress. J. Geophys. Res., 78, 3619-3620.
4. Beard, K. V., 1976: Terminal velocity and shape of cloud and precipitation drops aloft. J. Atmos. Sci., 33, 851-864.
5. Billings, J. J., and D. F. Holland, 1969: Vibrating water drops in electric fields. J. Geophys. Res., 74, 6881-6886.
6. Brazier-Smith, P. R., M. Brook, J. Latham, C. P. R. Saunders, and M. H. Smith, 1971: The vibration of electrified water drops. Proc. Roy. Soc., London, A 322, 523-534.
7. O'Konski, C. T., and H. C. Thatcher, 1953: The distortions of aerosol droplets by an electric field. J. Phys. Chem., 57, 955-958.
8. Taylor, G., 1964: Disintegration of water drops in an electric field. Proc. Roy. Soc., London, A 280, 383-397.
9. Brazier-Smith, P. R., 1971a: The stability of a water drop oscillating with finite amplitude in an electric field. J. Fluid Mech., 50, 417-430.
10. Brazier-Smith, P. R., 1971b: Stability and shape of isolated and pairs of water drops in an electric field. Phys. of Fluids, 14, 1-6.
11. Abbas, M. A., and J. Latham, 1969: The disintegration and electrification of charged water drops falling in an electric field. Quart. J. Roy. Meteor. Soc., 95, 63-76.
12. Richards, C. N., and G. A. Dawson, 1973: Stresses on a raindrop falling at terminal velocity in a vertical electric field. Phys. Fluids, 16, 796-800.
13. Ausman, E. L., and M. Brook, 1967: The distortion and disintegration of water drops in strong electric fields. J. Geophys. Res., 72, 6131-6135.
14. Griffiths, R. F., and J. Latham, 1972: The emission of corona from falling drops. J. Meteor. Soc., Japan, 50, 416-422.
15. Wilson, C. T. R., and G. I. Taylor, 1925: The bursting of soap bubbles in a uniform electric field. Proc. Camb. Phil. Soc., 22, 728-730.
16. Nolan, J. J., 1926: The breaking of water drops by electric fields. Proc. Roy. Irish Academy, 37, 28-39.
17. Macky, W. A., 1931: Some investigations on the deformation and breaking of water drops in strong electric fields. Proc. Roy. Soc., London, A 133, 565-587.
18. Dawson, G. A., and C. N. Richards, 1970: Discussion of the paper by Latham and Myers. J. Geophys. Res., 75, 4589-4588.
19. Smythe, W. P., 1950: Static and Dynamic Electricity, 2nd Ed. 616 pp., McGraw-Hill, New York.

032  
N82 23450

REPORT OF  
OF FOUR

## Raindrop oscillations

K. V. Beard

Department of Atmospheric Sciences, University of Illinois  
1101 W. Springfield, Urbana, Illinois 61801  
and  
Meteorology Section, Illinois State Water Survey  
P. O. Box 5050, Station A, Champaign, Illinois 61820

### Abstract

Raindrops measured by two orthogonal cameras were classified by shape and orientation to determine the nature of the oscillation. A physical model based on potential energy was then developed to study the amplitude variation of oscillating drops. The model results show that oscillations occur about the equilibrium axis ratio, but the time average axis ratio is significantly more spherical for large amplitudes because of asymmetry in the surface potential energy. A generalization of the model to oscillations produced by turbulence yields average axis ratios that are consistent with the camera measurements. The model results for average axis ratios have been applied to rainfall studies with a dual-polarized (vertical/horizontal) radar.

### Introduction

The equilibrium shape of a falling drop is the result of a balance between surface tension, aerodynamic forces, and hydrostatic and internal pressures. Drops which have been observed in laminar flow wind tunnels<sup>1</sup> and in still air<sup>2</sup> assume shapes that are consistent with the equilibrium calculations of Pruppacher and Pitter<sup>3</sup>. Under turbulent conditions, however, drops are not quiescent since they undergo continuous oscillations<sup>4,5</sup>. In fact, photographs of raindrops in the atmosphere indicate that the average shape departs significantly from equilibrium<sup>6</sup>. Although these departures have usually been neglected, they take on a renewed importance with recent advances in radar meteorology that exploit the shape and orientation of scatterers to obtain a quantitative or qualitative description of precipitation<sup>7</sup>.

The following study consisted of two major efforts. The first was to determine raindrop shape from the photographic record, and the second was to construct a physical model of the changing shape to compute the time average axis ratio for the analysis of dual-polarization radar data. The application of the model is discussed in another paper<sup>8</sup>.

### Data analysis

In the late 1950's Jones studied the shape of natural falling raindrops using two cameras with optical axes 90° apart<sup>6</sup>. From photographs he was able to determine the axial ratio and volume of 1783 drops. Jones' data has been replotted in Figure 1 to show the average axial ratio (vertical/horizontal) with the 95% confidence interval as a function of equivalent volume diameter. The solid line in Figure 1 represents the equilibrium drop shape calculated by Pruppacher and Pitter<sup>3</sup>. As the 95% confidence intervals shows, the mean axial ratio for raindrops is significantly more spherical than equilibrium. Raindrops larger than 4 mm were also found to be more spherical than equilibrium, but were not photographed in adequate numbers to yield a good estimate of the mean. Although the total sample of 1783 raindrops is relatively modest, a preliminary inspection of measurements using a single camera<sup>9</sup> with several hundred thousand raindrops between 2 and 6 mm diameter shows similar results.

Data from Jones was re-analyzed to determine the nature of raindrop distortions. A simple ellipsoidal shape was assumed which is consistent with an oscillation of the fundamental mode. Rotation was not considered as a cause of drop distortion since the energy required is much larger than for oscillations<sup>10</sup>. Each data point was analyzed for characteristic shape by comparing the measured vertical and horizontal dimensions. Smaller drops were found to be predominately spheres and larger drops predominantly ellipsoids. It was apparent from the shape analysis that raindrops do not oscillate just in the vertical axisymmetric mode because of the significant percentage of horizontal ellipsoids.

The type of oscillation was examined by combining shapes suggestive of the vertical axisymmetric oscillations and those shapes suggestive of horizontal oscillations. The result was consistent with the wind tunnel observations of Nelson and Gokale<sup>11</sup> that small drops ( $D \leq 3$  mm) prefer the axisymmetric oscillation ( $m = 0$  degeneracy of the fundamental mode) and of Blanchard<sup>5</sup> that large drops ( $D \geq 5$  mm) prefer the horizontal oscillation ( $m = 2$ ).

The latter is apparently enhanced by aerodynamics since the external pressure should provide a positive feedback to the horizontal deformation. Support for an aerodynamic effect is found in the observation of stable horizontal "prolates" for very large drops<sup>5</sup>.

The drop was assumed to have only surface, gravitational and kinetic energies. The minimum in the surface plus gravitational energy was calculated numerically. Agreement with wind tunnel data and the numerical result of Pruppacher and Pitter for the equilibrium axis ratio was within 1% for diameters less than 5 mm (Figure 1) demonstrating that the aerodynamic and hydrodynamic pressures are much less important than the hydrostatic pressure in determining the axis ratio.

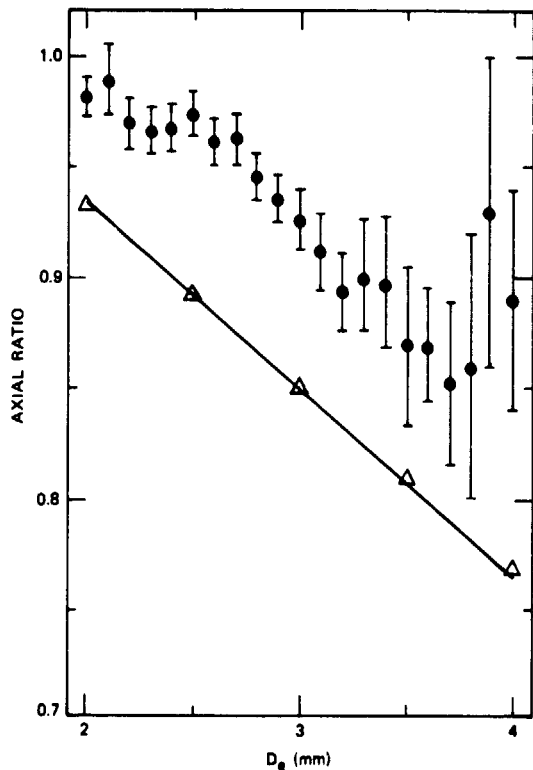


Figure 1. Drop axial ratio as a function of equivalent spherical volume diameter. Circles are for raindrops (Jones), and the curve for equilibrium shaped water drops (Pruppacher and Pitter). Confidence intervals for the mean have been added to the original raindrop data at the 95% significance level based upon the estimated standard deviation and sample size. Triangles are present model for equilibrium shape.

with gravity ( $g = 980 \text{ cm sec}^{-2}$ ,  $\rho_w = 0.998 \text{ g cm}^{-3}$  and  $\sigma = 73 \text{ dynes cm}^{-1}$ ) for both  $\nu = 0.01 \text{ cm}^2 \text{ sec}^{-1}$  and  $\nu = 0$ , yielded values of  $\overline{AR}$  only slightly less than the mean of the undamped turning points.

Asymmetric oscillations of the fundamental mode ( $m = 2$  degeneracy) is currently under investigation. A set of equations similar to those given above is used to solve the temporal behavior of the axis ratio.

Analytical and numerical solutions are more difficult to obtain than the axisymmetric case since oscillations occur in the shape of a general ellipsoid. Preliminary analysis indicates that the time average axis ratio for the asymmetric oscillation of a raindrop can be approximated by the mean of the turning points defined by the potential energy well.

The surface plus gravitational energy function was used as a potential energy "well" for anharmonic oscillations of an ellipsoidal drop. The equation of axisymmetric motion for the fundamental mode was obtained from the energy relation

$$PE_0 - PE = KE = m(V_a^2 + V_b^2 + V_c^2)/5 \quad (1)$$

by solving for the temporal change in axis ratio

$$\dot{AR} = 6AR^{4/3} V_a/D \quad (2)$$

where

$$V_a = (5KE/m)^{1/2} (1 + 2AR^2)^{-1/2} \quad (3)$$

and

$$AR = c/a = c/b \quad (4)$$

with a constant volume constraint

$$D = 8abc. \quad (5)$$

An analytical solution for small amplitude yielded the Rayleigh oscillation time ( $\tau_R$ ) using the factor of 1/5 in the kinetic energy relation. Linear dissipation was added to the calculation by assuming  $\dot{KE} = B KE$  where B was determined from the result of Lamb<sup>12</sup> for a complete cycle.

Numerical integrations were made for  $D = 0.12 \text{ cm}$  to compare with the Navier-Stokes simulation of Foote<sup>13</sup> for the axisymmetric oscillation without gravity with  $\rho_w = 1 \text{ g cm}^{-3}$  and  $\sigma = 73 \text{ dynes cm}^{-1}$ . The present model for the large amplitude oscillation of Foote (where  $AR_0 = 1/1.7$ ) gives the same oscillation times (i.e.,  $1.04 \tau_R$  for  $\nu = 0.06 \text{ cm}^2 \text{ sec}^{-1}$  and  $1.06 \tau_R$  for  $\nu = 0$ ), and shows similar temporal variations in the surface and kinetic energies, and in axis ratio with 57% of the time spent as a prolate spheroid. The axis ratio averaged over one cycle for the above two cases, and also for  $D = 0.3$  and  $0.6 \text{ cm}$

ORIGINAL PAGE IS  
OF POOR QUALITY

Three candidates for the cause of raindrop oscillations were examined: drop interactions, turbulence in the air and pumping by wake shedding. A drop interaction model was used to obtain the oscillation energy from a balance between the average collisional energy and viscous dissipation. The time average axis ratio was found to be considerably larger than equilibrium for drops with  $D \geq 3$  mm in heavy rainfall. In contrast, preliminary results for wake forcing indicate that appreciable oscillations occur only for  $D \leq 2$  mm.

For turbulent forcing the oscillation energy was related to turbulence in the inertial subrange using the distance traveled by a raindrop during an oscillation. This gave a unique scaling for the oscillation energy with raindrop size and dissipation rate. Mean axis ratios for the average oscillation energy were calculated from a balance between input of turbulent energy and dissipation by viscosity. The results provided a reasonable fit to the mean axis ratios of the camera data and a suitable envelope for the observed amplitudes. It was concluded that atmospheric turbulence and also drop interactions can produce significant increases in average axis ratio of raindrops resulting in an appreciable change in radar backscatter cross sections.

Acknowledgments

I thank Art Jameson and Dave Johnson for their helpful suggestions during the course of this investigation. This work was partially supported by the National Science Foundation under grant NSF ATM79-18365.

References

1. Pruppacher, H. R., and K. V. Beard, "A Wind Tunnel Investigation of the Internal Circulation and Shape of Water Drops Falling at Terminal Velocity in Air," Quart. J. Roy. Meteor. Soc., Vol. 96, pp. 247-256. 1970.
2. Magono, C., "On the Shape of Water Drops Falling in Stagnant Air," J. Meteor., Vol. 11, pp. 77-79. 1954.
3. Pruppacher, H. R., and R. L. Pitter, "A Semi-Empirical Determination of the Shape of Cloud and Raindrops," J. Atmos. Sci., Vol. 28, pp. 86-94. 1971.
4. Gunn, R., "Mechanical Resonance in Freely Falling Rain Drops," J. Geophys. Res., Vol. 54, pp. 383-385. 1949.
5. Blanchard, D. C., "The Behavior of Water Drops at Terminal Velocity in Air," Trans. Amer. Geophys. Union, Vol. 31, pp. 836-842. 1950.
6. Jones, D. M. A., "The Shape of Raindrops," J. Meteor., Vol. 16, pp. 504-510. 1959.
7. Seliga, T. A., and V. N. Bringi, "Potential Use of Radar Differential Reflectivity Measurements of Orthogonal Polarizations for Measuring Precipitation," J. Appl. Meteor., Vol. 15, pp. 69-76. 1975.
8. Jameson, A. R., K. V. Beard, and J. Bresch, "Complications in Deducing Rain Parameters from Polarization Measurements," Proc. of the 20th Conf. on Radar Meteor., (In press). 1981.
9. Mueller, E. A., and A. L. Sims, Investigation of the Quantitative Determination of Point and Areal Precipitation by Radar Echo Measurements. Tech. Report ECOM-00032-F, 88 pp. (NTIS AD645-218). 1966.
10. Brown, R., The Shape and Stability of Three-Dimensional Interfaces. Ph.D. Dissertation, University of Minnesota. 1979.
11. Nelson, A. R., and N. R. Gokhale, "Oscillation Frequencies of Freely Suspended Water Drops," J. Geophys. Res., Vol. 77, pp. 2724-2727. 1972.
12. Lamb, H., Hydrodynamics. Dover Publications, New York, 738 pp. 1932.
13. Foote, G. B., "A Numerical Method for Studying Liquid Drop Behavior: Simple Oscillation," J. Comput. Phys., Vol. 11, pp. 507-530. 1973.

## Drop rebound in clouds and precipitation

Harry T. Ochs, III and K. V. Beard

Meteorology Section, Illinois State Water Survey  
P. O. Box 5050, Station A, Champaign, Illinois 61820Abstract

The collection efficiency has been measured for 17 size pairs of relatively uncharged drops in over 500 experimental runs using two techniques. The results indicate that collection efficiencies fall in a narrow range of 0.60 to 0.70 even though the collector drop was varied between 63 and 326  $\mu\text{m}$  and the size ratio from 0.05 to 0.33. In addition the measured values of collection efficiencies ( $E$ ) were below the computed values of collision efficiencies ( $E$ ) for rigid spheres. Therefore it has been concluded that rebound was occurring for these sizes since inferred coalescence ( $\epsilon = F/E$ ) efficiencies are about 0.6 to 0.8. At a very small size ratio ( $r/R = p = 0.05$ ,  $R = 326 \mu\text{m}$ ) the coalescence efficiency inferred from our experiment is in good agreement with the experimental findings for a supported collector drop. At somewhat larger size ratios ( $0.11 \leq p \leq 0.33$ ) our inferred values of  $\epsilon$  are well above results of supported drop experiments, but show a slight correspondence in collected drop size dependency to two models of drop rebound. At a large size ratio ( $p = 0.73$ ,  $R = 275$ ) our inferred coalescence efficiency is significantly different than all previous results.

Experimental study on cloud drops

An experiment has been developed<sup>1</sup> to investigate the possibility of rebound for colliding cloud drops as postulated by Levin et al.<sup>2</sup> The collection efficiency is being determined from the amount of tracer captured by a stream of widely separated drops falling at terminal velocity through a monodisperse cloud of chemically tagged droplets.

Design and procedure

The current experimental setup is shown in figure 1. The cloud is produced by a vibrating orifice device (TSI Model 3050). With careful adjustment of the transducer frequency, the liquid jet is disrupted into a stream of uniform size drops which is free of smaller satellites and also larger multiplerts. Recombination of the drops is greatly reduced by dispersion in an axial jet of turbulent air and by subsequent dilution. Both air streams are saturated slightly above room temperature to prevent evaporation. The tracer solution of lithium sulfate (0.1%  $\text{Li}^+$ ) is fed to the cloud droplet generator from the solution reservoir under pressure. The amount of tracer is apparently much less than has been used in previous collection studies<sup>3,4</sup> and has a negligible effect in the physical properties of the cloud water (e.g., surface tension). The reference pressure is adjustable and remains essentially constant by virtue of a large, nitrogen reservoir. An electrically neutral cloud is achieved with an ion discharge device (TSI 3054). The cloud is continuously generated during the experiment and flows at 11 lpm through a cloud chamber 1.3 m long and 10.6 cm in diameter.

Sampling ports are located in the chamber to permit the insertion of slides coated with a dye and gelatin mixture for an evaluation of the droplet sizes. The stain produced by the droplets was calibrated by using the direct output of the droplet generator, and was found to be consistent with the results of a similar method used by Liddell and Wooten<sup>5</sup>. For a typical experiment the droplets in the cloud chamber were found to be composed of over 98% singlets. A typical standard deviation for the singlet distribution was 1.5%. The droplet concentration was measured from photographs taken with a strobe and 35 mm camera. The illumination was arranged in a vertical plane of well defined thickness by two cylindrical lenses and two slits. Typical concentrations vary between 1 and 75  $\text{cm}^{-3}$  depending on the size of droplet being used with the smaller droplets yielding a higher concentration.

An orifice device was also used to produce the collector drops<sup>6</sup>. Drops with a wide vertical spacing (several centimeters) were separated from the main stream with an electronically controlled charging ring and high voltage deflection plates. The drops were allowed to reach terminal velocity before entering the top of the cloud chamber. The vertical spacing was determined from the terminal velocity and the production rate. The charge on the collector drops was determined with a laboratory built electrometer. The charge on individual drops was measured with an oscilloscope to a sensitivity of about  $10^{-16}$  Coulombs per drop.

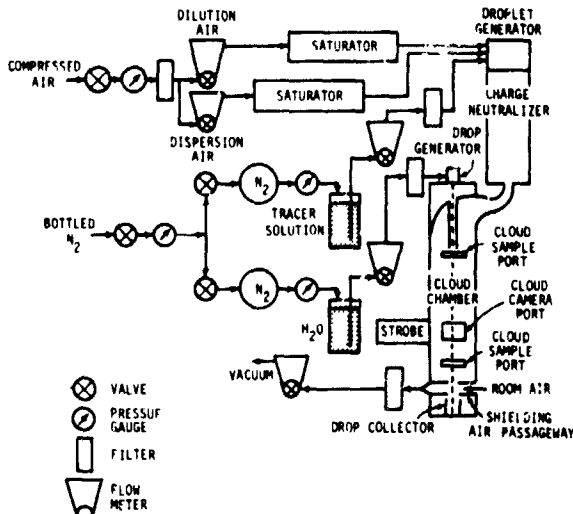


Figure 1. Diagram of experimental setup used to measure the collection efficiencies of cloud drops.

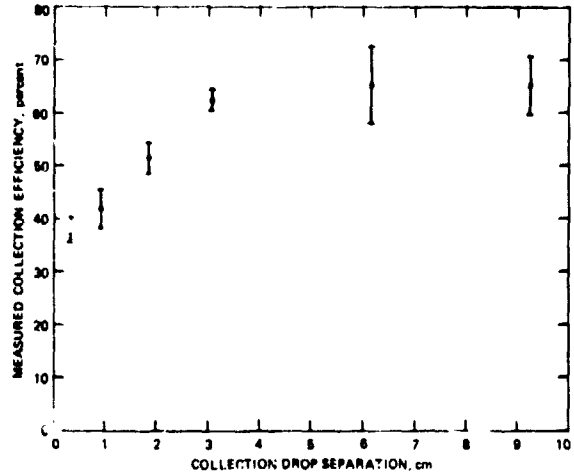


Figure 2. Collection efficiency as a function of R-drop separation for  $R = 95 \mu\text{m}$  and  $r = 19 \mu\text{m}$ .

During an experimental run the drops were collected beneath the cloud chamber in a polypropylene jar for a known period and covered for later analysis. After chemical analysis the collection efficiency was determined from experimental parameters using the following equation:

$$E = M / [\pi R^2 (1+p)^2 \Delta V n m X t N] \quad (1)$$

where  $M$  is the amount of lithium measured for an experimental run and the term in brackets is the amount of lithium expected from capture of all cloud droplets in the geometric path of the collector drops (i.e., unity collection efficiency). The term  $\pi R^2 (1+p)^2$  is the geometric cross section for the drop-droplet interaction. Multiplication of this cross section by the relative terminal velocity ( $\Delta V$ ) and the number concentration of droplets ( $n$ ) results in the number of cloud droplets encountered geometrically per unit time by a single collector drop. Further multiplication by the mass of one cloud droplet ( $m$ ) and mass fraction of lithium in one cloud droplet ( $X$ ) results in the amount of lithium encountered geometrically per unit time by a single collector drop. Finally, the lithium encountered by all collector drops is found from multiplication by the interaction time for one collector drop ( $t$ ) and the total number of collector drops for one experimental run ( $N$ ).

The number of collector drops ( $N$ ) was calculated from the drop generation rate and the experimental time. The amount of lithium for each run ( $M$ ) was determined by atomic absorption analysis. The size of the collector drop ( $R$ ) and cloud droplets ( $r$ ) was used to obtain the size ratio ( $p$ ), and the relative terminal velocity ( $\Delta V$ ) using the equations in Beard<sup>7</sup>. The cloud droplet concentration ( $n$ ) was determined photographically by the method discussed above. The initial droplet size was used to determine droplet mass ( $m$ ), whereas the initial lithium was fixed by the concentration of the tracer in the cloud water solution ( $X = 0.001$ ). The interaction time ( $t$ ) was determined from the fall speed of the collector drop, the downward air velocity in the cloud chamber and the cloud chamber height. Accurate knowledge of the air velocity was unnecessary because its magnitude was  $\leq 4\%$  of collector drop velocity.

#### Error analysis

The most obvious potential source of error in an experiment of this type is chemical contamination. Beyond checking for inconsistent or unrepeatable data several precautions and tests were made to assess and eliminate this problem. New polypropylene jars with plastic lids were always used for sample acquisition. During the course of an experiment several unopened jars were included for chemical analysis. Also experimental runs were made without any collector drops falling through the system to test for cloud droplet contamination in the jars. The jars in these runs were handled identically to the jars with collector drops. Chemists, trained in microanalysis, performed the atomic absorption measurements necessary to determine the amount of  $\text{Li}^+$  in each sample. Our tests have shown that total errors from chemical contamination and analysis are less than 3%.

Since electric charge on both the collector and collected drops can alter both the collision and coalescence efficiencies, we have been careful to minimize charge effects. The cloud droplets were passed through a charge neutralizer (TSI) designed to achieve a Boltzmann charge distribution at much higher flows than used in our experiment. We have computed that the mean magnitude of charge on a cloud droplet is  $< 2 \times 10^{-18}$  C. Our method of charge minimization for the collector drop leads to a charge magnitude  $< 3 \times 10^{-16}$  C. Considering the extremely small charge on the cloud droplets only induced charge effects are of possible significance in our experiment. The stronger influence of oppositely charged drops of a magnitude of  $\geq 10^{-14}$  C is necessary to significantly affect coalescence.

The final and possibly most subtle source of experimental error is a depletion effect. Since one collector drop follows the next through the center of the cloud column, there is the potential for depletion of the cloud droplet concentration by the stream of collector drops. In the data analysis this effect would be reflected as an anomalously low collection efficiency. Figure 2 shows the depletion effect for 19  $\mu\text{m}$  cloud droplets and 95  $\mu\text{m}$  collector drops. All data were taken at a sufficient collector drop separation to eliminate the depletion shown in Figure 2.

### Results

The measured collection efficiencies are shown in Figure 3 as a function of cloud droplet size. Also shown for comparison are experimental and theoretical findings at comparable collector drop sizes. Our 1980 measurements (closed triangles) were extended to a wider range of droplet sizes in 1981 (closed circles). Although charge control was improved in 1981 there is no apparent systematic difference between '80 and '81 data. Each data point has an uncertainty of about  $\pm 10\%$ . In every instance our measured collection efficiency lies below the theoretical collision efficiencies, whereas other work at smaller droplet sizes is more comparable to the computed efficiencies. There is a tendency evident in our results of a convergence with theoretical efficiencies at smaller droplet sizes. No apparent trend in the experimental data with collector drop size can be deduced, perhaps because of experimental scatter. The theoretical efficiencies, however, also are rather insensitive to collector drop size in the investigated range.

Coalescence efficiencies calculated from our experimental data on collection efficiencies and theoretical collision efficiencies are shown in Figure 4. In addition to our experimental error of about  $\pm 10\%$  there is an uncertainty in  $\epsilon$  from the use of computed collision efficiencies. For instance, our values of  $\epsilon$  would increase by about 15% with the use of deAlmeida's<sup>9</sup> collision efficiencies.

Some correspondence is found between our results and coalescence theories. For example, our data lie somewhat above the geometric coalescence factor ( $\epsilon = (1+p)^{-2}$ ) of Whelpdale and List<sup>10</sup>. On the other hand, our data falls somewhat below one of the several models of Arbel and Levin<sup>11</sup> (their Table 4). Their other results do not correspond as well. Our results all lie above the empirical formula of Levin and Machnes<sup>12</sup> based on an extrapolation of their findings for larger collector drops.

The experiments were conducted at two levels of charge. In 1980 the charge was maintained to  $10^{-15} \leq |Q_R - Q_r| \leq 10^{-14}$  Coulombs whereas in 1981 the charge was lowered to about  $3 \times 10^{-16}$  Coulombs for all data. No systematic differences were found in the data obtained at these two charge levels. Thus, charges of these magnitudes, which are found in weakly or moderately electrified clouds, apparently are too weak to significantly enhance coalescence. It therefore follows that the experiment should be extended to higher levels of charge to determine the magnitude needed to suppress the rebounding of falling drops. In addition, the amount of charge transferred by rebound in the range  $10^{-18} \leq |Q_R - Q_r| \leq 10^{-13}$  Coulombs should also be measured to help determine the viability of the induction mechanism for cloud electrification.

### Conclusions

Collection efficiencies were measured for 15 pairs of drop sizes in the range of  $63 \leq R \leq 98 \mu\text{m}$  and  $11 < r < 26 \mu\text{m}$ . The resulting efficiencies were all in the 60-70% range, most lying significantly below the computed hydrodynamic collision efficiencies. The physical basis of a nearly constant collection efficiency in this range may be due to a critical contact angle for rebound<sup>11</sup> or geometric coalescence factor<sup>10</sup> with hydrodynamic effects, if any, masked by experimental scatter.

The inferred coalescence efficiencies of 63-83% were only somewhat consistent with the coalescence models of Whelpdale and List<sup>10</sup> and of Arbel and Levin<sup>11</sup>. Both our empirical results and the models show a decrease in  $\epsilon$  with increasing droplet size. In contrast to the models, however, no systematic change in efficiency was found as a function of collector

C - 4

drop size. Even the qualitative agreement in r-drop dependency could be fortuitous since our measurements at other size ratios (reported in the following sections) show no correspondence with the models.

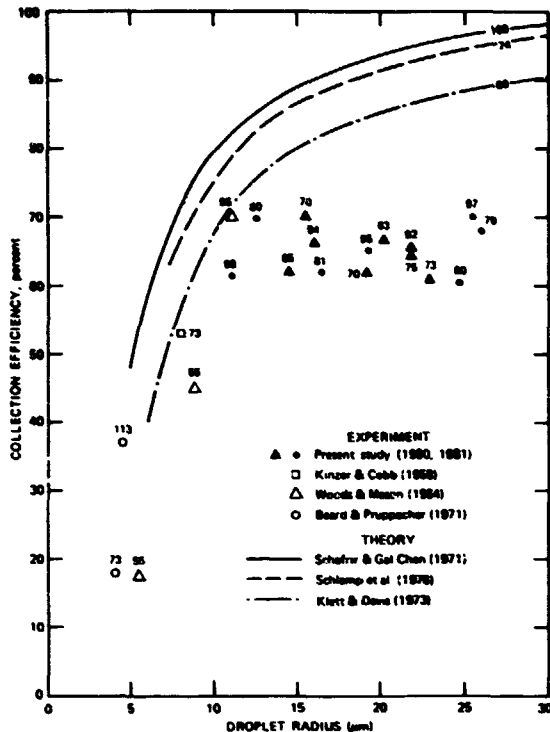


Figure 3. Collection efficiency as a function of r-drop radius.

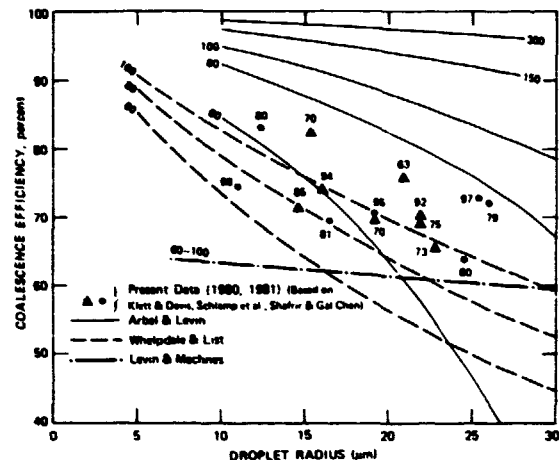


Figure 4. Coalescence efficiency as a function of r-drop radius.

#### Experimental study on accretion

A slight modification was made to the apparatus described in the previous section to permit the generation of collector drops of precipitation size for a study of the collection of much smaller cloud drops. The large capacity water feed system and the generator controls (described in the next section) were connected to the cloud drop experiment. Other aspects of the experimental arrangement remained unchanged.

The water feed rate and the generation frequency were selected so that 326  $\mu\text{m}$  collector drops reached within 1% of terminal velocity before entry into the cloud chamber. A drop charge of  $< 2 \times 10^{-15}$  Coulombs was maintained with the technique described in the previous section. A collection efficiency of  $0.59 \pm 10\%$  was measured for accretion with 17  $\mu\text{m}$  cloud droplets ( $p = 0.95$ ) from 12 experimental runs at 2 different vertical separations (32 and 64 cm). A coalescence efficiency of  $\epsilon = 0.63$  has been inferred from a collision efficiency of  $E = 0.94$  based on computations for small size ratios<sup>13</sup>. Our result is nearly the same as Levin and Machnes<sup>11</sup> ( $\epsilon = 0.61$ ) even though their empirical formula is a fit to a pure coalescence study (i.e., the "collector" drop was supported). We may have reached a small enough size ratio where the collision and coalescence mechanisms are relatively uncoupled. This important finding suggests that for accretion the collection efficiency may be calculated from computed collision efficiencies where  $E \sim 1$  and empirical coalescence studies where  $\epsilon \sim 0.6$ , that is  $E \sim 0.6$ . A few more measurements are desirable to verify this hypothesis for the accretion process at other sizes and size ratios.

#### Experimental study on precipitation drops

A study of the collection efficiency of small precipitation drops has been initiated<sup>14</sup>. The experiment is designed so that the drops interact initially at *terminal velocity* and the closure velocity and impact angle are determined by the natural system. This approach circumvents the difficulty of trying to combine the results of coalescence studies<sup>12, 15, 16</sup> with collision theory.

ORIGINAL PAGE IS  
OF POOR QUALITY

Design and procedure

An apparatus has been designed and constructed to measure the collection efficiency of small precipitation drops with size ratios  $0.6 \leq p \leq 1$ . In the following paragraphs, this system will be described. The present system can readily be used to measure collection efficiencies for drops  $R < 400 \mu\text{m}$  with  $p > 0.6$ .

Drops are produced by perturbing a liquid jet using a method first demonstrated by Rayleigh<sup>17</sup>. Adam et al.<sup>6</sup> described a technique for producing unequal sized drop pairs from a single jet. A sinusoidal voltage is applied to a piezoelectric transducer which induces capillary waves on the jet resulting in uniform drop production. The excitation frequency is periodically switched between two values to produce drops of one size followed by drops of another size. The drops can be charged and deflected between high voltage electrodes. When pulses of controlled width and voltage are superimposed on the charging voltage then selected drops from either group of drops can be generated with a negligible charge. As the main stream is deflected between the high voltage electrodes the uncharged drops fall as repetitive drop pairs.

Several design changes, some of which are indicated in Figure 5, have been made to improve the system of Adam et al.<sup>6</sup> First TTL digital logic has been adopted for the majority of the electronic controls. By using a 10 MHz crystal controlled oscillator, good frequency control and long term stability is achieved. Digital counters are used to divide the clock frequency by integer numbers selected by thumbwheel switches indicated by A and B in Figure 5. Thus, square waves of varying frequencies can be generated, and then amplified to drive the transducer.

The integers  $N_A$  and  $N_B$  are also selected by thumbwheel switches. These integers control the number of cycles of frequency  $A^*$  and  $B^*$  (corresponding to the integers A and B) between changes in frequency. Thus, after  $N_A$  cycles of frequency  $A^*$ ,  $N_B$  cycles of frequency  $B^*$  are generated and the sequence is repeated. A rotary switch (not shown) is used to select either frequency  $A^*$  and  $B^*$  or alternative packets of  $A^*$  and  $B^*$ .

The flip-flop circuit used to switch the two data selectors also triggers the four indicated time delays. These delays control the timing of the pulses that are used to generate the uncharged drops and trigger the strobe and camera. Electronic controls not shown in Figure 5 allow the camera to be triggered before the strobe so that the strobe flash occurs at the instant when the shutter has fully opened.

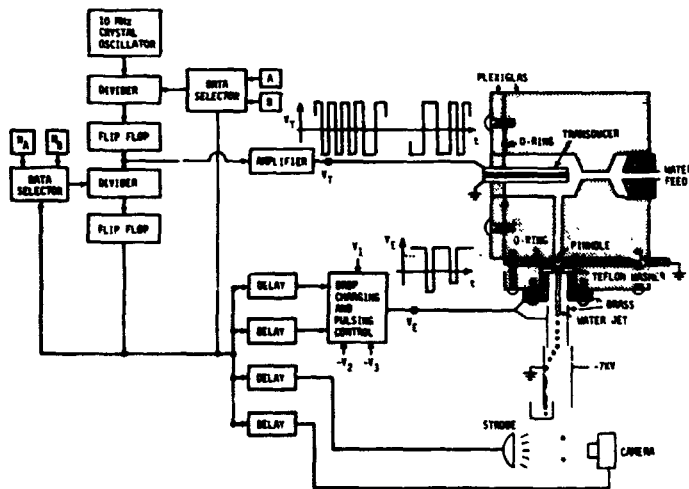


Figure 5. Diagram of drop generator and control circuits for experiment to measure collection efficiencies of small precipitation drops.

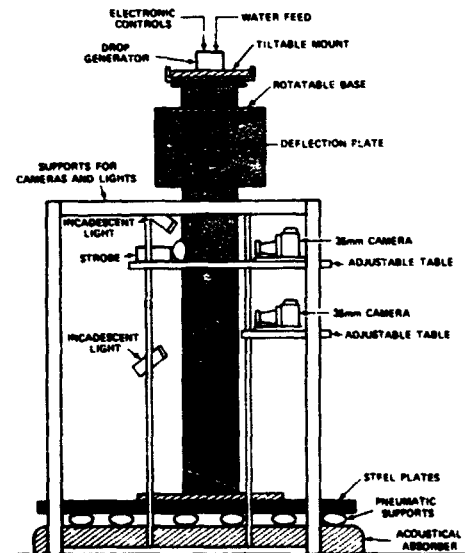


Figure 6. Experimental apparatus for the precipitation drop experiment.

This drop generating system has several advantages over the system described in Adam et al. The use of a square wave to drive the transducer appears to have improved the system performance. Troublesome satellite drops are almost never formed in the stable frequency range. This may result from sharper edges on the perturbation imposed on the liquid jet. The size ratio obtained can be extended using a lower harmonic during jet breakup. However, the use of higher multiplets is restricted to  $< 100 \mu\text{m}$  radius because larger drops tend to break apart when pulsed out. Thus, the singlet range of  $0.6 \leq p \leq 1$  might be extendable down to  $p \sim 0.5$  when the small drops are  $\leq 60 \mu\text{m}$  radius.

The drop generator is mounted on a platform that can be adjusted to about  $15^\circ$  from level so that the water jet can readily be directed vertically downward (Figure 6). The platform is located on top of a small plexiglas enclosure that can be rotated to align drop pairs parallel to the film plane. The experiment occurs in a 100 cm tall plexiglas chamber with a square cross section of  $100 \text{ cm}^2$ . The drops fall through this chamber and collide in a saturated environment at room temperature after they have each attained their terminal velocities. Data on drop trajectories is obtained photographically.

At the onset of an experiment the repetition rate can be set high enough such that the drops appear stationary under stroboscopic light. Individual small and large drops can be pulsed out of the stream and adjusted to fall vertically between high voltage electrodes. At this point the drop stream may appear as shown in Figure 7, however, in practice a much larger initial separation is chosen so that both drops will achieve terminal velocity before they approach each other. Since both the large and small drops are generated from the same stream it is impossible to produce both sizes at their terminal velocities.

The drop pairs must be separated in time so that each event is unaffected by the preceding one. Greater time separation is achieved by simply adding more trailing large drops to the drop cycle. Since the delay for the pulses is always measured from the point at which the first small drop is produced, these delays are unaffected by the addition of trailing large drops and the drop pairs can be made arbitrarily far apart. As more large drops are added the pulses must be slightly readjusted since aerodynamic factors have changed. This is done by viewing the position of streaks produced by the drops as they pass the incandescent light. As a practical matter drop events are usually separated by about 0.5 s. After the events have been adequately separated minor readjustments are made to enhance the probability of an interaction.

Two polyethylene lined 55 gallon drums partially filled with distilled water are used as a water feed system for the drop generator. Pressure is supplied from bottled nitrogen. Because of the large water surface the flow remains essentially constant for several hours. The water reservoirs and experimental chamber are each on an isolation platform to reduce interference from building vibrations. These platforms consist of massive steel plates suspended pneumatically above an acoustic absorber.

Streak and strobe photographs are obtained near the top of the 100 cm column. The streaks are created by an incandescent lamp located  $30^\circ$  above the camera axis and on the opposite side of the chamber. The collection efficiency is determined from the maximum horizontal separation measured for coalescence. An observed coalescence that results from drops falling in a plane more than about 15 degrees out of parallel with the film plane will result in a measurement that is at least 3% too low. Therefore, the platform which supports the drop generator is turned to align the plane of the falling drops parallel to the camera film plane so that the streak photograph represents the best possible measure of the horizontal separation. A position for a second camera at right angles to the first camera has been constructed for an unambiguous measure of the horizontal separation.

A free running strobe light placed about  $45^\circ$  to one side of the optical axis creates successive exposures on the film. Using the frequency of the strobe flashes, the fall speed of each drop can be computed. Triggered strobe observations are also used to verify the vertical drop separation at the point where the streaks are recorded. Another camera is triggered at the point where the drops come together to record the results (miss, coalescence, rebound, or possibly breakup) in the form of streak photographs.

## Results

The apparatus just described has been used to measure the collection and coalescence efficiencies for a 275-200  $\mu\text{m}$  drop pair. Two cameras are used to obtain the necessary data. The upper camera recorded streak data for a measure of the initial horizontal offset of the drops that is used to determine the maximum separation for collection (i.e., the collection efficiency). In addition multiple strobe exposures were used to verify fall speeds. Figure 8a depicts a sample of the data taken with the upper camera. The lower camera was used to record streak images of the interaction to determine whether a collection event had occurred. Figure 8b shows the characteristic signature of a coalescence event whereas Figure 8c shows a rebound event with an indication of the oscillation due to deformation at impact. No

evidence of partial coalescence has been noticed. Data from the lower camera was also used to estimate the rebound probability from the fractional number of rebound events out of the total of rebound and coalescence events. To obtain the coalescence efficiency (or probability) the rebound probability is subtracted from unity.



Figure 7. Stream of charged drops and one uncharged pair falling between high voltage plates.

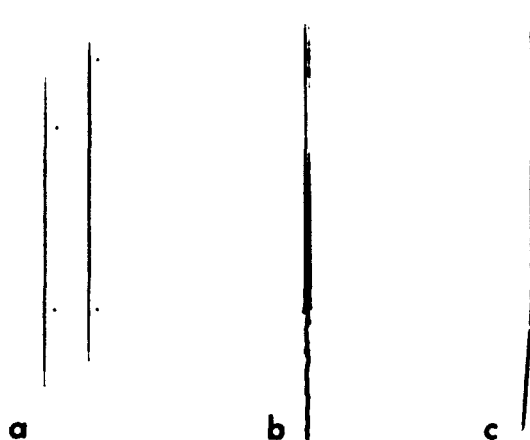


Figure 8. Camera data showing: (a) horizontal separation, upper camera; (b) coalescence event, lower camera; and (c) rebound event, lower camera.

The drop sizes were determined by weighing a timed sample of uniform droplets from the stream. By knowing the frequency at which the drops were produced, their mass could be determined. This method leads to less than a 1% error in determining the drop radius. However, it was not possible to set up the experiment in precisely the same manner from day to day resulting in a 5% variation in the radius of each drop. Both drops were falling approximately 3% faster than their terminal velocities when approached within 100 radii of each other, and their relative velocity was about 4% high.

To date, we have obtained and analyzed data from several hundred photographed events. Out of 56 collision events (either coalescence or rebound) we have determined the coalescence efficiency to be  $0.72 \pm 0.05$  and the collection efficiency to be  $0.71 \pm 0.05$ . This result is consistent with an expected collision efficiency close to unity.

Park<sup>16</sup> has obtained the only data on unsupported drops in the size range used in this experiment. His data was obtained by firing streams of drops at each other and not by using drops at terminal velocity. Our data point lies outside the rebound region based on his data. The coalescence efficiency of Levin and Machnes<sup>12</sup> for this size pair with one drop supported is only 0.36. They acknowledged that this experimental approach was only an approximation to the collection problem since it artificially divides a "continuous" process into collision and coalescence. The degree of approximation in such an experiment can only be determined by comparison with data on collection as obtained in our initial experiment. The comparison shows, at least for small precipitation drops of similar size, that such approximate coalescence studies may result in a large uncertainty.

#### Acknowledgments

This work was supported by the National Science Foundation under grant ATM79-14170.

#### References

1. Beard, K. V., H. T. Ochs, and T. S. Tung, "A Measurement of the Efficiency for Collection between Cloud Drops," *J. Atmos. Sci.*, Vol. 36, pp. 2479-2483. 1979.
2. Levin, Z., M. Neiburger, and L. Rodriguez, "Experimental Evaluation of Collection and Coalescence Efficiencies of Cloud Drops," *J. Atmos. Sci.*, Vol. 30, pp. 944-946. 1973.
3. Picknett, R. G., "Collection Efficiencies for Water Drops in Air," *J. Air Water Pollut.*, Vol. 3, pp. 160-167. 1960.

ORIGINAL PAGE IS  
OF POOR QUALITY

4. Woods, J. D., and B. J. Mason, "Experimental Determination of Collection Efficiencies for Small Water Drops in Air," Quart. J. Roy. Meteor. Soc., Vol. 90, pp. 373-381. 1964.
5. Liddell, H. F., and N. W. Wootten, "The Detection and Measurements of Water Droplets," Quart. J. Roy. Meteor. Soc., Vol. 83, pp. 263-266. 1957.
6. Adam, J. R., R. Cataneo, and R. G. Semonin, "The Production of Equal and Unequal Size Droplet Pairs," Rev. Sci. Instrum., Vol. 42, pp. 1847-1849. 1971.
7. Beard, K. V., "Terminal Velocity and Shape of Cloud and Precipitation Drops Aloft," J. Atmos. Sci., Vol. 33, pp. 851-864. 1976.
8. Pruppacher, H. R., and J. D. Klett, Microphysics of Clouds and Precipitation, Reidel. 1978.
9. de Almeida, F. C., "Collision Efficiency, Collision Angle and Impact Velocity of Hydrodynamically Interacting Cloud Drops: A Numerical Study," J. Atmos. Sci., Vol. 34, pp. 1286-1292. 1977.
10. Whelpdale, D. M., and R. List, "The Coalescence Process - Raindrop Growth," J. Geophys. Res., Vol. 76, pp. 2836-2856. 1971.
11. Arbel, N., and Z. Levin, "The Coalescence of Water Drops I and II," Pure Appl. Geophys., Vol. 115, pp. 869-914. 1977.
12. Levin, Z., and B. Machnes, "Experimental Evaluation of the Coalescence Efficiency of Colliding Water Drops," Pure Appl. Geophys., Vol. 115, pp. 845-867. 1977.
13. Beard, K. V., and S. N. Grover, "Numerical Collision Efficiencies for Small Raindrops Colliding with Micron Size Particles," J. Atmos. Sci., Vol. 31, pp. 543-550. 1974.
14. Ochs, H. T., and K. V. Beard, "The Collection Efficiency of Similarly Sized Precipitation Drops," Proceedings of the Conference on Cloud Physics and Atmospheric Electricity, Issaquah, Washington. 1978.
15. Brazier-Smith, P. F., S. G. Jennings, and J. Latham, "The Interaction of Falling Water Drops: Coalescence," Proc. R. Soc. Lond., A, 326, pp. 393-408. 1972.
16. Park, R. W., Behavior of Water Drops Colliding in Humid Nitrogen. Ph.D. Thesis, Dept. of Chemical Engineering, University of Wisconsin. 1970.
17. Rayleigh, Lord, "On the Instability of Jets," Proc. Lond. Math. Soc., Vol. 10, pp. 4-13. 1878.

## The geophysical importance of bubbles in the sea

Ramon J. Cipriano

Atmospheric Sciences Research Center, State University of New York at Albany  
1400 Washington Avenue, Albany, New York 12222

### Abstract

Sea salt is by far the major constituent cycled through the earth's atmosphere each year. Bursting bubbles in the oceans appear to be primarily responsible. These salt particles play a role in the formation of maritime clouds, which in turn affect the earth's radiation budget. Along with the salt are carried various chemical pollutants and potentially pathogenic microorganisms, often in highly enriched form. Both jet and film drops are produced by bursting bubbles. This paper summarizes our present knowledge of the droplet production and enrichment mechanisms, with particular emphasis on the unsolved problems.

### Introduction

Each year the oceans of the world inject  $10^9$ - $10^{10}$  tons of salt into the atmosphere.<sup>1</sup> This is 1 or 2 orders of magnitude greater than inputs from all other sources. Bursting bubbles from whitecaps appear to be primarily responsible. There is good evidence suggesting that most of the condensation nuclei involved in maritime cumulus and stratocumulus cloud formation consist of or are derived from sea salt.<sup>2,3,4,5</sup> These cloud types are ubiquitous and affect the global radiation budget. Their microphysical structure is fundamentally different from continental clouds, allowing them to produce rain much more efficiently,<sup>6</sup> which in turn affects the residence time of smaller particles in the marine atmosphere.<sup>7</sup> The marine aerosol exhibits a geochemical fractionation or enrichment which generally increases with decreasing particle size.<sup>8,9,10,11</sup> Various pollutants such as PCBs, DDT, heavy metals, and radionuclides are transferred from sea to air, often in highly concentrated form.<sup>12</sup> Microorganisms such as bacteria and viruses are found concentrated in aerosols from bursting bubbles,<sup>13,14,15,16</sup> with consequent health implications if pathogens are involved.<sup>17</sup>

### Droplet production mechanisms

#### Film drops

Two types of droplets are produced when bubbles burst. Film drops form from the disintegration of the protruding bubble film. The details of this process are unknown, largely because the film rupture has never actually been observed. Two difficulties present themselves. First, the rupture is quite rapid: for a 250  $\mu\text{m}$  diameter bubble, the film collapses in about  $3 \times 10^{-7}$  sec.<sup>18</sup> But this is now well within the reach of current time-lapse capabilities. A more serious problem is the size of the film drops, for recent evidence suggests most are of submicron dimensions. Thus any photographic scheme which allows observation of the entire film collapse will lack sufficient resolution to reveal many of the individual droplets formed by the collapse.

Most important of the variables controlling film drop production is bubble size: bubbles smaller than about 300  $\mu\text{m}$  diameter produce few or none; 1 mm bubbles produce up to 20 or 30, and this increases to a maximum of about 1000 for 6 mm bubbles; most of the film droplets are ejected in a cloud several centimeters above the water surface.<sup>18,19</sup> However, for a given bubble diameter, the film drop production can be a fraction of the maximum numbers just quoted. Two variables influencing this (there are undoubtedly others) are the "cleanliness" of the bubble (i.e., the amount of surfactant adsorbed to the bubble as it rises), and the bubble surface lifetime (delay between the arrival of the bubble at the water surface and the film collapse). Film drop production generally decreases with increasing bubble dirtiness and surface lifetime (for reasons still hypothetical), although there are exceptions to this. Bubble surface lifetime is itself related to bubble cleanliness, for reasons also poorly understood.

Data on film drop size distributions are scant. Blanchard and Syzdek<sup>20</sup> used glass slides coated with MgO to determine the film drop size distribution of drops resolvable with the light microscope for 740  $\mu\text{m}$  diameter bubbles. The distribution peaked at about 4-6  $\mu\text{m}$ , as shown in Figure 1.

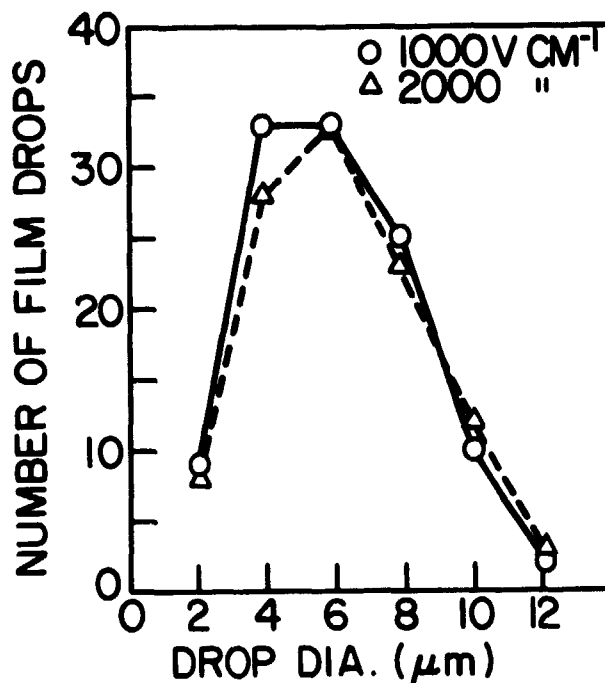


Figure 1. Film drop size distribution (2  $\mu\text{m}$  bandwidth) obtained from 30 bubbles of 740  $\mu\text{m}$  diameter bursting in a  $3.3 \times 10^3$  ppm nutrient broth solution. Film drops were collected electrostatically, at the indicated field strength, on glass slides coated with MgO. Data from Blanchard and Syzdek (1975).

The maximum film drop production mentioned above was determined with a thermal gradient diffusion cloud chamber, which is capable of growing drops of  $<0.01 \mu\text{m}$  diameter to 5-10  $\mu\text{m}$ . The cloud of droplets so produced tends toward monodispersity regardless of the initial size distribution. However, data obtained by the author suggests that for larger bubbles ( $>1 \mu\text{m}$  dia.), most film drops are submicroscopic. For example, when the aerosol produced by bursting of 1.8 mm dia. bubbles in seawater was examined simultaneously with a TSIR 3020 condensation nuclei counter (capable of counting hygroscopic particles  $<0.01 \mu\text{m}$  dia.) and a Royco optical particle counter (dia.  $>0.3 \mu\text{m}$ ), the Royco count was only 10-30% of the 3020 count.

Further evidence suggesting submicron film drop production was obtained from a laboratory model of a breaking wave, shown in Figure 2. Seawater, circulated by a centrifugal pump, falls from a height of 33 cm into a circular tank 0.5 m in diameter. The aerosol produced by the upwelling plume of bubbles was passed through a Sinclair diffusion battery, the penetration through which is determined by particle size.<sup>21</sup> Figure 3 shows the penetration curves of the model wave aerosol at 90% and 75% relative humidity, compared with the penetration curves of monodisperse aerosols of 0.05  $\mu\text{m}$ , 0.02  $\mu\text{m}$ , and 0.01  $\mu\text{m}$  radii. Although drops other than film drops are produced by the experimental configuration shown in Figure 2, there are good reasons to believe the submicron drops revealed in Figure 3 are indeed film drops.<sup>22</sup>

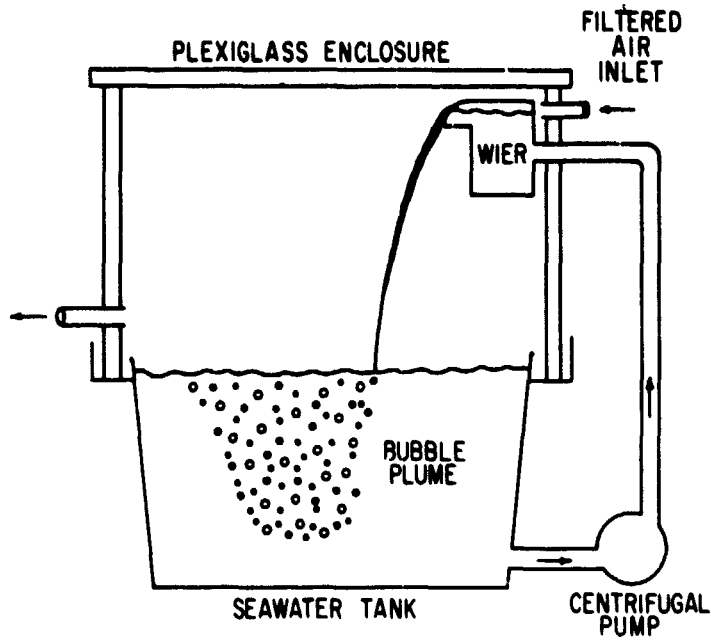


Figure 2. Scale drawing of a laboratory simulation of a breaking wave or whitecap. Tank diameter is 0.5 m, waterfall height 33 cm.

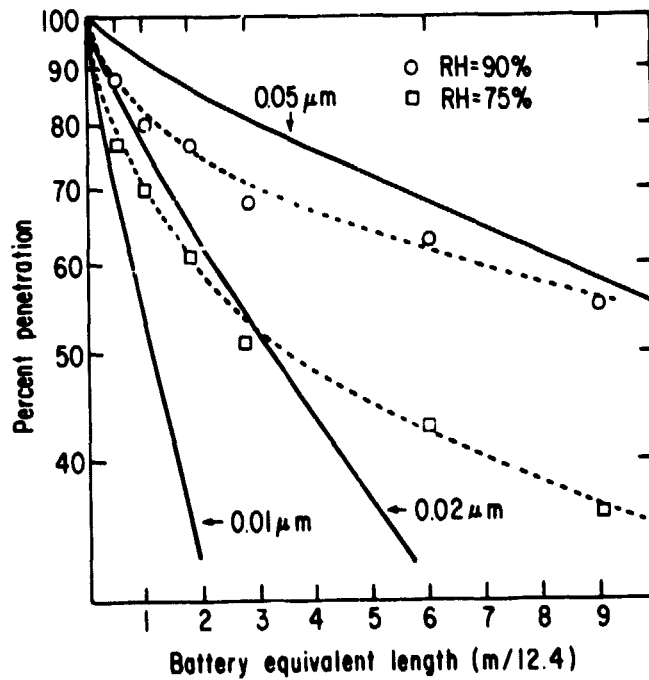


Figure 3. Diffusion loss of the model wave aerosol at 90% relative humidity, together with calculated diffusion loss for monodisperse aerosols of 0.05 μm, 0.02 μm, and 0.01 μm radii.

## Jet Drops

Jet drops are also produced by bursting bubbles. These are formed by the collapse of the cavity remaining after the film rupture. A jet of water is propelled upwards from the center of this cavity, becomes unstable, and breaks into discrete droplets. Surface tension is the major energy source.<sup>18</sup> Jet drops are about one-tenth the bubble diameter.<sup>23</sup> The number of jet drops per bubble decreases from as many as five or six for a 300  $\mu\text{m}$  diameter bubble to only one for bubbles larger than about 3 mm.

The breakup of the jet into individual droplets has been observed for a large bubble (1.7 mm dia.) by time-lapse photography with  $3 \times 10^{-4}$  sec resolution.<sup>24</sup> Details of jet breakup for smaller bubbles are as yet unobserved, although certainly well within current capabilities. The calculated top jet drop ejection speed increases with decreasing drop size, reaching  $8 \times 10^3$  cm sec<sup>-1</sup> at 70  $\mu\text{m}$  bubble diameter.<sup>18</sup> (Film drop ejection speeds are unknown.) Top jet drop ejection height reaches a maximum of nearly 20 cm for 200  $\mu\text{m}$  drops. The upper bound jet drop diameter relevant to atmospheric processes is, of course, determined by sedimentation, 20  $\mu\text{m}$  being a reasonable value. The lower bound jet drop diameter is unknown; direct observations extend only to  $\sim 7$   $\mu\text{m}$ . The existence of submicron jet drops is at this point hypothetical; it is, however, doubtful that such drops are produced in large numbers in nature, since bubbles smaller than 10  $\mu\text{m}$  diameter are rapidly forced into solution due to surface tension.<sup>23,25</sup>

## Droplet enrichment mechanisms

Material can adsorb to the surface of a bubble both as it rises (bubble scavenging), and also as it penetrates the bulk water surface, if a monolayer of material is floating there. Film drops are formed from the bubble surface itself. Material which comprises the jet drops, particularly the top drop, is skimmed from the surface of the bubble cavity by a capillary wave which in effect acts as a microtome.<sup>26</sup> Thus it might be expected that the composition of both jet and film drops can be vastly different from that of the bulk water in which the bubbles burst. The enrichment of bacteria in jet drops has already been demonstrated,<sup>15</sup> and evidence strongly suggestive of film drop bacterial enrichment now exists.<sup>22</sup> In nature, both bubble scavenging and bulk surface microlayer transfer surely operate. Which of the two mechanisms predominates is unknown. Strong arguments favor scavenging,<sup>27</sup> particularly in cases where the flux of upwelling bubbles is great, for this causes divergence of the water surface adequate to push aside floating monolayers.

## Relevance to geophysics

The relative contribution of jet and film drops to the marine aerosol and its enrichment is a complex problem. In view of the relationships between jet and film drop size distributions versus bubble size, the shape of the bubble spectrum in whitecaps is of critical importance. The size distribution of sea salt particles is such that most of the salt mass is contributed by drops larger than 1  $\mu\text{m}$ , whereas these comprise a small fraction of the total number. Most cloud condensation nuclei (CCN) are smaller than 1  $\mu\text{m}$ .<sup>4,6</sup> Comparison of the bubble and aerosol spectra produced by the model whitecap shown in Figure 1 suggests that the global salt mass flux is controlled by jet drops, from bubbles smaller than 1 mm, and that the CCN flux is controlled by film drops, from bubbles larger than 1 mm.<sup>3,22</sup> It is important to determine the validity of this laboratory simulation: there is evidence that a feedback mechanism exists whereby the addition of surface active material to the oceans, by man or otherwise, can lead to a significant modification of film and jet drop production.<sup>28</sup>

The processes of drop formation and enrichment mentioned here must apply to some extent to bubbles in all types of liquids. It is anticipated that new parallels will be found in many other disciplines.

## References

1. Blanchard, D. C., and A. H. Woodcock, "The Production, Concentration, and Vertical Distribution of the Sea-Salt Aerosol," Annals N. Y. Acad. Sci., Vol. 338, pp. 330-347. 1980.
2. Blanchard, D. C., "The Oceanic Production Rate of Cloud Nuclei," J. Rech. Atmos., Vol. 4, pp. 1-6. 1969.
3. Cipriano, R. J., and D. C. Blanchard, "Bubble and Aerosol Spectra Produced by a Laboratory Breaking Wave," J. Geophys. Res., in press.
4. Dinger, J. E., E. B. Fowell, and T. A. Wojciechowski, "On the Source and Composition of Cloud Nuclei in a Subsident Air Mass over the North Atlantic," J. Atmos. Sci. Vol. 27, pp. 791-797. 1970.
5. Woodcock, A. H., "Smaller Salt Particles in Oceanic Air and Bubble Behaviour in the Sea," J. Geophys. Res., Vol. 77, pp. 5316-6321. 1972.
6. Mason, B. J., The Physics of Clouds, Clarendon Press, Oxford, pp. 79-80. 1971.

7. Junge, C., "Our Knowledge of the Physico-Chemistry of Aerosols in the Undisturbed Marine Environment," J. Geophys. Res., Vol. 77, pp. 5183-5200. 1972.
8. Barker, D. R., and H. Zeitlin, "Metal Ion Concentrations in Sea-Surface Microlayer and Size-Separated Atmospheric Aerosol Samples in Hawaii," J. Geophys. Res., Vol. 77, pp. 5076-5086. 1972.
9. Chesselet, R., J. Morelli, and P. Buat-Menard, "Variations in Ionic Ratios between Reference Sea Water and Marine Aerosols," J. Geophys. Res., Vol. 77, pp. 5116-5131. 1972.
10. Duce, R. A., A. H. Woodcock, and J. L. Moyers, "Variation of Ion Ratios with Size among Particles in Tropical Oceanic Air," Tellus, Vol. 19, pp. 369-379. 1967.
11. Hoffman, G. L., and R. A. Duce, "Consideration of the Chemical Fractionation of Alkali and Alkaline Earth Metals in the Hawaiian Marine Atmosphere," J. Geophys. Res., Vol. 77, pp. 5161-5169. 1972.
12. GESAMP: Joint Group of Experts on the Scientific Aspects of Marine Pollution. Interchange of Pollutants between the Atmosphere and the Oceans, Rep. Stud. GESAMP (13), 55 pp. 1980.
13. Baylor, E. R., M. B. Baylor, D. C. Blanchard, L. D. Syzdek, and C. Appel, "Virus Transfer from Surf to Wind," Science, Vol. 198, pp. 575-580. 1977.
14. Bezdek, H. F., and A. F. Carlucci, "Surface Concentration of Marine Bacteria," Limnol. Oceanogr., Vol. 17, pp. 566-569. 1972.
15. Blanchard, D. C., and L. D. Syzdek, "Concentration of Bacteria in Jet Drops from Bursting Bubbles," J. Geophys. Res., Vol. 77, pp. 5087-5099. 1972.
16. Rejkal, T. W., P. A. LaRock, and J. W. Winchester, "Water-to-Air Fractionation of Bacteria," Appl. Environ. Microbiol., Vol. 39, pp. 335-338. 1980.
17. Wendt, S. L., K. L. George, B. C. Parker, E. Gruff, and J. O. Falkinham, III, "Epidemiology of Infection by Nontuberculous Mycobacteria, III: Isolation of Potentially Pathogenic Mycobacteria from Aerosols," Am. Rev. Respir. Dis., Vol. 122, pp. 259-263. 1980.
18. Blanchard, D. C., "The Electrification of the Atmosphere by Particles from Bubbles in the Sea," Prog. Oceanogr., Vol. 1, pp. 71-202. 1963.
19. Day, J. A., "Production of Droplets and Salt Nuclei by the Bursting of Air-Bubble Films," Quart. J. R. Met. Soc., Vol. 90, pp. 72-78. 1963.
20. Blanchard, D. C., and L. D. Syzdek, "Electrostatic Collection of Jet and Film Drops," Limnol. Oceanogr., Vol. 20, pp. 762-774. 1975.
21. Sinclair, D., and L. Hinchliffe, "Production and Measurement of Submicron Aerosols, II." In: Assessment of Airborne Particles, Chapter 10 (Ed. by T. T. Mercer, P. E. Morrow and W. Stober), Charles C. Thomas. 1972.
22. Cipriano, R. J., Bubble and Aerosol Spectra Produced by a Laboratory Simulation of a Breaking Wave, Ph.D. dissertation, State University of New York at Albany. 1979.
23. Blanchard, D. C., and A. H. Woodcock, "Bubble Formation and Modification in the Sea and Its Meteorological Significance," Tellus, Vol. 9, pp. 145-158. 1957.
24. Kientzler, C. F., A. B. Arons, D. C. Blanchard and A. H. Woodcock, "Photographic Investigation of the Projection of Droplets by Bubbles Bursting at a Water Surface," J. Geophys. Res., Vol. 6, pp. 1-7. 1954.
25. Johnson, B. D., and R. C. Cooke, "Organic Particle and Aggregate Formation Resulting from the Dissolution of Bubbles in Seawater," Limnol. Oceanogr., Vol. 25, pp. 653-661. 1980.
26. MacIntyre, F., "Geochemical Fractionation during Mass Transfer from Sea to Air by Breaking Bubbles," Tellus, Vol. 22, 451-461. 1970.
27. Blanchard, D. C., "Bubble Scavenging and the Water-to-Air Transfer of Organic Material in the Sea," Advances in Chemistry, No. 145. Applied Chemistry at Protein Interfaces, American Chemical Society. 1975.
28. Blanchard, D. C., and E. J. Hoffman, "Control of Jet Drop Dynamics by Organic Material in Seawater," J. Geophys. Res., Vol. 83, pp. 6187-6191. 1978.

Fluid dynamical description of relativistic nuclear collisions

J. R. Nix and D. Strottman

Theoretical Division, Los Alamos National Laboratory  
Los Alamos, New Mexico 87545

Abstract

On the basis of both a conventional relativistic nuclear fluid dynamical model and a two-fluid generalization that takes into account the interpenetration of the target and projectile upon contact, we calculate collisions between heavy nuclei moving at relativistic speeds. This is done by solving the relevant equations of motion numerically in three spatial dimensions by use of particle-in-cell finite-difference computing techniques. We study the effect of incorporating a density isomer, or quasistable state, in the nuclear equation of state at three times normal nuclear density, as well as the effect of doubling the nuclear compressibility coefficient. For the reaction  $^{20}\text{Ne} + ^{238}\text{U}$  at a laboratory bombarding energy per nucleon of 393 MeV, the calculated distributions in energy and angle of outgoing charged particles are compared with recent experimental data both integrated over all impact parameters and for nearly central collisions.

Introduction

Our colloquium on drops and bubbles has brought together people in such diverse disciplines as astrophysics, fluid dynamics, and nuclear physics, working with physical systems ranging in size from stars through water drops to atomic nuclei. Having already heard from astrophysicists and fluid dynamicists, it is time now to turn our attention from some of the largest objects in the universe to some of the smallest.

An atomic nucleus, with diameter about  $10^{-14}$  m and mass about  $10^{-25}$  kg, is about  $10^4$  times as dense as water. Discovered in 1911 by Sir Ernest Rutherford, it is to lowest order a collection of positively charged protons and uncharged neutrons held tightly together by short-range nuclear forces. As first suggested by Niels Bohr in 1936, a nucleus behaves in some respects like a uniformly charged drop of liquid with surface tension.

The liquid-drop model has been widely used to explain the breakup of a heavy nucleus into two smaller fragments in the process of nuclear fission, as well as to explain many features associated with collisions between two nuclei. Until recently, the bombarding energy in such collisions has been fairly low, with the result that the nuclear density remains close to its equilibrium value and the excitation energy is relatively low. However, a few years ago accelerators were developed that can accelerate heavy nuclei to relativistic speeds, and we are now beginning to explore what happens when nuclei become highly compressed and excited.

The collision of heavy nuclei at high energy is extremely complicated, lying somewhere in between two limiting possibilities that have been used to describe it. At one extreme, the process could be dominated by a series of collisions between individual particles making up the nuclei or produced in the reaction. This first limit, which would be realized if the particle mean free path were much longer than the nuclear force range, has been studied in terms of microscopic approaches such as the relativistic intranuclear cascade, where the basic input is experimentally measured two-particle cross sections.<sup>1-3</sup>

At the other extreme, the process could be dominated by coherent collective-field effects, resembling instead the collision of two drops of nuclear fluid. This second limit would be realized if there are many degrees of freedom, sufficient time during the collision to establish local equilibrium, and a short mean free path for stopping a particle. In relativistic nuclear collisions of the type considered here, the first two conditions are satisfied moderately well whereas the last condition is more uncertain. Estimates based on collisions between two particles in free space give relatively long mean free paths, but the mean free path could be reduced significantly inside a nuclear medium because of many-body effects or a nuclear phase transition.<sup>4</sup> This second limit has been studied by several different groups around the world in terms of fluid dynamical models, where the basic input is the nuclear equation of state. We will be concentrating here on recent work performed at Los Alamos within this approach.<sup>5-7</sup>

### Nuclear equation of state

One reason for studying relativistic nuclear collisions is to learn about the nuclear equation of state, the fundamental relationship specifying how pressure depends upon density and thermal energy. At present we have experimental information about this important function only in the vicinity of the equilibrium ground state. However, theoretical speculations suggest that it may be extremely complicated, with nuclear matter undergoing one or more phase transitions as its density is increased.<sup>5</sup> This is illustrated schematically in Figure 1, which shows how the ground-state energy per nucleon  $E_0(n)$ , or zero-temperature compressional energy per nucleon, might depend upon nucleon number density  $n$ . We know experimentally that the equilibrium energy per nucleon  $E_0(n_0) = -16$  MeV, that the equilibrium density  $n_0 = 1.5 \times 10^{14}$  nucleons/m<sup>3</sup>, and that the nuclear compressibility coefficient  $K = 210$  MeV. What happens away from equilibrium is currently unknown, but doubling the nuclear density from its normal value could lead to a pion condensate, or a state containing a large number of bound pions. Compression to several times normal density could result in a density isomer, or a quasistable state existing at other than normal density. Still further compression could produce quark matter, in which the quarks that comprise nucleons become free. To determine whether or not any of these phase transitions actually exist in nuclei is the exciting challenge that we face!

In addition to the above compressional energy, nuclear matter at rest can contain thermal energy, so that the total internal energy per nucleon is

$$E(n, I) = E_0(n) + I, \quad (1)$$

where  $I$  is the thermal energy per nucleon, which is itself a function of  $n$  and either the entropy per nucleon  $S$  or the temperature  $T$ . The pressure  $p$  is then given by<sup>5-7</sup>

$$p = n^2 \left. \frac{\partial E(n, I)}{\partial n} \right|_S = n^2 \frac{dE_0(n)}{dn} + n^2 \left. \frac{\partial I}{\partial n} \right|_S, \quad (2)$$

containing separate contributions from the compressional energy and the thermal energy.

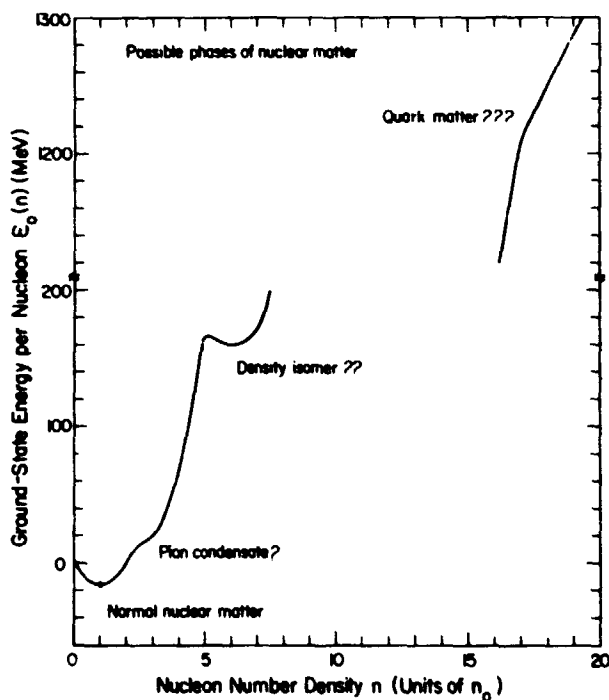


Figure 1. Compressional energy, illustrating three conjectured nuclear phase transitions.

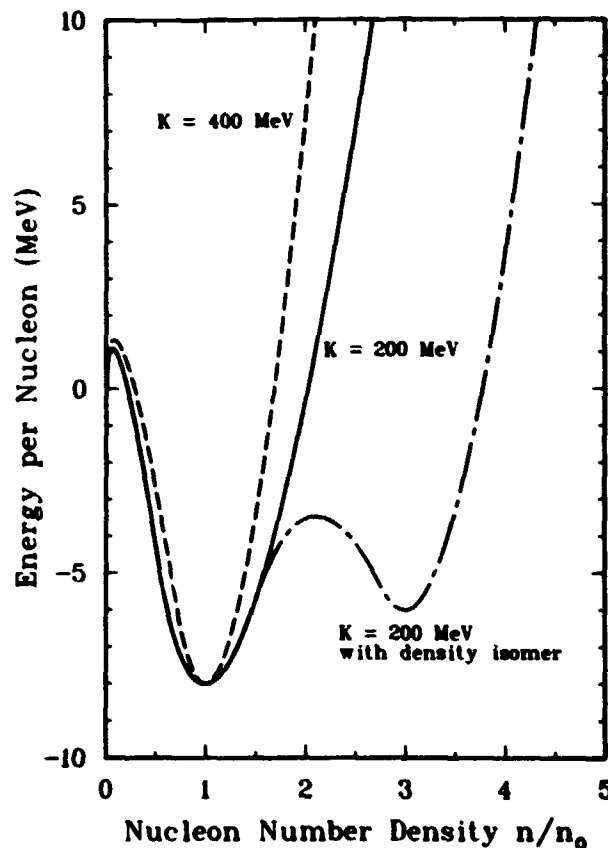


Figure 2. Compressional energy in three of our nuclear equations of state.

For the ground-state energy per nucleon  $E_0(n)$  we use both an old functional form<sup>6</sup>

$$E_0(n) = a n^{2/3} - b n + c n^{5/3} \quad , \quad (3)$$

with positive constants  $a$ ,  $b$ , and  $c$  that yield a compressibility coefficient  $K = 294.8$  MeV, and a new functional form<sup>7</sup> producing the three curves shown in Figure 2. The solid line shows the result for compressibility coefficient  $K = 200$  MeV, and the dashed line shows the effect of doubling the compressibility coefficient to 400 MeV. The dot-dashed curve shows the result for a density isomer at a density that is three times normal nuclear density, with an energy 2 MeV higher than at normal density and with the same curvature. In each of these three cases we use the value  $E_0(n_0) = -8$  MeV to simulate the loss in binding energy for finite nuclei arising from surface and Coulomb energies. The new functional form has the property that the speed of sound approaches the speed of light in the limit of infinite compression. This is achieved by parametrizing  $E_0(n)$  for  $n$  greater than a critical value in terms of three smoothly joined parabolas in the square root of the density, so that in the limit of infinite compression it increases linearly with density.

For the thermal contribution to the pressure we use the result<sup>5-7</sup>

$$P_{\text{thermal}} = n^2 \left. \frac{\partial I}{\partial n} \right|_S = \frac{2}{3} n I \quad , \quad (4)$$

which is derived from the nonrelativistic Fermi-gas model.

#### Relativistic nuclear fluid dynamics

In a complete nuclear fluid dynamical calculation, we would need to take into account nuclear energy, Coulomb energy, nuclear viscosity, thermal conductivity, and single-particle effects, as well as the production of additional particles and the associated radiative loss of energy from the system. However, in nuclear collisions of the type considered here, these effects are small compared to those caused by the dominant kinetic, compressional, and thermal energies, and are consequently neglected.

The covariant relativistic fluid dynamical equations that we solve express the conservation of nucleon number, momentum, and energy, for a specified nuclear equation of state. In units in which the speed of light  $c = 1$ , these equations are<sup>5-7</sup>

$$\frac{\partial N}{\partial t} + \nabla \cdot (\vec{v}N) = 0 \quad , \quad (5)$$

$$\frac{\partial \vec{M}}{\partial t} + \nabla \cdot (\vec{v}\vec{M}) = -\nabla p \quad , \quad (6)$$

and

$$\frac{\partial E}{\partial t} + \nabla \cdot (\vec{v}E) = -\nabla \cdot (\vec{v}p) \quad , \quad (7)$$

where  $N$ ,  $\vec{M}$ , and  $E$  are respectively the nucleon number density, momentum density, and energy density (including rest energy) in the laboratory reference frame and  $\vec{v}$  is the velocity of matter relative to the laboratory frame. The three laboratory-frame quantities are related to rest-frame quantities by

$$N = \gamma n, \quad (8)$$

$$\vec{M} = \gamma^2 (\epsilon + p) \vec{v} \quad , \quad (9)$$

and

$$E = \gamma^2 (\epsilon + p) - p \quad , \quad (10)$$

where  $\gamma = (1 - v^2)^{-1/2}$  and  $\epsilon$  is the internal energy density in the rest frame, which is related to the internal energy per nucleon of Eq. (1) by

$$\epsilon = [m_0 + E(n, I)]n \quad , \quad (11)$$

including the nucleon mass  $m_0$ .

For a given nuclear equation of state and for given initial conditions, we solve these equations numerically in three spatial dimensions by use of a particle-in-cell finite-difference computing method.<sup>5-8</sup> In this technique, the fluid is represented by discrete Lagrangian computational particles, which move through a mesh consisting of fixed cubical Eulerian cells. From finite-difference representations of Eqs. (5)-(7), the values of  $N$ ,  $M$ , and  $E$  for each cell are calculated at later times in terms of preceding values. The values of  $n$ ,  $v$ ,  $\epsilon$ , and  $p$  throughout the mesh are obtained by means of a partial algebraic reduction followed by the iterative solution of a transcendental equation in one unknown.

Some examples of the solutions are shown in Figure 3 for the reaction  $^{20}\text{Ne} + ^{238}\text{U}$  at a laboratory bombarding energy per nucleon of 250 MeV, corresponding to an incident speed that is 62% the speed of light. The nuclear equation of state is given by Eqs. (2)-(4). Each column presents a side view of the matter distribution evolving in time for a different impact parameter. The initial frame in each case shows a  $^{238}\text{U}$  target bombarded from above by a Lorentz-contracted  $^{20}\text{Ne}$  projectile. The projectile and target are represented by computational particles, which are initially aligned so that in the direction perpendicular to the page only a single point is visible. However, as the impulse resulting from the collision propagates throughout the system this alignment is destroyed and additional particles come into view.

The characteristic features of the time evolution vary systematically with impact parameter. In nearly central collisions the target and projectile are substantially deformed, compressed, and excited, with curved shock waves produced. These are followed by rarefaction waves and an overall expansion of the matter into a moderately wide distribution of angles. At the other extreme, in peripheral collisions the projectile is fragmented into a portion that proceeds roughly straight ahead at its original velocity and another portion that deposits its energy in the target. This disturbs the target much less violently than in nearly central collisions, and its deformation, compression, and excitation are therefore much less.

We show in Figure 4 the effect of varying the nuclear equation of state on nearly central collisions at the higher laboratory bombarding energy per nucleon of 393 MeV, corresponding to an incident speed that is 71% the speed of light. The results for the different equations of state are very similar to one another, but for our equation of state with a density isomer the expansion starts somewhat later because the matter is compressed to a higher density than for our two conventional equations of state.

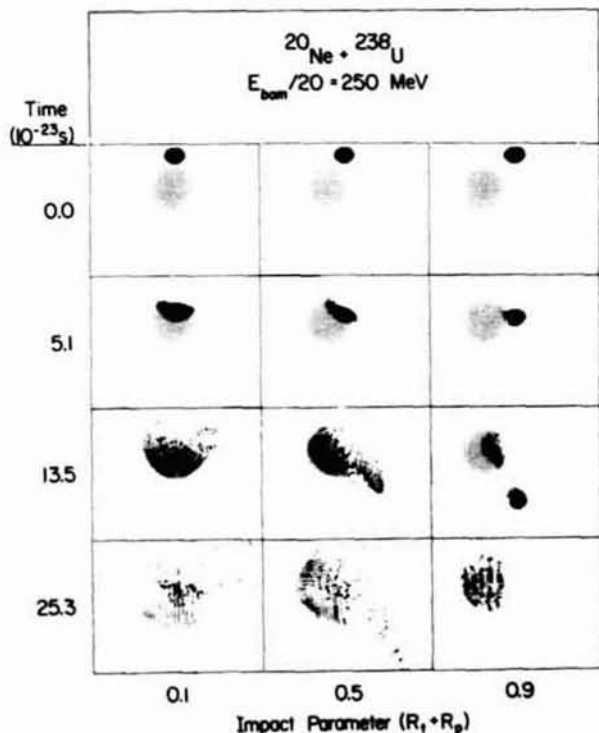


Figure 3. Time evolution of the matter distribution for three impact parameters.

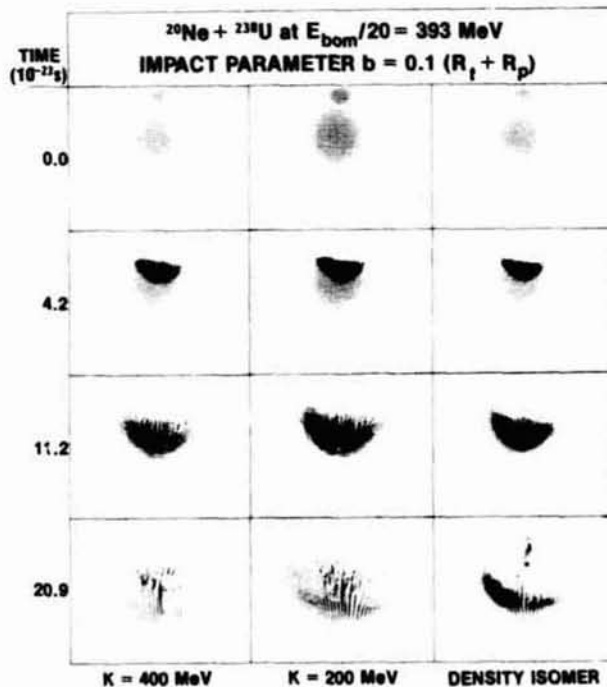


Figure 4. Time evolution of the matter distribution for three nuclear equations of state.

For our conventional equation of state with compressibility coefficient  $K = 200$  MeV, the matter is compressed to a maximum rest-frame density of  $3.9 n_0$  and remains above  $2 n_0$  for  $1.0 \times 10^{-22}$  s. For our stiffer equation of state with  $K = 400$  MeV the matter is compressed to a maximum rest-frame density of  $3.4 n_0$  and remains above  $2 n_0$  for  $0.7 \times 10^{-22}$  s. For our softer equation of state with a density isomer the matter is compressed to a maximum rest-frame density of  $5.1 n_0$  and remains above  $3 n_0$  for  $1.4 \times 10^{-22}$  s and above  $2 n_0$  for  $1.9 \times 10^{-22}$  s.

#### Comparison with experimental data

For the reaction  $^{20}\text{Ne} + ^{238}\text{U}$  at a laboratory bombarding energy per nucleon of 393 MeV, Sandoval et al.<sup>9</sup> have recently measured at the Berkeley Bevalac the distributions in energy and angle of outgoing charged particles, including contributions from protons, deuterons, tritons,  $^3\text{He}$  particles, and  $^4\text{He}$  particles. Also, by selecting only those events containing large numbers of associated charged particles, Stock et al.<sup>10</sup> have measured for nearly central collisions the distributions in energy and angle of outgoing charged particles, including contributions from protons, deuterons, and tritons. Unfortunately, this selection does not eliminate possible contributions from large impact parameters, for which the high-energy yield in forward directions is larger than for central collisions. These experimental data in the form of energy spectra at four laboratory angles ranging from  $30^\circ$  to  $150^\circ$  are shown by the solid circles in Figure 5, where they are compared with histograms calculated for our conventional equation of state with compressibility coefficient  $K = 200$  MeV. We have also made similar comparisons with results calculated for the other two equations of state illustrated in Figure 2.

Our calculated distributions are obtained by constructing from the velocity vectors at some large time the energy and angular distributions for the expanding matter. The small amount of matter that already has passed through the top and side boundaries of the computational mesh is also included. By integrating over the appropriate ranges of impact parameter, we compute the double-differential cross section corresponding both to all impact parameters and to central collisions constituting 15% of the total cross section. The cross section for the outgoing matter distribution is then converted into the cross section  $d^2\sigma/dE d\Omega$  for outgoing charged particles under the assumption of uniform charge density. Some measure of the fairly large numerical inaccuracies inherent in fluid dynamical calculations can be determined from the fluctuations in the histograms, which are obtained using angular bins of  $10^\circ$  width.

Examining first the results for all impact parameters given in left-hand side of Figure 5, we see that at low energy the calculated results are for all angles higher than the experimental results. This is because of our neglect of binding, which causes the entire system to completely disintegrate into slowly moving matter for an arbitrarily small impulse. At higher energy the calculations with all equations of state reproduce, to within numerical uncertainties, the experimental data at all angles. We have found that the nuclear equation of state has little effect on the single-particle-inclusive cross section  $d^2\sigma/dE d\Omega$  integrated over all impact parameters.

We turn now to the results for central collisions, which are given in the right-hand side of Figure 5 for our conventional equation of state with  $K = 200$  MeV. At intermediate angles the results calculated with the three equations of state are very similar to one another, to within numerical uncertainties. However, at  $\theta = 30^\circ$  the slope of the energy spectrum decreases significantly as we go from a stiff equation of state with  $K = 400$  MeV through an intermediate one with  $K = 200$  MeV to a soft one that contains a density isomer. Also, at  $\theta = 150^\circ$  the results calculated for the density isomer are somewhat higher than those calculated for the two conventional equations of state. These differences arise because the softer density-isomer equation of state leads to higher initial density and thermal energy per nucleon, which increases the thermal contribution to the cross section in regions where it would otherwise be small.

Because of our neglect of binding, at low energy the calculated results for central collisions are also higher than the experimental results for all angles and equations of state except for  $\theta = 150^\circ$  with the two conventional equations of state, where the rapid expansion in the backward direction suppresses the cross section. At higher energy the calculations with all equations of state reproduce, to within numerical uncertainties, the experimental data at all angles except  $\theta = 30^\circ$ , where the calculated energy spectra for all three equations of state have significantly larger slopes than the experimental spectrum. This important discrepancy for central collisions in the forward direction could arise from several different possibilities, but the most likely is that upon contact the target and projectile interpenetrate substantially. This interpenetration can be taken into account, while retaining some degree of coherent collective flow, by means of a nuclear two-fluid model, to which we now turn our attention.

### Nuclear two-fluid dynamics

In the nuclear two-fluid model coupled relativistic equations of motion are solved for separate target and projectile nuclear fluids.<sup>5,11</sup> The terms in the equations that couple the two nuclear fluids are obtained from the cross section and mean longitudinal momentum transfer for free nucleon-nucleon collisions. At low relative velocities the target and projectile fluids merge, in which case conventional relativistic nuclear fluid dynamics (which we alternatively refer to as one-fluid dynamics) is recovered.

The equations of motion for the target and projectile nuclear fluids express the conservation of nucleon number, energy, and momentum, plus the transfer of energy and momentum between the two fluids. For a given fluid, the relativistic equations of motion are analogous to Eqs. (5)-(7) for conventional nuclear fluid dynamics, but contain in addition coupling terms that describe the transfer of energy and momentum from one fluid to the other as they interpenetrate. In particular, when the relative velocity of the two fluids is large compared to the Fermi velocity of the nucleons comprising each fluid, the relativistic equations of motion for fluid 1 are<sup>5,11</sup>

$$\frac{\partial N_1}{\partial t} + \nabla \cdot (\vec{v}_1 N_1) = 0 \quad , \quad (12)$$

$$\frac{\partial \vec{M}_1}{\partial t} + \nabla \cdot (\vec{v}_1 \vec{M}_1) = -\nabla p_1 - D(\gamma_1 \vec{v}_1 - \gamma_2 \vec{v}_2) \quad , \quad (13)$$

and

$$\frac{\partial E_1}{\partial t} + \nabla \cdot (\vec{v}_1 E_1) = -\nabla \cdot (\vec{v}_1 p_1) - D(\gamma_1 - \gamma_2) \quad ; \quad (14)$$

those for fluid 2 are obtained by interchanging the subscripts 1 and 2. The drag function  $D$  involves the nucleon number densities and velocities of the two fluids, as well as the

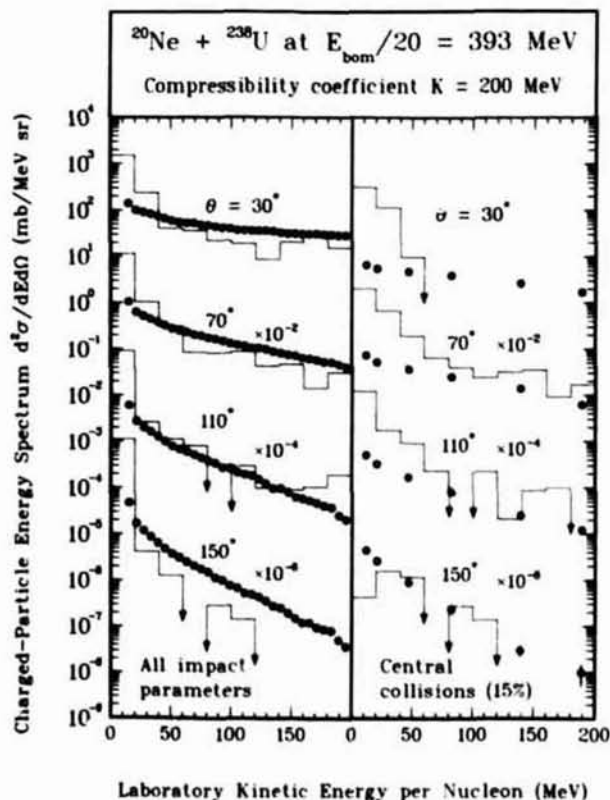


Figure 5. Comparison of calculated histograms with experimental points (Refs. 9 and 10).

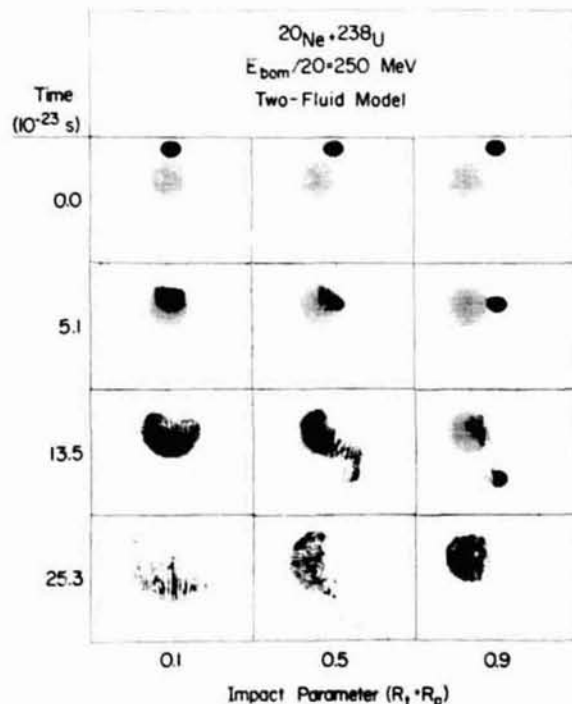


Figure 6. Time evolution of the matter distribution calculated in the two-fluid model.

cross section and average longitudinal momentum transfer for free nucleon-nucleon collisions. For the nuclear equation of state specified by Eqs. (2)-(4), these equations of motion are solved by use of a two-fluid generalization of the relativistic particle-in-cell technique.<sup>5, 8, 11</sup>

We show in Figure 6 some examples of the two-fluid solutions for the reaction  $^{20}\text{Ne} + ^{238}\text{U}$  at a laboratory bombarding energy per nucleon of 250 MeV. These results are qualitatively similar to those shown in Figure 3 for conventional nuclear fluid dynamics, especially during the later stages of the process. However, because the target and projectile interpenetrate somewhat before they begin to respond to the presence of the other, the initial compression is less and the amount of matter emerging in the backward direction is less in the two-fluid model than in conventional nuclear fluid dynamics.

Figure 7 shows the resulting energy spectra calculated for central collisions in both the one-fluid and two-fluid models with the same equation of state, along with the experimental data of Stock et al.<sup>10</sup> For the three angles  $\theta = 70^\circ, 110^\circ,$  and  $150^\circ$ , the two models reproduce equally well, to within numerical uncertainties, the experimental data at high energy and are both larger than the experimental data at low energy because of our neglect of binding. For  $\theta = 30^\circ$ , the two-fluid model agrees with the experimental data substantially better than does the one-fluid model, although the slope calculated from the two-fluid model is still somewhat larger than the experimental slope. However, as shown earlier for the one-fluid model, a softer nuclear equation of state than the one used here would increase slightly the calculated high-energy yield in forward directions.

An alternative and perhaps more illuminating way of making the comparisons for central collisions is in the form of angular distributions for fixed outgoing laboratory momentum per nucleon, as shown in Figure 8. The experimental angular distributions for low outgoing momenta contain a small peak that shifts to smaller angles and finally disappears for higher outgoing momenta. Unfortunately, this peak could be the result of either the neglect of  $^3\text{He}$ ,  $^4\text{He}$ , and heavier composite particles, whose yields are concentrated at low energies and forward directions, or the Coulomb interaction, which provides a transverse driving force for slow-moving charged particles.

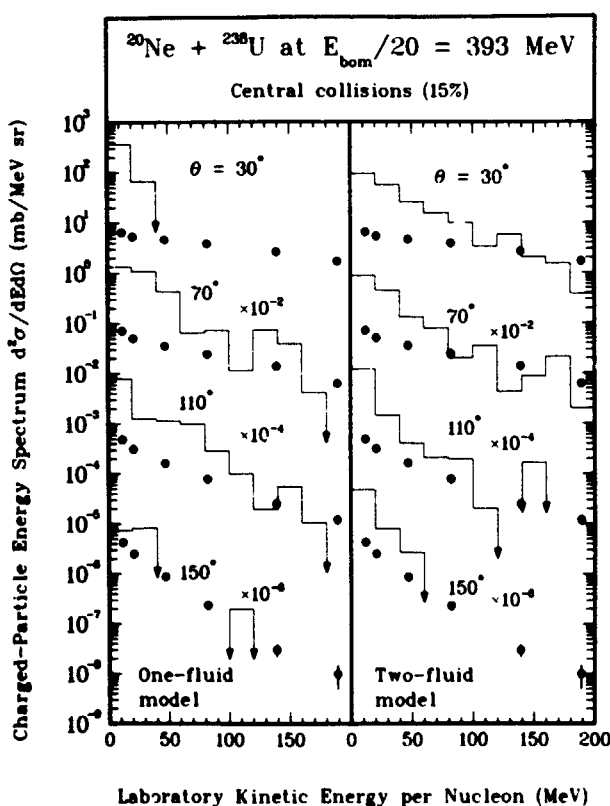


Figure 7. Comparison of calculated histograms with experimental points (Ref. 10).

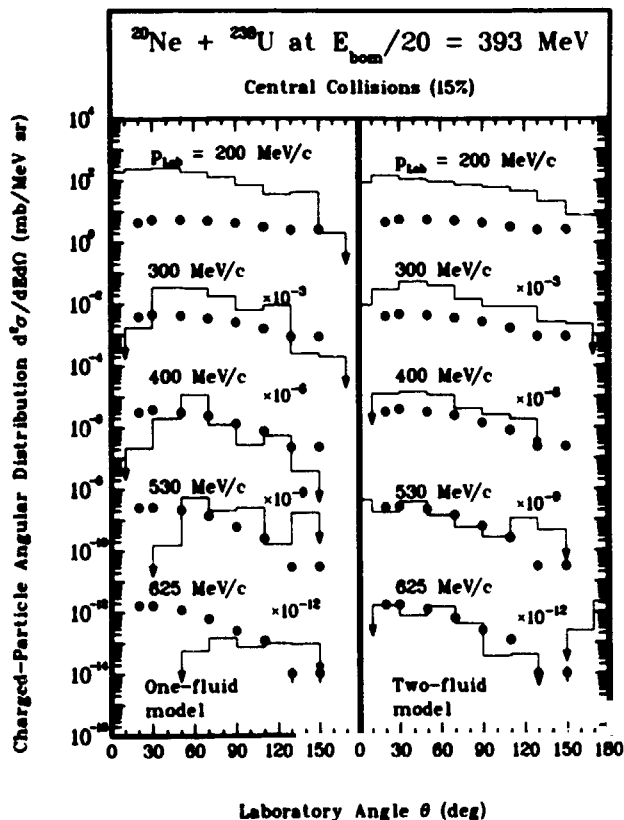


Figure 8. Comparison of calculated histograms with experimental points (Ref. 10).

The histograms are calculated with energy bins of 20 MeV. Because of our neglect of binding, the results for the lowest outgoing momentum calculated in both the one-fluid and two-fluid models are much larger than the experimental data. With increasing outgoing momentum, the one-fluid model predicts angular distributions that are narrower than the experimental distributions and that are peaked at increasingly larger angles, which is opposite to the experimental trend. However, as shown by Stöcker et al.,<sup>3</sup> the agreement between the one-fluid model and experiment would be improved by superimposing the remaining thermal energy at a freezeout density at which fluid dynamics ceases to be valid. The two-fluid model predicts angular distributions with peaks that shift to smaller angles with increasing outgoing momentum, as is observed experimentally. For intermediate outgoing momenta the experimental data are lower in absolute value than the two-fluid calculations, but for the two highest outgoing momenta the experimental data agree with the two-fluid calculations to within their numerical uncertainties. By comparison, microscopic models based on independent two-particle collisions yield for central collisions angular distributions that are essentially forward peaked at all outgoing energy.<sup>1-3</sup>

### Conclusions

With some qualifications, we conclude that in relativistic nuclear collisions the target and projectile interpenetrate substantially upon contact, but that some degree of coherent collective flow is involved. Although conventional relativistic nuclear fluid dynamics is deficient in several respects, relativistic nuclear two-fluid dynamics satisfactorily describes many aspects of relativistic nuclear collisions. Because the calculated results are not very sensitive to the input nuclear equation of state, we do not yet know whether or not there are any phase transitions as the nuclear density is increased. The answer to this question is relevant not only to atomic nuclei but also to neutron stars, illustrating once again how drops and bubbles help unify our understanding of physical systems differing in size by twenty orders of magnitude.

### Acknowledgments

We are grateful to R. Stock, Y. Yariv, Z. Fraenkel, and B. Schürmann for enlightening discussions and for providing us with their experimental data and theoretical calculations prior to publication. This work was supported by the U. S. Department of Energy.

### References

1. Yariv, Y. and Fraenkel, Z., "Intranuclear Cascade Calculation of High Energy Heavy Ion Collisions: Effect of Interactions between Cascade Particles," Phys. Rev. C, Vol. 24, pp. 488-494. 1981. Also private communication.
2. Schürmann, B. and Chemtob, M., "Direct Versus Thermal Particle Emission in High-Energy Heavy-Ion Collisions: Multiplicity-Selected Proton Inclusive Spectra," Z. Phys. A, Vol. 294, pp. 371-376. 1980. Also private communication.
3. Stöcker, H., Riedel, C., Yariv, Y., Csernai, L. P., Buchwald, G., Graebner, G., Maruhn, J. A., Greiner, W., Frankel, K., Gyulassy, M., Schürmann, B., Westfall, G. D., Stevenson, J. D., Nix, J. R., and Strottman, D., "Nuclear Fluid Dynamics versus Intranuclear Cascade--Possible Evidence for Collective Flow in Central High Energy Nuclear Collisions," Lawrence Berkeley Laboratory Preprint No. LBL-12634. 1981.
4. Gyulassy, M. and Greiner, W., "Critical Scattering and Pionic Instabilities in Heavy Ion Collisions," Ann. Phys. (N. Y.), Vol. 109, pp. 485-527. 1977.
5. Nix, J. R., "Theory of High-Energy Heavy-Ion Collisions," Prog. Part. Nucl. Phys., Vol. 2, pp. 237-284. 1979.
6. Amsden, A. A., Harlow, F. H., and Nix, J. R., "Relativistic Nuclear Fluid Dynamics," Phys. Rev. C, Vol. 15, pp. 2059-2071. 1977.
7. Nix, J. R. and Strottman, D., "Effect of a Density Isomer on High-Energy Heavy-Ion Collisions," Phys. Rev. C, Vol. 23, pp. 2548-2556. 1981.
8. Harlow, F. H., Amsden, A. A., and Nix, J. R., "Relativistic Fluid Dynamics Calculations with the Particle-in-Cell Technique," J. Comp. Phys., Vol. 20, pp. 119-129. 1976.
9. Sandoval, A., Gutbrod, H. H., Meyer, W. G., Stock, R., Lukner, C., Poskanzer, A. M., Gosset, J., Jourdain, J. C., King, C. H., King, G., Nguyen, V. S., Westfall, G. D., and Wolf, K. L., "Spectra of p, d, and t from Relativistic Nuclear Collisions," Phys. Rev. C, Vol. 21, pp. 1321-1343. 1980.
10. Stock, R., Gutbrod, H. H., Meyer, W. G., Poskanzer, A. M., Sandoval, A., Gosset, J., King, C. H., King, G., Lukner, C., Nguyen, V. S., Westfall, G. D., and Wolf, K. L., "Emission Patterns in Central and Peripheral Relativistic Heavy-Ion Collisions," Phys. Rev. Lett., Vol. 44, pp. 1243-1246. 1980. Also private communication.
11. Amsden, A. A., Goldhaber, A. S., Harlow, F. H., and Nix, J. R., "Relativistic Two-Fluid Model of Nucleus-Nucleus Collisions," Phys. Rev. C, Vol. 17, pp. 2080-2096. 1978.

V. 30  
N82 23454

Studies of the Nuclear Equation of State Using Numerical Calculations  
of Nuclear Drop Collisions

C. T. Alonso, J. M. LeBlanc, and J. R. Wilson  
Lawrence Livermore National Laboratory, P. O. Box 808, L-18, Livermore, CA. 94550

Abstract

A numerical calculation for the full thermal dynamics of colliding nuclei has been developed. Preliminary results are reported for the thermal fluid dynamics in such processes as Coulomb scattering, fusion, fusion-fission, bulk oscillations, compression with heating, and collisions of heated nuclei.

I. Introduction

The preceding paper by Ray Nix summarized high-energy nuclear collision calculations using relativistic fluid dynamics. In this paper we shall discuss lower-energy nuclear collisions, and we shall change the emphasis from predicting outgoing multi-particle distributions to attempting to calculate the interior thermal properties of the nuclear fluid during and after a collision process. We present this study as an example of a methodology for treating the dynamics of any hot compressible fluid drop with known material properties. In our particular case we have arrived at the material properties of our exotic nuclear fluid by solving a meson field equation integrally with the thermal dynamics. For more common materials the thermal fluid dynamic methods presented here can be used in a more straightforward manner with an analytical equation of state.

The original motivation for this study came, not from nuclear physics or from fluid dynamics, but from a critical problem in astrophysics: as increasingly more accurate modelling is being included in calculations of stellar collapse, it is becoming more difficult to get those calculations to result in a supernova explosion (1). The calculations end, not with a bang, but with a whimper. Supernova explosions, while not a common sight, are definitely known to occur, of course, and the astrophysicists amongst us would like to be able to predict when they occur.

A major remaining uncertainty in stellar collapse calculations is the equation of state of nuclear matter (NEOS). The equation of state is a fundamental relationship between the pressure and the density and internal energy of a fluid. In order to predict supernova explosions, the current collapse calculations of J. Wilson seem to demand rather radical departures from the currently fashionable NEOS.

The material description of a star nearing the end of its collapse is given in Table I. At densities around  $10^{14}$  gm/cm<sup>3</sup> the constituent nuclei are almost touching and the temperature of the nuclear material is around 8 - 10 MeV. The heat capacity of the nucleus will determine whether the nuclei can thermally disintegrate under these conditions. Thermal disintegration is important because a free nucleon gas creates extra thermal pressures that help to generate an explosion.

Heavy nuclei, in the laboratory at least, exhibit a large number of excited states, and their extrapolated heat capacity appears to be so large that the nuclear matter is too "stiff" during collapse, producing non-exploding stars. While we don't understand all the implications at this time, J. Wilson's collapse computations might be interpreted to mean that supernova explosions require a "softer" NEOS at high densities and temperatures than current nuclear theory predicts.

Until recently, laboratory heavy-ion experiments were confined to nuclear matter near zero temperatures, and extrapolations to higher densities and temperatures led to widely varying results. During the last decade, however, high-energy heavy-ion accelerators have allowed nuclear researchers to observe experimentally the collisions of heavy nuclei and their subsequent excitation and breakup. The goal from the NEOS point of view is to obtain some information about the heating and compression of the composite nuclear fluid before it disintegrates. In heavy ion collisions excitation temperatures as high as 80 MeV are not uncommon (as deduced from the Maxwellian distribution of the emitted fragments; see Figure 1) (2). At low excitation energies the temperature dependence is that of a Fermi gas and at high excitations the temperature follows a classical Boltzmann gas law. High compressions have not yet been definitively observed, though there is intense interest in creating high compression because of a theoretically-predicted phase transition at about twice normal density. At this density the nuclear matter might exhibit a pion condensation, a state which contains many bound pions. Even higher compression might lead to a "density isomer", a stable state of very high density (3).

Thus it is extremely important, for the astrophysicist as well as for the nuclear physicist, that we understand the NEOS at high densities and temperatures. One way to approach this understanding is to adopt a NEOS and study its consequences for heavy ion collisions, looking for predicted phenomena that will help to pin down the exact form of the NEOS. We have begun such a study. In the next section we describe the NEOS approach taken by J. Wilson for our initial studies.

Mass	15 M <sub>sun</sub>
Temperature	8-10 MeV
Density	2-5 × 10 <sup>14</sup> gm/cm <sup>3</sup>
Infall	50,000 km/sec
Radius (Fe core)	10 <sup>8</sup> cm
Time since Fe burn depletion	0.3 sec
Neutrino radiation rate (equivalent of visible luminosity of 10 <sup>10</sup> of the largest galaxies in the universe)	10 <sup>47</sup> W

Table I: Stellar collapse conditions just before bounce.

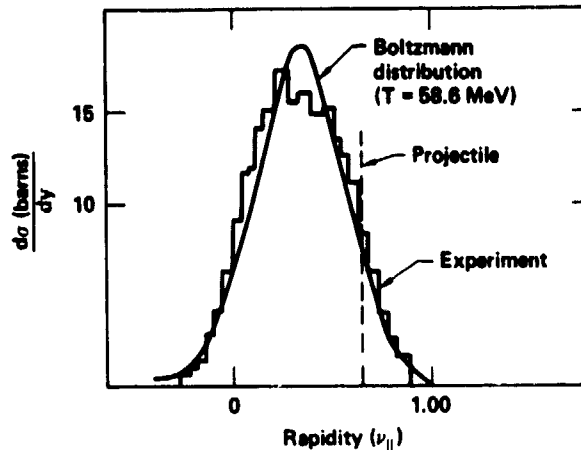


Figure 1: Maxwellian distribution of fragments from the heavy-ion collision  $^{20}\text{Ne}$  on  $^{238}\text{U}$  at 250 MeV/amu.

## II. The Equation of State

There are at present two approaches generally used to represent the NEOS: first, the use of effective two-nucleon potentials such as the Skyrme interaction (4); and second, a direct calculation of the equilibrium energy per nucleon in terms of the underlying meson field such as the Walecka NEOS (5). All nuclear fluid dynamics (NFD) calculations up to the present have used the first approach; in this paper we report preliminary results from an effort to use the second approach in conjunction with NFD.

The Wilson nuclear equation of state used in this work was derived by solving the classical meson field equations using a Lagrangian energy density given by

$$\mathcal{L} = \frac{1}{2} \left[ g^{ij} \left( \frac{\partial \phi}{\partial x^i} \frac{\partial \phi}{\partial x^j} + \frac{\partial \psi}{\partial x^i} \frac{\partial \psi}{\partial x^j} \right) + m_*^2 \phi^2 \right] + \rho + \epsilon + g\rho\phi + 4\pi eZ\psi \quad (1)$$

where  $\phi$  is a scalar field with effective mass  $m_* = m_\pi(1 + \rho/\rho_0)$ ,  $\psi$  represents the electrostatic field, and  $\rho_0$  and  $g$  are adjustable parameters. The density of nuclear matter is  $\rho$ , the internal energy per nucleon is  $\epsilon$ , and  $Ze$  is the electric charge per nucleon. This choice of Lagrangian was motivated mostly by a desire for simplicity since our lengthy two-dimensional calculations include both dynamic and thermal effects. Also it was felt that the astrophysical calculations for which this model was intended contained greater uncertainties in other quantities than would be introduced by this simple but partially ad hoc Lagrangian.

Whereas the standard approach begins with a microscopic Lagrangian and eliminates the quantum meson fields by replacing them with classical averages, Wilson's approach begins with a combination of microscopic fields and macroscopic densities which is designed to reproduce most of the known properties of nuclear matter. In particular, by including the density-dependent effective meson  $m_*$ , he retrieves in a simple manner the saturation properties induced by the repulsive vector field in more elaborate models.

Wilson's approach is related to the Thomas-Fermi class of approximations used in nuclear and atomic theory. The use of this unusual means of arriving at the equation of state has to be justified by a comparison with more refined NEOS models and with experimental data.

Our NEOS parameters are determined by fitting the dimensionless variables  $g$ ,  $\rho_0$ , and  $m$  so that they reproduce the binding energy, the measured density profiles, and the period of compressible radial oscillations ("breathing mode"), for the complete spectrum of nuclear masses. The fitted values are  $g=0.68$ ,  $\rho_0=0.32$ , and  $m=0.73$ . It is a significant achievement that a model with these three constants alone can reproduce all of the above data. Figure 2 shows the resulting binding energy vs. mass curve compared with experimental values. Figure 3 compares the predicted density profiles for  $^{208}\text{Pb}$  and  $^{56}\text{Fe}$  with the experimentally deduced profiles. The equation of state is plotted in Figure 4. The compressibility implied by this NEOS is 200 MeV, which is close to the experimental value of 210 MeV. For comparison we also show in Figure 4 the state-of-the-art (zero-temperature) NEOS of Walecka (5) as well as the Skyrme NEOS used by Stocker et.al. in their recent studies of nuclear collisions (6). The latter implies a rather high compressibility of 295 MeV, and the Walecka NEOS is even stiffer at higher densities. The Wilson NEOS used in our studies is relatively soft, which may be more appropriate for supernova applications.

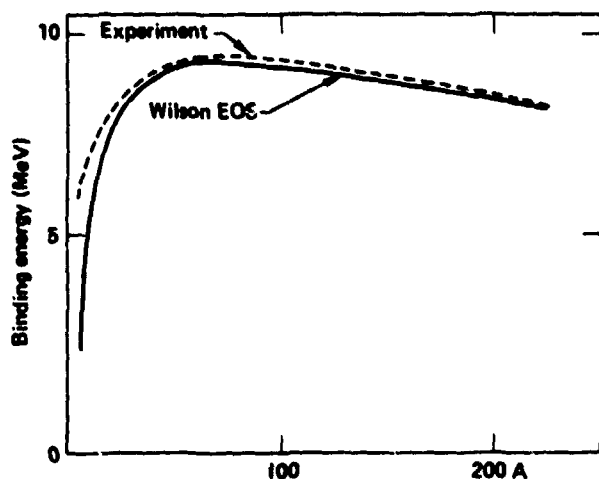


Figure 2: Comparison of experimental binding energies with Wilson's predictions for all masses A.

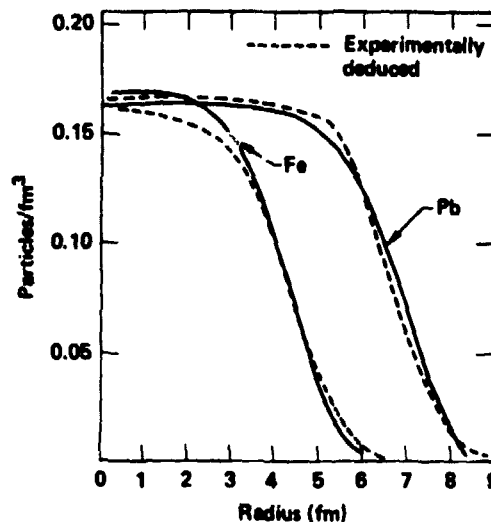


Figure 3: Density profiles for Fe and Pb predicted by the Wilson nuclear equation of state.

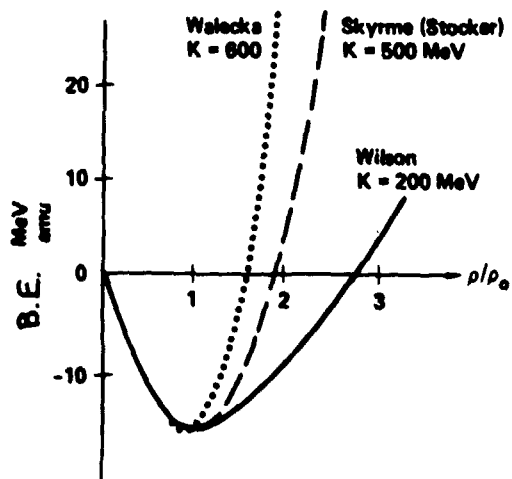


Figure 4: Comparison of current equations of state.

The work presented in this paper represents ongoing studies of dynamic heavy-ion collision processes. These studies compare our predictions using the above Wilson NEOS with experimental data and with the results of other dynamic models. Our main goals are to evaluate the consequences of this NEOS and to explore the effects of temperature, density and pressure gradients on the collision dynamics, both for cold and hot nuclear matter. These calculations are unique in that they simultaneously treat the full macroscopic thermal and dynamic fluid processes, including shock waves, while directly solving a classical scalar meson field equation for the nuclear binding. While the results shown here are for central collisions of inviscid identical nuclei, we also have the capability of treating central collisions of any two nuclei with classical viscosity.

### III. Thermal Physics

Many effective interactions used in current NFD calculations include compressional but not thermal effects. The compressional part of the internal energy is usually represented by a three or four-term expansion of the internal energy as powers of the local density. In our calculations we treat both thermal and compressional contributions to the internal energy. The compressional contributions are calculated directly from the meson field Lagrangian as a function of the internal energy, as described above; the thermal contributions are calculated as described below.

Thermal effects are included in these calculations by directly computing thermal pressures, using the thermal energy of a nonrelativistic Fermi gas:

$$\epsilon_{th} = \int (P_{th} + Q) dV \quad (2)$$

Here  $Q$  is a tensor von-Neumann artificial viscosity. The pressure is obtained from a  $\gamma=5/3$  law:

$$P_{th} = \frac{2}{3} \rho \epsilon_{th} \quad (3)$$

This equation is valid for all temperatures. The degeneracy energy and pressure are given by

$$\epsilon_{deg} = \rho^{2/3} \left[ Z^{5/3} + (1-Z)^{5/3} \right] \quad (4)$$

and

$$P_{deg} = \frac{2}{3} \rho \epsilon_{deg} \quad (5)$$

in units where  $\hbar = 10^{-13}$  cm,  $t = 1/3 \times 10^{-23}$  sec, and  $m = 1$  amu (the velocity of light is unity).

The temperature is not an explicit variable, so we obtain it from the internal energy through a temperature-defining relation given by:

$$\epsilon_{total} = \epsilon_{deg} + \epsilon_{th} = \left[ \epsilon_{deg}^2 + \frac{aT^2 + bT^4}{1 + cT^2} \right]^{1/2} \quad (6)$$

The constants  $a$ ,  $b$ , and  $c$  were derived theoretically to give the correct expression in the limit of a cool Fermi gas ( $x=kT/cdeg$ ):

$$\epsilon_{th} = 1 + \frac{3}{10} \pi^2 x^2 \quad (7)$$

the correct expression in the limit of a hot Boltzmann gas:

$$\epsilon_{th} = \frac{3}{2} x \quad (8)$$

and the exact thermal energy in the transition region where the chemical potential is equal to  $kT$ .

Thus this temperature-defining relation has been fitted to vary smoothly from low to high temperature regimes. The appropriate numerical values are  $a = 2.96$ ,  $b = 1.5$ , and  $c = 0.66$ .

#### IV. Computational Method

To solve the full thermal dynamical problem, J. LeBlanc has employed sophisticated hybrid Eulerian-Lagrangian finite difference techniques developed over the years at the Lawrence Livermore National Laboratory. Three conservation equations are solved simultaneously in an Eulerian frame:

- (1) the equation of continuity

$$\frac{d\rho}{dt} = \frac{\partial\rho}{\partial t} + \bar{u} \cdot \bar{\nabla}\rho = -\rho \bar{\nabla} \cdot \bar{u} \quad (9)$$

- (2) energy conservation

$$\frac{d(\rho\epsilon_{th})}{dt} = \frac{\partial(\rho\epsilon_{th})}{\partial t} + \bar{u} \cdot \bar{\nabla}(\rho\epsilon_{th}) = -\rho\epsilon_{th} \bar{\nabla} \cdot \bar{u} - (\rho_{th} + Q) \bar{\nabla} \cdot \bar{u} \quad (10)$$

- (3) momentum conservation

$$\begin{aligned} \frac{d(\rho\bar{u})}{dt} &= \frac{\partial(\rho\bar{u})}{\partial t} + \bar{u} \cdot \nabla(\rho\bar{u}) = -\nabla(P_{tot} + Q) \\ &\quad - \rho \nabla \left[ g\phi + \frac{g\phi^2}{\rho_0} m^2 (1 + \rho/\rho_0) + eZ\psi \right] \end{aligned} \quad (11)$$

where  $Q$  is the von Neumann artificial viscosity for shocks. The fields  $\phi$  and  $\psi$  are solved by iterating two Poisson's equations:

(4) meson field:  $\nabla^2 \phi - m_*^2 \phi = g\rho$  where  $m_* = m(1 + \rho/\rho_0)$  (12)

(5) electrostatic field:  $\nabla^2 \psi = 4\pi\rho Ze$  (13)

These five equations represent the full thermal dynamics of this compressible system.

In our calculations the fundamental variables are the pressures; the internal energy is calculated from  $P_{th}dV$ , while the zone accelerations are calculated from  $P_{total}$ , which includes the degeneracy pressure. Leaving out some technical details, we could describe this process as taking  $\gamma$ -law excursions off the  $T=0$  degeneracy adiabat.

Figure 5 displays the sequential operations performed by the computer code. The Eulerian mesh typically contains around 2000 nodes (the dots shown in the graphics). The basic Lagrangian parts (the pressures and accelerations at time  $t$ ) are calculated first. Next the Eulerian terms are calculated using a second-order accurate implicit scheme on two staggered time-levels. Finally the meson and electrostatic fields are calculated using an overrelaxation method. The whole calculation is extremely fast, taking on the average 60  $\mu\text{sec}/\text{cycle}$  on a 7600. The time step  $\delta t$  is calculated according to several stability and accuracy algorithms, and then the code cycles on to calculate everything for time  $t + \delta t$ . The output is edited in the form of graphics and files on fiche or in movies if desired.

In particular we edit plots of momentum vectors and contours of density, temperature, pressure, and the accelerating potential. Examples are displayed in subsequent figures.

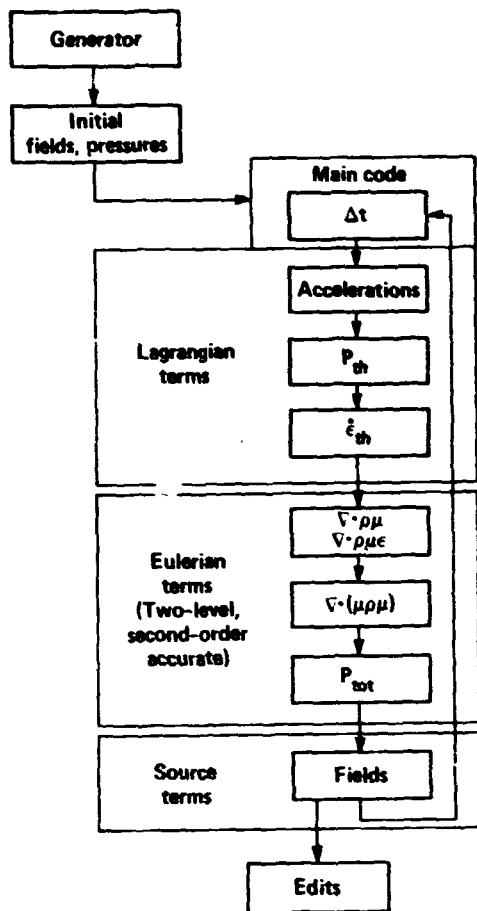


Figure 5: Flow chart for advanced Eulerian thermal hydrodynamics code of J. LeBlanc

## HEAD-ON COLLISION TRAJECTORIES

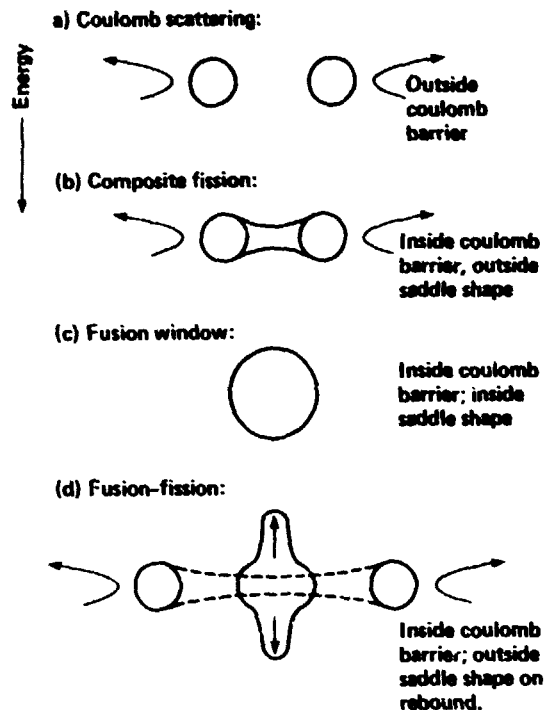


Figure 6: Possible features of symmetric heavy ion collisions as a function of projectile energy.

## V. Nuclear Collisions

In this section we present a variety of collision phenomena predicted by this model, along with comparisons with other dynamic nuclear model predictions and with experimental data. At the lowest bombarding energies we do not expect our results to be accurate because we neglect predominant quantal shell effects. Low-energy collisions are subsonic and basically incompressible. When we increase the relative projectile velocity to the nuclear sound speed, around  $v/c = .16$ , the collisions become supersonic and then interesting compressible and thermal effects are predicted. Of course in a detailed thermal calculation the compressibility

$$K = 9\rho^2 \frac{\partial^2 \epsilon}{\partial \rho^2} \quad (14)$$

depends on the local state of the matter, and therefore so does the sound speed

$$c_s = \left. \frac{\partial P}{\partial \epsilon} \right|_s \quad (15)$$

If local conditions are such that  $c_s$  is smaller than in the stiff ground-state nuclear matter, then interesting compressions are possible.

In our collision calculations we are seeking detailed knowledge about such thermal compression effects. Our hope is that with detailed thermal understanding we will have more control over predicting the compression and dynamics than has heretofore been possible. We shall now review generally what happens in these collisions as the projectile energy is increased.

1. Head-On Collision Trajectories

Figure 6 illustrates head-on collisions, in the center-of-mass system, of two identical nuclei. Five general types of process are possible, in order of increasing energy. If the incoming kinetic energy is so low that the long-range Coulomb repulsion absorbs all the initial kinetic energy before the shorter-range nuclear forces can fuse the nuclei together, then the nuclei turn around and accelerate backward, as shown in trajectory (a). At slightly higher energies the attractive "proximity force" (which is like the molecular Van der Waals force) can partially fuse the nuclei. If the initial kinetic energy is used up before a stable "saddle shape" is reached, then the repulsive Coulomb forces predominate and the partially fused system separates again, as in trajectory (b).

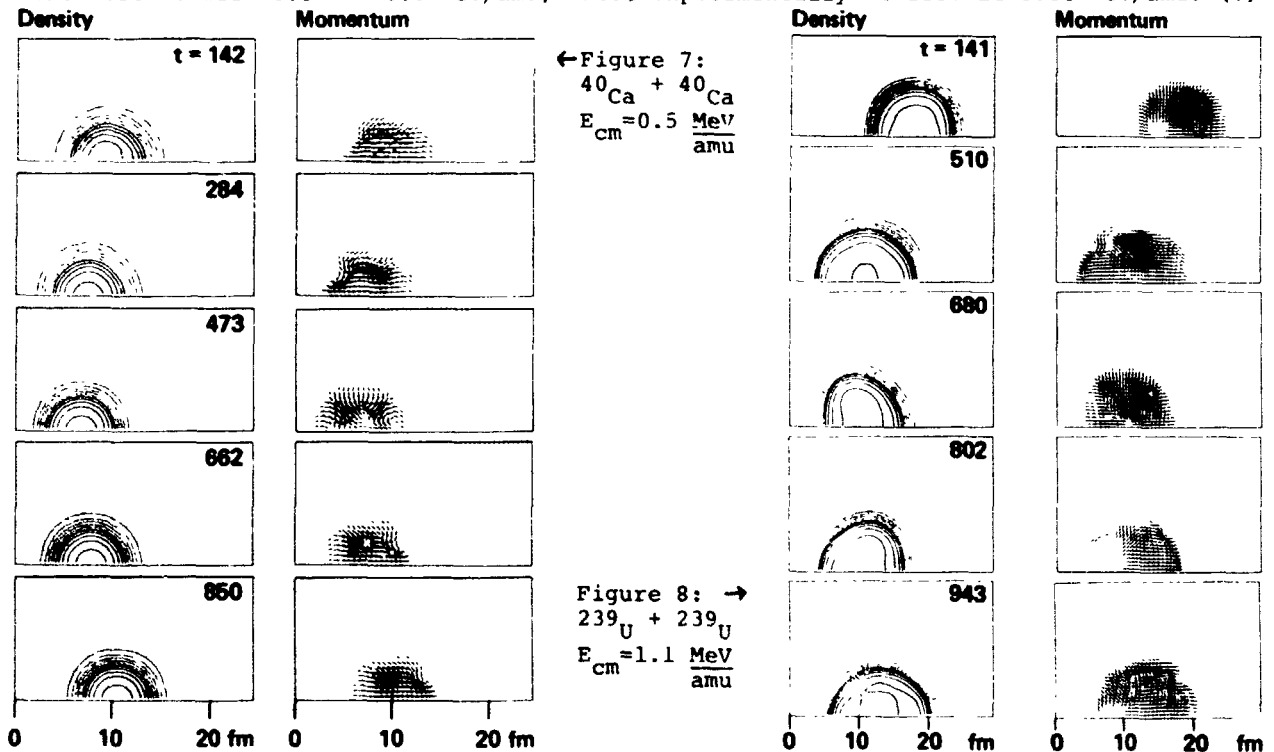
At even higher energies it is possible, at least for the lighter nuclei, to fuse the composite system inside the saddle shape (where attractive nuclear forces just balance the repulsive Coulomb forces), at the same time absorbing most of the initial kinetic energy. This results in a stable fused compound nucleus as in (c). At medium-high energies the nuclei fuse to form a flat disk, which then rebounds out to an elongated spheroid. Here the kinetic energy remains so high that the system fissions on rebound, producing the fusion-fission process of trajectory (d). These higher-energy collisions can result in some exotic shapes. Finally, at relativistic energies the nuclei tend to splat into an expanding disk whose disintegration was discussed by the previous speaker.

The existence of a "fusion window" (c) between composite fission (b) and fusion-fission (d) depends on the size of the compound system. Theoretically a compound nucleus with no kinetic energy reserves will undergo fission if its "fissility"

$$X \sim 0.02 Z^2/A = \text{Coulomb energy/surface energy} \quad (16)$$

exceeds unity. For head-on collisions this occurs roughly for identical projectiles heavier than Sm. Thus we would predict that colliding Ca nuclei would have a fusion window but U nuclei would not. The fusion window was of great interest a decade ago because it made the generation of "superheavy" elements possible. Subsequent experiments implied that the fusion window was much narrower than predicted, probably because of viscous dissipation during the collision. We plan to study viscous effects, but the simulations presented here are for inviscid nuclear matter.

Figure 7 shows the results of our Coulomb scattering calculation of Ca on Ca at an initial kinetic energy of 0.5 MeV/amu in the CMS. The maximum temperature remains relatively cool at 2 MeV and the compression ( $\rho/\rho_0$  where  $\rho_0 = 0.145 \text{ amu/fm}^3$ ) remains near the normal nuclear value. Our computer runs place the fusion barrier somewhere between 0.5 and 0.6 MeV/amu, while experimentally it lies at 0.66 MeV/amu. (7)



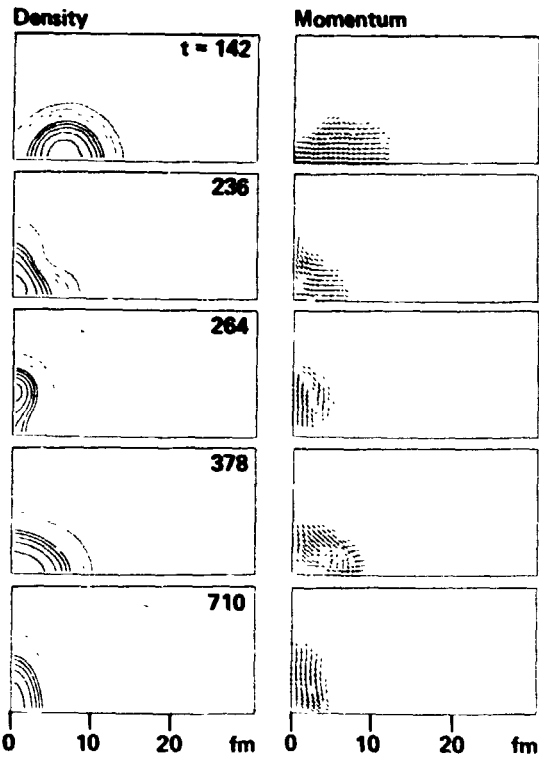


Figure 9:  $^{40}\text{Ca} + ^{40}\text{Ca}$  at  $E_{\text{cm}} = 1.5 \frac{\text{MeV}}{\text{amu}}$

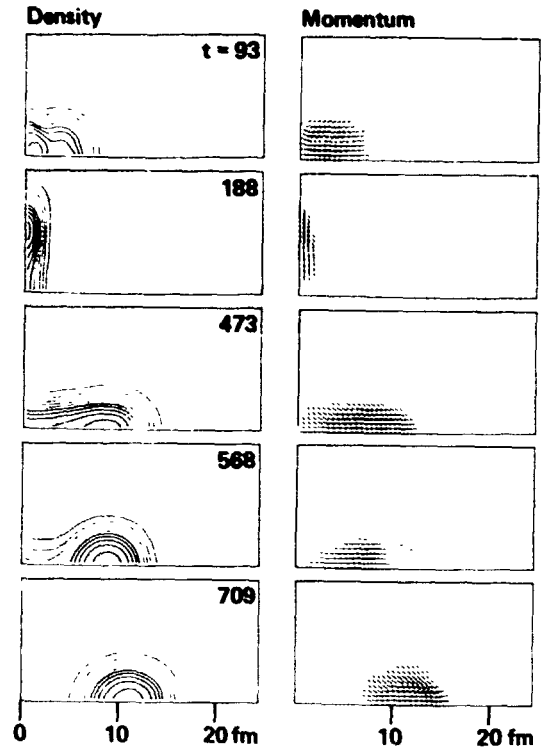


Figure 10:  $^{40}\text{Ca} + ^{40}\text{Ca}$  at  $E_{\text{cm}} = 5 \frac{\text{MeV}}{\text{amu}}$

That is, we currently underestimate the barrier, perhaps indicating a little too much nuclear binding. Time-dependent Hartree-Fock (TDHF) calculations, on the other hand, tend to overestimate the barrier to between 0.7 and 0.9 MeV/amu, depending on the choice of interaction force (7).

A Coulomb scattering calculation for a  $^{239}\text{U}$  collision is shown in Figure 8. Notice the interesting sequence of distorted shapes during closest approach.

Figure 9 shows a fusion process (Ca on Ca) at 1.5 MeV/amu. The composite system necks into a prolate spheroid and then flattens into an oblate disk, from which it rebounds into a spheroid without a neck. This fused compound nucleus then oscillates very much like a classical charged liquid drop, as shown by the later frames in Figure 9. During the initial shock of fusion the compression reached a maximum of 1.3 and the average temperature was around 5 MeV, indicating strong local heating. The temperature tends to increase quickly during the initial fusion process and then to build up slowly thereafter (see Figure 14).

Next in this sequence, Figure 10 shows a high-energy Ca on Ca collision at 5 MeV/amu which demonstrates fusion followed by fission on the rebound. Here the oblate disk gets very extended but the nuclear forces are able to pull it back so that it shoots out into an extended prolate shape which soon fissions. The maximum compression at impact was 1.4. During the expanded oblate stage the average compression was sub-nuclear at 0.7, and the average temperature cooled down to 3 MeV.

If this collision is simulated at even higher energies, then the oblate disk expands so much that it does not stop, and the composite system is presumed to disintegrate into small particles.

Thus our Ca on Ca calculations display the appropriate behavior as a function of initial kinetic energy. The dynamic fusion window for Ca on Ca appears to occur for  $E_{\text{cm}}$  between 0.6 MeV/amu and 4 MeV/amu for the case of this low-viscosity nuclear fluid. The lower limit agrees with the experimental of 0.66 MeV; the upper limit has not been measured to our knowledge. We have not yet established our upper limit precisely; it is somewhere between 3 and 5 MeV/amu.

ORIGINAL PAGE IS  
OF POOR QUALITY

Figure 11 displays the collision and subsequent fission of a  $^{239}\text{U}$  system at  $E_{\text{cm}}=1.8$  MeV/amu. The accelerating potential contours are plotted here. The collision results in a ternary fission of the composite. At lower energies a binary fission results from the collision.

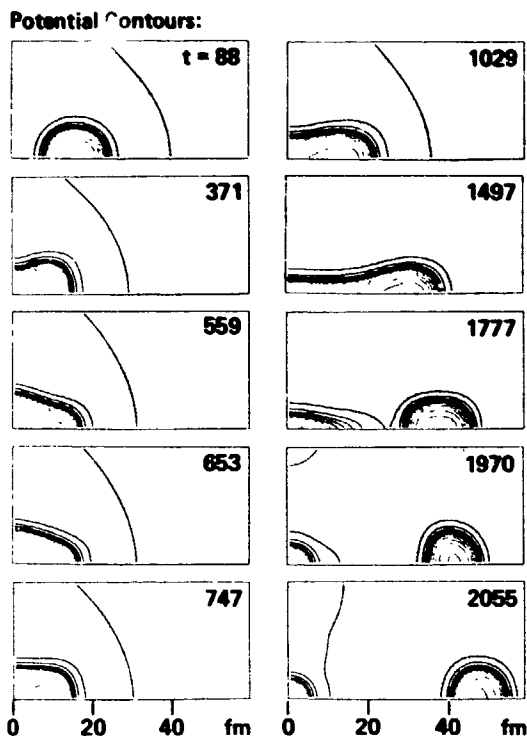


Figure 11:  $^{239}\text{U} + ^{239}\text{U}$  at  $E_{\text{cm}}=1.8$   $\frac{\text{MeV}}{\text{amu}}$

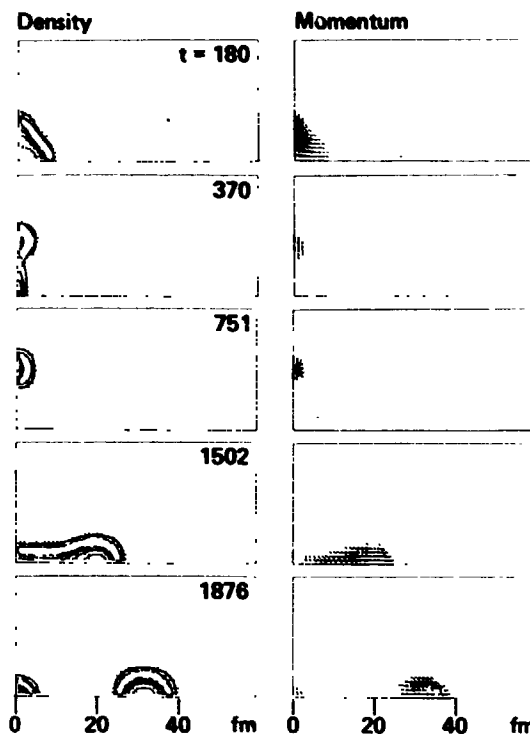


Figure 12:  $^{150}\text{Sm} + ^{150}\text{Sm}$  at  $E_{\text{cm}}=5.2$   $\frac{\text{MeV}}{\text{amu}}$

A final example of collision dynamics is shown in Figure 12. Here  $^{150}\text{Sm}$  collides with itself at 5.2 MeV/amu in the center of mass. The interesting feature is the toroidal shape that forms from the oblate disk. Similar toroidal shapes have been observed in TDHF calculations. We also see them in higher-energy  $^{239}\text{U}$  collisions. The torus expands out with low compression and then collapses in on itself with high compression. The composite then fissions on the rebound.

## 2. Composite Nucleus Oscillations

During and after a low-energy fusion collision, the composite nucleus exhibits two kinds of oscillation. During the collision it undergoes a series of rapid energy oscillations associated with compression waves in the heated composite. After the fusion is complete the heated compound nucleus oscillates in a roughly classical liquid drop manner. These processes are exhibited in Figure 13, where we show the total kinetic energy as a function of time for the collision of two Kr nuclei at 0.5 MeV/amu in the CMS.

The period of the surface oscillations after fusion is  $18 \times 10^{-22}$  sec, which is close to the period predicted by the classical expression for frequency of surface oscillations of a charged liquid drop. Thus at these lower energies the thermal effects generated during the collision do not greatly affect the overall classical kinetic behavior of the compound nucleus. This predicted oscillation behavior can also be taken as evidence that our code is working reasonably at low energies.

At higher collision energies a stable compound nucleus is not formed because it fissions on rebound. The heated fission fragments, however, also undergo roughly classical oscillations as they move apart from each other.

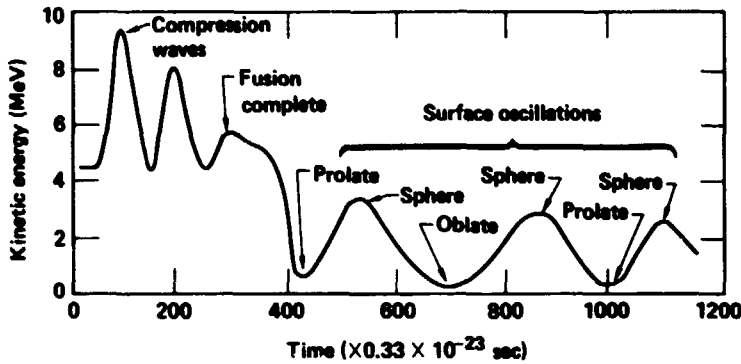


Figure 13: Kinetic energy oscillations of compound nucleus from  $^{80}\text{Kr} + ^{80}\text{Kr}$  at  $E_{cm} = 0.5 \text{ MeV/amu}$ .

### 3. Compression and Heating

Above nuclear excitations of the order of 50 MeV, shell effects disappear in heavy nuclei. This corresponds to a temperature of about 6 MeV using the usual conversion for a Fermi gas: (8)

$$E^* = a T^2 \approx \left( \frac{A_1 + A_2}{8} \right) T^2 \quad (17)$$

At such temperatures, macroscopic features like shapes and fission barriers are influenced by the excitation, and heating effects are important in medium- and high-energy nuclear physics. In collapsing stars the compressed nuclear fluid is at temperatures of 2 - 10 MeV, so thermal changes in the nuclei comprising the material could affect the bulk properties of the star. Figure 14 compares experimentally deduced fragment temperatures with the theoretical Fermi and Boltzmann limits (8).

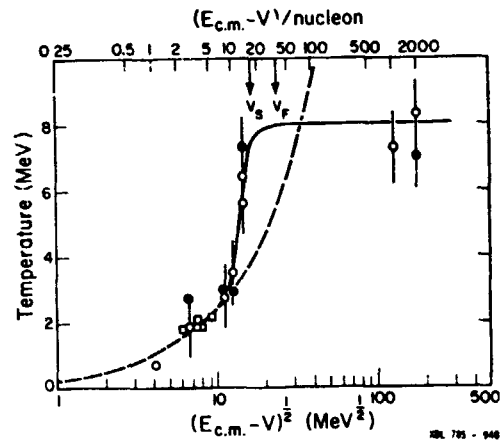
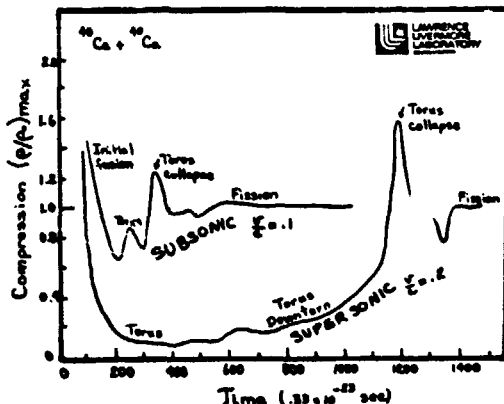


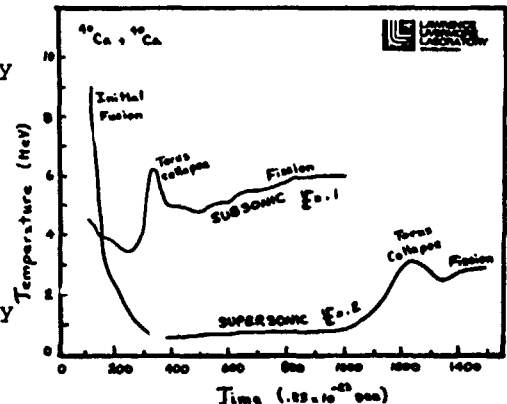
Figure 14: Nuclear Temperatures.

Compression during collisions is of great interest because of the possibility of phase changes. At twice the ground state nuclear density a pion condensation has been predicted. Figure 15 compares the maximum compressions obtained during a barely subsonic  $^{40}\text{Ca}$  fusion collision at 5 MeV/amu and a supersonic collision at 19 MeV/amu. The outstanding feature is the rapid expansion into an underdense torus for the supersonic case. This is accompanied by cooling as shown by the corresponding temperature curves in Figure 16. When the torus collapses, a compression of 1.6 results. It is possible that careful engineering of nuclear dynamics could produce compressions near 2.0. The subsonic collisions remain mostly incompressible, with some compression followed by expansion during the fusion process.



← Figure 15: Maximum compression history for  $^{40}\text{Ca}$  on  $^{40}\text{Ca}$  at  $E_{cm} = 5 \text{ MeV/amu}$ .

→ Figure 16: Average temperature history corresponding to Figure 15.



Thermal expansion also accompanies the higher-energy collisions. As the nuclei fuse the composite heats up and expands. These thermal properties translate into a temperature-dependence for such macroscopic quantities as the surface tension, the Coulomb energy, and the volume energy, as pointed out by Sauer et. al. (9). The static thermal ( $T=2$  MeV) Hartree-Fock calculations of the latter produced smaller changes in the density profile than we see in our heated  $^{40}\text{Ca}$  nuclei.

At high temperatures the fission barrier is lowered due to a decrease in surface tension. We plan to study this process in more detail in the future. Conversely, nuclear material at high temperatures, as in stellar material, might be expected to exhibit different fusion windows and cross sections, both because of thermal expansion and because of softer surface density profiles. We will now discuss this interesting possibility.

#### 4. Collisions of Heated Nuclei:

Our results for collisions of hot nuclei are very preliminary. This type of calculation was accomplished by allowing two cold "laboratory" nuclei to execute a fusion-fission reaction, and then to let the heated fission fragments impact their mirror images by means of reflection boundary conditions on the right-hand mesh boundary. We did this in order to achieve realistic velocity, temperature, and potential profiles in the "initial" heated nucleus.

The reasons for studying collisions of hot nuclei are twofold; first, to examine nuclear collisions in the astrophysical environment; and second, to explore possible ways of creating abnormal nuclear composites using secondary collision fragments in the laboratory. The latter should really be studied using heated projectiles and cold targets, and we have begun such studies as well.

A successful fusion of the hot fission fragments from a  $^{239}\text{U}$  ternary fusion-fission reaction is shown in Figure 17. Unfortunately our code did not edit the masses of the independent fragments, but this hot fused composite is evidently very massive, with a radius around 8.5 fm. This intriguing result should await a careful examination of this new type of calculation before it is to be believed.

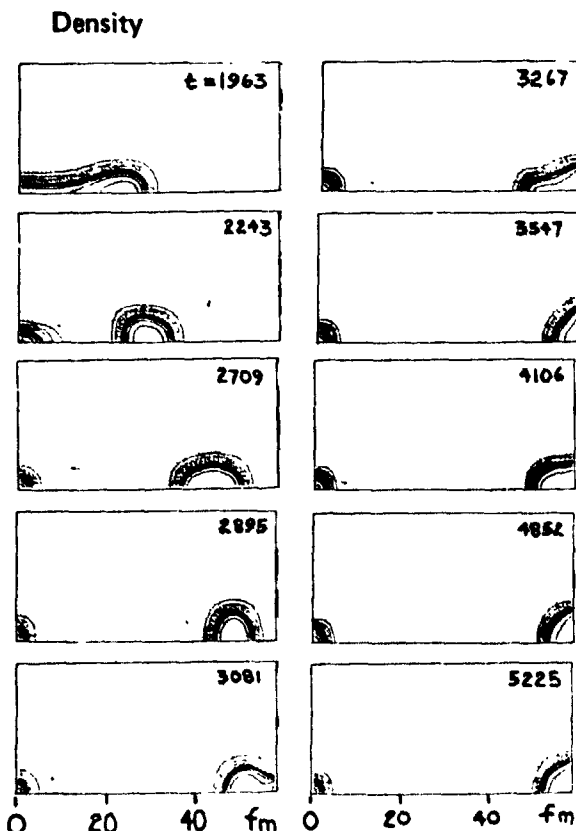


Figure 17: Collision of hot secondary fragment with its mirror image (on RHS).

The results are indeed very preliminary, but there is a suggestion here that the fusion window might be enlarged by pre-conditioning the projectile to higher temperatures or an expanded radius. (However, we have not included viscous effects yet, and the classical viscosity, which goes to  $T^{1/2}$ , will tend to close the fusion window.) Surface oscillations of the secondary fragment could also be used to change the fusion window if the period is engineered, for example, to present an oblate disk shape to the next target nucleus. To observe these phenomena we should concentrate on secondary reactions, tailoring the primary energy to produce the desired characteristics in the secondary.

A phenomenon which may be related has recently been reported by Friedlander et. al. (10). They observe that some secondary fragments display an anomalously short mean free path for their charge. We would like to suggest that these "anomalons" may be secondaries from central collisions that were heated and then expanded and cooled, resulting in a larger geometric cross section than would be calculated for a normal nucleus of that mass. However, for this explanation to be possible the heated nuclei would have to stay in an expanded state for very long times ( $10^{-11}$  sec). This might occur if they cannot radiate away their internal energy. We plan to investigate this possibility quantitatively.

## VI. Conclusions

We have developed a computational method for treating the full thermal dynamics of nonrelativistic compressible nuclear matter. In particular we have begun a systematic study of central collisions of heavy nuclei. Preliminary results were presented for such processes as Coulomb scattering, fusion, fusion-fission, bulk oscillations, compression, heating, and collisions of heated nuclei.

Our main goal at this point was to exercise the calculation through the above variety of difficult-to-model phenomena to verify that it gives generally reasonable results. The predicted behavior in the above processes agrees qualitatively with experimental experience: e.g. low-mass projectiles fuse into a stable compound nucleus; high mass projectiles undergo a fusion-fission process; low-energy projectiles turn around under the influence of Coulomb forces; and perturbed nuclear drops oscillate in a classical manner. In producing such overall good behavior we have shown that the Wilson nuclear equation of state gives reasonable dynamical results.

We have barely begun to analyze the current predictions quantitatively. Much information is contained in these calculations. Besides reproducing some known laboratory phenomena, we have also predicted some interesting features which may or may not be real: temporary toroidal shapes are common in the higher-energy collision calculations, and the high-mass composites tend to fission in a ternary manner with a light remnant in the center of mass. These ternary processes can be checked experimentally if they persist when our calculations are made more quantitative. We also see some very preliminary evidence that pre-heated secondary nuclei can fuse more easily than cold primary nuclei. This would have important implications in both nuclear physics and astrophysics.

Our next step will be to try to systematically fine-tune the code predictions of the available experimental data to a point where the calculations are quantitatively accurate. Our immediate goal is to calculate the detailed temperature, pressure, and density gradients (including shock waves) during both cold and heated nuclear collisions. If this can be done, then the opportunities presented to us are enormous. In a long-range view, one can envision an era of nuclear fluid engineering in which one can carefully control the dynamics of nuclear collisions to produce abnormal composites, perhaps with applications totally unheard of today.

## Acknowledgments

We wish to thank Virginia Taylor for typing and laying out this manuscript.

## References

1. J. Wilson and R. Bowers, "Energy and Technology Review", Lawrence Livermore National Laboratory, February 1980, p. 17.
2. H. Gutbrod et. al., Phys. Rev. Lett. 37, 667 (1976)
3. A. B. Migdal, Sov. Phys. JETP 34, 1184 (1972)
4. T. H. R. Skyrme, Nuc Phys 9, 615 (1959)
5. J. D. Walecka, Annals of Physics 83, 491 (1974)
6. H. Stocker, R. Y. Cusson, J. A. Maruhn, and W. Greiner, Z. Physik A294, 125 (1980)
7. David Scott, LBL-7727, 74 (1976)
8. David Scott, LBL-7727, 117 (1978)
9. G. Saver, H. Chandra, and U. Mosel, Nuc. Phys. A264, 221 (1976)
10. E. M. Friedlander et. al., Phys. Rev. Lett. 45, 1084 (1980)

The size and shape of equilibrium capillary surfaces

Robert Finn

Department of Mathematics, Stanford University, Stanford, California 94305

Abstract

The classical theory of capillarity is concerned largely with size and shape estimates in symmetric asymptotic configurations. Recent developments have led to global results for all symmetric cases, and to new qualitative information on asymptotic properties. Also new stability criteria have been found. It has been discovered that asymmetric situations can lead to behavior that differs strikingly from the symmetric case. When gravity vanishes, capillary surfaces in the accustomed sense may not appear. The question of characterizing those tubes in which surfaces can be found has partially been settled. New progress has been made toward determining the effects of contact angle hysteresis in cases of particular interest.

In 1805, P. S. Laplace (Tr. méc. cél., Suppl. au livre X) introduced the notion of the mean curvature  $H$  of a surface and derived for it, in the representation  $z = u(x,y)$ , the expression

$$2H = \operatorname{div} Tu, \quad \text{with} \quad Tu \equiv \frac{1}{\sqrt{1 + |\nabla u|^2}} \nabla u \quad (1)$$

The context in which this basic contribution appeared was not an abstract study of the geometry of surfaces; it lay instead in his effort to clarify conceptually and describe quantitatively the rise of liquid in a capillary tube. For that problem there holds  $2H = \kappa u$ , where  $\kappa > 0$  is a physical constant, and thus the physical problem is transformed by (1) into an analytical and geometrical one.

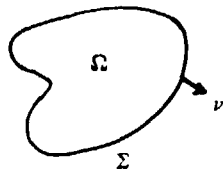


Figure 1

In the same year 1805, T. Young gave a formal reasoning supporting the view that the surface meets the bounding walls in an angle  $\gamma$  depending only on the materials; thus,  $\nu \cdot Tu = \cos \gamma$  on the boundary  $\Sigma$  of a section  $\Omega$  of the tube (Figure 1). Thus one has to solve a nonlinear equation under a nonlinear boundary condition.

For the problem considered, not a single nontrivial explicit solution is known. However, Laplace integrated (1) approximately in the case of a "narrow" circular tube of radius  $a$  to obtain the celebrated formula

$$u_0 \sim L(a; \gamma) \equiv 2 \frac{\cos \gamma}{\kappa a} - \frac{a}{\cos \gamma} \left( 1 - \frac{2}{3} \frac{1 - \sin^3 \gamma}{\cos^2 \gamma} \right) \quad (2)$$

for the height  $u_0$  on the axis of symmetry (Figure 2).

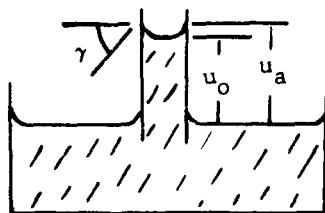


Figure 2

Laplace did not prove (2), nor did he indicate how small  $a$  must be in order to achieve a prescribed accuracy. The first proof that (2) is correct was given by D. Siegel (Pacific J. Math., 1980). Later, Finn (ZAMM, 1981) gave a simpler proof with improved error estimates. The method derives from a discovery of Laplace, that the volume of fluid lifted in the tube is given explicitly by  $2\pi a \kappa^{-1} \cos \gamma$ . The volume is compared with that lifted by certain spherical caps through  $u_0$ . One is led to the relations

$$L(a; \gamma) < u_0 < u_0^+ < 2 \frac{\cos \gamma}{\kappa a} \quad (3)$$

where  $u_0^+$  is the unique nontrivial solution of the equation

$$u_0^4 - \frac{2}{\kappa a} u_0^3 \cos \gamma + \frac{2}{\kappa} u_0^2 - \frac{16}{3\kappa^3 a^2} \left[ 1 - \left( 1 - \frac{\kappa^2 a^2}{4} u_0^2 \right)^{3/2} \right] = 0. \quad (4)$$

Thus, the Laplace formula provides a strict lower bound for  $u_0$ .

The method leads also to a new bound for the height  $u_a$  at the contact line (Fig. 2)

$$u_a < \frac{2}{\kappa a} \cos \gamma + \frac{a}{\cos \gamma} \left( \frac{1}{1 + \sin \gamma} - \frac{1 - \sin^3 \gamma}{3 \cos^2 \gamma} \right). \quad (5)$$

Also a lower bound analogous to the upper bound in (3) can be given.

The size of a capillary tube is best measured in terms of the nondimensional parameter  $B = \kappa a^2$ . (For a water-air interface on the earth's surface,  $\kappa \sim 29$ .) If  $B \ll 1$ , (3) and (5) yield quite precise estimates. For larger  $B$ , one writes the equation in the parametric form

$$\frac{dr}{d\psi} = \frac{r \cos \psi}{\kappa r u - \sin \psi}, \quad \frac{du}{d\psi} = \frac{r \sin \psi}{\kappa r u - \sin \psi} \quad (6)$$

in terms of the inclination angle  $\psi$  of a vertical section of the solution surface. (6) can be integrated approximately to obtain a hierarchy of estimates, valid for all  $B$  and asymptotically exact both for small and large  $B$  (Finn, Moscow Math. Soc., vol. dedicated to Vekua, 1978; Siegel, Pacific J. Math., 1980; Finn, Pacific J. Math., 1980). We mention the results

$$\sqrt{\frac{p+1}{p}} \sqrt{\frac{2}{\kappa} (1 - \cos \psi) + \frac{p+1}{4} u_0^2} < u < 2 \frac{\sin \psi}{\kappa r} + \sqrt{\frac{2}{\kappa} (1 - \cos \psi) - \frac{\sin^2 \psi}{\kappa^2 r^2} + \frac{u_0^2}{2}} \quad (7)$$

with  $p = \sqrt{1 + \frac{\kappa r^2}{1 + \cos \psi}}$ . These (and other related) formulas yield the first general estimates valid in the range  $1 < B < 10$ . They also have remarkable monotonicity properties, which lead to precise estimates for the meniscus height  $q = u_a - u_0$ .

Brulois (Dissertation, Stanford University, 1981) has given a formal iterative procedure leading to an arbitrarily good upper bound for  $u_0$ .

The above methods can be modified and extended to apply also to the problem of the "sessile" liquid drop, and they lead to general estimates for the parameters describing its shape (Figure 3). Here the "physical" prescribed data are in general the volume  $V$

and  $\gamma$ , rather than  $a$  and  $\gamma$  as above. It turns out there is a "reciprocity" between the two problems, becoming arbitrarily exact for small and for large  $B$  (Finn, Pacific J. Math., 1980).

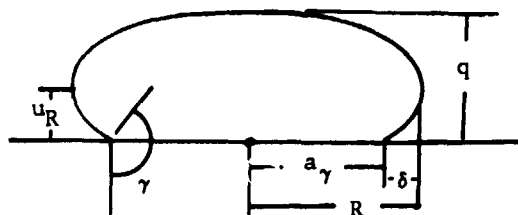


Figure 3

$$\lambda^3(\gamma) = \frac{3}{4 \sin^3 \gamma} \int_0^\gamma \sin^3 \theta d\theta.$$

Then if  $\gamma \neq \pi$  there holds

$$\lim_{B \rightarrow 0} \frac{q}{B} = \lambda^2(\gamma) \quad (8)$$

while if  $\gamma = \pi$  we find

$$\lim_{B \rightarrow 0} \frac{B^2}{B} = \frac{3}{2} \quad (9)$$

Thus, the rate of decrease of wetted surface is nonuniform in contact angle. If  $\gamma = \pi$  the drop rests--for small  $B$ --on a negligibly small surface (Figure 4). It seems likely that this surface acts as a point of support about which the drop can rotate rigidly when disturbed slightly, thus establishing new points of contact with the supporting plane and leading to a kind of "rolling" instability (Finn, J. Reine Angew. Math., to appear).

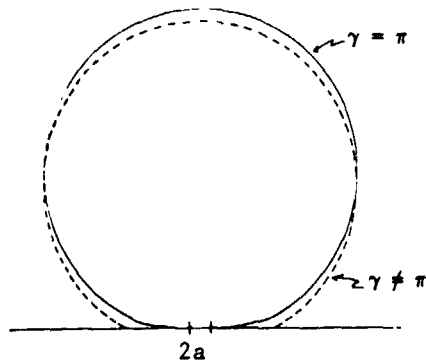


Figure 4

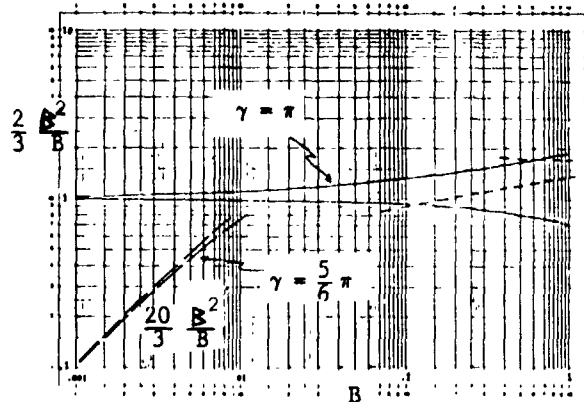


Figure 5

The nonuniformity is illustrated in Figure 5, which shows--on logarithmic scale--upper and lower bounds for the expression in (9) when  $\gamma = \pi$ , and for ten times that expression when  $\gamma = \frac{5}{6} \pi$ .

For large drops, one finds the exact asymptotic relation for the "overhang"

$$\lim_{B \rightarrow \infty} \sqrt{\kappa}(R - a) = \sqrt{2} - \log(1 + \sqrt{2}) - 2 \cos \frac{\gamma}{2} + \log \cot \frac{\gamma}{4} \quad (10)$$

If  $\gamma = \pi$ , this relation simplifies to

$$\lim_{B \rightarrow \infty} \sqrt{\kappa}(R - a) = \sqrt{2} - \log(1 + \sqrt{2}) \quad (11)$$

Also,  $R$ ,  $a$  can be estimated in terms of  $B$ .

The behavior of liquid in a capillary tube with asymmetric section  $\Omega$  can differ in striking ways from what happens with a circular section. For surfaces of the form  $z(x,y)$  general estimates can be obtained by comparison with symmetric surfaces, using maximum principles that are idiosyncratic for the equation. An important distinction between these principles and the classical ones for elliptic equations is that the comparison on the boundary need be prescribed only up to a set of Hausdorff measure zero. The distinction has as consequence the following result (Concus and Finn, Acta Math., 1974):

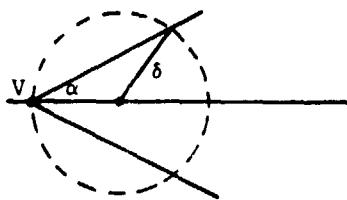


Figure 6

Let  $u(x,y)$  be a capillary surface over a section  $\Omega$  which contains the intersection of a ball  $B_\delta$  of radius  $\delta$  and a wedge of opening  $2\alpha$  (Figure 6). Then if  $\alpha + \gamma > \pi/2$ , there holds  $u < \frac{2}{\kappa\delta} + \delta$ ; if  $\alpha + \gamma < \pi/2$ , then  $u \rightarrow \infty$  at  $V$ . Thus the solutions depend discontinuously on the boundary data. Figure 7 shows a "kitchen sink" experiment that exhibits the discontinuity for water in a wedge formed by two plastic plates.



Figure 7



Figure 8

The problem was studied further by L. Simon (Pacific J. Math., 1980) who proved that if  $\alpha + \gamma > \pi/2$ ,  $\alpha < \pi/2$ , then  $u(x,y)$  is differentiable up to  $V$ . In independent work, N. Korevaar (Pacific J. Math., 1980) found the surprising result that if  $\alpha > \pi/2$ , there exist solutions that are bounded and discontinuous at  $V$ .

Concus and Finn (Math. Z., 1976) showed there exist sections  $\Omega$ ,  $\Omega' \subset \Omega$ , such that  $\Omega$  raises more fluid over  $\Omega'$  than  $\Omega'$  does. The problem was studied further by Finn (Vekua volume, l.c.) who gave general conditions under which this behavior will or will not occur. Siegel (Pacific J. Math., l.c.) gave another condition under which the "smaller" tube must raise a larger volume over its section.

For a capillary tube in outer space (zero gravity), solutions of the problem as posed do not in general exist. At a corner, as in Figure 6, there can be no solution when  $\alpha + \gamma < \pi/2$  (Concus and Finn, Acta Math., 1974). Physically, the fluid flows out along the corner, to infinity or to the top of the container, whichever comes first. For a regular polygon the above condition is best possible: if  $\alpha + \gamma \geq \pi/2$  a lower spherical cap yields an explicit bounded solution. Figure 8 shows the results of an experiment conducted in the NASA drop tower in Cleveland and verifying the predicted behavior.

For a general section  $\Omega$  it appears to be not easy to find existence criteria. The case  $\gamma = 0$  was studied by Chen (Pacific J. Math., 1980), who gave a simple geometric sufficiency condition. For general  $\gamma$ , Finn (Manuscripta Math., 1979) reduced the question to that of properties of vector fields over  $\Omega$ . Applying the results to polygonal domains, he found that in a parallelogram of arbitrary side ratio a solution exists if and only if  $\alpha + \gamma \geq \pi/2$  at the smaller vertex angle  $2\alpha$ . Thus, a solution exists in any rectangle if  $\gamma \geq \pi/4$ . However, the existence can fail for any  $\gamma \neq \pi/2$ , in trapezoids obtained from rectangles by arbitrarily small deformations.

This behavior was clarified recently by Finn (Indiana Univ. Math. J., to appear), who showed that a solution surface exists if and only if there is no subarc  $\Gamma$  of a semicircle of radius  $R_\gamma = \frac{\Omega}{\Sigma \cos \gamma}$ , meeting  $\Sigma$  in angles  $\gamma$  as indicated in Figure 9, for which

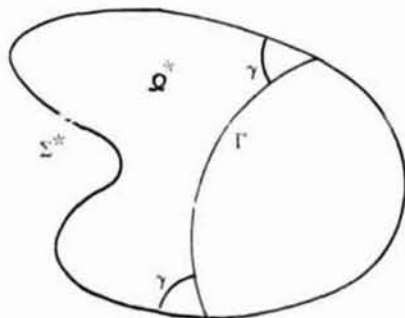


Figure 9

$$\varphi(\Gamma) = \Gamma - \Sigma^* \cos \gamma + \frac{1}{R_\gamma} \Omega^* \leq 0. \quad (12)$$

Here the lengths and areas  $\Sigma$ ,  $\Omega$ , ... are as indicated in Figures 1, 9.

Consider a situation in which  $\varphi(\Gamma) = 0$ , and in which there is no  $\Gamma$  for which  $\varphi(\Gamma) < 0$ . Let  $\gamma_j \downarrow \gamma$ . Then there is a corresponding sequence of solution surfaces with boundary angle  $\gamma_j$ , tending to a solution with boundary angle  $\gamma$  on  $\Omega \setminus \Omega^*$ , and tending to infinity on  $\Gamma$  and throughout  $\Omega^*$ . The solution is asymptotic at  $\Gamma$  to a vertical cylinder of radius  $R_\gamma$ . The cylinder acts as a barrier across which the solution surface cannot be extended.

The behavior just described actually occurs in a trapezoidal section. Also, letting the smaller base  $\rightarrow 0$  while the nonparallel sides meet (at  $V$ ) in a fixed angle  $2\alpha$ ,  $\Gamma$  will tend to  $V$  while  $\gamma \rightarrow (\pi/2) - \alpha$ ; thus, the above angle theorem appears as a limiting case.

Gerhardt (Pacific J. Math., 1980) considered tubes closed at the bottom and partially filled with liquid. He showed there always exist energy minimizing solutions (with or without gravity) which may have the value  $z = 0$  on part of the base. In this region, the solutions appear to admit the physical interpretation of a thin film covering the base.

A drop hanging from a horizontal plane (Figure 10) behaves very differently from the sessile drop. The solution section is uniquely determined by the height  $u_0$  at the vertex and

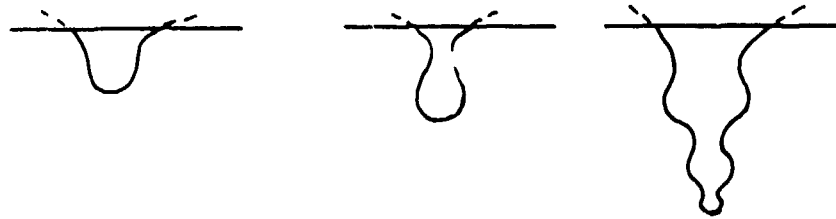


Figure 10

consists, for any  $u_0$ , of a curve that can be continued analytically to infinity without limit secs or double points (Concus and Finn, Philos. Trans. Roy. Soc., 1979). There exists also a singular solution  $v(r) \sim -(\sqrt{\kappa} r)^{-1}$  (Concus and Finn, Invent. Math., 1975; Huh, Dissertation, Dept. Chem. Eng., University of Minnesota, 1969). It is conjectured that as  $u_0 \rightarrow -\infty$ , the "drop" solutions tend, uniformly in compacta, to  $v(r)$ . A proof of a somewhat weaker result appears in Concus and Finn (Philos. Trans. Roy. Soc., l.c.).

Conditions for stability of the pendent drop have been given by E. Pitts, by Michael and by others. Most recently, the problem was treated in full generality by Wente (Pacific J. Math., 1980). Wente showed in particular that the occurrence of an inflection in the meridional section need not preclude stability.

The reasoning of Young on the constancy of  $\gamma$  is based on a hypothesis that all material forces are central. In the presence of resistive forces the behavior can be very different. Finn and Shinbrot consider a drop of liquid on a horizontal surface, with  $\gamma$  initially determined as in the Young theory. If liquid is now slowly added, the wetted surface may remain constant while the angle  $\gamma$  increases. If resistance is very large, then continued addition of liquid will eventually lead to a value  $\gamma > \pi$ , which is physically impossible as then the drop would penetrate the supporting plane. It follows that a geometrically imposed instability must occur when  $\gamma$  increases past  $\pi$ , forcing the wetted surface to increase. It can be shown (Finn, J. Reine Angew. Math., l.c.) that an upper bound for the critical  $B$  is determined as the unique solution of the relation

$$B^3 - \frac{3}{2} B B - \frac{9}{4} B^2 = 0. \quad (13)$$

Finn and Shinbrot interpret the above behavior by postulating a resistance force whose area density  $F$  is potential,  $F = -\nabla\psi$ , and which is formally equivalent to a distribution of linear density  $\varphi$  directed normally on  $\Sigma$ . They then apply that interpretation to the



Figure 11

more complicated situation of a drop on an inclined plane, initially under zero gravity and meeting the plane in the (Young) angle  $\gamma_0$ , and then subjected to slowly increasing gravity (Figure 11). Under hypotheses, that  $\psi$  depends only on the pressure at the interface, and that the effect can be separated into a radial "squishing" term as occurs for the horizontal plate and a "sliding" term due to the inclination, they are led to a relation of the form (for small  $B$ )

$$\cos \gamma = \cos \gamma_0 + \epsilon(\psi) + \alpha \sin \psi \sin \theta - \beta \sin^2 \psi \sin^2 \theta . \quad (14)$$

Here  $\alpha, \beta$  are constants,  $\alpha$  is explicitly known and of order  $\epsilon$ , and  $\epsilon$  is decreasing in  $\psi$ .  $\beta$  has order  $\epsilon^2$ ,  $\epsilon$  has order  $\epsilon$  if  $\psi < \pi/2$  and order  $\epsilon^2$  if  $\psi = \pi/2$ . Again a geometrically imposed instability appears, and in fact does so for surprisingly small values of  $\epsilon$ .

## The stability of the axially symmetric pendent drop

Henry C. Wente

Department of Mathematics, University of Toledo  
Toledo, Ohio 43606

### Abstract

We analyze the axially symmetric pendent drop as it occurs in three different physical settings: Problem A, constant pressure, fixed circular opening (the siphon); Problem B, constant volume, fixed circular opening (the medicine dropper); Problem C, prescribed volume, constant angle of contact with a horizontal plate. As examples, the following results are verified. For Problem B we show that if the opening is small enough to support a stable pendent drop with a bulge, then as the exposed volume is increased, stable pendent drops with both a neck and a bulge will be formed. For Problem C we show that with increasing volume the profile curves for the family of stable pendent drops will develop an inflection point before instability arises.

### Introduction

We first analyze the equilibrium and stability criteria for each of the problems.

#### Problem A

Here the drop is to protrude downward from a fixed circular opening of radius  $F$ , held at the level  $u = \bar{u}$  where  $u$  is the vertical coordinate with positive direction upward and  $u = 0$  is the zero pressure level of the fluid. ( see Figure 1). If  $X$  is the exposed body of the fluid and  $\Omega$  is the liquid-air interface with  $A(\Omega)$  its area, the potential energy of the configuration is

$$E_0(\Omega) = \sigma A(\Omega) + \rho g \int_X z dV. \quad (1)$$

$\sigma$  is the surface tension of the liquid-air interface,  $\rho$  is the density of the fluid, and  $g$  is the gravitational constant. The condition for equilibrium is that the first variation of the potential energy  $\delta E_0(\Omega, N) = 0$  for all normal perturbations  $N$  of  $\Omega$  which vanish on the boundary. The Euler Equations yield

$$2H = -ku \quad \text{on } \Omega, \quad k = \rho g / \sigma. \quad (2)$$

$H$  is the mean curvature of the surface measured so that it is positive at the drop tip. By a suitable scaling we may assume that  $k = 1$ . The condition for stability is that the second variation be positive for all non-trivial normal perturbations.

$$\delta^2 E_0(\Omega, N) > 0 \quad \text{for all } N \neq 0, \text{ but } N = 0 \text{ on } \partial\Omega. \quad (3)$$

#### Problem B

As in Problem A the fixed circular opening of radius  $F$  lies in a horizontal plane, but now the exposed volume is prescribed (see Figure 1). Now the condition for equilibrium is that the first variation of the energy  $\delta E_0(\Omega, N) = 0$  for all perturbations  $N$ , vanishing on the boundary and for which the first variation of the volume is also zero. By the method of Lagrange multipliers we obtain

$$\delta(E_0 + \lambda V)(\Omega, N) = 0 \quad \text{for some constant } \lambda \quad (4)$$

and all normal perturbations  $N$  vanishing on the boundary. This yields the condition

$$2H = -ku + \lambda', \quad \text{where } k = \rho g / \sigma \text{ and } \lambda' \text{ is a constant.} \quad (5)$$

By a vertical translation of coordinates we may take  $\lambda'$  to be zero, reducing (5) to the condition (2), and with the vertical coordinate of the opening at the level  $u = \bar{u}$ .

The condition for stability is that

$$\delta^2(E_0 + \lambda V)(\Omega, N) > 0 \quad (6)$$

for all non-trivial normal perturbations  $N$ , which vanish on the boundary and for which the first variation of the volume is zero.

### Problem C

The drop is now pendent from a homogeneous horizontal plate. The potential energy is now

$$E(\Omega) = E_0(\Omega) - \sigma\beta|\Sigma| \quad (7)$$

where  $\beta$  is a physical constant and  $|\Sigma|$  is the area of contact of the liquid with the plate. Setting the first variation equal to zero for all volume preserving perturbations yields the conditions

$$\begin{aligned} \text{a) } 2H &= -ku + \lambda \quad \text{for some constant } \lambda, k = \rho g/\sigma \\ \text{b) } \cos\alpha &= \beta \end{aligned} \quad (8)$$

Here  $\alpha$  is the angle of contact of the liquid-air interface with the horizontal plate measured interior to the fluid. Again we may choose  $k = 1$ , and by a vertical translation of coordinates may set  $\lambda = 0$ , with the horizontal plate at a level  $u = \bar{u}$ . Clearly it is necessary that  $|\beta| \leq 1$  so that  $0 \leq \alpha \leq \pi$ . There are no possible pendent drops when  $\alpha = \pi$  so that we may consider  $0 \leq \alpha < \pi$  ( $-1 < \beta \leq 1$ ). As in Problem B the condition for stability is that the second variation  $\delta^2(E + \lambda V)(\Omega, N)$  be positive for all non-trivial normal perturbations for which the first variation of volume is zero. (see Figure 1).

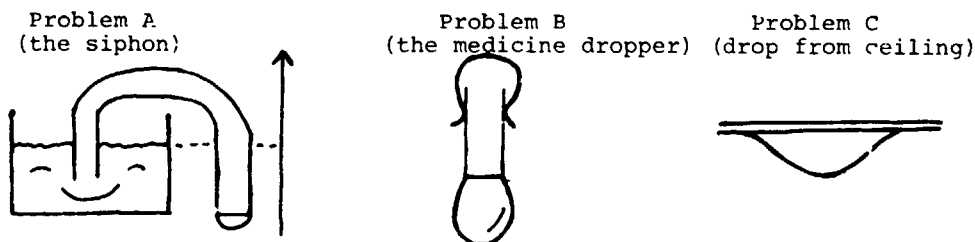


Figure 1. The various drop configurations.

### Description of the Profile curves

Suitably normalized, the differential equation for the profile curve whose surface of revolution represents the liquid-air interface (satisfying (2) with  $k = 1$ ) is

$$\begin{aligned} \text{a) } r'(s) &= \cos \psi & r(0) &= 0 \\ \text{b) } u'(s) &= \sin \psi & u(0) &= u_0 \\ \text{c) } \psi'(s) &= -(\sin \psi/r) - u & \psi(0) &= 0. \end{aligned} \quad (9)$$

The solutions to this system have been carefully studied by many people. In particular, I should mention the work of D.W. Thomson<sup>1</sup>, F. Bashforth and J.C. Adams<sup>2</sup>, and recently P. Concus and R. Finn<sup>3</sup>.

There is a unique solution,  $\{r(s, \kappa), u(s, \kappa), \psi(s, \kappa)\}$ , to the system satisfying the initial conditions,  $r(0, \kappa) = 0$ ,  $u(0, \kappa) = u_0 = -2\kappa$ ,  $\psi(0, \kappa) = 0$ , where  $\kappa$  is the mean curvature at the drop tip. The solution exists for all  $s$  and all  $\kappa$  and is analytic in both variables. We note that  $u \equiv 0$  gives a solution and that reflection of any solution about the  $r$ -axis yields another solution. Drops with  $u_0 < 0$  represent pendent drops and the solutions corresponding to  $u_0 > 0$  represent "emerging" bubbles. We now list other important properties of the family of solutions.

1. For "small"  $u_0 < 0$  the solution can be expressed non-parametrically with  $u$  as a function of  $r$  over the entire positive  $r$ -axis, and  $u(r) \sim u_0 J_0(r)$  where  $J_0(r)$  is the Bessel function of order zero.

2. There is a value  $u_0^*$  ( $u_0^* \approx -2.5678$ ) such that the profile curve with drop tip at  $u_0^*$  attains a simultaneous vertical tangent and inflection point at  $(r_1^*, u_1^*)$  where  $r_1^* \approx .91$  and  $u_1^* \approx -1.1$ . For  $0 < r < r_1^*$  the curve is convex while for  $r$  greater than  $r_1^*$  the curve may again be expressed non-parametrically  $u = u(r)$ .

3. For  $u_0^* < u_0 \leq 0$  the solutions may be expressed in non-parametric form,  $u = u(r)$ , for all  $r$ .

4. For  $u_0 < u_0^*$  the profile curves attain a vertical tangent at a point  $(r_1, u_1)$  where  $0 < r_1 < r_1^*$  and  $u_1 < u_1^*$ . The curves form a bulge at this point and  $r$  decreases to a value  $r_2$ , and forms a neck at  $(r_2, u_2)$  where  $u_2 < 0$ .  $r_1$  and  $u_1$  are increasing functions of  $u_0$  for  $u_0 < u_0^*$  with  $\lim_{u_0 \rightarrow 0} r_1 = 0$  and  $\lim_{u_0 \rightarrow -\infty} u_1 = -\infty$ .

5. For  $u_0 \ll u_0^*$  the profile curves form a sequence of bulges and necks until it crosses the  $r$ -axis with  $r'(s)$  and  $u'(s)$  both positive from which point on the curves may be expressed non-parametrically  $u = u(r)$  out to  $r = \infty$ .

6. The first inflection point on a profile curve with tip at  $u_0 < 0$  occurs at a point  $(\hat{r}, \hat{u})$  where  $\hat{u} < 0$ .  $\hat{r}$  and  $\hat{u}$  are monotonically increasing functions of  $u_0$  for  $u_0 < 0$ . If  $u_0 < u_0^*$ , so that the profile curve has both a neck and a bulge, then the first inflection point lies between the first neck and first bulge.

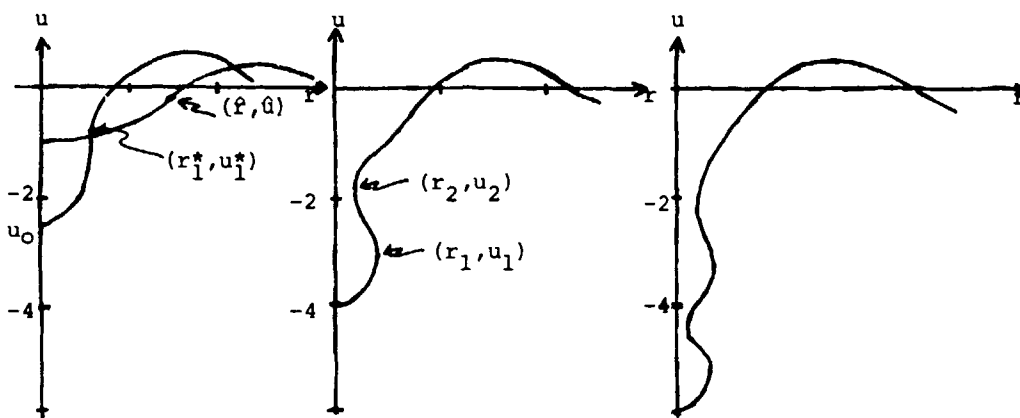


Figure 2. Possible drop configurations

#### Analysis of stability

Our method for determining the stable configurations for each of the problems proceeds as follows. Take a given profile curve  $\{r(s, \kappa), u(s, \kappa), \psi(s, \kappa)\}$  and let  $(\bar{r}, \bar{u})$  be a point on the curve,  $r = r(\bar{s}, \bar{\kappa})$  and  $\bar{u} = u(\bar{s}, \bar{\kappa})$ . The profile curve from the drop tip to this point generates a possible pendent drop whose exposed volume  $V$ , can be calculated.

$$V = \text{volume of drop} = \pi \bar{r}(\bar{r}\bar{u} + 2\sin \bar{\psi}) \quad (10)$$

The volume gives us a fourth function of the parameters  $s$  and  $\kappa$ ,  $V = V(s, \kappa)$ . For each of our three problems two of the four functions are prescribed. This generates a mapping from the  $(s, \kappa)$ -plane (the parameter space) into a two-dimensional "control" space. The analysis of this map determines stability for each of the problems.

#### Stability for problem A

Here the appropriate map is  $A(s, \kappa)$  where it is defined by

$$A(s, \kappa) = (r(s, \kappa), u(s, \kappa)). \quad (11)$$

The "control" space for this problem is the  $(r, u)$ -plane. It is easily checked that the derivative of  $A$ ,  $DA(s, \kappa)$  is invertible when  $s$  equals zero. Let  $O$  be the set of all points in the  $(s, \kappa)$ -plane where the derivative is invertible.

Definition.  $O_S$  contained in  $O$  is that component of  $O$  in the parameter space which contains the line  $s = 0$ .

Theorem 1. Every point  $(\bar{s}, \bar{\kappa})$  in  $O_S$  determines a stable pendent drop for Problem A. (i.e. the drop generated by the profile curve  $(r(s, \kappa), u(s, \kappa))$  for  $0 < s < \bar{s}$ ). Any point outside  $O_S$  determines an unstable pendent drop for Problem A.

This theorem is essentially classical.

It follows that the "control set"  $A(O_S)$ , is an open set in the  $(r,u)$ -plane. A point  $(\bar{r}, \bar{u})$  determines a stable configuration for problem A if and only if it is a member of the set  $A(O_S)$ . We now wish to describe the regions  $O_S$  and  $A(O_S)$ . Since  $A(O_S)$  is symmetric about the coordinate axes, we may restrict ourselves to the case  $r \geq 0, u \leq 0$

**Theorem 2.** Choose  $\kappa > 0$  and consider the profile curve  $(r(s, \kappa), u(s, \kappa)), s \geq 0$ . There is a smallest positive value  $\delta$ , such that  $(s, \kappa)$  is in  $O_S$  for  $0 < s < \delta$  while  $(\delta, \kappa)$  is on the boundary of  $O_S$ . On the interval  $0 < s \leq \delta$ , we have  $r'(s) = \cos \psi$  positive so that  $0 < \psi < (\pi/2)$ .

Therefore the corresponding profile curve  $(r(s, \kappa), u(s, \kappa))$   $0 < s < \delta$  may be expressed in nonparametric form  $u = f(r, \kappa)$ , for  $0 < r < \rho$  where  $\rho = r(\delta, \kappa)$  and  $\hat{u} = f(\rho, \kappa)$ . The point  $(\rho, \hat{u})$  lies on the boundary of  $A(O_S)$ . It is the conjugate point to the drop tip along this profile curve.

Since  $r'(s)$  is positive, we may use  $r$  as an independent variable rather than  $s$ . Points  $(\bar{r}, \bar{u})$  on the boundary of  $A(O_S)$  are determined by the condition that the derivative  $D\hat{A}(r, \kappa)$  be singular where  $\hat{A}(r, \kappa) = (r, f(r, \kappa))$  and  $u = f(r, \kappa)$  is the nonparametric representation of the curve. This occurs when  $f_\kappa(r, \kappa)$  equals zero. (i.e. the point  $(\bar{r}, \bar{u})$  is on the envelope  $\Gamma_A$ , of the family of profile curves.

**Theorem 3.** The first envelope  $\Gamma_A$ , of the family of profile curves  $u = f(r, \kappa)$  for  $\kappa > 0$  ( $u_0 \leq 0$ ) and  $r$  positive, is the graph of a smooth (analytic) function  $u = e(r)$  for  $0 < r \leq \alpha_0$  where  $\alpha_0$  is the first positive zero of the zero order Bessel function,  $J_0(r)$ . This function has the following properties.

$$\lim_{r \rightarrow 0^+} e(r) = -\infty, \quad \lim_{r \rightarrow \alpha_0} e(r) = 0$$

The derivative  $e'(r)$  is positive on the interval  $0 < r < \alpha_0$  with  $e'(\alpha_0) = 0$  and  $\lim_{r \rightarrow 0^+} e'(r) = +\infty$  as  $r$  approaches zero.

The entire envelope is thus a smooth curve without self-intersections which possesses a cusp only at  $(\alpha_0, 0)$ . (see Figure 3)

Consequences.

I. The mapping  $A(s, \kappa)$  is a diffeomorphism of  $O_S$  onto its image  $A(O_S)$ .

II. For  $(\bar{r}, \bar{u})$  in  $A(O_S)$  where  $\bar{r} < r_1^*$ , the profile curve for the stable pendent drop is convex. For  $\bar{r}$  near  $\alpha_0$  ( $\bar{r} < \alpha_0$ ) and  $(\bar{r}, \bar{u})$  in  $A(O_S)$ , the profile curve will contain an inflection point, and so the stable pendent drop loses convexity. (Figure 3)

III. There are no "inaccessible" stable pendent drops for Problem A. The vertical line  $r = \bar{r}$  ( $\bar{r}$  less than  $\alpha_0$ ) intersects  $A(O_S)$  in a connected interval. Thus the stable pendent drop corresponding to the point  $(\bar{r}, \bar{u})$  may be reached from the stable zero pressure solution ( $u \equiv 0$ ) corresponding to the point  $(\bar{r}, 0)$  in  $A(O_S)$  merely by increasing the pressure ( $p = -u$ ) continuously from 0 to  $-\bar{u}$ . (see Figure 3.)

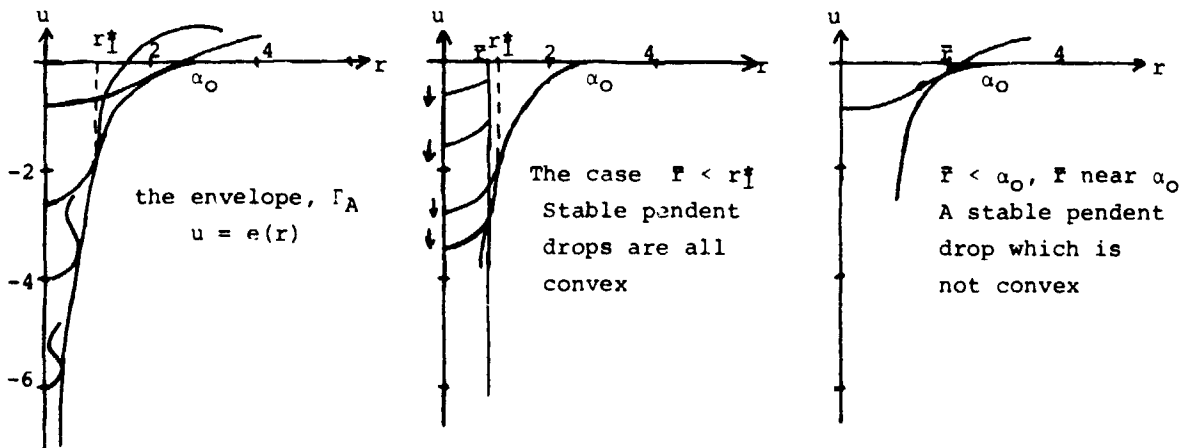


Figure 3. The envelope  $\Gamma_A$ , stable configurations for problem A

Stability for problem B.

The constraints are now the radius of the tube  $r$ , and the exposed volume  $V$ . Thus the control space is the  $(r,V)$ -plane and we are led to study the mapping  $B(s,\kappa)$  from the parameter space to the control space defined by

$$B(s,\kappa) = (r(s,\kappa), V(s,\kappa)) \tag{12}$$

As in problem A we let  $O$  be the open set in the  $(s,\kappa)$ -plane where the derivative  $DB(s,\kappa)$ , is invertible. However, since  $B(0,\kappa) = (0,0)$  the line  $s = 0$  lies outside the set  $O$ .

Fix  $\bar{\kappa}$  and consider the curve  $B(s,\bar{\kappa})$  for positive  $s$ . There exists a smallest positive value  $s_B$ , such that the derivative  $DB(s,\bar{\kappa})$  is invertible for  $0 < s < s_B$  but singular when  $s = s_B$ . Let  $(r_B, u_B)$  be the corresponding point on the profile curve  $(r(s,\bar{\kappa}), u(s,\bar{\kappa}))$ , where  $r_B = r(s_B,\bar{\kappa})$  and  $u_B = u(s_B,\bar{\kappa})$ . It is a classical result that if  $(\bar{r}, \bar{u})$  is a point on the profile curve prior to  $(r_B, u_B)$  then the corresponding pendent drop generated by the profile curve up to  $(\bar{r}, \bar{u})$  is "symmetrically" stable for problem B, while if the profile segment contains the point  $(r_B, u_B)$  then the generated drop is unstable for problem B.

Definition. We call the point  $(r_B, u_B)$  the "Volume-constrained" conjugate point on the profile curve relative to the drop tip.

Note. The axisymmetric pendent drop is said to be symmetrically stable if the second variation  $\delta^2(E_0 + \lambda V)(\Omega, N)$  is positive for all non-trivial symmetric normal perturbations  $N$ , of  $\Omega$  which vanish on the boundary and for which the first variation of volume is zero. If the profile curve can be expressed non-parametrically in the form  $r = r(u)$ , then symmetric stability implies stability.<sup>4</sup> In this case we observe that the angle of inclination  $\psi$ , must be non-negative. However, if the angle of inclination becomes negative on some portion of the profile curve (the corresponding drop is of re-entrant type), then the drop is unstable for problem B due to a non-symmetric perturbation. This fact was noted by D.H. Michael and P.G. Williams<sup>4</sup>. For an alternative discussion see reference 5.

Definition.  $O_S$  is the subset of  $O$  consisting of all points  $(s,\kappa)$  where  $0 < s < s_B$  where  $s_B$  depends on  $\kappa$ . It follows that  $(s,\kappa)$  determines a stable configuration if it is in  $O_S$  and an unstable configuration if it lies outside of  $\bar{O}_S$ .

We now wish to describe  $O_S$  and its image  $B(O_S)$  contained in the "control space", the  $(r,V)$ -plane.

Theorem 4.  $O_S$  is a connected open set in the  $(s,\kappa)$ -plane bounded on the left by the line  $s = 0$ , and on the right by an analytic curve  $\gamma$ , which is the graph of a positive analytic function  $s_B = \sigma(\kappa)$ .

Therefore  $O_S$  is a open set in the parameter space and  $B(O_S)$  is an open set in the control space.

Theorem 5. Let  $(r_B, u_B)$  be the volume-constrained conjugate point on the profile curve  $(r(s,\kappa), u(s,\kappa))$ . At the point  $(r_B, u_B)$  the derivative,  $r'(s)$  is positive. The point  $(r_B, u_B)$  is located between the first and second inflection points on the profile curve. If the profile curve possesses a bulge (and hence a neck) then  $(r_B, u_B)$  is located above the neck. As  $\kappa$  approaches zero the point  $(r_B, u_B)$  approaches the point  $(\alpha_1, 0)$ , where  $\alpha_1$  is a root of the equation  $rJ_0(r) + 2J_0'(r) = 0$ . (see Figure 4)

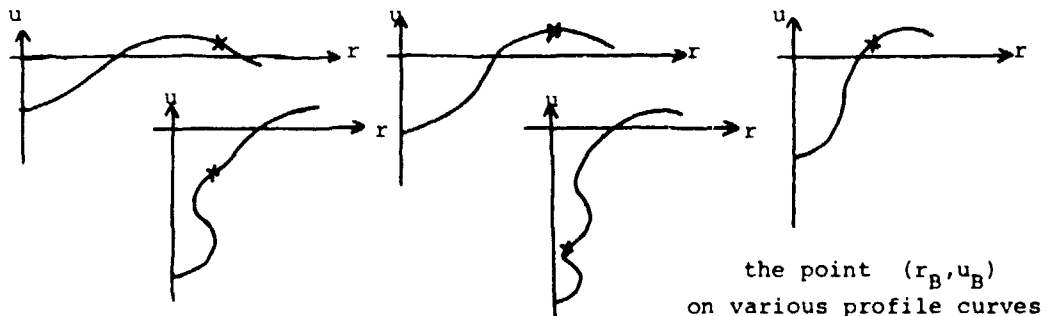


Figure 4. Locations of the volume-constrained conjugate point

By Theorem 4 the curve  $\gamma$  is an analytic arc parameterized by  $\kappa$ . Its image  $B(\gamma)$  is a parameterized curve in the  $(r,V)$ -plane and, as in problem A, it is the envelope,  $\Gamma_B$ , of the family of curves  $(r(s,\kappa),V(s,\kappa))$ . Thus  $\Gamma_B$  may be expressed in the form  $(r(\kappa),V(\kappa))$  where  $r(\kappa) = r(\sigma(\kappa),\kappa)$  and  $V(\kappa) = V(\sigma(\kappa),\kappa)$  are analytic functions of  $\kappa$ . Furthermore

$$\lim_{\kappa \rightarrow \infty} (r(\kappa),V(\kappa)) = (0,0) \quad \text{and} \quad \lim_{\kappa \rightarrow 0} (r(\kappa),V(\kappa)) = (\alpha_1,0)$$

By Theorem 5 we know that a given curve  $B(s,\kappa)$ , touches the envelope at a point where  $r'(s)$  is positive. Thus, in a neighborhood of this point,  $(r_B, V_B)$ , we may express the curves  $B(s,\kappa)$  non-parametrically in the form  $V = g(r,\kappa)$ . If the envelope is smooth it will be tangent to the family of curves  $V = g(r,\kappa)$ , and itself would have a non-parametric representation  $V = G(r)$ . A point on the envelope of the family of curves  $V = g(r,\kappa)$ , is determined by the condition  $g_\kappa(r,\kappa) = 0$  while the condition for smoothness is that  $g_{\kappa\kappa}(r,\kappa) \neq 0$ . Since the envelope  $\Gamma_B = B(\gamma)$  is a parameterized analytic curve it will be smooth except perhaps at isolated points where the derivatives  $r'(\kappa)$  and  $V'(\kappa)$  both vanish. At such points the possibility of a cusp arises. One such cusp occurs at  $(\alpha_1,0)$ .

Conjecture. That part of the envelope  $\Gamma_B$  which lies in the half-space  $V > 0$  is a smooth curve which may be expressed non-parametrically in the form  $V = G(r)$ ,  $0 < r < \alpha_1$ , with  $G(0) = G(\alpha_1) = 0$  and  $G'(\alpha_1) = 0$ . There is a single value  $r^*$  where  $G'(r^*) = 0$ .

Computer calculations <sup>6</sup> strongly indicate that the conjecture is valid, but a complete proof of this is lacking at present. (see Figure 5)

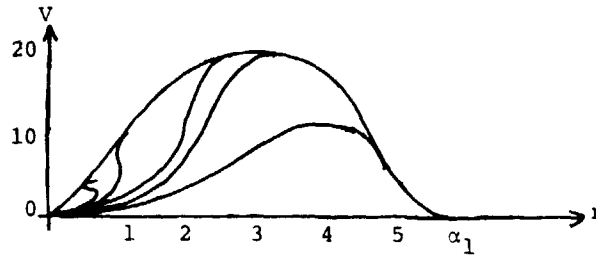


Figure 5. The curves  $B(s,\kappa)$  and their envelope,  $\Gamma_B$ .

If the envelope is a smooth curve, then it follows that the map  $B(s,\kappa)$  is a diffeomorphism of  $O_S$  onto its image  $B(O_S)$ . In this case any vertical line  $r = \bar{r}$  in the control space would intersect  $B(O_S)$  in a connected interval. The stable pendent drop corresponding to  $(\bar{r},V)$  is accessible from the flat drop  $u \equiv 0$ , corresponding to the point  $(\bar{r},0)$  in the control space, through a smooth one-parameter family of stable pendent drops of increasing volume and fixed radius for the aperture until a maximum volume is reached. This is the procedure used by E. Pitts in his paper. <sup>7</sup>

If the envelope were not smooth and contained cusps, then the possibility arises that the mapping  $B(s,\kappa)$  is not a one-to-one map of  $O_S$  onto its image, or that for some  $\bar{r}$  the intersection of the line  $r = \bar{r}$  with the set  $B(O_S)$  is not connected. In either case there would exist stable pendent drops corresponding to some control value  $(\bar{r},V)$  which could not be connected to  $(\bar{r},0)$  in the manner described above.

If we follow the "usual" procedure of trying to describe those drops which are accessible from the initial drop  $u \equiv 0$ , corresponding to the point  $(\bar{r},0)$  then we have the theorem:

Theorem 6. (a) If  $\bar{r} < r_1^*$  then as we increase the volume from zero there will be produced a one-parameter family of stable pendent drops for Problem B. Through an initial range of volumes  $0 < V < V_1(\bar{r})$ , the profile curves will be convex and the drops will develop a bulge. When the exposed volume reaches  $V_1(\bar{r})$ , the profile curve will develop an inflection point at the edge of the drop. With increasing volumes the drops lose convexity, but before the limit of stability is reached pendent drops possessing both a neck and a bulge will evolve.

(b) For  $\bar{r} > \beta_1$  where  $J_1(\beta_1) = 0$  the "drop"  $u \equiv 0$  is unstable for problem B due to non-symmetric perturbations. For  $\bar{r} < \beta_1$  the drop  $u \equiv 0$  is stable and with increasing volume the profile curves for the family of stable pendent drops will develop an inflection point before the limit of stability is reached.

(c) For any radius  $\bar{r}$ , drop height increases monotonically with volume throughout the range of stability.

The result (a) of Theorem 6 was observed in the limiting case of small drop with narrow necks by A.K. Chesters <sup>8</sup>.

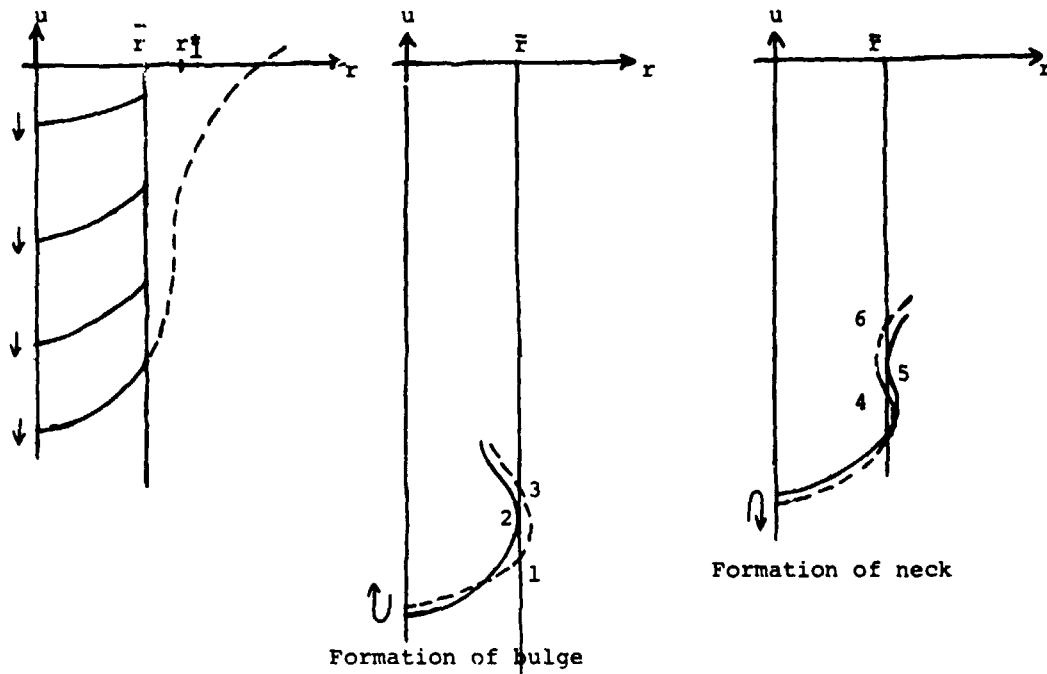


Figure 6. Drop formation for Problem B

Stability for problem C.

The control parameters are now the angle of inclination  $\psi$ , and the volume  $V$ , giving

$$C(s, \kappa) = (\psi(s, \kappa), V(s, \kappa)) \tag{13}$$

as our mapping from the parameter space to the control space. Again we let  $O$  be the set of all points  $(s, \kappa)$  where the derivative  $DC(s, \kappa)$ , is invertible and we observe that the line  $s = 0$  does not meet the set  $O$  since  $C(0, \kappa) = (0, 0)$ . For each  $\bar{\kappa}$ , there is a positive value  $s_c$  depending on  $\bar{\kappa}$ , such that  $DC(s, \bar{\kappa})$  is invertible for  $0 < s < s_c$  but is singular at  $s_c$ . Let  $O_S$  be the set of all points in  $O$  of the form  $(s, \bar{\kappa})$  where  $0 < s < s_c$ .

Theorem 7.  $O_S$  is an open simply-connected set bounded on the left by the line  $s = 0$  and on the right by a curve  $\gamma_c$  which is the graph of a positive analytic function  $s_c = s_c(\kappa)$  where  $\lim_{\kappa \rightarrow \infty} s_c(\kappa)$  is zero as  $\kappa$  becomes infinite.

Definition. For a given profile curve  $(r(s, \bar{\kappa}), u(s, \bar{\kappa}))$   $s \geq 0$ , the volume-constrained focal point for problem C is the point  $(r_c, u_c)$  on the curve with  $r_c = r(s_c, \bar{\kappa})$ ,  $u_c = u(s_c, \bar{\kappa})$ .

If a profile curve is to generate a physically meaningful configuration for problem C, it is necessary that the angle of inclination  $\psi$ , be non-negative along the segment of the profile curve generating the drop. Otherwise the drop would intersect the face. This eliminates from consideration the re-entrant drops. Therefore we let  $O'_S$  be the set of those points  $(\bar{s}, \bar{\kappa})$  in  $O_S$  for which the angle of inclination is positive,  $0 < s < \bar{s}$ .

Theorem 8. The profile curve segment corresponding to any member of  $O'_S$  generates a stable configuration for problem C. If the point  $(\bar{s}, \bar{\kappa})$  lies outside the closure of the set  $O'_S$ , then the generated drop is unstable for problem C.

Remark: This result which was essentially "classical" for problems A and B, is somewhat more difficult for problem C.

In other words, let  $(r_c, u_c)$  be the volume-constrained focal point for problem C on some profile curve. Suppose that  $(r_c, u_c)$  comes before the point where the angle of inclination is zero. If  $(\bar{r}, \bar{u})$  is a point on the profile curve prior to  $(r_c, u_c)$  then the corresponding pendent drop is stable for problem C, while if  $(\bar{r}, \bar{u})$  comes after  $(r_c, u_c)$  then the resulting drop is unstable.

**Theorem 9.** The volume-constrained focal point  $(r_C, u_C)$  for a given profile curve lies between the first and second inflection points. It comes ahead of the volume-constrained conjugate point for problem B,  $(r_B, u_B)$ .

**Theorem 10.** The set  $C(O'_S)$  is symmetric about the line  $\psi = 0$ . It is bounded on the left by the line  $\psi = 0$ . The rest of  $C(O'_S)$  is bounded by  $C(\gamma_C)$  where  $\gamma_C$  is the curve described in Theorem 7.

As in problem B, the set  $C(\gamma_C)$  is the envelope  $\Gamma_C$  of the family of curves  $(\psi(s, \kappa), V(s, \kappa))$ . By Theorem 9 each curve in the family will touch the envelope at a point where  $\psi'(s)$  is negative. Therefore in a neighborhood of the touching point each of these curves may be expressed non-parametrically  $V = h(\psi, \kappa)$ . The envelope is determined by the condition  $h_\kappa(\psi, \kappa) = 0$ . It will be a smooth curve if  $h_{\kappa\kappa}(\psi, \kappa) \neq 0$ . If the angle  $\psi$  is positive, then  $dV/d\psi = h_\psi(\psi, \kappa) = V/\psi$  is negative, and where it is smooth, the envelope will be the graph of a decreasing function.

**Conjecture.** That part of the envelope  $\Gamma_C$ , which lies in the first quadrant of the  $(\psi, V)$ -plane is the graph of a smooth function  $V = V(\psi)$   $0 < \psi < \pi$ , with  $V'(0) = 0$ ,  $V'(\psi)$  negative for  $0 < \psi < \pi$ , and  $V'(\pi) = 0$ .

Computer calculations strongly support the conjecture.<sup>6</sup> If the conjecture is true, then (as in problem B) the map  $C$  would be a diffeomorphism of  $O'_S$  onto its image, and the intersection of a vertical line  $\psi = \bar{\psi}$ , with  $C(O'_S)$  would be a connected interval. This would imply that as we move vertically along the line  $\psi = \bar{\psi}$  from  $(\bar{\psi}, 0)$  to  $(\bar{\psi}, V_{\max})$  in the control space, the corresponding drops would generate the entire family<sup>max</sup> of stable pendent drops for problem C. If the conjecture were not true, then as was the case for problem B, the procedure just described would fail to pick up some stable pendent drops for Problem C. (see figure 7.)

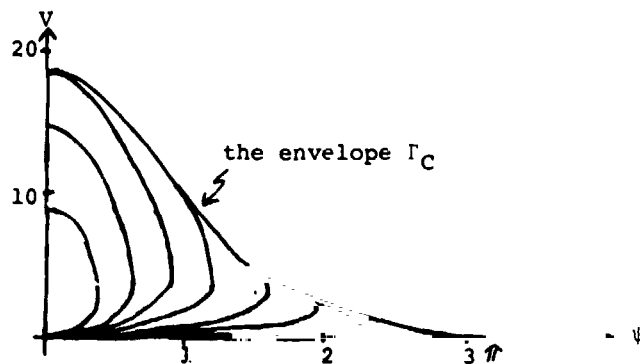


Figure 7. The curves  $C(s, \kappa)$  and their envelope  $\Gamma_C$

The following theorem identifies those stable pendent drops that are accessible from drops of very small volume.

**Theorem 11.** (a) For any angle of contact  $\bar{\psi}$ ,  $0 < \bar{\psi} < \pi$ , stable drops of small volume are convex and resemble spherical caps. These drops are generated by profile curves whose tip is at  $u_0$ , where  $u_0$  is large and negative. At a certain positive volume  $V_1$ , where  $V_1$  depends on  $\bar{\psi}$ , the profile curve generating the drop will develop an inflection point at its edge. This drop is stable. As the volume is increased, further stable pendent drops are formed, and the inflection point on the profile curves will move to the interior. With increasing volume the limit of stability will be reached before a second inflection point appears.

(b) If  $\bar{\psi} = 0$  all profile curves corresponding to pendent drops of positive volume contain an inflection point. Drops of small volume correspond to small values for  $u_0$  at the drop tip. As  $u_0$  is decreased stable pendent drops of increasing volume are formed. The drop generated by that profile curve whose tip is at  $u_0 = u_0^* = -2.5678$  is unstable. (Computer results indicate that the stable pendent drop of maximum volume occurs with  $u_0 = -1.6$  with a volume of 18.4)

(c) For any angle of contact drop height increases monotonically with volume throughout the range of stability.

**Remark.** For example, if the angle of contact  $\psi = (\pi/2)$ , it follows that with increasing volume and before the point of instability is reached, pendent drops containing both a neck and a bulge will appear.

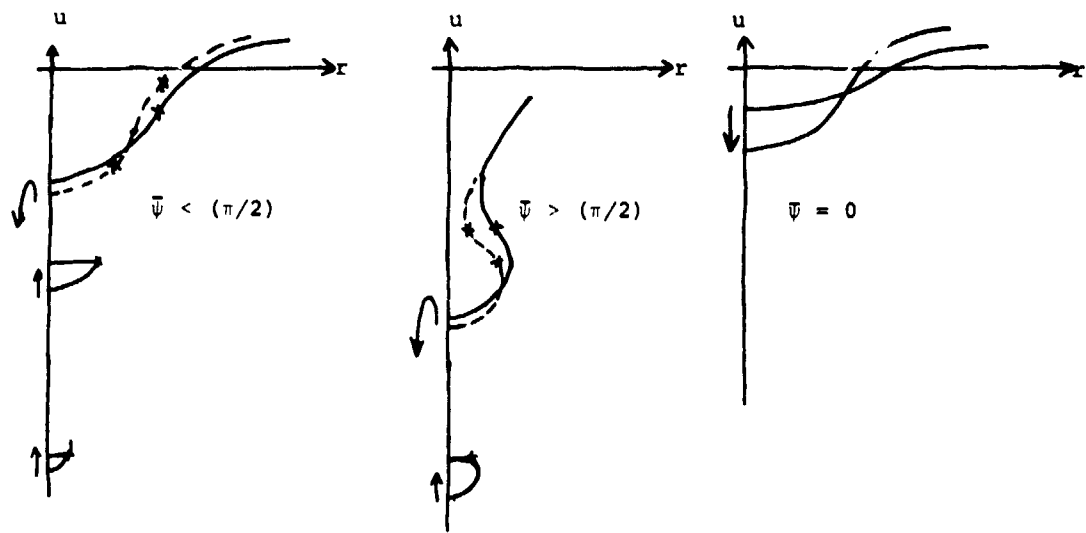


Figure 8. Drop formation for problem C

Justification of the stability criterion.

As noted earlier, any re-entrant drop (drop for which the angle of inclination becomes negative) is necessarily unstable. Otherwise a stable symmetric pendent drop represents a strong local minimum of energy for any of the problems discussed. A nice proof is based on the method of H.A. Schwarz in his proof of the isoperimetric property of the sphere. For example, relative to Problem C we can show the following result.

Theorem 12. Let  $(X, \Omega)$  be a stable pendent drop for problem C with exposed volume  $\bar{V}$ , and angle of contact  $\psi$ . Consider any other pendent drop  $(Y, S)$  whose contained volume is  $\bar{V}$ . For each horizontal plane  $P$ , below the supporting plane, let  $A(P)$  be the cross-sectional area of  $Y \cap P$ , and let  $V(P)$  be the volume of the drop lying below the plane  $P$ . Let  $r(P)$  be the radius of the circle whose area is  $A(P)$ . Suppose that the pair  $(r(P), V(P))$  determines a stable pendent drop for problem B and for every plane  $P$ . Then the energy  $E(\Omega)$  (see (7)) is less than or equal to  $E(S)$ , with equality only if  $(X, \Omega) = (Y, S)$ .

The method of proof is to first symmetrize  $(Y, S)$  producing a new drop of less energy and the same volume, which we then compare to the given stable drop.

Acknowledgments

The research work leading to this paper was supported in part by NSF grant MPS75-07402, a Summer faculty fellowship from the University of Toledo, and SFB72 at the University of Bonn, Germany.

References

1. Thomson, D.W., On Growth and Form, 2nd edition, Cambridge Univ. Press, 1973.
2. Bashforth, F. and Adams, J.C., An Attempt to Test the Theories of Capillary Action, Cambridge Univ. Press, 1883.
3. Concus, P. and Finn, R., The Shape of a Pendent Liquid Drop, Philos. Trans Roy. Soc. London Ser.A, 292 (1979) 207-223.
4. Michael, D.H. and Williams, P.G., The Equilibrium and Stability of Axisymmetric Pendent Drops, Proc. Roy. Soc. London A, 351 (1976) 117-128.
5. Wente, H.C., The Stability of the Axially Symmetric Pendent Drop, Pac. J. of Math. Vol. 88, No.2 (1980) 421-470.
6. Boucher, E.A., Evans, M.J.B., and Kent, H.J., Capillary Phenomena, II. Equilibrium and Stability of Rotationally Symmetric Fluid Bodies, Proc. Roy. Soc. London, Ser.A, 349 (1976) 81-100.
7. Pitts, E., The Stability of Pendent Liquid Drops, Part 2, Axial Symmetry, J. Fluid Mech., 63 Part 3 (1974) 487-508.
8. Chesters, A.K., An Analytical Solution for the Profile and Volume of a Small Drop of Bubbles Symmetrical about a Vertical Axis, J. Fluid Mech. 81 Part 4 (1977) 609-624.

Capillary surface discontinuities above re-entrant corners

N. J. Korevaar

Mathematics Research Center, University of Wisconsin-Madison  
610 Walnut Street, Madison, Wisconsin 53706

A capillary surface  $S$  is the (equilibrium) interface between two adjacent fluids that are also contacting rigid walls. Because the interface is in equilibrium one has information about the mean curvature of  $S$  and its contact angle  $\gamma$  with the bounding walls. The general problem in the mathematical theory of capillarity is to use this geometric information to deduce properties of  $S$ .

In this paper we study a particular configuration for which  $S$  is the interface between two fluids in a vertical capillary tube, in the presence of a downward pointing gravitational field.  $S$  is the graph a function  $u$  whose domain is the (horizontal) cross section  $\Omega$  of the tube. The mean curvature of  $S$  is proportional to its height above a fixed reference plane,  $\gamma$  is a prescribed constant and may be taken between zero and  $\pi/2$ .

The particular question we study here is, are there domains  $\Omega$  for which  $u$  is a bounded function but does not extend continuously to  $\partial\Omega$ ? We find simple domains to show that the answer is yes and study the behavior of  $u$  in those domains.

In section 1 of this note we fix notation and briefly formulate the non-parametric capillary problem described in the second paragraph above.

In section 2 we review an important comparison principle that has been used (in the literature) to derive many of the results in capillarity. It allows one to deduce the approximate shape of a capillary surface by constructing comparison surfaces with mean curvature and contact angle close to those of the (unknown) solution surface. In the context of non-parametric problems the comparison principle leads to height estimates above and below for the function  $u$ . We describe an example from the literature where these height estimates have been used successfully. We indicate areas of possible future applications. In section 3 we construct the promised domains for which the bounded  $u$  does not extend continuously to the boundary. The point on the boundary at which  $u$  has a jump discontinuity will be the vertex of a re-entrant corner having any interior angle  $\theta > \pi$ . Using the comparison principle we study the behavior of  $u$  near this point.

Much of this paper uses material from the note, "On the behavior of a capillary surface at a re-entrant corner"<sup>6</sup> and from other sections of the Ph.D. dissertation, "Capillary surface behavior determined by the bounding cylinder's shape"<sup>7</sup>, by this author.

Section 1: The non-parametric capillary problem

For a Lipschitz domain  $\Omega$  in  $\mathbb{R}^2$  a function  $u \in C^2(\Omega) \cap C^1(\bar{\Omega})$  is a classical solution to the capillary problem in a gravitational field if

$$\operatorname{div} Tu = 2H(S_u) = \kappa u \quad \text{in } \Omega, \tag{1}$$

$$Tu = \frac{Du}{\sqrt{1 + |Du|^2}}, \quad Du = \operatorname{grad} u, \quad H(S_u) = \text{mean curvature of } S_u, \quad \kappa > 0,$$

$$Tu \cdot n = \cos \gamma \quad \text{on } \partial\Omega, \tag{2}$$

$$0 < \gamma < \pi \quad \text{prescribed, } n = \text{exterior normal to } \partial\Omega.$$

Physically  $S_u$  describes the capillary surface formed when a vertical cylinder with horizontal cross section  $\Omega$  is placed in an infinite reservoir of liquid having zero rest height. Then

$$\kappa = \frac{\rho g}{\sigma} \quad \text{where } \rho = \text{density of liquid} \\ g = (\text{downward}) \text{ acceleration of gravity} \\ \sigma = \text{surface tension between liquid and air}$$

$$\cos \gamma = \frac{\sigma_1}{\sigma} \quad \sigma_1 = \text{surface attraction between liquid and cylinder}.$$

(More generally, by picking the reference height  $u = 0$  appropriately,  $S_u$  can be the interface between any two different density fluids occupying a capillary tube. Then  $\rho$  is the density difference between the two fluids,  $\sigma_1$  is the difference in surface attraction

between the two fluids and the bounding cylinder, and  $\sigma$  is the surface tension between the two fluids).

Geometrically  $\text{div Tu}$  is twice the mean curvature of the surface  $S_u$ . In some sense this is the average amount the surface is curving: Writing the surface locally as a graph above its tangent plane at a point  $P$ ,  $\zeta = \phi(\eta)$ , then one can verify that at  $P$   $\text{div Tu}$  is the trace of the Hessian of  $\phi$ . The correct choice of orthogonal coordinates  $\eta$  (called the principal directions) makes the Hessian a diagonal matrix. Then  $\text{div Tu}$  is the sum of the curvatures (second derivatives of  $\phi$ ) in these principal directions and  $H(S_u)$  is the average.

Geometrically  $\gamma$  is the contact angle between the (downward normal to the) capillary surface  $S_u$  and the (exterior normal to the) bounding cylinder  $\partial\Omega \times \mathbb{R}$  (see Figure 1). Thus if the cylinder is of uniform composition  $\gamma$  is constant. We consider that case here. By considering the function  $-u$  if necessary (locking at the capillary tube upside down) we can assume

$$0 < \gamma < \pi/2. \quad (3)$$

The most natural way to prove the existence of capillary surfaces is to solve the variational problem associated to (1), (2):  $u$  should minimize the energy

$$\tilde{E}(f) = \int_{\Omega} (\sigma\sqrt{1 + |Df|^2} + \frac{\rho g}{2} f^2) - \int_{\partial\Omega} \sigma_1 f$$

or equivalently

$$E(f) = \int_{\Omega} \sqrt{1 + |Df|^2} + \frac{\kappa}{2} f^2 - \int_{\partial\Omega} v f, \quad v = \sigma \cos \gamma \quad (4)$$

over the appropriate space of functions. The three terms making up the energy functional are (in order) surface energy, potential energy from gravity, wetting energy. Emmer<sup>4</sup> and Finn-Gerhardt<sup>5</sup> have studied the existence of variational solutions to the capillary problem in Lipschitz domains  $\Omega$ . (In particular, existence theorems are guaranteed for the particular piecewise smooth domains considered in section 3.) When it exists the function  $u$  is unique, real analytic in  $\Omega$  and satisfies (1) classically. Wherever  $\partial\Omega$  is smooth enough ( $C^4$ ),  $u$  extends smoothly and satisfies the boundary condition (2) classically. (In particular  $u$  can never be discontinuous at a point where  $\partial\Omega$  is smooth.)

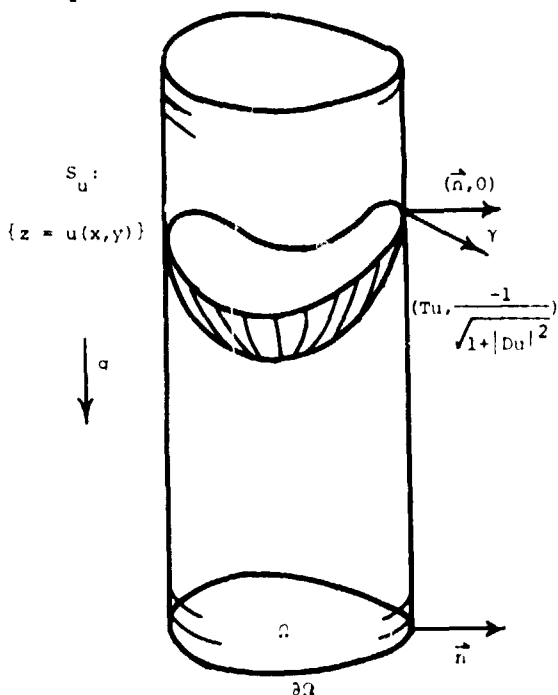


Figure 1: Configuration for the non-parametric capillary problem.

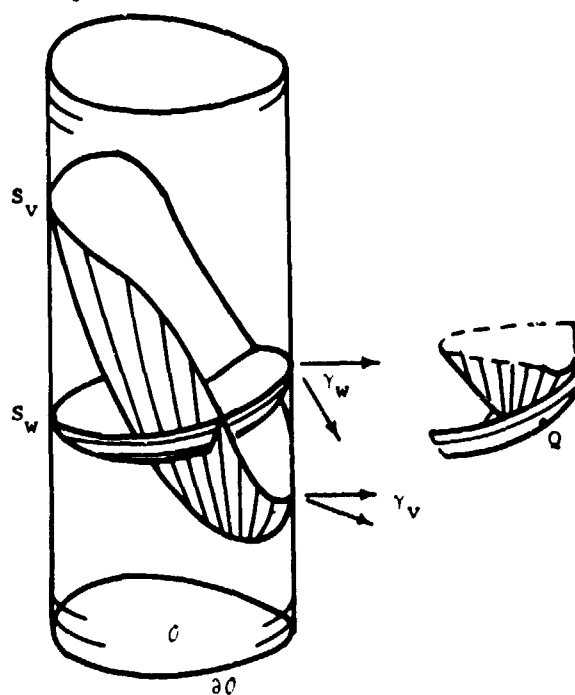


Figure 2. The comparison principle: If  $\gamma < \gamma_w$  on  $\partial\Omega$  (wherever  $v < w$ ), then any last point of contact between  $S_v$  and  $S_w$  occurs inside  $\Omega \times \mathbb{R}$ . At such a point,  $H(S_v) > H(S_w)$ .

## Section 2: The comparison principle

Let  $\Omega$  be the domain being studied for the capillary problem. Let  $O$  be a (bounded) subdomain (possibly all of  $\Omega$ ). Let  $n$  be the exterior normal to  $\partial O$ . For a function  $u$  let  $\gamma_u$  denote the contact angle of  $S_u$  with the subcylinder  $\partial O \times \mathbb{R}$ . That is,  $Tu \cdot n = \cos \gamma_u$ . The comparison principle for non-parametric surfaces of related mean curvature and contact angle is:

**Theorem 2.1:** Let  $v, w \in C^2(O)$  and suppose that

- (i) wherever  $v < w$  in  $O$ ,  $\operatorname{div} Tv < \operatorname{div} Tw$
- (ii) wherever  $v < w$  on  $\partial O$ ,  $Tv \cdot n > Tw \cdot n$  (i.e.  $\gamma_v < \gamma_w$ )

Then  $v$  is never actually less than  $w$ ,  $v \geq w$ .

As applied to mean curvature and contact angle Theorem 2.1 is due to Concus and Finn<sup>3</sup>. It is a special case of a very general comparison principle for elliptic equations with suitable boundary conditions.

We roughly sketch the classical proof of this theorem, assuming that  $\partial O$  is smooth, that  $v, w \in C^1(\bar{O})$  and that (ii) is replaced by the stronger

- (ii) wherever  $v < w$  on  $\partial O$ ,  $\gamma_v < \gamma_w$ .

(See Figure 2.)

Suppose  $S_v$  does not lie entirely above  $S_w$ . Then lift  $S_v$  until it reaches a point  $Q$  of last contact with  $S_w$ . (Lifting  $S_v$  does not affect its mean curvature or contact angle with  $\partial O \times \mathbb{R}$ ). The condition (ii) implies that wherever  $v < w$  on  $\partial O$ ,  $S_v$  rises more steeply than  $S_w$  to meet  $\partial O \times \mathbb{R}$ . Hence  $Q$  cannot be a boundary point, on  $\partial O \times \mathbb{R}$ , and must instead be contained in  $O \times \mathbb{R}$ . Since  $Q$  is a point of last contact (the lifted)  $S_v$  and  $S_w$  are tangent there. But (the lifted)  $S_v$  contacts  $S_w$  at  $Q$  and never lies beneath it, so we must have  $H(S_v) > H(S_w)$  there. This contradicts (i). Thus  $S_v$  did actually lie above  $S_w$ .

Filling in the details to the preceding proof one would see that it is only the ellipticity of the mean curvature operator that is used (for both the boundary and interior arguments).

There is another (less intuitive but still simple) proof that uses the divergence structure of the elliptic equation (1), (2). Using this proof and the fact that  $|Tu| \leq 1$  it is possible to see that  $\partial O$  can be Lipschitz and that the boundary condition (ii) need only be attained in a certain weak sense. In particular the comparison principle will hold for the piecewise smooth domains considered in section 3 and for the solutions  $u$  to the capillary problems in these domains.

The specific form of Theorem 2.1 that we need for section 3 is:

**Corollary 2.2:** Let  $O$  be piecewise smooth. Let  $u, v, w \in C^2(O)$  and suppose the contact angle for these three surfaces exists on the smooth parts of  $\partial O$ . Suppose

$$\begin{aligned} \operatorname{div} Tv &< kv, & \operatorname{div} Tu &= ku, & \operatorname{div} Tw &> kw & \text{ in } O & & (5) \\ \gamma_v &< \gamma_u, & & & \gamma_w &> \gamma_u & \text{ on } \partial O. & & \end{aligned}$$

Then  $v \geq u \geq w$  in  $\bar{O}$ .

**Proof:** We show  $v \geq u$ : Condition (ii) of Theorem 2.1 is satisfied on all of  $\partial O$ . Condition (i) is satisfied since  $v < u$  implies  $\operatorname{div} Tv < kv < ku \leq \operatorname{div} Tu$ . Thus  $v \geq u$ .

**Remark 2.3:** Note that the comparison principle sounds backwards: If  $v$  has "less" mean curvature and "less" contact angle,  $S_v$  lies above  $S_u$ . If  $w$  has "more" mean curvature and "more" contact angle,  $S_w$  lies beneath  $S_u$ .

**Remark 2.4:** One of the most successful uses of the comparison principle has been to study the seemingly strange behavior of capillary surfaces above domains with corners, in the presence of gravity. This study was undertaken by Concus-Finn<sup>3</sup> who showed that above a corner with interior angle  $\theta$  satisfying  $\theta < \pi - 2\gamma$ ,  $u$  approaches infinity as the vertex is approached. In contrast they showed that for  $\theta > \pi - 2\gamma$ ,  $u$  is bounded, uniformly as the corner is closed. In the unbounded case they actually constructed a comparison surface

that describes  $u$  to within a constant. The methods we use in section 3 are very similar in spirit to theirs.

There are other instances in the literature where the non-parametric comparison principle yields interesting height estimates, but I feel the general comparison technique has not yet been fully utilized, as the following three remarks indicate:

Remark 2.5: Mean curvature and contact angle (i.e. capillarity) make sense in the more general parametric setting of surfaces. The proof of the comparison principle that I sketched roughly can also make sense in the parametric setting: If there are two surfaces  $S_1$  and  $S_2$  of "known" mean curvature (known in the sense that the mean curvature is determined by the perhaps unknown position of the surface), each making "known" contact angle with a fixed third surface  $S_3$ , then by considering appropriate families of transformations of  $S_1$  relative to  $S_2$  (not necessarily by rigid motions), one can conclude location bounds on possible parametric capillary surfaces.

Remark 2.6: There is a connection between comparison surfaces such as those in (5) and the energy functional (4). Roughly speaking if  $f$  is a candidate to minimize (4) and if one knows of supersolutions  $v$  or subsolutions  $w$  in the sense of (5) then one can assume without loss of generality that  $f$  lies beneath  $v$  and above  $w$ . This can be very useful in proving existence theorems, where it is often important to bound the minimizing sequence. For example, one can give direct proofs of the existence theorems for "admissible domains" in the sense of Finn-Gerhardt<sup>5</sup> using this observation and the direct variational techniques of Emmer<sup>3</sup>. For parametric variational problems the connection with the comparison principle has to do with the families of surfaces described in Remark 2.5. I am currently investigating this area and believe it will yield existence theorems for parametric capillary surfaces (of the type pictured in Figure 3) depending naturally on the geometry of the fixed bounding walls.

Remark 2.7: Relatively little numerical work has been done computing capillary surfaces. (There has been some<sup>1</sup>.) The effective use of comparison surfaces can reduce the amount of computing time needed by giving a priori bounds above and below for the candidate functions (Remark 2.5). This can be especially useful in domains for which the capillary surface behaves in a singular fashion but for which good comparison surfaces can still be constructed, (for example the narrow wedges described in Remark 2.4 and the domains of section 3).

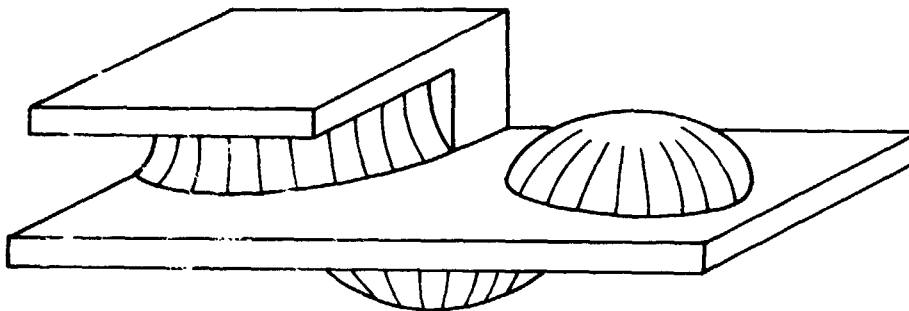


Figure 3: Some capillary surfaces.

### Section 3: Re-entrant corner domains

Let  $\theta$  and  $\gamma$  satisfy

$$\pi < \theta < 2\pi, \quad 0 < \gamma < \pi/2. \quad (6)$$

We will construct a domain for which a bounded solution  $u$  to (1), (2) exists, but having a corner of interior angle  $\theta$  at which there is a jump discontinuity in  $u$ . (The arguments can be modified to include the case  $\gamma = 0$ . If  $\gamma = \pi/2$ ,  $u \equiv 0$ . All other cases reduce to one of these (3).)

Determine the domain scale by fixing  $R > 0$  (Figure 4). Since  $\theta > \pi$  we can pick  $\theta_1$  and  $\theta_2$  satisfying

$$\theta_1 > \pi - \gamma, \quad \pi/2 > \theta_2 > \gamma, \quad \theta_1 + \theta_2 = \theta. \quad (7)$$

For positive  $\epsilon$  less than  $R \sin^2 \theta_2$ , let  $\Omega_\epsilon$  be a bounded domain, of which the intersection with  $B_{3R}(0)$  is shown in Figure 4, and which has  $C^4$  boundary except at  $P_0$  and  $P_1$ .  $B_{3R}(0)$  is the disc of radius  $3R$  centered at the origin.)

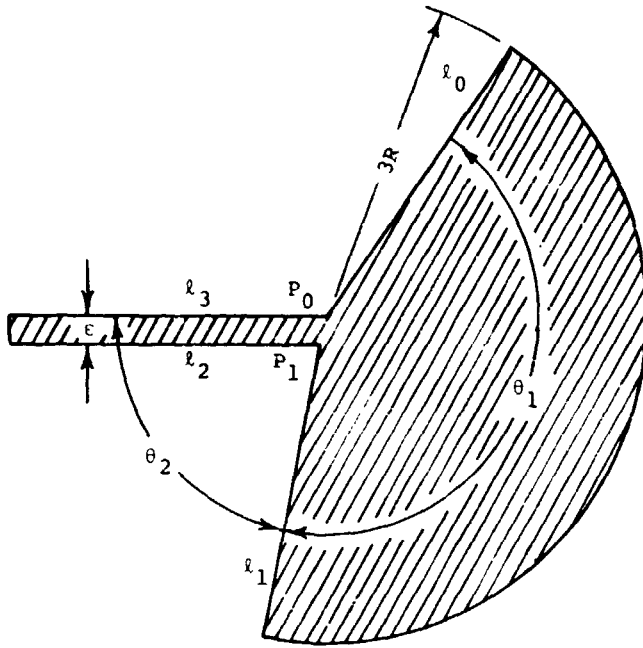


Figure 4: The intersection of  $\Omega_\epsilon$  with the disc of radius  $3R$ .

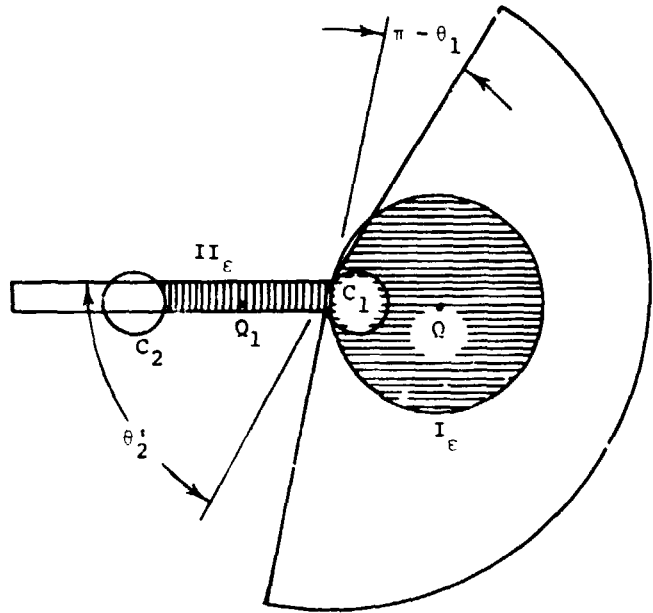


Figure 5: The subdomains  $I_\epsilon$  and  $II_\epsilon$ .  $B_R(Q)$  is tangent to  $l_1$  at  $P_0^\epsilon$ .  $C_1$  is the circle through  $P_0$  and  $P_1$  that hits  $l_3$  with angle  $\theta_2'$ .

**Lemma 3.1:** There exists a unique solution to (1), (2) in any  $\Omega_\epsilon$ . It is bounded above, non-negative, and extends smoothly to the smooth parts of  $\partial\Omega_\epsilon$ .

**Proof:** The existence, regularity and boundedness follow from the references mentioned in section 1. The fact that  $u > 0$  follows immediately from the comparison principle (Cor. 2.2), comparing  $u$  to  $w \equiv 0$  on the entire domain  $\Omega_\epsilon$ .

We are interested in the behavior of  $u_\epsilon$  near  $P_0$ , as  $\epsilon$  approaches 0. We will show that  $u_\epsilon$  stays uniformly bounded in one sector touching  $P_0$  whereas in another it gets uniformly large. It follows that  $u_\epsilon$  eventually has a jump discontinuity at  $P_0$ .

Let  $I_\epsilon$  be the subdomain of  $\Omega_\epsilon$  shown in Figure 5. Then we have

**Lemma 3.2:**  $u_\epsilon$  is uniformly bounded in  $I_\epsilon$ , independently of  $\epsilon$ .

**Proof:** We use the comparison principle, taking  $\Omega = I_\epsilon$ . Our candidate for a supersolution is a function  $v$  whose graph is a lower hemisphere lying above  $B_R(Q)$ . Its contact angle with  $B_R \cap \partial\Omega = B_R \cap l_1$  is exactly  $\pi - \theta_1$ . (If a plane slices a sphere the contact angle is the same along the entire circle of contact.) But by (7),  $\pi - \theta_1 < \gamma$ . Along

$\partial B_R(Q) \cap \Omega$  the hemisphere is vertical,  $\gamma_v = 0 < \gamma_u$  since  $u$  is smooth there. Thus  $v$  satisfies the supersolution boundary condition of Cor. 2.2. We must lift the hemisphere high enough to make

$$\operatorname{div} T v \leq \kappa v. \quad (8)$$

But  $\operatorname{div} T v = 2H(S_v) = 2/R$ , so (8) is satisfied if

$$v > 2/R\kappa.$$

This can be accomplished by placing the south pole at height  $2/R\kappa$ . Since the lower hemisphere varies in height by  $R$ , the comparison principle implies

$$u_\epsilon \leq v \leq 2/R\kappa + R \text{ in } I_\epsilon. \quad (9)$$

This estimate is independent of  $\epsilon$ . (See Figure 6.) Q.E.D.

Now fix  $\theta'_2$  with  $\gamma < \theta'_2 < \theta_2$  and let  $\Pi_\epsilon$  be the subregion of  $\Omega_\epsilon$  as described in Figure 5. Then we have

**Lemma 3.3:**  $u_\epsilon$  approaches  $\infty$  uniformly in  $\Pi_\epsilon$  as  $\epsilon$  approaches zero.

**Proof:** We apply the comparison principle with  $\partial = \Pi_\epsilon$ . Our candidate  $w$  for a subsolution is the "underside" of a torus. We take the unique (vertical) torus in  $R^3$  containing  $C_1$  and  $C_2$  (Figure 5). It is generated by rotating  $C_1$  about an axis parallel to the  $y$ -axis and going through  $Q_1$ , the point midway between  $C_1$  and  $C_2$ . Then in  $\Pi_\epsilon$  the "underside"  $T = S_w$  of the torus is the graph of

$$w(x,y) = [(R - \sqrt{r^2 - (y - y_1)^2})^2 - (x - x_1)^2]^{1/2},$$

where  $(x_1, y_1) = Q_1$ .  $T$  contacts  $I_3 \times R$  with contact angle  $\theta'_2 > \gamma$  and contacts  $I_2 \times R$  with contact angle of at least  $\theta'_2$ . It is vertical along  $C_1$  and  $C_2$  and has contact angle  $\gamma_w = \pi > \gamma_u$  (since  $u$  is smooth along these arcs). Thus  $w$  satisfies the subsolution boundary condition of Cor. 2.2. In order to be a subsolution it must therefore be low enough to satisfy

$$\operatorname{div} Tw > \kappa w.$$

But the mean curvature of a torus can be calculated and satisfies

$$\operatorname{div} Tw > \frac{1}{r} - \frac{1}{R-r}. \quad (10)$$

So it suffices to satisfy  $(\frac{1}{r} - \frac{1}{R-r}) > \kappa w$ , i.e.

$$w < \frac{1}{\kappa} \left( \frac{1}{r} - \frac{1}{R-r} \right). \quad (11)$$

This can be done by placing the highest part of  $S_w$  at the height (11). Since the total height of  $S_w$  varies by no more than  $R$ , we then have

$$w > \frac{1}{\kappa} \left( \frac{1}{r} - \frac{1}{R-r} \right) - R$$

and by the comparison principle,

$$u_\epsilon > w > \frac{1}{\kappa} \left( \frac{1}{r} - \frac{1}{R-r} \right) - R \text{ in } \Pi_\epsilon. \quad (12)$$

But  $r$  is proportional to  $\epsilon$  and  $R$  is fixed, so (12) implies that  $u_\epsilon$  approaches infinity uniformly in  $\Pi_\epsilon$  as  $\epsilon$  approaches zero.

Combining Lemmas 3.1-3.3 immediately yields the desired:

**Theorem 3.4:** For  $\epsilon$  sufficiently small the solution  $u_\epsilon$  to the capillary problem (1), (2) in  $\Omega_\epsilon$  cannot be extended continuously to the vertex of the re-entrant corner of angle  $\theta$ .

One can study the behavior of  $u_\epsilon$  near the vertex more carefully. Consider for example the particular case  $\theta = 3/2\pi$ ,  $\theta_1 = \pi$ ,  $\theta_2 = \pi/2$ . (This is the domain one gets by pushing two vertically held microscope slides close together in a bowl of water.) Since  $u_\epsilon$  becomes vertical near  $P_0$  the capillary surface must "look like" the picture in Figure 7: It has essentially no curvature in the vertical direction and its level sets are approximately circular arcs with curvature  $\kappa z$ . In fact, one can construct comparison surfaces having exactly that form near  $P_0$  (and then modified slightly near their high and low points to conform to the comparison principle). An easy calculation then implies that the jump in  $u$  at  $P_0$  is given by

$$\limsup_{P \rightarrow P_0} u_\epsilon(P) - \liminf_{P \rightarrow P_0} u_\epsilon(P) = \frac{2\cos\gamma}{\epsilon\kappa} + O(1) \quad (13)$$

as  $\epsilon$  approaches zero. For distilled water and air  $\kappa$  is approximately  $13 \text{ cm}^{-2}$  and between water and glass the contact angle is near zero, so that one should be able to see a jump of about 1 cm. by taking

$$\epsilon = 2/13 \text{ cm}.$$

This is quite narrow. Experimentally, better success will be obtained by using two fluids of approximately the same density (so that  $\kappa$  is considerably reduced). (Also, for a jump of only 1 cm. the  $O(1)$  term in (13) could still play a destructive role.)

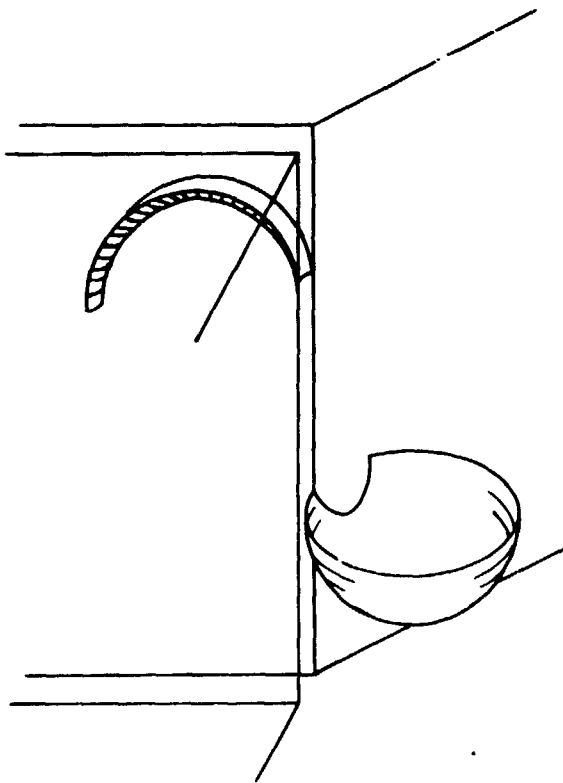


Figure 6: A lower hemisphere contacting  $\partial\Omega_\epsilon \times \mathbf{R}$  with angle less than  $\gamma$ . The "underside" of a torus with angle of contact greater than  $\gamma$ .

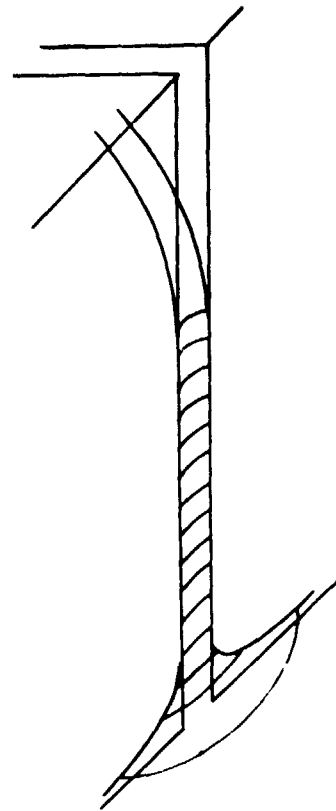


Figure 7: The asymptotic behavior of  $u_\epsilon$ . (Here  $\theta = \frac{3\pi}{2}$ ,  $\theta_1 = \pi$ ,  $\theta_2 = \pi/2$ ).

Remark 3.5: What happens in the complimentary case of convex corners? As remarked in section 2, if  $\theta < \pi - 2\gamma$   $u$  approaches infinity uniformly. Simon has shown that in the case  $\pi - 2\gamma < \theta < 2\pi$   $u$  actually extends to be  $C^1$  at the vertex<sup>8</sup>. Therefore it seems that the only way  $u$  can have a jump discontinuity is if there is a re-entrant corner. This is actually correct:  $u$  extends continuously to a point on the boundary of a Lipschitz domain if the boundary is locally  $C^1$  or locally convex there<sup>7</sup>.

#### Acknowledgment

Sponsored by the United States Army under Contract No. DAAG29-80-C-0041. This material is based upon work supported by the National Science Foundation under Grant No. MCS-7927062, Mod. 1.

#### References

1. Brown, R. A., "Finite Element Methods for the Calculation of Capillary Surfaces," J. Comp. Physics, Vol. 33, pp. 217-235. 1979.
2. Concus, P. and Finn, R., "On the Behavior of a Capillary Free Surface in a Wedge," Proc. Nat. Acad. Sci., Vol. 63, pp. 292-299. 1969.
3. Concus, P. and Finn, R., "On Capillary Free Surfaces in a Gravitational Field," Acta. Math., Vol. 132, pp. 207-223. 1974.
4. Enmer, M., "Esistenza, Unicit  e Regolarita nelle Superfici di Equilibrio nei Capillari," Ann. Univ. Ferrara Sez. VII, Vol. 18, pp. 79-94. 1973.
5. Finn, R. and Gerhardt, C., "The Internal Sphere Condition and the Capillarity Problem," Ann. Mat. Pura Appl. IV, Vol. 112, pp. 13-31. 1977.

6. Korevaar, N., "On the Behavior of a Capillary Surface at a Re-entrant Corner," Pacific J. Math., Vol. 88, pp. 379-385. 1980.
7. Korevaar, N., Capillary Surface Behavior Determined by the Bounding Cylinder's Shape, Ph.D. dissertation, Stanford University. 1981.
8. Simon, L., "Regularity of Capillary Surfaces Over Domains with Corners," Pacific J. Math., Vol. 88, pp. 363-377. 1980.
9. Simon, L. and Spruck, J., "Existence and Regularity of Capillary Surfaces with Prescribed Contact Angle," Arch. Rational Mech. Anal., Vol. 61, pp. 19-34. 1976.

## Fluid models and simulations of biological cell phenomena

H. P. Greenspan

Department of Mathematics, Massachusetts Institute of Technology  
 Room 2-343, 77 Massachusetts Avenue, Cambridge, MA 02139

Abstract

One aspect of Biofluid research concerns the dynamics of coated droplets. Of specific interest is the manner in which the shape of a droplet, the motion within it as well as that of aggregates of droplets can be controlled by the modulation of surface properties and the extent to which such fluid phenomena are an intrinsic part of cellular processes. From the standpoint of biology, an objective is to elucidate some of the general dynamical features that affect the disposition of an entire cell, cell colonies and tissues. Conventionally averaged field variables of continuum mechanics are used to describe the overall "global" effects which result from the myriad of small scale molecular interactions. By this means, an attempt is made to establish cause and effect relationships from correct dynamical laws of motion rather than by what may have been unnecessary invocation of metabolic or life processes. The distinction between what must be a life process and what may really be the result of more ordinary inanimate mechanisms is an important and central question, the resolution of which will lead to a deeper understanding of biological activity as well as the origin of life.

Several topics are discussed where there are strong analogies between droplets and cells. These are: encapsulated droplets -- cell membranes; droplet shape -- cell shape; adhesion and spread of a droplet -- cell motility and adhesion; foams and multiphase flows -- cell aggregates and tissues. Evidence is presented to show that certain concepts of continuum theory such as surface tension, surface free energy, contact angle, bending moments, etc. are relevant and applicable to the study of cell biology.

1. Introduction

A primary objective of biologists is to understand the structure and function of basic molecular complexes that constitute life processes. At this fundamental level of inquiry -- the direct bio-chemical interactions between molecules -- fluid dynamics is not applicable (although mathematical analysis, presently eschewed, could be used more effectively). However, when the focus of study turns to the explanation of the comparatively large scale phenomena that result from a myriad of molecular reactions, continuum theory becomes a natural and often preferred means of investigation as it does when the corresponding transition in physics is made from single to many particle systems. This in fact is a pertinent analogy that well illustrates the anticipated role of continuum mechanics in biology. To say that the movements of or within a cell are explained by the contractile capability of certain protein molecules is about as satisfying, and as predictive, as the knowledge that all mechanics follows directly, in some way, from the application of Newton's laws of motion to each and every constituent particle of a medium. It is not generally recognized within biology that (a) the large scale dynamical consequences of the interaction of very many particles need not be discernible on the molecular scale or even predictable from that standpoint; (b) the net effect on the aggregate can be distinctive, new phenomena which transcend the behavior of the individual elements such as waves, instabilities, patterns and structure. As a result, there is a paucity of cell physiological data that is relevant to continuum formulations and very few experiments attempt to measure the variables and parameters that characterize the rheology of a medium or its dynamic response. (Even less can be said about acceptance or the use of mathematics and mathematical models.) Unfortunately, biologists, like other scientists, can scarcely maintain control over the vast flow of information within their own specialties. However, the present situation does exemplify the opportunities and challenges inherent in the renewed and growing contact between two venerable disciplines, and these will be stressed here.

Continuum mechanics offers to cell biology, the means to study tissue morphogenesis, growth and differentiation, cell processes that involve dynamic change, motion and flow, as well as the conditions that maintain equilibrium. The description of patterns, flows and structures in terms of continuum state variables and rheological parameters will provide understanding of the dynamical principles that govern global phenomena. The use of dimensional analysis will enable data to be interpreted and correlated; experiments will be suggested and experimental techniques adapted; theoretical models and analogies will help formulate and test hypotheses and provide for detailed analysis of special events.

In return biology gives the continuum mechanician a miraculous "fluid" medium, an awe

inspiring chemical, metabolic system where almost anything conceivable can occur and seems actually to occur somewhere. With such wondrous material, what must be a life process and what can be the result of more ordinary inanimate dynamics become central questions to be resolved. The polymerization of contractile fibers is a favored omnibus explanation of much cellular activity but although this is indeed a most important mechanism, non-metabolic dynamic processes often give a simpler interpretation of events. This does not mean that when an inanimate mechanism is adequate, a more complicated life process is unnecessary. But it does require a rationalization of why in evolutionary developments a complex process has substituted for a simpler one. Questions of this type must lead to deeper understanding of biological processes.

Biological fluid dynamics, that is the fluid dynamics of cells and tissues, concerns that most complex material rheology yet studied. Although in most circumstances flows are slow, cellular material is chemically active in the extreme, most definitely a non-Newtonian colloid, emulsion or mixture subject to temporal and spatial changes of state from sol to gel, all within an ensemble or organelles of various compositions and functions -- minute deformable domains enclosed by a lipid/protein membranes of extraordinary properties. Moreover, even the simplest hydrodynamic analogies and simulations of cells and tissues lead to unsolved fluid problems of current interest in chemical engineering, microhydrodynamics, polymeric and interface sciences.

Corresponding topics in biology and fluid dynamics are roughly the following: cell rheology -- viscoelasticity; cell membranes -- interfaces and monolayers; cell shape -- droplet dynamics; cell adhesion and motility -- liquid adhesion and spreading; cell aggregates -- foams, emulsions and multi-phase mixtures. Some specific problems will illustrate these connections and the feedback that continually generates new questions.

## 2. Survey

Some of the biological phenomena which my colleagues and I have studied using continuum theory are cell cleavage, cell adhesion and motility, cell membranes (as monolayer coatings on droplets), cell cultures and capillary growth.

There are essentially two classes of problems represented here. One concerns motion of and within a cell and the other deals with the dynamics of cell aggregates. In the former, the relevant length scale is the size of the cell, which though small, is still very much greater than molecular distances. In the latter the cell itself may be viewed as the basic element of the tissue fluid as long as the phenomenological scales are many cell lengths. (However, both scales are usually microscopic in the literal sense. Large and small distances are referred to then as microscopic or submicroscopic and ultrafine, respectively.)

A continuum theory based on surface tension, slow viscous flow and an approximate momentum equation similar to Darcy's law, was formulated<sup>1</sup> to describe the growth and movement of certain cell cultures in response to a distribution of nutrient. In this model, a new cell forms, expands to proper size, and pushes aside neighboring cells of the culture. The forces of displacement are transmitted with attenuation throughout the cell population. The total pressure developed in this way causes internal migration of cells and a drift of the entire colony as it builds in the direction of a richer supply of nutrient. The internal motion is assumed to be proportional to the negative gradient of the pressure and a surface tension force proportional to the mean curvature of the tumor surface maintains the colony as a compact and continuous mass. In essence then, the culture is similar to an incompressible fluid within a variable domain in which there are sources and sinks. This theory and elaborations of it<sup>2</sup> are found to yield good agreement with observations.

The competition between surface and interior forces that control the shape of the colony, motivated an examination of dynamic instability of such cultures<sup>3</sup>. This analysis established the conditions in which the slight surface distortions that arise lead to the possible division of or disintegration of the colony. This like other analyses<sup>4</sup> makes the important point to biologists that instabilities are a natural part of biological development.

This example of the control of shape by surface tension, and the form of the most prominent mode of instability suggested that cell cleavage could also be approached along similar lines. A theory of cytokinesis was presented<sup>5</sup> in which cytoplasmic streaming, furrow development, contractile ring formation and division are all direct and related effects of a dynamical instability that is caused by the modulation of tension at or near the membrane surface during anaphase. Based on earlier work<sup>6</sup>, a completely fluid model of cleavage dynamics was constructed in which an effective surface tension simulates the sum of all forces exerted within the boundary structure of a cell. The dynamical process hypothesized was shown to be unstable and once triggered develops rapidly without further stimulation. The primary pattern of instability exhibits the typical shape of furrow formation at the equator; the time scale of this excitation is also consistent with

observations. However, this first model is much too simple to be an entirely realistic description of a cell, but it, with the accompanying experiments on the division of oil droplets and subsequent continuum analysis of the cell membrane as a thin elastic shell<sup>7</sup>, well illustrate the capabilities of surface forces and the manner in which they may be implicated in the division process.

A common theme in all this work is the control of droplet shape by surface forces that arise from the distribution of a surfactant on a pure interface, or from a material which is in fact a separate surface fluid. Several droplet problems were examined in order to explore the range of phenomena associated with surface flows and to develop greater intuition regarding the possible relevance of such effects in cell biology. For example, it has been shown<sup>8</sup> that the deposition of mass to the surface layer is in itself sufficient to cause spiculation of a droplet if the layer material is nearly incompressible, i.e., the surface compressional modulus is large. At early times, the surface layer does indeed behave like a true incompressible fluid and crenations form. But these protuberances decrease in size and in number as the compressibility of the real coating takes effect, until finally the droplet again becomes spherical. Essentially too much surface area for the contained volume causes ripples. The manner in which excess area is actually accommodated by fully nonlinear changes of droplet shape -- whether by bumps, invagination, folds, or a break up into smaller droplets -- is a question under examination.

It is known that the deposition and desorption of surfactants also leads to interface instabilities<sup>9</sup>, and in the combination of these effects (and a more complex model of the surface) lies a possible explanation of at least the onset of crenation, villation, and spiculation of real cells<sup>10</sup>.

The collapse of surface monolayers is a closely related instability problem of interest which is being examined simultaneously. The mathematical formalism developed for droplets applies in this case as well.

A similar approach based on "thin shell" theory of solid mechanics was used to construct a model of capillary growth in tissue<sup>11</sup>. Here the surface area of the capillary "cylinder" which consists of endothelial cells, increases as the cells divide. This leads to sinuous and bulbous instabilities of the column. These distortions seem essentially the same as those of capillaries observed in situ<sup>12</sup> and in fact, the theory provides an explanation of and qualitative agreement with experimental data.

The use of an effective surface tension to model the membrane and subcortical structure of the cell naturally gave rise to the question of whether adhesion and motility of cells<sup>13</sup> could also be simulated by droplets<sup>14</sup>.

Interfacial tensions between membrane, substratum and ambient medium must be a part of the physical mechanism by which an almost spherical cell rapidly flattens after mitosis. Chemical changes in the cell surface at division probably increase the affinity of membrane molecules for those of the substratum or solid boundary providing thereby the main forces for the initial extension of a cell. The intrinsic process may be somewhat analogous to the spread of a liquid droplet on a solid. Although the cell attaches to the surface at only thousands of sites mainly along its periphery<sup>15</sup>, while there are many billions of binding sites for a liquid droplet, this is still probably a sufficiently large sample for the same kind of statistical averaging to apply that underlies a continuum theory. It would then follow that such concepts as surface free energy, spreading and contact angle have loose analogs in cell adhesion and motility. (It should be noted that the spreading of a liquid droplet is in many respect an unsolved problem. The exact nature of the boundary conditions at the advancing liquid/solid boundary is unclear<sup>16</sup> and this reflects the uncertainty about the physics of fluid attachment of a surface which implies the condition of no-slip.)

We advanced a model<sup>17</sup> for the movement of a small droplet on a surface specifically adapted for the high viscosity of cells. This was based on the lubrication equations and used the concept of dynamic contact angle to describe the forces that act on the fluid at the contact line. The specific problems solved with this theory were the spreading and retraction of a circular droplet; the advance of a thin two-dimensional layer; the creeping of a droplet on a coated surface to a region of greater adhesion; the distortion of droplet shape owing to surface contamination. A more intensive analysis of the equations<sup>18</sup> showed that an advancing droplet becomes more pear-shaped in outline, with a broader advancing contact line and a narrower retreating edge. This has some of the features of motile cells; however, numerical methods will have to be employed to examine further the shape and stability of the edge contour.

The similarities between the spread of a cell and of a droplet that were noted by Greenspan and Folkman<sup>19</sup>, have been exploited to a remarkable degree in the experiments of Folkman and Moscona<sup>20</sup>. They have shown that the shape of a cell can determine whether DNA

synthesis will be permitted; the technique used was to control the degree of spreading on coated the plastic slips, i.e., by modifying the interfacial tension in the known manner. The fact that cell shape can be proven to correlate with cell function substantiates some of the earlier hypotheses relating shape and function<sup>1</sup>. There is now considerable evidence<sup>2</sup> that surface tension and contact angle are meaningful and useful concepts in cell biology, but more work is required before the advantages of this viewpoint are accepted.

The study of the dynamics of encapsulated droplets has been extended by considering a surface coating which is an oriented, polar fluid of either a monolayer or a bilayer structure. The general theory of polar fluids<sup>3</sup> was adapted for such surface flows<sup>4</sup> and general constitutive laws were determined that relate surface stress, strain, bending moment and a non-Newtonian rheology<sup>5</sup>. The bending moment of the membrane arises from the preferred orientation of the molecules that form the surface layer. Its importance has been discussed in connection with the shape of the red blood cell<sup>6</sup> and with the growth of capillaries in tissues<sup>7</sup>. In both cases, the bending moment appears as a stabilizing factor because it acts to undo distortions of an equilibrium configuration and to cut off the growth of incipient wave instabilities below a certain wave length. However, this is not as yet a general conclusion valid in all circumstances. The interplay of moments, variable surface tension (pressure) and chemical exchange with the bulk fluid by the deposition and desorption of surfactants could easily produce a range of new, interesting and surprising effects.

We are currently examining the dynamics of liquid/liquid foams (i.e., coated droplets in an aqueous medium) with the focus on an accurate description of the motion that results from the addition of surfactants. The behavior of such systems is in many ways analogous to assemblages of cells in cultures and colonies. For example, spiral patterns of motion are observed in such biliquid foams<sup>8</sup>; likewise the development of "similar" spirals in cultured epidermal cells has also been described<sup>9</sup>. Whether the underlying mechanical and visco-elastic processes are also analogous remains to be seen<sup>10</sup>. One difficulty is that the fluid dynamics of foams is essentially an undeveloped area whose theoretical formulation is not completely understood. Accordingly, we have had to begin with certain fundamental, idealized problems that are several levels removed from biological applications, and this has indeed become a separate program of research.

The results of such a study should also be directly relevant to our continuing investigation of the growth and movement of certain cell cultures and solid tumors in response to a changing chemical environment. Development of a more elaborate compressible fluid model of tissues is necessary in order to substantiate or to generalize the empirical dynamical law that has been assumed. We would then be better positioned to inquire about the dynamic response of cultures to stimuli, and the effects of spatially varying rheological properties.

#### References

1. Greenspan, H.P., "Models for the Growth of a Solid Tumor by Diffusion", Studies in Applied Mathematics, 51, pp. 317-340. 1972.
- 2a. McElwain, D. and Ponzio, P., "Model for the Growth of a Solid Tumor with Non-Uniform Oxygen Consumption", Math. Biosci. 35, pp. 267-279. 1977.
- 2b. McElwain, D. and Morris, L., "Apoptosis as a Volume Loss Mechanism in Math Models of Solid Tumor Growth", Math. Bio. Sci. 39, pp. 147-157. 1978.
- 2c. Li, Conan, K.N., "The Glucose Distribution in 9L Rat Brain Multicell Tumor Spheroids and its Effect on Cell Necrosis." 24 page preprint.
3. Greenspan, H.P., "On the Growth and Stability of Cell Cultures and Solid Tumors", J. Theor. Biol. 56, pp. 229-242. 1976.
- 4a. Odell, G. et al., "A Mechanical Model for Epithelial Morphogenesis", J. of Math. Biology, 9, pp. 291-295. 1980.
- 4b. Odell, G., et al., "The Mechanical Basis for Morphogenesis I: Epithelial Folding and Invagination. To appear in Developmental Biology. 1981.
- 5a. Greenspan, H.P., "On the Dynamics of Cell Cleavage", J. of Theor. Biol. 65, pp. 79-99. 1977.
- 5b. Greenspan, H.P., "On the Deformation of a Viscous Droplet Caused by Variable Surface Tension", Studies in Applied Mathematics, 57, pp. 45-58. 1977.
- 5c. Greenspan, H.P., "On Fluid-Mechanical Simulations of Cell Division and Movement", J. Theor. Biol. 70, pp. 124-134. 1978.
- 6a. Butschli, O., Investigation on Microscopic Foams and on Protoplasm, Black (London).
- 6b. Harvey, E., "Tension at the Cell Surface", Protoplasmatologia, 11, 1954.
- 6c. Hiramoto, Y., "Mechanics and Mechanism of Cleavage in Sea-Urchin Egg", Symp. Soc. Exp. Bio. 22. 1968.
- 6d. Rappaport, R., "Cytokinesis in Animal Cells", Intl'l Rev. Cytol 31, pp. 169-213. 1971.
7. Pujara, P. and Lardner, T.J., "A Model for Cell Division", J. Biomech., 12, pp. 293-

299. 1979.

8. Greenspan, H.P. and Landman, K.A., "On the Crenation of Coated Droplets", to be published in Studies in Applied Mathematics. (1981).
- 9a. Scriven, L.E. and Miller, C.A., "The Oscillations of a Fluid Droplet Immersed in Another Fluid", J. Fluid Mech. 32, pp. 417-435. 1968.
- 9b. Saville, D.A., "The Effects of Interfacial Tension Gradients on the Motion of Drops and Bubbles", The Chemical Engineering Journal, 5, pp. 251-259. 1973.
- 9c. Sorensen, T.S., "Chemical and Hydrodynamical Analysis of Stability of a Spherical Interface", J. of Colloid. and Interface Sci. 56, pp. 191-205. 1976.
- 10a. Bragina, E.E. et al., "Formation of Bundles of Microfilaments During Spreading of Fibroblasts on the Substrate", Exp. Cell Res. 97, pp. 241-248. 1976.
- 10b. Wasserman, P.M. et al., "Cytochalasin Induced Pseudo-Cleavage", J. Cell Sci. 21, 523-535. 1976.
- 10c. Fischer, T. et al., "The Red Cell as a Fluid Droplet", Science 202, pp. 894-896. 1978.
11. Waxman, A.M., "A Continuum Approach to Blood Vessel Growth: I. Axisymmetric Elastic Structures", J. Theor. Biol. 91, pp. 273-301. 1981.
12. Folkman, J., "The Vascularization of Tumors", Scientific American, 234, pp. 58-73. 1976.
- 13a. Carter, S.B., "Haptotaxis and the Mechanism of Cell Mobility", Nature, 213, pp. 261-264. 1967.
- 13b. Harris, A., "Behavior of Cultured Cells on Substrata of Variable Adhesiveness", Exp. Cell Res. 77, pp. 285-297. 1973.
- 13c. Albrecht-Buehler, G., "Phagokinetic Tracks", Cell 12, pp. 333-339. 1977.
- 14a. Schonhorn, H. et al., "Kinetics of Wetting of Surfaces by Polymer Melts", J. of Applied Physics 37, pp. 4967-4973. 1966.
- 14b. Pegram, S.M. and Maroudas, N.G., "Early Events in Fibroblast Adhesion to Glass", Exp. Cell Res. 96, pp. 416-422. 1975.
- 15a. Harris, A., "Location of Cellular Adhesions to Solid Substrata", Dev. Biol. 35, pp. 97-114. 1973.
- 15b. Revel, J.P. et al., "Adhesion of Culture Cells to their Substratum", Exp. Cell Res., 84, pp. 207-218. 1974.
- 15c. Gershman, H. and Rosen, J.J., "Cell Adhesion and Cell Surface Topography", J. Cell Bio. 76, pp. 639-651. 1978.
16. Dussan, E.B., "On the Spreading of Liquids on Solid Surfaces: Static and Dynamic Contact Line", Annl. Rev. Fluid Mech. 11, pp. 371-400. 1979.
17. Greenspan, H.P., "On the Motion of a Small Viscous Droplet that Wets a Surface", J. Fluid Mech. 84, pp. 125-143. 1978.
18. Greenspan, H.P. and McCay, B., "On the Wetting of a Surface by a Very Viscous Fluid", Studies in Applied Mathematics 64, pp. 95-112. 1981.
19. Greenspan, H.P. and Folkman, J., "Hypothesis of Cell Adhesion and Actin Cables", J. Theor. Biol. 65, pp. 397-398. 1975.
20. Folkman, J. and Moscona, A., "Role of Cell Shape in Growth Control", Nature, 273 pp. 345-349. 1978.
21. Folkman, J. and Greenspan, H.P., "Influence of Geometry on Control of Cell Growth", Biochimica et Biophysica Acta. 417, pp. 211-236. 1975.
- 22a. Van Oss, C.J., "Phagocytosis as a Surface Phenomena", Ann. Rev. of Microbiol., 32, pp. 19-39. 1978.
- 22b. Tanford, C., "Hydrostatic Pressure in Small Phospholipid Vesicles", Proc. Nat'l. Acad. Sci., 76, pp. 3318-3319. 1979.
23. Cowin, S.C., "The Theory of Polar Fluids", Advances in Applied Mechanics, 14, pp. 279-347. 1974.
24. Waxman, A., "Blood Vessel Growth as a Problem in Morphogenesis: A Physical Theory", Microvascular Research 22, pp. 32-42. 1981.
- 25a. Sheetz, M. et al., "Biological Membranes as Bilayer Couples III. Compensatory Shape Changes Induced in Membranes", J. of Cell Biology, 70, pp. 193-203. 1976.
- 25b. Evans, E.A. and Hochmuth, R.M., "Mechanochemical Properties of Membranes", Current Topics in Membranes and Transport, 10, Ed. F. Bonner, Academic Press, 64 pages. 1978.
26. Sebba, F., "Macrocluster Gas-Liquid and Biliquid Foams and their Biological Significance", A.C.S. Symposium Series 9 Coll. Dispersions and Micellar Behavior, 18, pp. 18-39. 1975.
27. Green, H. and Thomas, J., "Pattern Formation by Cultured Human Epidermal Cells", Science, 300 pp. 1385-1393. 1978.
- 28a. Phillips, H. and Steinberg, M., "Embryonic Tissues as Elastic Viscous Fluids", 11, Dev. Biol. 59, pp. 124-134. 1977.
- 28b. Phillips, H. and Steinberg, M., "Embryonic Tissues as Elastic-Viscous Liquids", J. Cell Sci. 30, pp. 1-20. 1978.
- 28c. Thurston, G.B. and Davis, S.F., "The Visco-Elastic Properties of a Soap-Stabilized Oil-In-Water Emulsion", J. of Colloid. and Interface Sci. 69, pp. 199-208. 1979.

Capillary forces exerted by liquid drops caught between crossed cylinders:  
A 3-D meniscus problem with free contact line

T. W. Patzek and L. E. Scriven

Department of Chemical Engineering & Materials Science,  
University of Minnesota, Minneapolis, Minnesota 55455

Abstract

The Young-Laplace equation is solved for three-dimensional menisci between crossed cylinders, with either the contact line fixed or the contact angle prescribed, by means of the Galerkin/finite element method. Shapes are computed, and with them the practically important quantities: drop volume, wetted area, capillary pressure force, surface tension force, and the total force exerted by the drop on each cylinder.

1. Problem statement

A liquid drop between solid fibers (Fig. 1) constitutes a three-phase system whose thermodynamic description may become quite involved (cf. Huh 1969). However, even without gravity, if the fluid-solid contact line differs from a circle, or two coaxial circles, the drop surface generally forms a three-dimensional meniscus of constant curvature, difficult to approximate from experiment and non-trivial to compute from theory. In large drops, gravity joins surface tension in the molding of shape and the situation becomes even more complex. The surface energy of the system in the absence of gravity is

$$E = \sigma_{LV} S_{LV} + (\sigma_{LS} - \sigma_{SV}) S_{LS} + E_0 \quad (1)$$

liq/vap   liq/sol-sol/vap   sol/vap datum

Here the solid surface is rigid and the solid-liquid vapor interactions are described by the constant interfacial tensions  $\sigma_{LV}$ ,  $\sigma_{LS}$ , and  $\sigma_{SV}$ .

Equilibrium drop shapes make the surface energy stationary, i.e.  $\delta E = 0$  for all perturbations that leave the drop volume fixed,  $\delta V = 0$ , and either the contact line fixed,  $\delta x_{LSV} = 0$ , or the contact angle unchanged,  $(\mathbf{n}_{LV} \cdot \mathbf{n}_S = \cos \beta$ , where  $\beta$  is the contact angle). These conditions define a variational problem equivalent to the Young-Laplace equation of capillarity — a normal stress balance — with appropriate boundary conditions at the contact line:

$$\delta E = \int_{S_{LV}} \left[ \frac{P_V - P_L}{\sigma_{LV}} - 2H_{LV}(x_{LV}) \right] \delta x_{LV} \cdot \mathbf{n}_{LV} \, dS +$$

capillary pressure →  $\frac{P_V - P_L}{\sigma_{LV}}$   
 interface mean curvature →  $2H_{LV}(x_{LV})$   
 interface location →  $x_{LV}$   
 normal interface perturbation →  $\delta x_{LV} \cdot \mathbf{n}_{LV}$   
 unit normal to interface →  $\mathbf{n}_{LV}$

$$+ \oint_{L_{LSV}} \left[ \mathbf{n}_{LV} \cdot \mathbf{n}_S - \frac{\sigma_{SV} - \sigma_{LS}}{\sigma_{LV}} \right] \delta x_{LV} \cdot \mathbf{t}_{LSV} \times \mathbf{n}_S \, dL = 0 \quad (2)$$

normal contact line perturbation, parallel to solid surface →  $\delta x_{LV} \cdot \mathbf{t}_{LSV}$   
 unit tangent to contact line →  $\mathbf{t}_{LSV}$   
 unit normal to solid surface →  $\mathbf{n}_S$   
 cosine of contact angle  $\beta$  →  $\mathbf{n}_{LV} \cdot \mathbf{n}_S$

Eq. [2] makes plain that the vanishing variation forces the Young-Laplace residual,  $2H_{LV} - (P_V - P_L)/\sigma_{LV}$ , and likewise the Young-Dupré residual,  $\cos \beta - (\sigma_{SV} - \sigma_{LS})/\sigma_{LV}$ , to be orthogonal (as viewed in the appropriate function space) to admissible normal perturbations.

A drop of liquid trapped between two perpendicular cylinders of equal radii is of interest. When the cylinders touch, their point of contact is taken as the origin (Fig. 2). Spherical coordinates are used to obtain a single-valued representation of the liquid-vapor interface. A sphere of radius R, equal to the cylinder diameter, is chosen as the base surface and is centered at the origin.

The unknown position of the interface, measured in the units of R, is

$$x_{LV} = f(\theta, \phi) e_r \quad [3]$$

Analogously, the interface perturbation is

$$\delta x_{LV} = \zeta(\theta, \phi) e_r \quad [4]$$

Furthermore, in the case of spherical representation, Weingarten's formulas relate the mean curvature of the interface to the divergence of the unit normal on the unit sphere  $\Omega$ :

$$2H_{LV} = - \frac{1}{f(\theta, \phi)} \nabla_{\Omega} \cdot n_{LV} \quad [5]$$

This, together with the divergence theorem, leads to the weak form of Eq. [2]:

$$\int_{\Omega} \left[ -n_{LV} \cdot (\nabla_{\Omega} (f\zeta) - 2\zeta e_r) + \frac{P_V - P_L}{\sigma_{LV}} \zeta f^2 \right] d\Omega +$$

↙ projected domain on unit sphere

$$+ \int_{\Lambda} f \zeta n_{LV} \cdot m_{\Omega} dA +$$

↙ projected binormal of contact line

↘ projected contact line

$$+ \int_{L_{LSV}} (n_{LV} \cdot n_S - \cos \beta) \zeta e_r \cdot t_{LSV} \times n_S dL = 0 \quad [6]$$

## 2. Galerkin/finite element method

The main steps of the finite element algorithm can be outlined as follows:

- (i) The problem is nonlinear and so an initial estimate of drop shape (and contact line position) is needed that falls within the domain of convergence of the iteration method. Estimate from either analysis of a limiting case or experimental observations or a blend of both. The last leads to the inside surface of a small torus as an initial guess.
- (ii) To discretize the problem, partition the corresponding spherical domain (Fig. 3) into curvilinear quadrilaterals between the equally spaced spines  $\phi = \text{constant}$  (cf. Kistler 1981). The spines remain fixed but the nodes of the quadrilaterals can move along them. Let the number of nodes in the partition be N.
- (iii) Construct a finite element basis function  $\Psi^i(\theta, \phi)$  for the subdomain around each node (cf. Brown, Orr, and Scriven 1979):
  - choose the biquadratic polynomial on the  $(\xi, \eta)$ -unit square,
  - map each quadrilateral isoparametrically  $(\theta, \phi) \rightarrow (\xi, \eta)$  onto the unit square. This procedure transforms the original, free boundary domain  $\Omega$  in  $(\theta, \phi)$ -coordinates into a fixed square in the map  $(\xi, \eta)$  (Strang and Fix 1973).
- (iv) Approximate the drop shape as

$$f(\theta, \phi) = \sum_{i=1}^N \alpha_i \Psi^i \left[ \theta(\xi, \eta), \phi(\xi, \eta) \right]$$

- nodal values  $\alpha_i$  are the coefficients to be found.

(v) Approximate the shape perturbation as

$$\zeta(\theta, \phi) = \sum_1^N \gamma_i \psi^i \left[ \theta(\xi, \eta), \phi(\xi, \eta) \right]$$

- take  $\gamma_i$  as arbitrary coefficients. Because the  $\gamma_i$ 's are arbitrary, the Galerkin weighted residuals — to which Eq. [6] transforms under (iv) and (v) — must vanish at equilibrium. This brings out the *direct* link between the *Galerkin* and *variational* approach.
- (vi) Solve the resulting N nonlinear algebraic equations for the coefficients  $\alpha_i$  using Newton's method.
  - update the original domain in each iteration
  - use the Jacobian for continuation in the parameter  $(p_V - p_L)/\sigma_{LV}$  or V.
- (vii) Terminate iteration when the  $L_\infty$  norm of residuals, i.e. the largest residual, is smaller than a preset value, e.g.  $10^{-6}$  (as was actually used).

The algorithm was programmed in Fortran and executed on a CDC CYBER-74 computer. It took ca. 2 sec/iteration for 169 unknowns and three to at most five iterations to converge.

A sequence of drop shapes in order of increasing volume is shown in Fig. 4 ( $R(p_V - p_L)/\sigma_{LV} \equiv \text{LAMBDA}$ ). As capillary pressure decreases, the liquid forms drops of increasing volume and finally encircles both cylinders. The plotted drops are stable, including the largest one — the surface of which covers more than half of the cylinder cross-section.

### 3. Practical quantities

Drops of liquid caught between crossed fibers of non-woven fabrics draw them together by capillary action and, when the liquid solidifies, fasten the fibers together. Similar phenomena occur in paper, where water at times forms droplets by capillary condensation from humid air. Liquid drops between fibers are also present at certain stages of oily soil removal by detergent action. Furthermore, drop behavior between crossed cylinders is important to direct measurement of adhesive forces between solid surfaces in the presence of capillary-condensed liquids (Fisher and Israelachvili 1981). These and other applications call for computation of the following practically important quantities:

- (i) drop volume V
- (ii) wetted area of each cylinder A
- (iii) capillary forces exerted by drop

- capillary pressure force  $(p_V - p_L) \int_{S_{LV}} \mathbf{e}_z \cdot \mathbf{n}_{LV} \, dS$

- surface tension force  $\sigma_{LV} \int_{L_{LSV}} \mathbf{e}_z \cdot \mathbf{m}_{LV} \, dL$

- their sum: total force holding crossed cylinders together.

Fig. 5 shows that the total force on the cylinders increases with the wettability of the solid by the liquid. As can be seen from Fig. 6, the components of total force vary widely with the drop volume but their sum increases slowly and approaches an asymptotic limit as the volume shrinks to zero. That limit is  $4\pi\sigma_{LV}(R/2)\cos\beta$  (Fisher and Israelachvili 1981), and becomes a good approximation for  $R(p_V - p_L)/\sigma_{LV} \sim 10^4$ , i.e. for very small drops. If the mean curvature is taken as the independent parameter, the drop volume grows extremely sensitive to it as the contact angle decreases (Fig. 7), whereas the total force again approaches the limit (Fig. 8).

### Summary and conclusions

What is described here is an extension of earlier analyses of three-dimensional meniscus shapes (Orr, Brown and Scriven 1977).

Besides yielding equilibrium shapes of drops with *fixed contact lines*, as in past 3-D analyses, the algorithm used here also gives shapes of drops with a *prescribed contact angle*, which is sometimes a closer approximation to reality.

Computations for other cases of 3-D menisci making a prescribed contact angle can be treated similarly. Augmented by a block-Lanczos method for solving the related

ORIGINAL PAGE  
BLACK AND WHITE PHOTOGRAPH

eigenproblem (see Brown and Scriven 1980), the algorithm tests stability with respect to admissible perturbations with the contact line fixed. The case of prescribed contact angle is more difficult but is also being treated in the continuation of this work.

The results show that total capillary force between cylinders increases with decreasing contact angle, i.e. with better wetting. Capillary force also increases with *decreasing* drop volume, approaching an asymptotic limit. However, the wetted area on each cylinder decreases with decreasing drop volume, which raises the question of the optimum drop volume to strive for, when permanent bonding is sought from solidified liquid. For then the strength of the bond is likely to depend upon the area of contact, which is the wetted area when the bonding agent was introduced in liquid form.

Acknowledgment

This research was supported by the NASA Fund for Independent Research.

References

- R. A. Brown, F. M. Orr Jr., and L. E. Scriven, Three-Dimensional Menisci: Numerical Simulation by Finite Elements, *J. Colloid Interface Sci.* 60 137 (1977).
- R. A. Brown, F. M. Orr Jr., and L. E. Scriven, Static Drop on an Inclined Plate: Analysis by the Finite Element Method, *J. Colloid Interface Sci.* 73 76 (1980).
- R. A. Brown and L. E. Scriven, The Shapes and Stability of Captive Rotating Drops, *Phil. Trans. Roy. Soc.* 297 51 (1980).
- C. Huh, Capillary Hydrodynamics, Interfacial Instability and the Solid/Liquid/Fluid Contact Line, Ph.D. Thesis, University of Minnesota (1969).
- L. R. Fisher and J. N. Israelachvili, Direct Measurement of the Effect of Meniscus Forces on Adhesion . . . , *J. Colloid Interface Sci.* submitted (1981).
- L. R. Fisher and J. N. Israelachvili, Experimental Studies on the Applicability of the Kelvin Equation to Highly Curved Nonlinear Menisci, *J. Colloid Interface Sci.* submitted (1981).
- S. F. Kistler, First International Fluid Mechanics Winter (Summer) Seminar, INTEC - Santa Fe, 18-21 August 1981.
- G. Strang and G. J. Fix, *An Analysis of the Finite Element Method*, Prentice-Hall, Inc., Englewood Cliffs, N. J. (1973).



Fig. 1. Liquid drop caught between crossed cylinders

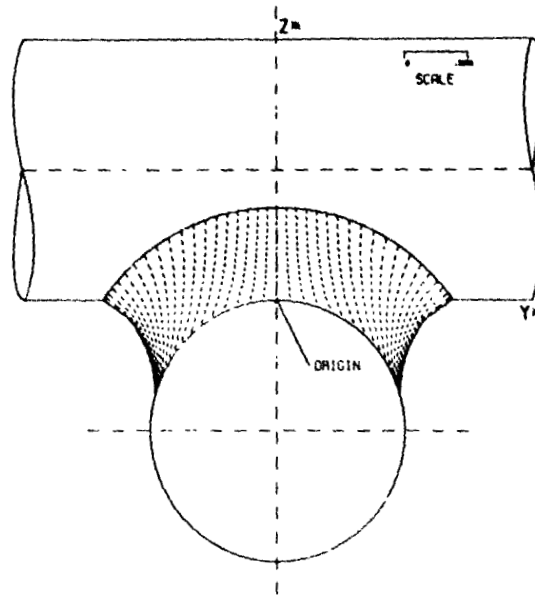


Fig. 2  
Two cylinders of equal radii crossed  
at right angle — coordinate system

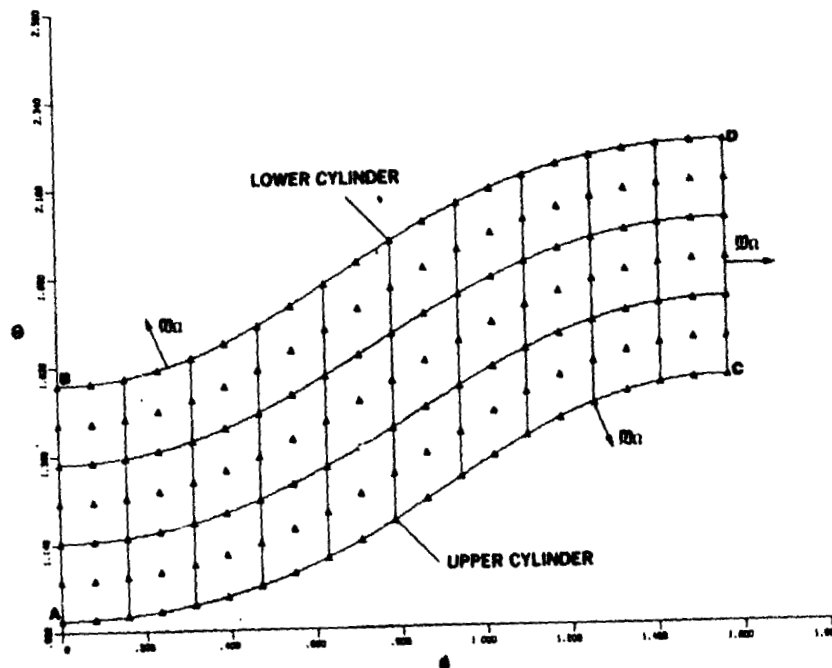


Fig. 3  
Typical computational domain in spherical coordinates

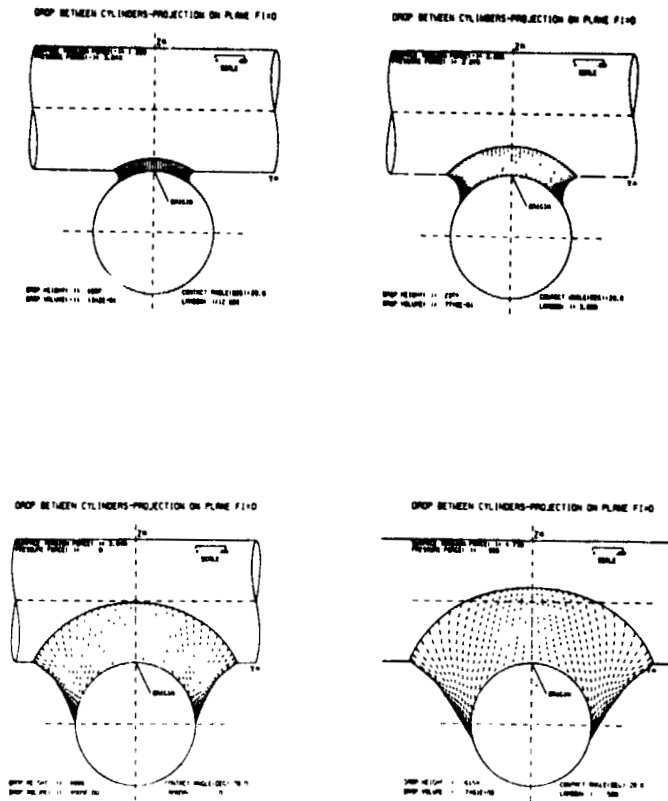


Fig. 4

Sequence of drop shapes in order of increasing volume.  
Dimensionless capillary pressure  $R(p_V - p_L)/\sigma_{LV} = \text{LAMBDA}$ .

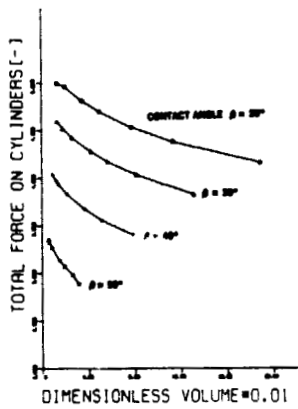


Fig. 5

Total force exerted by drop  
on each cylinder vs. drop volume.

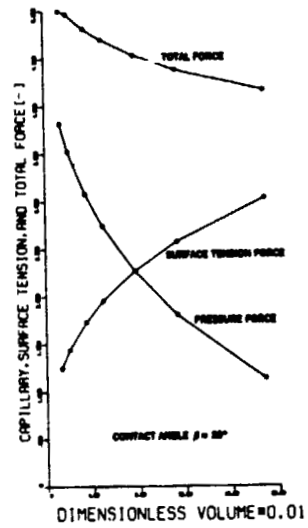


Fig. 6

Components of the total force  
vs. drop volume.

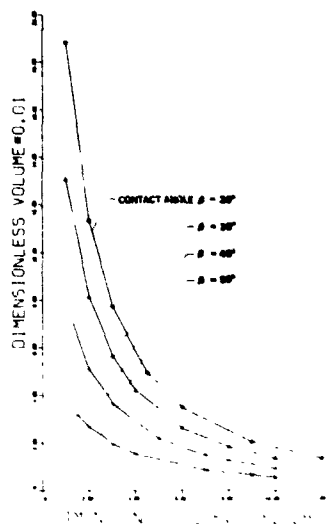


Fig. 7  
Drop volume vs.  
capillary pressure

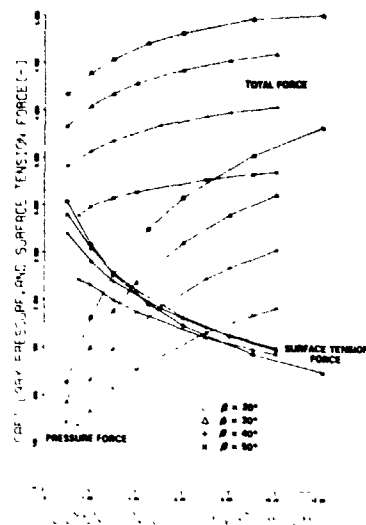


Fig. 8  
Forces exerted by  
drop on each cylinder  
vs. capillary pressure

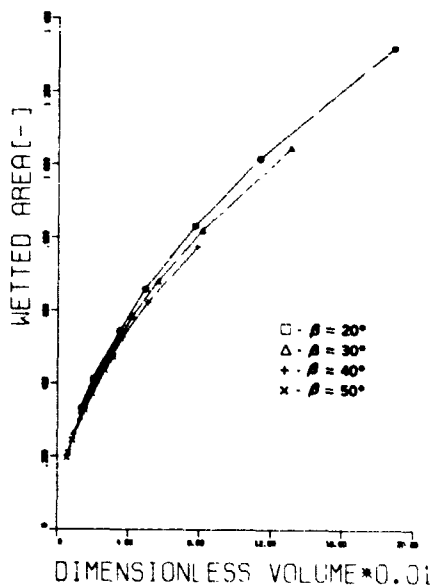


Fig. 9  
Wetted area on each cylinder vs. drop volume

The motion of a drop on a rigid surface

L. M. Hocking

Department of Mathematics, University College  
Gower Street, London WC1E 6BT, England

Abstract

The assumptions of a region of slip near a moving contact line (to remove the force-singularity) and a constant contact angle are used to obtain the equation for the shape of a thin drop of liquid resting on a horizontal plane. Three asymptotic expansions are matched together to obtain an expression for the rate at which the drop spreads. Some cases of sliding motion are also examined. Although the technique is presented here for thin drops only, it can also be applied to drops of arbitrary size.

Introduction

The chief difficulty that has to be overcome in an attempt to describe the motion of a drop in contact with a rigid surface is the determination of the correct boundary conditions to be applied at the contact line where the surface of the drop meets the rigid surface. If the drop is spreading over the surface, or if it is sliding along it, or both, the contact line is moving and it is well known that in these circumstances application of the no-slip boundary condition leads to a solution containing an unacceptable singularity. For certain purposes this singularity can be ignored but if, for example, we wish to determine the rate at which the drop spreads or the speed at which it slides, a dynamical balance of the forces acting must be achieved, which proves to be impossible in the presence of the force-singularity. To circumvent this difficulty, the most widely used device is to replace the no-slip boundary condition in the vicinity of the contact line by one allowing a certain amount of slip there. The argument in favour of this proposal is that large stresses occur near the contact line, associated with the rapid change in direction of the fluid motion there, and the molecular forces which are usually sufficient to prevent any slip between fluid and solid may be unable to control these large stresses. Of course, what is really required is a good molecular theory for the junction between drop, solid and surrounding air. Failing such a theory, some model boundary condition may be proposed in the hope that its exact form is of little consequence and that it will at least enable finite answers to be produced in answer to questions involving the force balances associated with the motion and that these answers can then be tested experimentally. The simplest model boundary condition is one which replaces the usual no-slip condition by one which allows a small amount of slip, proportional to the local velocity gradient. If  $u$  is the velocity parallel to the plane surface and  $z$  is measured normally away from it, the proposed boundary condition is

$$u - \lambda \partial u / \partial z = 0 \tag{1}$$

for a fluid in contact with a solid boundary at rest. The slip coefficient  $\lambda$  is a measure of the length over which slip is significant. Although its value is unknown, if the slip is produced by molecular effects we might expect a value of the order of  $10^{-9}$  m. Such slip is only expected to occur close to the contact line and the boundary condition should revert to its usual form elsewhere. However, the very small size suggested for  $\lambda$  indicates that the slip condition can be used everywhere with negligibly small error. As we shall see, allowing for slip near the contact line gives speeds proportional to  $1/|\ln \lambda|$  which is of much greater significance than any erroneous inclusion of terms proportional to  $\lambda$ .

When we have decided to use a slip boundary condition for problems involving moving contact lines, the stresses near the contact line are still large and we may consequently expect that there will be a significant distortion of the shape of the free surface near the contact line. The large stresses will be balanced by capillary effects, which are proportional to the curvature of the surface. In order to provide sufficient boundary conditions for the shape of the free surface to be calculated, it is necessary to specify the angle at which the free surface meets the plane. Observations of contact angles seem to show that the angle increases with the speed of advance of the contact line, and decreases when the contact line is retreating. For stationary drops, the contact angle is not uniquely defined but can take any value between certain limits. The evidence for the dynamic behaviour of the contact angle is based on observations which do not take account of any rapid change of slope in the very small distance from the edge of the drop where, as we have seen, large stresses are present. It may well be that the contact angle measured at the edge itself does not change with speed and the dynamic behaviour refers only to an apparent contact angle, only relevant at some distance from the edge. Evidence

in favour of this contention has been provided by Lowndes<sup>1</sup> who has produced numerical calculations for the motion of a meniscus along a tube using the slip hypothesis and keeping the actual contact angle fixed. He was able to show that apparent contact angles could be found from his calculated meniscus shapes which were in good agreement with observed values and that marked changes in slope occurred in the immediate vicinity of the edge.

The calculations of Lowndes<sup>1</sup> show that a self-consistent rational framework for dealing with moving contact lines is provided by the assumptions of slip at the edge and a fixed contact angle. This framework has been used to discuss the spreading and sliding of a drop which is thin enough for lubrication theory to be used<sup>2</sup>. These problems are time-dependent and an estimate of the speeds involved depends crucially on the slip hypothesis. Both the meniscus problem and the drop problems needed considerable numerical calculation, although the use of lubrication theory reduced the amount required to a large extent. The equations for the spreading and sliding drop problems involve a small parameter, the slip coefficient, which suggests that matched asymptotic expansions could yield the desired answers without recourse to extensive numerical calculation. An attempt at such a procedure was made before the numerical results were obtained, but was not successful. The present paper, however, shows that matched asymptotic expansions can be used to obtain the rate of spread of a thin drop and, with certain restrictions, the rate at which a drop slides down a plane. The key to success was the realisation that, as well as expected inner and outer expansions, an intermediate region was required across which the inner and outer regions could be matched. The method employed has some similarities to the one set out by Lacey<sup>3</sup>, except that he used a multiple scale approach and did not carry the solution sufficiently far.

Although the methods to be described here can be applied to a variety of problems, for simplicity they are explained with reference to the problems examined before<sup>2</sup>. The drop is assumed to be thin and two-dimensional and it is also assumed that it is small enough for the Bond number to be small, that is, for gravity to be less significant than capillarity. In the first problem, the drop is placed on a horizontal plane and allowed to spread until its equilibrium position is reached. The quantity to be determined is the rate of spread of the drop as a function of its width. In the second problem, the drop is placed on an inclined plane, when both spreading and sliding may occur. The final width of the drop and the speed at which it slides are the quantities to be determined in this case.

#### Formulation

The application of lubrication theory to the problems to be solved is straightforward and has been described in detail before<sup>2</sup>. The simplified forms of the Stokes equations enable the velocity components to be found in terms of the pressure and the application of the normal stress condition and the kinematic boundary condition at the free surface yields an equation for the height  $\bar{h}(x, \bar{t})$  of the drop, where  $\bar{x}$  is measured parallel to the plane surface and  $\bar{t}$  is the time. The equation for  $\bar{h}$  is

$$\frac{3\mu}{\sigma} \frac{\partial \bar{h}}{\partial \bar{t}} + \frac{\partial}{\partial \bar{x}} \left[ \bar{h}^2 (\bar{h} + 3\bar{\lambda}) \left\{ \frac{\partial^3 \bar{h}}{\partial \bar{x}^3} + \frac{g\rho \sin \theta}{\sigma} \right\} \right] = 0, \quad (2)$$

where  $\mu$  is the fluid viscosity,  $g$  gravity,  $\sigma$  surface tension,  $\bar{\lambda}$  the slip coefficient and  $\theta$  the inclination of the plane to the horizontal. Lubrication theory is only valid if the slope of the drop surface is everywhere small, so the contact angles must be small. A non-dimensional form of (2) is

$$\frac{\partial \bar{h}}{\partial \bar{t}} + \frac{\partial}{\partial \bar{x}} \left[ \bar{h}^2 (\bar{h} + \bar{\lambda}) \left\{ \frac{\partial^3 \bar{h}}{\partial \bar{x}^3} + K \right\} \right] = 0, \quad (3)$$

where

$$\bar{h} = a_0 \alpha_a h, \quad \bar{x} = a_0 x, \quad \bar{t} = 3\mu a_0 t / \sigma \alpha_a^3, \quad \bar{\lambda} = a_0 \alpha_a \lambda / 3, \quad K = a_0^2 \rho g \sin \theta / \sigma \alpha_a, \quad (4)$$

and  $a_0$  is a length scale associated with the size of the drop and  $\alpha_a$  is a typical value of the (small) contact angle.

The extent of the plane covered by the drop can be fixed by two more unknowns,  $a_1(t)$  and  $a_2(t)$ , so that  $a_2 \leq x \leq a_1$  and

$$h(a_1(t), t) = h(a_2(t), t) = 0. \quad (5)$$

The volume of fluid in the drop remains constant throughout the motion and the length scale can be chosen so that

$$\int_{a_2}^{a_1} h(x, t) dx = \frac{2}{3}. \quad (6)$$

The other conditions on  $h$  relate to the slope of the surface of the drop at its edges. The proposal indicated in the introduction shows that, when the contact line is moving in a direction from the interior of the drop to the exterior (an advancing edge), the contact angle is fixed at its static value, which we can take to be the scaling factor  $\alpha_a$ . For a retracting edge, when the motion is in the opposite direction, the contact angle is equal to the minimum static angle  $\alpha_r$ . At a stationary edge the contact angle can lie anywhere between  $\alpha_r$  and  $\alpha_a$ . The boundary conditions to be applied at the edges are, therefore,

$$\begin{aligned} \text{at } x = a_1: & \quad -\partial h/\partial x = 1 & \text{if } da_1/dt > 0, \\ & \beta \leq -\partial h/\partial x \leq 1 & \text{if } da_1/dt = 0, \\ & -\partial h/\partial x = \beta & \text{if } da_1/dt < 0, \end{aligned} \quad (7)$$

$$\begin{aligned} \text{at } x = a_2: & \quad \partial h/\partial x = \beta & \text{if } da_2/dt > 0, \\ & \beta \leq \partial h/\partial x \leq 1 & \text{if } da_2/dt = 0, \\ & \partial h/\partial x = 1 & \text{if } da_2/dt < 0, \end{aligned} \quad (8)$$

where  $\beta = \alpha_r/\alpha_a$  and  $0 \leq \beta \leq 1$ .

The final information needed to specify the problem completely is the initial state, that is, the values of  $a_1(0)$ ,  $a_2(0)$  and  $h(x,0)$ . From arbitrary initial states, one expects a fairly rapid transient phase during which the shape of the drop changes without significant spreading taking place. This is because the rate of spread is controlled by conditions at the contact line where large stresses resist the motion. No such restriction is placed on the distortion of the drop surface when the edges are fixed. Since the initial phase is of little significance to the general spreading problem it will be ignored here. The height of the drop is then a function of time only through its dependence on the positions of the edges. Thus the solutions to be obtained are of similarity type and the initial shape of the drop will be assumed to agree with these solutions for the given initial positions of the edges.

#### Spreading

The simplest problem of the type being considered is when the drop spreads on a horizontal surface. If we suppose that the drop starts from a position where the apparent contact angles are greater than the static value, the edges of the drop will move outwards. If the drop is initially symmetric about its mid-position, it will remain so and we may write  $a_1(t) = -a_2(t) = a(t)$  and consider the interval  $0 \leq x \leq a$  only. The problem then takes the form

$$\dot{a} \frac{\partial h}{\partial a} + \frac{\partial}{\partial x} \left[ h^2 (h + \lambda) \frac{\partial^3 h}{\partial x^3} \right] = 0, \quad (9)$$

$$h = 0, \quad -\partial h/\partial x = 1 \quad \text{at } x = a, \quad (10)$$

$$\partial h/\partial x = 0 \quad \text{at } x = 0, \quad (11)$$

$$\int_0^a h \, dx = 1/3, \quad (12)$$

where  $\dot{a} = da/dt$  and  $h$  is a function of  $x$  and  $a$ , in line with the intention to ignore any initial transient phase. As already explained, the rate of spread is expected to be small so that we can expand in powers of some small parameter  $\epsilon(\lambda)$ , where  $\lambda \ll \epsilon \ll 1$  but the dependence of  $\epsilon$  on  $\lambda$  is yet to be determined. Hence we can write

$$\dot{a} = \epsilon u_1 + \epsilon^2 u_2 + \dots, \quad (13)$$

and, in the outer region where  $x$  is  $O(1)$ ,  $h = h_0 + \epsilon h_1 + \dots$ . From equation (9) the equations satisfied by  $h_0$  and  $h_1$  are

$$\frac{\partial}{\partial x} \left[ h_0^3 \frac{\partial^3 h_0}{\partial x^3} \right] = 0, \quad (14)$$

$$\frac{\partial}{\partial x} \left[ h_0^3 \frac{\partial^3 h_1}{\partial x^3} \right] = -u_1 \frac{\partial h_0}{\partial a} \quad (15)$$

and these have to be solved subject to the conditions (10), (11) and (12), except that the condition on the slope at the edge of the drop is not to be applied in this outer region. The solutions are

$$h_0 = \frac{1}{2a^3} (a^2 - x^2), \quad (16)$$

$$h_1 = u_1 a^4 \left[ (a+x) \ln(a+x) + (a-x) \ln(a-x) - 2a \ln 2a + \frac{3}{2a} (a^2 - x^2) \right] \quad (17)$$

so that, near the edge of the drop where  $a - x$  is small,

$$h \sim \frac{a-x}{a^2} + \epsilon u_1 a^4 (a+x) \left[ \ln \frac{a-x}{2a} + 2 \right]. \quad (18)$$

The inner region is close to the edge of the drop and is where slip is important. In this region we write

$$x = a - \lambda X, \quad h(x, a) = \lambda H(X, a), \quad H = H_0 + \epsilon H_1 + \dots \quad (19)$$

The equation satisfied by  $H$  with a term  $O(\lambda)$  omitted is

$$\dot{a} \frac{\partial H}{\partial X} + \frac{\partial}{\partial X} \left[ H^2 (H+1) \frac{\partial^3 H}{\partial X^3} \right] = 0 \quad (20)$$

and the boundary conditions are

$$H = 0, \quad \partial H / \partial X = 1 \quad \text{at } X = 0, \quad (21)$$

and  $\partial H / \partial X$  is not more than logarithmically infinite as  $X \rightarrow \infty$ . The solution is

$$H = X + \frac{1}{2} \epsilon u_1 \left[ (X+1)^2 \ln(X+1) - X^2 \ln X - X \right] + \dots, \quad (22)$$

so that, for  $X \rightarrow \infty$ ,

$$H \sim X + \epsilon u_1 X \ln X. \quad (23)$$

Although (18) and (23) both contain logarithmic terms, it is not possible to match these two expansions together and an intermediate expansion is required. This region is of width  $O(\epsilon)$ , and the match can be achieved if we choose

$$\epsilon = 1 / \ln(\lambda^{-1}). \quad (24)$$

The variables to be used in this region are defined by

$$y = \epsilon \ln X, \quad Q(y) = H/X, \quad (25)$$

and the governing equation (20) becomes, after one integration,

$$\dot{a} + Q(Q + e^{-y/\epsilon}) (\epsilon^3 \frac{\partial^3 Q}{\partial y^3} - \epsilon \frac{\partial Q}{\partial y}) = 0. \quad (26)$$

Neglecting the exponentially small term, the solution is

$$Q^3 = c_0 + \epsilon c_1 + 3(u_1 + \epsilon u_2) y + O(\epsilon^2), \quad (27)$$

which matches with the inner solution (23) if we choose  $c_0 = 1$ ,  $c_1 = 0$ . To match with the outer solution (18) we write

$$y = 1 + \epsilon \ln(a - x) \quad (28)$$

and obtain

$$h \sim (a-x) \left[ (1 + 3u_1)^{1/3} + \epsilon (1 + 3u_1)^{-2/3} (u_1 \ln(a-x) + u_2) + O(\epsilon^2) \right]. \quad (29)$$

Comparing this with the outer solution, we can see that the logarithmic term and the constant term both match if

$$1 + 3u_1 = a^{-6}, \quad u_2 = u_1 (2 - \ln 2a), \quad (30)$$

so that the rate of spread of the drop is given approximately by

$$\dot{a} = \epsilon (1 + \epsilon (2 - \ln 2a)) (a^{-6} - 1), \quad (31)$$

or, to the same order of accuracy,

$$3 \ln \left( \frac{2a}{\lambda e^2} \right) \frac{da}{dt} = a^{-6} - 1. \quad (32)$$

The objective of determining the rate of spread of the drop as a function of its width has thus been achieved. If the leading term only in the outer expansion is included an apparent contact angle is given by the value of  $a^{-2}$ , from (18). With variables in their dimensional forms, equation (32) yields the expression

$$\alpha_a \left\{ 1 + \frac{9\mu U}{\sigma a^3} \ln \left( \frac{2\tilde{a}\alpha_a}{3\lambda e^2} \right) \right\}^{1/3} \quad (33)$$

for the apparent contact angle at the edge of a drop of width  $2a$  advancing with speed  $U$  when the static contact angle is small. But the inclusion of the second term in the outer expansion destroys the validity of the concept of an apparent contact angle as a directly measurable quantity since, with the extra term included, the slope does not tend to a constant at the edge of the drop within the outer region. It is, however, still possible to define the quantity (33) as a derived contact angle as it could be measured by finding the curvature of the drop at its mid-point, for example, thus taking into account the outer solution but not requiring any measurement to be made in the vicinity of the edge.

#### Sliding

The second problem is when the drop is placed on an inclined plane. The drop is no longer symmetric and both edges have to be treated. As before, the Bond number is small, and gravity enters the problem only through the positive parameter  $K$  defined in (4), which measures the component of gravity down the plane. Any transient behaviour is again ignored, so that we suppose the height of the drop to depend on the co-ordinate  $x$  measured along the plane and on the positions of the two edges, but not directly on the time. The same three regions encountered in the spreading problem are present, but because both edges have to be treated, it is convenient to introduce a change of variable. If we write  $h(x,t) = f(s, a_1, a_2)$ , where

$$x = \frac{1}{2}(a_1 + a_2) + \frac{1}{2}(a_1 - a_2) s, \quad (34)$$

the range covered by the independent variable  $s$  is from  $-1$  to  $1$ . In the outer region, we can write  $f = f_0 + f_1 + \dots$ , and the equation for  $f_0$  is

$$\frac{\partial^3 f_0}{\partial s^3} + K = 0, \quad (35)$$

and the solution which vanishes at the edges and which satisfies the volume condition (6) is

$$f_0 = \frac{1-s^2}{a_1 - a_2} \left\{ 1 + \frac{Ks}{48}(a_1 - a_2)^4 \right\}. \quad (36)$$

Since  $f_0$  must be non-negative for  $s$  in  $[-1, 1]$ , this solution is only acceptable if  $0 < b < 1$ , where

$$b = \frac{K}{48} (a_1 - a_2)^4. \quad (37)$$

This condition may be broken either in the initial stage or during the spreading of the drop. In either case, a different approach from that used here must then be employed. The failure of the condition implies that regions are developing where the drop becomes very thin and although this is an interesting possible behaviour, this aspect of the problem is not investigated here, and we assume that  $b < 1$  throughout the motion.

The second term in the expansion in the outer region satisfies the equation

$$\frac{16}{(a_1 - a_2)^5} \frac{\partial^3 f_1}{\partial s^3} = \frac{\dot{a}_1(1+s)(1+b) + \dot{a}_2(1-s)(1-b)}{(1-s^2)^2(1+bs)^3}. \quad (38)$$

The boundary conditions on  $f_1$  are

$$f_1 = 0 \text{ at } s = -1 \text{ and at } s = 1, \quad \int_{-1}^1 f_1 ds = 0, \quad (39)$$

and the solution can be found in closed form after a great deal of algebra. The only quantities of interest are the asymptotic values for the height of the drop near the two edges and these are given by

$$h \sim \frac{4(a_1-x)(1+b)}{(a_1-a_2)^2} + \frac{(a_1-a_2)^4(a_1-x)}{16(1+b)^2} \left[ \dot{a}_1 \left\{ \ln \frac{(1-b)(a_1-x)}{(1+b)(a_1-a_2)} + \frac{1-2b}{1-b} \right\} - \dot{a}_2 \frac{1}{1-b} \right], \quad (40)$$

$$h \sim \frac{4(x-a_2)(1-b)}{(a_1-a_2)^2} + \frac{(a_1-a_2)^4(x-a_2)}{16(1-b)^2} \left[ -\dot{a}_2 \left\{ \ln \frac{(1+b)(x-a_2)}{(1-b)(a_1-a_2)} + \frac{1+2b}{1+b} \right\} + \dot{a}_1 \frac{1}{1+b} \right]. \quad (41)$$

The solutions in the inner and intermediate regions are similar to those found in the spreading problem, except that the edges may be moving in either direction or be stationary. The conditions (7) apply at the lower edge  $x = a_1$  and when they are applied, and the resulting inner expansions matched via the intermediate expansion to the outer solutions, we obtain the equation

$$\left\{ \ln \left( \frac{(a_1-a_2)(1+b)}{\lambda(1-b)} S(\dot{a}_1) \right) - \frac{1-2b}{1-b} \right\} \dot{a}_1 + \frac{\dot{a}_2}{1-b} = \frac{1}{3} \left\{ \frac{2^6(1+b)^3}{(a_1-a_2)^6} - S^3(\dot{a}_1) \right\} \quad (42)$$

where  $S$  is a step function, defined by

$$S(x) = 1 \text{ for } x > 0, \quad S(x) = \beta \text{ for } x < 0, \quad (43)$$

When the edge is at rest, (42) is replaced by  $\dot{a}_1 = 0$ . The corresponding results for the upper edge  $x = a_2$ , where the conditions (8) apply, are

$$\left\{ \ln \left( \frac{(a_1-a_2)(1-b)}{\lambda(1+b)} S(-\dot{a}_2) \right) - \frac{1+2b}{1+b} \right\} \dot{a}_2 + \frac{\dot{a}_1}{1+b} = -\frac{1}{3} \left\{ \frac{2^6(1-b)^3}{(a_1-a_2)^6} - S^3(-\dot{a}_2) \right\} \quad (44)$$

when the edge is moving, and  $\dot{a}_2 = 0$  when it is at rest.

These equations are sufficient to determine the future behaviour of the drop from any given initial position of the edges. The drop may not move at all, or one or both edges may move in either direction as the drop spreads or contracts. The most interesting possibility is when the drop spreads and slides, approaching a final state in which the width of the drop and its speed down the plane attain constant values. This final state can be found by setting  $\dot{a}_1 = \dot{a}_2 = U$  and  $a_1 - a_2 = 2a$ . From (42) and (44), with  $b$  replaced by its value in terms of  $K$  and  $a$  from (37), we obtain the equations

$$U = \frac{\frac{2K}{a^2} \left( 1 + \frac{1}{27} a^8 K^2 \right) - 1 + \beta^3}{3 \ln \left( \frac{4a^2 \beta}{\lambda^2} \right) + \frac{12a^8 K^2}{9 - a^8 K^2}}, \quad (45)$$

$$\frac{\ln \left( \frac{2a}{\lambda} \frac{3 + \dot{a}^4 K}{3 - \dot{a}^4 K} \right) + \frac{6a^4 K}{3 - \dot{a}^4 K}}{\ln \left( \frac{2a}{\lambda} \frac{3 - \dot{a}^4 K}{3 + \dot{a}^4 K} \right) - \frac{6a^4 K}{3 + \dot{a}^4 K}} = \frac{a^6 - \left( 1 + \frac{1}{3} \dot{a}^4 K \right)^3}{\left( 1 - \frac{1}{3} \dot{a}^4 K \right)^3 - \beta^3 a^6}. \quad (46)$$

There are too many parameters for it to be easy to make general statements about the motion. An approximate set of criteria can be found by retaining only the dominant terms on the left-hand sides of (42) and (44), that is, the logarithmic terms. Then it follows that

$$\begin{aligned} \dot{a}_1 &= 0 \quad \text{if } \beta < a^{-2} (1 + a^4 K/3) < 1, \\ \dot{a}_2 &= 0 \quad \text{if } \beta < a^{-2} (1 - a^4 K/3) < 1. \end{aligned} \quad (47)$$

A static final state is only possible if these two conditions on the width of the drop overlap, which they do if  $0 \leq K \leq K_C$ , where

$$K_C = \frac{3}{4}(1 - \beta^2) \quad (48)$$

while for  $K > K_C$  the drop will slide. If there is no contact angle hysteresis, that is, if  $\alpha_r = \alpha_a$ , the drop will slide however small the inclination of the plane.

#### Extensions and conclusions

Although only thin two-dimensional drops have been considered here, the method is applicable to many other cases. The spreading of a thin drop by both capillarity and gravity and without the restriction to two-dimensionality has been examined<sup>4</sup>. The capillary spreading of a drop which is not thin, so that the simplifications of lubrication theory are not available, has also been examined and the results compared with those obtained experimentally<sup>5</sup>. Further work on the sliding problem, with the extension to three-dimensionality and the lifting of the restriction on the gravity parameter  $K$  is planned.

The aim of this paper has been to show that the moving contact line problem can, in certain circumstances, be solved in a satisfactory manner. The solutions for which experimental corroboration is available<sup>1,5</sup> indicate that the proposed boundary conditions can be used with some confidence. The results obtained here and elsewhere<sup>4,5</sup> show that the application of these conditions need not involve a large amount of refined numerical analysis to resolve the solution near the contact line.

#### References

1. Lowndes, J., "The numerical simulation of the steady movement of a fluid meniscus in a capillary tube," J.Fluid Mech., vol. 101, pp. 631-645, 1980.
2. Hocking, L.M., "Sliding and spreading of thin two-dimensional drops," Quart.J.Mech.Appl. Math., vol. 34, pp.37-55, 1981.
3. Lacey, A.A., "The motion with slip of a thin viscous droplet over a solid surface." To be published in J.Fluid Mech.
4. Hocking, L.M., "The spreading of a thin drop by gravity and capillarity." Submitted to Quart.J.Mech.Appl.Math.
5. Hocking, L.M. and Rivers, A.D., "The spreading of a drop by capillary action." Submitted to J.Fluid Mech.

Profiles of electrified drops and bubbles

O. A. Basaran and L. E. Scriven

Department of Chemical Engineering & Materials Science,  
 University of Minnesota, Minneapolis, Minnesota 55455

Abstract

Axisymmetric equilibrium shapes of conducting drops and bubbles, (1) pendant or sessile on one face of a circular parallel-plate capacitor or (2) free and surface-charged, are found by solving simultaneously the free-boundary problem consisting of the augmented Young-Laplace equation for surface shape and the Laplace equation for electrostatic field, given the surface potential. The problem is nonlinear and the method is a finite element algorithm employing Newton iteration, a modified frontal solver, and triangular as well as quadrilateral tessellations of the domain exterior to the drop in order to facilitate refined analysis of sharply curved drop tips seen in experiments. The stability limit predicted by this computer-aided theoretical analysis agrees well with experiments of Wilson and Taylor (1925). The instability and mechanism of charged droplet ejection are under theoretical and experimental study.

1. Introduction

The shape of a conducting fluid interface is affected by mobile surface charge. The distribution of mobile free, surface charge is affected in turn by the shape of the interface. At equilibrium, charge distributes to make uniform the potential of the interface. But surface charge creates an electrical pressure that competes with capillary pressure (the resultant of surface tension in a curved interface) and hydrostatic pressure to control the shape.

Only cylindrical and spherical equilibrium drops have yielded to classical analysis (Rayleigh 1882, Basset 1894, Taylor 1969, Michael and O'Neill 1972). Shapes that depart from standard coordinate surfaces can be analyzed by modern computer-aided mathematics with finite element basis functions (Gifford 1979).

Observations of electrified drops and bubbles stand in need of accurate theoretical analysis of shapes and stability. Free drops were studied by Nolan 1926, Macky 1931, Doyle, Moffett and Vonnegut 1964, and others; supported drops, by Zeleny 1914, 1917, Wilson and Taylor 1925, Macky 1930, Krohn 1974, and others. The results of analysis will pertain to such fields as spray generation in technology and cloud physics in science.

2. Observations of charged sessile soap-bubbles

A soap-bubble sitting on the lower, wetted plate of a circular parallel-plate capacitor appears hemispherical in the absence of field. As the field strength is raised the bubble elongates along the field direction. Because the plate is wetted the circular contact line slides freely and the contact angle remains approximately 90°. The prolate shape sequence seen at field strengths up to a critical value is a family of stable equilibrium shapes: four members are shown in Fig. 1. Computer-aided theoretical analysis is used to track this shape family in section 6.

Increasing the field strength even slightly beyond the critical value leads to a dynamic succession. The end of the bubble rapidly narrows and becomes conical. Filaments are subsequently ejected from the end of the bubble, this spitting being accompanied by intense vibrations of the tip. Such observations were originally reported by Wilson and Taylor (1925) and Macky (1930).

3. Statement of the two cases analyzed

The two situations treated here are shown in Fig. 2:

Case 1.

Axisymmetric drop or bubble sessile (pendant) on one face of a circular parallel-plate capacitor (Fig. 2a).

Case 2.

Free surface-charged drop in absence of an external imposed field (Fig. 2b).

4. Governing dimensionless groups, equations and boundary conditions

The relevant dimensionless groups are compiled in Table 1. In the case of the free

drops we choose to work with the potential at the drop surface relative to "infinity" instead of specifying the charge on the drop. The two alternatives are of course fully equivalent.

The governing equations of electrostatics and capillary hydrostatics and boundary conditions are summarized in Figs. 3 and 4.  $U$  is of course the electrostatic potential. In the normal stress balances at the interfaces  $2H$  is twice the dimensionless mean curvature, a nonlinear function of first and second derivatives of the drop profiles;  $K$  is a reference pressure,  $E^2$  represents the electrical pressure created by surface charge, and  $4Gz$  is the hydrostatic pressure created by a gravitational field (supposed absent in Case 2).

### 5. Computer-aided analysis

Theoretical computation of drop shape requires solving a system made nonlinear by the free boundary and by the curvature and electrical pressure in the augmented Young-Laplace equation. The procedure is:

- (i) Estimate drop shape and electrostatic potential from either an analysis of limiting case or experimental observation.
- (ii) Partition, or tessellate, the one-dimensional domain (drop profile) into curve segments and the two-dimensional domain (surrounding space) into quadrilaterals between spines  $\theta = \text{constant}$  (cf. Kistler 1981) as indicated in Fig. 5.
- (iii) In the 2-D domain construct finite element basis functions  $\Psi^i(r, \theta)$  for the sub-domain around each node:
  - choose the biquadratic polynomial on the  $(\epsilon, \eta)$ -unit square;
  - map each quadrilateral isoparametrically onto the unit square (Fig. 6).
- (iv) In the 1-D domain exploit the fact that the 1-D basis functions  $\phi^i(\theta)$  when mapped isoparametrically onto  $0 \leq \epsilon \leq 1$  are simply and very conveniently the isoparametrically mapped  $\psi^i(\epsilon, \eta \equiv 0)$  (cf. Kistler 1981).
- (v) Approximate the interface shape as

$$f(\theta) = \sum_{i=1}^M q_i \phi^i[\theta(\epsilon)]$$

and the potential as

$$U(r, \theta) = \sum_{i=1}^N U_i \Psi^i[r(\epsilon, \eta), \theta(\epsilon, \eta)].$$

- (vi) Form Galerkin weighted residuals and require them to vanish
- (vii) Solve the resulting  $N + M + 1$  nonlinear algebraic equations for the unknown coefficients  $(q_i, U_i, K)$  by Newton iteration:
  - derivatives with respect to  $q_i$ 's are calculated by ganging nodes along spines;
  - the domain is updated at each iteration;
  - convergence approaches quadratic rate;
  - the Jacobian is valuable for continuation in the parameters and evaluation of stability.
- (viii) Modify the frontal solver (Irons 1970, Hood 1976, 1977) to handle the constraint of fixed volume and use it for the linear equation set in Newton iteration.
  - The presence of a free boundary makes the frontal solver cost-effective.
- (ix) Terminate iteration when the norm of the largest component of correction vector is sufficiently small.
- (x) Change the parameter (typically  $E_\infty$  or  $U_0$ ), estimate a shape by continuation and begin anew.
  - Prefer the secant version of first-order continuation because it is easier to use than the tangent version and it maintains near-quadratic convergence with bigger parameter changes than does zeroth-order continuation.
- (xi) Concentrate computational power where needed:
  - refine the tessellation in regions of sharp gradients;
  - derive Robin boundary condition to account for asymptotic far field behavior and thereby shrink the computational domain.

An example of the last point is shown in Fig. 7: a finite element mesh of triangles and rectangles which proved computationally efficient.

### 6. Results

Calculations were programmed in FORTRAN and made on the Control Data Corporation CYBER 74 at the University of Minnesota. 3 sec/iteration was typical for  $N + M + 1 = 183$  unknowns and 2-4 iterations were required to converge.

*Case 1. Results for axisymmetric supported bubble ( $G = 0$ )*

Finite element calculations for a bubble meeting one of the capacitor plates at a fixed contact angle of  $90^\circ$  simulate theoretically experiments with electrified soap-bubbles

described in section 2 (cf. Wilson and Taylor 1925 and Macky 1930). Moreover, if the spacing between the plates is much larger than the bubble radius, both experiment and theory model a drop freely floating in a uniform applied electric field in the absence of gravity. Drop shapes and equipotentials for a bubble of volume  $2\pi/3$  are plotted as function of the parallel-plate electric field  $E_\infty$  in Fig. 8, which shows that bubble profiles are prolate in the field direction. This theoretical analysis using finite element basis functions can be made as accurate as the computer allows and it already confirms Taylor's (1964) spheroidal approximation.

Results for a bubble of volume  $2\pi/3$  with its contact line fixed are plotted in Fig. 9. The theoretical analysis predicts that bubble shape tends toward conical.

Families of drops of volume  $2\pi/3$  with either the contact line fixed or the contact angle prescribed are plotted in parameter space in Fig. 10. In both cases the family loses stability at a turning point, bubbles with contact line fixed being the more stable of the two. The stability limit predicted for the fixed contact angle case by this computer-aided theoretical analysis is within 3% of the value 0.321 obtained experimentally by Wilson and Taylor (1:25).

Aspect ratio as function of parallel-plate electric field  $E_\infty$  is plotted in Fig. 11. When contact angle is fixed the critical bubble is elongated 1.82/1.37 times as much as one with contact line fixed.

How surface charge distributes on supported bubbles is plotted in Fig. 12. The ordinate is the ratio of local surface charge density on the bubble to charge density on the plate far from the bubble. Because electrical pressure goes as the square of charge density, electrical pressure at the bubble tip attains values from 40 to 50 times as large as that between two parallel-plates for the larger of the two voltages shown.

*Case 2. Results for axisymmetric free surface-charged drop*

Though the sphere is an equilibrium shape at all values of charge  $q$  it was shown by Lord Rayleigh (1882; see also Hendricks and Schneider 1962) that a sphere of radius  $R$  is unstable to any perturbation proportional to the Legendre polynomial of order  $n$ ,  $P_n(\cos \theta)$ , if the charge exceeds

$$q > 4\pi\sqrt{(n+2)\epsilon_0\sigma R^3}$$

or, in dimensionless form,

$$Q > 2\pi\sqrt{2(n+2)} \quad \text{or} \quad U_0 > \sqrt{\frac{n+2}{2}}$$

Instability first appears for the  $n = 2$  mode, i.e. the second spherical harmonic, and the criteria  $Q = 4\pi\sqrt{2}$  or  $U_0 = \sqrt{2}$  are known as the Rayleigh limit. The finite element analysis predicts the first instability to occur at  $U_0 = 1.42$ , which is in good agreement with the value  $\sqrt{2}$ , and to correspond to bifurcation from the trunk family of spheres (Fig. 13). The theoretical analysis also reveals that bifurcation at the Rayleigh limit is *subcritical*, thereby confirming Taylor's (1964) surmise from his spheroidal approximation. A secondary bifurcation is found at  $U_0 = 1.40$  along this branch family of prolate shapes. The theoretical analysis accurately predicts the bifurcation points of the higher modes, but these are not shown in Fig. 13.

### 7. Concluding Remarks

Charge repulsion can overcome the attractive-like action of surface tension and when it does it limits the surface charge that can be stably carried by a fluid interface: at the limiting charge density the interface becomes unstable.

Computer-aided analysis with finite element basis functions can handle relatively complicated equilibrium profiles of electrified drops. The finite element algorithm developed here is not limited in its applicability in contrast to the method of Borzabadi and Bailey (1978), who calculated profiles of drops hanging from a tube connected to a high voltage source.

Additional results will be reported elsewhere. With the flow field inside the drop accounted for, the methods developed here and certain others should make it possible to analyze the dynamic succession in unstable drops and settle the long-standing question of how charged drops break up.

### Acknowledgments

The authors would like to thank K. A. Amundson for assisting with the construction of the parallel-plate capacitor and taking the photographs, and R. E. Benner, N. E. Bixler and S. F. Kistler for extensive discussion and valuable insights into finite element analysis of free boundary problems. This research was supported by NASA Fund for Independent Research.

### References

- A. B. Basset, Waves and Jets in a Viscous Liquid, *Am. J. Math.* 16 13 (1894).
- E. Borzabadi and A. G. Bailey, The Profiles of Axially Symmetric Electrified Pendant Drops, *J. Electrostatics* 5 369 (1978).
- A. Doyle, D. P. Moffett, and B. Vonnegut, Behavior of Evaporating Electrically Charged Droplets, *J. Colloid Sci.* 19 136 (1964).
- W. A. Gifford, The Shapes and Stability of Charged, Rotating Liquid Drops, Ph.D. Thesis, University of Minnesota (1979).
- C. D. Hendricks and J. M. Schneider, Stability of a Conducting Droplet Under the Influence of Surface Tension and Electrostatic Forces, *Am. J. Phy.* 31 450 (1962).
- P. Hood, Frontal Solution Program for Unsymmetric Matrices, *Int. J. Num. Meth. Engng.* 10 379 (1976).
- P. Hood, Note on Frontal Solution Program for Unsymmetric Matrices, *Int. J. Num. Meth. Engng.* 11 1055 (1977).
- B. M. Irons, A Frontal Solution Program for Finite Element Analysis, *Int. J. Num. Meth. Engng.* 2 5 (1970).
- S. F. Kistler, First International Fluid Mechanics Winter (Summer) Seminar, INTEC-Santa Fe, 18-21 August 1981.
- V. E. Krohn, Electrohydrodynamic Capillary Source of Ions and Charged Droplets, *J. App. Phy.* 45 1144 (1974).
- W. A. Macky, The Deformation of Soap-Bubbles in Electric Fields, *Proc. Camb. Phil. Soc.* 26 421 (1930).
- W. A. Macky, Some Investigations of the Deformation and Breaking of Water Drops in Strong Electric Fields, *Proc. Roy. Soc. Lond.* A133 565 (1931).
- D. H. Michael and M. E. O'Neill, The Bursting of a Charged Cylindrical Film, *Proc. Roy. Soc. Lond.* A328 529 (1972).
- J. J. Nolan, The Breaking of Water-Drops by Electric Fields, *Proc. Roy. Irish Acad.* 37 28 (1926).
- Lord Rayleigh, On the Equilibrium of Liquid Conducting Masses Charged with Electricity, *Phil. Mag.* 14 184 (1882).
- G. I. Taylor, Disintegration of Water Drops in an Electric Field, *Proc. Roy. Soc. Lond.* A280 383 (1964).
- G. I. Taylor, Electrically Driven Jets, *Proc. Roy. Soc. Lond.* A313 453 (1969).
- C. T. R. Wilson and G. I. Taylor, The Bursting of Soap-Bubbles in a Uniform Electric Field, *Proc. Camb. Phil. Soc.* 22 728 (1925).
- J. Zeleny, On the Conditions of Instability of Electrified Drops, with Applications to the Electrical Discharge from Liquid Points, *Proc. Camb. Phil. Soc.* 18 71 (1914).
- J. Zeleny, Instability of Electrified Liquid Surfaces, *Phys. Rev.* 10 1 (1917).

ORIGINAL PAGE  
BLACK AND WHITE PHOTOGRAPH

TABLE 1  
Governing dimensionless groups

SUPPORTED DROP	FREE DROP
$E_0 =$ PARALLEL-PLATE ELECTRIC FIELD, $(\frac{\epsilon_0 R^2}{2\sigma})^{1/2} \frac{U_0}{h}$	$U_0 =$ POTENTIAL AT DROP SURFACE WITH RESPECT TO INFINITY, $(\frac{\epsilon_0 R^2}{2\sigma})^{1/2} u_0$
$G =$ GRAVITATIONAL BOND NUMBER, $\frac{\rho \Delta \rho R^2 g}{\sigma}$	$Q =$ NET CHARGE ON DROP, $(\frac{1}{2\epsilon_0 R^2 \sigma})^{1/2} q$
$R =$ EITHER RADIUS OF CONTACT CIRCLE OR RADIUS OF HEMISPHERE OF EQUAL VOLUME (SPECIFIED CONTACT ANGLE CASE)	$R =$ RADIUS OF SPHERE OF EQUAL VOLUME
$\Delta \rho =$ DENSITY DIFFERENCE BETWEEN SURROUNDINGS AND DROP	
$K =$ DATUM PRESSURE DIFFERENCE, $(p - p_{\text{atm}}) R / \sigma$ AT $z = 0$	$K =$ EXCESS DROP PRESSURE OVER AMBIENT PRESSURE, $(p - p_{\text{atm}}) R / \sigma$

$\epsilon_0 =$  PERMITTIVITY OF FREE SPACE,  $\sigma =$  SURFACE TENSION

ELECTRIFIED SOAP-BUBBLE MAKING  $\sim 90^\circ$  CONTACT ANGLE WITH THE PLATE

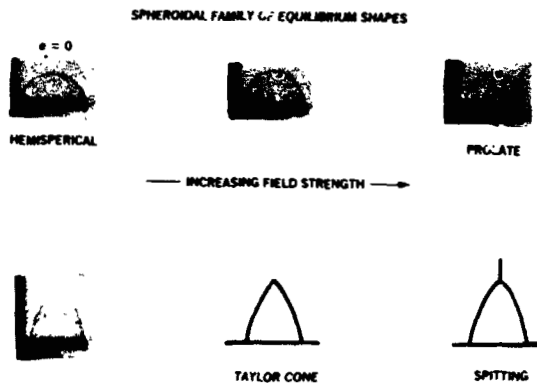


Figure 1. Observations of a charged sessile soap-bubble.

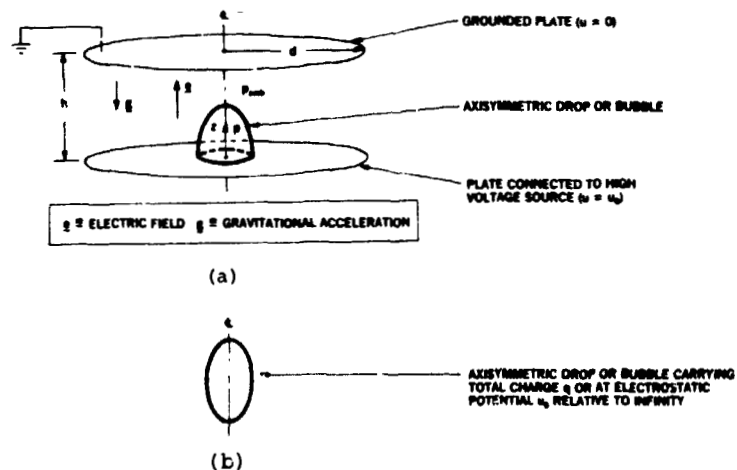


Figure 2. (a) Axisymmetric drop or bubble sessile (pendant) on one face of a circular parallel-plate capacitor; (b) free surface-charged drop (no applied field).

ORIGINAL PAGE  
BLACK AND WHITE PHOTOGRAPH

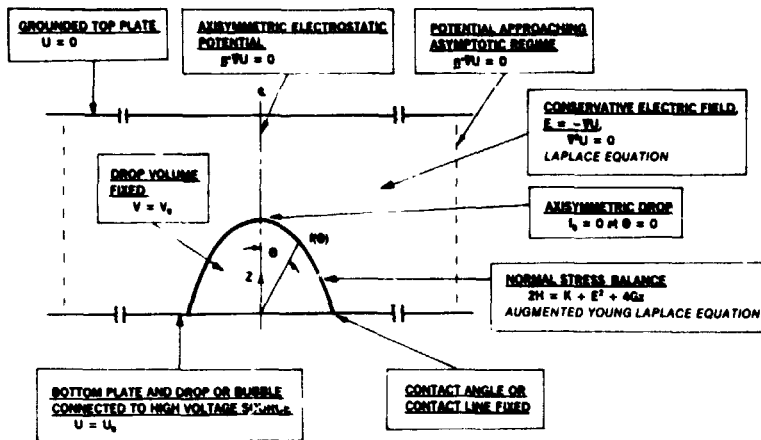


Figure 3. Governing equations and boundary conditions (Case 1).

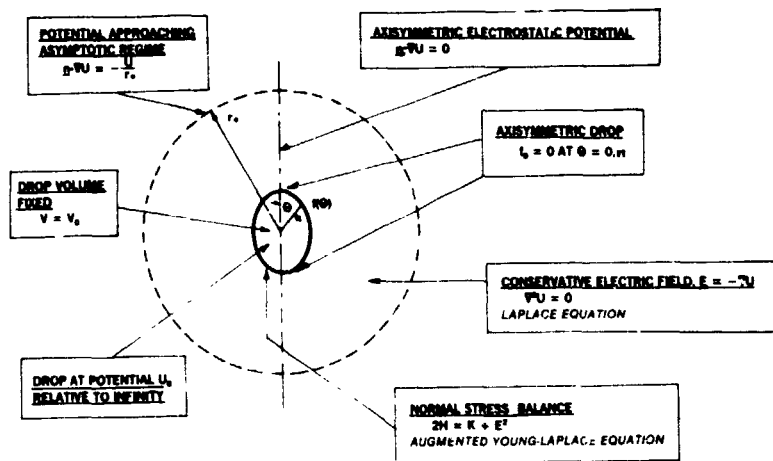


Figure 4. Governing equations and boundary conditions (Case 2).

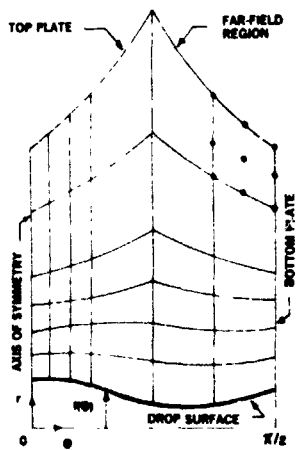


Figure 5. Spherical coordinate representation.

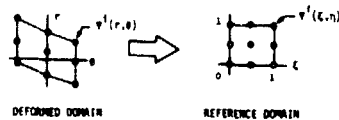


Figure 6. Isoperimetric mapping, i.e. mapping by the polynomial function of the finite element function itself.

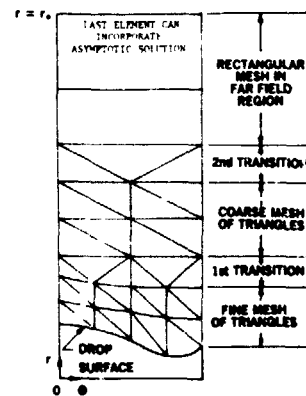


Figure 7. Computationally efficient finite element mesh for electrified drop problems.

ORIGINAL PAGE IS  
OF POOR QUALITY.

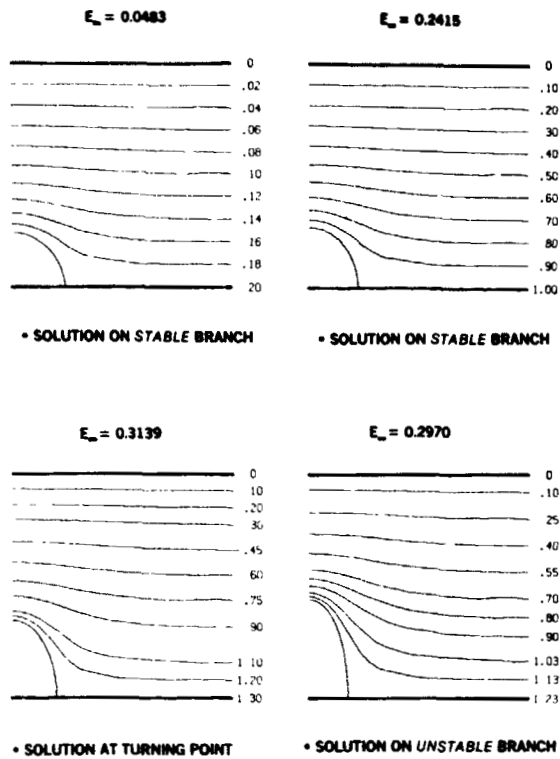


Figure 8. Drop shapes and equipotentials for fixed contact angle ( $90^\circ$ ) case.

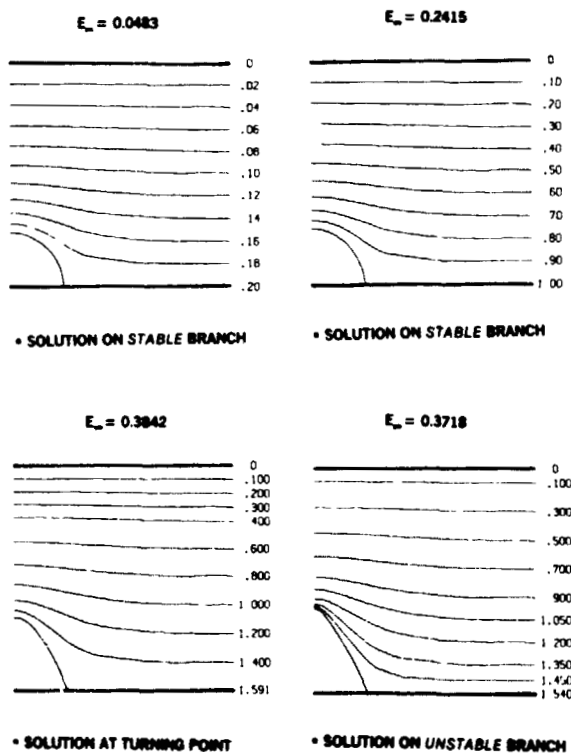


Figure 9. Drop shapes and equipotentials for fixed contact line case.

ORIGINAL PAGE  
BLACK AND WHITE PHOTOGRAPH

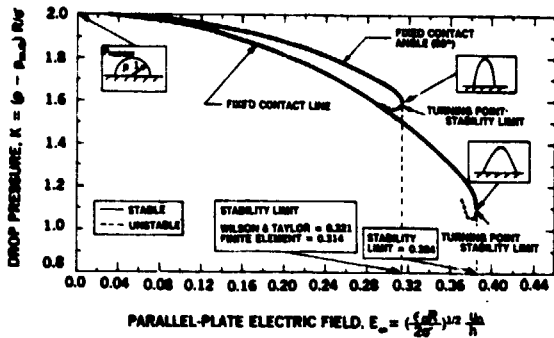


Figure 10. Solution families in parameter space for axisymmetric supported bubble ( $G = 0$ ).

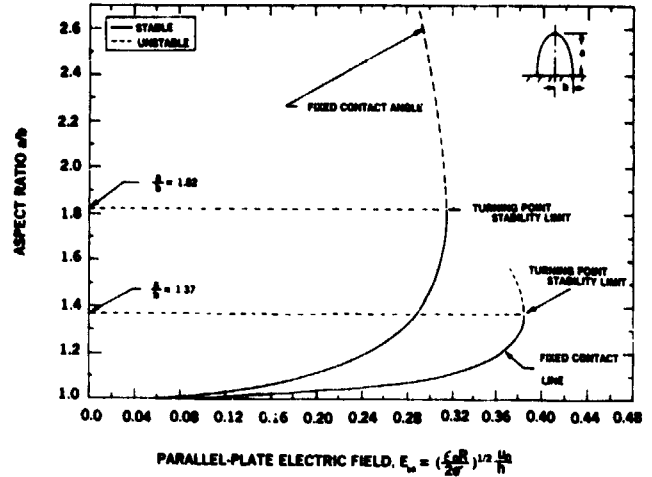


Figure 11. Aspect ratio  $a/b$  as a function of parallel-plate electric field  $E_\infty$ .

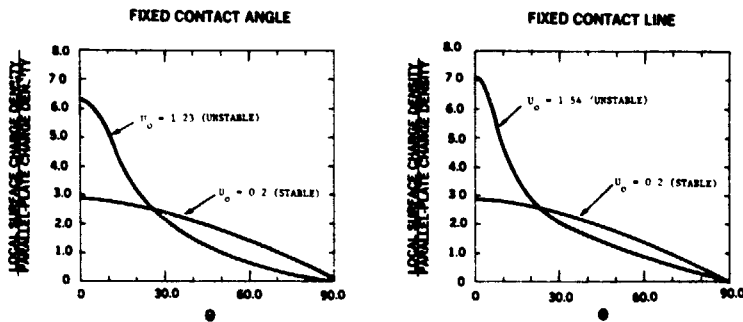


Figure 12. Distribution of surface charge on sessile bubbles.

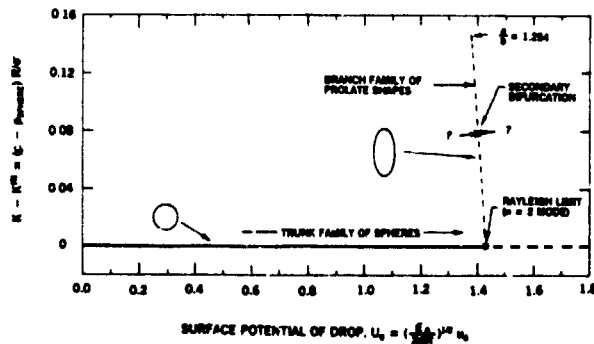


Figure 13. Bifurcation diagram in parameter space for free surface-charged drop (no externally applied field).

A numerical method for integrating the kinetic equations of droplet spectra evolution by condensation/evaporation and by coalescence/breakup processes

Isaac M. Erukashvily

Department for Research and Development, Israel Meteorological Service,  
 P. O. Box 25, Bet-Dagan, Israel

Abstract

An extension of the method of moments is developed for the numerical integration of the kinetic equations of droplet spectra evolution by condensation/evaporation and by coalescence/breakup processes. The number density function  $n_k(x,t)$  in each separate droplet packet between droplet mass grid points  $(x_k, x_{k+1})$  is represented by an expansion in orthogonal polynomials with a given weighting function. In this way droplet number concentrations, liquid water contents and other moments in each droplet packet are conserved and the problem of solving the kinetic equations is replaced by one of solving a set of coupled differential equations for the number density function moments. The method is tested against existing analytic solutions of the corresponding kinetic equations. Numerical results are obtained for different coalescence/breakup and condensation/evaporation kernels and for different initial droplet spectra. Also droplet mass grid intervals, weighting functions and time steps are varied.

Introduction

There are three major difficulties in numerical computation of droplet spectra evolution by condensation/evaporation and coalescence/breakup processes, which occur as a result of interaction between droplets and vapour-air environment.

a) The relaxation time of condensation/evaporation process is much smaller than the relaxation time of coalescence/breakup process and therefore the numerical computations of these processes require a different time steps.

b) A correct approximation of droplet number density function  $n_k(x,t)$  is required in each separate droplet packet between droplet mass grid points  $(x_k, x_{k+1})$ . In Berr's approximation<sup>1,2</sup> of number density function neither the number concentration nor the liquid water content of droplets are conserved. In Bleck's method<sup>3,4</sup> it is impossible to estimate the error of the approximate numerical solution and an assumption is made that in each separate droplet packet all droplets are spread over the whole mass interval  $(x_k, x_{k+1})$ . This Bleck's uniform distribution hypothesis gives as a result a significant increase of the mass conversion velocity from small droplets to large drops.

c) The problem of correct computation of water vapour supersaturation taking into account the release of latent heat of condensation/evaporation during the time step used for the numerical computation of the condensation/evaporation processes.

Method of moments

In this study an extension of Bleck's method<sup>3</sup> and of the method of moments<sup>5,6</sup> is developed for numerical integrating the kinetic equations of droplet spectra evolution by condensation/evaporation and coalescence/breakup processes. Each separate droplet mass interval  $(x_k, x_{k+1})$ , where  $x_{k+1} = sx_k$  is considered as a droplet packet with its own number concentration, liquid water content and other moments. The unknown number density function  $n_k(x,t)$  in each droplet packet is represented by an expansion in orthogonal polynomials with a given weighting function

$$n_k(z,t) = W_k(z,t) \sum_{i=0}^{\infty} a_{ik}(t) G_{ik}(z) \quad (1)$$

where  $z = x/x_k$  represents the nondimensional mass of droplets in the packet  $(x_k, x_{k+1})$ .  
 $W_k(z,t)$  -- weighting function.

$G_{ik}(z)$  -- are polynomials orthogonal in the range  $(1,s)$  with weighting function  $W_k(z,t)$ .

$a_{ik}(t)$  -- are the expansion coefficients which are expressed as linear combinations of the number density function moments and depend on the moments of  $W_k(z,t)$  as well.

In this way droplets number concentration, liquid water content and other moments are conserved in each separate droplet packet and the problem of solving the kinetic equations is replaced by one of solving an infinite set of coupled differential equations for the number density function moments. However, approximating  $n_k(z,t)$  by means of first  $L$  terms of the expansion (1) and also replacing the expansion coefficients  $a_{ik}(t)$  by means of linear combinations of number density function moments we obtain a finite set of

ORIGINAL PAGE IS  
OF POOR QUALITY

coupled differential equations to compute the first L moments of the  $n_k(z,t)$ . Note that the approximation of the  $n_k(z,t)$  by means of the first L terms of the expansion (1) assumes that the expansion coefficients for  $i < L$ ,  $i=L+1, \dots$  are zero, that is

$$a_{Lk}(t)=0; \quad a_{L+1,k}(t)=0; \quad \dots \quad (2)$$

By (2) the larger order moments of the number density function may be determined by means of the first L moments of the  $n_k(z,t)$ .

The accuracy of the approximation of  $n_k(z,t)$  by means of the first L terms of the expansion (1) in droplet packet  $(x_k, x_{k+1})$  depends on the choice of  $W_k(z,t)$  as well as on the choice of droplet mass grid points. The number density function  $n(x,t)$  is a distribution function which in experiments is determined only for the range  $(x, x+dx)$ . If droplet mass increment  $dx$  is much smaller than  $x$ , the  $n(x,t)$  in each range  $(x, x+dx)$  represents a piecewise constant function and an arbitrary moment of  $n(x,t)$  in the range  $(x, x+dx)$  is expressed by means of the zero-order moment  $dN(x,t)=n(x,t)dx$ ; therefore also the number density function  $n(x,t)$  is determined by zero-order moment  $dN(x,t)$  and does not depend on the choice of the weighting functions in the range  $(x, x+dx)$ .

For the numerical computations of the kinetic equations it is impossible to choose droplet mass grid points for which  $(x_{k+1}-x_k)$  is much smaller than  $x_k$ ; therefore for such grid points the zero-order approximation of the expansion (1) ( $L=1$ ) will be incorrect for an arbitrary weighting function  $W_k(z,t)$ . So, if for numerical solution of the corresponding kinetic equations we have chosen the droplet mass grid points  $x_{k+1}=sx_k$ , then we have to define for what value of the grid intervals  $(x_{k+1}-x_k)$  the first-order approximation of (1) ( $L=2$ ) will be correct that is will be not dependent on the choice of the weighting function  $W_k(z,t)$ . It is shown that for  $s$  equal or smaller than two the first-order approximation of the expansion (1) that is the approximation of  $n_k(z,t)$  by means of the first two moments is sufficiently correct.

The relations are obtained to compute the zero-order and the first-order approximations of the polynomial expansion (1) for an arbitrary range  $(l,s)$  and for an arbitrary weighting functions.

It should be noted that the first-order approximation of the expansion (1) ( $L=2$ ) describes not only the case where the droplets in the packet  $(x_k, x_{k+1})$  are spread over the whole mass interval  $(x_k, x_{k+1})$ , but also the case where the droplets in the packet  $(x_k, x_{k+1})$  are located only in the part of the whole mass interval  $(x_k, x_{k+1})$ .

Numerical method for integrating the condensation/evaporation kinetic equation

In this study a separate treatment of microphysics of condensation/evaporation process (without advection phenomena) is adopted and this process for sufficiently small time steps is considered as a space-homogenous process. Such consideration is based on the assumption that the time integration is broken up into separate treatment of the dynamic tendency and of the microphysical processes which control the vapour supersaturation field.

Differential equations which describe the microphysics of the droplet spectra evolution by condensation/evaporation processes can be written as:

$$\frac{\partial n(x,t)}{\partial t} + \frac{\partial}{\partial x} \left\{ \left( \frac{dx}{dt} \right) n(x,t) \right\} = 0 \quad (3)$$

$$\frac{dx}{dt} = K \frac{S(t)x^{2/3} - R_x^{1/3} + \phi(c)x^{2/3}}{x^{1/3} + \xi} \quad (4)$$

$$S(t) = Q(t) - Q_s(t) \quad (5)$$

$$Q(t) + I_s(t) = Q(0) + M(0) \quad (6)$$

$$\rho_l c_p \frac{dT}{dt} = L_0 \frac{dM(t)}{dt} \quad (7)$$

$$\frac{dQ_s(T)}{dT} = \frac{Q_s(T)}{T} \left( \frac{L_0}{R_v T} - 1 \right) \quad (8)$$

where  $S(t)$ -water vapour supersaturation;  $M(t)$ - droplets total liquid water content;  $Q(t)$ -water vapour density;  $Q_s(t)$ - water vapour saturation density at temperature  $T(t)$ . The equation (3) represents the condensation/evaporation kinetic equation; (4)-represents the individual droplet diffusional growth equation which includes the terms due to surface tension (B) and solute effects- $\phi(c)$ ; (6) represents the mass conservation equation; (7)- the first law of thermodynamics; (8)- the Clapeyron-Clausius equation.

Multiplying (3) by  $x^m dx$  and integrating from  $x_k(t)$  to  $x_{k+1}(t)$ , and also taking into account that  $n(x,t)dx = n_0(y)dy$  we have the set of number density function moments equations-

$$\frac{dM_k^m(t)}{dt} = m \int_{x_k(t)}^{x_{k+1}(t)} x^{m-1} (dx/dt) n(x,t) dx = m \int_{x_k(0)}^{x_{k+1}(0)} (x(y,t))^{m-1} (dx(y,t)/dt) n_0(y) dy \quad (9)$$

where

$$M_k^m(t) = \int_{x_k(t)}^{x_{k+1}(t)} x^m n(x,t) dx = \int_{x_k(0)}^{x_{k+1}(0)} (x(y,t))^m n_0(y) dy$$

represents the  $m$ -order moment of the number density function in the droplet packet with nonfixed grid points  $(x_k(t), x_{k+1}(t))$ , that is in the droplet packet which for  $t=0$  is contained within grid points  $(x_k(0), x_{k+1}(0))$  and for time  $t$  transfers in the droplet packet  $(x_k(t), x_{k+1}(t))$  as a result of the droplets diffusional growth.

For  $t=0$  we have initial conditions:

$$n(x,0) = n_0(y); \quad x(y,0) = y; \quad x_k(0) = x_k; \quad x_{k+1}(0) = x_{k+1}$$

From equation (9) we have for  $m=0$  and  $m=1$

$$\frac{dN_k(t)}{dt} = 0; \quad \frac{dM_k(t)}{dt} = \int_{x_k(0)}^{x_{k+1}(0)} (dx(y,t)/dt) n_0(y) dy \quad (10)$$

where  $N_k(t) = M_k^0(t)$  and  $M_k(t) = M_k^1(t)$  represent the number concentration and liquid water content respectively in the droplet packet with nonfixed grid points  $(x_k(t), x_{k+1}(t))$ . Using (10) we have for the droplets total liquid water content

$$\frac{dM(t)}{dt} = \sum_{k=1}^J \int_{x_k(0)}^{x_{k+1}(0)} (dx(y,t)/dt) n_0(y) dy \quad (11)$$

where  $J$ -the total number of droplet packets.

Picard's method of successive approximations is used for the integration of differential equation (4) with the initial condition for  $t=0$   $x=y$ . It is assumed that the droplet individual diffusional growth rate in the  $(j+1)$ -th approximation is determined by the droplet mass in  $j$ -th approximation. Substituting (4) in (11) and approximating  $n_0(y)$  by means of the first two moments  $N_k(0)$  and  $M_k(0)$  we obtain the first relationship between total liquid water content of droplets and between water vapour supersaturation:

$$\frac{dM^{(j)}(t)}{dt} = S^{(j)}(t) \phi^{(j-1)}(t) + \psi^{(j-1)}(t)$$

where

$$\phi^{(j-1)}(t) = -K \sum_{k=1}^J \int_{x_k(0)}^{x_{k+1}(0)} ((x^{(j-1)}(y,t))^{2/3} n_0(y) dy) / ((x^{(j-1)}(y,t))^{1/3} + R)$$

$$\psi^{(j-1)}(t) = K \sum_{k=1}^J \int_{x_k(0)}^{x_{k+1}(0)} (dy) ((-B(x^{(j-1)}(y,t))^{1/3} + \phi(c)(x^{(j-1)}(y,t))^{2/3}) n_0(y) / ((x^{(j-1)}(y,t))^{1/3} + R))$$

are the condensation/evaporation integrals.

The second relationship between  $M^{(j)}(t)$  and  $S^{(j)}(t)$  can be derived using the equations (5)-(8). Expanding  $Q_s(t)$  in Taylor's series, we have for sufficiently small time steps, (that is for time steps for which  $(T(t)-T(0)) \ll T(0)$  is satisfied)

$$S^{(j)}(t) = S(0) - (1+F) M^{(j)}(t) - M(0) \quad (12)$$

where

$$F = (((Q_s(T(0))L_0) / (r_1 c_p T(0))) ((L_0 / R_v T(0)) - 1))$$

and  $L_0$  represents the latent heat of water vaporization. Such an approach gives the possibility to obtain the analytic relationships to compute the unknown values of  $x(y,t)$ ,  $x_k(x_k(0),t)$ ,  $M_k(\cdot)$ ,  $M(t)$ ,  $S(t)$ ,  $Q(t)$ ,  $T(t)$ ,  $Q_s(t)$  for sufficiently small time steps  $\tau$ , ( $0 < t < \tau_1$ ) which may be much smaller than the time step used for the numerical computation. The coalescence/breakup processes. The redistribution of the liquid water mass from the droplet packets between nonfixed grid points  $(x_k(t), x_{k+1}(t))$  among the droplet packets located between fixed grid points  $(x_k, x_{k+1})$  which are used for the numerical computation of the coalescence/breakup processes can be computed without too much difficulty.

Note that according to (10) the number concentration  $n_k(t)$  in the droplet packets with nonfixed grid points  $(x_k(t), x_{k+1}(t))$  is constant and for initial monodisperse droplet spectrum  $M(t) = N_0 Q(x(t))$  where  $N_0$  represents the total number concentration of droplets. Therefore for the initial monodisperse droplet spectrum and for the case  $B=0$  and  $\phi(c)=0$  in equation (4) there exists the analytic solution of the set of differential equations (4), (11), (12) which may be used for the test of the numerical method developed in this study.

#### Numerical method for integrating the coalescence/breakup kinetic equation

The coalescence/breakup kinetic equation for the droplet number density function  $n(x,t)$  can be written as:

$$\frac{\partial n(x,t)}{\partial t} = -n(x,t) \int_{x_1}^{x/2} \sigma(x,y) n(y,t) dy + \int_{x_1}^{x/2} \sigma(x-y,y) n(x-y,t) n(y,t) dy - n(x,t) P(x) + \int_x n(y,t) Q(y,x) P(y) dy \quad (13)$$

In this equation  $\sigma(x,y)$  represents the coalescence kernel for two droplets of mass  $x$  and  $y$ ;

$x_1$  is the smallest mass in the spectrum of droplets,  $P(x)$  - the probability that a droplet of mass  $x$  will break up during a unit time and  $Q(y,x)$  - the droplet number density function, formed due to breakup of a parent drop of mass  $y$ .

Multiplying (13) by  $x^m dx$  and integrating (13) from  $x_k$  to  $x_{k+1} = sx_k$  yields

$$\frac{\partial M_k^m(t)}{\partial t} = \int_{x_k}^{sx_k} x^m n(x,t) dx \int_{x_1}^{sx_k} \sigma(x,y) n(y,t) dy + \int_{x_k}^{sx_k} x^m dx \int_{x_1}^{sx_k} \sigma(x-y,y) n(x-y,t) n(y,t) dy - \int_{x_k}^{sx_k} x^m n(x,t) P(x) dx + \int_{x_k}^{sx_k} x^m dx \int_x^{sx_k} n(y,t) Q(y,x) P(y) dy \quad (14)$$

where

$$M_k^m(t) = \int_{x_k}^{sx_k} x^m n_k(x,t) dx = x_k^m \int_1^s z^m n_k(z,t) dz \quad (15)$$

represents the  $m$ -th order moment of the number density function of droplets in the packet  $(x_k, x_{k+1})$ . According to Bleck, the first two double integrals on the right side of (14) can be computed sectionally over small areas. Using this idea also for the computation of the last two integrals in (14), we have

$$\frac{\partial M_k^m(t)}{\partial t} = - \sum_{i=1}^J A_{i,k-1}^{m,k-1} M_{i,k-1}^{m,k-1} + \sum_{i=1}^J A_{i,k}^{m,k} M_{i,k}^{m,k} + \sum_{i=k}^J B_{i,k}^{m,k} M_{i,k}^{m,k} - B_k^{m,k} M_k^{m,k} \quad (16)$$

where  $k=1, 2, \dots, J$ ;  $J$  is the number of droplet packets:  $m=0, 1, 2, \dots$ ; and  $m$  is the order of moments. In the set of differential equations (16)  $A_{i,k}^{m,k}$ ,  $A_{i,k-1,k}^{m,k}$ ,  $A_{i,k,k}^{m,k}$  are coalescence double integrals which describe the kinetics of the coalescence process. The last two terms in (16) describe the droplet breakup process.

The computation of the coalescence and breakup double integrals requires the values of the unknown number density function  $n(x,t)$  in each separate droplet packet. Therefore approximating again the number density function  $n_k(z,t)$  by means of the first  $L$  terms of the expansion (1) and replacing the expansion coefficients  $a_{ik}(t)$  by means of linear combinations of  $M_k^m(t)$ , we have from (16) a finite set of coupled differential equations to compute the first  $L$  moments of the  $n_k(z,t)$  in each separate droplet packet.

There exist conservation relations between the coalescence double integrals, which for  $m=0$  and  $m=1$  describe the droplets number concentration conservation and liquid water content conservation respectively during the coalescence interaction between two droplet packets.

The detailed method for numerical integrating of the coalescence/breakup kinetic equation is contained in .

#### Numerical computations and concluding remarks

The unknown number density function  $n_k(z,t)$  in each separate droplet packet  $(x_k, x_{k+1})$  ( $x_{k+1} = sx_k$ ) is represented by an expansion in orthogonal polynomials with a given weighting function in the range  $(x_k, x_{k+1})$ . In this way the problem of solving the condensation/evaporation and coalescence/breakup kinetic equations is replaced by one of solving a set of coupled differential equations for the moments of the number density function  $n_k(z,t)$ .

The method of moments developed in this study, is tested against existing analytic solutions of the corresponding kinetic equations. Numerical results are obtained for different coalescence/breakup kernels, for different individual droplet diffusional growth rate and for different initial droplets spectra. Also droplet mass grid points intervals, weighting functions and integration time steps are varied.

The results of the numerical computations of the droplet spectra evolution by condensation/evaporation processes indicate that the convergence of the Picard's method of the successive

ORIGINAL PAGE IS  
OF POOR QUALITY

approximations for the equation (4) for small time intervals is sufficiently rapid. For monodisperse initial droplet spectra a comparison between numerical results computed by the method of this study and between existing analytic solution of droplet spectra evolution by condensation process is made. It is shown that a simultaneous use of the Picard's method and of the method of moments gives reasonable results which are very close to the existing analytic solution.

For the numerical integration of the coupled differential equations for  $N_k(t)$  and  $M_k(t)$  which are derived from (16), the forward time differencing is adopted. For practical computations the droplet mass grid points  $x_{k+1}=2x_k$  are the most convenient. The results of the numerical computations indicate that if the chosen weighting function is close to the unknown number density function  $n_k(z,t)$ , the difference between numerical results computed by means of the zero-order approximation and by means of the first-order approximation of the expansion (1) is sufficiently small. The results of numerical computations also show that the difference between numerical results computed by means of the first-order approximation of the expansion (1) with different  $M_k(z,t)$  is not large and even if the chosen weighting functions are not close to the unknown number density function  $n_k(z,t)$ , the use of the first-order approximation of the expansion (1) for different  $M_k(z,t)$  gives numerical results which are close to the existing analytic solutions. Therefore one important aspect of the method of moments is its ability to estimate for a given kernels the efficiency of the chosen weighting function, that is the sufficiency of the zero-order approximation of the expansion (1) when there is no analytic solution. A preliminary numerical results are obtained to study the influence of the condensation/evaporation processes on the droplet spectra evolution by the coalescence/breakup processes.

Thus, the convergence of the expansion of the number density function  $n_k(z,t)$  in terms of orthogonal polynomials with a given weighting functions in the range  $(1,s)$  ( $s \leq 2$ ) is sufficiently rapid and for droplet mass grid points  $x_{k+1}=sx_k$  ( $s \leq 2$ ) the approximation of  $n_k(z,t)$  by means of the first two terms of the expansion (1) is sufficiently correct.

Acknowledgments

The author wishes to thank Dr. Sh. Tsitsvashvily, Mr. A. Manes, Dr. K. Beheng and Mr. D. Decker for valuable discussions. The author also is thankful to Ms. N. Namtalishvily and Ms. D. Shvarts for manuscript preparation.

References

1. Berry, E. X., "Cloud droplet growth by collection" J. Atmos. Sci., vol. 24, pp 688-701. 1967.
2. Beheng, K. D., "Numerical simulation of graupel development". J. Atmos. Sci., vol. 35, pp. 683-689. 1978.
3. Bleck, R., "A fast approximative method for integrating the stochastic coalescence equation" J. Geophys. Res., vol. 75, pp. 5165-5171. 1970
4. Soong, S. T. "Numerical simulation of warm rain development in an axisymmetric cloud model" J. Atmos. Sci., vol. 31, pp. 1262-1285. 1974.
5. Erukashvily I. M. "On the solution of the kinetic coagulation equation" Izv. Akad. Nauk SSSR, ser. Geofiz., No 10, pp. 944-948. 1964.
6. Erukashvily I. M. "On the problem of a kinetic theory of gravitational coagulation in spatially heterogeneous clouds". Izv. Akad. Nauk SSSR, ser. Geofiz., No 11, pp. 1043-1045. 1964.
7. Erukashvily I. M. "A numerical method for integrating the kinetic equation of coalescence and breakup of cloud droplets" J. Atmos. Sci., vol.37, pp.2521-2534. 1980.

245

N82 23463

Bubble in a corner flow

Jean-Marc Vanden-Broeck

Mathematics Department and Mathematics Research Center, University of Wisconsin-Madison  
Madison, Wisconsin 53706

Abstract

The distortion of a two-dimensional bubble (or drop) in a corner of angle  $\delta$ , due to the flow of an inviscid incompressible fluid around it, is examined theoretically. The flow and the bubble shape are determined as functions of the angle  $\delta$ , the contact angle  $\beta$  and the cavitation number  $\gamma$ . The problem is formulated as an integrodifferential equation for the bubble surface. This equation generalizes the integrodifferential equations derived by Vanden-Broeck and Keller<sup>1,2</sup>. The shape of the bubble is found approximately by using the slender body theory for bubbles presented by Vanden-Broeck and Keller<sup>2</sup>. When  $\gamma$  reaches a critical value  $\gamma_0(\beta, \delta)$ , opposite sides of the bubble touch each other. Two different families of solution for  $\gamma < \gamma_0$  are obtained. In the first family opposite sides touch at one point. In the second family contact is allowed along a segment. The methods used to calculate these two families are similar to the ones used by Vanden-Broeck and Keller<sup>3</sup> and Vanden-Broeck<sup>4</sup>.

1. Introduction and formulation

We consider the steady potential flow around a gas bubble or liquid drop in a corner of angle  $\delta$ . The contact angle is denoted by  $\beta$  (see Figure 1). We shall write "bubble" to mean either bubble or drop. We take into account the surface tension  $\sigma$  at the interface, but we ignore the flow inside the bubble, assuming that the pressure is a constant  $p_0$  throughout it.

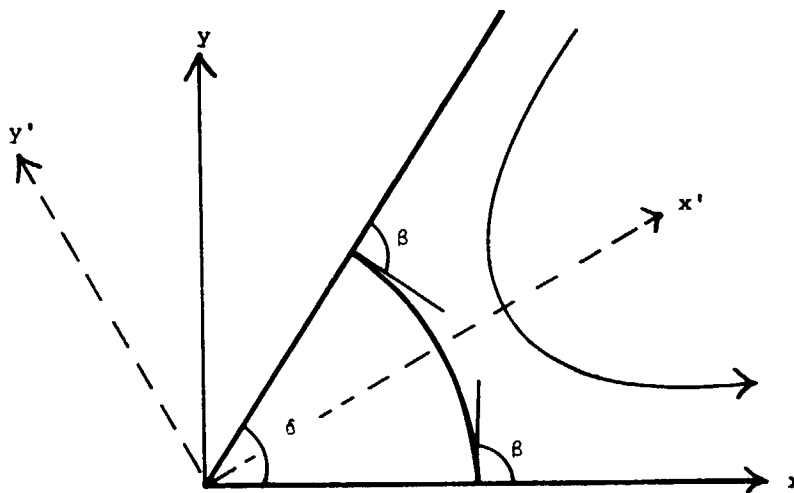


Figure 1. Sketch of the bubble and the coordinates

In order to formulate this problem we assume that the complex potential without the bubble is  $\frac{\delta \alpha}{\pi} (x + iy)^{\pi/\delta}$ , where  $\alpha$  is a constant and  $x$  and  $y$  are Cartesian coordinates.

We introduce dimensionless variables by choosing  $\left(\frac{2\sigma}{\rho \alpha^2}\right)^{\frac{\delta}{2\pi-\delta}}$  as the unit length and  $\alpha \left(\frac{2\sigma}{\rho \alpha^2}\right)^{\frac{\pi-\delta}{2\pi-\delta}}$  as the unit velocity. We also introduce the dimensionless potential  $b\phi$  and

stream function  $b\psi$ . Here,  $b > 0$  is a dimensionless constant to be chosen so that  $\phi = \frac{1}{2}$  and  $\phi = -\frac{1}{2}$  at the stagnation points on the walls  $y = 0$  and  $y = x \tan \delta$ , respectively. We denote the streamline along the two walls and along the bubble boundary by  $\psi = 0$ . In these variables  $b(\phi + i\psi) \sim \frac{\delta}{\pi} (x + iy)^{\frac{\delta}{\pi}}$  at infinity or, equivalently

$$x + iy \sim \left(\frac{\pi b}{\delta}\right)^{\frac{\pi}{\delta}} (\phi + i\psi)^{\frac{\delta}{\pi}} \quad (1)$$

at infinity.

The flow occupies the region  $\psi > 0$  of the  $\phi, \psi$  plane, and the bubble boundary corresponds to the segment  $-\frac{1}{2} < \phi < \frac{1}{2}$  of the axis  $\psi = 0$ . The problem of finding the flow consists of determining  $x + iy$  as an analytic function of  $\phi + i\psi$  in the half plane  $\psi > 0$  satisfying Equation (1) at infinity. Then the bubble surface is given by setting  $\psi = 0$  in  $x(\phi + i\psi)$  and  $y(\phi + i\psi)$  and letting  $\phi$  range from  $-\frac{1}{2}$  to  $\frac{1}{2}$ . The contact angle conditions require that the bubble surface meets the walls at the angle  $\beta$ , which yields

$$\frac{y_\phi}{x_\phi} = \begin{cases} \tan \beta & \text{as } \phi \rightarrow \frac{1}{2} \\ -\tan(\beta - \delta) & \text{as } \phi \rightarrow -\frac{1}{2} \end{cases} \quad (2)$$

On the bubble surface the pressure in the fluid, which is given by the Bernoulli equation, must differ from  $p_b$  by  $\sigma k$ , where  $k$  is the curvature of the interface. This leads to the boundary condition

$$p_s - \frac{\rho q^2}{2} = p_b - \sigma k \quad \text{on } -\frac{1}{2} < \phi < \frac{1}{2}, \quad \psi = 0. \quad (3)$$

Here,  $p_s$ ,  $\rho$  and  $q$  are, respectively, the stagnation pressure, the density and the speed of the fluid outside the bubble. In dimensionless variables (3) becomes

$$q^2 = k - \gamma \quad \text{on } -\frac{1}{2} < \phi < \frac{1}{2}, \quad \psi = 0, \quad (4)$$

where  $\gamma$  is the cavitation number defined by

$$\gamma = \frac{p_b - p_s}{\sigma} \left(\frac{2\sigma}{\rho a^2}\right)^{\frac{\delta}{2\pi - \delta}} \quad (5)$$

The problem can be further simplified by requiring the bubble to be symmetric about the line  $y = x \tan \frac{\gamma}{2}$ . This implies that

$$y_\phi(\phi, 0) = y_\phi(-\phi, 0) \cos \delta - x_\phi(-\phi, 0) \sin \delta, \quad 0 < \phi < \frac{1}{2}. \quad (6)$$

By using Equation (6) we can restrict our analysis to the interval  $0 < \phi < \frac{1}{2}$ .

## 2. Reformulation as an integrodifferential equation

It is convenient to reformulate the boundary value problem as an integrodifferential equation by considering the function

$$(\phi + i\psi)^{1 - \frac{\delta}{\pi}} (x_\phi + iy_\phi) - \left(\frac{\pi b}{\delta}\right)^{\frac{\delta}{\pi}} \frac{\delta}{\pi},$$

which is analytic in the half plane  $\psi > 0$  and vanishes at infinity as a consequence of Equation (1). Therefore, on  $\psi = 0$ , its real part is the Hilbert transform of its imaginary part. The imaginary part vanishes on  $\psi = 0$ ,  $|\phi| > \frac{1}{2}$  and therefore the Hilbert transform yields

$$\begin{aligned} \phi^{1-\frac{\delta}{\pi}} x_{\phi}(\phi, 0) - \left(\frac{\pi b}{\delta}\right)^{\frac{\delta}{\pi}} \frac{\delta}{\pi} &= \frac{1}{\pi} \int_0^{1/2} \frac{(\phi')^{1-\frac{\delta}{\pi}} y_{\phi}(\phi', 0)}{\phi' - \phi} d\phi' \\ &+ \frac{1}{\pi} \int_{-1/2}^0 \frac{(-\phi')^{1-\frac{\delta}{\pi}} [-y_{\phi}(\phi', 0) \cos \delta + x_{\phi}(\phi', 0) \sin \delta]}{\phi' - \phi} d\phi'. \end{aligned} \quad (7)$$

We now use the symmetry condition (6) to rewrite (7) in the form

$$x_{\phi}(\phi, 0) = \left(\frac{\pi b}{\delta}\right)^{\frac{\delta}{\pi}} \phi^{\frac{\delta}{\pi}-1} + \frac{\phi^{\frac{\delta}{\pi}-1}}{\pi} \int_0^{1/2} (\phi')^{1-\frac{\delta}{\pi}} y_{\phi}(\phi', 0) \left(\frac{1}{\phi' - \phi} + \frac{1}{\phi' + \phi}\right) d\phi'. \quad (8)$$

Next we express the boundary condition (4) in terms of  $x_{\phi}$  and  $y_{\phi}$  noting that  $q^2 = b^2(x_{\phi}^2 + y_{\phi}^2)^{-1}$ . Then (4) becomes

$$\frac{b^2}{x_{\phi}^2 + y_{\phi}^2} = \frac{y_{\phi} x_{\phi\phi} - x_{\phi} y_{\phi\phi}}{(x_{\phi}^2 + y_{\phi}^2)^{3/2}} - \gamma, \quad |\phi| < \frac{1}{2}, \quad \psi = 0. \quad (9)$$

Now (8) and (9) together constitute a nonlinear integrodifferential equation for  $y_{\phi}(\phi)$  in the interval  $0 < \phi < \frac{1}{2}$ ,  $\psi = 0$ . The contact angle conditions (2) complete the formulation of the problem for  $y_{\phi}(\phi, 0)$  and  $b$ .

For  $\gamma = \pi$ , the equation defined by (8) and (9) reduces to the integrodifferential equation derived by Vanden-Broeck and Keller<sup>1</sup>. The particular case  $\beta = \frac{\pi}{2}$  represents half of a free bubble.

For  $\gamma = \beta = \frac{\pi}{2}$ , the equations (8) and (9) reduce to the integrodifferential equation derived by Vanden-Broeck and Keller<sup>2</sup>. This case represents a quarter of a free bubble in a straining flow.

The integrodifferential equation defined by (8) and (9) can be solved numerically for arbitrary values of  $\beta$ ,  $\gamma$  and  $\delta$  by using the numerical procedures described by Vanden-Broeck and Keller<sup>1,2</sup>.

In the next section, we shall find the shape of the bubble approximately by using the slender body theory for bubbles presented by Vanden-Broeck and Keller<sup>1</sup>.

### 3. Slender body approximation

For  $\gamma$  large the bubble tends to an arc of a circle of radius  $\gamma^{-1}$ . As  $\gamma$  decreases numerical solutions show that the bubble elongates in the direction of the line which bisects the angle between the two walls. Then it develops a horn or spike which large curvature near its end. Finally when  $\gamma$  reaches a critical value  $\gamma_0(\beta, \delta)$ , opposite sides of the bubble touch each other. For  $\beta < \frac{\delta}{2}$  the contact point is at  $x = y = 0$ . For  $\beta > \frac{\delta}{2}$  the contact point is away from  $x = y = 0$ . Typical profiles for  $\delta = \pi$  and  $\delta = \beta = \frac{\pi}{2}$  can be found in Vanden-Broeck and Keller<sup>1,2</sup>. These profiles were obtained by solving numerically the integrodifferential equation of Section 2.

For  $\gamma \sim \gamma_0(\beta, \delta)$  the bubble is slender. Therefore we shall use the slender body theory for bubbles presented by Vanden-Broeck and Keller<sup>1</sup> to get an approximate description of the flow around the bubble. In the lowest order, the flow about a symmetric slender bubble is approximated by the flow about a rigid plate lying along the center line of the bubble. In the present case the center line of the bubble consists of a straight segment of some length  $a$  lying along the line  $y = x \tan \delta/2$ . We introduce the coordinates  $x', y'$  (see Figure 1) and find the potential  $b\phi(x', y')$  of the flow about these plates requiring that

at infinity  $b(\phi + i\psi) \sim \frac{\delta}{\pi} (x + iy)^{\frac{\delta}{\pi}}$ . Evaluating the potential on the plate  $y' = 0, x' > 0$  we obtain

$$b\phi(x',0) = \frac{\delta}{\pi} \left[ a \frac{2\pi}{\delta} - x' \frac{2\pi}{\delta} \right]^{1/2}. \quad (10)$$

By differentiating (10) we find that the flow speed  $q$  on the plate is

$$q(x',0) = x' \frac{2\pi}{\delta}^{-1} \left( a \frac{2\pi}{\delta} - x' \frac{2\pi}{\delta} \right)^{-1/2}, \quad x' > 0. \quad (11)$$

Before using  $q$  to get the bubble shape, we shall determine the length  $a$ . We do so by requiring the suction force  $F$ , exerted by the flow on the end of the spike, to balance the surface tension  $2\sigma$ . As we see in Ref. 5 [p. 412, Eq (6.5.4)],  $F = \pi\rho A^2/4$ . Here  $A$ , is the coefficient in the expansion  $b\phi \sim Ar^{1/2} \cos \frac{\theta}{2}$  in terms of polar coordinates with their origin at the end of the plate. Upon setting  $F = 2\sigma$  and introducing dimensionless variables we obtain

$$A^2 = \frac{4}{\pi}. \quad (12)$$

From (10) we find  $A^2 = \frac{2\delta}{\pi} a \frac{2\pi}{\delta}^{-1}$ , so (12) yields

$$a = \left( \frac{2}{\delta} \right)^{\frac{\delta}{2\pi-\delta}}. \quad (13)$$

We next use (11) for  $q$  in (4) and approximate the curvature  $k$  by  $-\eta_{x'x'}(x')$ . Here the equation of the bubble is  $y' = \eta(x')$ . Then (4) becomes

$$\eta_{x'x'} = -x' \frac{4\pi}{\delta}^{-2} \left( a \frac{2\pi}{\delta} - x' \frac{2\pi}{\delta} \right)^{-1} - \gamma. \quad (14)$$

At the end of the spike we require

$$\eta(a) = 0. \quad (15)$$

In addition the contact angle condition yields

$$\eta'(a) = -\tan(\beta - \frac{\delta}{2}). \quad (16)$$

Here  $a$  is defined by the equation

$$\eta(a) = a \tan \frac{\delta}{2}. \quad (17)$$

The function  $\eta(x')$  is easily obtained by integrating (14) twice with the auxiliary conditions (15) and (16). In the particular case  $\delta = \pi$ , the result of the integration is

$$\eta(x') = (a^2 - x'^2)(\gamma - 1)/2 - \frac{1}{2} a(a + x') \log(a + x') - \frac{1}{2} a(a - x') \log(a - x') + a^2 \log 2a + (a - x') \tan(\beta - \frac{\pi}{2}). \quad (18)$$

For  $\delta = \pi$ , (13) becomes

$$a = \frac{2}{\pi}. \quad (19)$$

Vanden-Broeck and Keller<sup>1</sup> have shown that the approximate solution (17), (18) is in fair agreement with the exact numerical solution of (8) and (9) for  $\beta \sim \frac{1}{2}\pi$  and  $\gamma \sim \gamma_0(\beta, \pi)$ .

For  $\gamma < \gamma_0(\beta, \delta)$  (14)-(16) yield unphysical profiles in which opposite sides of the bubble cross over. In the next two sections we construct physically acceptable families of solutions for  $\gamma < \gamma_0(\beta, \delta)$ . We shall present these results in the important particular case  $\delta = \pi$ .

#### 4. Solution with one point of contact

To obtain solutions for  $\gamma < \gamma_0(\pi, \beta)$  we require the free surface to be in contact with itself at one point. Then the bubble contains a small sub-bubble near its tip (see Figure 2). We denote by  $c$  the  $x'$  coordinate of the contact point.

We describe the profile of the bubble by the equations  $y' = \eta_1(x')$   $0 < x' < c$  and  $y' = \eta_2(x')$   $c < x' < a$ . Then by symmetry we have

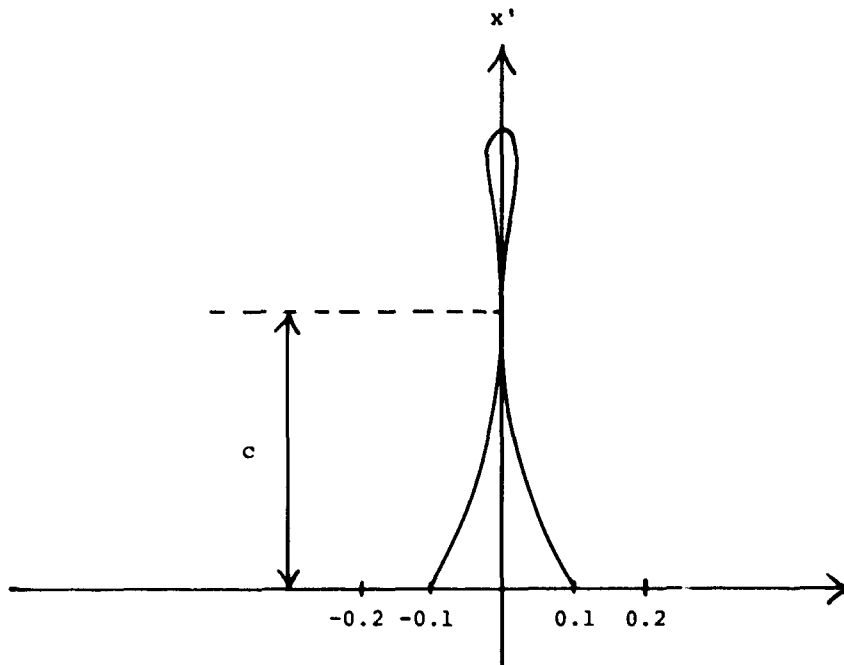


Figure 2. Profile of the bubble with one point of contact for  $\gamma = \gamma_0 \approx -1.7$  and  $\beta = 2\pi/3$ . The vertical scale is the same as the horizontal scale. The cavitation number in the sub-bubble is equal to  $\gamma_0$ .

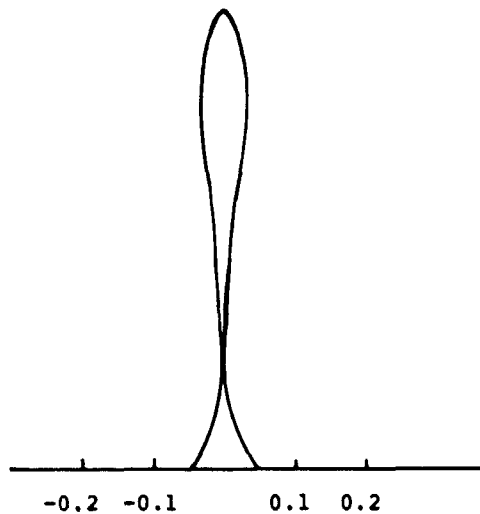


Figure 3. Profile of the bubble with one point of contact for  $\gamma = -4.5$  and  $\beta = 2\pi/3$ . The vertical scale is the same as the horizontal scale. The cavitation number in the sub-bubble is  $\mu = -0.6$ .

$$\eta_1(c) = \eta_2(c) = 0 \quad (20)$$

$$\eta_1'(c) = \eta_2'(c) = 0. \quad (21)$$

The conditions (15) and (16) yield

$$\eta_2(a) = 0 \quad (22)$$

$$\eta_1'(0) = -\tan(\beta - \frac{\pi}{2}). \quad (23)$$

The functions  $\eta_1(x')$  and  $\eta_2(x')$  are obtained by integrating (14) twice. The four constant of integrations and the value of  $c$  have to be evaluated to satisfy the six conditions (20)-(23). This yields a system of six equations with five unknowns. Therefore we cannot expect this system of equations to have a solution for any value of  $\gamma$  other than  $\gamma_0(\beta, \pi)$ .

The physical reason why the problem does not have a solution for  $\gamma \neq \gamma_0$  is that it requires the cavitation number in the sub-bubble to be the same as in the main bubble. It is to be expected that the cavitation number within the sub-bubble will have some value other than  $\gamma$ , which we cannot prescribe. Following the general philosophy of the method used by Vanden-Broeck and Keller<sup>3</sup> we shall introduce the unknown cavitation number  $\mu$  in the interval  $c < x' < a$ .

Integrating (14) twice we obtain

$$\begin{aligned} \eta_1(x') = & (a^2 - x'^2) \frac{\gamma - 1}{2} - \frac{1}{2} a(a + x') \log(a + x') \\ & - \frac{1}{2} a(a - x') \log(a - x') + A + Bx', \end{aligned} \quad (24)$$

$$\begin{aligned} \eta_2(x') = & (a^2 - x'^2) \frac{\mu - 1}{2} - \frac{1}{2} a(a + x') \log(a + x') \\ & - \frac{1}{2} a(a - x') \log(a - x') + E + Dx'. \end{aligned} \quad (25)$$

Here  $A, B, E$  and  $D$  are the four constants of integration. Using the six conditions (20)-(23) we obtain a system of six algebraic equations for the six unknowns  $A, B, E, D, \mu$  and  $c$ . This system can easily be solved and yields a unique solution for any  $\gamma$  in the interval  $-\infty < \gamma < \gamma_0(\beta, \pi)$ . Typical profiles for  $\beta = \frac{2\pi}{3}$  are shown in Figures 2 and 3. The value of  $\gamma_0$  is approximately equal to  $-1.7$ . As  $\gamma$  decreases the size of the sub-bubble increases and the size of the main bubble decreases. For  $\gamma = -\infty$ ,  $\mu = -0.39$  and the main bubble vanishes. It is interesting to note that the present solution also exists in the interval  $\gamma_0 < \gamma < \gamma^*$ . Here  $\gamma^*$  is the value of  $\gamma$  for which  $\eta_1'(c) = 0$ . A similar result was found by Vanden-Broeck and Keller<sup>3</sup>.

The results are summarized in Figure 4. The solution before contact described in Sections 2 and 3 correspond to the interval  $\gamma_0 < \gamma < \infty$ . It is represented by the straight line  $\mu = \gamma$  in Figure 4. The other curve in Figure 4 corresponds to the present solution. It exists in the interval  $-\infty < \gamma < \gamma^*$ . Therefore there are two possible solutions in the interval  $\gamma_0 < \gamma < \gamma^*$ .

##### 5. Solution with an interval of contact

In this section we derive another solution for  $\gamma < \gamma_0(\beta, \pi)$  by requiring the bubble to be collapsed between  $x' = f$  and  $x' = g$  (see Figure 5). We describe the profile of the bubble by the equations  $y' = \eta_1(x')$ ,  $0 < x' < f$  and  $y' = \eta_2(x')$ ,  $g < x' < a$ . The functions  $\eta_1(x')$  and  $\eta_2(x')$  must satisfy the following conditions

$$\eta_2(a) = 0 \quad (26)$$

$$\eta_1'(0) = -\tan(\beta - \frac{\pi}{2}), \quad (27)$$

$$\eta_1(f) = \eta_2(g) = 0, \quad (28)$$

$$\eta_1'(f) = \eta_2'(g) = 0. \quad (29)$$

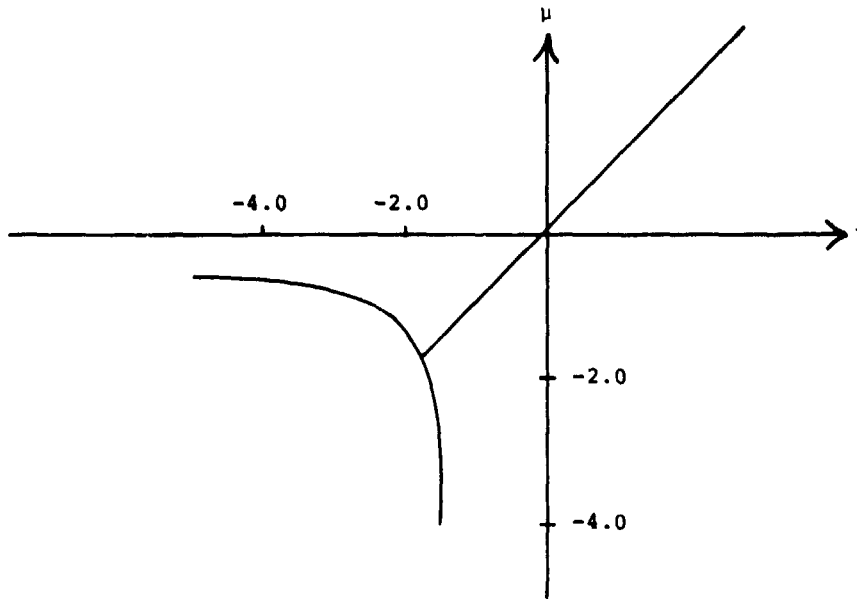


Figure 4. The cavitation number  $\mu$  as a function of  $\gamma$ .

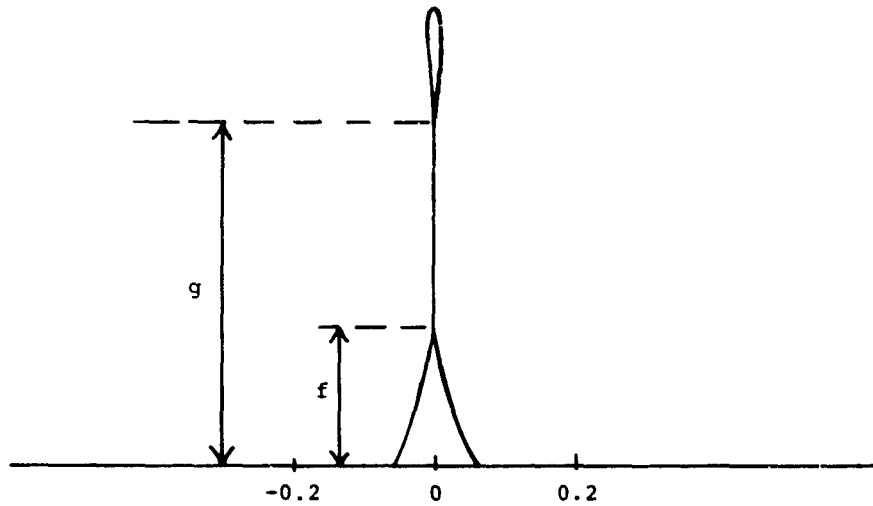


Figure 5. Profile of the bubble with one segment of contact for  $\gamma = -3.0$  and  $\beta = 2\pi/3$ . The vertical scale is the same as the horizontal scale. The values of  $f$  and  $g$  are respectively 0.19 and 0.47.

The functions  $\eta_1(x')$  and  $\eta_2(x')$  are obtained by integrating (14) twice. They are therefore given by the relations (24) and (25). The six constants  $A, B, E, D, g$  and  $f$  are found by satisfying the six conditions (26)-(29). We note that the present solution can be found with the same cavitation number everywhere.

A typical profile for  $\beta = \frac{2\pi}{3}$  is shown in Figure 5. As  $\gamma$  decreases the sizes of the main bubble and of the sub-bubble decrease. Furthermore the length of the contact segment increases as  $\gamma$  decreases. For  $\gamma = -\infty$ , the bubble reduces to a straight segment of length  $a$  lying on the  $x'$  axis.

Finally let us mention that the equilibrium of forces require the segment of contact to be a "film of impurities" characterized by a surface tension equal to  $2\sigma$ . This is very unlikely to occur in reality. Therefore the bubble with a segment of contact is physically unrealistic. However, this mathematical solution is physically relevant to describe the deformation of an inflated membrane. For details see Vanden-Broeck<sup>4</sup>.

#### Acknowledgments

Sponsored by the United States Army under Contract No. DAAG29-80-C-0041. This material is based upon work supported by the National Science Foundation under Grant No. MCS-7927062, Mod. 1.

#### References

1. Vanden-Broeck, J. M. and Keller, J. B., "Deformation of a Bubble or Drop in a Uniform Flow", J. Fluid Mech., Vol. 101, pp. 673-686. 1980.
2. Vanden-Broeck, J. M. and Keller, J. B., "Bubble or Drop Distortion in a Straining Flow in Two Dimensions", Phys. Fluids, Vol. 23, pp. 1491-1495. 1980.
3. Vanden-Broeck, J. M. and Keller, J. B., "A New Family of Capillary Waves", J. Fluid Mech., Vol. 98, pp. 161-169. 1980.
4. Vanden-Broeck, J. M., "Contact Problems Involving the Flow Past an Inflated Aerofoil", J. Appl. Mech. (in press).
5. Batchelor, G. K., Introduction to Fluid Dynamics, Cambridge University Press 1967.

Asymptotic expansions and estimates for the capillary problem

Frédéric Paul Brulois

Department of Mathematics, The University of Iowa  
Iowa City, Iowa 52242

Abstract

This paper analyzes the asymptotic properties for small Bond number  $B$  of the equilibrium capillary interface interior to a circular cylindrical tube vertically dipped in an infinite reservoir of liquid. (The Bond number  $B$  is a dimensionless parameter which is the ratio of gravitational to capillary forces.) The formal expansion in powers of  $B$  of the solution to the differential equation describing the equilibrium surface (as can be obtained by standard perturbation methods) is proved to be truly asymptotic—to all orders and uniformly in the variable and parameter  $\gamma$ , the contact angle.

Sequences of general estimates, in closed form, from above and from below, are also given for the solution and related functions. The  $m^{\text{th}}$  term in these sequences are asymptotically exact to order  $m$ . An idiosyncrasy of the problem, crucial in obtaining these estimates, is the absolute monotonicity of the structural function of the system in integral form.

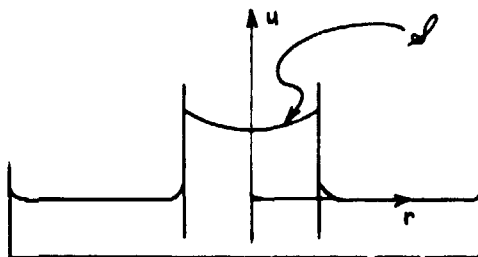


Figure 1.

Introduction

We consider the classical capillary problem of describing the equilibrium fluid interface  $\mathcal{A}$  interior to a circular cylindrical tube vertically dipped into an infinite reservoir of liquid (Fig. 1). Let  $u(r)$  be the height (above the level in the outer reservoir) of the surface  $\mathcal{A}$  as a function of the distance  $r$  to the axis of the tube. Then  $u(r)$  is a solution of the following boundary value problem

$$\frac{1}{r} \left( r \frac{u_r}{\sqrt{1+u_r^2}} \right)_r = Bu \tag{1}$$

$$u_r(0+) = 0 \tag{2}$$

$$u_r(1-) = \tan\left(\frac{\pi}{2} - \gamma\right). \tag{3}$$

In this formulation, the quantities  $r$ ,  $u$ ,  $\gamma$ , and  $B$  are dimensionless;  $\gamma$  is the contact angle of  $\mathcal{A}$  with the boundary cylinder ( $0 \leq \gamma \leq \pi$ ), and  $B = \rho g R^2 / T > 0$  is the Bond number with  $\rho$  the density difference across  $\mathcal{A}$ ,  $g$  the gravitational acceleration,  $R$  the radius of the cylinder, and  $T$  the surface tension. We refer for background to previous papers<sup>3,4,5,6,10</sup> and, in particular to<sup>1,2</sup>, for detailed proofs of most of the theorems.

Boundary value problem (1,2,3) has a unique solution; this solution will be studied indirectly by the shooting method. Set  $v(r,h,B)$  to be the unique solution of the following initial value problem

$$\frac{1}{r} \left( r \frac{v_r}{\sqrt{1+v_r^2}} \right)_r = 2h + Bv \tag{4}$$

$$v(0,h,B) = 0 \quad (5)$$

$$v_r(0,h,B) = 0. \quad (6)$$

Set also  $\sigma(r,h,B) = \frac{v_r}{\sqrt{1+v_r^2}}(r,h,B)$  and  $s = \sin(\frac{\pi}{2} - \gamma)$ . (The parameter  $h$  is the mean

curvature at the apex of the corresponding surface of revolution and  $\sigma$  is the sine of the slope angle of  $v$ ) Then there exists a unique  $h = h(B,s)$  such that  $\sigma(1,h,B) = s$ ; this is also the unique  $h$  such that the function  $2h/B + v(\cdot,h,B)$  is the solution of (1,2,3). Consequently, set

$$u(r,B,s) = \frac{2h(B,s)}{B} + v(r,h(B,s),B). \quad (7)$$

For the above existence and uniqueness results, see, for example, [6] or [2].

Instead of the initial value problem (4,5,6), we shall use an equivalent integral system for the pair  $(\sigma,v)$ , namely,

$$\sigma(r,h,B) = hr + \frac{B}{r} \int_0^r \rho v(\rho,h,B) d\rho \quad (8)$$

$$v(r,h,B) = \int_0^r g(\sigma(\rho,h,B)) d\rho \quad (9)$$

where the structural function  $g$  is given by

$$g(y) = \frac{y}{\sqrt{1-y^2}} = \sum_{n=0}^{\infty} \frac{\binom{2n}{n}}{2^{2n}} y^{2n+1}, \quad \text{for } |y| < 1. \quad (10)$$

Note that  $g$  is absolutely monotonic on the interval  $(0,1)$ , i.e., has nonnegative derivatives on all orders on  $(0,1)$ . This fact is essential in obtaining the estimates below.

The approach will consist in first obtaining asymptotic results (resp. estimates) for the solution  $\sigma(r,h,B)$ ,  $v(r,h,B)$  of the initial value problem (in integral form), then deriving from these results similar ones for  $h(B,s)$  and then  $u(r,B,s)$ .

#### Absolute monotonicity and analyticity of $\sigma$ and $v$

Since (4) is singular at  $r = 0$ , we need to show that the pair  $(\sigma,v)$  is locally analytic at  $r = 0$  and depends analytically on the parameters  $h$  and  $B$ . This can be done in a number of ways (cf., for example, Wentz<sup>1</sup>); alternatively<sup>1</sup>, it can be observed that the "one dimensional solution"  $(\bar{\sigma}, \bar{v})$  (i.e., the profile curve of the capillary surface between two vertical parallel plates) is a majorant for  $(\sigma,v)$ . Since  $(\bar{\sigma}, \bar{v})$  is solution of a regular initial value problem, we conclude, by the method of majorants, that

Proposition 1: For every  $\eta, \beta > 0$ , there exists  $\rho > 0$  such that the functions  $\sigma(r,h,B)$  and  $v(r,h,B)$  are analytic in the domain  $|r| < \rho$ ,  $|h| < \eta$ ,  $|B| < \beta$  in  $\mathbb{C}^3$ .

Now the absolute monotonicity of  $g$  on  $(0,1)$  yields that  $\sigma(r,h,B)$  and  $v(r,h,B)$  are absolutely monotonic in all three variables for positive values of  $r$ ,  $h$ , and  $B$ . This can be checked by power series substitution into system (8,9). Thus the triple power series expansion of  $\sigma$  and  $v$  at  $(0,0,0)$  has nonnegative coefficients. This last fact together with Pringsheim's Theorem below implies that this expansion is convergent on the maximal interval  $0 < r < \rho = \rho(h,B)$  where  $\sigma(\cdot,h,B)$  and  $v(\cdot,h,B)$  can be continued as a solution of integral system (8,9). Since  $\sigma(\cdot,h,B)$  and  $v(\cdot,h,B)$  are monotonic and bounded, we obtain convergence up to the boundary of the disc of convergence.

Proposition 2: The power series expansions of  $\sigma(\cdot,h,B)$  and  $v(\cdot,h,B)$  at  $r = 0$  converge absolutely and uniformly in the closed convex disc  $|r| \leq \rho(h,B)$ . Moreover  $0 < \rho(h,B) < \infty$  and, at  $r = \rho(h,B)$ ,  $\sigma(r,h,B) = 1$ .

Corollary 3: The triple power series expansions of  $\sigma$  and  $v$  at  $(r,h,B) = (0,0,0)$  converge absolutely and uniformly in the closed domain

$$D = \{(r,h,B) \in \mathbb{C}^3: |r| \leq \rho(|h|, |B|)\}. \quad (11)$$

Pringsheim's Theorem: Let

$$f(z) = \sum_{n=0}^{\infty} c_n z^n \quad (12)$$

and  $R$  the radius of convergence of power series (12). Suppose  $c_n \geq 0$ , for all  $n \geq 0$ . Then  $z = R$  is a singular point of  $f$ .

#### Asymptotic expansions

**Theorem 4:** For each  $m \geq 0$ , the series expansions in powers of  $B$  of the functions  $h(B,s)$ ,  $\sigma(r,h(B,s),B)$ ,  $v(r,h(B,s),B)$ , and  $u(r,B,s)$  are asymptotic to order  $m$  uniformly in  $r$  and  $s$  over the entire range  $0 \leq r \leq 1$ ,  $-1 \leq s \leq 1$ , as  $B \rightarrow 0$ .

**Proof (outline):** By symmetry, we may restrict ourselves to  $s \geq 0$ . Recall that  $h(B,s)$  is the unique solution of

$$\sigma(1,h,B) = s. \quad (13)$$

Now  $\sigma(1,h,0) = h$  and  $\sigma(1,\cdot,\cdot)$  is analytic at each point  $(h,0)$  where  $h$  is in the complex disc  $|h| < 1$ . Since  $\sigma_h(1,h,0) = 1$ , the implicit function theorem implies that  $h(B,s)$  is analytic at each point  $(0,s)$  where  $s$  is in the complex disc  $|s| < 1$ . A compactness argument shows that, for each  $s_0$  with  $0 < s_0 < 1$ , there exists  $B_0 > 0$  such that  $h(B,s)$  is analytic in  $|B| \leq B_0$ ,  $|s| \leq s_0$  and

$$h(B,s) = \sum_{n=0}^{\infty} B^n \xi_n(s) \quad \text{where} \quad \xi_n(s) = \frac{1}{n!} \frac{\partial^n h}{\partial B^n}(0,s). \quad (14)$$

This yields the asymptotic statement for  $h(B,s)$  away from  $s = 1$ , i.e., contact angle  $\gamma = 0$ .

The neighborhood of  $s = 1$  requires a special treatment and the use of the parametric system for the profile curve (parametrized by arclength). The corresponding function  $\bar{h}(B,\alpha)$  where  $\alpha = \frac{\pi}{2} - \gamma$  is shown to be analytic in a neighborhood of  $(0, \frac{\pi}{2})$  by the implicit function theorem. Thus  $h(B,s) = \bar{h}(B, \arcsin s)$ . We conclude, since the function arcsine is continuous at  $s = 1$ .

The other three functions are handled in a similar way. QED.

In particular,  $\xi_n(1) = \lim_{s \rightarrow 1^-} \xi_n$  exists. This settles in the negative the problem of possible nonuniformity as  $s \rightarrow 1$  (cf. [1]).

In Tables 1, 2, 3, and 4 below, we give the first few coefficient-functions of each expansion as can be obtained by standard perturbation techniques. Previously Laplace<sup>7</sup>, Poisson<sup>8</sup>, Rayleigh<sup>9</sup>, and Concus<sup>3</sup> computed formally these asymptotic expansions to various orders. We should also mention that Siegel<sup>10</sup> had proved recently the first term of those expansions to be truly asymptotic.

First we need

$$\sigma(r,h,B) = \sum_{n=0}^{\infty} (Br^2)^n \lambda_n(hr) \quad (15)$$

$$v(r,h,B) = r \sum_{n=0}^{\infty} (Br^2)^n \mu_n(hr) \quad (16)$$

(where the series converge in  $D$ ) and recurrence formulas for the functions  $\lambda_n$  and  $\mu_n$

$$\lambda_0(x) = x \quad (17)$$

$$\lambda_n(x) = \frac{1}{x^{2n+1}} \int_0^x \xi^{2n} \mu_{n-1}(\xi) d\xi \quad (18)$$

$$\mu_n(x) = \frac{1}{x^{2n+1}} \int_0^x \xi^{2n} \sum_{p=0}^n g^{(p)}(\xi) \sum \frac{(\lambda_1^{l_1} \dots \lambda_n^{l_n})(\xi)}{l_1! \dots l_n!} d\xi \quad (19)$$

where the second summation in (19) is for  $l_1 + \dots + l_n = p$  and  $l_1 + 2l_2 + \dots + nl_n = n$ .

Table 1. First few  $\lambda_n$

$$\begin{aligned}\lambda_0(x) &= x \\ \lambda_1(x) &= \frac{1}{6} \frac{1+2\sqrt{1-x^2}}{(1+\sqrt{1-x^2})^2} x \\ \lambda_2(x) &= \frac{1}{6x^3} \left[ \frac{x^2}{(1+\sqrt{1-x^2})^2} + \log \frac{1+\sqrt{1-x^2}}{2} \right] \\ \lambda_3(x) &= \frac{1}{x^7} \left[ \frac{1}{72} \frac{1}{\sqrt{1-x^2}} - \frac{13}{36} + \frac{11}{24} \sqrt{1-x^2} - \frac{1}{18} (1-x^2) - \frac{1}{18} (1-x^2)^{3/2} \right. \\ &\quad \left. - \frac{1}{12} (1+\sqrt{1-x^2}) (5-3\sqrt{1-x^2}) \log \frac{1+\sqrt{1-x^2}}{2} \right]\end{aligned}$$

Table 2. First few  $\mu_n$

$$\begin{aligned}\mu_0(x) &= \frac{1}{x} (1-\sqrt{1-x^2}) = \frac{x}{1+\sqrt{1-x^2}} \\ \mu_1(x) &= \frac{1}{6x^3} \left[ \frac{1}{\sqrt{1-x^2}} - 1 + 2 \log \frac{1+\sqrt{1-x^2}}{2} \right] \\ \mu_2(x) &= \frac{1}{x^5} \left[ \frac{1}{72} \frac{1}{(1-x^2)^{3/2}} - \frac{1}{24} \frac{1}{\sqrt{1-x^2}} - \frac{5}{36} + \frac{1}{6} \sqrt{1-x^2} \right. \\ &\quad \left. + \frac{1-3\sqrt{1-x^2}}{6\sqrt{1-x^2}} \log \frac{1+\sqrt{1-x^2}}{2} \right]\end{aligned}$$

Table 3. First few  $\xi_n$

$$\begin{aligned}\xi_0 &= \lambda_0 \\ \xi_1 &= -\lambda_1 \\ \xi_2 &= \lambda_1 \lambda_1' - \lambda_2 \\ \xi_3 &= \lambda_1 \lambda_2' + \lambda_2 \lambda_1' - \lambda_1 \lambda_1'^2 - \frac{1}{2} \lambda_1^2 \lambda_1'' - \lambda_3\end{aligned}$$

Table 4. Expansions for the BVP

$$\begin{aligned} \sigma(r, h(B, s), B) &= sr + B[r^2 \lambda_1(sr) - \lambda_1(s)] \\ &+ B^2[r \lambda_1(s) \lambda_1'(s) - r^3 \lambda_1(s) \lambda_1'(sr) + r^4 \lambda_2(sr) - r \lambda_2(s)] + \dots \end{aligned}$$

$$\begin{aligned} v(r, h(B, s), B) &= r \mu_0(sr) + B[r^3 \mu_1(sr) - r^2 \lambda_1(s) \mu_0'(sr)] \\ &+ B^2[r^2 \lambda_1(s) \lambda_1'(s) \mu_0'(sr) - r^2 \lambda_2(s) \mu_0'(sr) - \frac{1}{2} r^3 \lambda_1^2(s) \mu_0''(sr) \\ &- r^4 \lambda_1(s) \mu_1'(sr) + r^5 \mu_2(sr)] + \dots \end{aligned}$$

$$u(r, B, s) = \frac{2h(B, s)}{B} + v(r, h(B, s), B)$$

Estimates

The coefficient-functions  $\lambda_n$  and  $\mu_n$  are odd, analytic in the unit disc, and absolutely monotonic in the interval  $(0, 1)$ . This yields the following lower estimates by truncation of the series (15) and (16), for each  $m \geq 0$ ,

$$\sigma(r, h, B) \geq \sum_{n=0}^m (Br^2)^n \lambda_n(hr) \tag{20}$$

$$v(r, h, B) \geq r \sum_{n=0}^m (Br^2)^n \mu_n(hr) \tag{21}$$

for  $(r, h, B) \in D^+ = D \cap [0, \infty)^3$ .

Using the fact that the right hand side of (20) is increasing in  $h$  and setting  $h = h(B, s)$  and  $r = 1$  in (20), we get the upper estimate

$$h(B, s) \leq \hat{h}_m(B, s) \tag{22}$$

where  $\hat{h}_m(B, s)$  is the unique nonnegative solution of equation

$$\sum_{n=0}^m B^n \lambda_n(h) = s. \tag{23}$$

Estimates on the other side are obtained by induction on  $m$  from integral system (6,9), using Picard's method of successive approximations and a careful estimation of each iterate. The proof uses strongly the absolute monotonicity of the function  $g$ . For each  $m \geq 0$ , we get the upper estimates

$$\sigma(r, h, B) \leq \sum_{n=0}^{m-1} (Br^2)^n \lambda_n(hr) + (Br^2)^m \lambda_m(\sigma(r, h, B)) \tag{24}$$

$$v(r, h, B) \leq r \sum_{n=0}^{m-1} (Br^2)^n \mu_n(hr) + r (Br^2)^m \mu_m(\sigma(r, h, B)) \tag{25}$$

for  $(r, h, B) \in D^+$ . Using the fact that the right hand side of (24) is increasing in  $h$  and setting  $h = h(B, s)$  and  $r = 1$  in (24), we get, for  $m \geq 1$ , the lower estimate

$$h(B, s) \geq \check{h}_m(B, s) \tag{26}$$

where  $\check{h}_m(B, s)$  is

- (i) 0, if  $B^m \geq s/\lambda_m(s)$ ,
- (ii) the unique nonnegative solution of equation

$$\sum_{n=0}^{m-1} B^n \lambda_n(h) + B^m \lambda_m(s) = s, \quad (27)$$

$$\text{if } B^m \leq s/\lambda_m(s).$$

Now, setting  $h = h(B,s)$  in (20) and (21) and using (26),

$$\sigma(r, h(B,s), B) \approx \sum_{n=0}^m (Br^2)^n \lambda_n(\check{r}\check{h}_m(B,s)) \quad (28)$$

$$v(r, h(B,s), B) \approx r \sum_{n=0}^m (Br^2)^n \mu_n(\check{r}\check{h}_m(B,s)). \quad (29)$$

Similarly, setting  $h = h(B,s)$  in (24) and (25) and using (22),

$$\sigma(r, h(B,s), B) \approx \sum_{n=0}^{m-1} (Br^2)^n \lambda_n(\hat{r}\hat{h}_m(B,s)) + (Br^2)^m \lambda_m(sr) \quad (30)$$

$$v(r, h(B,s), B) \approx r \sum_{n=0}^{m-1} (Br^2)^n \mu_n(\hat{r}\hat{h}_m(B,s)) + r (Br^2)^m \mu_m(sr). \quad (31)$$

Estimates (22,26,28,29,30,31) are valid for  $m \geq 1$ ,  $B \geq 0$ ,  $0 \leq s \leq 1$ , and  $0 > r \geq 1$ ; they are all asymptotically exact to order  $m$ , as  $B \rightarrow 0$ .

Some of these estimates had been obtained previously by Finn<sup>4,5</sup> and Siegel<sup>10</sup>.

#### References

1. Brulois, F., Ph.D. dissertation, Stanford Univ. 1981.
2. Brulois, F., "Estimates for axially symmetric capillary surfaces," to appear.
3. Concus, P., "Static menisci in a vertical right circular cylinder," J. Fluid Mech., Vol. 34, pp. 482-495. 1968.
4. Finn, R., "The sessile liquid drop I: Symmetric case," Pacific J. Math., Vol. 88, pp. 541-587. 1980.
5. Finn, R., "On the Laplace formula and the meniscus height for a capillary surface," to appear.
6. Johnson, W. E., and L. M. Perko, "Interior and exterior boundary value problems from the theory of the capillary tube," Arch. Rat. Mech. Anal., Vol. 29, pp. 125-143. 1968.
7. Laplace, P. S., Traité de mécanique céleste, Tome 4, Supplément au Livre X, "Sur l'action capillaire," Bauthier-Villars, Paris 1806.
8. Poisson, S.D., Nouvelle théorie de l'action capillaire, Bachelier, Paris 1831.
9. Rayleigh, J. W. S., "On the theory of the capillary tube," Proc. Roy. Soc. London, Ser. A 92, pp. 184-195. 1915.
10. Siegel, D., "Height estimates for capillary surfaces," Pacific J. Math., Vol. 88, pp. 471-515. 1980.
11. Wentz, H. C., "The stability of the axially symmetric pendant drop," Pacific J. Math., Vol. 88, pp. 421-470. 1980.

N82 23465

The numerical analysis of the rotational theory for the formation of lunar globules

James Ross<sup>1</sup>, John Bastin<sup>2</sup>, and Kris Stewart<sup>3</sup>

<sup>2</sup>Queen Mary College

<sup>3</sup>University of New Mexico

<sup>1</sup>San Diego State University Department of Mathematical Sciences  
San Diego, California, 92182

Lunar globules are smooth glassy objects which were discovered by the astronauts on the moon. These objects are small - most are less than a tenth of a millimeter in diameter - though some are a good deal larger. The shapes of the globules vary on a continuum from spheres to prolate spheroids to dumbbells. Figure 1 contains two photographs, one of a prolate globule and one of a dumbbell shaped globule.

Several theories have been proposed for their creation. All these theories assume that molten rock is shot from the surface of the moon, solidifies in space above the moon and then falls back to the surface.

The rotational theory which we study in this paper makes the following assumptions: The volume of the molten rock does not change during cooling. The angular momentum is conserved. There are no internal motions because of the high viscosity of the molten rock, i.e., in equilibrium the globule is rotating as a rigid body. Finally, we assume that the kinetic reaction of the globule to the forces is fast relative to the rate of cooling, i.e., we assume that the globule reaches equilibrium at constant energy. For more discussion of this theory see [1].

Most thermodynamists would agree that with these assumptions equilibrium will be achieved at a local minimum of the internal energy and that the relevant part of the internal energy is

$$E = \frac{1}{2} I(\Omega) \omega^2 + T \cdot A(\partial\Omega)$$

Here  $\Omega$  is the region occupied by the globule in a coordinate system fixed in the body.  $I(\Omega)$  is the moment of inertia of the globule with respect to its axis of rotation.  $A(\partial\Omega)$  is the surface area of the globule.  $T$  is a positive constant which describes the surface tension properties of the molten rock (this number is effectively constant over wide variations of temperature), and  $\omega$  is the angular velocity.

We remark that from the standpoint of rational thermokinetics there is a need to justify these claims theoretically. However, we will assume here that equilibrium will be achieved at a local minimum of this internal energy expression.

We therefore consider the mathematical problem:

$$\text{Minimize:} \quad E = \frac{1}{2} I \omega^2 + T \cdot A(\partial\Omega) \quad (1)$$

$$\text{Subject to:} \quad \text{Volume}(\Omega) = V(\Omega) = k_1 = \text{given constant}$$

$$I\omega = k_2 = \text{given constant.}$$

It is sometimes more convenient to consider the problem in the following equivalent form.

$$\text{Minimize:} \quad \bar{E} = \frac{ck_2^2}{I} + A(\partial\Omega) \quad (2)$$

$$\text{Subject to:} \quad V(\Omega) = k_1 = \text{given constant}$$

The class of globules over which we minimize will always be some subset of the smoothly bounded axisymmetric (with respect to the axis of rotation) configurations. Here axisymmetric with respect to the z-axis means that if  $(x, y, z)$  is a point in the globule then so is  $(-x, -y, z)$ .

We would first like to point out that for this variational problem there is no configuration for which  $E$  (or  $\bar{E}$ ) attains its absolute minimum, so that we can only expect to find a local minimum. To see this, consider problem (2). Let  $\epsilon > 0$  be given. By detaching two small identical pieces from the sphere at volume  $k_1$  and placing them symmetrically on either side of the remainder of the sphere on an axis which is perpendicular to the axis of rotation, it is possible by pushing the two small pieces far away from the sphere to obtain a configuration,  $\Omega$ , such that  $\bar{E}(\Omega) = a_1 + \epsilon$  where  $a_1$  is the surface area of the sphere of volume  $k_1$ . Thus the absolute minimum for  $\bar{E}$  is  $a_1$  if it exists. But clearly no configuration has this value for  $\bar{E}$  provided that  $k_2 \neq 0$ , since the sphere of volume  $k_1$  is the only possibility.

Applying the classical methods of the calculus of variations we obtain as the Euler-Lagrange equation for this problem the equation:

$$C(p) = -(Ar^2 + B), \quad (3)$$

where  $C(p)$  is the mean curvature of the surface  $\partial\Omega$  at the point  $p \in \partial\Omega$ ,  $r^2 = x^2 + y^2$  where we have taken the  $z$ -axis is the axis of rotation, and  $A$  and  $B$  are constants which involve Lagrange multipliers and must be chosen to satisfy the constraints. It is reassuring to note that this equation can be obtained directly by balancing the forces at each point on  $\partial\Omega$  without considering the variational problem at all. Since the pressure inside the globules must be greater than the outside pressure, we may conclude that the constants  $A$  and  $B$  are positive. Here we have adopted the convention that inward curvature is negative.

It is possible to write this equation as a free boundary value problem for a nonlinear partial differential equation. But this problem seems difficult to treat even numerically. We will introduce additional symmetries into the problem so that we are led to consider an approximate problem involving ordinary differential equations.

#### The oblate solutions

There exist exact solutions to (3) which are surfaces of revolution with respect to the  $z$ -axis (the axis of rotation). By taking advantage of the assumed symmetries, we see that these solutions will be solutions to the free boundary value problem.

$$\begin{aligned} f f'' &= (1 + (f')^2)(1 - 2f(1 + (f')^2)^{1/2}(Af^2 + B)) \\ f'(0) &= 0 : f(b) = 0, f'(b) = -\infty. \end{aligned} \quad (4)$$

Here,  $f$  and  $b$  are unknown and  $A$  and  $B$  are positive constants which must be chosen to satisfy the constraints. The function  $x = f(z)$  generates the surface of the globule when rotated about the  $z$ -axis. Remarkably, this equation can be integrated exactly in terms of elliptic integrals. (See Chandrasekhar [2].) However, it is easier to do numerically. These solutions while they are exact solutions to the Euler-Lagrange equation (3), they almost surely are not local minima for our variational problem except possibly near the sphere i.e., for small values of the angular momentum. Nevertheless, there is a smooth one parameter family of these solutions for a given volume starting with the sphere ( $k_2 = 0$ ) and becoming more and more oblate. A convenient parameter to index these solutions is,  $I$ , their moment of inertia. Table 1 contains some important numbers for a few members of this family.

#### The approximate prolate and dumbbell solutions

Motivated by the fact that the actually occurring shapes are close to being surfaces of revolution with respect to an axis (which we call the  $x$ -axis) which is perpendicular to the axis of rotation, we consider the variational problem modified so as to include in the class of possible globules only those which are surfaces of revolution with respect to the  $x$ -axis. Now the appropriate functional to minimize is

$$\begin{aligned} \int_0^b \frac{\rho\pi}{8} f^4 \omega^2 + \frac{\rho\pi}{2} f^2 x^2 \omega^2 + 2\pi T f \sqrt{1 + (f')^2} \\ + \lambda_1 \pi f^2 + \lambda_2 \left[ \frac{\rho\pi}{4} f^4 + \rho\pi f^2 x^2 \right] \omega dx \end{aligned}$$

where the function  $y = f(x)$  generates the surface of the globule by rotation about the  $x$ -axis,  $\rho$  is the density, and  $\lambda_1$  and  $\lambda_2$  are Lagrange Multipliers. Here  $\omega$  is treated as a parameter. As before, both  $f$  and  $b$  are unknown. This leads to the free boundary value problem,

$$f f'' = (1 + (f')^2) (1 - 2f(1 + (f')^2)^{1/2} (Ax^2 + \frac{A}{2} f^2 + B)) \quad (5)$$

$$f'(0) = 0; f(b) = 0, f'(b) = -\infty.$$

As before, the positive constants A and B must be chosen to satisfy the constraints. As in the oblate case, if we fix the volume, we can generate, numerically, a continuous one parameter family of solutions starting at this sphere and proceeding through prolate shapes to dumbbell shapes with narrower and narrower necks. Again, I, the moment of inertia is an increasing parameter along this family of deformations of the sphere. Figure 2 contains graphs of some of the members of this family. The volumes of all the globules in this graph are equal. The reader is asked to compare the shapes in this figure with the photographs in Figure 1. Mathematically, this equation is more difficult to handle than (4). It cannot be integrated in terms of elliptic integrals and no existence theorem is known for this free boundary value problem. Table 2 contains extensive information about this family. The number e is defined as the thickness at the axis of rotation divided by the

length of the globule. The number, D, is defined by  $D = \frac{A}{B^3}$ . We note that both of these numbers are invariant under similarity transformations and that if a globule is a solution to our free boundary value problem then so is any similar globule. Both Tables 1 and 2 were computed assuming that the volume is one and that the density is one.

We have, therefore, two families of deformations of the sphere each parameterized by, I, the moment of inertia of the globule with respect to its axis of rotation. We denote the oblate family by  $\Omega_0(I)$  and the prolate family by  $\Omega_p(I)$ . For given I, the two corresponding members are local minimum for the variational problem modified in two ways. First, we add the constraint that  $I = \text{const}$ . Second, we restrict the variations allowed to be such that they produce in the case of the oblate family surfaces which are surfaces of revolution with respect to the axis of rotation (the x-axis) and in the prolate family surfaces which are surfaces of revolution with respect to the x-axis. We caution that if more general variations are allowed the prolate family globule cannot be a local minimum since they do not satisfy (3). While the oblate family globule is also not a local minimum, at least sufficiently far from the sphere, even though it does satisfy (3).

The first constraint,  $I = \text{constant}$ , is eliminated by considering  $\bar{E}$  as a function of I along either of the families. We have

$$\bar{E}(I) = \frac{ck_2^2}{I} + A(I).$$

At a minimum for the problem where the constraint,  $I = \text{constant}$ , is dropped but the restrictions on the variations are retained we must have  $\frac{d\bar{E}}{dI} = 0$ . That is  $I \frac{dA}{dI} = c K_2^2$ .

Also we must have  $\frac{d^2\bar{E}}{dI^2} > 0$ . Some simple calculations show that this condition is equivalent

to the condition  $\frac{d}{dI} (I \frac{dA}{dI}) > 0$  assuming that  $\frac{d\bar{E}}{dI} = 0$  at the point considered. An examination of Table 2 leads to the conclusion that these globules are no longer a minimum beyond globule #25. That is beyond this point the globules are clearly unstable. If this theory is correct, the dumbbell shaped globule in Figure 1 is near the limit of stability. If it were much narrower at the neck it would break apart.

#### Comparison of the energies

We assume now that this volume of all globules is fixed at one. If  $k_2$  is sufficiently small, there is exactly one local minimum for the modified variational problems along each of the families  $\Omega_0(I)$  and  $\Omega_p(I)$ . The value of  $\bar{E}$  at a point where  $\frac{d\bar{E}}{dI} = 0$  is given by the

expression  $I \frac{dA}{dI} + A$  which forms the last column in the tables. By inspecting Tables 1 and 2

we see that for a given  $k_2$  the energy,  $\bar{E}_p(k_2)$  of the minimizing globule from the  $\Omega_p(I)$  family is smaller than the energy  $\bar{E}_0(k_2)$  at the minimizing globule from the  $\Omega_0(I)$  family from globules #16 or #17 on to the end of the table, while up to that point  $\bar{E}_0(k_2)$  is

smaller than  $\bar{E}_p(k_2)$ . However, since there exist perturbations of any of the prolate family globules which produce an even smaller energy there are globules near the prolate family which produce smaller values of  $\bar{E}$  nearer to the sphere than globule #16.

We conjecture that there is a one parameter family of globules which start from the sphere and develops essentially like the prolate family but which contains true local minimum for the variational problem (1). (Chandrasekhar [2] expects that the oblate spheroids are stable near the sphere and that a bifurcation occurs along this family which contains ellipsoids with different lengths for all three axes.)

### Conclusion

The good agreement between the actual shapes of the Lunar globules and the numerical results in Figure 2 certainly lend some support to the rotational theory. However, since the existence of true local minima has not been established and since the theoretical understanding of the thermokinetics is still to be attained, there is certainly room for doubt.

### The numerical computation

The simplification of the variational problem yields a second order ordinary differential equation (ODE) for  $f(x)$

$$\frac{d^2 f}{dx^2} = \frac{1}{f(x)} \left( 1 + \left( \frac{df}{dx} \right)^2 \right) \left[ 1 - 2f(x) \sqrt{1 + \left( \frac{df}{dx} \right)^2} (Ax^2 + B + C(f(x))^2) \right] \quad (6)$$

and one must find a positive value of the independent variable, say  $x_f$ , so that the following boundary conditions hold

$$\left. \frac{df}{dx} \right|_{x=0} = 0; \quad f(x_f) = 0; \quad \left. \frac{df}{dx} \right|_{x=x_f} = -\infty \quad (7)$$

i.e., the function should start off flat from the  $f$ -axis and should cross the  $x$ -axis going straight down.

The numerical solutions present in this paper were computed using 14 digit precision BASIC on a Z-80 based microcomputer employing two routines from the small machine oriented library of mathematical software, SCRUNCH [4] to solve this variant of a two-point boundary value problem by simple shooting. ZEROIN, a robust root finder developed by L. F. Shampine and R. C. Allen, Jr. which uses a careful combination of bisection and the secant rule, was used to find the missing end point,  $x_f$ . RKF45, a fourth/fifth order Runge-Kutta-Fehlberg method originally coded by H. A. Watts and L. F. Shampine for solving the initial value problem for systems of first order differential equations with automatic step selection and reliable error control, integrated the ODEs for each trial value of  $x_f$ .

The differential equations and boundary conditions were reformulated in terms of arc length and integrated from  $x=x_f$  to  $s=0$  using a suggestion of C. W. Gear to avoid the singularities present at the boundaries and the instability due to a large, positive eigenvalue of the ODE system (6) at  $x=x_f$ . Changing the direction of integration caused the system to be initially stiff due to the large, negative eigenvalue present, but this causes no problem due to the small step sizes typically necessary to start the integration. Letting  $x = x(s)$ ;  $y = y(s) = f(x(s))$ , the problem actually computed was

$$\begin{aligned} \frac{d^2 x}{ds^2} &= -2 \frac{dy}{ds} (Ax^2 + B + Cy^2) - \frac{dy}{ds} \left( \frac{dx}{ds} \frac{1}{y(s)} \right) \\ \frac{d^2 y}{ds^2} &= 2 \frac{dx}{ds} (Ax^2 + B + Cy^2) + \frac{dx}{ds} \left( \frac{dx}{ds} \frac{1}{y(s)} \right) \end{aligned} \quad (8)$$

with boundary conditions at  $x_f = x(0)$ :

$$x(0) = x_f; \quad \left. \frac{dx}{ds} \right|_{s=0} = 0; \quad y(0) = 0; \quad \left. \frac{dy}{ds} \right|_{s=0} = 1 \quad (9)$$

and defining the total length of the arc,  $s_T$ , by the condition  $x(s_T) = 0$

$$x(s_T) = 0; \quad \left. \frac{dx}{ds} \right|_{x=s_T} = -1; \quad y(s_T) = \text{positive}; \quad \left. \frac{dy}{ds} \right|_{s=s_T} = 0. \quad (10)$$

The singularity still present at the starting point  $x_f$  due to the term  $\frac{dx}{ds} \frac{1}{y(s)}$  in (8) is avoided by using the approximation

$$\left. \left( \frac{dx}{ds} \frac{1}{y(s)} \right) \right|_{s=0} \approx - (Ax^2 + B + Cy^2) \Big|_{\substack{x=x_f \\ y=0}} = - (Ax_f^2 + B)$$

which comes from using the first two terms of a Taylor series for  $\frac{dx}{ds}$  and  $y(s)$  near  $s=0$  and the known properties of the problem.

The final BASIC program takes as input the values of the parameters A and B (using the relation that  $C = A/8$ ) and an interval  $(x_1, x_2)$  in which to search for the unknown  $x_f$ , the root of the function

$$G(x) \equiv \left. \frac{dy}{ds} \right|_{s=s_T}$$

obtained by integrating (8) backwards from the trial starting point  $x$  using initial conditions (9) until the function crosses the  $y$ -axis. The differential equations were integrated using a mixed relative and absolute error tolerance of  $10^{-6}$  and the root was found to a similar mixed tolerance of  $10^{-5}$ . These tolerances were easily met using the 14 digit BASIC now that the problem is formulated in a numerically stable manner. Once the missing value  $x_f$  was obtained, the initial value problem (8 and 9) was solved and the values  $(x, y)$  obtained at each step of the integration were plotted using a simple line-printer/plotter routine.

Table 1

C V=1	20	25	50	75	150
I	.12768	1.9094	.19978	.20477	.21300
A	4.8833	4.9297	4.9742	5.0022	5.0523
$\frac{dA}{dI}$	3.499	5.034	5.611	6.087	7.107
$I^2 \frac{dA}{dI}$	.1105	.1835	.2239	.2553	.3235
$I \frac{dA}{dI} + A$	5.505	5.891	6.065	6.249	6.566

Table 2

#	e	D	I	A	$\frac{dA}{dT}$	$I^2 \frac{dA}{dT}$	$I \frac{dA}{dT} + A$
1	1	0	.15401	4.8363	.26		
2	1.05	.125	.15554	4.8367	1.09		
3	1.07	.25	.15691	4.8382	1.98		
4	1.10	.5	.15934	4.8430	2.59		
5	1.14	.75	.16181	4.8494	3.22		
6	1.21	1.25	.16694	4.8659	4.14		
7	1.43	2.5	.18516	4.9413	4.52		
8	1.45	2.625	.18815	4.9548	4.55		
9	1.47	2.6375	.18848	4.9563	4.57		
10	1.48	2.6875	.18986	4.9626	4.46	.161	5.81
11	1.49	2.71875	.19078	4.9667	4.54	.165	5.83
12	1.50	2.75	.19175	4.9711	4.50	.166	5.83
13	1.55	3.05	.20779	5.0433	4.38	.189	5.95
14	1.92	3.0	.23741	5.1729	4.13	.233	6.15
15	2.02	2.875	.25021	5.2257	3.99	.250	6.22
16	2.15	2.6875	.26628	5.2898	3.87	.275	6.32
17	2.15	2.6375	.26770	5.2953	3.88	.278	6.33
Dumbell 18	2.18	2.625	.27139	5.3096	3.78	.278	6.34
19	2.26	2.5	2.8150	5.3478	3.62	.287	6.37
20	2.41	2.25	.30217	5.4227	3.42	.312	6.46
21	2.58	2.0	.32432	5.4984	3.20	.336	6.54
22	2.67	1.75	3.4908	5.5775	2.98	.363	6.62
23	2.95	1.5	.37758	5.6623	2.75	.392	6.70
24	3.21	1.25	.41136	5.7552	2.34	.396	6.72
25	3.98	.75	.50533	5.9755	1.98	.506	6.98
26	4.66	.5	.57291	6.1059	1.52	.500	6.98
27	6.30	.25	.65168	6.2258	1.02	.431	6.88
28	9.15	.125	.68487	6.2595			

ORIGINAL PAGE  
BLACK AND WHITE PHOTOGRAPH!!



Figure 1

Photographs supplied courtesy of Dr. Gertrude Hinsch, Department of Biology, University of South Florida and Dr. H. Fertig, Max Plank Institute für Kern Physik, Heidelberg, Germany.

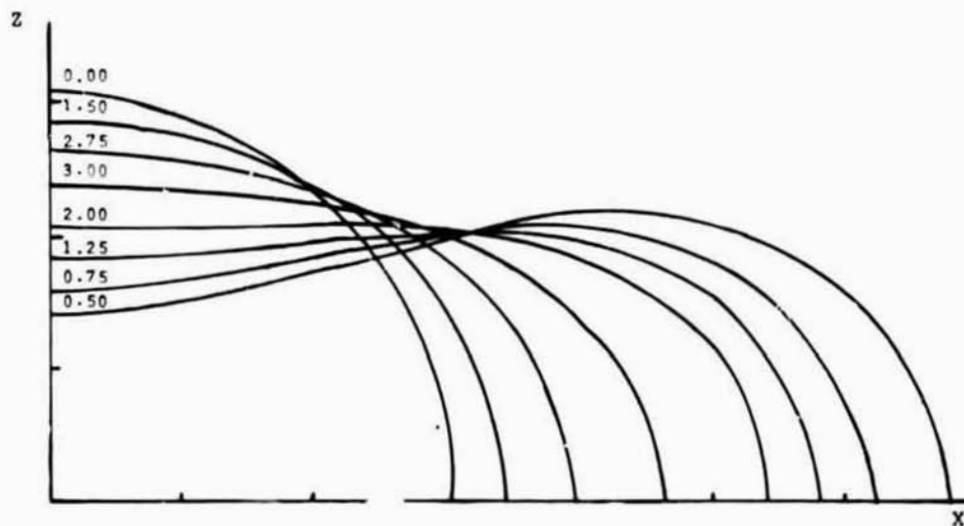


Figure 2

The numbers appearing on the graph are values of D.

#### Bibliography

1. Bastin, J. A., & W. J. French, The formation of lunar globules. Proc. Geo. Soc. Land No. 1664. 238 (1970).
2. Chandrasehkar, S., The stability of a rotating liquid drop. Proc. Roy. Soc. London, A, 1-26 (1965).
3. Fulchiganoni, Funicciello, Iaddeucci, & Trigila, Geochim Cosmochim Acta. 2, 937 (1971).
4. Stewart, K., Numerical computations on very small machines. California Software, 704 Solana Avenue, Albany, CA, 94706 (1979).

243  
N82 23466

Numerical methods and calculations for droplet flow, heating and ignition

H. A. Dwyer\*, B. R. Sanders  
D. Dandy†

Sandia National Laboratories  
Livermore, California 94550

Abstract

A new numerical method has been devised and employed to solve a variety of problems related to liquid droplet combustion. The basic transport equations of mass, momentum and energy have been formulated in terms of generalized nonorthogonal coordinates, which allows for adaptive gridding and arbitrary particle shape. In this paper example problems are solved for internal droplet heating, droplet ignition and high Reynolds number flow over a droplet.

Introduction

This paper presents initial results of a research effort whose end goals are the calculation of single and multiple liquid droplet combustion flows. The complete problem of even single droplet combustion presents a severe challenge for present day numerical methods because of the multiple space and time scales which can be introduced into the problem. These scales are the result of high Reynolds and Peclet numbers as well as flame formation around the droplet. In order to resolve all the physical phenomena that are contained in the problem, it is necessary to use the grid points in a numerical solution method very efficiently. A major new advance in the efficient location of grid points is the use of generalized nonorthogonal coordinates and adaptive grids.<sup>1,2,3</sup> It will be shown, and has been shown, that these methods greatly enhance the ability to calculate complex flows.

In the present paper major simplifications have been made in the flow equations to isolate physical phenomena and test the efficiency of the numerical methods employed. The most limiting simplification will be that of constant overall density, however as will be shown, the numerical significance of the results are not damaged by the assumptions made.

Basic transport equations

The equations for momentum, energy, and mass transport will now be written in terms of generalized coordinates, and the numerical methods employed discussed. The starting point is the equations in terms of axially-symmetric cylindrical coordinates, and the equations for stream function ( $\psi$ ), vorticity ( $\omega$ ), temperature ( $T$ ) and reactant species density ( $\rho_a$ ), which are the following:

$$\frac{\partial}{\partial z} \left( \frac{1}{r} \frac{\partial \psi}{\partial z} \right) + \frac{\partial}{\partial r} \left( \frac{1}{r} \frac{\partial \psi}{\partial r} \right) = \omega \quad (1)$$

$$\frac{\partial}{\partial t} (\rho r \omega) + \frac{\partial}{\partial r} (\rho r v \omega) + \frac{\partial}{\partial z} (\rho r w \omega) - \rho v \omega = \frac{\partial}{\partial r} \left( r \frac{\partial}{\partial r} (\mu \omega) \right) + \frac{\partial}{\partial z} \left( r \frac{\partial}{\partial z} (\mu \omega) \right) - \frac{\mu \omega}{r} \quad (2)$$

$$\text{where } u = - \frac{1}{r} \frac{\partial \psi}{\partial r} \text{ and } v = \frac{1}{r} \frac{\partial \psi}{\partial z} \quad (3)$$

$$\frac{\partial}{\partial t} (\rho r C_p T) + \frac{\partial}{\partial r} (\rho r C_p v T) + \frac{\partial}{\partial z} (\rho r C_p w T) = \frac{\partial}{\partial r} \left( r k \frac{\partial T}{\partial r} \right) + \frac{\partial}{\partial z} \left( r k \frac{\partial T}{\partial z} \right) + r \rho_a \Delta h_a K_a e^{-E_a/RT} \quad (4)$$

$$\frac{\partial}{\partial t} (r \rho_a) + \frac{\partial}{\partial r} (r v \rho_a) + \frac{\partial}{\partial z} (r w \rho_a) = \frac{\partial}{\partial r} \left( r D_a \frac{\partial \rho_a}{\partial r} \right) + \frac{\partial}{\partial z} \left( r D_a \frac{\partial \rho_a}{\partial z} \right) - r \rho_a K_a e^{-E_a/RT} \quad (5)$$

\*Professor, Department of Mechanical Engineering, University of California Davis.

†Current address, Department of Chemical Engineering, California Institute of Technology, Pasadena, California 91103.

Research supported by U.S. Department of Energy, Office of Basic Energy Sciences, Division of Engineering, Mathematical and Geosciences.

where the following notation has been used for physical constants:  $K_a$ -pre-exponential reaction constant;  $E_a$ -activation energy;  $R$ -gas constant;  $k$ -thermal conductivity,  $\rho$ -overall density; and  $\Delta h_a$ -chemical heat release. Also, the independent variables  $t$ ,  $r$  and  $z$  are the time, radial coordinate and axial position, respectively. (A more detailed explanation of the chemical reaction terms will be given later in the paper.)

A major difficulty with the above formulation is that the surface of the droplet does not lie naturally on a constant value of the independent variables  $r$  and  $z$ . However, this difficulty can be removed immediately by transforming to generalized nonorthogonal coordinates  $\xi$ ,  $\eta$ , and thereby making the droplet surface correspond to  $\eta=0$ . In order to simplify notation it will first be useful to rewrite equations (1) through (5) in a vector form

$$\frac{\partial \hat{Q}}{\partial t} + \frac{\partial \hat{E}}{\partial r} + \frac{\partial \hat{F}}{\partial z} = \frac{\partial \hat{R}}{\partial r} + \frac{\partial \hat{S}}{\partial z} + \hat{H} \quad (6)$$

where

$$\hat{Q} = \begin{pmatrix} 0 \\ \rho r w \\ \rho r C_p T \\ r \rho_a \end{pmatrix} \quad \hat{E} = \begin{pmatrix} 0 \\ \rho r v w \\ \rho r v C_p T \\ r v \rho_a \end{pmatrix} \quad \hat{F} = \begin{pmatrix} 0 \\ \rho r u w \\ \rho r u C_p T \\ r u \rho_a \end{pmatrix}$$

$$\hat{R} = \begin{pmatrix} \frac{1}{r} \frac{\partial \psi}{\partial r} \\ r \frac{\partial}{\partial r} [\mu \omega] \\ r k \frac{\partial T}{\partial r} \\ r D_a \frac{\partial \rho_a}{\partial r} \end{pmatrix} \quad \hat{S} = \begin{pmatrix} \frac{1}{r} \frac{\partial \psi}{\partial z} \\ r \frac{\partial}{\partial z} [\mu \omega] \\ r k \frac{\partial T}{\partial z} \\ r D_a \frac{\partial \rho_a}{\partial z} \end{pmatrix} \quad \hat{H} = \begin{pmatrix} -\omega \\ -\frac{\mu \omega}{r} + \rho v w \\ r \rho_a \Delta h_a K_a e^{-E_a/RT} \\ -r \rho_a K_a e^{-E_a/RT} \end{pmatrix}$$

Transforming to the variables  $r$ ,  $\xi$  and  $\eta$  equation (6) becomes

$$\frac{\partial \hat{Q}}{\partial t} + \frac{\partial \hat{F}}{\partial \xi} + \frac{\partial \hat{F}}{\partial \eta} = \frac{\partial \hat{R}}{\partial \xi} + \frac{\partial \hat{S}}{\partial \eta} + \hat{H} \quad (7)$$

where the following new vectors have been defined

$$\hat{Q} = \frac{\hat{Q}}{J}$$

$$\hat{E} = \frac{1}{J} (\hat{Q}_\xi + \hat{E}_r + \hat{F}_z)$$

$$\hat{F} = \frac{1}{J} (\hat{Q}_\eta + \hat{E}_r + \hat{F}_z)$$

$$\hat{R} = \frac{1}{J} (\hat{R}_r + \hat{S}_z)$$

$$\hat{S} = \frac{1}{J} (\hat{R}_r + \hat{S}_z)$$

$$\hat{H} = \frac{\hat{H}}{J}$$

and the transformation metrics, or areas and volumes, are given by

$$J = \frac{1}{z_{\xi} r_{\eta} - z_{\eta} z_{\xi}}$$

$$\xi_z = Jr_{\eta} \quad \xi_r = -Jz_{\eta} \quad \xi_t = -z_{\xi}\xi_z - r_{\xi}\xi_r$$

$$\eta_z = -Jr_{\xi} \quad \eta_r = Jz_{\xi} \quad \eta_t = -z_{\eta}\eta_z - r_{\eta}\eta_r$$

It can easily be seen that the resulting equations are more complex, however the digital computer is extremely well equipped to handle this type of algebraic complexity, and with some additional programming a much more valuable research tool is obtained. The equations as they are written in (7) will easily handle arbitrary-shaped particles as well as particles whose shape is changing as a function of time. However, the major advantage of the above formulation is that it allows the use of adaptive grid procedures to be employed, and this feature will be shown to be one of the single most important advances in the efficient use of numerical methods to solve complex physical problems.

An interesting feature of these equations is that they allow for the use of variable transport properties  $\mu$ ,  $k$  and  $D_a$ , although the overall density must be constant. To the authors' knowledge this is the first time that a variable transport property formulation of the stream function-vorticity equations has been given. This formulation will be a complete description of the mass and energy transport processes inside the droplet, where constant overall density is assumed.

#### Numerical methods

The original plan for the numerical solution method was to employ a fully implicit iterative scheme to solve the set of transport equations given previously. In order to solve these equations an alternating-direction-implicit (ADI) scheme was employed together with a Newton procedure to linearize the equations where necessary. The resulting equations are block tridiagonal, and the efficient solver of Hindmarsh<sup>5</sup> was used to obtain the solution. This procedure proved to be unstable because of the large sensitivity that the stream function has to all errors. The coupling of the vorticity and stream function equations, plus generalized coordinates, and block solutions along a line, causes the truncation error to give very inaccurate values of stream function near the boundary. A major part of the problem is due to the fact that the stream function can change by four or five orders of magnitude from the body surface to the free stream. The values of the stream function near the surface are very small and truncation error in the outer part of the flow overwhelms the small stream function values near the surface. The solution to the problem is point relaxation of the stream function equation on a previously calculated vorticity distribution, followed by iteration between the stream function and vorticity equations. This point relaxation method does not couple all the truncation errors together, and very good results were obtained.

The numerical method that was finally employed had the following features:

- I. Stream function-vorticity equations
  - a. First-order backward, implicit time differences for time derivatives.
  - b. Second-order central differences in space.
  - c. ADI solution of the vorticity equation.
  - d. Point relaxation of the stream function equation.
  - e. Global iteration on both equations.
- II. Energy and species equations
  - a. The same space and time differencing as the vorticity equation.
  - b. Newton linearization of the nonlinear terms.
  - c. Block tridiagonal solution with an ADI marching technique.

The above numerical method is somewhat ad hoc in that it uses two difference methods within itself to determine a solution, however the individual methods reflect the numerical nature of the equations being solved. The block tridiagonal solution of the energy and species equation is excellent for chemical reactions, while the point iteration method allows the stream function to converge accurately and smoothly on the vorticity distribution.

#### Criterion for grid placement

The basic criterion for grid placement that was employed in the present paper will now be presented. The computational space,  $\xi$  and  $\eta$ , has been normalized so that their numerical values go between zero and one, and the grid points are fixed in time. In the physical

space the grid points will be placed and moved in time to achieve the resolution of high gradient regions. Along a given arc in the physical space the grid points will be distributed in proportion to the gradient of the dependent variable. If the distance along a given arc in physical space is denoted by  $S$ , a mathematical statement of the relationship between the computational and physical space is

$$d\xi = \left| \frac{\partial T}{\partial S} \right| ds$$

where  $S$  is the distance measured on the  $n = \text{constant}$  arc, and  $T$  the dependent variable of the transport equation being solved, in this paper the dependent variable is temperature. In order to normalize, allow for "optimization," and remove singularities, the above equation is cast into the following form

$$\xi(x, y, t) = \frac{\left[ \int_0^S (1 + b \left| \frac{\partial T}{\partial S} \right|) ds \right]}{\left[ \int_0^{S_{\max}} (1 + b \left| \frac{\partial T}{\partial S} \right|) ds \right]}$$

where  $b$  is an adjustable constant used for "optimization" of the grid distribution.

The above equation has some interesting features which will now be discussed briefly. For the case  $b = 0$  a uniform distribution of points on the nonorthogonal arc is obtained, while for large  $b$ , constant values of the variable  $T$ , or isotherms, are selected. The coordinate location equation is solved in an explicit sense at the old time step, and the details can be found in the paper by Dwyer et al.<sup>2</sup> Also, it should be mentioned that the accuracy in solving the equation does not influence directly the accuracy of the finite difference solution. With the use of these generalized coordinates and an adaptive grid technique a powerful new method is available for numerical solution.

In the present paper the adaptive gridding procedure has only been employed in the calculation of the temperature and species concentrations, and has not been used for the stream function-vorticity part of the method. The stream function and vorticity have been calculated from a predetermined grid, however the use of adaptive gridding for the fluid dynamics is being implemented at the present time.

### Results

The results which will be presented illustrate mainly the capability of the calculation method, and do not give a complete description of droplet combustion. The problems which have been solved are the following:

1. Ignition and flame propagation about hot particles.
2. Separated flow around liquid droplets.

A description of each of these results will now be given.

The first problem solved was to calculate the ignition and flame propagation about a spherical particle. The reaction mechanism is very simple and consisted of a premixed fuel A reacting and going over to species B. The nondimensional form of the energy and species equations are

$$\frac{\hat{D}T}{Dt} = \frac{1}{Pe} \frac{1}{\partial x_i} \left( \frac{\partial \hat{T}}{\partial x_i} \right) + \hat{\rho}_a N_{DA} e^{-\theta_a/\hat{T}}$$

$$\frac{\hat{D}\rho_a}{Dt} = \frac{1}{Pe} \frac{\partial}{\partial x_i} \left( \frac{\partial \hat{\rho}_a}{\partial x_i} \right) - \hat{\rho}_a N_{DA} e^{-\theta_a/\hat{T}}$$

where  $Pe = \frac{U_m d}{\alpha}$  Peclet Number, based on maximum velocity  $U_m$  inside the droplet

$N_{DA}$  = Dimensionless Pre-Exponential Reaction Coefficient.

$\theta_a$  = Activation Temperature,  $E_a/R$ .

and it has been assumed that all transport coefficients are constant, and that the thermal diffusivity and species diffusivity are equal.

For this ignition model problem the velocity field was assumed to be that given by Stokes flow, and the overall density was assumed constant. The value for the Peclet number was chosen to be 200 and  $\theta_a=4$  for an initial temperature of premixed reactant of  $\hat{T}=1.2$ . The spherical particle surface will be raised impulsively to  $\hat{T}=1.0$  and the adiabatic flame temperature in terms of dimensionless temperature is  $\hat{T}_{AD} = 1.2$ .

The values for the pre-exponential coefficient were chosen to be characteristic of hydrocarbon fuels, thus the basic time scales of the processes are similar to a moderate Reynolds number particle in a premixed hydrocarbon gas (however, the simulation is highly simplified as can be easily seen). The first results for the numerical simulation are shown in Figures (1) through (4) for  $N_{DA} = 2.2 \cdot 10^3$ , which corresponds to a rather thin flame compared to particle diameter. Figures (1) and (2) show the coordinate system (top) and isotherm distribution for a uniform grid simulation. A careful study of the isotherm distribution shows oscillations in the flame, and this is due to the high cell Peclet numbers.

The oscillations are more severe as the flame moves away from the body, because of the natural increase in grid cell size occurring in spherical coordinates. As the flame approaches the computational boundary there is only one point to describe the flame structure. This lack of resolution results in temperature and species oscillations in the calculation, incorrect flame speed and eventually termination of the calculation due to negative values of temperature and species.

A second more accurate calculation with the same number of grid points, but with the adaptive grid strategy employed is shown in Figures (3) and (4). The most dramatic feature of the calculation is the bunching of the grid points inside the flame structure. This removes all the numerical oscillations, and the overall flame speed agrees well with the results of Otey and Dwyer.<sup>10</sup> The results of this calculation thus show dramatically the usefulness and capabilities of the adaptive grid procedure for combustion problems.

A second calculation with a reduced reaction rate ( $N_{DA} = 2.2 \cdot 10^3$ ) is shown in Figures (5) through (8). In this case the flame is much thicker and the coordinate adaption is only very slight. However, the ignition and flame propagation processes are much more interesting. Figure (5) exhibits the isotherm distribution at an early time with a maximum temperature of  $\hat{T} = 1.0$  occurring at the particle surface. As time increases an ignition process occurs at the rear stagnation point (Figure (6)) and then a steady state reaction zone is set up on the leeward side of the particle (Figures (7)-(8)). It is easily seen from the isotherm distribution that the surface location where the gas temperature rises above the wall temperature quickly stabilizes on the leeward side of the particle surface. These results show that the present calculation methods will resolve ignition phenomena in particle dynamics.

The final results to be presented are a demonstration of the ability of the numerical methods to calculate the fluid flow around and inside droplets. Shown in Figures (9) through (11) are the distribution of stream function and vorticity for a solid particle in a flow with a Reynolds number of 100, based on particle diameter. Figure (9) exhibits the distribution of stream function outside the particle, while Figure (10) shows the stream function inside the separation bubble (the top figure is the coordinate distributions). A more dramatic representation of high Reynolds number influences can be seen in Figure (11) where the normalized vorticity contours are given. The bunching of the contours on the windward side of the particle is clear evidence of the start of boundary layer formation and separation.

All of the above results agree well with the calculations of Le Clair.<sup>7</sup> Figure (12) exhibits the streamline pattern inside of a liquid droplet at an external flow Reynolds number of 200. For this calculation the ratios of liquid droplet to gas viscosity and density are respectively

$$\frac{\mu_d}{\mu_g} = 50 \quad \frac{\rho_d}{\rho_g} = 1000$$

which are typical values of interest to combustion problems. Therefore, it seems that the methods we are employing are quite encouraging, and give strong promise of giving new results for the complete problem of droplet combustion.

#### Conclusions

A raw collection of numerical techniques has been assembled to solve problems of heat, mass and momentum transport in droplet combustion systems. The major new features of this collection of methods are the following:

1. Generalized Nonorthogonal Coordinates
2. Adaptive Gridding on Temperature Gradients
3. Block Tridiagonal Solution of Energy and Species Equations
4. Point Iteration of the Stream Function on the Vorticity Distribution

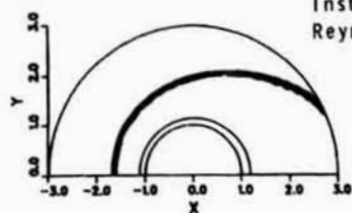
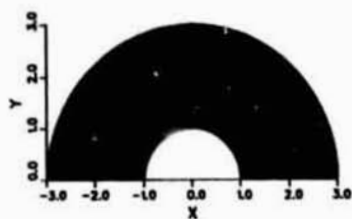
All of the above methods have shown themselves stable and capable of giving improved results for the fluid flow, heat transfer, and mass transfer problems solved.

The physical problems solved in the paper were moderate Reynolds number flow over both solid and liquid droplets, as well as a study of ignition around a hot solid particle in a Stokes flow. The fluid flow studies reproduced the results of other investigators, and thus verified the accuracy of the methods employed. The study of ignition about a hot particle showed clearly that ignition can be delayed until the leeward side of the particle, and a flame can be stabilized in the wake of the particle. These results seem to be new, and the future inclusion of variable density will allow for a complete description of particle ignition. Also, it should be mentioned again that the high-reaction-rate ignition studies would not be possible without adaptive gridding, because of its efficient use of grid points.

#### References

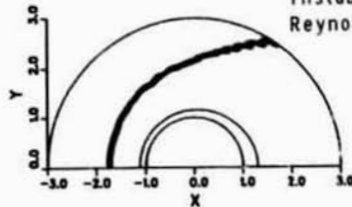
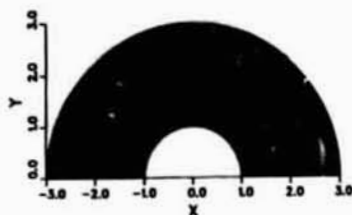
1. Dwyer, H. A., Kee, R. J., Barr, P. K., and Sanders, B. R. "Transient Droplet Heating at High Peclet Number," A.S.M.E. Winter Annual Meeting, Symposium on Computers and Fluids, November 1981.
2. Dwyer, H. A., Kee, R. J., and Sanders, B. R., "Adaptive Grid Method for Problems in Fluid Mechanics and Heat Transfer," *AIAA J.*, Vol. 18, No. 10, October 1980, p. 1205.
3. Steger, J. L., "Implicit Finite-Difference Simulation of Flow About Arbitrary Two-Dimensional Geometries." *AIAA Journal*, Vol. 16, July 1978, pp. 679-686.
4. Roache, P., *Computational Fluid Dynamics*, Hermosa Publishers, Albuquerque, New Mexico, 1971
5. Hindmarsh, A. C., "Solution of Block-Tridiagonal Systems of Linear Algebraic Equations," Report UCID-30150, Lawrence Livermore Laboratory, February 1977.
6. Otey, G. and Dwyer, H. A., "A Numerical Study of the Interaction of Fast Chemistry and Diffusion," *AIAA J.*, Vol. 17, June 1979, pp. 606-613.
7. Le Clair, B. P., Hamielec, A. E., Pruppacher, H. R. and Hall, W. D., "A Theoretical and Experimental Study of the Internal Circulation in Water Drops Falling at Terminal Velocity in Air," *Journal of Atmospheric Sciences*, V. 29, pp. 728-740.

ORIGINAL PAGE  
BLACK AND WHITE PHOTOGRAPH



Instability Due to Large Cell Reynolds Number

Fig. 1. Flame propagation with a uniform grid,  $N_{DA} = 2.2 \cdot 10^5$ .



Instability Due to Large Cell Reynolds Number

Fig. 2. Flame propagation with a uniform grid,  $N_{DA} = 2.2 \cdot 10^5$ .

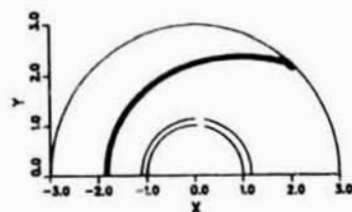
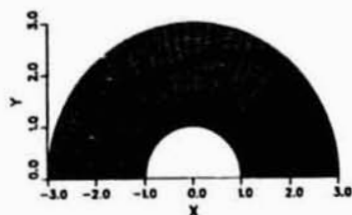


Fig. 3. Flame propagation with an adaptive grid,  $N_{DA} = 2.2 \cdot 10^5$ .

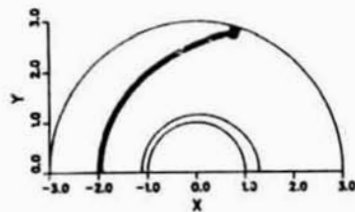
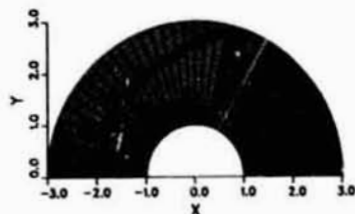


Fig. 4. Flame propagation with an adaptive grid,  $N_{DA} = 2.2 \cdot 10^5$ .

$$\tau = \frac{\alpha t}{R^2} = 0.04$$

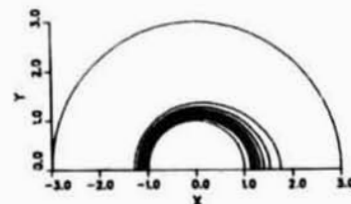
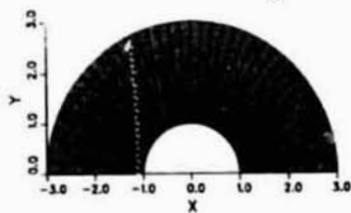


Fig. 5. Preignition isotherm distribution.

$$\tau = \frac{\alpha t}{R^2} = 0.06$$

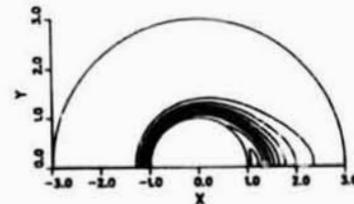
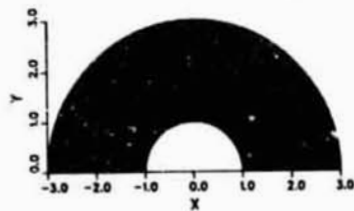


Fig. 6. Ignition isotherm distribution.

$$\tau = \frac{aI}{R^2} = 0.08$$

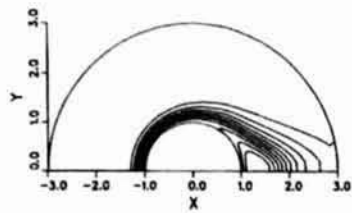
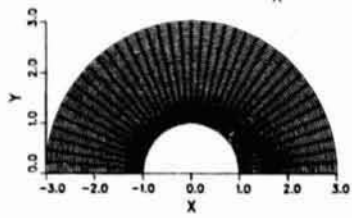


Fig. 7. Postignition isotherm distribution.

$$\tau = \frac{aI}{R^2} = 0.1$$

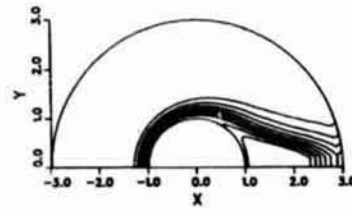
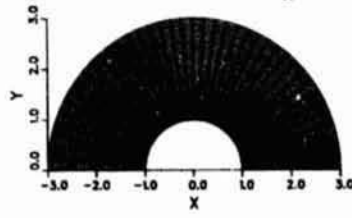


Fig. 8. Postignition isotherm distribution.

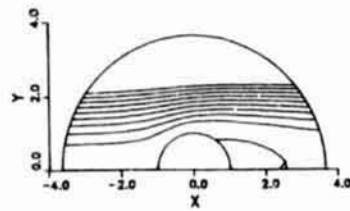
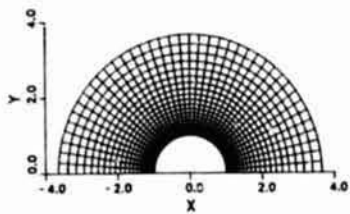


Fig. 9. External streamlines; solid particle,  $Re = 50$ .

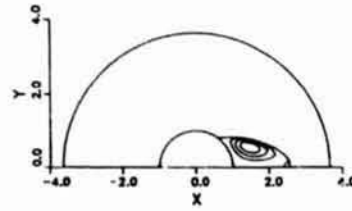
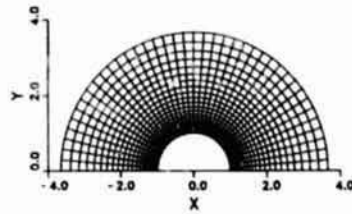


Fig. 10. Separation bubble streamlines; solid particle,  $Re = 50$ .

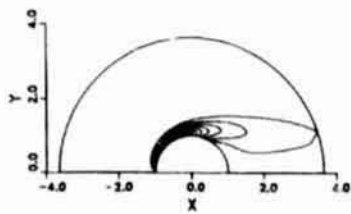
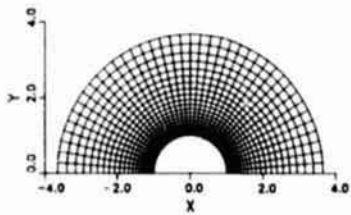
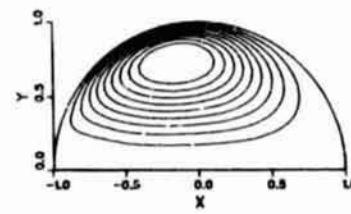
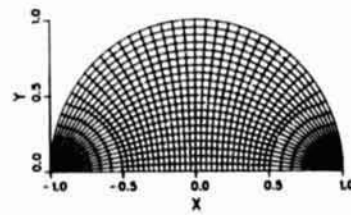


Fig. 11. Vorticity distribution; solid particle,  $Re = 50$ .



$$P_Q/P_a = 1000$$

$$\mu_Q/\mu_a = 50$$

Fig. 12. Streamline distribution; liquid droplet,  $Re = 100$ .

Effects of rotation and magnetic field on the onset of convective instability  
in a liquid layer due to buoyancy and surface tension

Gabb'ita Sundara Rama Sarma

Institut für Theoretische Strömungsmechanik,  
Deutsche Forschungs- und Versuchsanstalt für Luft- und Raumfahrt  
Bunsenstrasse 10, D-3400 Göttingen, Federal Republic of Germany

Abstract

Thermocapillary stability characteristics of a horizontal liquid layer heated from below rotating about a vertical axis and subjected to a uniform vertical magnetic field are analyzed under a variety of thermal and electromagnetic boundary conditions. Results based on analytical solutions to the pertinent eigenvalue problems are discussed in the light of earlier work on special cases of the more general problem considered here to show in particular the effects of the heat transfer, nonzero curvature and gravity waves at the two-fluid interface. Although the expected stabilizing action of the Coriolis and Lorentz force fields in this configuration are in evidence the optimal choice of an appropriate range for the relevant parameters is shown to be critically dependent on the interfacial effects mentioned above.

Introduction

In recent years there has been a resurgence of interest in understanding the origins and possible means of controlling convective instability, especially in configurations relevant to material sciences in general and material processing in particular within the framework of the current space programs. In this context some of the basic aspects of this problem area have been under investigation<sup>1-4</sup> by the present author. The contribution to be presented here is part of a continuing effort at the DFVLR to analyze some of the basic fluid dynamic aspects relevant to the material science configurations, especially in the context of space experiments under reduced gravity conditions and the related ground based research.

Since references<sup>1-4</sup> give the general background and motivation for the particular problem considered here and cite the relevant literature, we shall restrict ourselves here only to a report of some of the recent results obtained and discuss them in the light of those available in the literature. While references 1-4 deal exclusively with the zero gravity situation, we consider here specifically the simultaneous action of surface tension and gravity in this classical Bénard - Marangoni configuration.

Formulation of the problem

We consider an infinite, horizontal, Boussinesq liquid layer of mean thickness  $d$  rotating about a vertical axis at a constant angular speed  $\Omega$  and subjected to a uniform magnetic induction field of strength  $B_0$  under various typical boundary conditions to be detailed later. Figure 1 illustrates the configuration schematically and is followed by a list of the symbols for dimensional quantities occurring in the later development. The details of the formulation incorporate the features introduced by Scriven and Sternling<sup>5</sup> and Smith<sup>6</sup> extending the pioneering work of Pearson<sup>7</sup>.

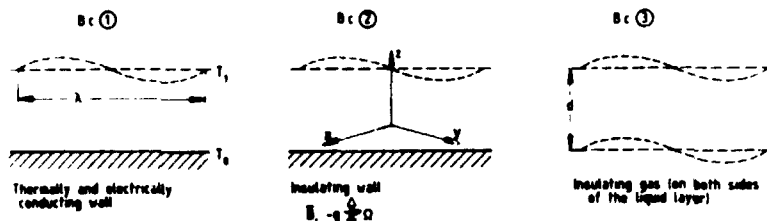


Figure 1. The Bénard - Marangoni configuration

List of symbols

$\beta$ = Coefficient of thermal volume expansion, $-\frac{1}{\rho} \frac{\partial \rho}{\partial T}$	$\vec{B}$ = Magnetic induction field
$\gamma$ = Electrical conductivity	$B_0$ = Magnitude of the applied $\vec{B}$ -field
$\Delta T$ = Applied temperature difference ( $T_0 - T_1$ )	$K$ = Thermal conductivity
$\zeta_0$ = Amplitude of the disturbance wave at the two-fluid interface	$T$ = Temperature
$\eta_m$ = Magnetic diffusivity $(\gamma \mu_m)^{-1}$	$c_0$ = specific heat
$\kappa$ = Thermal diffusivity, $K/\rho c_0$	$d$ = Mean thickness of the liquid layer
$\lambda$ = Disturbance wavelength, $2\pi/\sqrt{k_x^2 + k_y^2}$	$g$ = Acceleration due to gravity
$\mu$ = Dynamic viscosity	$h$ = heat transfer coefficient at the disturbed interface
$\mu_m$ = Magnetic permeability	$k_x, k_y$ = Disturbance wave numbers in the x-y-directions
$\nu$ = Kinematic viscosity	$p$ = Time constant in the exponential growth/decay factor of a disturbance normal mode
$\rho$ = Density	
$\sigma$ = Interfacial energy at the two-fluid interface	
$\Omega$ = Angular speed of rotation	

The liquid layer has nominally constant temperatures  $T_0, T_1$  ( $T_0 > T_1$ ) respectively at its lower and upper horizontal boundaries. For the sake of definiteness and simplicity the characteristics of the adjoining media are somewhat idealized. They are specified for the three cases ①, ②, ③ of the boundary conditions (b.c.) as follows.

In b.c. ① we take the bottom boundary as a thermally and electrically perfect solid conductor. In b.c. ② the bottom boundary is a thermally and electrically perfect insulator. In both cases the upper adjoining medium is taken as an electrically insulating gas extending in the z-direction to infinity. The heat transfer to the gas from the liquid layer can be simplified (without going into the details of the possible flow in the upper medium) in terms of an effective heat transfer coefficient  $h(T)^{5,7}$  for the two-fluid interface. A detailed discussion of this simplification was given by Pearson<sup>7</sup>. In b.c. ③ we consider the situation where the same ambient gas is present on both sides of the liquid layer.

The onset of convective instability in such a liquid layer with an initially uniform linear temperature profile can be formulated as a linear eigenvalue problem for the disturbance amplitudes of the flow variables using the standard normal modes procedure<sup>8</sup>. We non-dimensionalize the problem using  $d, d^2/\nu, \kappa/d, \kappa/d^2, 4\pi\gamma\kappa B_0/d, \Delta T$  respectively as the reference quantities for length, time, velocity, vorticity, electric current density and temperature. The stability of the configuration with respect to an infinitesimal normal mode of disturbance may then be stated in terms of the following eigenvalue problems in dimensionless form.

$$(D^2 - a^2)(D^2 - a^2 - p_2)(D^2 - a^2 - p_1)W - Ta(D^2 - a^2 - p_2)DZ - Q(D^2 - a^2)D^2W = Ra \cdot a^2(D^2 - a^2 - p_2)\theta \quad (1)$$

$$(D^2 - a^2 - p_3)\theta + W = 0 \quad (2)$$

$$(D^2 - a^2 - p_1)Z + Ta \cdot DW + QDX = 0 \quad (3)$$

$$(D^2 - a^2 - p_2)X + DZ = 0 \quad (4)$$

where  $D \equiv (1/d) \cdot d/dz$  and  $W, Z, X, \theta$  are respectively the dimensionless disturbance amplitudes of the z-components of velocity, vorticity and electric current density and of temperature.

The boundary conditions are to distinguish not only between cases ①, ②, ③ specified earlier but also as to whether the neutrally stable oscillatory ( $p_1 \neq 0$ ) or stationary ( $p_1 = 0$ ) modes are considered while determining the stability boundary for the configuration.

(a) Neutral modes oscillatory ( $p_1 \neq 0$ )

$$\text{B.c. ①} \quad W(0) = 0 = DW(0) = \theta(0) = Z(0) = DX(0) \quad (5)$$

$$\text{B.c. ②} \quad W(0) = 0 = DW(0) = D\theta(0) = Z(0) = X(0) \quad (6)$$

$$\text{B.c. ③} \quad W(0) = p_3 \frac{\zeta_0}{d} \quad (\text{Kinematic condition at the two-fluid interface}) \quad (7)$$

For  $Nu = \frac{hd}{K\Delta T} > 0$

$$\frac{Cr}{(Bo + a^2)} \{ (D^2 - p_1 - 3a^2)DW(0) \} - \left\{ \frac{D\theta(0)}{Nu} + \theta(0) \right\} = 0 \quad (8)$$

$$(D^2 + a^2)W(0) - \frac{a^2 \cdot Ma D\theta(0)}{Nu} = 0 \quad (9)$$

For  $Nu = 0$

$$D\theta(0) = 0 \quad (10)$$

$$\frac{p_3 Cr}{a^2 (Bo + a^2)} \{ (D^2 - 3a^2 - p_1) DW(0) \} - W(0) = 0 \quad (11)$$

$$p_3 (D^2 + a^2)W(0) + Ma \cdot a^2 \{ p_3 \theta(0) - W(0) \} = 0 \quad (12)$$

B.c. at  $z = d$  for cases ①, ②, ③ are of the same form as those for case ③ at  $z = 0$ .

(b) Neutral modes stationary ( $p_1 = 0$ )

The conditions (11), (12) above are to be replaced by

$$W(0) = 0 \quad (\text{which covers also (7) above}) \quad (13)$$

$$D^2 W(0) + a^2 \cdot Ma \theta(0) + \frac{Ma \cdot Cr}{(Bo + a^2)} \{ -D^3 W(0) + 3a^2 DW(0) \} = 0 \quad (14)$$

Again the b.c. at  $z = d$  are of the same form for cases ①, ②, ③ as those for case ③ at  $z = 0$ .

The dimensionless numbers occurring in the above formulation are  $Bo = \rho g d^2 / \sigma$  (Bond),  $Cr = \kappa \mu / \sigma d$  (crispation),  $Ma = |(\partial \sigma / \partial T) \Delta T| / \mu \kappa$  (Marangoni),  $Nu = dh / \kappa \Delta T$  (Nusselt),  $Pr = \nu / \kappa$  (Prandtl),  $Pr_m = \nu / \eta_m$  (magnetic Prandtl),  $Q = B_0^2 d^2 \gamma / \mu$  (Chandrasekhar),  $Ra = g \beta \Delta T d^3 / \nu \kappa$  (Rayleigh),  $Ta = 2 \Omega d^2 / \nu$  (Taylor),  $a = 2 \pi d / \lambda$  (disturbance wave number),  $p_1 = \rho d^2 / \nu$  (frequency factor for oscillatory disturbance mode),  $p_2 = Pr_m \cdot p_1$ ,  $p_3 = Pr \cdot p_1$ . The last four parameters are characteristics of a disturbance normal mode in the hydromagnetic thermocapillary stability discussion of the configuration whereas the first nine describe the basic configuration.

Briefly<sup>5,6</sup> the boundary conditions (5), (6) state the no-slip condition and the thermal and electromagnetic properties associated with the boundaries whereas (8), (9) cover the requirements<sup>5,6</sup> of stress balance along and normal to the two-fluid interface incorporating the thermocapillary terms and also taking into account the nonzero interfacial curvature ( $Cr$ ), gravity waves ( $Bo$ ) and heat transfer contribution at the disturbed interface ( $Nu$ ).

The existence of oscillatory modes in this configuration especially at large  $Ta$  is well-known for the buoyancy-driven case<sup>8</sup> and was also demonstrated in the surface tension-driven case. The oscillatory modes become important at low  $Pr$  but it was found<sup>1</sup> that at least for  $Bo = 0$  the incipient instability is stationary rather than oscillatory since the corresponding critical Marangoni number is higher than that for the stationary mode which is independent of  $Pr$ . It turns out that for small  $Bo \neq 0$  the critical  $Ma_c$  tends to decrease and  $a_c \rightarrow 0$  with large  $Ta$  whereas the oscillatory modes were shown by asymptotic analysis<sup>1</sup> to occur at large  $Ma_c \sim Ta \gg 1$ , as a short wave instability with  $a \sim \sqrt{Ta}$ . Thus we have some plausible evidence to suppose that in this configuration, where the effects of the magnetic field ( $Q \neq 0$ ) which inhibits the onset of buoyancy-driven oscillatory modes (for  $Pr > Pr_m$ )<sup>8</sup> are also included, the stationary modes precede the oscillatory ones at onset of instability.

Since the practical interest in the present investigation lies ultimately in the suppression of convective instability<sup>1-4</sup>, consider here the case  $p_1 = 0$  in the following. If, however, the solution of the complete eigenvalue problem with  $p_1 \neq 0$  posed above does lead to oscillatory modes we have then only to compare the corresponding minimum critical Marangoni number with  $Ma_c$  computed here.  $Ma_c$  is in any case an upper bound for stability of the configuration.

The stationary modes of convective instability are given by nontrivial solutions to the homogeneous boundary value problems given by (1) - (10), (13), (14) for the different cases ①, ②, ③. The secular conditions for the existence of nontrivial solutions to the respective homogeneous boundary value problems have been obtained by using the exact analytical solutions (combinations of trigonometric and hyperbolic functions) of (1) - (4) in the appropriate boundary conditions. The neutral stability characteristics of the configuration are then analyzed from the resulting transcendental secular relationship in terms of the dimensionless parameters of the problem. Since we have a large number of dimensionless groups here, we shall have to choose a suitable range of their values with some class of applications in view. As indicated in references<sup>1-4</sup> the interface curvature effects are already in evidence for such small values of  $Cr = 10^{-3}, 10^{-4}$  yielding stability characteristics quite different from those for  $Cr = 0$ . Using the thermophysical property data available in the literature<sup>9-11</sup> the parameter ratio  $Bo/Cr = g d^3 / \nu \kappa$  at  $g = 9.81 \text{ m/s}^2$  with  $d = \text{mm}$  has values of  $O(10^7)$  as

shown in Table 1 for some substances of interest

**Table 1. Typical values for Bo/Cr**

Silicone oil (Dow-Corning 200)	Cu-melt	Al-Cu-melt	GaAs-melt	Si-melt
$4.5 \times 10^2$	$6.07 \times 10^2$	$5.1 \times 10^2$	$7.1 \times 10^2$	$1.82 \times 10^3$

The corresponding values for different levels of gravity and the appropriate size of the layer for experiments in space missions can be estimated from Table 1. We can also use them for estimating parameters such as Ra and Bo say by choosing  $Cr = 10^{-3}, 10^{-4}$  to demonstrate the effects of nonzero interfacial curvature. It is found that  $Cr = 10^{-3}, 10^{-4}$  for Silicone oil (Dow-Corning 200)<sup>10</sup>, used frequently for convection experiments, when  $d = \text{mm, cm}$  respectively. Thus for experiments in a terrestrial laboratory in the mm size and in an orbital laboratory in the cm range can be covered by considering  $Bo = 0.05, 0.5$  and  $Cr = 10^{-3}, 10^{-4}$  to emphasize the effects of interfacial waves. Table 2 gives some representative values for Q and Ta.

**Table 2. Values of Q at  $B_0 = 0.5$  tesla and Ta at  $\Omega = 500$  rpm for  $d = \text{mm}$**

	Silicone oil DC 200	Al-melt	GaAs- melt	Si-melt	Cu-melt
Q	—	$9.02 \times 10^2$	$5.57 \times 10^2$	$1.14 \times 10^2$	$8.43 \times 10^2$
Ta	0.524	$1.95 \times 10^2$	$3.37 \times 10^2$	$2.98 \times 10^2$	$2.48 \times 10^2$

### Results and discussion

The eigenvalue relationships giving the stability characteristics of the present configuration under b.c. ①, ②, ③ have been obtained by investigating various special cases:  $Ta = 0, Q \neq 0$ ;  $Ta \neq 0, Q = 0$ ;  $Ta, Q \gg 1$ ;  $Ta \gg 1, Q = 0, p_1 \neq 0$  all with  $Pa = 0 = Bo$  i.e., under zero gravity bringing out the essential differences between  $Cr = 0$  and  $Cr \neq 0$ .

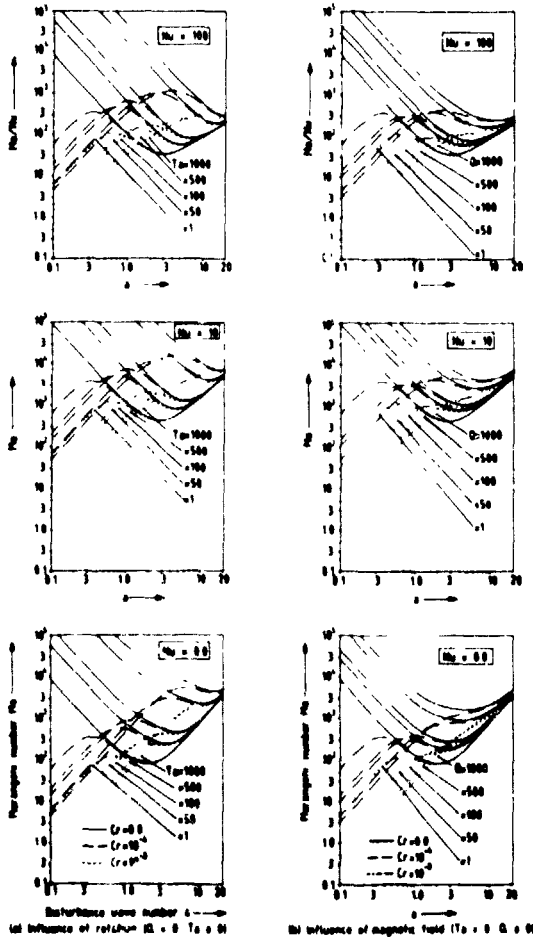


Figure 2. Neutral stability curves for the onset of thermocapillary convective instability in a liquid layer under zero gravity: Effects of interfacial curvature (Cr) and heat transfer (Nu) under the influence of (a) rotation alone and (b) magnetic field alone for b.c. ①. The unstable domain is above the respective curves.

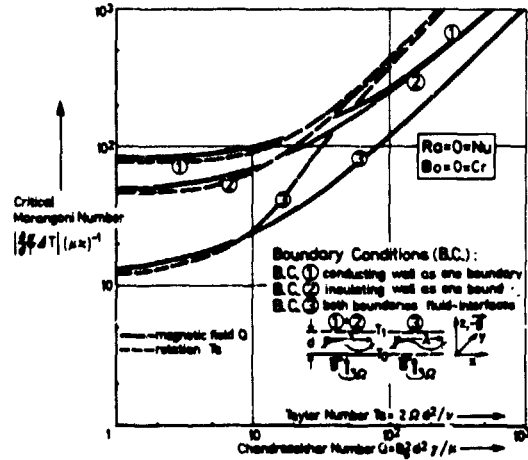


Figure 3. Variation of  $Ma_c$  with rotation (Ta) and magnetic field (Q) neglecting interfacial effects ( $Cr = 0 = Nu$ ) under zero gravity for b.c. ①, ②, ③.

Figure 2 shows the neutral stability curves of the present configuration under the action of (a) rotation alone and (b) magnetic field alone for different  $Nu$ ,  $Cr$  at  $Bo = 0 = Ra$  for b.c. ①. We notice first of all the radical departure of the stability characteristics for  $Cr \neq 0$  from those of  $Cr = 0$ , namely, that there exists strictly speaking no minimum critical Marangoni number when  $Cr \neq 0$  as was first shown by Scriven and Sternling<sup>5</sup> for  $Ta = 0 = Q$ . Asymptotic analysis in the limit  $a \rightarrow 0$  shows that  $Ma \sim f(Ta, Q) (Nu+1)/a^2$ ,  $a \rightarrow 0$  for  $Cr = 0$  whereas  $Ma \sim g(Ta, Q) (Nu+1)a^2/Cr$ ,  $a \rightarrow 0$  for  $Cr \neq 0$  under b.c. ①. The numerical results shown confirm this limiting behaviour as well (note the linearity of the curves for small  $a$ ). The above formulas incidentally include the factor  $(Nu+1)$  missing in those of reference 5 (Table 1, p.333) for  $Ta = 0 = Q$ .

For sufficiently small  $Cr/g(Ta, Q)$  we may speak of a quasi-critical Marangoni number  $Ma_c$  which is approximately equal to that calculated using  $Cr = 0$  in earlier literature<sup>1,2,3</sup>. Since the unstable long wave band increases in size with  $Ta$  and  $Q$  (for  $Ta \gg 1$ ,  $Q \ll 1$ ;  $Ta \ll 1$ ,  $Q \gg 1$  respectively the corresponding band widths are  $O(Cr/Ta)$  and  $O(Cr/Q)$ ,  $Cr$  must indeed accordingly be smaller for this approximation to hold at higher  $Ta, Q$ . As shown in Figure 2 the effects of heat transfer ( $Nu \neq 0$ ) at the two-fluid interface are stabilizing in that the unstable domain is pushed upward along the  $Ma$ -axis with increasing  $Nu$ .

Figure 3 shows the monotonically increasing stabilization potentially to be achieved by increasing rotation ( $Ta$ ) and magnetic field ( $Q$ ) under the three typical b.c. ①, ②, ③ which, it may be noted, are in decreasing order of stability amongst themselves. The results shown agree with those in references 12,14 for  $Cr = 0$ . Asymptotically  $Ma_c = 0(Q)$  for  $Q \gg 1$ ,  $Ta \ll 1$  and  $Ma_c = 0(Ta)$  for  $Ta \gg 1$ ,  $Q \ll 1$ . Note that the asymptotic range is attained faster by  $Ta$  than by  $Q$  due to the influence of rotation on the flow field in general and vorticity in particular. The differences between the b.c. persist longer in the case of magnetic field. The situation is analogous in the case of buoyancy<sup>6</sup>.

Apart from their formal interest the results shown in Figures 2, 3 for  $Cr = 0$  may also be seen as useful approximations for sufficiently small  $Cr$  and at low levels of gravity provided the long wave instabilities are considered relatively harmless. The relevant ranges of the parameters will become apparent in the later discussion.

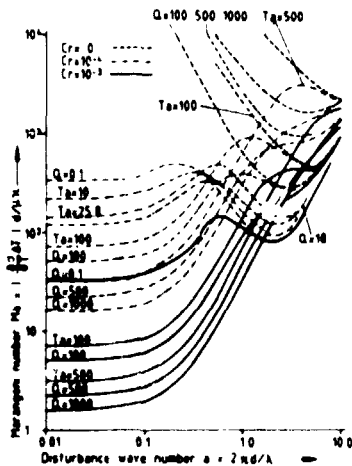


Figure 4. Neutral stability curves for b.c. ① with  $Nu = 0$ ,  $Bo = 0.05$  at low gravity ( $Ra = 0.1$ ) for different  $Ta$  ( $Q = 0.1$ ) and  $Q$  ( $Ta = 0.1$ )

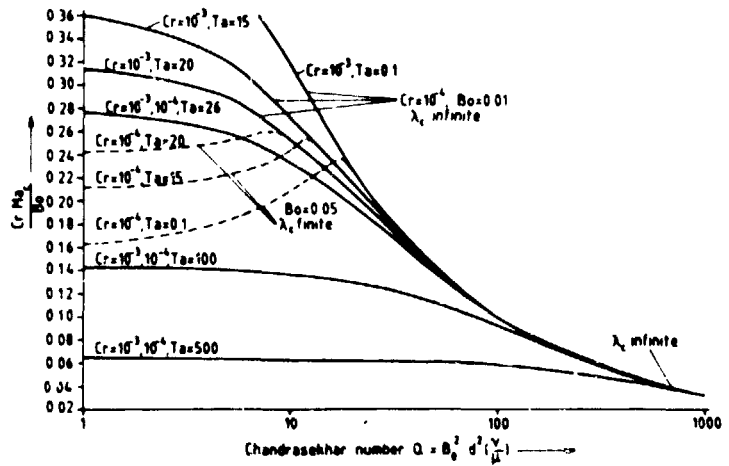


Figure 5. Correlation of the critical Marangoni number  $Ma_c$  with  $Bo/Cr$  for b.c. ① with  $Nu = 0$ ,  $Ra = 0.1$  at  $Cr = 10^{-3}, 10^{-4}$ ;  $Bo = 0.01, 0.05$

Figure 4 shows the further departure of the stability characteristics of the configuration from those at  $Cr = 0$  when we consider low Bond number and crispation effects together. We notice first of all the reinstatement of an absolute minimum critical  $Ma_c$  for the onset of convective instability as was first shown by Smith<sup>6</sup> for  $Ta = 0 = Q$ . The neutral stability curves for  $Cr = 10^{-3}$  show two minima, one at  $a = 0$  and the other at finite  $a$ . Even for  $Cr = 10^{-4}$  the same feature can be reproduced at  $Bo = 0.5$ . This is due to the fact that the long wave stability characteristics depend on the ratio  $Bo/Cr$  and not individually on  $Bo, Cr$ . The occurrence of double minima has been confirmed for  $Bo/Cr \geq 200$ . The lesser of the two minima is then the critical  $Ma_c$  for the onset of instability. For small  $Ta (< 25.8)$  and small  $Q (< 18)$  we observe that the critical wavelength  $\lambda_c$  corresponding to  $Ma_c$  is finite whereas at higher  $Ta$  and  $Q$ ,  $\lambda_c$  is infinite at onset of instability. It may also be mentioned that when  $\lambda_c$  is

# ANALYSIS OF POOR QUALITY

finite it does correspond to the value for  $Cr = 0$ .  $Ma_c$  clearly decreases monotonically with larger  $Ta, Q$  and the corresponding  $\lambda_c$  is then infinite. Thus, allowing for gravitational waves and crimpation effects leads to long wave instability at a low but finite  $Ma_c$  for large  $Ta$  and  $Q$ .

Figure 5 shows the correlation of  $Ma_c$  with  $Bo/Cr$  for b.c. ① with  $Nu = 0$ ,  $Ra = 0.1$  at  $Cr = 10^{-3}, 10^{-4}$ ;  $Bo = 0.01, 0.05$ . Along the continuous parts of the curves  $\lambda_c$  is infinite and along the broken ones  $\lambda_c$  is finite. The latter situation is found to occur at low  $Ta (< 25.8)$  and  $Q < Q^*$  ( $Q^* = 18, 12, 8.5$  respectively for  $Ta = 0.1, 15, 20$ ) and large enough  $Bo/Cr$ . The last provision is to be recognized along the curves for  $Ta < 26$  where the respective curves split off at  $Q^*$  into two branches applying separately for  $Bo = 0.01$  ( $\lambda_c \rightarrow \infty$ ) and  $Bo = 0.05$  ( $\lambda_c$  finite) eventhough both correspond to the same value of  $Cr = 10^{-4}$ . For large enough  $Ta$  and  $Q$  values the correlation with  $Bo/Cr$  is universal and  $a_c = 0$ . Furthermore we notice that at large  $Q$  ( $\sim 800$ ) all the curves for  $Ta \leq 500$  merge. This implies a certain "saturation effect" as far as the influence of rotation is concerned while acting together with the magnetic field as a stabilizing agent.

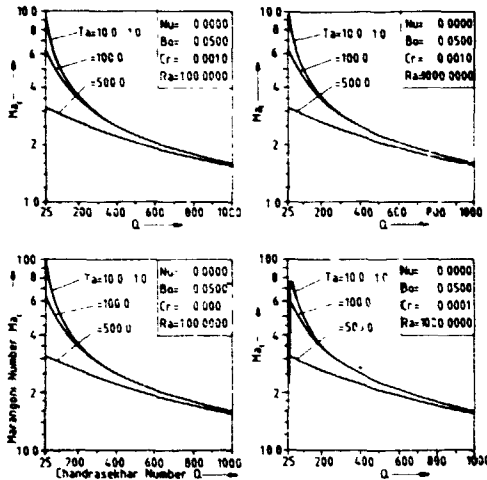


Figure 6. Variation of  $Ma_c$  with rotation ( $Ta$ ) and magnetic field ( $Q$ ) for b.c. ① with  $Nu = 0$

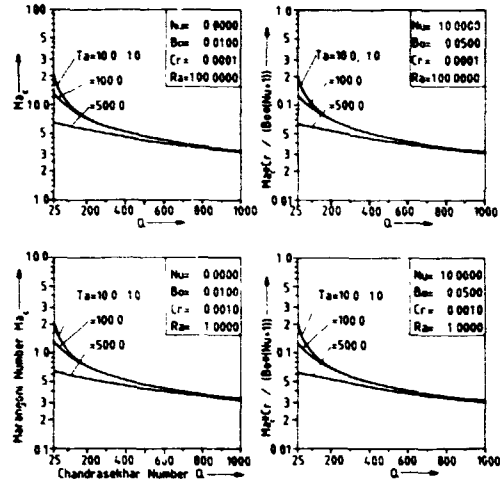


Figure 7. Variation of  $Ma_c$  with  $Bo, Cr, Nu$  for b.c. ①

Figure 6 shows the variation of  $Ma_c$  with  $Ta$  and  $Q$  ( $Q \geq 25$ ) wherein the monotonic decrease of  $Ma_c$  is to be noted even for  $Bo/Cr = 500$  in contrast to the initial increase observed in Figures 4, 5 for lower  $Ta, Q$ . (In Figures 6 - 8 the respective constant parameter values are indicated in the inset.) The computations show that  $Ma_c$  hardly changes with  $Ra$ . In fact for  $Cr = 10^{-3}, Bo = 0.05$  the upper right quadrant of Figure 6 shows that even up to  $Ra = 1000$ ,  $Ma_c$  is that given by the long wave limit  $(Ma_c)_{a=0}$ . However for higher  $Bo/Cr$  ( $= 500$  shown) the buoyancy effects become noticeable from  $Ra > 300$  for  $Ta = 0.1, 10$  at  $Q = 25$  since now  $Q^*$  increases for  $Ta = 0.1, 10$  from 18, 12 respectively at low  $Ra$  ( $= 0.1$ ) to 47, 46 at moderate  $Ra$  ( $= 1000$ ). This is indicated in the lower right hand quadrant of Figure 6. This latter range, where buoyancy effects become noticeable, is distinguished by the broken curve along which  $\lambda_c$  is finite. (The curves for  $Ta = 0.1, 10$  are hardly to distinguish on the scale drawn but they end, when extended, respectively at approximately  $Q_0 = 16.5$  and  $13.2$  on the  $Q$ -axis.)

Figure 7 shows the correlation of  $Ma_c$  with  $(Bo/Cr)(Nu+1) f(Ta, Q)$  for different combinations of  $Bo, Cr, Nu$ . The coefficient functions  $f(Ta, Q)$  shown have been confirmed numerically for various combinations of the parameters as long as the buoyancy effects are not noticeable. The "universality" of these correlation functions depends slightly on the parameter range but is found to be within a few percent at  $a = 0.02$  chosen to represent the limit  $a \rightarrow 0$ . Another feature to be noted from Figures 4 - 7 is that  $a_c \rightarrow 0$  as  $Ta, Q$  increase and  $a_c = 0$  for all  $Ta, Q$  greater than some not too large a value. This is in contrast to the common finding of the earlier studies<sup>12-14</sup> (wherein  $Cr$  was set equal to zero a priori), namely, that  $a_c$  increases with  $Ta$  and  $Q$ . Here we see that as long as the buoyancy effects do not dominate, the stationary form of instability sets in only at  $a_c = 0$  for sufficiently large  $Ta$  and  $Q$ .

Now we turn to the effect of the boundary conditions on the stability characteristics of the configuration. In all the three cases of b.c. ①, ②, ③ the same trends in the variation of  $Ma_c$  are observed for low  $Ra$ .  $Ma_c$  is proportional to  $Bo/Cr$  and decreases monotonically

# ORIGINAL PAGE IS OF POOR QUALITY

with  $Ta$ ,  $Q$  for low  $Bo/Cr$  as demonstrated in Figure 8(a) for  $Bo/Cr = 10, 100$ .

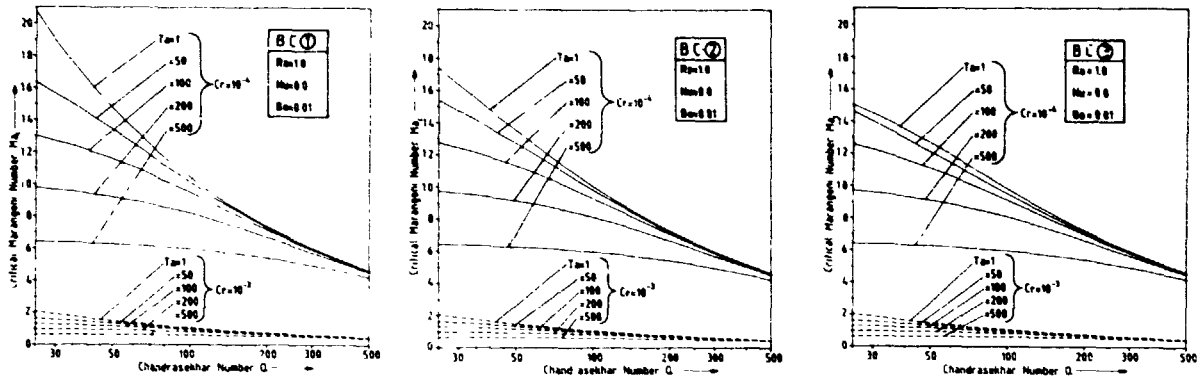


Figure 8(a). Effect of boundary conditions on the variation of  $Ma_c$  at  $Bo/Cr = 10, 100$

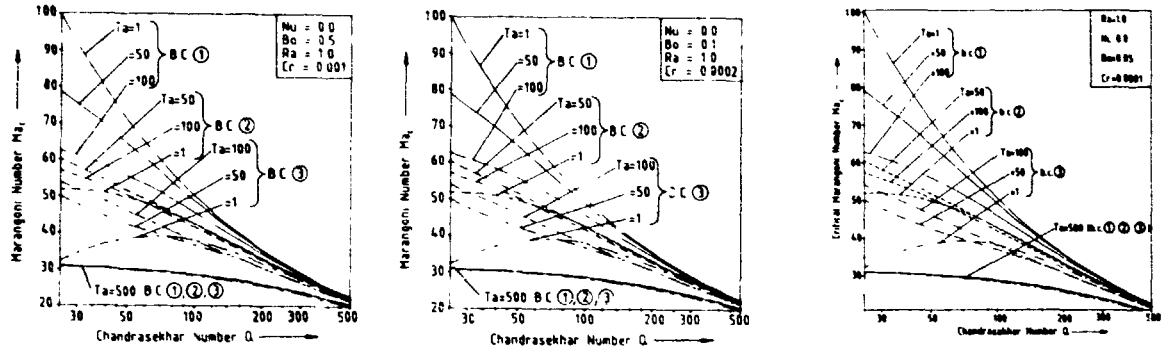


Figure 8(b). Effect of boundary conditions on the variation of  $Ma_c$  at  $Bo/Cr = 500$

We also note that at low  $Ta$  and  $Q$ ,  $Ma_c$  for b.c. ① is higher than that for b.c. ② and the latter in turn is higher than that for b.c. ③. This indicates the decreasing degree of stability imparted by the degrees of freedom allowed by the three types of boundary conditions ①, ②, ③ in that order. This feature is similar to that for the buoyancy-drive, convective instability<sup>8</sup> although the boundary conditions there are different. For large  $Ta$  and  $Q$ , however we notice (cf.  $Q > 500$ , or  $Ta = 500$ ) the boundary conditions can no longer be distinguished from each other. In the present case the role of the b.c. is further enhanced via the dependence on  $Bo/Cr$ . The lower  $Bo/Cr$ , the lesser is the influence of b.c. even at low  $Ta, Q$  (cf.  $Ta = 1, 50$  for  $Bo = 0.01, Cr = 10^{-3}$  shown by dashed curves in the lower part of Figure 8(a).)

Complementary to the results in Figure 8(a) those in 8(b) demonstrate that for larger  $Bo/Cr$  ( $= 500$  for three different combinations of  $Bo, Cr$ ) a more pronounced effect of the boundary conditions on the variation of  $Ma_c$  and in particular that  $Ma_c$  can decrease as well as increase with  $Ta$  and  $Q$  depending on the range of parameters. Again at large  $Ta, Q$  the distinction between the boundary conditions decreases.

### Conclusions

The onset of stationary convective instability driven by both density- and surface-tension-gradients in a horizontal liquid layer heated from below can be suppressed by means of rotation about a transverse axis and by a transverse magnetic field. But the stabilizing influence of these two agencies is subject to considerable qualifications in view of the effects of curvature and gravity waves at the two-fluid interface. The larger the ratio  $Bo/Cr$ , the greater the range of stabilizing action in terms of  $Ta, Q$  for all the boundary conditions considered and relatively greater for b.c. ② and ③ than for b.c. ①. The influence of the individual b.c. ①, ②, ③ becomes indistinguishable at larger  $Ta, Q$  and at lower  $Bo/Cr$ . Since  $Ma_c$  decreases with  $Ta, Q$  (for sufficiently large  $Ta, Q$ ) and  $a_c \rightarrow 0$ , an optimal parameter range for the combined stabilizing action of rotation and magnetic field must be

sought appropriately. Allowance for heat transfer the ambient gas is generally stabilizing.

In the low gravity situation (small  $Bo$  and  $Ra < 100$ ) the buoyancy effects do not perceptibly influence the onset of instability except at low  $Ta$  and  $Q$ . In this range the onset of instability is at a finite wave number  $a_c \neq 0$  which is independent of  $Bo$ ,  $Cr$  as may be expected. ( $Ma_c$  corresponds otherwise to  $a_c = 0$  and as shown  $\propto Bo/Cr$  for  $Nu = 0$ .) The general problem of interaction between buoyancy and surface tension will be considered in a later report but it seems legitimate to draw a partial conclusion on the basis of results shown here, namely, that the buoyancy-dominated situation tends to prefer finite wave length instability while the capillarity-dominated situation including the effects of interfacial curvature and interfacial gravity waves tends to favour the infinitely long wave mode of instability. This conclusion is qualitatively in contrast to that of earlier studies on this configuration ignoring the interfacial effects altogether ( $Bo = 0 = Cr$ ). This stems only from the nonzero  $Bo/Cr$  and does not explicitly depend on the (finite) value of the mean surface tension<sup>1-5</sup>.

The question of oscillatory modes of instability has been bypassed here on the basis of asymptotic results indicating that the incipient instability is stationary for large  $Ta$  ( $Q = 0$ ). The results for the finite range of  $Ta$  and  $Q$  need of course to be examined in order to confirm whether  $Ma_c$  calculated here is indeed the absolute minimum critical Marangoni number for the onset of instability.

#### References

1. Sarma, G.S.R., "On Oscillatory Modes of Thermocapillary Instability in a Liquid Layer Rotating about a Transverse Axis", *Physico Chemical Hydrodynamics* (in Press), 1981.
2. Sarma, G.S.R., "Marangoni Convection in a Liquid Layer under the Simultaneous Action of a Transverse Magnetic Field and Rotation", *Adv. Space Res.*, Vol. 1, pp. 55-58. 1981.
3. Sarma, G.S.R., "Marangoni Convection in a Liquid Layer Subjected to Rotation about a Transverse Axis", *Proc. 3<sup>rd</sup> European Symp. on Material Sciences in Space*, Grenoble 24-27 April 1979, - ESA SP-142, pp. 359-362. 1979.
4. Sarma, G.S.R., "Marangoni Convection in a Fluid Layer under the Action of a Transverse Magnetic Field", *Space Research*, Vol. XIX, pp. 575-578. 1979.
5. Scriven, L.E. and Sternling, C.V., "On Cellular Convection Driven by Surface-Tension Gradients: Effects of Mean Surface Tension and Surface Viscosity", *J. Fluid Mech.*, Vol. 19, pp. 321-340. 1964.
6. Smith, K.A., "On Convective instability Induced by Surface-Tension Gradients", *J. Fluid Mech.*, Vol. 24, pp. 401-414. 1966.
7. Pearson, J.R.A., "On Convection Cells Induced by Surface Tension", *J. Fluid Mech.*, Vol. 4, pp. 489-500. 1958.
8. Chandrasekhar, S., Hydrodynamic and Hydromagnetic Stability, Oxford University Press 1961.
9. Bourgeois, S.V., "Buoyant and Capillary Natural Convection in Infinite Horizontal Liquid Layers Heated Laterally", *Letters in Heat and Mass Transfer*, Vol. 2, pp. 223-236. 1975.
10. Palmer, H.J. and Berg, J.C., "Convective Instability in Liquid Pools Heated from Below", *J. Fluid Mech.*, Vol. 47, pp. 779-787. 1971.
11. Chang, C.E. and Wilcox, W.R., "Inhomogeneities due to Thermocapillary Flow in Floating Zone Melting", *J. Crystal Growth*, Vol. 28, pp. 8-12. 1975.
12. Nield, D.A., "Surface Tension and Buoyancy Effects in the Cellular Convection of an Electrically Conducting Liquid in a Magnetic Field", *ZAMP*, Vol. 17, pp. 131-139. 1966.
13. Namikawa, T., Takashima, M. and Matsushita, S., "The Effect of Rotation on Convective Instability Induced by Surface Tension and Buoyancy", *J. Physical Soc. Japan*, Vol. 28, pp. 1340-1349. 1970.
14. Vidal, A. and Acrivos, A., "The Influence of Coriolis Force on Surface-Tension-Driven Convection", *J. Fluid Mech.*, Vol. 26, pp. 807-818. 1966.

N82 23468

A variational approach to the study of capillarity phenomena

Michele Emmer, Eduardo Gonzalez, and Italo Tamanini

Università di Roma, Università di Lecce, and Università di Trento  
Istituto Matematico, Piazzale Aldo Moro, 00185 Roma; Istituto Matematico, Via Arnesano,  
73100 Lecce; a.d Dipartimento di Matematica, 38050 Povo (Trento), Italy.

Abstract

We consider the problem of determining the free surface of a liquid in a capillary tube, and of a liquid drop, sitting first on a horizontal plane and then on more general surfaces. With some modifications, the method applies to the study of pendent drops and of rotating drops as well.

Introduction

Several capillarity phenomena, such as the rise of water in tubes of narrow bore, and the formation of liquid drops or bubbles, can conveniently be studied from the general point of view of the Calculus of Variations. Such a possibility, which clearly originates in the energy-minimizing character of the observed equilibrium configurations, has the remarkable advantage of providing a unified treatment of the mathematical questions that arise in a variety of particular phenomena.

By using a well-known argument, based on the principle of virtual work, one is led to a variational formulation of the physical problem, in which a certain functional (representing the global energy of the system under consideration) has to be minimized, subject to some "natural" constraints, such as prescribed boundary conditions or fixed volume constraints. In general, the energy functional will consist of a "surface integral" plus a "volume integral": the latter corresponds to body forces, of which gravity is a typical representative, while the former results, for example, from the consideration of the forces acting on the surface of separation between the liquid and the gas surrounding it.

Now, the point is, that the classical definition of "surface area" is rather inadequate for treating this type of problem, mainly because it applies to smooth or Lipschitz-continuous surfaces only - a class which is not closed under the usual limit operations.

The difficulties arising from the presence of a surface integral become even more evident when compared with the relatively simple treatment of the corresponding volume integral, which is generally well-defined on measurable sets and enjoys (at least in the simplest cases) nice variational properties.

A satisfactory theory of surface area for a general class of surfaces of codimension one in  $\mathbb{R}^n$ ,  $n \geq 2$ , has been developed by E. De Giorgi in the fifties.<sup>1</sup> It is a remarkable fact that some classical questions, concerning the existence and regularity of capillary surfaces, have been answered only quite recently, using the variational techniques introduced by De Giorgi, or even more general methods pertaining to the field of Geometric Measure Theory.<sup>2</sup>

The definition of "functions of Bounded Variation", together with the main results of the corresponding BV-functions theory, will be recalled in the next section. As a first application of the theory, we shall discuss in section 2 the "standard" capillary problem, i.e. the determination of the free surface of a liquid in a thin tube of general cross section, which results from the simultaneous action of surface tension, boundary adhesion and gravity. It turns out that in this case the existence of the solution surface depends heavily on the validity of a simple geometric condition about the mean curvature of the boundary curve of the cross section of the capillary tube. Some particular examples of physical interest will also be discussed.

Section 3 is devoted to the study of liquid drops, sitting on, or hanging from, a fixed horizontal plane. The symmetry of the solutions (which can actually be proved, as a consequence of a general symmetrization argument) now plays the chief role in deriving both the existence and the regularity of energy-minimizing configurations. When symmetry fails (this is the case, for example, when the "contact angle" between the drop and the plate is not constant, or when the supporting surface is not itself symmetric), then more sophisticated methods must be used. Extensions in this direction will be outlined in section 4.

We refer to the papers listed in the (fairly incomplete) bibliography at the end of the present paper for a deeper treatment of the subject, as well as for the discussion of related problems.

Functions of bounded variation

Given an open subset  $\Omega$  of  $\mathbb{R}^n$ ,  $n \geq 2$ , we denote by  $BV(\Omega)$  the function space of Lebesgue integrable functions  $f$  over  $\Omega$ , whose distributional gradient  $Df$  is a vector measure with finite total variation on  $\Omega$ ;  $\int_A |Df|$  will denote the total variation of the measure  $Df$ , evaluated at  $A \subset \Omega$ .

When  $A$  is open we obtain:

$$\int_A |Df| = \sup \left\{ \int f(x) \operatorname{div} G(x) dx : G \in C_0^1(A; \mathbb{R}^n), |G| \leq 1 \right\}$$

As a first result we can prove the lower semicontinuity of the map  $f \rightarrow \int |Df|$ , with respect to the local convergence on  $\Omega$ ; that is, if  $f_j \in BV(\Omega)$  for every  $j$  and

$$\lim_{j \rightarrow +\infty} \int_A |f_j - f| dx = 0$$

for every  $A \subset\subset \Omega$  (i.e.,  $A$  open and bounded with  $\bar{A} \subset \Omega$ ), then:

$$\int_{\Omega} |Df| \leq \liminf_{j \rightarrow +\infty} \int_{\Omega} |Df_j|.$$

Furthermore, we have the following compactness property: if  $f_j \in BV(\Omega)$ , and for every  $A \subset\subset \Omega$  and for every  $j$  it holds

$$\int_A |Df_j| \leq c(A)$$

with  $c(A)$  independent of  $j$ , then there exists a subsequence of  $\{f_j\}$ , locally converging in  $\Omega$  to some limit function  $f$ .<sup>3</sup>

If  $f \in BV(\Omega)$  and  $\Omega$  has a Lipschitz-continuous boundary  $\partial\Omega$ , then we can define the "trace" of  $f$  on  $\partial\Omega$  (still denoted by  $f$ ), which is summable on  $\partial\Omega$  and satisfies<sup>4</sup>

$$\int_{\partial\Omega} |f| \leq (1+L^2)^{1/2} \int_{\Omega} |Df| + c(\Omega) \int_{\Omega} |f| \quad (1)$$

where  $L$  (the Lipschitz constant of  $\partial\Omega$ ) and  $c(\Omega)$  depend only on the geometry of  $\Omega$  but not on  $f$ .

By specializing the above definitions and properties to the case when  $f$  is the characteristic function  $\phi_E$  of a measurable set  $E \subset \Omega$ , we get a parallel theory of sets of finite perimeter, where by definition:

$$\text{"perimeter of } E \text{ in } \Omega" = \int_{\Omega} |D\phi_E|$$

A straightforward application of the Gauss-Green theorem shows that this quantity coincides with the area of  $\partial E \cap \Omega$ , at least when  $\partial E$  is a smooth  $(n-1)$ -dimensional surface in  $\Omega$ . The connection between BV-functions and sets of finite perimeter is given by the coarea formula:

$$\int_{\Omega} |Df| = \int_{-\infty}^{+\infty} dt \int_{\Omega} |D\phi_{F_t}| \quad (2)$$

where  $f \in BV(\Omega)$  and  $F_t = \{x \in \Omega : f(x) < t\}$ .<sup>3</sup>

Moreover<sup>5</sup>, if  $E = \{(x, t) : x \in \Omega, t < f(x)\}$ , then it holds

$$\int_{\Omega \times \mathbb{R}} |D\phi_E| = \int_{\Omega} \sqrt{1 + |Df|^2}$$

where the second integral represents the total variation on  $\Omega$  of the vector measure, whose  $n+1$  components are respectively the Lebesgue measure on  $\mathbb{R}^n$ , and the distribution derivatives  $D_i f$ ,  $i=1, \dots, n$ . When  $f$  is Lipschitz-continuous on  $\Omega$ , this yields of

course the area of the graph of  $f$  over  $\Omega$ .

### Capillary surfaces in cylindrical vertical tubes

Let us consider a capillary tube, open at both ends and partially immersed into a liquid; for simplicity, we may assume that the liquid rises in the tube, so that - in view of the preceding discussion - the energy corresponding to a certain configuration of the liquid within the tube, described by the graph a function  $f \geq 0$ , can be expressed as

$$\mathcal{J}(f) = \int_{\Omega} \sqrt{1+|Df|^2} - \nu \int_{\partial\Omega} f + \frac{\kappa}{2} \int_{\Omega} f^2 \quad (3)$$

Here,  $\Omega$  (open and bounded in  $\mathbb{R}^2$ , with Lipschitz boundary  $\partial\Omega$ ) denotes the cross section of the tube,  $f \in BV(\Omega)$ , and  $\kappa, \nu$  are physical constants, with  $\kappa > 0$  and  $0 < \nu \leq 1$ . It is easily seen that  $f \equiv 0$  is the trivial solution of  $\mathcal{J}(\cdot) \rightarrow \min$ , when  $\nu \leq 0$ , while  $\inf \mathcal{J}(\cdot) = -\infty$  when  $\nu > 1$ .

We can immediately check that a configuration of minimal energy (i.e., a solution to the problem  $\mathcal{J}(\cdot) \rightarrow \min$ ) satisfies the equations

$$\begin{cases} \operatorname{div} Tf(x,y) = \kappa f(x,y) & \text{in } \Omega \\ Tf(x,y) \cdot n(x,y) = \nu & \text{on } \partial\Omega \end{cases}$$

where  $Tf = \frac{Df}{\sqrt{1+|Df|^2}}$ , and  $n(x,y)$  denotes the outward unit normal to  $\partial\Omega$  at  $(x,y)$ .

This is true if, for example,  $\partial\Omega$  is of class  $C^1$  and  $f \in C^2(\Omega) \cap C^1(\bar{\Omega})$ .

This way, we realize that the mean curvature of a capillary surface is, at any point  $(x,y,f(x,y)) \in \Omega \times \mathbb{R}$ , proportional (with constant  $\kappa$ ) to its height above the reference plane  $z = 0$ , and that  $\nu$  corresponds to the cosine of the contact angle between the surface and the walls of the tube.

The classical approach consisted in solving the above system of equations in the special case when  $\Omega$  was a disc of radius  $R$ , and  $f = f(r)$ ,  $r = (x^2 + y^2)^{1/2}$  (axially symmetric solutions). In this case, one is led to the ordinary differential equation

$$\left( \frac{rf_r}{\sqrt{1+f_r^2}} \right)_r = \kappa rf(r) \quad \text{for } 0 < r < R$$

with the boundary conditions:  $f_r(0) = 0$ ,  $f_r(R) = \nu \cdot (1-\nu^2)^{-1/2}$ .

In order to prove the existence of a solution  $f$  to the problem  $\mathcal{J}(\cdot) \rightarrow \min$ , we make the following assumption on the domain  $\Omega$ :

$$\int_{\partial\Omega} \phi_E \leq \alpha \int_{\Omega} |D\phi_E| + \beta \int_{\Omega} \phi_E \quad (4)$$

for every  $E \subset \Omega$ , with  $\alpha \geq 1$  and  $\beta > 0$ . From (4) and the coarea formula (2) we get

$$\int_{\partial\Omega} f \leq \alpha \int_{\Omega} |Df| + \beta \int_{\Omega} f$$

for every  $f \in BV(\Omega)$  with  $f \geq 0$ . By introducing this last inequality in (3) we find:

$$\mathcal{J}(f) \geq (1-\nu\alpha) \int_{\Omega} |Df| + \frac{\kappa}{4} \int_{\Omega} f^2 - \frac{\nu^2 \beta^2}{\kappa} \cdot |\Omega|,$$

where  $|\Omega|$  denotes the Lebesgue measure of  $\Omega$ . In particular, if  $\nu \leq 1/\alpha$  we obtain  $\inf \mathcal{J}(\cdot) \geq -\nu^2 \beta^2 |\Omega| / \kappa$ , while if  $\nu > 1/\alpha$ , then for any minimizing sequence  $f_j$ , satisfying  $\mathcal{J}(f_j) \rightarrow \inf \mathcal{J}(\cdot)$ , we obtain:

$$\int_{\Omega} |Df_j| \leq \frac{\text{const.}}{1-\nu\alpha}, \quad \int_{\Omega} f_j^2 \geq \text{const.}$$

so that, in view of the results in section 1, we conclude that a subsequence of  $\{f_j\}$  converges to a function  $f$ , which clearly solves our problem; as a consequence of the strict convexity of the energy functional, such a solution is in fact unique.

The hypothesis (4) now comes into discussion: clearly, it is implied by the trace estimate (1), so that capillary surfaces always exist for  $v$  in the range  $0 < v < (1+L^2)^{-1/2}$ , with  $L$  = Lipschitz constant of  $\partial\Omega$ ; that this is in fact an "almost necessary" condition can easily be seen with the aid of some simple examples.<sup>7</sup> For a domain  $\Omega$  in the form of a circular sector, no solution with bounded energy can exist when  $v > (1+L^2)^{-1/2}$  (that is, when  $\theta + 2\gamma < \pi$ , where  $\theta$  is the angle of the sector and  $\gamma$  is the contact angle). The discontinuity at  $\theta + 2\gamma = \pi$  is also confirmed by physical experiments.<sup>7</sup>

On the other hand,<sup>6</sup> interior corners do not affect the solution: in the special case when  $\Omega$  satisfies an Internal Sphere Condition of radius  $R > 0$  (i.e., when each point in  $\Omega$  belongs to some ball  $B_R \subset \Omega$ ), then (4) holds with  $\alpha = 1$ , and it can be shown, by using a result of Concus and Finn,<sup>6</sup> that the solution exists for every  $v$  with  $0 < v \leq 1$ .

In conclusion, we remark that the variational method does not work when  $\kappa = 0$ , i.e. in the absence of gravity; one can actually show<sup>8</sup> that the solutions  $f_\kappa$ , corresponding to values  $\kappa > 0$ , go uniformly to  $+\infty$  in  $\Omega$ , as  $\kappa \rightarrow 0^+$ .

### Sessile drops and pendent drops

The energy of a liquid drop, sitting on the horizontal plane  $\{z=0\}$  in  $\mathbb{R}^3$ , can be written in the following way:

$$\mathcal{F}_\kappa(E) = \int_{z=0} |D\phi_E| + v \int_{z=0} \phi_E + \kappa \int_{z=0} z\phi_E \quad (5)$$

where  $E$  denotes the region of the half-space  $\{z > 0\}$  occupied by the liquid. The first integral in (5) represents the area of the free boundary of the drop, the second integral gives the area of the region of contact, and the third integral corresponds to gravity. As usual, we assume  $\kappa \geq 0$  and  $v \in (-1, 1]$ , since for  $v = -1$  no solution can occur. The same functional, with  $\kappa < 0$ , represents the energy of a pendent drop; in both cases, a volume constraint has to be imposed, namely  $|E| = v > 0$ .

Now, it can be shown<sup>10</sup> that by replacing each horizontal section of a given configuration  $E$  by a disc of the same area, centered on the  $z$ -axis, a new configuration  $E'$  results, which is of less energy than  $E$  (in fact,  $\mathcal{F}_\kappa(E) = \mathcal{F}_\kappa(E')$  iff  $E$  is already axially symmetric).

From this fact, by using the obvious estimate

$$\int_{z=0} \phi_E \leq \int_{z=0} |D\phi_E|$$

which implies

$$\mathcal{F}_\kappa(E) \geq \frac{1+v}{2} \int |D\phi_E|$$

for every  $E$ , if  $\kappa \geq 0$ , one gets easily the existence of a minimum of  $\mathcal{F}_\kappa(\cdot)$ , when  $\kappa \geq 0$ . On the other hand, when  $\kappa < 0$  the situation is completely different, and we can look only for local solutions of  $\mathcal{F}_\kappa(\cdot) \rightarrow \min$ , since clearly  $\inf \mathcal{F}_\kappa(\cdot) = -\infty$  in this case.

To this aim, we introduce the following definition:  $E$  is a local minimum of the energy functional (a pendent drop) if  $|E| = v$ , and there exist  $T > 0$  and  $\alpha \in (0, 1)$  such that  $E$  is contained in the region  $\{0 < z < \alpha T\}$  and, for every  $F \subset \{0 < z < T\}$  with  $|F| = v$ , there holds  $\mathcal{F}_\kappa(E) \leq \mathcal{F}_\kappa(F)$ .

In order to prove the existence of pendent drops, we start by observing that, when  $\kappa = 0$  (that is, in the absence of gravity), the minimum  $E_0$  of  $\mathcal{F}_0(\cdot)$  is a portion of a ball, completely determined from the data  $v$  and  $\nu$ . With this in mind, we choose  $T$  greater than the maximum height of  $E_0$  and find the solution  $E_\kappa$  of the problem  $\mathcal{F}_\kappa(\cdot) \rightarrow \min$ , restricted to the configurations  $E \subset \{0 < z < T\}$ .

An easy calculation shows that  $E_\kappa \rightarrow E_0$  as  $\kappa \rightarrow 0$  as a consequence of general results concerning the convergence of surfaces of prescribed mean curvature, we get that for  $|\kappa|$  small enough, the solution  $E_\kappa$  is actually contained in  $\{0 < z < \alpha T\}$  for a suitable  $\alpha \in (0, 1)$ ,<sup>11</sup> thus concluding the proof of the existence of pendent drops of given volume, in a weak gravitational field. Estimates on the effective smallness of  $|\kappa|$  are also explicitly known.

For example, Giusti<sup>12</sup> showed that pendent drops exist, if the product  $|\kappa|v^{2/3}$  does not exceed a constant, which can be written down explicitly, and which depends only on the value of the contact angle between the free surface of the drop and the plane  $\{z=0\}$ .

### Concluding comments

The regularity (analyticity) of the equilibrium surface of a liquid in a capillary tube can be derived from general regularity results for hypersurfaces of least area or, more generally, of prescribed mean curvature in  $\mathbb{R}^n$ .<sup>13</sup> The boundary behaviour of the solutions has also been studied, and several results in this direction are presently known.<sup>14</sup>

As far as the regularity of liquid drops is concerned, we note firstly that the free surface of a drop sitting on a horizontal plane, being rotationally symmetric, can also be described (locally) as the graph of a suitable function  $f$ , defined on a 2-dimensional domain. It turns out that  $f$  minimizes a functional of the type:

$$\int \sqrt{1 + |Df|^2} + \text{gravity} + \lambda f$$

where the Lagrange multiplier  $\lambda$  takes into account the volume constraint. From this, the interior analyticity of the free surface of the drop follows at once.<sup>15</sup>

Secondly, it is not difficult to prove that the configuration representing a sessile drop is a convex set.<sup>16</sup> We then conclude that its free surface is in fact smooth up to the plane  $\{z=0\}$ , and that the cosine of the contact angle coincides with  $\psi$ .

Much more difficult is the study of liquid drops, when symmetry ceases to exist. However, some partial results have recently been obtained, such as the existence and regularity of solutions, corresponding to drops sitting on (or hanging from) a surface  $z = \psi(x,y)$  in  $\mathbb{R}^3$ , satisfying  $\psi(r) \rightarrow +\infty$  for  $r = (x^2 + y^2)^{1/2} \rightarrow +\infty$ . From this "growth condition at infinity", which however is not satisfied in a number of interesting and still open situations, the necessary compactness results can easily be derived.<sup>17</sup>

A theorem, which extends to minima of area-like functionals, subject to a volume constraint, the regularity theory for minimal boundaries, is now available.<sup>17,18</sup> A technique, developed in connection with its proof, can also be used to prove the existence of liquid drops, in rotation around an axis through the center of mass, and held together by surface tension.

In its simplest formulation, the problem asks for a local minimum of the functional

$$\mathcal{F}_\omega(E) = \int_{\mathbb{R}^3} |D\phi_E| - \omega \int_{\mathbb{R}^3} (x^2 + y^2) dx dy dz, \quad \omega > 0 \quad (6)$$

subject to a volume constraint ( $|E| = 1$ ) and to a further constraint about the center of mass (which must coincide with the origin of the space).

The presence of the kinetic energy excludes, in general, the symmetry of the solutions. Anyway, following the treatment of the pendent drop problem, one can show<sup>19</sup> the existence of relative minima of the energy functional, when  $\omega$  is small enough, that is, when the rotation is sufficiently slow.

The proof of this result, which can only be outlined here, proceeds as follows: firstly, we define  $E$  to be a local minimum of the energy functional (6), if there exists  $R > R_0 = (3/4\pi)^{1/3}$  such that  $E \subset\subset C_R$  and, for every admissible  $F \subset\subset C_R$ , satisfying the above constraints, it holds  $\mathcal{F}_\omega(E) \leq \mathcal{F}_\omega(F)$ .

Here,  $C_R$  denotes the cylindrical container

$$C_R = \{(x,y,z) \in \mathbb{R}^3 : x^2 + y^2 \leq R^2, |z| \leq R\}.$$

Then, we can easily prove that for every  $\omega \geq 0$ , and every  $R > R_0$ , there exists a solution  $E_\omega$  to the problem  $\mathcal{F}_\omega(E) \rightarrow \min$ , restricted to the admissible configurations  $E \subset C_R$ . Such a solution, however, will not generally satisfy the condition  $E_\omega \subset\subset C_R$  for a local minimum.

Next, we observe that for a fixed  $R > R_0$ , the solutions  $E_\omega$  we have found in this way, converge, as  $\omega \rightarrow 0^+$ , to the ball  $E_0 = \{(x,y,z) : x^2 + y^2 + z^2 < R_0^2\} \subset\subset C_R$ . The local convergence  $E_\omega \rightarrow E_0$  is unfortunately too weak to conclude that  $E_\omega \subset\subset C_R$  for  $\omega$  small enough. But we can prove, and this is actually the crucial point of the entire demonstration, that if  $\omega$  is sufficiently small (and positive), then there exists a value  $r \in (R_0, R)$  such that

$$\int_{\partial C_R} \phi_{E_\omega} = 0$$

From this result, the fact that  $E_\omega \subset\subset C_R$  for  $\omega$  small can be proved as follows. Define:

$$G = E_\omega \cap C_r \quad \text{and} \quad \alpha = |E_\omega - C_r|$$

and choose  $F = (1-\alpha)^{-1/3}G$  (that is,  $F$  is constructed by expanding  $G$ , with a coefficient  $(1-\alpha)^{-1/3} > 1$ ). Clearly,  $|F| = 1$ . Since  $\alpha \rightarrow 0$  as  $\omega \rightarrow 0$ , it is clear that when  $\omega$  is small, by means of a suitable translation  $F \rightarrow \tilde{F}$  we obtain eventually an admissible configuration  $\tilde{F} \subset C_R$ , whence

$$\mathcal{F}_\omega(E_\omega) \leq \mathcal{F}_\omega(\tilde{F}) \quad (7)$$

On the other hand, the difference  $\mathcal{F}_\omega(E_\omega) - \mathcal{F}_\omega(\tilde{F})$  can easily be estimated from below by the quantity:

$$\left[ 1 - (1-\alpha)^{-2/3} \right] \int_{\mathbb{R}^3} |D\phi_G| + \text{const.} \alpha + \text{const.} \alpha^{2/3}$$

Now, from the Taylor expansion of the coefficient between square brackets, we conclude that  $\mathcal{F}_\omega(E_\omega) - \mathcal{F}_\omega(\tilde{F}) > 0$  if  $\alpha$  is positive and small, which would contradict (7). Therefore, for  $\omega$  small enough,  $\alpha$  must be 0, so that the corresponding solution  $E_\omega$  is contained in  $C_R \subset C_R$ .

In conclusion, we remark that the preceding argument, when used in connection with general regularization techniques,<sup>20</sup> allows the proof of the analyticity of the solution  $E_\omega$  as well.

#### References

1. De Giorgi, E., Colombini, F., Piccinini, L., Frontiere orientate di misura minima e questioni collegate, Pisa, Editrice Tecnico Scientifica 1972.
2. Taylor, J., "The structure of singularities in soap-bubble-like and soap-film-like minimal surfaces", *Annals of Math.* 103, 489-539, 1976.
3. Giusti, E., Minimal surfaces and functions of bounded variation, Notes on Pure Math., Canberra 1977.
4. Emmer, M., "Esistenza, unicit  e regolarit  nelle superfici di equilibrio nei capillari", *Ann. Univ. Ferrara*, 18, 79-94, 1973.
5. Miranda, M., "Superfici cartesiane generalizzate ed insiemi di perimetro localmente finito sui prodotti cartesiani", *Annali Sc. Norm. Sup. Pisa*, 18, 515-542, 1964.
6. Tamanini, I., "Il problema della capillarit  su domini non regolari", *Rend. Sem. Mat. Univ. Padova*, 56, 169-191, 1977.
7. Finn, R., "Capillarity Phenomena", *Russian Math. Surveys* 29, 133-153, 1974.
8. Concus, P., Finn, R., "On capillary free surfaces in a gravitational field", *Acta Math.* 132, 207-223, 1974.
9. Emmer, M., "On the behaviour of the surfaces of equilibrium in the capillary tubes when gravity goes to zero", to appear on *Rend. Sem. Mat. Univ. Padova*.
10. Gonzalez, E., "Sul problema della goccia appoggiata", *Rend. Sem. Matem. Univ. Padova* 55, 289-302, 1976.
11. Gonzalez, E., Massari, U., Tamanini, I., "Existence and regularity for the problem of a pendent liquid drop", *Pacific Journal of Mathematics*, 88, 399-420, 1980.
12. Giusti, E., "The pendent water drop. A direct approach", *Boll. U.M.I.*, 17-A, 458-465, 1980.
13. Massari, U., "Esistenza e regolarit  delle ipersuperfici di curvatura media assegnata in  $\mathbb{R}^n$ ", *Arch. Rat. Mech. Anal.* 55, 357-382, 1974.
14. Simon, L., Spruck, J., "Existence and regularity of a capillary surface with prescribed contact angle", *Arch. Rat. Mech. Anal.* 61, 19-34, 1976.
15. Gonzalez, E., "Sulla regolarit  della goccia appoggiata", *Rend. Sem. Mat. Univ. Padova* 58, 25-33, 1977.
16. Gonzalez, E., Tamanini, I., "Convessit  della goccia appoggiata", *Rend. Sem. Mat. Univ. Padova* 58, 35-43, 1977.
17. Giusti, E., "The equilibrium configuration of liquid drops", *J. reine angew. Math.* 321, 53-63, 1981.
18. Gonzalez, E., Massari, U., Tamanini, I., "On the regularity of boundaries of sets minimizing perimeter with a volume constraint", to appear in *Indiana Univ. Math. J.*
19. Albano, S., Gonzalez, E., "Rotating drops", to appear.
20. Tamanini, I., "Boundaries of Caccioppoli sets with H lder-continuous normal vector", to appear.

## Mechanics of couple-stress fluid coatings

Allen M. Waxman

Biomedical Engineering & Instrumentation, National Institutes of Health  
Bldg. 13, Rm. 3W-13, Bethesda, MD 20205Abstract

We outline here, the formal development of a theory of viscoelastic surface fluids with bending resistance - their kinematics, dynamics, and rheology. It is relevant to the mechanics of fluid drops and jets coated by a thin layer of immiscible fluid with rather general rheology. This approach unifies the hydrodynamics of two-dimensional fluids with the mechanics of an elastic shell in the spirit of a Cosserat continuum.

Introduction

Recently, Waxman<sup>1,2</sup> has developed a formal theory of viscoelastic surface fluids in which bending resistance was incorporated in a purely phenomenological way. Motivation for this two-dimensional continuum theory stems from a variety of applications: interfacial stability, emulsion rheology, red blood cell deformability, and coated drop and jet mechanics. The mechanics of Newtonian surface fluids, accounting for the evolving surface geometry, was first considered by Scriven<sup>3</sup> (as detailed by Aris<sup>4</sup>). Extension to viscoelastic surface rheologies<sup>2</sup> and the inclusion of bending resistance<sup>1</sup> in the formalism then followed.

Bending rigidity arises from the finite thickness structure of the fluid coating, e.g. surface tension at the multiple interfaces of a compound drop or jet, a layer of normally oriented rod-like molecules such as those which form the lipid bilayer membrane of biological cells, and electrically charged or polarized monolayers at a fluid interface. Whatever the molecular origins of the bending rigidity may be, the associated bending moments (or couple-stresses) may be included in the mechanics of the surface phase in a purely phenomenological way. However, it would clearly be of interest to see if averaging techniques could indeed reduce the mechanics of finite thickness fluid coatings to that of couple-stress surface fluids. Such averaging methods underlie the development and success of elastic shell theory.<sup>5</sup> The direct approach which we have adopted is motivated by the notion of a Cosserat surface which has been exploited by the shell theorists for some time now.<sup>6</sup>

We view our model continuum as a two-dimensional viscoelastic fluid, isotropic in the surface, and associate with each material point on this surface a 'director' (viz. an arrow) oriented along the local normal with its center of mass located at the surface. Changes in surface shape imply a reorientation of these directors which manifests itself dynamically in two ways: reorientation corresponds to curvature changes which generate bending moments, in addition the rate of reorientation corresponds to an internal angular momentum of the surface phase over and above any surface vorticity. We shall see that the director dynamics enters into the surface equations of motion through an asymmetric surface stress tensor and a transverse shearing stress.

There are three distinct facets to the formulation of surface continuum mechanics and we shall try to outline here the important ideas and results associated with each: the kinematics of evolving surface geometries, the conservation laws governing the mechanics of surface continua, and the rheological equations of state governing the surface stress and moment tensors. Further details may be found elsewhere.<sup>1,2</sup>

Evolving surface geometries

As the surface phase is generally located at the interface between two bulk fluids, motions in the bulk lead to a distortion of the interface and hence, an evolution of the surface phase geometry. In order to discuss the mechanics of surface continua we must be able to track the surface as it moves through space. In addition, since various key geometrical quantities (e.g. metric and curvature tensors) enter into the dynamical equations, it is useful to derive evolution equations for these quantities. But first we must establish a coordinate system on the surface. Following Scriven<sup>3</sup>, we construct a set of 'fixed surface coordinates'  $u^{\alpha}$  ( $\alpha=1,2$ ) which label geometric points on the surface. As the surface evolves, these fixed coordinates move through space along the local normal to the surface; they are unaffected by any flow of the surface material tangential to the surface. Associated with these fixed coordinates are local tangent vectors  $\mathbf{g}_{\alpha}$  which then define a metric tensor for the surface  $a_{\alpha\beta} = \mathbf{g}_{\alpha} \cdot \mathbf{g}_{\beta}$ . A base vector triad at each point on the surface consists of these tangent vectors  $\mathbf{g}_{\alpha}$  and the local unit normal  $\mathbf{n}$  to the surface. Thus, for example, the velocity  $\mathbf{v}$  of the surface phase through space may be decomposed according to  $\mathbf{v} = v^{\alpha} \mathbf{g}_{\alpha} + v^{(n)} \mathbf{n}$ .

Here,  $v^a$  are the contravariant components of surface velocity and  $v^{(n)}$  (a scalar) is the component of velocity in the direction of the local normal.

Let the surface be embedded in an inertial space described by general coordinates  $x^i$  ( $i=1,2,3$ ) with corresponding base vectors  $g_i$ . The surface location is expressed by a relation between the fixed surface coordinates and the space coordinates:  $x^i = x^i(u^\alpha, t)$ . It can be shown that the evolution of the surface geometry through space is governed by the equation

$$\frac{\partial x^i}{\partial t} = v^{(n)} n^i, \quad (1)$$

where the local normal to the surface has been decomposed as  $n = n^i g_i$ . That is, the fixed surface coordinates move through space in the direction of the local normal and do so at a rate given by the normal component of velocity of the surface phase. One may also obtain evolution equations for the metric ( $a_{\alpha\beta}$ ) and curvature ( $b_{\alpha\beta}$ ) tensors associated with the fixed surface coordinate system.

$$\frac{\partial a_{\alpha\beta}}{\partial t} = -2 v^{(n)} b_{\alpha\beta} \quad (2)$$

$$\frac{\partial b_{\alpha\beta}}{\partial t} = v^{(n)}{}_{,\alpha\beta} - v^{(n)} b_{\alpha}{}^{\gamma} b_{\gamma\beta} \quad (3)$$

Equation (2) expresses the fact that a normal velocity distribution over a curved surface leads to a stretching of the fixed surface coordinates (viz. the radial expansion of a spherical surface). Equation (3) describes geometric shape changes via an evolving curvature. The first term, being the second covariant derivative of the normal velocity over the surface, leads to new geometric forms (a first derivative would only express a tilting of the surface). The second term in (3) incorporates the effects of a changing surface metric in the shape changes (e.g. an expanding sphere has a changing radius of curvature though it remains spherical). Simple evolution equations may also be derived for the tangent and normal vectors as well as the Christoffel symbols of the fixed surface coordinate system. As may be seen from equations (1) - (3), the evolution of the surface geometry may be decoupled from the tangential flow of the surface phase in so far as it depends only on the normal component of velocity. However, the normal velocity is implicitly coupled to the tangential flow through the equations of motion governing the surface phase.

#### Surface equations of motion

The surface equations of conservation of mass, momentum, and angular momentum may all be derived in the fixed surface coordinate system through the use of the Reynolds transport theorem generalized to surface flows. If we may neglect mass exchange between the surface phase and the neighboring bulk fluids on the timescales of interest, then the conservation of surface mass leads to the following continuity equation for the surface mass density  $\gamma$ :

$$\frac{\partial \gamma}{\partial t} + (\gamma v^a)_{,a} - 2H v^{(n)} \gamma = 0. \quad (4)$$

The first two terms in (4) resemble those found in the continuity equation for bulk fluids. The third term is associated with the stretching of the fixed surface coordinates (cf. eq.2)  $H = \frac{1}{2} b_{\alpha}{}^{\beta}$  being the local mean curvature of the surface. If we bring this term to the right-hand side of (4) it appears as a 'mass sink' ( $H < 0$  for a sphere) in that it represents a fixed amount of mass being spread over an ever increasing surface area (for  $H < 0$  and  $v^{(n)} > 0$ ).

The conservation of linear surface momentum leads us to the following equations of motion for the surface continuum. They may be thought of as dynamical boundary conditions which couple the adjacent bulk phases.

$$\gamma A^a = (f^a + \gamma G^a) + (T^{a\beta}{}_{,\beta} - g^{\beta} b_{\beta}{}^a) \quad (5a)$$

$$\gamma A^{(n)} = (f^{(n)} + \gamma G^{(n)}) + (T^{a\beta} b_{a\beta} - g^a{}_{,\alpha}) \quad (5b)$$

The right-hand sides of (5) closely resemble the equilibrium shell equations.<sup>5</sup> They represent the net tangential and normal forces acting on an element of surface. The surface stress tensor  $T^{a\beta}$  and transverse shear stress  $g^a$  will be discussed further below; they manifest themselves in local stress vectors (forces per unit length) acting on a curve bounding a small element of surface,  $T^{a\beta}$  leading to an in-plane stress,  $g^a$  corresponding to a stress normal to the surface along the bounding curve. These are usually termed internal stresses. External stresses act on a small element of surface and arise from body forces (e.g. gravitational and electrostatic forces) represented in (5) by  $G^a = G^a g_a + G^{(n)} g$ , and from the neighboring bulk fluids exerting normal and tangential stresses on the surface phase embodied in  $f^a = f^a g_a + f^{(n)} g$ . Expressions for  $f^a$  and  $f^{(n)}$  are given elsewhere.<sup>1,3,4</sup> On the left-hand sides

ORIGINAL PAGE IS  
OF POOR QUALITY

of (5) we have the tangential and normal components of surface acceleration given by

$$A^{\alpha} = \frac{\partial v^{\alpha}}{\partial t} + v^{\beta} v^{\alpha}_{,\beta} - 2 v^{(n)} v^{\beta} b_{\beta}^{\alpha} - v^{(n)} v^{(m)}_{,\beta} a^{\alpha\beta} \quad (6a)$$

$$A^{(n)} = \frac{\partial v^{(n)}}{\partial t} + 2 v^{\beta} v^{(n)}_{,\beta} + v^{\alpha} v^{\beta} b_{\alpha\beta}. \quad (6b)$$

In addition to the intrinsic derivatives of velocity in equation (6), there are terms resembling centripetal and Coriolis accelerations. They arise from the time varying base vectors associated with the evolving surface coordinate system, i.e. the evolving surface is a non-inertial reference frame. In equation (5b), we see how tangential stresses conspire with the curvature to generate a normal force (a generalization of the in-plane stress condition). Similarly, the transverse shear in (5a) generates a tangential force due to the curvature.

Considerations of angular momentum conservation lead to expressions for the transverse shear stress  $g^{\alpha}$  and the antisymmetric part of the surface stress tensor  $T^{(\alpha\beta)}$ . (We decompose  $T^{\alpha\beta}$  into a sum of symmetric and antisymmetric parts,  $T^{\alpha\beta} = T^{(\alpha\beta)} + T^{[\alpha\beta]}$ .) We find

$$g^{\alpha} = M^{\sigma\alpha}_{,\sigma} + \epsilon^{\alpha\sigma} (H_{\sigma} - \gamma \dot{\chi}_{\sigma}), \quad (7)$$

$$T^{[\alpha\beta]} = \frac{1}{2} (b_{\sigma}^{\alpha} M^{\sigma\beta} - b_{\sigma}^{\beta} M^{\sigma\alpha}) - \frac{1}{2} \epsilon^{\alpha\beta\gamma} H^{(n)}, \quad (8)$$

where  $M^{\sigma\alpha}$  is the surface moment (or couple-stress) tensor. In equations (7) and (8),  $\epsilon^{\alpha\beta}$  is the contravariant alternating tensor of the surface,  $H_{\sigma}$  and  $H^{(n)}$  are components of any externally imposed torque on the surface phase (e.g. magnetic couples), and  $\dot{\chi}_{\sigma}$  represents the tangential components of internal angular momentum associated with the tumbling motion of the directors. A complicated expression may be derived for  $\dot{\chi}_{\sigma}$ , but what is important is that it is determined entirely by the velocity field of the surface phase and the surface geometry (along with a presumed moment of inertia). Thus, it introduces no new unknowns into the equations of motion. In arriving at (8) we have assumed that each director spins about its local normal at a rate equal to one-half the local surface vorticity. That is, they are viscously coupled to their surface phase environments and hence, there is no normal component of internal angular momentum. We may use (7) and (8) to eliminate  $g^{\alpha}$  and  $T^{[\alpha\beta]}$  from the equations of motion (5). These equations simplify enormously for slow flows where we may neglect all terms associated with the inertia of the surface phase. It remains for us to give expressions for the symmetric surface stress and moment tensors  $T^{(\alpha\beta)}$  and  $M^{\sigma\alpha}$ .

#### Surface rheology

We concern ourselves here with surface fluids which are isotropic in the surface, and summarize the rheological laws discussed in detail by Waxman.<sup>1,2</sup> Allowing the surface phase to support an in-plane 'hydrostatic stress' in the absence of any motion, we write

$$T^{(\alpha\beta)} = -\pi a^{\alpha\beta} + \mathcal{J}^{\alpha\beta}. \quad (9)$$

Here,  $\pi$  is an isotropic surface pressure (or minus the net surface tension). It is related to the density, temperature, and chemistry of the surface phase and neighboring bulk phases via a thermodynamic equation of state. For incompressible surface continua,  $\pi$  becomes a dynamic variable to be solved for along with the surface velocity field. The symmetric tensor  $\mathcal{J}^{\alpha\beta}$  embodies the viscous and elastic components of stress. (An explicit dependence of  $\pi$  on  $\gamma$  already represents an area elasticity.)

The Newtonian surface fluid is the simplest example of a viscous surface phase. It is described by a linear relation between stress and rate-of-strain;

$$\mathcal{J}^{\alpha\beta} = C^{\alpha\beta\gamma\delta} S_{\gamma\delta} \quad (10a)$$

$$C^{\alpha\beta\gamma\delta} = \kappa a^{\alpha\beta} a^{\gamma\delta} + \epsilon (a^{\alpha\gamma} a^{\beta\delta} + a^{\alpha\delta} a^{\beta\gamma} - a^{\alpha\beta} a^{\gamma\delta}) \quad (10b)$$

with  $\kappa$  and  $\epsilon$  being coefficients of surface dilational and shear viscosity, respectively. The surface rate-of-strain is given by

$$S_{\gamma\delta} = \frac{1}{2} (v_{\gamma,\delta} + v_{\delta,\gamma}) - v^{(n)} b_{\gamma\delta}. \quad (11)$$

The first term represents the rate-of-deformation due to gradients in the tangential flow, the second term represents the geometric straining associated with the evolving surface

metric (cf. eq.2).

A simple viscoelastic surface fluid which exhibits both stress relaxation in a finite time and delayed elasticity is the 'corotational Jeffreys surface fluid' described L,

$$Y^{\alpha\beta} + \lambda \frac{D_s Y^{\alpha\beta}}{Dt} = C^{\alpha\beta\gamma\delta} \left\{ S_{\gamma\delta} + \omega \frac{D_s S_{\gamma\delta}}{Dt} \right\} \quad (12)$$

Here,  $C^{\alpha\beta\gamma\delta}$  is of the form (10b), and  $\lambda > \omega > 0$  are stress relaxation and strain retardation time constants. The time-derivative operator in (12) represents a rate-of-change as seen from a frame which is translating and corotating (but not codeforming) with an element of surface material. It is the surface analogue of the Jaumann time-derivative. Its derivation and properties are discussed in detail in the work of Waxman.<sup>2</sup> Equation (12) is a quasi-linear rheological law of the rate-type; nonlinear modifications of (12) have also been discussed.<sup>2</sup>

A simple law for the bending moment tensor is motivated by Hookean elasticity. It describes a surface capable of storing potential energy in bending and relates the moment tensor to a measure of bending strain in a linear fashion;

$$M^{\alpha\beta} = C^{\alpha\beta\gamma\delta} K_{\gamma\delta}. \quad (13)$$

Again,  $C^{\alpha\beta\gamma\delta}$  is of the form (10b) with  $K$  and  $\epsilon$  representing independent (positive) moduli of bending rigidity. An appropriate choice of bending strain for surface fluids is<sup>2</sup>

$$K_{\gamma\delta} = -(b_{\gamma\delta} - B_{\gamma\delta}), \quad \text{where} \quad (14a)$$

$$\frac{D_s B_{\gamma\delta}}{Dt} = 0, \quad B_{\gamma\delta} = \hat{b}_{\gamma\delta} \quad \text{at } t=0. \quad (14b)$$

That is,  $K_{\gamma\delta}$  measures the deviation of curvature from a comparison curvature  $B_{\gamma\delta}$  which represents an initial reference curvature  $\hat{b}_{\gamma\delta}$  evolved forward in time in a corotational way. Viscoelastic moment relations of the rate-type may be constructed from (13) through the use of the surface corotational time-derivative operator.

#### Conclusions

It is hoped that the dynamical formulation outlined here for couple-stress surface fluids will provide a useful approximation to the dynamics of thin fluid coatings in evolving geometries. Application to the mechanics of cell membranes is anticipated in the near future.

#### References

1. Waxman, A.M. "Dynamics of a Couple-Stress Fluid Membrane" (preprint), 1981.
2. Waxman, A.M. "A Corotational Time Derivative for Surface Tensors, Constitutive Relations and a New Measure of Bending Strain" J. Non-Newtonian Fluid Mech (in press), 1981.
3. Scriven, L.E. "Dynamics of a Fluid Interface" Chem. Eng. Sci., vol.12, p.98, 1960.
4. Aris, R. Vectors, Tensors, and the Basic Equations of Fluid Mechanics, Prentice-Hall, 1962.
5. Green, A.E. & Zerna, W. Theoretical Elasticity, 2nd edn, Oxford Univ. Press, 1968.
6. Green, A.E., Naghdi, P.M. & Wainwright, W.L. "A General Theory of a Cosserat Surface" Arch. Rat. Mech. Anal., vol.20, p.287, 1965.

COLLOQUIUM PARTICIPANTS

**Carol T. Alonso**

Lawrence Livermore National Laboratory,  
P.O. Box 808, L-18  
Livermore, CA 94550

**Osman A. Basaran**

University of Minnesota  
421 Washington Ave. S.E.  
Minneapolis, MN 55455

**Kenneth V. Beard**

University of Illinois  
Urbana, IL 61801

**Robert E. Benner**

University of Minnesota  
421 Washington Ave. S.E.  
Minneapolis, MN 55455

**Thomas P. Bernat**

Lawrence Livermore National Laboratory  
P.O. Box 5508  
Livermore, CA 94550

**John F. Brady**

Department of Chemical Engineering, 66-556  
Massachusetts Institute of Technology  
Cambridge, MA 02139

**Robert A. Brown**

Department of Chemical Engineering, 66-468  
Massachusetts Institute of Technology  
Cambridge, MA 02139

**Frédéric P. Brulois**

Department of Mathematics  
The University of Iowa  
Iowa City, IO 52240

**John R. Carruthers**

Hewlett-Packard Laboratories  
3500 Deer Creek Road  
Palo Alto, CA 94304

**G. S. P. Castle**

University of Western Ontario  
London, Ontario, CANADA N6A 5B9

**Georges Chahine**

Hydronautics, Inc.  
7210 Pindell School Road  
Laurel, MD 20707

**Chih-Wen Chen**

Lawrence Livermore National Laboratory  
L-482  
Livermore, CA 94550

**Robert J. L. Chimenti**

Exxon Research & Engineering Co.  
P.O. Box 45  
Linden, NJ 07036

**Ramon J. Cipriano**

Atmospheric Sciences Research Center  
State University of New York  
1400 Washington Ave.  
Albany, NY 12222

**Paul Concus**

Lawrence Berkeley Laboratory  
University of California  
Berkeley, CA 94720

**Arvid P. Croonquist**

Jet Propulsion Laboratory  
Pasadena, CA 91109

**Joseph M. Crowley**

Department of Electrical Engineering  
University of Illinois at Urbana-Champaign  
Urbana, IL 61801

**J. S. Darrozès**

Université Paris VI  
Campus Univ. Bat 502 Orsay  
Orsay, FRANCE 91405

**H. Ted Davis**

University of Minnesota  
421 Washington Ave. S. E.  
Minneapolis, MN 55455

**Dennis Dees**

University of California at Berkeley  
Berkeley, CA 94720

## COLLOQUIUM PARTICIPANTS (Continued)

**Richard L. DeWitt**  
NASA – Lewis Research Center  
21000 Brookpark Road  
Cleveland, OH 44135

**Robert Doremus**  
Rensselaer Polytechnic Institute  
Troy, NY 12181

**Daniel D. Elleman**  
Jet Propulsion Laboratory  
Pasadena, CA 91109

**Michele Emmer**  
University of Rome  
00100 Roma, ITALY

**I-an Feng**  
Jet Propulsion Laboratory  
Pasadena, CA 91109

**Robert Finn**  
Department of Mathematics  
Stanford University  
Stanford, CA 94305

**Bob Frazer**  
Jet Propulsion Laboratory  
Pasadena, CA 91109

**Jacob E. Fromm**  
IBM Research  
5600 Cottle Road  
San Jose, CA 95193

**Jack J. Fulwyler**  
Becton Dickinson FACS Systems  
490-B Lakeside Drive  
Sunnyvale, CA 94087

**Christopher Fung**  
University of Toronto  
60 St. George St.  
Toronto, Ontario, CANADA M5S 1A7

**Paul M. Gammell**  
Jet Propulsion Laboratory  
Pasadena, CA 91109

**Harvey P. Greenspan**  
Department of Mathematics  
Massachusetts Institute of Technology  
Cambridge, MA 02139

**Charles D. Hendricks**  
Lawrence Livermore National Laboratory  
P.O. Box 5508  
Livermore, CA 94550

**Leslie Hocking**  
University College  
London, UNITED KINGDOM WC1E 6BT

**Marylou Ingram**  
University of Miami  
1475 Northwest 12 Avenue  
Miami, FL 33101

**Nathan Jacobi**  
Jet Propulsion Laboratory  
Pasadena, CA 91109

**T. B. Jones**  
Xerox Corporation  
Bldg. 129 800 Phillips Rd.  
Webster, NY 14580

**James M. Kendall, Jr.**  
Jet Propulsion Laboratory  
Pasadena, CA 91109

**Kyckyon Kim**  
University of Illinois  
406 W. Green St.  
Urbana, IL 61801

**Joel Koplik**  
Schlumberger-Doll Research  
P.O. Box 307  
Ridgfield, CT 06877

**Nick Korevaar**  
University of Wisconsin  
610 Walnut St.  
Madison, WI 53706

**Kerry Landman**  
Southern Methodist University  
Dallas, TX 75275

## COLLOQUIUM PARTICIPANTS (Continued)

**W. E. Langlois**

IBM Research  
5600 Cottle Road  
San Jose, CA 95124

**John Latham**

University of Manchester  
P.O. Box 88  
Manchester, UNITED KINGDOM M60 1QD

**Chung Law**

Department of Mechanical Engineering  
Northwestern University  
Evanston, IL 60201

**Adeniyi Lawal**

Department of Chemical Engineering, 66-468  
Massachusetts Institute of Technology  
Cambridge, MA 02139

**Gary Leal**

California Institute of Technology  
Pasadena, CA 91125

**Norman R. Lebovitz**

University of Chicago  
5734 S. University Ave.  
Chicago, IL 60637

**Dennis H. Le Croisette**

Jet Propulsion Laboratory  
Pasadena, CA 91109

**C. P. Lee**

Jet Propulsion Laboratory  
Pasadena, CA 91109

**Mark C. Lee**

Jet Propulsion Laboratory  
Pasadena, CA 91109

**Yves Malmejac**

Laboratoire d'Etude de la Solidification  
Centre d'Etudes Nucleaires de Grenoble  
85 X - 38041 Grenoble Cedex, FRANCE

**Tom Marshall**

University of Mississippi  
403 S. 5th Street, #9  
Oxford, MS 38655

**Philip L. Marston**

Washington State University  
Pullman, WA 99164

**Edward C. Monahan**

Department of Meteorology  
Naval Postgraduate School  
Monterey, CA 93940

**J. R. Nix**

Los Alamos National Laboratory  
Los Alamos, NM 87545

**H. T. Ochs**

Illinois State Water Survey  
Box 5050  
Champaign, IL 61820

**Tim Oolman**

University of California, Berkeley  
Berkeley, CA 94705

**William Oran**

NASA Headquarters  
7th and Independence Avenues  
Washington, D.C. 20546

**Tadeusz W. Patzek**

University of Minnesota  
421 Washington Ave. S.E.  
Minneapolis, MN 55455

**Robert F. D. Perret**

Lawrence Livermore National Laboratory  
Livermore, CA 94550

**Roy Rasmussen**

University of California, Los Angeles  
450 Hilgard  
Los Angeles, CA 90024

**Carl J. Remenyik**

University of Tennessee  
Perkins Hall, Room 317  
Knoxville, TN 37916

**Won-Kyu Rhim**

Jet Propulsion Laboratory  
Pasadena, CA 91109

## COLLOQUIUM PARTICIPANTS (Continued)

**Carl E. Rosenkild**

Lawrence Livermore National Laboratory  
P.O. Box 808  
Livermore, CA 94550

**James Ross**

San Diego State University  
7732 Topaz Lake Ave.  
San Diego, CA 92119

**Gregory Ryskin**

California Institute of Technology  
Pasadena, CA 91106

**Billy R. Sanders**

Sandia Laboratory  
P.O. Box 969  
Livermore, CA 94550

**C. P. R. Saunders**

University of Manchester  
P.O. Box 88  
Manchester, UNITED KINGDOM M60 1QD

**E. Schatzman**

Observatoire de Nice BP 252  
Nice Cedex 06007, FRANCE

**L. E. Scriven**

University of Minnesota  
421 Washington Ave. S.E.  
Minneapolis, MN 55455

**Franklin Serduke**

Lawrence Livermore National Laboratory  
P.O. Box 808  
Livermore, CA 94550

**S. A. Sheffield**

Sandia Laboratories  
P.O. Box 5800  
Albuquerque, NM 87185

**Nicholas K. Sheridon**

Xerox Research Center  
3333 Coyote Hill Rd.  
Palo Alto, CA 94304

**Marvin Shinbrot**

Department of Mathematics  
University of Victoria  
P.O. Box 1700  
Victoria, B.C., CANADA V8W 2Y2

**Joseph I. Silk**

Department of Astronomy  
University of California, Berkeley  
Berkeley, CA 94720

**W. E. Slack**

National Research Council, Canada  
NAE, Bldg. U-61, Montreal Road  
Ottawa, Ontario, CANADA K1A 0R6

**R. S. Subramanian**

Clarkson College of Technology  
Potsdam, NY 13676

**W. J. Swiatecki**

Lawrence Berkeley Laboratory  
No. 1 Cyclotron Rd.  
Berkeley, CA 94720

**James Tegart**

Martin Marietta Corporation, Denver  
381 W. Davies Ave.  
Littleton, CO 80120

**Samuel Temkin**

Rutgers University  
New Brunswick, NJ 08903

**Lloyd M. Trefethen**

Tufts University  
Medford, MA 02155

**Eugene Trinh**

Jet Propulsion Laboratory  
Pasadena, CA 91109

**John Tsamopoulos**

Department of Chemical Engineering, 66-468  
Massachusetts Institute of Technology  
Cambridge, MA 02139

## COLLOQUIUM PARTICIPANTS (Continued)

**Jean-Marc Vanden-Broek**  
University of Wisconsin  
610 Walnut Street  
Madison, WI 53706

**J. P. B. Vreeburg**  
National Aerospace Laboratory NLR  
P.O. Box 90502  
1006 BM Amsterdam, THE NETHERLANDS

**Chris Walcek**  
University of California, Los Angeles  
405 Hilgard  
Los Angeles, CA 90024

**Taylor Wang**  
Jet Propulsion Laboratory  
Pasadena, CA 91109

**Allen Waxman**  
National Institutes of Health  
Bldg. 13, Room 3W-13  
Bethesda, MD 20205

**Morton S. Weiss**  
Lawrence Livermore National Laboratory  
P.O. Box 808, L-71  
Livermore, CA 94550

**Henry C. Wente**  
University of Toledo  
Toledo, OH 43606

**Forman Williams**  
Princeton University  
Princeton, NJ 08540

ALPHABETICAL INDEX OF AUTHORS

- Alonso, C. T., 268  
 Annamalai, P., 26  
 Avellan, François, 182
- Basaran, O. A., 322  
 Base, T. E., 120  
 Bastin, John, 350  
 Beard, K. V., 244, 247  
 Bernat, T., 96  
 Brulois, Frédéric Paul, 344
- Cammack, L., 203  
 Castle, G. S. P., 120  
 Cipriano, Ramon J., 255  
 Cole, Robert, 26  
 Croonquist, Arvid P., 31, 203  
 Crowley, Joseph M., 63
- Dandy, D., 358  
 Darrozès, J. S., 157  
 Davis, H. Ted, 129  
 Dominick, Sam, 187  
 Doremus, Robert H., 1  
 Dwyer, H. A., 358
- Elleman, D. D., 7, 31, 107  
 Emmer, Michele, 374  
 Erukashvily, Isaac M., 330  
 Erdoğan, M. Emin, 71
- Feng, I-an, 107  
 Finn, Robert, 280  
 Fromm, J., 54
- Gonzalez, Eduardo, 374  
 Goosby, S. G., 166  
 Greenspan, H. P., 303  
 Guerri, L., 175
- Hendricks, Charles D., 88, 94, 124  
 Hess, C. F., 112  
 Hocking, L. M., 315
- Inculet, I. I., 120
- Jacobi, Nathan, 31  
 Jones, T. B., 17
- Kendall, James M., 79  
 Kim, K., 96  
 Korevaar, N. J., 295
- Langley, D. S., 166  
 Latham, J., 227  
 Law, C. K., 39  
 Leal, L. G., 151  
 LeBlanc, J. M., 268  
 Lee, Mark C., 107  
 Ligneul, P., 157  
 LoPorto-Arione, S. E., 166  
 Lucca, G., 175
- Marston, P. L., 166  
 Meyyappan, M., 15  
 Mok, L., 96
- Nix, J. R., 260
- Ochs, Harry T., III, 247
- Patzek, T. W., 308  
 Prosperetti, A., 175  
 Pruppacher, H. R., 239
- Rasmussen, R., 239  
 Resch, François, 182  
 Rhim, W. K., 7  
 Ross, James, 350  
 Ryskin, G., 151
- Saffren, M., 7  
 Sanders, B. R., 358  
 Sarma, Gabbita Sundara Rama, 366  
 Schatzman, E., 222  
 Scriven, L. E., 308, 322  
 Shankar, N., 26  
 Sheffield, Stephen A., 112  
 Silk, Joseph, 214  
 Slack, W. E., 195  
 Stewart, Kris, 350  
 Strottman, D., 260  
 Subramanian, R. Shankar, 15, 26
- Tagg, R., 203  
 Tamanini, Italo, 374  
 Tegart, James, 187  
 Trinh, E. H., 143  
 Trolinger, J. D., 112
- Vanden-Broeck, Jean-Marc, 336
- Walcek, C., 239  
 Wang, P. K., 239

## ALPHABETICAL INDEX OF AUTHORS (Continued)

Wang, Taylor G , 31, 107, 143, 203

Waxman, Allen M , 380

Wente, Henry C., 286

Wilcox, William R , 15

Wilson, J R , 268

Young, Ainslie T , 107